

ABSTRACT

Preclinical Characterization of Small Molecule Compounds as Therapeutics for Cancer and Chagas' Disease: Tumor Vascular Disrupting Agents and Cysteine Protease Inhibitors

Samuel O. Odutola, Ph.D.

Mentor: Mary Lynn Trawick, Ph.D.

The purpose of this study was the pre-clinical exploration of specific small molecule compounds as vascular disrupting agents and cysteine protease inhibitors, targeted towards the development of therapeutic agents for the treatment of cancer and Chagas' disease. Disruption of tumor vasculature is a selective approach to cancer therapy that results in tremendous tumor necrosis while leaving normal blood vessels relatively unaffected. The first part of this study describes an examination of the vascular disrupting ability and the mechanism of action of the indole-based tubulin-binding compound, OXi8006, and its water-soluble phosphate prodrug OXi8007. Treatment of rapidly proliferating human umbilical vein endothelial cells, used as a model for the tumor vasculature, with OXi8006 caused a dramatic disruption of the microtubule network and subsequent increase in cell contractility as observed from increased actin stress fiber and focal adhesion formation. The induced signaling cascade included increased phosphorylation of myosin light chain and focal adhesion kinase, and activation

of the LIM kinase-cofilin pathway. It was demonstrated that these events were mediated by the intracellular G protein switch RhoA and its downstream target RhoA kinase, via the microtubule-binding guanine nucleotide exchange factor GEF-H1.

A separate research project focused on the evaluation of synthetic thiosemicarbazone inhibitors of cysteine proteases as anticancer agents. Cathepsins L, K, and B are cysteine proteases that are implicated in tumor growth and metastasis. In addition, the cysteine protease cruzain, an essential enzyme in the life cycle of the parasite *Trypanosoma cruzi*, is a validated therapeutic target for Chagas' disease. In this project, preliminary in vitro analyses of a group of synthetic thiosemicarbazones were carried out in order to characterize their potency and mode of inhibition against these enzymes. A number of compounds were found to be potent inhibitors of each enzyme. Results demonstrated that the most potent inhibitors in this library have slow binding, slowly reversible, competitive mechanisms of inhibition. Furthermore, results suggested that the best thiosemicarbazone inhibitors form a reversible covalent bond with each enzyme. Cathepsin L inhibitors were able to delay cell migration and cell invasion of the MDA-MB-231 breast cancer cell line in a concentration dependent manner.

Preclinical Characterization of Small Molecule Compounds as Therapeutics for Cancer and Chagas'
Disease: Tumor Vascular Disrupting Agents and Cysteine Protease Inhibitors

by

Samuel O. Odutola, B.A.

A Dissertation

Approved by the Institute of Biomedical Studies

Robert R. Kane, Ph.D., Director

Submitted to the Graduate Faculty of
Baylor University in Partial Fulfillment of the
Requirements for the Degree
of
Doctor of Philosophy

Approved by the Dissertation Committee

Mary Lynn Trawick, Ph.D., Chairperson

Robert R. Kane, Ph.D.

Chris Kearney, Ph.D.

Myeongwoo Lee, Ph.D.

Kevin G. Pinney, Ph.D.

Accepted by the Graduate School
May 2017

J. Larry Lyon, Ph.D., Dean

Copyright © 2017 by Samuel O. Odutola

All rights reserved

TABLE OF CONTENTS

LIST OF FIGURES	viii
LIST OF TABLES.....	xix
LIST OF ABBREVIATIONS.....	xxii
ACKNOWLEDGMENTS	xxxii
ATTRIBUTIONS	xxxv
CHAPTER ONE	1
Introduction.....	1
Background and Significance	1
Small Molecule Drug Discovery in Cancer	2
Small Molecule Drug Discovery in Parasitic Diseases.....	7
Statement of Purpose	9
CHAPTER TWO	13
Introduction to Vascular Targeting Agents	13
Tumor Vasculature.....	13
Approaches to Anti-Vascular Tumor Therapy	17
Tumor Angiogenesis.....	18
Angiogenesis Inhibiting Agents.....	20
Vascular Disrupting Agents.....	24
The Microtubule System.....	32
In Vitro Models for VDA Evaluation: HUVECs and MDA-MB-231.....	38
CHAPTER THREE	42
The Vascular Disrupting activity of OXi8006 in Endothelial Cells and Its Phosphate Prodrug OXi8007 in Breast Tumor Xenografts.....	42
Abstract.....	43
Introduction.....	45
Materials and Methods.....	48
Results.....	55
Discussion.....	77

Contributions of Individual Co-Authors	84
CHAPTER FOUR.....	87
Evaluation of Mechanism of Action of VDAs in Vitro: The Roles of GEFs and Various Signaling Proteins	87
Rho Family GTPases	89
ROCK	92
Focal Adhesion Kinase (FAK).....	95
GEF-H1	96
Materials and Methods.....	98
Results and Discussion	107
Summary	121
CHAPTER FIVE	126
Introduction to Cysteine Proteases	126
Papain-Like Cysteine Proteases: Sequence, Structure, Mechanism, Expression, Substrate Specificity, and Physiological Functions	127
Substrate-Binding Sites.....	134
Cysteine Protease Intracellular and Tissue Distribution.....	142
Role of Cysteine Proteases in Pathological Conditions.....	146
Introduction to Enzyme Kinetics	150
Experimental Design for Analysis of Cysteine Proteases.....	169
CHAPTER SIX.....	172
Chagas' Disease: Epidemiology, Pathology and Treatment.....	172
Roles of Parasitic Proteases in Mammals	172
Chagas Disease; History, Epidemiology and Pathology,.....	173
Chagas Disease; Symptoms and Diagnosis	174
Trypanosoma cruzi.....	182
Current Therapeutics for Chagas' Disease	190
Potential Targets for Chagas Disease Drug Development.....	192
Cruzain: A Validated Target for Drug Development	199
Biological Roles of Cruzain in T. cruzi Pathology	200
Structure of Cruzain.....	201
Cruzain Substrate Specificity and Mechanism of Action	205
Cruzain Inhibitors	207

CHAPTER SEVEN	212
Evaluation of Thiosemicarbazone Inhibitors of Cruzain as Therapeutics for Chagas' Disease	212
Material and Methods for the Biological Evaluation of Thiosemicarbazones Derivatives as Inhibitors of Cruzain	212
Experimental Section	218
Results and Discussion	225
Summary	252
CHAPTER EIGHT	255
Inhibition of Cysteine Cathepsins by Thiosemicarbazone Compounds	255
Materials and Methods for the Evaluation of Thiosemicarbazone Compounds as Cysteine Protease Inhibitors	255
Experimental Section	265
Results and Discussion	275
Summary	307
CHAPTER NINE.....	309
Conclusions.....	309
Vascular Disrupting Agents.....	309
Cysteine Protease Inhibitors	311
APPENDIX A.....	317
Immunofluorescence Microscopy Experiments	317
APPENDIX B	327
Wound Assays	327
REFERENCES	331

LIST OF FIGURES

Figure 1.1. A summary of the research presented in this dissertation	3
Figure 2.1. Normal vasculature (A and C) compared to tumor vasculature (B and D)	16
Figure 2.2. Comparison between AIAs and VDAs in effects on tumor vasculature	18
Figure 2.3. Summary of signaling events leading to up-regulation of angiogenesis in tumor vasculature	20
Figure 2.4. AIAs that have advanced through some stages of clinical development	22
Figure 2.5. Various classes of AIAs based on their mechanism of inhibition	23
Figure 2.6. VDA mechanism of action on pre-established tumor blood vessels	26
Figure 2.7. Tubulin binding sites of microtubule binding agents	30
Figure 2.8. Selection of small molecule VDAs investigated in clinical trials	33
Figure 2.9. Microtubule structure and dynamics	36
Figure 2.10. Structure of tubulin heterodimer at 3.5 Å resolution, in complex with colchicine and with the stathmin-like domain (SLD) of RB3 (PDB: 1SAO)	36
Figure 2.11. Binding of colchicine to tubulin heterodimers causes a conformational change on protofilaments	38
Figure 2.12. Phase contrast image of HUVECs	39

Figure 2.13. Phase contrast image showing confluent monolayer of HUVECs	40
Figure 2.14. MDA-MB-231 cells in culture (ATCC website)	41
Figure 3.1. Small molecule inhibitors of tubulin assembly: vascular disrupting agent CA4 and its phosphate prodrug CA4P; OXi8006 and its phosphate prodrug OXi8007	47
Figure 3.2. Representative confocal images of the morphological effects of OXi8006 treatment on activated HUVECs	57
Figure 3.3. Representative confocal images of a concentration dependent increase in microtubule disruption and stress fiber formation with OXi8006 treatment of activated endothelial cells	58
Figure 3.4 Representative images showing that activated endothelial cells exposed to a high concentration of OXi8006 demonstrate retraction from the gelatin substratum, contraction and rounding up of the cells	59
Figure 3.5. Representative confocal images demonstrating the morphological effects of OXi8007 treatment on activated HUVECs	60
Figure 3.6. OXi8006 treatment of activated endothelial cells results in increased MLC and FAK phosphorylation	63
Figure 3.7. Representative confocal images of a concentration dependent increase in actin stress fiber and focal adhesion formation accompanied by an increase in focal adhesion kinase (FAK) phosphorylation (pY397) with OXi8006 treatment of activated endothelial cells	64
Figure 3.8. OXi8006 induced increase in stress fiber formation and phosphorylation of FAK (pY397), but not microtubule disruption, is mediated by RhoA/RhoA kinase	65

Figure 3.9. Representative confocal images demonstrating that the increase in phosphorylation of myosin light chain (T18/S19) observed upon OXi8006 treatment of activated endothelial cells is mediated by RhoA and its downstream effector RhoA kinase (ROCK)	66
Figure 3.10. The cytotoxicity of tubulin binding VDAs and doxorubicin against nearly confluent HUVECs to model the low proliferating baseline of normal mature endothelium	68
Figure 3.11. OXi8006 and OXi8007 induced G2/M arrest in HUVECs. (A-C) Representative DNA histograms and (D, E) bar graphs show concentration dependent increase in the fraction of cells arrested at the G2/M phase upon OXi8006 and OXi8007 treatment	69
Figure 3.12. OXi8006 treatment disrupts pre-established endothelial capillary-like networks	72
Figure 3.13. OXi8007 treatment disrupts pre-established endothelial capillary-like networks	72
Figure 3.14. Dynamic BLI assessment of dose escalation response to OXi8007	74
Figure 3.15. MDA-MB-231-luc breast tumor response to OXi8007 treatment assessed by BLI	75
Figure 3.16. Histological evaluation of MDA-MB-231-luc tumor xenografts after OXi8007 administration confirmed vascular shutdown	76
Figure 3.17. Proposed VDA mechanism of action of OXi8007 in activated endothelial cells	83
Figure 4.1. Proposed VDA mechanism of action of OXi8007 in activated endothelial cells (modified from Figure 3.17)	88
Figure 4.2. Crystal Structure of Human RhoA (PDB ID: 1A2B)	93

Figure 4.3. Activation/Deactivation cycle of RhoGTPases	93
Figure 4.4. Downstream effectors of RhoA	94
Figure 4.5. Various signaling cascades initiated by activated ROCK	95
Figure 4.6. Representation of GEF-H1 Structure	97
Figure 4.7. Colocalization analysis of microtubules and GEFH1 in HUVECS	108
Figure 4.8. GEF-H1 RNAi qPCR	109
Figure 4.9. GEFH1 RNAi results in reduced protein expression in HUVECs	111
Figure 4.10. Effects of GEFH1 knockdown on OXi8006 treated HUVECs	112
Figure 4.11. Western blot experiment showing effect of GEFH1 knockdown on OXi8006 induced FAK phosphorylation	113
Figure 4.12. HUVECs cells stained with RGNEF	114
Figure 4.13. Representative confocal images showing p190 RhoGEF (RGNEF) depletion (via RNAi) has minimal effect on OXi8006 induced increase in HUVEC contractility	116
Figure 4.14. Representative confocal images showing effect of OXi8006 treatment on cofilin phosphorylation in HUVECs	117
Figure 4.15: Time course experiment showing effect of OXi8006 (1 μ M) on cofilin phosphorylation in HUVECs	118
Figure 4.16. Effect of LIM Kinase inhibition on OXi8006 treated HUVECs	120

Figure 4.17. Representative images of MDA-MB-231 cell monolayers showing effect of various concentrations of OXi8006 on wound closure over time	122
Figure 4.18. Bar graphs showing MDA-MB-231 wound closure over time at different OXi8006 concentrations	122
Figure 4.19. Graphical representation of rates of MDA-MB-231 wound closure due to different OXi8006 concentrations	123
Figure 4.20. Quantification of fluorescence microscopy images showing induction of annexin V binding due to various treatments (**** $p < 0.0001$, ** $p < 0.001$)	123
Figure 5.1. List of human cysteine cathepsin proteases	128
Figure 5.2. Amino acid sequence alignment of human lysosomal cathepsins and related parasite cysteine proteases	131
Figure 5.3. Amino acid Sequence of Cathepsin L. Legend: Blue, Heavy Chain; Red, Light Chain; Catalytic Residues, Green	132
Figure 5.4. Amino Acid Sequence of Cathepsin K (PDB ID: 3KX1)	132
Figure 5.5. Amino acid Sequence of Cathepsin B. Legend: Green, signal peptide; Red, pro-peptide; Pink, light chain of mature enzyme; Blue, Heavy chain of mature enzyme	132
Figure 5.6. Typical cysteine cathepsin (cathepsin L) fold viewed along the two-domain interface and the active site at the top	133
Figure 5.7. Typical procathepsin fold (1cj)	134
Figure 5.8. Diagrammatic representation of peptide substrate interaction with the active site pockets of a cysteine protease	135
Figure 5.9. Crystal Structure of Human Cathepsin L (PDB ID: 1ICF) [279]	137

Figure 5.10. Crystal Structure of Human Cathepsin K (PDB: 3KX1) [270]	138
Figure 5.11. Crystal Structure of Human Cathepsin B (PDB: 1HUC) [267]	139
Figure 5.12. Catalytic mechanism of cysteine proteases	144
Figure 5.13. Stabilization of the oxyanion generated by the cysteine protease catalytic reaction	145
Figure 5.14. Autoactivation of a cysteine protease due to low pH	147
Figure 5.15. Transactivation of a cysteine protease in acidic conditions	148
Figure 5.16. Diagrammatic representation of the tumor metastatic process	150
Figure 5.17. Simplified enzyme catalyzed reaction	150
Figure 5.18. Typical Michaelis-Menten Plot	152
Figure 5.19. Competitive inhibitor reaction scheme	154
Figure 5.20. Graphical representation of effect of competitive inhibitor on Michaelis-Menten kinetics	155
Figure 5.21. Uncompetitive inhibitor reaction scheme	156
Figure 5.22. Graphical representation of effect of uncompetitive inhibitor on Michaelis-Menten kinetics	156
Figure 5.23. Noncompetitive inhibitor reaction scheme	157
Figure 5.24. Effects of reversible inhibitors on enzyme kinetics	158

Figure 5.25. IC ₅₀ sigmoidal dose response curve	159
Figure 5.26. Reaction Progress Curves showing Uninhibited (black) and Inhibited Sample with a Slow Binding Inhibitor (red)	162
Figure 5.27. Determination of Inhibition Modality for Slow-Binding Inhibitors	164
Figure 5.28. Mechanisms for slow binding inhibition of enzymatic reactions	165
Figure 5.29. Graphical representation of slow binding reversible inhibition	166
Figure 5.30. Graphical representation of enzyme isomerization slow binding inhibition mechanism	168
Figure 5.31. Graphical Representation of the Morrison Equation	168
Figure 5.32. Experimental flowchart for analyzing compound inhibition of cysteine proteases	170
Figure 5.33: Structural scaffolds of thiosemicarbazone compounds tested as cysteine protease inhibitors	171
Figure 6.1. Projected worldwide number of <i>T. cruzi</i> infections	175
Figure 6.2. Chagas' disease progression	176
Figure 6.3. Artistic Rendition of Romãña's Sign	177
Figure 6.4. Suggested mechanisms of cardiac tissue destruction as a result of chronic Chagas' disease infection	181
Figure 6.5. Giemsa-stained <i>T. cruzi</i> trypomastigote in a thin-blood smear	183

Figure 6.6. Phylogram showing origin of <i>T. cruzi</i> clade	185
Figure 6.7. Geographic Distribution of <i>T. cruzi</i> strains across Central and South America	186
Figure 6.8. Life cycle and transmission of <i>T. cruzi</i>	187
Figure 6.9. Surface interactions between <i>T. cruzi</i> trypomastigote and Host cell	189
Figure 6.10: Models of <i>T. cruzi</i> internalization	191
Figure 6.11: Chemical structures of Nifurtimox and Benznidazole	191
Figure 6.12. Mechanism of dihydrofolate reductase in the biosynthesis thymidine monophosphate	193
Figure 6.13. Structure of methotrexate	194
Figure 6.14. Simplified ergosterol biosynthesis in fungi and protozoa	197
Figure 6.15. Azole ergosterol biosynthesis inhibitors that inhibit CYP51	198
Figure 6.16. Amino Acid Sequence of Pre-procruzain	202
Figure 6.17. Amino Acid Sequence of Cruzain (PDB:1ME3)	203
Figure 6.18. Crystal Structure of Cruzain (PDB:1ME3)	204
Figure 6.19. Cruzain active site with labelled subsites	205
Figure 6.20. Selection of potential antichagasic cruzain inhibitors	211

Figure 7.1. Fluorometric enzyme assay reaction	226
Figure 7.2. Fluorescence values of AMC plotted over time	227
Figure 7.3. AMC Calibration Curve	228
Figure 7.4. Catalytic activity of cruzain over time with varying substrate concentrations	229
Figure 7.5. Dependence of cruzain activity on substrate concentration. The curve was fit to the Michaelis-Menten equation via non-linear regression using GraphPad Prism 5.0 software	230
Figure 7.6. Potent thiosemicarbazone inhibitors of cruzain	238
Figure 7.7. Cruzain progress curves with varying concentrations of compound 23	239
Figure 7.8. Graphical representation of relationship between k_{obs} and 23	241
Figure 7.9. Cruzain progress curves with varying substrate concentration and 1 μ M of compound 19	242
Figure 7.10. Graphical representation of relationship between k_{obs} and substrate concentration when cruzain is inhibited with compound 19	243
Figure 7.11. Effect of increasing pre-incubation times on IC_{50} of compound 25 against cruzain	245
Figure 7.12. Graphical representation of Morrison Analysis of tight binding of 23 to cruzain	247
Figure 7.13. Graphical representation of Morrison Analysis of tight binding of 28 to cruzain	247

Figure 7.14. Reversibility curves for cruzain incubated with compound 14	248
Figure 7.15. First 500 s of reversibility reaction showing rapid recovery of cruzain activity	249
Figure 7.16. Molecular docking of compound 28 with cruzain (1ME3)	252
Figure 7.17. Compound 28 docked at the active site of cruzain with thiosemicarbazone carbon to Cys-25 sulfur distance labelled	253
Figure 7.18. Molecular docking of compound 24 with cruzain (1ME3)	254
Figure 8.1. Structure of Compound 46 , a phosphate analogue of compound 2	270
Figure 8.2. Invasion and Migration Assay Sample Fields	274
Figure 8.3. Cathepsin L/K catalyzed hydrolysis of Z-FR-AMC	277
Figure 8.4. Cathepsin B catalyzed hydrolysis of Z-RR-AMC	277
Figure 8.5. Graphical representation of the kinetic parameters for cathepsin L against Z-FR-AMC synthetic fluoregenic substrate	279
Figure 8.6. Graphical representation of the kinetic parameters for cathepsin K against Z-FR-AMC synthetic fluoregenic substrate	280
Figure 8.7: Potent thiosemicarbazone inhibitors ($IC_{50} < 100$ nM) of cathepsin L	290
Figure 8.8. Potent thiosemicarbazone inhibitors ($IC_{50} < 100$ nM) of cathepsin K	291
Figure 8.9: Thiosemicarbazone compounds selective for cathepsin L and/or K	292
Figure 8.12. Graphical representation of the relationship between k_{obs} and [22]	294

Figure 8.13. Graphical representation of the relationship between k_{obs} and [28]	295
Figure 8.14. Graphical representation of Morrison analysis of tight binding of compound 7 to cathepsin L	297
Figure 8.15. Conversion of compound 46 to compound 2	298
Figure 8.16. Alkaline phosphatase enzymatic assay	299
Figure 8.17. HPLC Chromatogram of Compounds 2 and 46	300
Figure 8.18. HPLC chromatogram of alkaline phosphatase treated compound 46	300
Figure 8.19. HPLC chromatogram of alkaline phosphatase treated compound 46 in 2% DMSO	301
Figure 8.20. Effect of alkaline phosphatase activity on cathepsin L inhibition by 46	302
Figure 8.21. Caspase 3 Inhibition Assay	303
Figure 8.22. MDA-MB-231 invasion and migration data for 10 and 25 μM of thiosemicarbazone compounds and E-64	306
Figure 8.23. Reversibility curves for cathepsin L incubated with compound 22 . Inset shows clearer view of slow recovery of enzyme activity over time	306
Figure 9.1. Overview of roles of cysteine cathepsins in invasion and metastasis.	314
Figure 9.2. Proposed mechanism for thiosemicarbazone inhibition of cysteine proteases	315

LIST OF TABLES

Table 3.1. OXi8006 and OXi8007 inhibited the growth of activated human umbilical vein endothelial cells (HUVECs) and human breast cancer cells (MDA-MB-231)	69
Table 4.1. QPCR cycling parameters	102
Table 5.1: Examples of Reversible Inhibitors in Clinical Use	153
Table 7.1A. Preparation of inhibitor stock solutions in pure DMSO	215
Table 7.1B. Preparation of inhibitor stock solutions in 35% DMSO	216
Table 7.2. Preparation of Cruzain Assay Buffer	217
Table 7.3. Preparation of Cruzain Stock Solution	217
Table 7.4. Dilution table for varying substrate concentrations (in 2.5% DMSO and water)	219
Table 7.6. IC ₅₀ values of benzophenone thiosemicarbazone compounds against cruzain	232
Table 7.7. IC ₅₀ values of thiochromanone thiosemicarbazone compounds against cruzain	233
Table 7.8. IC ₅₀ values of benzoyl benzophenone thiosemicarbazone compounds against cruzain	234
Table 7.9. IC ₅₀ values of benzophenone (with alkyl linkers) thiosemicarbazone compounds against cruzain	236

Table 7.10. Calculated Kinetic Parameters for Cruzain Progress Curves with compound 23	240
Table 7.11. Kinetic parameters for Cruzain substrate progress curves with compound 19	242
Table 7.12. Effect of Pre-incubation Time on IC ₅₀ Values with various compounds	243
Table 7.13. IC ₅₀ and K _i ^{app} values of potent thiosemicarbazone inhibitors of cruzain (5 minute preincubation)	246
Table 8.1. Preparation of Cathepsin L Assay Buffer	259
Table 8.2. Preparation of Cathepsin L Secondary Stock Solution	259
Table 8.3. Preparation of Cathepsin K Assay Buffer	262
Table 8.4. Preparation of Cathepsin K Secondary Stock Solution	262
Table 8.5. Preparation of cathepsin B assay buffer	264
Table 8.6. Preparation of cathepsin B secondary stock solutions	265
Table 8.7. IC ₅₀ values of benzophenone thiosemicarbazone compounds against cysteine cathepsins	284
Table 8.8. IC ₅₀ values of thiochromanone thiosemicarbazone compounds against cysteine cathepsins	285
Table 8.9. IC ₅₀ values of benzoyl benzophenone thiosemicarbazone compounds against cysteine cathepsins	286

Table 8.10. IC ₅₀ values of benzophenone thiosemicarbazone compounds (with alkyl chain linkers) against cysteine cathepsins	288
Table 8.11. Kinetic parameters obtained from non-linear regression analysis of progress curves of cathepsin L inhibited by compound 22	294
Table 8.12. K _I values of a selection of thiosemicarbazone inhibitors of cathepsin L	296

LIST OF ABBREVIATIONS

[E]	Enzyme concentration
[E _T]	Total enzyme concentration
[I]	Inhibitor concentration
[S]	Substrate concentration
°C	Degrees Celsius
3-D	3-Dimensional
A	Alanine
AA	Amino acid
Abz	3-Aminobenzoic Acid
AIA	Angiogenesis Inhibiting Agent
Ala	Alanine
AMC	7-Amino-4-Methylcoumarin
ANOVA	Analysis of Variance
ANG	Angiopoietin
Arg	Arginine
Asn	Asparagine
Asp	Aspartate
ATCC	American Type Culture Collection
ATG	Start codon
B2R	Bradykinin Receptor

bFGF	Basic Fibroblast Growth Factor
BLI	Bioluminescence Imaging
BM	Basement Membrane
BZ	Benznidazole
C	Cysteine
C-	Carboxy Terminal
C=O	Carbonyl, Carbonyl Bond
CA4	Combretastatin A 4
CA4-P	Combretastatin A 4 Phosphate
Cbz	Carboxybenzyl
Cdc42	Cell Division Control Protein 42
CDC	Center for Disease Control
C-N	Carbon-Nitrogen Angle
CYP51	Sterol 14 α Demethylase Cytochrome P450
Cys	Cysteine
D	Aspartate
DAPI	4',6-diamidino-2-phenylindole
DCE-MRI	Dynamic Contrast Enhanced Magnetic Resonance Imaging
DHFR	Dihydrofolate Receptor
DMEM	Dulbecco's Modified Eagle's Medium
DMSO	Dimethyl sulfoxide
DMXAA	5,6-Dimethylxanthenone-4-acetic Acid
DNA	Deoxyribonucleic Acid

DTT	Dithiothreitol
E	Glutamate
E	Enzyme
E-64	Irreversible Inhibitor Of Cysteine Proteases
EC	Enzyme Classification
EC	Endothelial Cell
ECM	Extracellular Matrix
EDTA	Ethylenediaminetetraacetic acid
EGF	Epidermal Growth Factor
EGFR	Epidermal Growth Factor Receptor
ELISA	Enzyme-Linked Immunosorbent Assay
ERK	Extracellular-Signal-Regulated Kinases
ER-	Estrogen Receptor
ES	Enzyme-Substrate Complex
F	Phenylalanine
FAA	Flavone Acetic Acid
FAK	Focal Adhesion Kinase
FBS	Fetal Bovine Serum
FBDD	Fragment Based Drug Discovery
FDA	United States Food And Drug Administration
FITC	Fluorescein Isothiocyanate
G	Glycine
g	Gram

GAP	GTPase Activating Protein
GDI	Guanine Nucleotide Dissociation Inhibitor
GDP	Guanine diphosphate
GEF	Guanine Nucleotide Exchange Factors
Gln	Glutamine
Glu	Glutamate
Gly	Glycine
GTP	Guanine Triphosphate
H	Histidine
h	Hour
HER2/neu	Human Epidermal Growth Factor Receptor 2
HIF-1 α	Hypoxia Inducible Factor 1 alpha
His	Histidine
HIV	Human Immunodeficiency Virus
HPV	Human Papillomavirus
HUVEC	Human Umbilical Vein Endothelial Cells
HTS	High Throughput Screening
I	Isoleucine
I	Inhibitor
IC ₅₀	Half Maximal Inhibitory Concentration
IFA	Indirect Immunofluorescence Assay
IGF-1	Insulin-Like Growth Factor 1

IL-8	Interleukin 8
IL-1 α	Interleukin 1 Alpha
Ile	Isoleucine
JNK	C-Jun N-Terminal Kinases
K	Lysine
kDa	Kilodalton
K_I	Inhibition Constant
K_I^{app}	Apparent Inhibition Constant
k_{cat}	Enzyme Turnover Number
K_d	Dissociation constant
K_M	Michaelis-Menten Constant
k_{obs}	Rate Constant For Conversion From The Initial Velocity Phase To The Steady State Velocity Phase.
k_{off}	Rate Of Dissociation
k_{on}	Rate Of Association
l	Liter
Leu	Leucine
Lys	Lysine
M	Methionine
M	Molar
MAPK	Mitogen-Activated Protein Kinases
MES	2-(N-morpholino)ethanesulfonic acid
Met	Methionine

MHC II	Major Histocompatibility Complex II
min	Minute
MLC	Myosin Light Chain
mM	Millimolar
MMP	Matrix Metalloprotease
MOPS	3-(N-morpholino)propanesulfonic acid
MP/MLCP	Myosin Light Chain Phosphatase
mRNA	Messenger Ribonucleic Acid
MW	Molecular Weight
N	Asparagine
N-	Amino
NaCl	Sodium Chloride
NADPH	Nicotinamide Adenine Dinucleotide Phosphate (Reduced)
NaOAc	Sodium Acetate Buffer
NaOH	Sodium Hydroxide
NF- κ B	Nuclear Factor Kappa-Light-Chain-Enhancer Of Activated B Cells
NH	Amino Group
nM	Nanomolar
NMII	Non muscle Myosin II
NO ₂	Nitrogen Dioxide
Nx	Nifurtimox
OXi8006	2-(3'-hydroxy-4'-methoxyphenyl)-3-(3'',4'',5''-trimethoxybenzoyl)-6-methoxyindole

OXi8007	2-(3'-disodium phosphate-4'-methoxyphenyl)-3-(3'',4'',5''-trimethoxybenzoyl)-6-methoxyindole
P	Proline
p38	P38 MAPK
p53	Tumor Protein 53
PAGE	Polyacrylamide gel electrophoresis
PBS	Phosphate Buffered Saline
PCR	Polymerase Chain Reaction
PDB	Protein Data Bank
PDGF	Platelet-Derived Growth Factor
PET	Positron emission Tomography
pH	Measure Of Hydrogen Ion Concentration
Phe	Phenylalanine
PI	Propidium Iodide
PI3K	Phosphatidylinositol 3-Kinase
PIP5-K	Phosphatidylinositol 4-Phosphate-5 Kinase
pM	Picomolar
pMLC	Phosphorylated Myosin Light Chain
PR-	Progesterone Receptor
Pro	Proline
PKN	Protein Kinase N
Q	Glutamine
QSAR	Quantitative Structure Activity Relationship

R	Arginine
r^2	Coefficient Of Determination
Rac	G-Protein
Ras	G-Protein
Rho	G-Protein
RNAi	RNA interference
ROCK	Rho Associated Coiled Coil Kinase
RTK	Receptor Tyrosine Kinases
S	Serine
S	Substrate
s	Second
SCID	Severe Combined Immunodeficiency
SDS	Sodium Dodecyl Sulfate
SE	Standard Error
sec	Second
Ser	Serine
siRNA	Small Interfering RNA
Src	Proto-Oncogene Tyrosine-Protein Kinase
SRB	Sulforhodamine B
SRF	Serum Response Factor
<i>T. cruzi</i>	Trypanosoma Cruzi
TGF- β	Transforming Growth Factor Beta
Thr	Threonine

TKI	Tyrosine Kinase Inhibitor
TM	Trademark
TNBC	Triple Negative Breast Cancer
TNF	Tumor Necrosis Factors
TNF- α	Tumor Necrosis Factor-Alpha
Trp	Tryptophan
TSC	Thiosemicarbazone
TUB	Tubulin
Tyr	Tyrosine
USA	United States of America
V	Valine
v	Velocity
Val	Valine
VDA	Vascular Disrupting Agent
VEGF	Vascular Endothelial Growth Factor
VEGFR	Vascular Endothelial Growth Factor Receptor
V_{MAX}	Maximum Velocity
v_{max}	Catalytic Rate Of An Enzyme Without The Presence Of An Inhibitor (Lowest Concentration, IC ₅₀ Determination)
v_{min}	Catalytic Rate Of An Enzyme With The Presence Of An Inhibitor (Highest Concentration, IC ₅₀ Determination)
v_o	Initial Velocity
v_s	Steady-State Velocity

W	Tryptophan
WHO	World Health Organization
Y	Tyrosine
Y	Fractional Activity
Y-27632	(R)-(+)-trans-4-(1-Aminoethyl)-N-(4-Pyridyl)cyclohexanecarboxamide dihydrochloride
Z-FR-AMC	N-Carbobenzoxy-L-Phenylalanyl-L-arginine Amide, Hydrochloride
Z-RR-AMC	N-Carbobenzoxy-L-Arginine-L-arginine Amide, Hydrochloride
α	Alpha
β	Beta
γ	Gamma
μ	Micro
μM	Micromolar
μm	Micrometer

ACKNOWLEDGMENTS

First and foremost I would like to thank God for bringing me to this point. I would not be here but for God's grace and I owe everything to the Lord almighty.

I would like to express my deep appreciation and gratitude to my advisor, Dr. Mary Lynn Trawick, for the guidance and mentorship she provided to me, throughout this process. Dr. Trawick's genuinely pleasant nature, humility, and patience made this experience much more pleasant for me than I expected. I am truly fortunate to have had the opportunity to work with her.

I am also thankful to members of the Trawick research group, past and present, who I have had the immense pleasure to work with. They all were instrumental to my graduate career and I am grateful. To Dr. Tracy Strecker, I would like to express my immense gratitude for all his help through this process and for his friendship throughout this time period. I am extremely grateful. To Emily Taylor, I would also like to express my appreciation for everything she volunteered her expertise to help me with. I am glad to have worked with her. To Dr. Jeff Schwartze, I am grateful for the opportunity to meet, work with, and become a friend of this outstanding medical professional. I would also like to thank past members of the Trawick group Dr. Amanda Charlton-Sevcik, Dr. Gustavo Chavarria, Morgan Cooper, and Yifan Wang. They all inspired and helped me in some form or another and I am very thankful.

In a similar vein I would also like to express my gratitude to Dr. Kevin Pinney. I am grateful for the opportunity to have worked with him and I am also very appreciative

of his generally pleasant attitude towards me over the years. I would also like to thank the various members of his research group.

I would also like to thank my committee members, Drs. Bob Kane, Chris Kearney and Myeongwoo Lee for their time and patience. I am immensely appreciative. You sirs are gentlemen and scholars.

I would also like to express my thanks to Mrs. Rhonda Bellert for all her help during my graduate career. I am very appreciative.

I would be remiss if I didn't express my gratitude to the various tremendous undergraduate students I have had an opportunity to mentor and work with over the course of my graduate career; Hijab Ahmed, Jesse Hilton, Alishba Khan, Chioma Ikedionwu, Prashant Appikarla, Isaac Lill and Tuata Dambo. I am glad to have gotten the opportunity to give a small contribution to their scholarly pursuits.

I would also like to thank my good friends Kika Anazia, Tayo Fadelu, Nnamdi Nwabudike and Afam Okagbue. It's a blessing to find an amazing group of friends that are there for you when you need it. Unfortunately, I gave up on looking for that group a long time ago and settled for you raggedy bunch. In all seriousness, I am very grateful for the invaluable friendship and support you all have given me over the years.

I would also like to express my immense gratitude to my darling girlfriend Oluwafunmilola Oyekan. Thank you so much for your love and support these past couple of years. You are one of a kind and I am truly blessed and lucky to have you in my life. My life would be a pale facsimile of what it is right now if I'd never met you.

I am also very grateful for my family away from home; Caleb, Chidera, Chinedu, Chinenye, Hadassah, Josh, Mummy Esther, and Mummy Grace. We may not be related

by blood but you all truly have been a family to me over the years and I am very grateful for your love and support.

Finally, I would like to thank my parents Dr. Adetunji Odutola and Mrs. Adetomike Odutola. To my Dad; I would like to say thank you for your love, your encouragement, your guidance, your prayers, and for being someone that I always aspired to emulate. To my mother; Mummy T, words will never be enough to express how thankful and grateful I am to you. I appreciate your love, your support, your encouragement, your faith in me, your constant worrying, your phone calls, and everything else. Thank you so much mom and I hope I can continue to make you proud.

ATTRIBUTIONS

The research presented in Chapter three of this dissertation is a peer-reviewed, published article with fifteen authors who participated to different extents in the various aspects the work published including conception and design of study, acquisition of data, analysis and interpretation of data, writing of the manuscript, and revision of the manuscript before submission and after review for publication. Furthermore, as is the case for most scientific research in the biomedical sciences, the work presented here is part of an extensive and ongoing collaboration - in this case between the the laboratories of Dr. Mary Lynn Trawick and Dr. Kevin Pinney at Baylor University, the research group of Dr. Ralph Mason at UT Southwestern in Dallas, and Mateon Therapeutics (formerly OXiGENE) Incorporated, a biopharmaceutical company located in San Francisco among other collaborators.

Dr. Tracy Strecker and Samuel Odutola were designated as co-first authors due to their equally significant contributions towards the publication of this paper. Both individuals contributed to the conception and design of the study including target selection in the mechanism study, as well as data acquisition and analysis. Specifically, Samuel Odutola, was responsible for designing, performing and evaluating the confocal immunofluorescence microscopy data. Samuel Odutola was also responsible for most of the statistical analysis conducted during evaluation of the data. Both Dr. Tracy Strecker and Samuel Odutola contributed to the acquisition and analysis of the western blot data presented in the study. Both individuals were responsible for the growth and culture of the cells used in the various cell assays presented in this study. Tracy Strecker was

responsible for acquiring the cytotoxicity data presented in the study, but Samuel Odutola played the major role in data analysis. Both individuals assisted in some of the other experiments presented including the flow cytometry experiments and the tube disruption assays. Samuel Odutola was also involved in some of the data analysis from the *in vivo* experiments, particularly the analysis of the immunohistochemical images, and he was responsible for putting the figures together, statistical analysis.

The co-first authors were both heavily involved in the drafting and revisions of the manuscript. Samuel Odutola was responsible for writing the first draft of the manuscript, making and incorporating revisions, and for assembling most of the figures. Tracy Strecker was also significantly involved in various revisions to the manuscript.

Drs. Mallinath Hadimani, Matthew MacDonough and Anjan Ghatak, who were members of the Pinney Research group under Dr. Kevin Pinney were responsible for the synthesis of the compounds analyzed in this study.

Morgan Cooper and Dr. Amanda Charlton-Sevcik were responsible for acquiring the flow cytometry data used in the study, while Justin Tidmore provided the data from the tube disruption assays.

Ramona Lopez, and Li Li and Dr. Li Liu, members and/or associated with the research group of Dr. Ralph Mason at UT Southwestern (Dallas) performed the *in vivo* mouse studies. Dr. Ralph Mason also contributed significantly to the conception and design of the study as well as revisions to the manuscript prior to submission.

Drs. David Chaplin, Kevin Pinney, and Mary Lynn Trawick played major roles in the design of the study. Dr. Mary Lynn Trawick had a major role in writing of the manuscript and Dr. Kevin Pinney and Dr. David Chaplin had significant roles in writing

of the manuscript. Members of the Pinney group synthesized the compounds analyzed, the in vivo work was carried out by Dr. Ralph Mason and his group, and the cell and molecular biology studies were performed by members of the Trawick group. Funding for the study was supported by the National Institutes of Health National Cancer Institute [Grant 5R01CA140674] (to K.G.P. and M.L.T. with subcontract to R.P.M.), and OXiGENE, Inc. (Grant to K.G.P. and M.L.T), which is now Mateon Therapeutics. Imaging was facilitated with the assistance of Resources of the Harold C. Simmons Cancer Center supported through an National Institutes of Health National Cancer Institute Cancer Center Support Grant [Grant 1P30 CA142543], specifically, the Southwestern Small Animal Imaging Resource, and Live Cell Imaging Resource. The IVIS Spectrum was purchased with support of 1S10RR024757.

CHAPTER ONE

Introduction

Background and Significance

In the fields of molecular biology, pharmacology and drug discovery, small molecule agents refer to low molecular weight (< 900 Daltons) organic compounds which can alter biological processes [1]. Small molecules typically bind to a specific biological target (such as a specific protein or nucleic acid) and act as effectors, leading to alteration of the activity or function of the target. Small molecules have numerous biological functions, including participation in cell signaling, as drugs in medicine, as pesticides in farming, and are also very important as research tools to probe biological functions in various research settings. These compounds can be natural (such as secondary metabolites) or artificial (such as antiviral drugs); they may have a beneficial effect against a disease (such as drugs) or may be detrimental (such as teratogens and carcinogens).

Larger structures such as nucleic acids, proteins and many polysaccharides are not small molecules, though their constituent monomers (ribo- or deoxyribonucleotides, amino acids, and monosaccharides, respectively) are often considered small molecules. Very small oligomers are also usually considered small molecules, such as dinucleotides, peptides such as the antioxidant glutathione, and disaccharides such as sucrose.

The use of small molecule agents as therapeutics is very common in the modern world. The size of small molecule compounds makes them more likely to rapidly diffuse

across cell membranes and bind to intracellular targets [1, 2]. The size of small molecule compounds is also significant in their use as therapeutics due to the fact that it enhances efficiency for bioavailability and ease of drug delivery. Furthermore, lower molecular weight compounds have been recommended for small molecule drug development based on the observation that clinical attrition rates are significantly reduced if the molecular weight is kept below 500 Daltons [3].

The major focus of the research projects presented here is to conduct analysis and optimization of small molecule compounds as possible candidates against druggable targets towards the development of therapeutics for cancer and Chagas disease (Figure 1.1). These analyses comprise a small portion of the overall drug discovery process, which is summarized in the section below.

Small Molecule Drug Discovery in Cancer

The sum total of research that goes into small molecule drug discovery in cancer typically involves four key steps: Target validation and selection, chemical hit and lead generation, lead optimization, and hypothesis-driven clinical trials.

The drug development process has numerous significant challenges. Clinical development of small molecule drugs has a very high attrition rate. Furthermore, expanding the envelope of druggability for less tractable targets, understanding and overcoming drug resistance, and designing intelligent and effective drug combinations are also challenging facets of the drug development process.

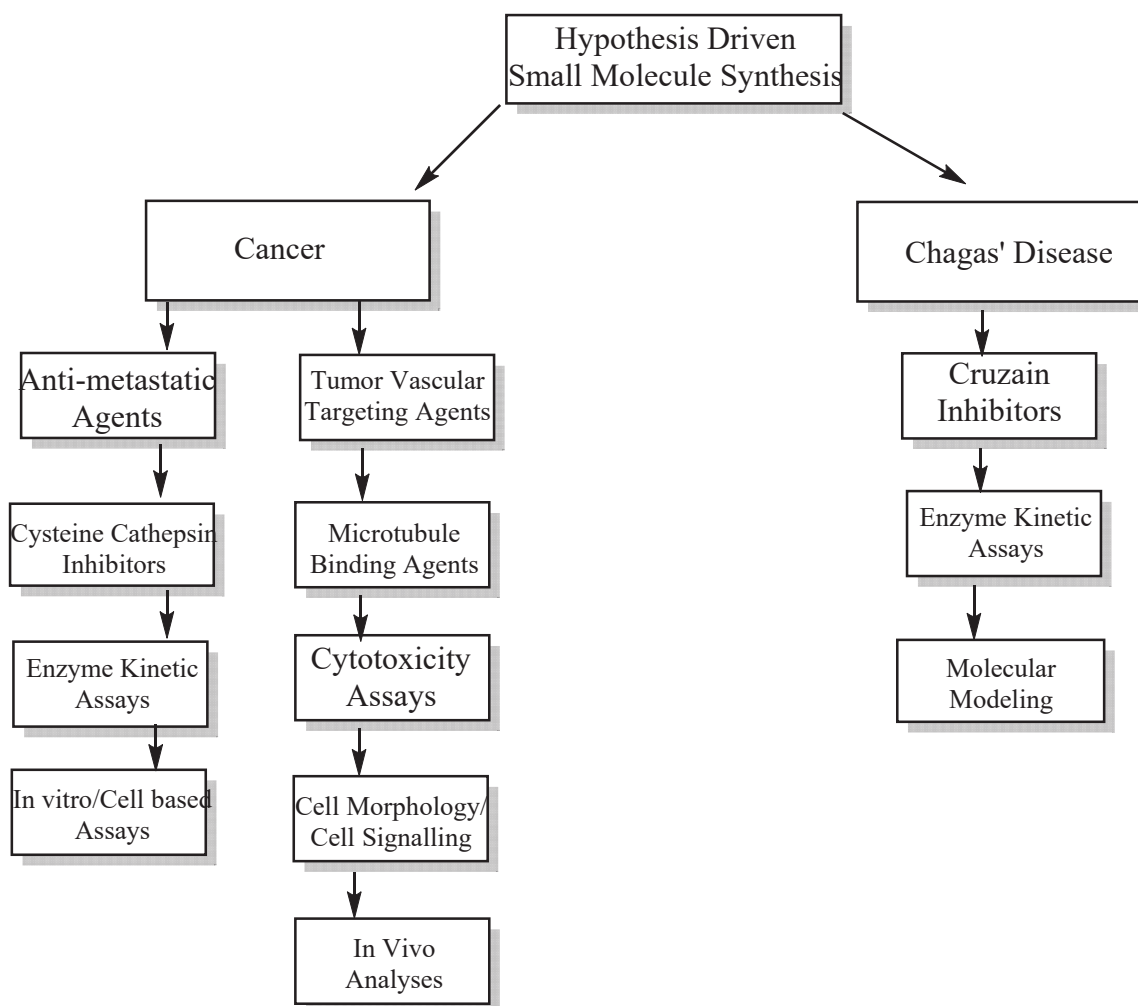


Figure 1.1. A summary of the research presented in this dissertation (Part of a larger collaborative small molecule development project between the Trawick and Pinney laboratories at Baylor University).

Target Selection and Validation

Target selection is the most important part of drug discovery as selection of a wrong target potentially leads to enormous waste of actual and opportunity costs [4]. Efficient drug discovery typically involves the selection of a new target for cancer drug discovery based on the strength of the evidence that the target represents a dependence or vulnerability for a particular group of cancer patients [5]. Such evidence is important not only to provide confidence that pharmacologically altering the function of the target

would lead to an antitumor effect, but also to help ensure that said drug would be selective for tumor versus normal healthy cells.

The assessment of the validity of a given cancer target can conceptually be focused on a number of key questions; is there sufficient evidence that the target is overactive or part of an over activated pathway that contributes to cancer growth, does it represent a vulnerability that can be exploited through synthetic lethality, and is there evidence that inhibition of the target will lead to the desired effect in patients (tumor regression and increased survival at well tolerated doses). Answering these questions involves a number of important steps. First, careful and systematic approaches to target selection are required (e.g. cancer genome sequencing, genome-wide RNA interference, and comprehensive cancer gene interaction profiling [6, 7]). Subsequently, it is important to conduct hypothesis driven experiments to assess whether the activity of proposed target can be altered by small molecules and validate that inhibition of targets will lead to the desired therapeutic outcomes [8]. In addition to this, it is also important to analyze targets to ascertain whether it contains a likely binding site for the drug. For instance, to bind with strong potency, a small molecule has to engage in a number of hydrophobic and polar interactions with its target. For drug-like molecules, this is generally only possible if the drug binds to an enclosed and hydrophobic pocket or cavity on the protein [9].

Hit and Lead Generation

After target selection, the next step in a small molecule cancer drug development program is generation of chemical hit matter (chemical compounds that appear to bind to and/or act on the drug target). Several different hit generation approaches have

successfully been employed and can be divided into four main categories: high throughput screening (HTS), fragment screening/fragment based drug discovery (FBDD), natural product screening and virtual screening.

High-throughput screening (HTS) is a very important and well used technique for hit generation. One advantage of HTS is that it is a relatively unbiased approach and can identify compounds with novel binding modes. HTS typically identifies compounds that bind with high affinity to targets in question. However, the process of screening and following up on the results can be time-consuming, as frequent false positives and undesired hits have to be eliminated. False positives often arise from compounds that aggregate [10] or interfere with the assay read out [11]. Undesired hits often have chemically reactive groups that react in an unspecific fashion with the target.

Target screening can also be achieved via fragment screening or fragment-based drug discovery (FBDD) [12]. This method is different from HTS in that only a limited number of compounds of relatively low molecular weights (<300 kDa) are screened with the aim of identifying weakly potent fragment hits ($\sim 100 \mu\text{M}$). This approach addresses one of the key challenges of HTS, which is the low odds of hit generation, as suitable HTS hits must engage in several interactions with the target in order to have sufficient potency to be identified. The disadvantage here is that the initial, weakly potent fragment hit has to be optimized through chemical modification to improve the potency into the range of a hit compound. This requires the detailed knowledge of the binding mode to the receptor (i.e. through crystal or NMR structures) thus limiting FBDD to targets where this information can be derived.

Screening of natural products is also an important method for discovery of cancer therapeutic candidates. Natural product based drug discovery projects had recently been less popular in the past two decades, for a few reasons including technical barriers to screening natural products in high-throughput assays against molecular targets, as well as the difficulties in supplying enough products and synthesizing complex natural small molecules [13]. However, natural products have once again gained traction as promising therapeutic candidates due to recent advances in screening technology [14], as well as the inherent advantages of natural products as therapeutic candidates such as the bioactivity of natural product secondary metabolites, the ubiquity of structural scaffolds and functionalizations found in natural products, as well as the fact that the Lipinski rule of five does not apply to natural products [13]. Several natural products have been discovered to be promising cancer therapeutic candidates [15, 16].

Another approach to hit and lead generation is virtual screening, which involves selecting compounds from large databases by using computational tools rather than physical screening. Virtual screening has obvious advantages over physical screening. It is significantly less resource-intensive and faster. In addition, even compounds that are not available can be evaluated by virtual screening and if found promising, can be bought or synthesized. Millions of compounds can thus be analyzed by virtual screening. It is important to keep in mind, however, that virtual screening is still a relatively coarse filter. Nevertheless, successful examples have been published [17].

Lead Optimization

Successful hit generation is followed by optimization of a lead structure through iterative rounds of medicinal chemistry design, synthesis and testing. This process

involves the simultaneous optimization of several compound properties such as potency, selectivity, tolerability, solubility, bioavailability and metabolic stability to generate a safe and efficacious drug [18].

Clinical Trials

The final and typically most resource/time intensive portion of small molecule drug development is the clinical trial. Clinical trials to develop chemotherapeutics have typically relied on a one-size-fits all paradigm in cancer research which has proven successful in the development of numerous cytotoxic drugs. However, this approach is rapidly becoming less favored as compelling evidence for the advantages of molecular, targeted and personalized cancer therapies is increasingly added to the chemotherapeutic landscape. In order to achieve this new focus, clinical trials for targeted drugs should be led by the biology and the clinical hypothesis. These trials should be hypothesis-testing and biomarker-led. They should be designed to test a strong scientific hypothesis, for example a drug acting on a specific molecular target should be efficacious in patients with a particular type of genetic aberration or certain molecular feature [19, 20].

Small Molecule Drug Discovery in Parasitic Diseases

Tropical parasites are responsible for a significant proportion of global health problems. Parasitic diseases affect hundreds of millions of people worldwide and cause significant mortality and devastating social and economic consequences [21]. However, there has been relatively little research and drug development into these diseases due to the fact that even though these diseases are globally massive in their impact, they mainly affect people in poor regions of the world. Thus, drug development in this area is

typically not seen as economically viable. Most of the drugs available to treat these diseases are decades old and typically have low efficacy, cause severe side effects, and are limited by drug resistance. Furthermore, only a few of the currently available drugs for parasitic diseases would be suitable for currently used discovery, preclinical and clinical development projects.

A modern and efficient drug development paradigm for these diseases would be somewhat similar to the cancer drug development paradigm described earlier. However, there are some unique considerations in antiparasitic drug discovery with respect to the selection of development candidates and target validation. Selection of drug candidates is contingent upon factors such as production and distribution costs, oral bioavailability, relatively broad range of chemical functionality, and low probability of development of resistance [22].

As far as target validation is concerned, it is important to ensure that there is a strong correlation between target inhibition and antiparasitic activity. Methods by which this may be achieved include comparison of the target in drug-sensitive versus drug-resistant parasites, as well as knockout of the parasite gene encoding the target [23]. It should be noted that although target validation is important, there are instances where direct validation cannot be achieved. However, failure to identify a target or elucidate a mechanism of action does not mean a promising drug candidate should not be further developed. A significant number of antiparasitic therapies both in clinical trials and currently in use do not have well-defined targets or mechanisms of action. There are a number of techniques by which the target validation process can be accomplished. These include gene knockouts [24], RNA interference (RNAi) [25], active site tags (in the case

of kinase and protease targets) [26], and small molecule inhibitors against mutants of the target [27].

Statement of Purpose

The research presented in this dissertation entails a small portion of the aforementioned facets of the drug discovery process. The overall goal of this project is to conduct some measure of target validation using small molecules that have been designed to bind to specific targets and alter their structure/activity in a therapeutically relevant manner. Furthermore, this research project aims to elucidate some of the mechanisms by which these small molecules can bind to and alter the structures and/or functions of these targets so as to gain a more robust understanding of the efficacy of these molecules as drug candidates. In addition, this project also aims to conduct some measure of lead optimization of potential vascular disrupting agents (VDAs) and cysteine protease inhibitors. Analyses of the effects of various structural motifs that are found in the libraries of compounds that were tested against these targets helps in the development and elucidation of important structure-activity relationship information which can aid in the synthesis of more potent candidate molecules against these particular targets.

Specific Aim I– Vascular Disrupting Agents

The first part of this research project involves the targeting of existing tumor vasculature by exploiting the structural components of tumor blood vessels using small molecule compounds known as vascular disrupting agents (VDAs). VDAs cause blood flow shutdown of the tumor vasculature leading to tumor necrosis. Vascular targeting has been shown to diminish the size of large tumors in animal studies but often leaves the

tumor periphery known as the viable rim intact. It should be noted however that no VDAs have been FDA approved as chemotherapeutics. Therefore, it is important to continue to contribute to the list of compounds that cause tumor vascular disruption as well as to further elucidate the mechanisms of action in vitro and in vivo.

Inspired by the well-established tubulin binding compounds that specifically bind at the colchicine binding site on tubulin dimers (combretastatin A-4 (CA4) and colchicine), a library of possible VDAs was designed and developed by members of the Kevin G. Pinney laboratory [28, 29] and analyzed as potential VDAs in a collaborative project with the Mary Lynn Trawick laboratory at Baylor University. From this compound library, an indole compound was chosen and evaluated as a promising VDA. One of the important goals of the research presented in this dissertation is to study the mechanisms of action of the lead indole compound its phosphate prodrug in activated human umbilical vein endothelial cells and MDA-MB-231 breast cancer cells. Specifically, this study aims to confirm these compounds as VDAs by ascertaining the effects of compound treatment on cytoskeletal components in endothelial and tumor cells. Furthermore, this study aims to elucidate the components of the signaling cascades as well as the downstream morphological effects that are elicited as a result of treatment of activated endothelial cells with these potential VDAs. Finally, this study aims to show some of the in vivo effects of these compounds in a breast cancer tumor xenograft model.

Specific Aim 2 – Cysteine Cathepsins

Chemotherapeutic agents should typically have several characteristics, including: potency, selectivity, solubility, stability, and low toxicity in patients. One of the major disadvantages when using non-specific chemotherapy as a cancer treatment is the

considerable list of negative side effects (i.e. vomiting, hair loss, skin rash). In targeted therapy, the inhibition of one specific enzyme or protein has the potential to limit the negative side effects caused by off-target reactions.

Cysteine cathepsins have generated a lot of research interest as specific chemotherapeutic targets due to their participation in numerous processes. Cathepsins L, B and K are members of this class of enzymes that have been extensively characterized, and have been implicated to play significant roles in tumor metastasis and progression. Cathepsins L and K play important roles in cancer metastasis; overexpression of these cathepsins is associated with a number of metastatic cancers. However, there are currently no cathepsin inhibitors that have been approved for therapeutic use.

In this portion of the research project, the main focus is to examine a group of small molecules as inhibitors of cathepsin L, for potential use in targeted therapies as anti-metastatic agents. These compounds were also assayed against cathepsins B and K in order to suggest compound moieties that may confer selectivity. These compounds, which have a thiosemicarbazone moiety, were synthesized by members of the Pinney laboratory.

Evaluation of these compounds as cathepsin L inhibitors involved a number of experimental procedures. Fluorometric based assays were utilized as a means to analyze inhibitory activities of these compounds against cysteine proteases (cathepsins B, L, and K), as well as to examine parameters such as reversibility, tightness of binding, and the mechanisms and mode of inhibition against cathepsin L. Cancer metastasis is characterized by increased cell invasion and cell migration. Therefore, two dimensional cell based assays were used to determine the ability of these compounds to inhibit the

invasion and migration of a metastatic breast cancer cell line through extracellular matrices.

Specific Aim 3 – Cruzain

Another cysteine protease, cruzain, is found in *Trypanosoma cruzi*, the causative agent of Chagas' disease. Chagas' disease, once considered to be strictly a tropical parasitic disease, is rapidly spreading to various non-tropical countries around the world. The parasitic infection is now considered a threat in some European countries and the United States. Cruzain plays important roles in the life cycle of *Trypanosoma cruzi* and is involved in host cell and organ invasion. There is currently no effective treatment for the eradication of the disease and efforts in the search for better alternatives are non-existing. The disease was considered a neglected condition, but this is rapidly changing due to the increasing number of patients in the United States and Europe.

In this project, a number of analogs in the aforementioned library of thiosemicarbazones were evaluated against cruzain towards suggesting promising therapeutic candidates against Chagas' disease. These studies were part of an ongoing collaboration between the Trawick and Pinney group (Baylor University). Evaluation of these compounds against cruzain included kinetic studies to determine inhibitory activities and mechanisms of inhibition, as well as some molecular modeling analyses so as to further elucidate the mechanisms by which these compounds inhibit the activity of cruzain.

CHAPTER TWO

Introduction to Vascular Targeting Agents

Tumor Vasculature

Targeting tumor vasculature as an anti-tumor strategy is an extensively researched area in the development of cancer therapeutics. The concept of vascular targeting was first described in the 1980s [30, 31], when the observation that physical occlusion of tumor blood vessels caused regression of solid tumors in mice, leading to the idea that pharmacologically obstructing tumor vasculature as a viable cancer therapeutic direction [30, 31]. The network of blood vessels that make up the tumor vasculature is very important for tumor growth and metastasis, as tumors require a rapidly growing and functional vascular system in order to provide oxygen and nutrients to the tumor cells. Tumors are not able to grow beyond 2 mm in size without development of this vascular system, with this development requiring the cells comprising the vascular network to adopt a highly angiogenic phenotype [32, 33].

The blood supply to the normal tissues of the body is maintained by an orderly and efficient vascular network and support system. Blood vessels are regulated by the balance of pro-angiogenic and anti-angiogenic molecular factors (maintained via metabolic demands) as well as a systematic network of lymphatic vessels which drain fluid and waste metabolic products from the interstitium. As a result, normal vascular networks are hierarchically organized, with mature vessels, made up of largely quiescent endothelial cells, that are evenly distributed to allow adequate perfusion of oxygen and

other nutrients to all cells (Figure 2.1A, C) [34, 35]. Normal vasculature is also well supported by pericytes and has adequate smooth muscle support. In tumors, the aggressive growth of the tumor cell population leads to the development of disorganized blood vessel networks that are fundamentally different from normal vasculature (Figure 2.1B, D)[34, 35]. Tumor vasculature is characterized by irregular structural dynamics and vessels that are immature, convoluted, and extremely permeable. Tumor vascular cells are constantly exposed to various pro-angiogenic factors which are secreted from the tumor, and are highly responsive to angiogenic signaling [36], leading to development of aberrant vascular morphology. Furthermore, the walls of the tumor vessels are poorly developed, having minimal vascular smooth muscle cell investiture, discontinuous endothelial-cell lining, poor connections between pericytes and endothelial cells, and having an irregular basement membrane [37, 38]. The endothelial cells that comprise the tumor vascular network tumor are often irregularly shaped, thus forming an uneven luminal layer that has loose interconnections and numerous intercellular spaces [39]. These features cause tumor vasculature to have a high intrinsic vascular permeability to macromolecules, leading to high interstitial fluid pressure on these vessels [40, 41]. The complex tumor vasculature is typically a chaotic tangle of vessels with a lack of conventional blood vessel hierarchy in which arterioles, capillaries, and venules are not clearly identifiable [42]. The accompanying lymphatic vessels are also inadequate, as well as being dilated, leaky and discontinuous. This leads to constitutively dilated and fluid-engorged vessels [43, 44]. Vessel diameters are also irregular and lengths between branching points are often very long [45]. This leads to high resistance to blood flow as well as low and intermittent blood flow rates through many tumor blood vessels. Finally,

tumor capillary blood contains abnormally high levels of deoxygenated blood, which, combined with heterogeneous blood flow, and large inter-capillary distances, contributes to micro-regional hypoxia in tumors [46, 47].

Functionally, the ability of the tumor vasculature to deliver nutrients via blood vessels and remove waste products via the lymphatic system is drastically diminished. Tumor vessels are much more permeable than normal vessels, resulting in accumulation of vascular contents and elevated interstitial fluid pressure [48]. Geometric resistance caused by irregular vessel shape and diameter leads to diminished blood flow and accompanying poor oxygen supply to tumor cells resulting in micro-regional hypoxia [48, 49]. These effects of these structural irregularities in tumor vasculature can readily be demonstrated by computer visualizations of normal and tumor vascular networks, as well as in reductions in calculated oxygen tension in areas of geometric resistance to blood flow [50].

It should be noted that these abnormal characteristics of tumor vasculature lead to atypical micro-environmental conditions that both enhance cancer progression and hinder non-vascular therapeutic anti-cancer strategies. The presence of micro-regional hypoxia is often associated with poor prognosis in patient outcomes in various cancer types [51]. Tumor hypoxia is also an important stimulus for angiogenesis. Hypoxia inducible factor-1 α (HIF-1 α) is the pivotal mediator in response to hypoxia, and increased activity of this protein in hypoxic regions leads to increased expression of vascular endothelial growth factors (VEGF) [52], a class of proteins that increase vascular permeability and promote endothelial cell growth and survival. Tumor hypoxia also leads to the up-regulation of other pro-angiogenic effectors, including angiopoietin-2 [53], nitric oxide synthase [54],

platelet-derived growth factor and basic and acidic fibroblastic growth factors [55], as well as leading to greater tumor survival by causing down-regulation of apoptosis in tumor cells [56]. Tumor hypoxia is also associated with resistance to both radiotherapy and chemotherapy [57-59]. All these factors, along with the importance of these vascular networks to tumor growth, further emphasize the importance of developing therapeutics to specifically target tumor vasculature.

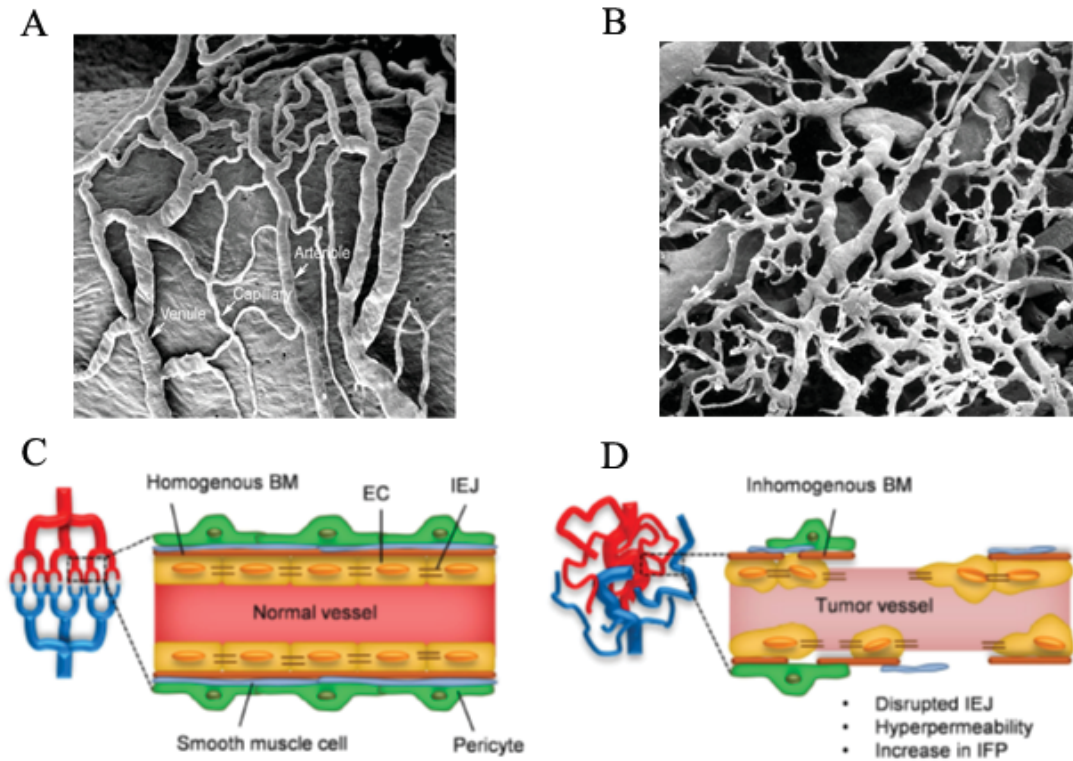


Figure 2.1. Normal vasculature (A and C) compared to tumor vasculature (B and D). Normal vasculature is well organized with mature vessels made up of evenly distributed endothelial cells. Tumor vasculature, on the other hand is disorganized, with structurally irregular endothelial cells, and an uneven luminal layer that has loose interconnections and numerous intercellular spaces Modified from [35] and [60].

Approaches to Anti-Vascular Tumor Therapy

Conventional therapeutic approaches to cancer typically involve targeting of tumor cells alone. However, cancer has recently been increasingly viewed as having three separate sections: tumor cells, the tumor vascular network, and the tumor surrounding stroma [61]. As an alternative to conventional chemotherapy, anti-vascular tumor therapy is directly focused on the tumor vascular network and not the tumor cells themselves. Agents used for anti-vascular tumor therapy can be divided into two broad categories; angiogenesis inhibiting agents (AIAs) and vascular disrupting agents (VDAs). These agents have distinct mechanisms and effects on the vascular networks that supply solid tumors (Figure 2.2). AIAs prevent the development of new tumor vasculature by inhibiting various steps in the process of angiogenesis, while tumor VDAs target and damage the already established tumor vessels.

Cancer therapy using an antivascular approach theoretically has a number of advantages over conventional chemotherapeutics used for treatment of malignant tumors;

- It is not restricted to a certain histologic tumor entity as all solid tumors depend on angiogenesis and the maintenance of functional microvasculature.
- The tumor microvasculature is well accessible to systemic treatment. In contrast to chemotherapy no endothelial barrier has to be crossed by the therapeutic substances.
- In contrast to the blood supply in organs, every single tumor blood vessel has to supply up to hundreds of critically dependent tumor cell layers. For that reason, anti-vascular therapy is potentially very effective.

- Angiogenesis in adult organisms is only induced under certain physiologic conditions, i.e. during the reproductive ovarian cycle or wound healing. An antagonism of angiogenesis is therefore a highly selective therapy promising less serious side effects.
- The endothelial cell is genetically stable and is therefore suggested to be a target that is less prone to development of drug resistance.

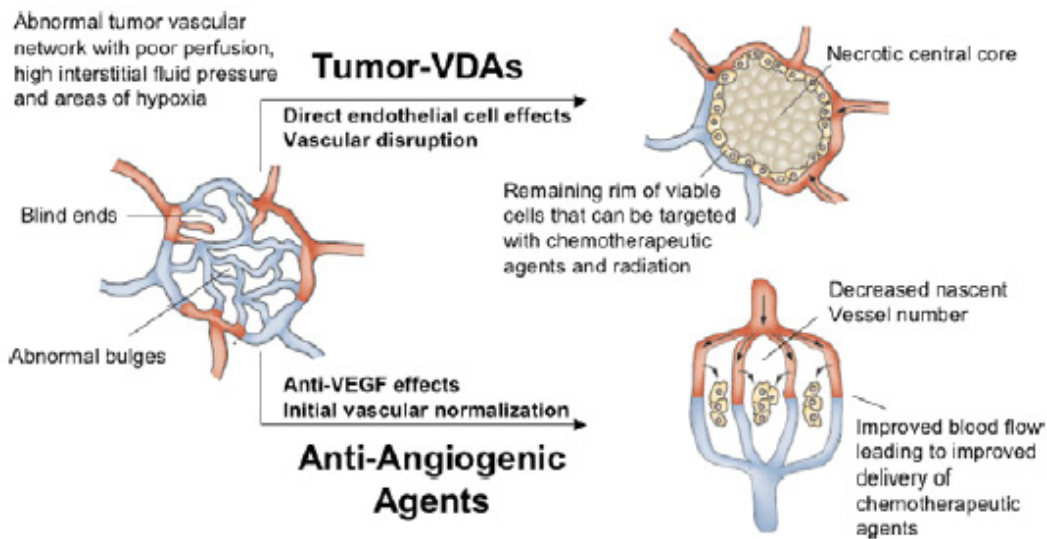


Figure 2.2. Comparison between AIAs and VDAs in effects on tumor vasculature [36]

Tumor Angiogenesis

As mentioned earlier, the development of tumor vasculature relies heavily on the presence of a highly angiogenic phenotype. Angiogenesis is a physiological process by which new blood vessels form from pre-existing ones. Tumor proliferation typically leads to the activation of this angiogenic phenotype so that the increased requirements of oxygen and nutrients can be satisfied [32, 33]. Furthermore, increased production and

release of anti-apoptotic factors from activated endothelial cells in the tumor neovasculature grants tumor cells with a distinct survival advantage [62]. The development of this angiogenic phenotype occurs due to a process known as the ‘angiogenic switch’, which results from an imbalance between endogenous angiogenesis inducers and inhibitors in such a way that increased angiogenesis is favored [63]. This switch is important for the progression of pre-malignant lesions into a vascularized malignant phenotype [64, 65]. Tumor angiogenesis is mediated via a multitude of growth factors, cytokines, lipids, matrix-degrading enzymes, receptor tyrosine kinases, and small molecules [66]. The angiogenic process comprises a large number of steps, leading to the activation of endothelial cells by the tumor via the secretion of pro-angiogenic growth factors which then bind to receptors on nearby dormant endothelial cells (ECs) that line the interior of vessels [33, 34] (Figure 2.3). Endothelial cell stimulation results in vasodilation and permeability of the vessels increase. This is accompanied by the recruitment of pericytes which is mediated by angiopoietin-2 (ANG2), platelet derived growth factor B (PDGF-B) and TIE2, a receptor tyrosine kinase with immunoglobulin-like and EGF-like domains [63, 67, 68]. Furthermore, matrix-degrading enzymes such as matrix metallo-proteases (MMPs) and heparanases, are secreted so as to dissolve the basement membrane and to remodel the extracellular matrix (ECM) as well as to liberate more pro-angiogenic growth factors (bFGF and VEGF) [69-71]. MMP secretion also causes endothelial cells to detach from the extracellular matrix and basement membrane. These cells then migrate and proliferate to sprout and form new branches from the pre-existing vasculature [34]. The angiogenic phenotype in tumor micro-environment can further be sustained by the recruitment of bone-marrow derived precursor endothelial

cells, stromal cells and circulating endothelial cells to migrate to the tumor vasculature. Stromal cells such as fibroblasts, mesenchymal stem cells and various bone marrow-derived myeloid cells including macrophages, TIE2-expressing monocytes, neutrophils and mast cells contribute to tumor angiogenesis through their production of growth factors, cytokines and proteases [72, 73].

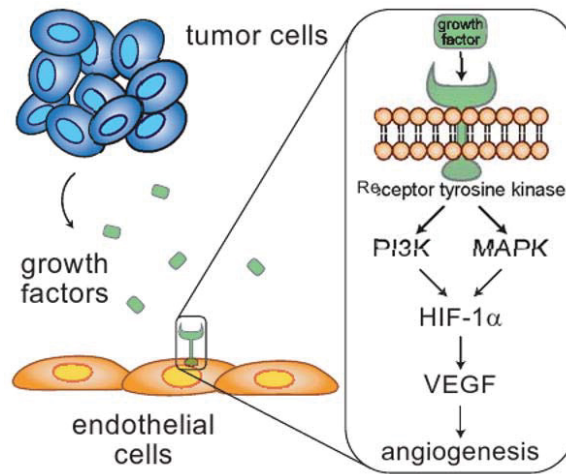


Figure 2.3. Summary of signaling events leading to up-regulation of angiogenesis in tumor vasculature [74]. Tumor cells release numerous growth factors that lead to increased angiogenic growth in endothelial cells in nearby vessels.

Angiogenesis Inhibiting Agents

Extensive research has been devoted to discovery of therapeutic strategies specifically targeting tumor angiogenesis. As such, a significant number of AIAs to target various aspects of the complex angiogenic process are under pre-clinical and clinical development (Figure 2.4). These agents can be generally classified into three distinct groups based on their modes of action; direct endogenous inhibitors that prevent tumor endothelial cell proliferation and migration, indirect inhibitors that block angiogenic

signaling, and miscellaneous agents that inhibit angiogenesis related processes and cells [75] (Figure 2.5).

Direct endogenous inhibitors of angiogenesis (Figure 2.5 A), such as angiostatin, endostatin, arrestin, vasostatin, canstatin, tumstatin and others, are fragments released on proteolysis of distinct ECM molecules. Endogenous inhibitors prevent vascular endothelial cell proliferation and migration in response to angiogenesis inducing factors such as VEGF, bFGF, interleukin 8 (IL-8) and PDGF [76, 77]. This direct anti-angiogenic effect may be mediated by interference with endothelial integrins along with several intracellular signaling pathways [78].

Indirect inhibitors of angiogenesis (Figure 2.5 B) prevent the expression and/or block the activity of pro-angiogenic proteins [79]. The most clinically relevant and extensively researched agents in this group are those which specifically target and inhibit the effects of VEGF. These include neutralizing antibodies to VEGF (e.g. bevacizumab) or VEGF receptors (VEGFRs) (e.g. ramucirumab), soluble VEGFR/VEGFR hybrids (e.g. VEGF-Trap), and tyrosine kinase inhibitors (TKIs) with selectivity for VEGFRs (e.g. sunitinib, pazopanib and sorafenib) [80-82]. Bevacizumab (Avastin) is a humanized monoclonal antibody against all isoforms of VEGF-A which has been FDA approved for the treatment of colorectal, lung, glioblastoma and renal cell carcinoma [80, 83]. Numerous clinical trials with bevacizumab have also shown promising efficacy against other cancers [84].

Table 1				
Drugs Developed Primarily for Antiangiogenic Effect				
Class	Drug	Description	Targets	Development Phase
Anti-VEGF	Bevacizumab (Avastin)	Monoclonal antibody	VEGF(-A), all isoforms	Marketed
	VEGF-trap	Soluble receptor	VEGF(-A), all isoforms	
	VEGF-AS (Veglin)	Antisense oligonucleotide	VEGF(-A), -C, -D	Phase I
Anti-VEGFR	PTK787 (vatalanib)	Small-molecule tyrosine kinase receptor inhibitor	VEGFR-1, -2, -3	Phase III
	SU011248	Small-molecule tyrosine kinase receptor inhibitor	VEGFR-2, PDGFR	Phase III
	ZD6474	Small-molecule tyrosine kinase receptor inhibitor	VEGFR-2, EGFR	Phase II
	AG-013736	Small-molecule tyrosine kinase receptor inhibitor	VEGFR, PDGFR, c-kit	Phase II
	CP-547,632	Small-molecule tyrosine kinase receptor inhibitor	VEGFR-2	Phase II
	Sorafenib (BAY 43-9006)	Small-molecule raf kinase inhibitor	VEGFR-2, PDGFR- β , R1-3, c-kit	Phase II
	CEP-7055	Small-molecule tyrosine kinase receptor inhibitor	VEGFR-1, -2, -3	Phase I
	IMC-1C11	Monoclonal antibody	VEGFR-2	Phase I
	AE-941 (Neovastat)	Shark-cartilage component	VEGF-VEGFR binding and MMP-2, -9	Phase III
Other anti-VEGF pathways	Erzastaurin (LY317615)	Acyclic bisindolyl-maleimide	Protein kinase C- β isozyme	Phase I
	Angiostatin	Recombinant human protein	Mimics innate mechanisms	Phase II
Human antiangiogenic factors	Endostatin	Recombinant human protein	Mimics innate mechanisms	Phase II
	Thrombospondin-1 mimetic (ABT-510)	Mimetic peptide	Mimics innate mechanisms	Phase II
	MEDI-522	Monoclonal antibody	$\alpha_v\beta_3$ integrin	Phase II
Anti-integrin agents	Cilengitide (EMD 121974)	Peptide	$\alpha_v\beta_3$ and $\alpha_v\beta_5$ integrins	Phase II
	CNTO 95	Monoclonal antibody	α_v integrins	Phase I
	BMS-275291	Nonhydroxamate small molecule	MMPs	Phase III
MMP inhibitors	Combretastatin A4	Small molecule	Tubulin	Phase II
Vascular-disruptive agents	5,6-Dimethyl-xanthone-4-acetic acid (DMXAA)	Flavonoid small molecule	Intratumoral macrophages (induction of TNF)	Phase I
	ZD6126	Small molecule	Tubulin	Phase I
	AVE8062	Small molecule	Tubulin	Phase I
Heparanase inhibitors	PI-88	Small molecule	Heparanase, VEGF	Phase I/II

EGFR = epidermal growth factor receptor; MMP = matrix metalloproteinase; PDGFR = platelet-derived growth factor receptor; TNF = tumor necrosis factor; VEGFR = vascular endothelial growth factor receptor.

Figure 2.4. AIAs that have advanced through some stages of clinical development [85]

VEGF-A can also be inhibited using soluble fusion proteins (VEGF-Trap), typically consisting of the VEGF-binding portions from the extracellular domains of human VEGF receptors 1 and 2 fused to the Fc portion of the human IgG1 immunoglobulin. These function by binding to and ‘trapping’ the different isoforms of VEGF-A, in addition to VEGF-B and placental growth factor [86, 87]. TKIs are small molecules with different chemical structures that have the ability to interact physically with the highly conserved kinase domain shared by different VEGFRs. These compounds inhibit the kinase activity of VEGFRs via a number of distinct mechanisms, and the resulting reduction in tyrosine phosphorylation leads to inhibition of downstream pro-angiogenic signal transduction [81, 88-90]. These compounds also inhibit the tyrosine kinase activity of PDGF receptors (PDGFRs), FGF receptors (FGFRs), EGFR, and Raf kinases, also resulting in antiangiogenic effects [81].

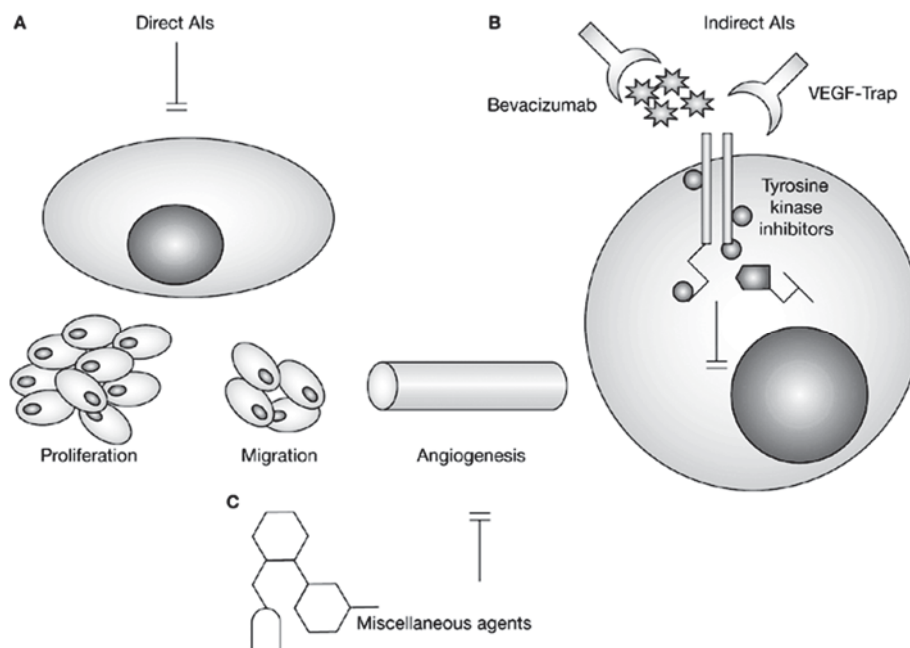


Figure 2.5. Various classes of AIAs based on their mechanism of inhibition. [91]

Tumor angiogenesis can also be inhibited by a number of miscellaneous agents (Figure 2.5 C) that target various aspects of the angiogenic process. These include;

- Matrix metalloprotease (MMP) and cysteine cathepsin inhibitors, which inhibit the enzymes responsible for degrading and remodeling by tumors so as to modify local micro-environment, an important step in the angiogenic process [92, 93].
- Tumor associated stromal cell therapy with compounds that disrupt tumor induced recruitment of stromal cells can indirectly inhibit tumor angiogenesis [83, 94, 95].
- Cell adhesion molecule targeted therapy to disrupt cell surface molecules such as α v-integrins, E-selectin, N-cadherin and VE-cadherin, which have been shown to play a role in tumor angiogenesis [96]. A prime example of this approach is research into the use of integrin antagonists such as peptidomimetics (e.g. cilengitide), monoclonal antibodies (e.g. volociximab), as well as oral small-molecule compounds in a number of cancer types [97].

Vascular Disrupting Agents

As mentioned earlier, VDAs target mainly the endothelial cells and pericytes that comprise the already established tumor vasculature, causing tumor ischemia and necrosis. VDAs are a group of compounds that specifically target endothelial cells via a limited number of pathways, with the end result being the disruption of the cytoskeleton and cell-to-cell junctions, and changes in endothelial cell shape. Subsequently, there is induction of a cascade of events, such as increased loss of endothelial cells from the vascular network, increased permeability to proteins and increased interstitial fluid pressure, which leads to a reduction in vessel diameter and plasma leakage. The end result is increased blood viscosity and decreased blood flow (Figure 2.6) [98]. Furthermore, the

exposed basement membrane components become activated through contact with platelets, contributing to vascular shutdown. The inhibition of blood flow and the consequent reduction in oxygen and nutrient supply induces necrosis of many tumor cells downstream. All these events are more selective in tumors than in normal endothelium, as tumor endothelial cells are more activated and rapidly growing. Through these various pathways, VDAs are able to induce extensive vascular shutdown and hemorrhagic necrosis of the tumor core in animal models; however, viable cells are often preserved at the peripheral rim, and these cells will rapidly repopulate the tumor. This rim of tumor cells probably survives because it derives nutritional support from nearby normal blood vessels, which are less responsive to VDAs due to the significant differences between normal and tumor blood vessels [98]. This suggests that VDAs are more likely to produce a meaningful clinical response when used in combination therapy with standard chemotherapeutic agents.

There are a number of potential advantages of VDAs over other approaches to anti-cancer therapy. Firstly, a significant bystander effect may take place, as one single blood vessel may provide oxygen and nutrients for thousands of tumor cells. Therefore, blockage or destruction of this solitary vessel may result in extensive downstream tumor cell deaths. The endothelial cells that make up the blood vessel do not need to be killed by the VDA. Rather, a change of cell structure or local initiation of the coagulation cascade may be all that is needed to cause vascular collapse. Furthermore, since the endothelial cells that make up the tumor vasculature are largely untransformed cells (albeit rapidly growing), there is reduced likelihood for development of drug resistance via genetic mutation [66]. Another advantage of VDAs is that their effects on local tumor

blood flow can be measured by non-invasive methods, including dynamic contrast-enhanced magnetic resonance imaging [DCE-MRI], positron emission tomography using ¹⁵O-PET, dynamic perfusion computed tomography, three-dimensional micro-bubble ultrasound, and dynamic bioluminescence imaging [67-69]. Finally, VDAs do not need to exert their effects for long, with studies suggesting significant tumor cell death starting at 2 hours post ischemia [99, 100]. Thus, even in cases where these agents are cleared rapidly in vivo, they can still be significantly efficacious. VDAs are divided into three main types; ligand-directed VDAs, cationic-liposome based VDAs, and small molecule VDAs.

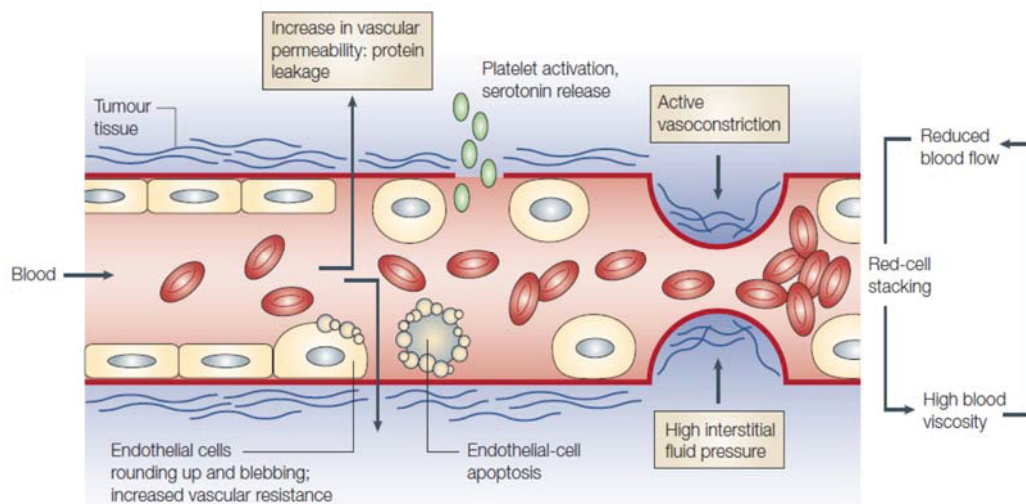


Figure 2.6. VDA mechanism of action on pre-established tumor blood vessels [98]

Ligand-Directed VDAs

Ligand-directed VDAs use antibodies or peptides against cell surface markers specific to tumor vascular cells so as to target effector molecules such as toxins or pro-coagulants to the tumor endothelium. There are several molecules that are upregulated in tumor vascular tissue as opposed to normal vasculature. These include antigens involved

in angiogenesis, thrombosis, and vascular remodeling, as well as cell adhesion molecules [101]. These agents cause exposure of the basement membrane, leading to vascular shutdown and subsequent widespread tumor cell necrosis [102]. The effector can induce vessel occlusion directly or indirectly or redirect host defenses attacking tumor vessels [101].

Cationic Liposome Based VDAs

Similar to ligand-directed VDAs, this approach to vascular disruption focuses on targeting compounds directly to the tumor vascular microenvironment. Previous studies have shown that cationic liposomes selectively target activated tumor endothelium while neutral and anionic liposomes do not [103, 104]. A variety of therapeutic substances (e.g. cytotoxic drugs, antisense oligonucleotides, vectors) can be encapsulated in cationic liposomes and thus selectively delivered to tumor vasculature. This selective targeting is possibly mediated by charge interaction of cationic liposomes with the more negatively charged cell surface of angiogenic endothelial cells relative to normal quiescent endothelial cells. The cell surface of activated endothelial cells is negatively charged for a number of reasons, including the presence of negatively charged lipid phosphatidylserine in the luminal membrane of tumor blood vessels [105], as well as up-regulation of negatively charged hyperglycosylated and hypersilylated membrane proteins in activated endothelial cells in vitro [106]. These negative binding sites possibly provide molecular targets for preferential binding of cationic liposomes within the angiogenic tumor endothelium. Studies have shown that cationic-liposomes loaded with cytotoxic substances, e.g. paclitaxel, specifically target tumor vasculature and produced improved anti-tumor effects compared to the agent alone [107-109].

Small Molecule VDAs

Small molecule VDAs function by exploiting the differences between normal and tumor endothelium to induce vascular shutdown of tumor blood vessels. Significant discovery and development of various small molecule compounds that cause selective tumor vascular shutdown has occurred over the past few years, with a number of compounds reaching the human clinical trial stage of development. Small molecule VDAs are divided into two distinct classes based on their mechanisms of action. The first class is represented by synthetic flavonoids that work through induction of local cytokine production. The second class comprises tubulin-binding agents. There are a significant number of these compounds that have shown some promise in human clinical trials.

Flavonoids

Flavonoids are a class of compounds based on the flavone ring structure. Flavone acetic acid (FAA), the first of this class of small molecule VDAs was originally synthesized as a non-steroidal anti-inflammatory agent, but was found to have widespread anti-cancer effects in pre-clinical studies [110, 111]. Unfortunately, FAA did not show much success in human clinical trials [112]. However, other synthetic flavonoid compounds showed more promise as VDAs. A prime example of these is DMXAA (5, 6-dimethylxanthenone-4-acetic acid), which was developed as a more active analogue of FAA. It is significantly more potent than FAA and has been shown to elicit rapid vascular shutdown in murine tumors [113, 114]. Flavonoids, DMXAA included, typically function via a mechanism involving the partial breakdown of the actin cytoskeleton, leading to DNA damage and subsequent induction of apoptosis in tumor endothelial cells [115, 116]. DMXAA also induces synthesis of tumor necrosis factor (TNF) (in tumor cells,

tumor vascular cells, and via the activation of macrophages), as well as the synthesis of nitric oxide [116-119]. The exact molecular target has not been completely elucidated, but it involves up-regulation of the nuclear transcription factor NFkB [115, 116], which leads to production of TNF and other cytokines. These vascular disrupting effects are further enhanced via the activation of platelets and serotonin [114, 116, 119, 120]. DMXAA showed promising results in phase I and II clinical trials [121, 122]. However, phase III clinical trials have thus far proven to be failures [123, 124].

Tubulin Binding Agents

Tubulin-binding small molecule vascular disrupting agents are an extensively researched group of compounds that function by a mechanism that is quite distinct from flavonoids. The small-molecule VDAs that are members of this class have a mode of action that includes an interaction with the tubulin-microtubule protein system, and potentially inhibit tubulin assembly into microtubules. Small molecules can bind to this system via one of four possible domains; the vinca-alkaloid and colchicine domains, located on the tubulin heterodimer, and the taxoid and laulimide binding domains located on the polymerized microtubule (Figure 2.7) [125]. The most clinically significant of these compounds are those that bind at the colchicine binding site located at the interface between the α and β -tubulin subunits of the tubulin heterodimer. These agents (usually having stilbene or heterocyclic structures) selectively target tumor endothelial cells by exploiting their dependence on the tubulin cytoskeleton to maintain cell shape [126]. Binding and destabilization of the tubulin cytoskeleton by these agents causes the induction of cell signaling cascades that lead to rapid changes in endothelial cell shape.

This rapid change of endothelial cell morphology leads to disruption of the endothelial cell layer, eventual vascular collapse, and necrosis or apoptosis of supported tumor cells.

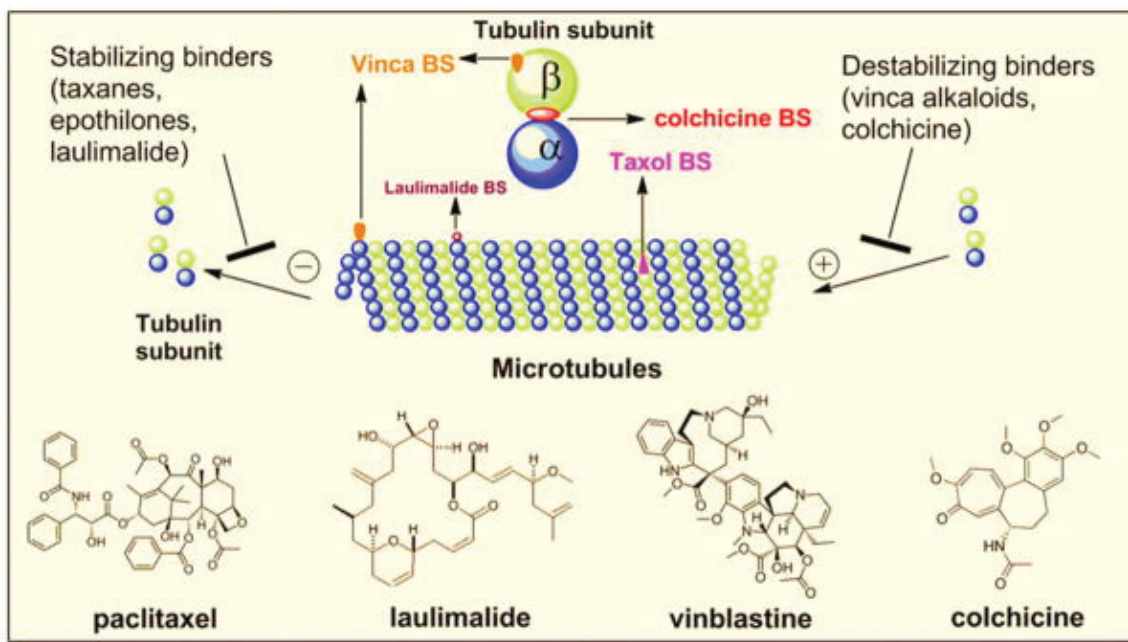


Figure 2.7. Tubulin binding sites of microtubule binding agents [125]

Colchicine was initially thought to have promise as a VDA due to its ability to disrupt tumor vasculature. However, the vascular disrupting effect was only seen to occur at doses that were toxic in animal models; therefore this significant toxicity precluded further clinical use [127]. Subsequent extensive research into compounds with similar tubulin binding and vascular disrupting characteristics as colchicine has led to the discovery of a library of small molecule compounds with promising antivascular effects. The most notable of these are the natural products obtained from the African willow tree (the combretastatins), of which combretastatin-A-4 (CA4) (as well as its phosphate pro-drug combretastatin-A-4-phosphate (CA4P)) (Figure 2.8) has been found to be one of the most effective [128, 129]. Treatment with CA4P causes rapid and selective vascular

shutdown in a range of human xenograft and rodent tumors [128-130]. CA4P is dephosphorylated by endogenous phosphatases yielding the parent compound CA4, which binds to tubulin at or near the colchicine-binding site, leading to microtubule depolymerization [128-131]. CA4P treatment causes significant impairment of tumor vascular function at doses as low as a tenth of the maximum tolerated dose [132]. However, there does remain a significant viable rim after CA4 treatment due to rapid regrowth of viable cells surviving at the tumor periphery [98, 132, 133]. In order to solve this problem, numerous studies into combination therapies with conventional chemotherapeutic agents such as cisplatin, taxol, doxorubicin, paclitaxel, carboplatin and 5-fluorouracil [128, 134-138], with anti angiogenic agents [139], and with radiation [100, 140] have been carried out. Other combretastatin compounds have also shown promise as tumor VDAs. A sodium phosphate prodrug of combretastatin A-1 (CA1P) has been proven to be ten times more potent than CA4P in preclinical models and is being rapidly developed as a tumor VDA (OXiGENE compound OXI4503) [141, 142]. Another CA4 derivative in clinical trials is AVE8062 (Aventis Pharma). This compound is a serine prodrug of CA4, which is cleaved by endogenous amino-peptidases to release the active parent drug [143]. Apart from the combretastatins, other tubulin-binding agents have potential as tumor VDAs. An analogue of colchicine, N-acetylcolchinol-O-phosphate (ZD6126), is currently undergoing preclinical and clinical testing [144]. ZD6126 is rapidly dephosphorylated by serum phosphatases to N-acetylcolchinol (NAC), a tubulin-binding agent that inhibits tubulin polymerization and causes microtubule destabilization, and results in significant anti-tumor activity against a variety of human xenograft models [145]. ZD6126 showed significant VDA activity at doses 1/8–1/16 of the MTD, as well

as selectivity for tumor blood vessels [145]. ZD6126 also enhanced the tumor response to radiation, giving a 1.3-fold increase in the slope of the radiation dose-response curve [144]. Auristatin PE (TZT1027) is a tubulin-binding agent derived from dolastatin 10 (isolated from a marine mollusk) that has profound vascular effects [146]. Arsenic trioxide (Trisenox, Cell Therapeutics) is used to treat patients with acute promyelocytic leukemia. Among other effects, it binds to tubulin and has vascular disrupting properties in solid tumors [147]. Other potential VDAs under current investigation include ABT-751 (Abbot Pharmaceuticals), MX-116407 (Maxim Pharmaceuticals), NPI-2358 (a diketopiperazine compound developed by Nereus Pharmaceuticals) and a number of others (as seen in Figure 2.8).

The Microtubule System

The eukaryotic cytoskeleton is composed of three distinct elements: actin microfilaments, intermediate filaments and microtubules. The latter represent a dynamic system, which is critically important for the spatial and temporal organization of eukaryotic cells and as such are a promising target for anticancer therapy. Microtubules are dynamic polymers which are made up of α/β tubulin dimers (Figure 2.9). They are hollow cylindrical structures, about 24 nm in diameter, built from 13 parallel protofilaments, which are in turn made up of α/β tubulin dimer subunits. Each α and β monomer has a GTP molecule bound to it

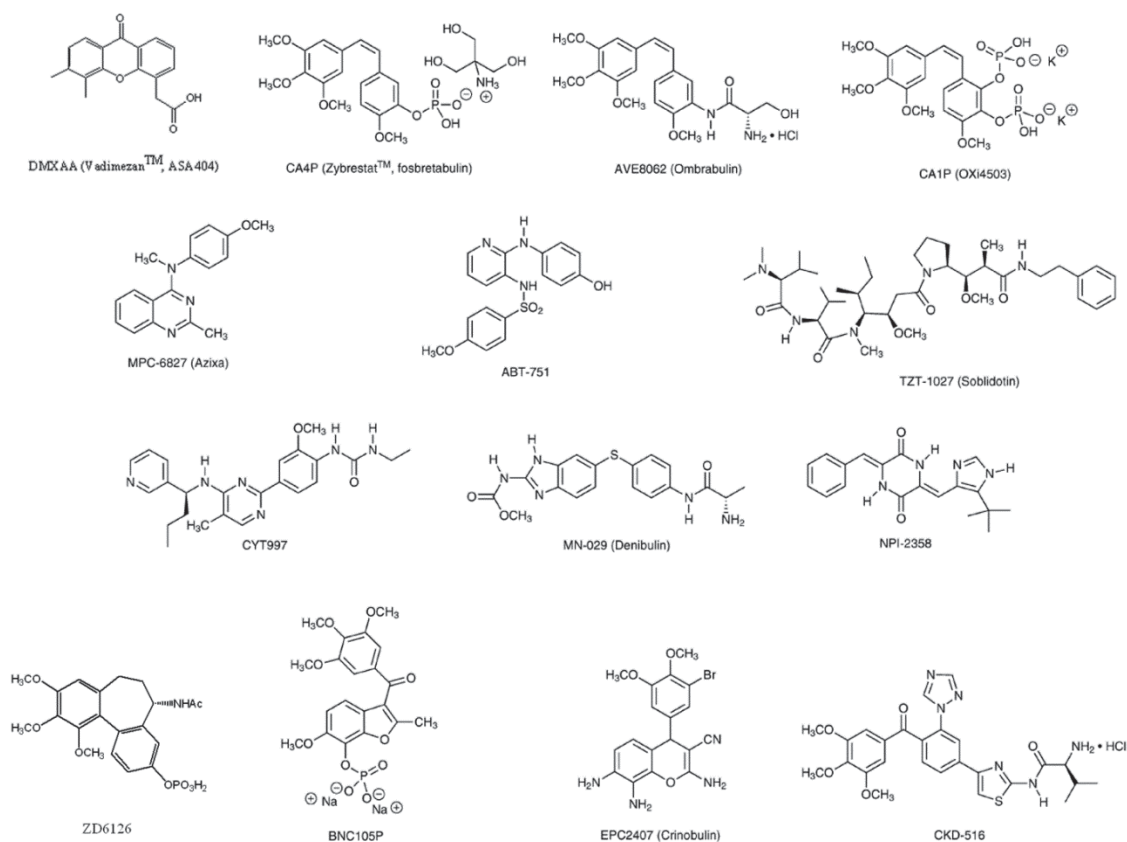


Figure 2.8. Selection of small molecule VDTAs investigated in clinical trials. Modified from [148]

The GTP that is bound to the α -tubulin is trapped at the dimer interface, while the GTP molecule bound to the β -tubulin can be readily hydrolyzed to GDP [149]. The process of tubulin assembly into microtubules occurs when one α/β subunit joins with another. When these heterodimer subunits self-assemble to form microtubules, two new types of protein-protein interactions are generated. Along the longitudinal axis of the microtubule, the “top” of one β -tubulin molecule forms an interface with the “bottom” of the α -tubulin molecule in the adjacent dimer subunit resulting in the formation of a protofilament. Perpendicular to these interactions, lateral contacts also form between neighboring protofilaments, with these connections typically being between monomers of

the same type (α - α and β - β). Together, these longitudinal and lateral associations are repeated to form the helical lattice structure of the microtubule [149-151]. Furthermore, each protofilament is assembled from subunits that all point in the same direction thereby resulting in a distinct structural polarity with a plus end with exposed β -tubulin and which grows most rapidly, and a minus end with α -tubulin. The minus end is usually oriented toward a centrosome, the center from which microtubules originate.

Microtubules are in a constant state of dynamic instability because the GTP at the plus end may become hydrolyzed to GDP before another tubulin subunit can join. While the presence of GTP at the plus end of the microtubule creates a 'GTP-cap' which contributes to the stability of the polymer, GDP-subunits rapidly dissociate from the microtubule. Therefore, there is a regulation of growth or shrinkage depending on the rate of hydrolysis and availability of GTP-tubulin subunits giving microtubules a characteristic known as dynamic instability (Figure 2.9) [150, 152-154]. This regulation is a vital component of various processes that are crucial to cell growth and proliferation such as mitosis, cell motility, maintaining cell shape, cellular transport, maintaining cell polarity, and cell signaling [151], and is especially crucial to the processes that control tumor vascular endothelial cell growth. The ability to interfere with this polymerization process is what makes tubulin-binding VDAs clinically relevant in cancer therapy.

Microtubule polymerization inhibitors, such as colchicine, disrupt polymerization of microtubules and interfere with tubulin dynamics via a mechanism that involves alteration of the binding capabilities of tubulin heterodimers to the microtubule polymer [155]. In order to elucidate this mechanism, the structures of the tubulin monomers and heterodimers (with bound colchicine) (Figure 2.10) have been analyzed via X-ray

crystallography and atomic modelling [156]. These studies on tubulin structure have shown α and β tubulin to be almost identical in principal structure, with each monomer composed of a core of two beta sheets surrounded by α helices. The monomer has compact structure, which can be divided into three functional domains: the N-terminal domain (which is the nucleotide-binding region), an intermediate domain containing the taxol-binding site, and the c-terminal domain where the binding site for motor proteins is located. The N-terminal, domain is composed of six parallel β -strands (S1–S6) alternating with helices (H1–H6). There are also six loops (T1–T6), which connect each strand with the start of the next helix, a structural motif that aids in binding the nucleotide [151, 155, 156].

Nucleotide binding in each monomer is completed by interaction with the N-terminal end of the core helix H7. The core helix connects the nucleotide binding domain with the smaller, second domain, formed by three helices (H8-H10) and a mixed beta sheet (S7-S10). The C-terminal region is formed by two antiparallel helices (H11-H12) that cross over the previous two domains [155, 156]. In order to clearly elucidate mechanism of colchicine disruption of tubulin polymerization, DAMA (N-deacetyl-N-(2-mercaptoacetyl)) colchicine was used to allow for the establishment of the location of the N-acetyl group and to explicitly define the orientation of colchicine at the binding site [157].

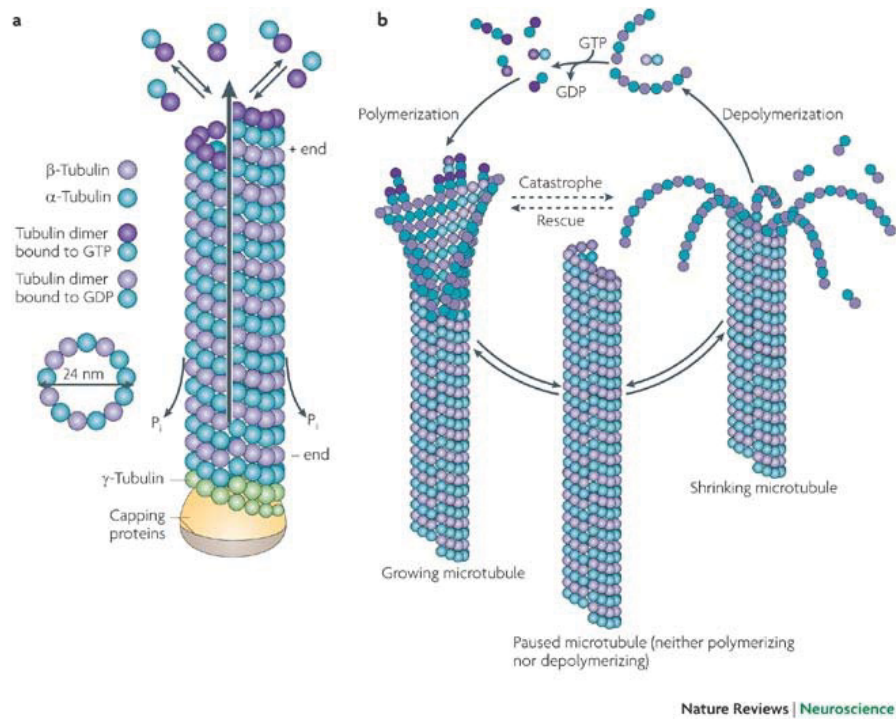


Figure 2.9. Microtubule structure and dynamics [154].

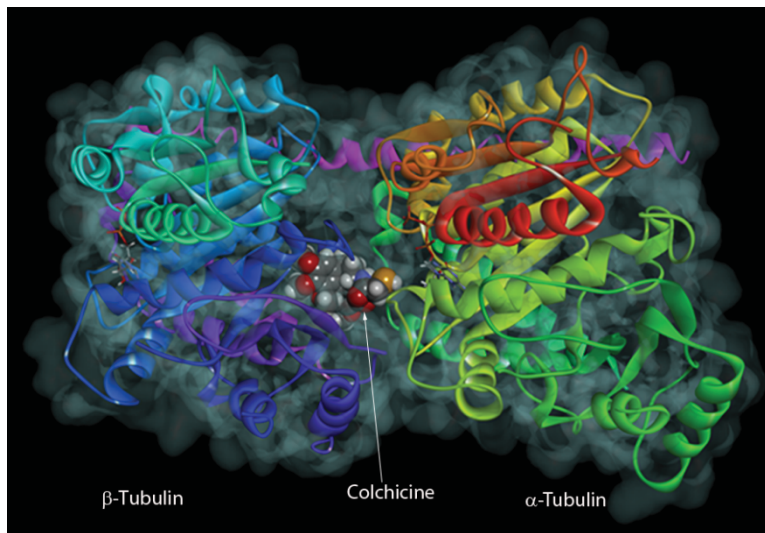


Figure 2.10. Structure of tubulin heterodimer at 3.5 Å resolution, in complex with colchicine and with the stathmin-like domain (SLD) of RB3 (PDB: 1SAO). The figure was prepared using Accelrys software.

DAMA colchicine was shown to bind on the β -subunit at a site surrounded by S8 (residues 313-320), S9 (residues 351-356), T7 loop (residues 244-251) and helices H7 (residues 224-243) and H8 (residues 252-260) [155, 157]. When bound, colchicine also interacts with the T5 loop (residues 173-182) of the adjacent α -subunit in addition to the β -subunit, allowing for stabilization of the colchicine bound tubulin heterodimer.

Microtubule polymerization is inhibited by low concentrations of colchicine due to the fact that it inhibits tubulin polymerization by binding to the ends of microtubules rather than to the soluble tubulin. Colchicine binding to the tubulin heterodimer leads to a conformational change in the heterodimeric tubulin structure (Figure 2.11) [157]. Kinetic analysis of the inhibition interaction has shown that tubulin–colchicine complex (TC-complex) disrupts polymerization by an “end conserving mechanism”. This means that such that the TC-complex does not completely prevent the tubulin addition to the polymer but only reduces the rate of tubulin addition that occurs along with the addition of the TC-complex at the microtubule ends[158]. Microtubules in a protofilament are stabilized through both lateral and longitudinal interactions [159]. The S7-H9 loop also known as the M loop (microtubule loop) is a very important component of these interactions. The M loop protrudes from one side of the protofilament and interacts with the H3 and several other loops. As such conformational changes on adjoining loops would affect the M loop and lead to microtubule destabilization. At sub-stoichiometric TC-complex concentrations, binding of the complex to microtubule disturbs formation of lateral contacts at the newly formed end of protofilaments due to displacement of the M loop. As a result, tubulin can no longer remain in straight conformation since it would lead to steric clash between colchicine and nearby residues along with GTP. This leads to

an increase in loss of lateral contacts, and reduction in polymerization. An increase in the concentration of colchicine results in a greater loss of lateral contacts, thereby leading to microtubule depolymerization.

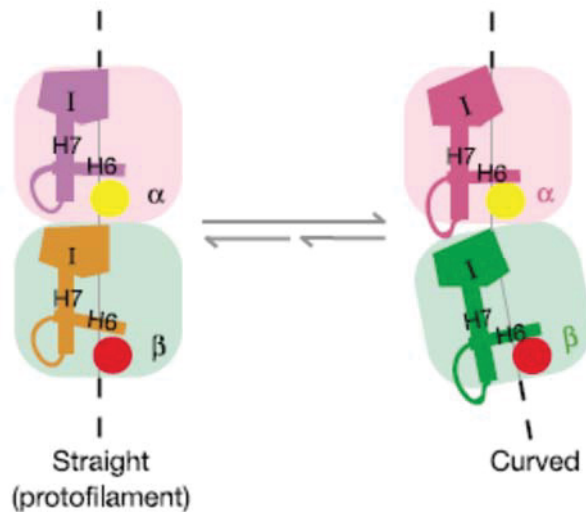


Figure 2.11. Binding of colchicine to tubulin heterodimers causes a conformational change on protofilaments [157]

In Vitro Models for VDA Evaluation: HUVECs and MDA-MB-231

Cell studies in this project were performed using mainly two different cell types; MDA-MB-231 breast cancer cell line and human umbilical vein endothelial cells (which are primary cells).

Human Umbilical Vascular Endothelial Cells

Human umbilical vein endothelial cells (HUVECs) provide a classic, important and widely used in vitro model system to study many aspects of endothelial function and disease, such as normal, abnormal and tumor-associated angiogenesis and/ or neovascularization, oxidative stress, hypoxia and inflammation related pathways in

endothelia under normal and pathological conditions, cellular and molecular events in the pathophysiology of atherosclerosis and plaque formation, cardiovascular-related complications associated with various diseases, mode of action and cardiovascular protection effects of various compounds, and in embryogenesis [160, 161]. Human umbilical vein endothelial cells (HUVEC) are isolated from the umbilical cord. The cells are homogenous, closely opposed, large, and polygonal with an oval, centrally located nucleus and indistinct cell borders (Figure 2.12). The cells grow in confluent monolayers with a cobblestone-like morphology with large dark nuclei (Figure 2.13). During proliferation, cells are small and evenly sized, display a high mitotic index and show no presence of smooth muscle cells. In order to more closely model rapidly growing tumor vascular endothelial cells in this study, HUVECs were analyzed only as sub-confluent cultures (40-70% confluence) and in media supplemented with a high concentration of growth factors.

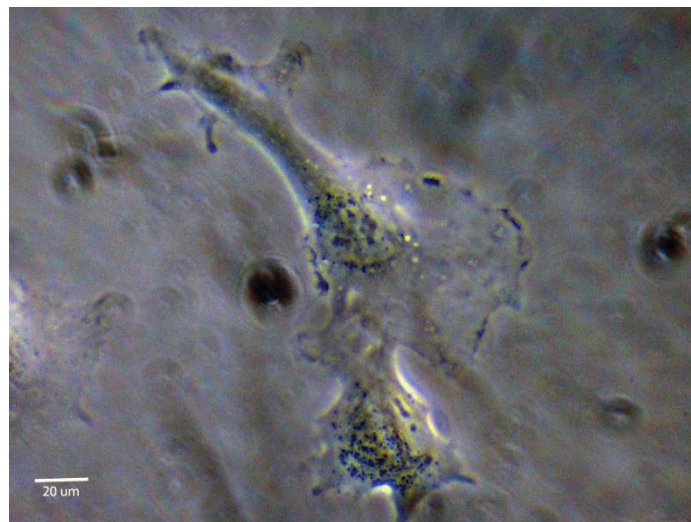


Figure 2.12. Phase contrast image of HUVECs.

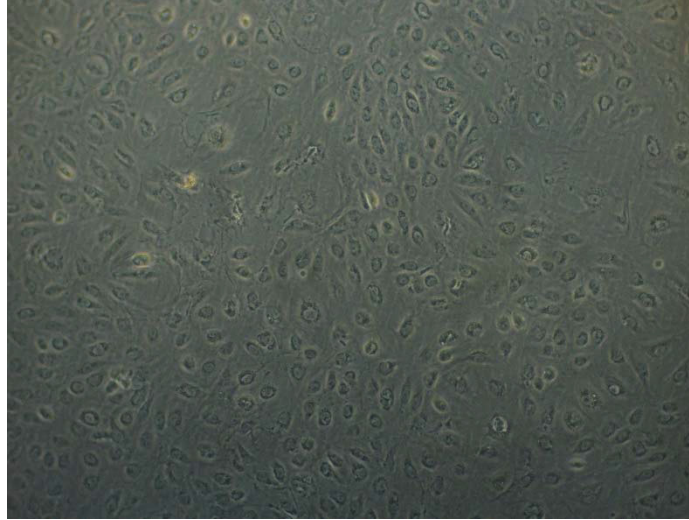


Figure 2.13. Phase contrast image showing confluent monolayer of HUVECs

MDA-MB-231 Cells

MDA-MB-231 is an epithelial-like breast cancer cell line derived from human metastatic mammary tissue. MDA-MB-231 cells have increased expression of epidermal growth factor (EGF) and transforming growth factor α (TGF α), and are aneuploid with chromosome counts near triploid range (ATCC). MDA-MB-231 cells have spindle shaped morphology although it is characteristic of this cell line to have some rounded up cells (Figure 2.14). MDA-MB-231 cells are about 100 μm in size for attached cells. This cell line is a triple negative breast cancer (TNBC), lacking estrogen receptors (ER-), progesterone receptors (PR-) and HER2. This triple negative indicates that the cancer growth is not estrogen and progesterone dependent and therefore the cell line does not respond to hormonal therapies such as tamoxifen. TNBC is often more aggressive and difficult to treat with an increased chance of re-occurrence and metastasis (nationalbreastcancer.org). Approximately 10-15% of all breast cancers are triple negative and often have poor patient outcome upon comparison to other breast cancer subtypes and therefore is a good model in the search for anticancer agents [162]. MDA-

MB-231 cells, like a number of other TNBCs, have a gain of function p53 mutation, leading to suppression of apoptosis in these cells which contributes to the poor patient outcome with this cancer type [162, 163]. Also, these cells tend to be well vascularized, and as such are likely to be responsive to VDA treatment.

ATCC Number: **HTB-26**™
Designation: **MDA-MB-231**

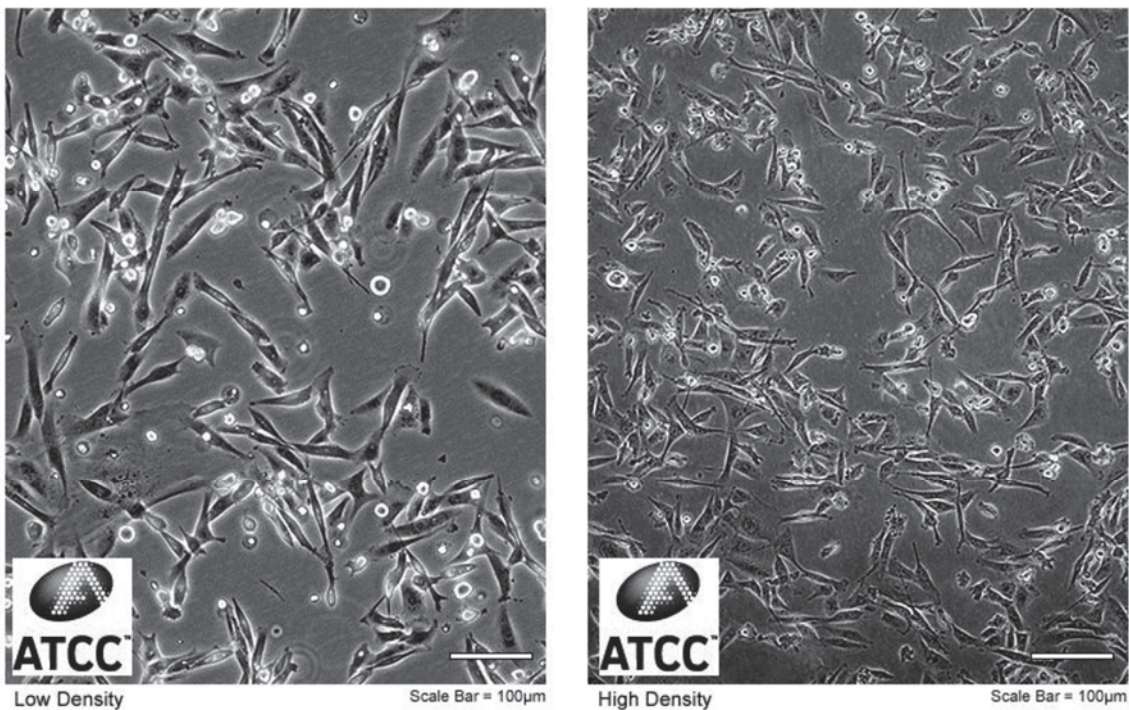


Figure 2.14. MDA-MB-231 cells in culture (ATCC website)

CHAPTER THREE

The Vascular Disrupting activity of OXi8006 in Endothelial Cells and Its Phosphate Prodrug OXi8007 in Breast Tumor Xenografts

This chapter published as: Strecker, T. E., Odutola, S. O., Lopez, R., Cooper, M. S., Tidmore, J. K., Charlton-Sevcik, A. K., ... & Trawick, M. L. (2015). The vascular disrupting activity of OXi8006 in endothelial cells and its phosphate prodrug OXi8007 in breast tumor xenografts. *Cancer letters*, 369(1), 229-241.

Tracy E. Strecker ^{a,*}, Samuel O. Odutola ^{b,*}, Ramona Lopez ^c, Morgan S. Cooper ^a, Justin K. Tidmore ^a, Amanda K. Charlton-Sevcik ^a, Li Li ^c, Matthew T. MacDonough ^a, Mallinath B. Hadimani ^a, Anjan Ghatak ^{a,†}, Li Liu ^c, David J. Chaplin ^d, Ralph P. Mason ^c, Kevin G. Pinney ^{a,b} and Mary Lynn Trawick ^{a,b}

^a Department of Chemistry and Biochemistry, Baylor University, Waco, TX 76798-7348

^b Institute of Biomedical Studies, Baylor University, Waco, TX 76798-7348

^c Department of Radiology, University of Texas Southwestern Medical Center, Dallas, TX 75390-9058

^d OXiGENE Inc., South San Francisco, CA 94080

*These authors contributed equally to this work.

†Dr. Anjan Ghatak deceased July 22, 2003.

Corresponding Author:

Mary Lynn Trawick, Ph.D.
Department of Chemistry and Biochemistry,
Baylor University
One Bear Place 97348,
Waco, TX, 76798-7348
(p) 254-710-6857
(f) 254-710-4272
Mary_Lynn_Trawick@baylor.edu

Abbreviations: ANOVA- analysis of variance, BLI- bioluminescence imaging, CA4-combretastatin A-4, CA4P-combretastatin A-4 phosphate, DAPI- 4', 6-diamidino-2-phenylindole, DMSO- dimethyl sulfoxide, DTT- dithiothreitol, FAK- focal adhesion kinase, FDA- Federal Drug Administration, FITC- fluorescein isothiocyanate, GI₅₀- median growth inhibitory concentration, HRP- horseradish peroxidase, HUVEC- human umbilical vein endothelial cells, MLC- myosin light chain, NMII- non-muscular myosin II, OXi8006- 2-(3'-hydroxy-4'-methoxyphenyl)-3-(3'',4'',5''-trimethoxybenzoyl)-6-methoxyindole, OXi8007- 2-(3'-disodium phosphate-4'-methoxyphenyl)-3-(3'',4'',5''-trimethoxybenzoyl)-6-methoxyindole, PBS- phosphate buffered saline, PI- propidium iodide, PLSD- protected least significant difference, PMLC- phosphorylated myosin light chain, ROCK- RhoA kinase, SCID- severe combined immunodeficiency, SDS- sodium dodecyl sulfate, SRB- sulforhodamine B, VDA- vascular disrupting agent, Y-27632- (R)-(+)-*trans*-4-(1-aminoethyl)-N-(4-pyridyl)cyclohexanecarboxamide dihydrochloride

Abstract

This study describes the vascular disrupting ability and the mechanism of action of the indole-based tubulin-binding compound, OXi8006, and its water-soluble phosphate prodrug OXi8007. Treatment of rapidly proliferating human umbilical vein endothelial cells (HUVECs), used as a model for the tumor vasculature, with OXi8006 or OXi8007 caused microtubule disruption followed by extensive reorganization of the cytoskeletal network. The mechanism of action involved an increase in focal adhesion formation associated with an increase in phosphorylation of both non-muscle myosin light chain

and focal adhesion kinase. These effects were dramatically diminished by an inhibitor of RhoA kinase, a downstream effector of RhoA. Cell cycle blockade at G2/M and cytotoxicity towards rapidly proliferating HUVECs were also observed. Capillary-like networks of HUVECs were disrupted by the action of both OXi8006 and OXi8007. The prodrug OXi8007 exhibited potent and rapid dose-dependent antivasculature activity assessed by dynamic bioluminescence imaging (BLI) in an MDA-MB-231-luc breast cancer xenograft mouse model. By 6 hours post treatment, over 93% of the BLI signal was abolished with only a slight recovery at 24 hours. These findings were confirmed by histology. The results from this study demonstrate that OXi8007 is a potent vascular disrupting agent acting through an anti-microtubule mechanism involving RhoA.

Keywords: vascular disrupting agent (VDA), microtubules, focal adhesion kinase (FAK), bioluminescence imaging (BLI), breast cancer

Introduction

Tumors require an expanding vasculature in order to grow and metastasize. The immature, chaotic, rapidly growing, activated tumor vascular endothelium is distinct from the largely quiescent, remodeled, and mature normal endothelium. These differences, along with the observation that a limited number of blood vessels supply a large number of cancer cells in the tumor, present the tumor vasculature as a selective target for cancer therapy [148, 164, 165]. Vascular disrupting agents (VDAs) [98, 133, 166] are a promising class of anticancer agents that act on the pre-existing tumor vasculature and are distinct from angiogenesis inhibiting agents such as bevacizumab (Avastin™) that inhibit the growth of new blood vessels but have limited effects on large tumors [167, 168]. The tubulin-microtubule system is an important anticancer target [169] and the mechanism of tubulin-binding, small-molecule VDAs is potentially two-fold. The major effect is the rapid and pronounced shutdown of blood flow to solid tumors, depriving cancer cells of necessary oxygen and nutrients and resulting in extensive tumor necrosis, while leaving blood flow to normal tissues intact [98, 133, 165, 170]. The secondary effect results from direct antimitotic activity against tumor cells. Treatment with combretastatin A-4 (CA4), a VDA that has advanced to human clinical trials, has been reported to inhibit tumor cell invasion, migration and metastasis [171]. Despite the encouraging positive pre-clinical studies and human clinical trial results of members of this class of anticancer agents, no VDA has yet been approved by the FDA [137-139, 172, 173]. Clearly this provides an opportunity to expand the compound landscape available for therapy.

OXi8006 is one of the first indole-based, colchicine-site binding, inhibitors of tubulin assembly into microtubules. Our previous studies demonstrated that OXi8006 was a potent inhibitor of tubulin polymerization ($IC_{50} = 1.1 \mu M$) and competed with radiolabeled colchicine at the colchicine binding site of tubulin [28]. We also found OXi8006 to be cytotoxic against three evaluated human cancer cell lines, NCI-H460, DU-145 and SK-OV-3, with an average GI_{50} of 25.7 nM [28]. The core indole molecular structure is now widely represented as a key component of a variety of inhibitors of tubulin assembly [174], but OXi8006 remains one of the most active compounds in this group with respect to tubulin binding and cytotoxicity. The very limited solubility of OXi8006 in aqueous solutions led to the synthesis of its water-soluble disodium phosphate prodrug OXi8007[28]. In preliminary studies, Color-Doppler ultrasound was used to image pronounced selective interference with the tumor vasculature upon OXi8007 treatment using a SCID mouse model bearing a human prostate tumor xenograft (PC-3) [28] indicating vascular disrupting properties. In separate studies, only a minimal effect was observed in a mouse model of the Ewing's sarcoma family (TC-32) of tumors [175]. In this study, we confirm the VDA properties and provide information on the biochemical and biological mechanism of action of OXi8006 and its phosphate prodrug OXi8007 (Figure 3.1) [28, 29, 176].

In order to elucidate the mechanism of OXi8006 action, we assessed the cytoskeletal effects in rapidly proliferating endothelial cells which were used as a model for the tumor vasculature [177-179]. We observed that OXi8006 rapidly initiated loss of microtubules, which elicited other cytoskeletal reorganizations and pronounced morphology changes. These effects suggested that RhoA and the RhoA kinase pathway

are involved in the cell signaling events leading to cell rounding and detachment [98]. Since focal adhesions are also significantly involved in regulating cell contraction and movement, we examined the activation status of focal adhesion kinase. The ability of OXi8006 to induce G2/M arrest, act as a cytotoxic agent against HUVECs, and to disrupt a preformed tubular network of endothelial cells, all hallmarks of VDA action, was also investigated. We demonstrate conclusively that OXi8007 is able to effectively disrupt the tumor vasculature in a human breast cancer xenograft model in SCID mice at a dose that was well tolerated (OXi8007 is converted to OXi8006 by the abundant non-specific phosphatase enzymes present *in vivo*).

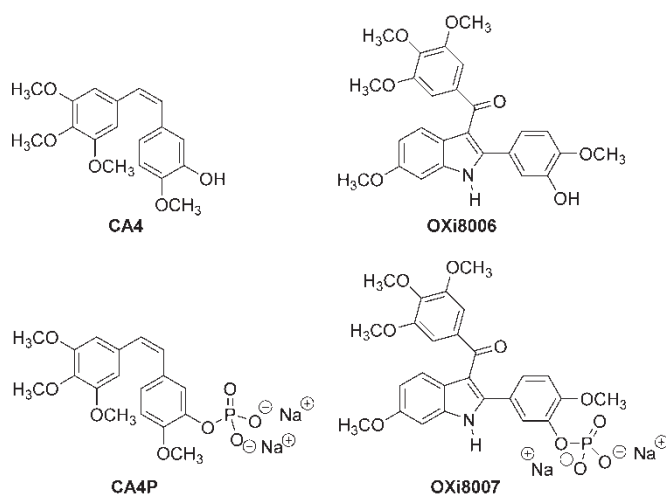


Figure 3.1. Small molecule inhibitors of tubulin assembly: vascular disrupting agent CA4 and its phosphate prodrug CA4P; OXi8006 and its phosphate prodrug OXi8007.

Materials and Methods

Compounds

CA4 and CA4P were obtained from OXiGENE Inc. (South San Francisco, CA), doxorubicin was obtained from Sigma-Aldrich, and OXi8006 and OXi8007 were synthesized as previously described [28, 29].

Cell Culture

HUVECs (Invitrogen) were grown on Collagen-I coated flasks (CELLCOAT®) in M200 medium (Invitrogen) supplemented with 1% gentamycin sulfate, 1% amphotericin B, and high growth factor supplement kit (Endothelial Cell Growth Kit-VEGF (ATCC)). HUVECs were not used beyond passage 5. MDA-MB-231 cells (ATCC) were cultured in DMEM supplemented with 10% fetal bovine serum (Gibco One Shot®) and 1% gentamycin sulfate, and passaged according to ATCC recommendations. Cells were maintained at 37 °C in a humidified atmosphere of 5% CO₂, for use in these experiments.

Fluorescence Imaging of Endothelial Cells

Actively proliferating HUVECs were cultured on glass coverslips coated with 1% gelatin. Cells were plated at 10,000 cells/coverslip in 6-well culture plates (Corning) using high growth factor supplemented medium and allowed to incubate at 37 °C for 48 hours (approximately 40% confluence) before being treated with compounds. Time dependent effects of compounds on HUVECs were measured using 10 nM compound for specific periods of time (5, 10, 15, 30, 60 and 120 minutes). Cells were also treated with increasing concentrations of compounds (2 nM-100 nM) for 2 h to observe dose

dependent effects. To demonstrate the response to higher compound concentrations, cells were exposed to 1 μ M of compound for 1 h. The effects of a Rho kinase inhibitor Y-27632 (Sigma Aldrich) were determined by pretreatment of cells (30 min) with 10 μ M of Y-27632 before incubation with compounds. Stock solutions were made by dissolving agents in DMSO, with a final concentration of DMSO less than 0.5% in media. After treatment, the cells were fixed and permeabilized via the addition of a solution that comprised 4% paraformaldehyde and 0.5% Triton X (Sigma-Aldrich) in PBS. Microtubules were detected using mouse anti- α -tubulin antibody (Sigma-Aldrich) followed by incubation with FITC-conjugated goat anti-mouse IgG (Jackson ImmunoResearch, West Grove, PA), actin fibers were stained using Texas-red conjugated phalloidin (Invitrogen), and nuclear staining was carried out with DAPI. Focal adhesions were stained with anti-vinculin antibody (Invitrogen) and FITC-conjugated goat anti-mouse IgG (Jackson ImmunoResearch). Focal adhesion kinase (FAK) and myosin light chain (MLC) phosphorylation were stained with anti-pFAK^{Y397} antibody (Abcam, Cambridge, MA) and anti-pMLC (Ser18/Thr19) antibody (Cell Signaling, Beverly, MA) respectively, with FITC and Cy5 conjugated goat anti-rabbit secondary antibodies (Jackson ImmunoResearch). Fluorescence and phase contrast images were collected using an Olympus FV 1000 confocal microscope and Olympus fluoview software (Olympus Imaging America Inc., Center Valley, PA) using a 60x oil immersion objective.

Western Blotting

Activated HUVECs were grown on collagen I coated T75 flasks to approximately 70% confluence and treated with 1 μ M OXi8006 for defined periods of time. A higher cell confluence was required to obtain sufficient protein, and with these conditions, a higher OXi8006 concentration was required to obtain similar effects to the morphology experiments on cover slips. OXi8006 was removed, and cells were briefly washed twice with 5 mL of ice cold PBS. Whole cell lysates were prepared by adding 400 μ L of lysis buffer per flask (50 mM tris base, 2% SDS, 10% glycerol, 50 mM DTT), one protease inhibitor cocktail tablet (1 per 10 mL, cOmplete ULTRA Tablets™, Roche, Indianapolis, IN), and one phosphatase inhibitor cocktail tablet (1 per 10 mL, PhoSTOP™, Roche). Lysates were sonicated (Misonix Sonicator 3000, Thermo-Fischer, Pittsburgh, PA) and protein concentrations determined via a Bradford assay. Lysates (45 μ g protein/sample) were combined with NUPAGE™ loading dye and 500 mM DTT solution, separated on NUPAGE™ 4-12% Bis-Tris gels (Invitrogen) and electroeluted to Immobilon-P™ PVDF membranes (EMD Millipore). Membranes were incubated with primary antibodies for pFAK^{Y397} (Abcam), FAK (Cell Signaling), pMLC (Cell Signaling), and β -actin (Sigma-Aldrich). Anti-rabbit HRP and anti-mouse HRP secondary antibodies were obtained from Jackson ImmunoResearch. Protein bands were visualized using ECL Prime™ blotting detection reagent (GE, Piscataway, NJ) and ImageQuant LAS 4000 imaging system (GE). Analysis of bands was done using Licor Image Studio 4.0 software.

Cell Cycle Analysis by Flow Cytometry

HUVECs were plated into Collagen-I coated 6-well plates (Corning) at a concentration of 200,000 cells/well. Cells were allowed to adhere for 48 h before a 24 h incubation period with compounds. Cells were trypsinized and then centrifuged at 800g for 10 minutes. After suspension in PBS, the cells were fixed with 70% ethanol and incubated overnight at -20°C. Fixed cells were centrifuged at 800g to remove ethanol and then resuspended in a PBS solution containing RNase A (20 µg/mL) and stained with propidium iodide (PI) (20 µg/mL). DNA content was measured using a FACSCalibur flow cytometer (Becton-Dickinson, San Jose, CA), and data were analyzed using CellQuest software (Becton-Dickinson).

Cytotoxicity Assay

The sulforhodamine B (SRB) assay was used to assess inhibition of human cell line growth as previously described [29, 180, 181]. Briefly, HUVECs and MDA-MB-231 cells were plated at 9,000 cells/well in 96-well plates (Corning) and incubated for 24 h or for 48 h (for a quiescent/confluent HUVEC population). Ten-fold serial dilutions of the compounds to be tested were then added to the wells. After 48 h of treatment, the cells were fixed with trichloroacetic acid, stained with SRB dye (Acid Red 52) (TKI, Tokyo), and dried. The dye was solubilized with 10 mM Tris base solution and plates were read at 540 nm with an automated Biotek Elx800 plate reader (Biotek, Winooski, VT). Absorbance values were then normalized to 630 nm to account for background absorbance [182]. A growth inhibition of 50% (GI₅₀ or the drug concentration causing a 50% reduction in the net protein staining relative to controls) was calculated from optical

density data with Excel software. Dose response curves were generated using Graphpad Prism 5.0.

Endothelial Tube Disruption Assay

HUVECs were plated in 24-well culture plates (Corning) that had been coated with 0.5 mL of 9.5 mg/mL MatrigelTM (Becton-Dickinson). Cells were plated at a concentration of 124,000 cells/well, at 37°C for 16 h in M200 supplemented with a high growth factor supplement kit. After 16 h, tube disruption was induced by treatment with varying concentrations of compounds for 2 h, after which the compound was removed and the cells were washed twice with fresh M200. Cells were imaged using an Axiovert 40 CFL inverted microscope (Zeiss, Thornwood, NY) at 5X magnification, and bright field images were collected with negative contrast using a Canon Powershot A640 digital camera mounted onto the microscope.

In Vivo Tumor Model

Human breast cancer cells, MDA-MB-231 (ATCC), were transfected with a lentivirus containing a firefly luciferase reporter. Highly expressing stable clones were isolated to create the cell line, MDA-MB-231-Luc [183]. Induction of tumors was carried out by injecting 10^6 cells mixed with 30% MatrigelTM (BD Biosciences, San Jose, CA) into the mammary fat pads of female SCID mice (University of Texas Southwestern Medical Center). Tumors were allowed to grow to approximately 5 mm in diameter, determined by caliper, before selection for BLI or histological analysis. All animal procedures were carried out in accordance with the Guide for the Care and Use of Laboratory Animals as adopted and promulgated by the U.S. National Institutes of Health

as well as the Institutional Animal Care and Use Committee approved protocols (University of Texas Southwestern Medical Center).

In Vivo Bioluminescence Imaging

Bioluminescence imaging was carried out as described previously [183]. Briefly, anaesthetized, tumor bearing mice (O₂, 2% isoflurane, Henry Schein Inc., Melville, NY) were injected subcutaneously in the fore-back neck region with 80 µL of a solution of luciferase substrate, *D*-luciferin (sodium salt, 120 mg/kg, in saline, Gold Biotechnology, St. Louis, MO). Mice were maintained under anesthesia (2% isoflurane in oxygen, 1 dm³/min,) while baseline bioluminescence imaging was performed using a Xenogen IVIS® Spectrum (Perkin-Elmer, Alameda, CA). A series of BLI images was collected over 35 minutes using the following settings: auto exposure time, f-stop = 2, Field of view = D, binning = 4 (medium). Light intensity-time curves obtained from these images were analyzed using Living Image® software. Mice were injected intraperitoneally with either 120 µl of saline (vehicle) or with OXi8007 in saline immediately after baseline BLI. Bioluminescence imaging was repeated, with new luciferin injections 2, 6 and 24 h later. Dose escalation studies using varying concentrations of OXi8007 (200-400 mg/kg) with three mice per concentration were performed except for 300 mg/kg where n=2. Subsequently, a separate cohort of mice (n=5) was treated with OXi8007 in saline (350 mg/kg) via intraperitoneal injection. BLI was again repeated for this cohort of mice after 2, 6 and 24 h. For comparison, other cohorts (n=5) of tumor bearing mice were treated with CA4P (120 mg/kg) or saline (control) IP and BLI was performed in a similar manner.

Immunohistochemistry

Histological analysis of tumor perfusion was carried out as previously described [184]. Tumor bearing mice were injected with saline or OXi8007. At each time point after injection (2, 6 and 24 h), the blue fluorescent dye Hoechst 33342 (10 mg/kg, Molecular Probes by Life Technologies, Eugene, OR) was injected into the tail vein of anaesthetized mice and the tumors were excised after 1 minute. Excised tumors were flash frozen in liquid nitrogen and stored at -80 °C. A series of 6 μ m sections from several regions of each tumor was collected, and the cryosections were immunostained with antibodies to the endothelial marker CD31, diluted 1:200 (BD Pharmingen, Purified Rat Anti-mouse CD31) followed by Cy3-conjugated secondary antibody 1:1000 (Jackson ImmunoResearch), and also stained with Hoechst 33342. Tumor sections were imaged with a Zeiss AxioScan Z1 confocal microscope using a 20X objective, and processed using ZEN 2012 software.

Statistical Methods

Data from the SRB assay are presented as mean \pm S.D. of a minimum of three independent experiments. Data from analysis of western blots are presented as mean \pm S.E.M. of a minimum of three independent experiments. In order to determine significant differences between treatment and control values, the Student's two-tailed *t* test was used, with analyses performed using Graphpad Prism 5.0. Analysis of dynamic BLI data was performed using Living Image software. Signal intensity was measured for regions of interest in tumors following luciferin injection, and maximum intensity was determined. Mean values \pm S.D. are presented for cohorts of tumors and statistical significance was assessed using an analysis of variance (ANOVA) on the basis of Fisher's Protected Least

Significant Difference (PLSD; Statview, SAS Institute, Inc., Cary, NC, USA). ANOVA was applied for comparison of multiple repeat measurements and the PLSD examined the importance of individual measurements on the overall population. Statistically significant data are denoted by: $*p < 0.05$, $**p < 0.01$, and $***p < 0.001$.

Results

OXi8006 Treatment Resulted in Profound Cytoskeletal Changes in Endothelial Cells

One characteristic of tubulin-binding VDAs is their disruption of cellular microtubules and a subsequent increase in actin stress fiber formation [185]. In tumor endothelium, this is followed by cell contraction and detachment from the substratum [186]. Indirect immunofluorescence staining showed that 10 nM OXi8006 caused disruption of microtubules in activated, rapidly proliferating HUVECs (grown in high growth factor containing VEGF, EGF, bFGF, IGF-1, and 2% FBS supplemented medium) used to model the tumor endothelium [177-179]. Starting at 5 minutes and progressing over the course of 2 h (Figure 3.2A), a profound loss of the microtubule network was observed. This was followed by actin cytoskeletal changes (starting approximately 30 minutes after treatment), as observed via Texas-Red conjugated phalloidin staining of F-actin (Figure 3.2B). F-actin in untreated cells is mainly found in bands in the cortical region at the periphery of cells as well as in a few fine filaments throughout the cell with some stress fibers observed. Microtubule disruption as effected by OXi8006 treatment resulted in significant formation of stress fibers across the cell body. At 10 nM OXi8006 concentration, a little over 50% of cells showed extensive stress fiber formation after 1 h, while at 2 h approximately 90% of cells showed this

effect. HUVEC cytoskeletal elements also responded to OXi8006 treatment in a dose dependent manner, with effects beginning at 10 nM, and increasing at 20 nM (Figure 3.3). Treatment with 100 nM OXi8006 for 2 h resulted in approximately 90% of HUVECs showing maximal stress fiber formation, with the remaining cells completely retracted from the substrate. HUVECs treated with OXi8006 (1 μ M) for 1 h demonstrated extensive cell contraction and rounding, as well as release of cells from the gelatin layer, with significant blebbing also observed in some cells (Figure 3.4). Treatment of HUVECs with OXi8007 showed similar effects although at higher concentrations (Figure 3.5).

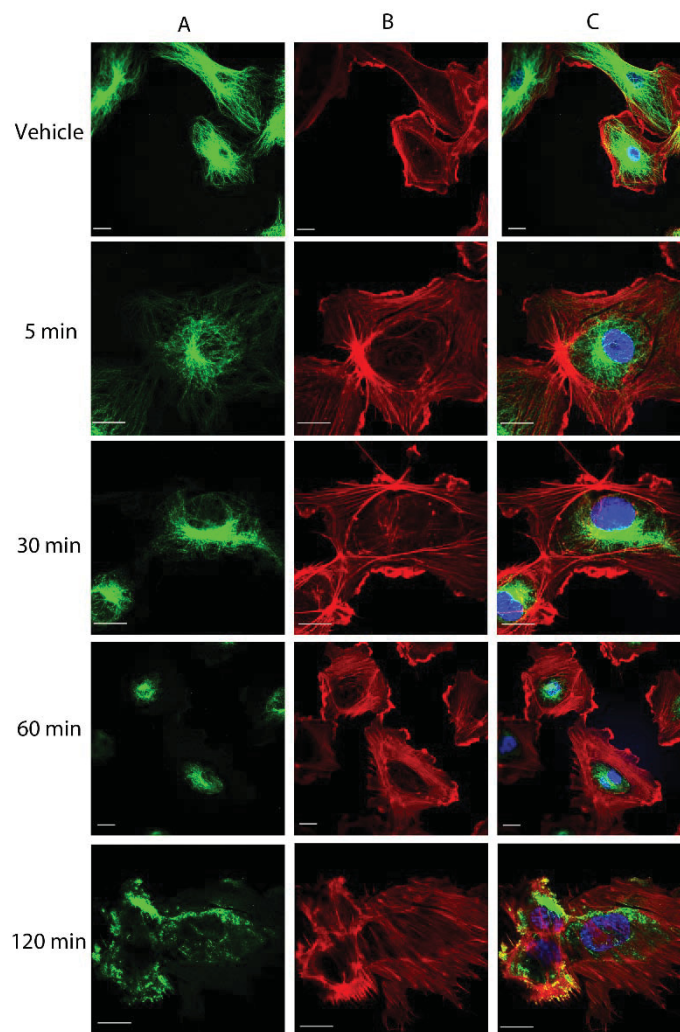


Figure 3.2. Representative confocal images of the morphological effects of OXi8006 treatment on activated HUVECs. Monolayers of rapidly growing HUVECs on gelatin-coated glass coverslips were treated with vehicle or 10 nM OXi8006 for the indicated times (5, 30, 60 and 120 min). Endothelial cells were fixed and stained with (A) anti- α -tubulin antibody (green, microtubules), (B) Texas red conjugated phalloidin (red, actin) and (C) DAPI (blue, nuclei), merged image. Bars, 20 μ m.

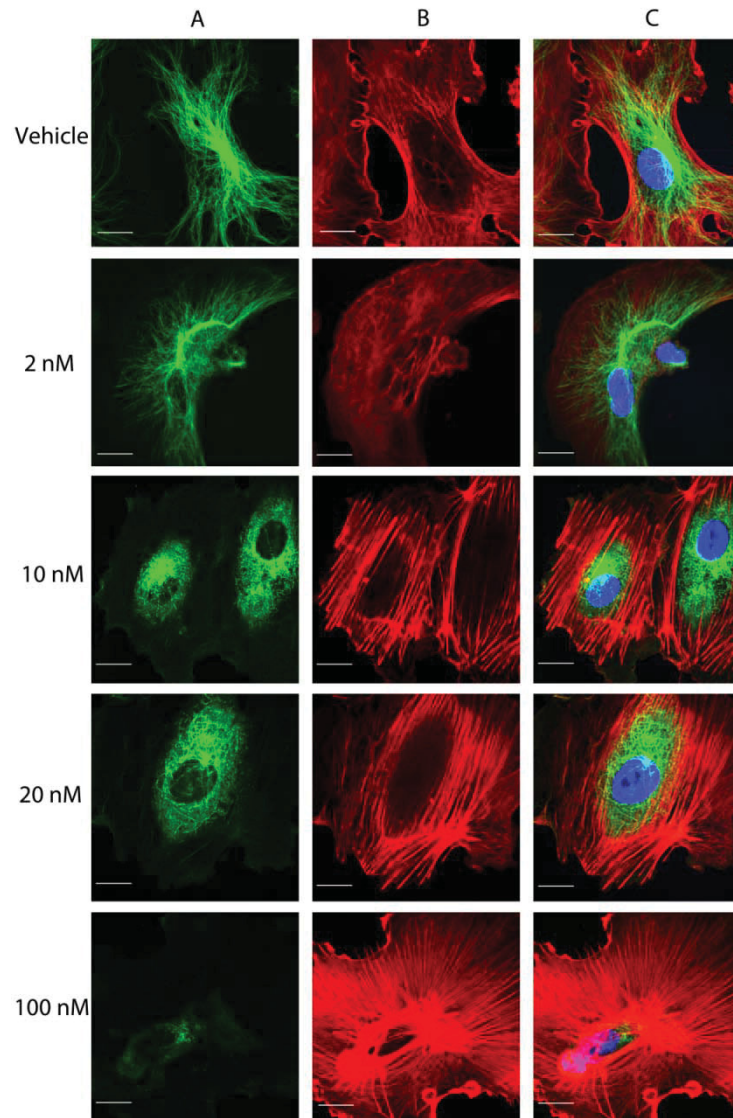


Figure 3.3. Representative confocal images of a concentration dependent increase in microtubule disruption and stress fiber formation with OXi8006 treatment of activated endothelial cells. Monolayers of rapidly growing human umbilical vein endothelial cells (HUVECs) on gelatin-coated glass coverslips were treated with vehicle or the indicated concentrations of OXi8006 (2, 10, 20 and 100 nM) for 2 h. The endothelial cells were fixed and stained with (A) anti- α -tubulin antibody (green, microtubules), (B) Texas red conjugated phalloidin (red, actin) and (C) DAPI (blue, nuclei), merged image. Bars, 20 μ m

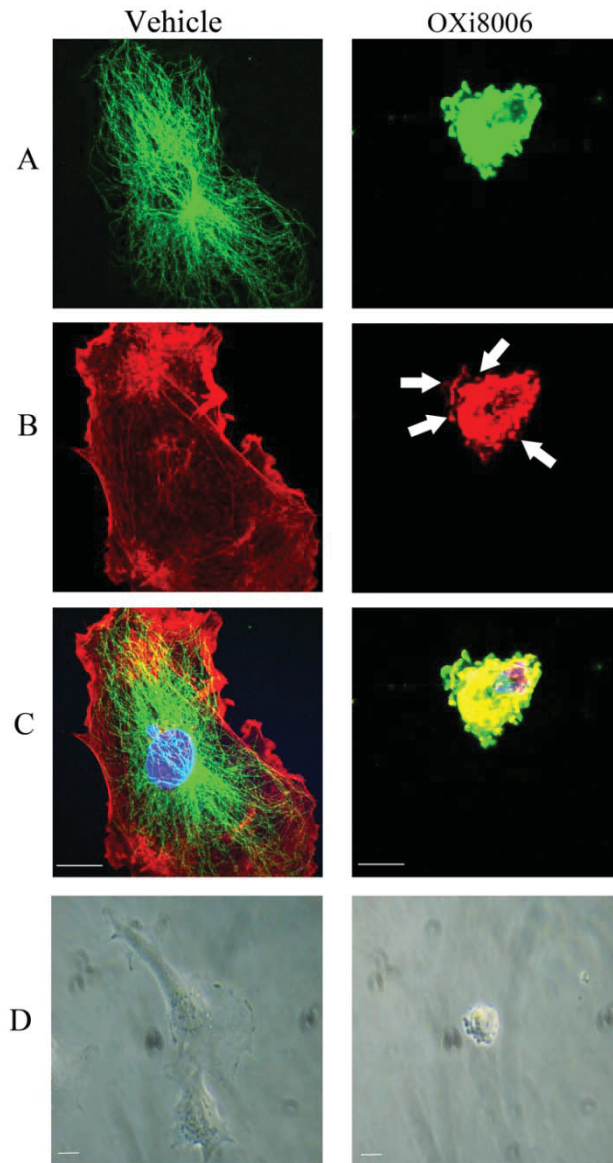


Figure 3.4 Representative images showing that activated endothelial cells exposed to a high concentration of OXi8006 demonstrate retraction from the gelatin substratum, contraction and rounding up of the cells. Many of the cells also demonstrated significant blebbing (arrows). Monolayers of rapidly growing HUVECs on gelatin-coated glass coverslips were treated with vehicle or 1 μ M of OXi8006 for 1 h. The endothelial cells were fixed and stained with (A) anti- α -tubulin antibody (green, microtubules), (B) Texas red conjugated phalloidin (red, actin) and (C) DAPI (blue, nuclei), merged image. (D) Representative phase contrast images of treated and untreated HUVECs are shown. Bars, 20 μ m

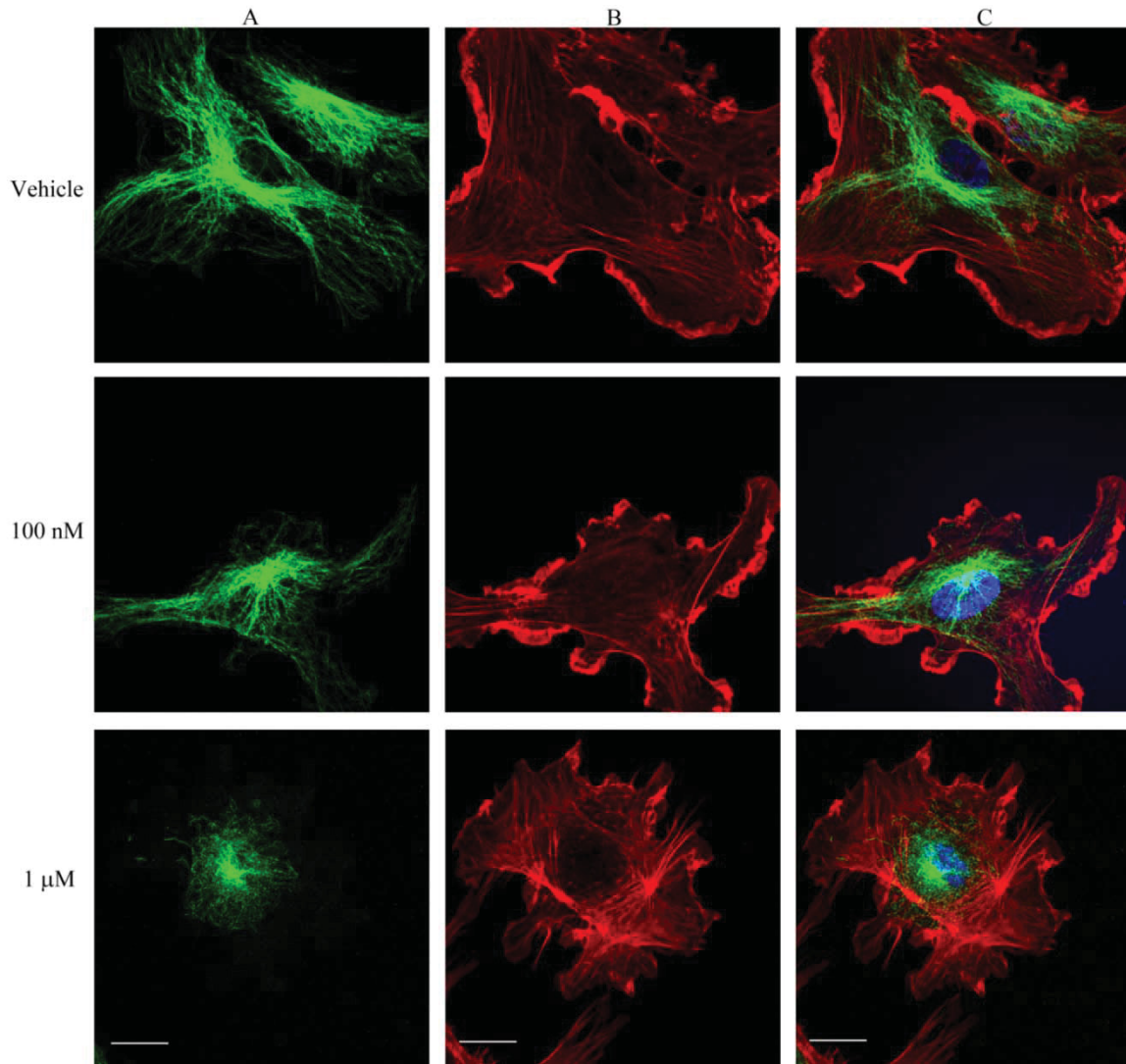


Figure 3.5. Representative confocal images demonstrating the morphological effects of OXi8007 treatment on activated HUVECs. Monolayers of rapidly growing HUVECs on gelatin-coated glass coverslips were treated with vehicle, 100 nM or 1 μ M OXi8007 for 2 h. Endothelial cells were fixed and stained with (A) anti- α -tubulin antibody (green, microtubules), (B) Texas red conjugated phalloidin (red, actin) and (C) DAPI (blue, nuclei), merged image. Bars, 20 μ m. While the effects of OXi8007 treatment on activated HUVECs are similar to those of OXi8006, OXi8007 is not as active as OXi8006 in this experiment (see Figure 3.2), presumably due to the time required for cleavage of the phosphate from OXi8007 to form OXi8006 by a non-specific phosphatase enzyme.

OXi8006 Treatment Increased HUVEC Contractility through Increased Myosin Light Chain Phosphorylation

Non-muscle myosin II plays an important role in actin bundling into stress fibers and the cell contractile system, and its activity is mediated via phosphorylation of the regulatory light chains of this protein. To examine the effects of OXi8006 on MLC signaling in HUVECs, western blot analysis was performed with an antibody to MLC phosphorylated at Thr-18 and Ser-19. After treatment of activated, sub-confluent HUVECs with 1 μ M OXi8006, an increase in MLC phosphorylation over time was observed, with maximal phosphorylation occurring at approximately 30 minutes followed by a decrease in phosphorylation (Figure 3.6 A, B). Indirect immunofluorescence staining of sub-confluent HUVECs treated with 100 nM OXi8006 also showed increased MLC phosphorylation, with pMLC co-localizing with OXi8006 induced actin stress fibers (Figure 3.6 E).

OXi8006 Treatment Induced an Increase in Focal Adhesion Formation and Focal Adhesion Kinase Signaling

Focal adhesions are assemblies of proteins that link actin stress fibers through integrins to the extracellular matrix. The formation of focal adhesions is a key component of cytoskeletal contractility and cellular adhesion [187-189]. Vinculin, a scaffolding protein that is recruited to focal adhesions, was used to assess the formation of focal adhesions by indirect immunofluorescence staining. OXi8006 induced microtubule disruption led to increased focal adhesion formation (as shown by an increase in vinculin staining (Figure 3.7)) localized to the ends of actin stress fibers (as seen from the merged images (Figure 3.7)). Focal adhesion kinase (FAK) activation through phosphorylation is a crucial step in the control of focal adhesion formation and turnover [187, 190].

Treatment with OXi8006 resulted in a concentration and time dependent downstream increase in FAK phosphorylation at Tyr-397 as observed via western blotting (Figure 3.6 C and D) and immunofluorescence staining (Figure 3.6 F). Western blotting showed an initial increase in phosphorylation occurring about 3 minutes after treatment, with maximal phosphorylation seen approximately 30 - 60 minutes after treatment followed by a decrease in phosphorylation.

OXi8006 Induced Changes in HUVEC Contractility and Adhesion were Mediated via RhoA

Previous studies implicated the intracellular switch RhoA and its downstream effector RhoA kinase (ROCK) in the mechanism of VDA action. In order to ascertain whether the RhoA signaling pathway is needed for the changes in HUVEC contractility and adhesion caused by OXi8006 treatment, the effects of Y-27632 (a compound that inhibits the activity of ROCK [191]) on OXi8006 mediated cytoskeletal changes were examined. Pre-treatment of cells with Y-27632 prevented OXi8006 induced formation of actin stress fibers and focal adhesions (Figure 3.8 A, C), and reduced the basal levels of actin bundling and focal adhesion formation in untreated HUVECs. However, pre-treatment with Y-27632 had no effect on microtubule disruption caused by OXi8006 treatment (Figure 3.8 B). Application of Y-27632 also prevented the OXi8006 induced increase in MLC phosphorylation (Figure 3.9). This demonstrated that inhibition of ROCK abrogates the downstream effects associated with OXi8006 induced microtubule disruption and highlights the importance of RhoA in this signaling pathway.

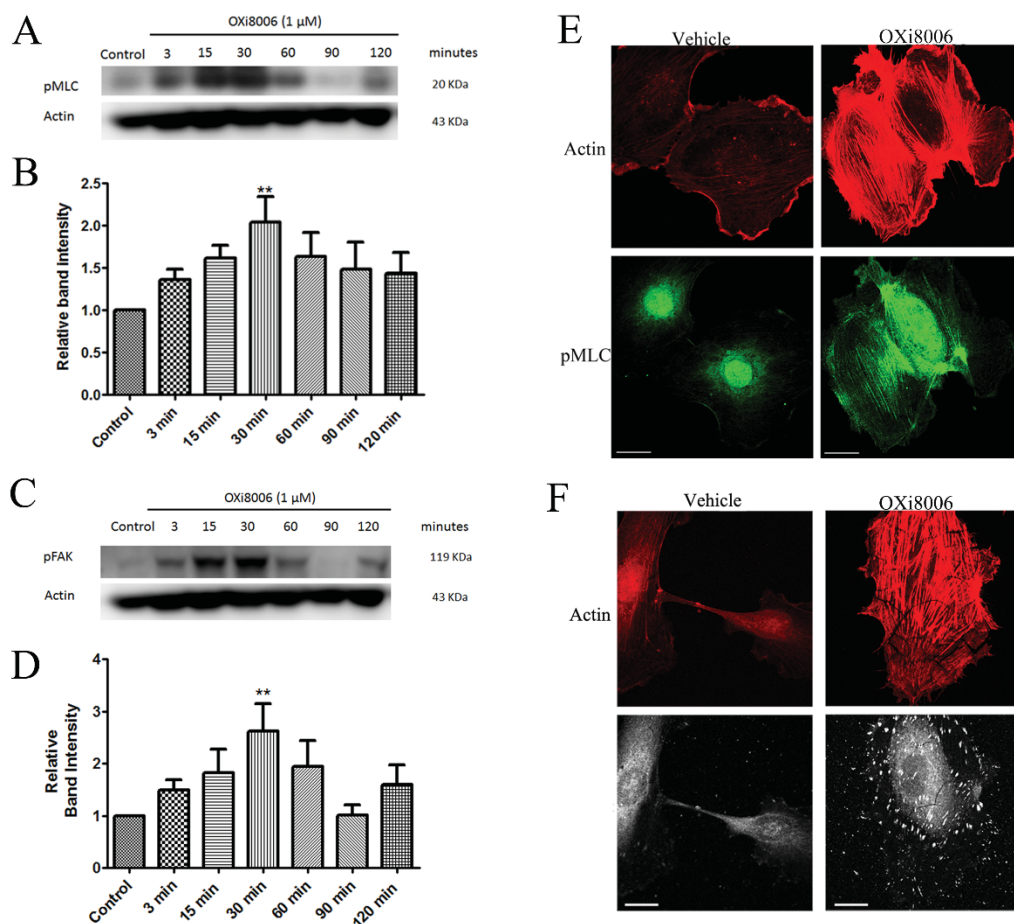


Figure 3.6. OXi8006 treatment of activated endothelial cells results in increased MLC and FAK phosphorylation. (A) Treatment (1 μ M) initiated increased MLC phosphorylation starting at 3 min and reaching a maximum at 30 min and then slowly decreasing. (B) Quantification of the optical density of the pMLC protein band (18 kDa) normalized to that of the actin band from Western blots of OXi8006-treated HUVEC lysates and untreated controls. (C) FAK phosphorylation (pY397) increased starting at 3 min, reaching a maximum at 30 min and then slowly decreasing. (D) Quantification of the optical density of the pFAK protein band (120 kDa) normalized to that of the actin band from western blots of OXi8006 treated HUVEC lysates and untreated controls. Data in bar graphs are presented as mean \pm S.E.M. ** $p < 0.01$. (E) Representative confocal images of cells treated with vehicle or 100 nM OXi8006 for 2 h and stained to show actin (red) and pMLC (green). (F) Representative confocal images of cells treated with vehicle or 100 nM OXi8006 showing increased actin stress fiber accompanied by an increase in FAK phosphorylation (pY397). Focal adhesions and pFAK were localized to each end of actin stress fibers. Cells were fixed and stained to show actin (red) and pFAK (white).

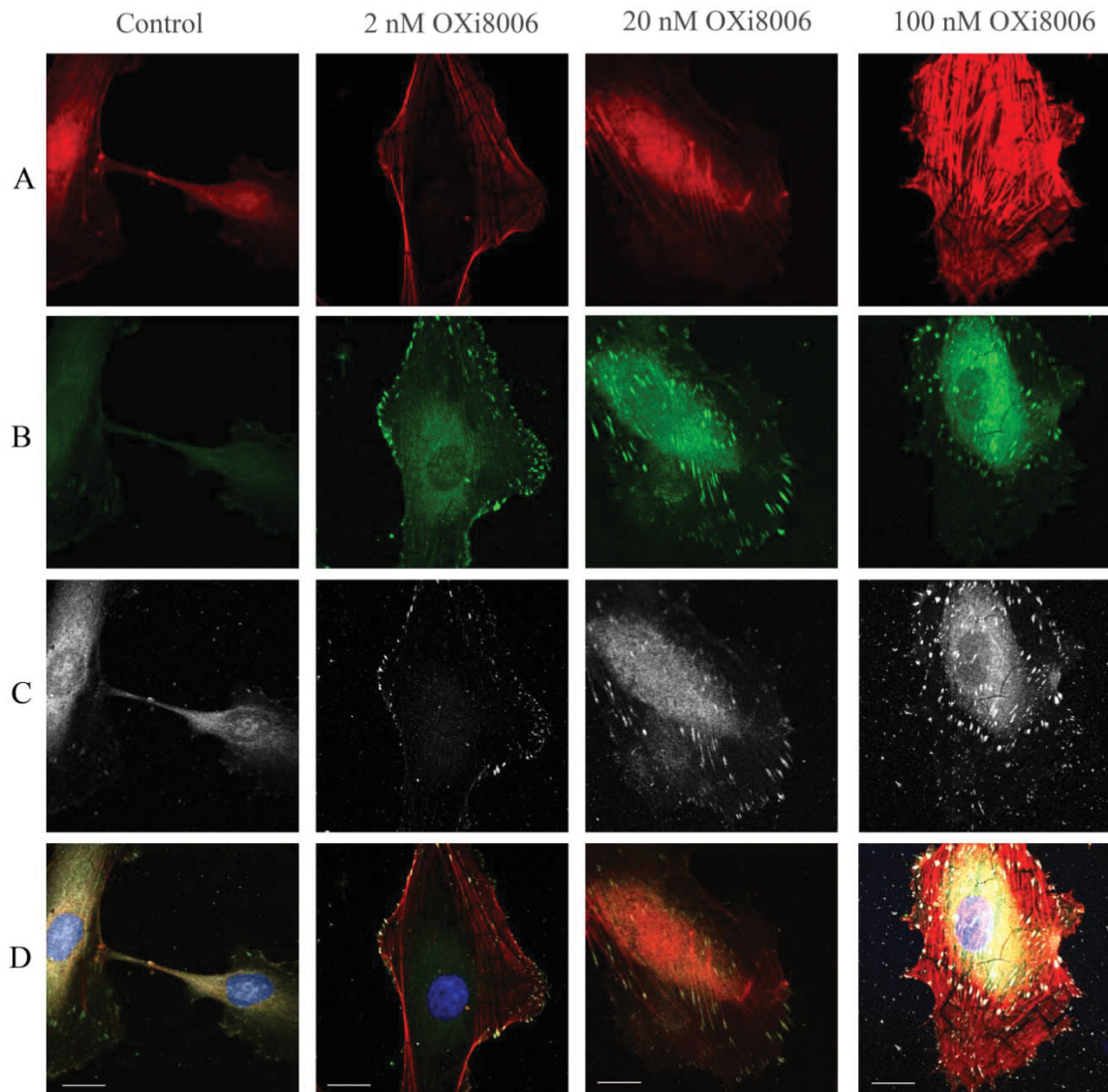


Figure 3.7. Representative confocal images of a concentration dependent increase in actin stress fiber and focal adhesion formation accompanied by an increase in focal adhesion kinase (FAK) phosphorylation (pY397) with OXi8006 treatment of activated endothelial cells. Focal adhesions and pFAK were localized to each end of actin stress fibers. Monolayers of rapidly growing HUVECs on gelatin-coated glass coverslips were treated with vehicle or the indicated concentrations of OXi8006 (2, 20 and 100 nM) for 2 h. The endothelial cells were fixed and stained with (A) Texas red conjugated phalloidin (red, actin), (B) anti-vinculin antibody (green, vinculin), (C) anti-FAK pY397 antibody (white, pFAK), and (D) DAPI (blue, nuclei), merged image. Bars, 20 μ m

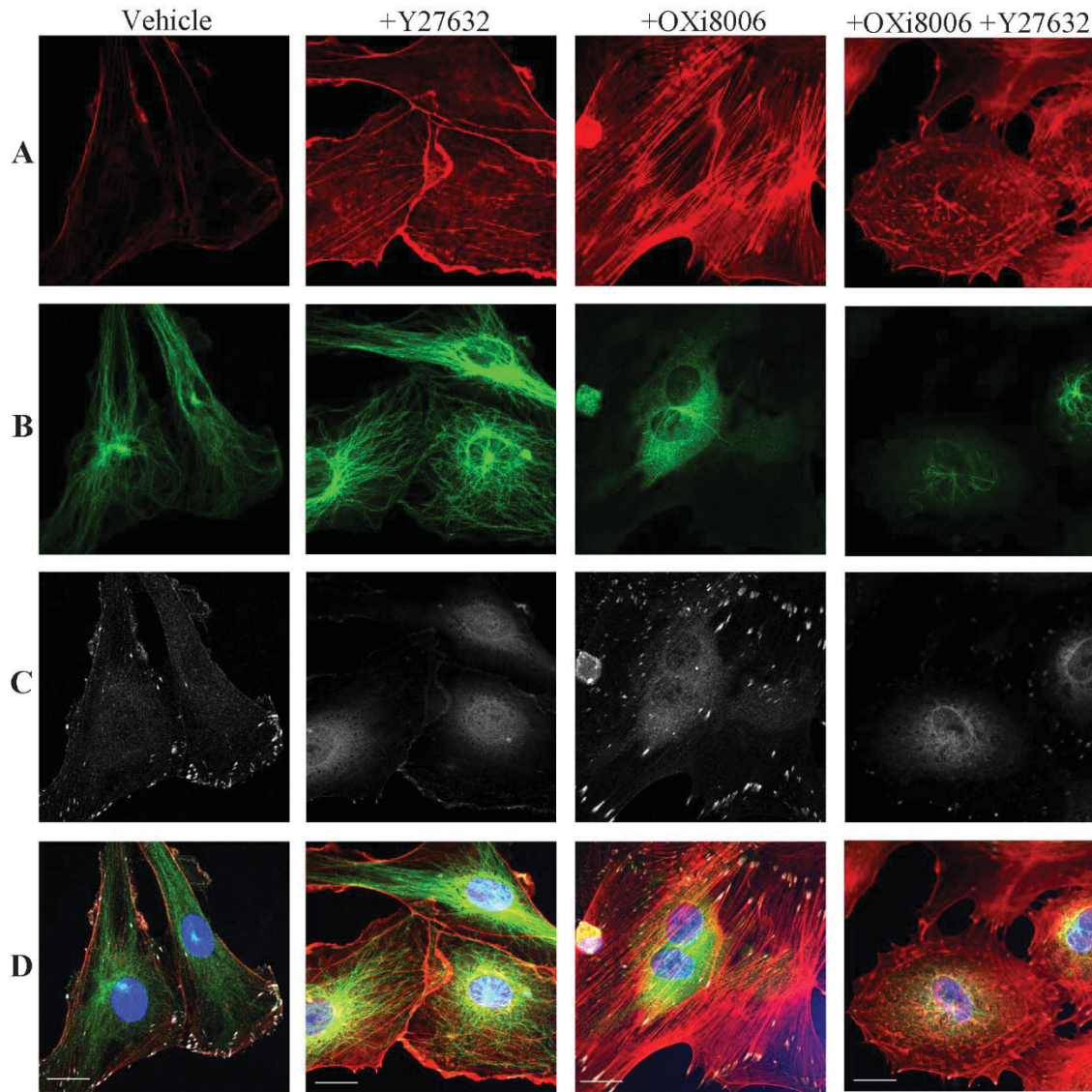


Figure 3.8. OXi8006 induced increase in stress fiber formation and phosphorylation of FAK (pY397), but not microtubule disruption, is mediated by RhoA/RhoA kinase. Monolayers of rapidly growing HUVECs on gelatin-coated glass coverslips were treated with vehicle, pre-treated for 30 min with 10 μ M of the ROCK inhibitor Y-27632 (+Y-27632), 100 nM OXi8006 for 2 h (+ OXi8006), or pre-treated for 30 min with 10 μ M of the ROCK inhibitor Y-27632 and then treated with 100 nM OXi8006 for 2 h (+Y-27632, + OXi8006). Representative confocal images for endothelial cells fixed and stained with (A) Texas red conjugated phalloidin (red, actin), (B) anti- α -tubulin antibody (green, microtubules), (C) anti-FAK pY397 antibody (white, pFAK), and (D) DAPI (blue, nuclei), merged image. Bars, 20 μ m.

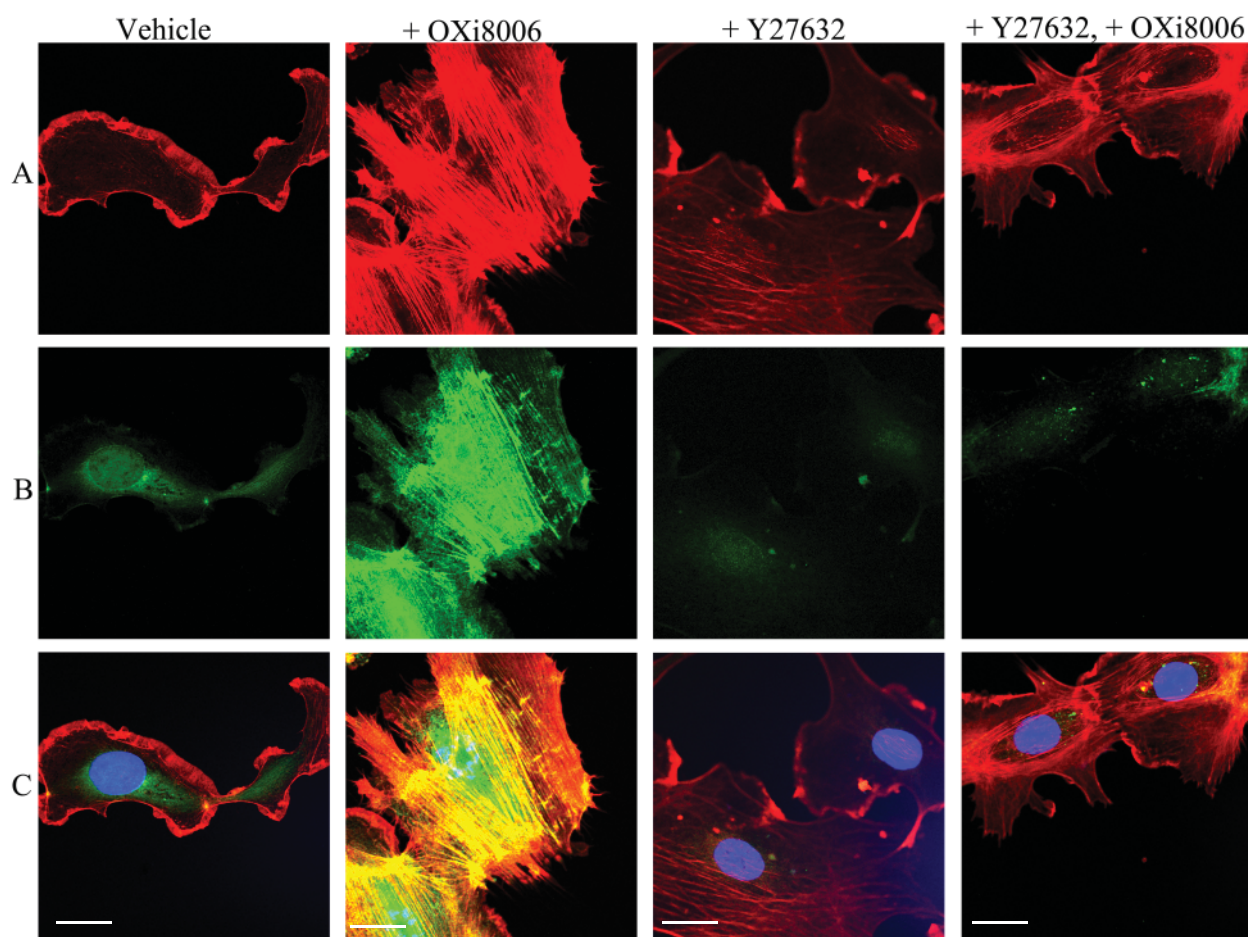


Figure 3.9. Representative confocal images demonstrating that the increase in phosphorylation of myosin light chain (T18/S19) observed upon OXi8006 treatment of activated endothelial cells is mediated by RhoA and its downstream effector RhoA kinase (ROCK). Monolayers of rapidly growing HUVECs on gelatin-coated glass coverslips were treated with vehicle (0.5% DMSO), pre-treated for 30 min with 10 μ M of the ROCK inhibitor Y-27632 (+Y-27632), treated with 100 nM OXi8006 for 2 h (+OXi8006), or pre-treated for 30 min with 10 μ M of the ROCK inhibitor Y-27632 and then treated with 100 nM OXi8006 for 2 h (+Y-27632, + OXi8006). The endothelial cells were fixed and stained with (A) Texas red conjugated phalloidin (red, actin), (B) anti-phosphomyosin light chain (T18/S19) antibody (green, pMLC), and (C) DAPI (blue, nuclei), merged image. Bars, 20 μ m.

Cytotoxicity and Cell Cycle Effects of OXi8006 and OXi8007

The cytotoxicity of OXi8006 and OXi8007 was evaluated against rapidly proliferating, sub-confluent HUVECs to model the activated tumor endothelium and compared to nearly confluent HUVECs as representative of the low proliferating baseline of normal mature endothelium. Cytotoxicity was evaluated using the standard SRB assay, and results showed that OXi8006 and its corresponding prodrug salt OXi8007 caused significant inhibition of cell growth of activated HUVECs (grown in medium supplemented with a high growth factor kit). The GI₅₀ values were in the low nanomolar range (Table 3.1). When HUVECs were grown to near confluence, there was a significant decrease in the cytotoxicity associated with OXi8006 treatment. Cytotoxicity reached a plateau and did not increase beyond 50% inhibition of cell growth, even at very high OXi8006 concentrations (> 100 μ M). Similar effects were observed for OXi8007 treatment of confluent HUVECs (Figure 3.10). The activity of OXi8006 and its corresponding prodrug salt OXi8007 were most effective on the most activated HUVECs. A progressive loss of activity was observed as the level of HUVEC confluence increased. OXi8006 and OXi8007 also caused significant inhibition of proliferation of the human triple negative breast cancer cell line MDA-MB-231 (Table 3.1).

One characteristic feature of tubulin-binding VDAs is their ability to induce antimitotic effects via blockade at the G2/M phase of the cell cycle with longer term exposure. HUVECs were treated with vehicle (0.5% DMSO in media), OXi8006 (0.01 - 0.1 μ M), and OXi8007 (0.025 – 1 μ M) for 24 h. Analysis of the HUVEC DNA profiles via flow cytometry showed that OXi8006 and OXi8007 treatment caused a pronounced

increase in the percentage of cells blocked at G2/M (4N DNA content) as compared with the amounts in the vehicle treated cells (Figure 3.11).

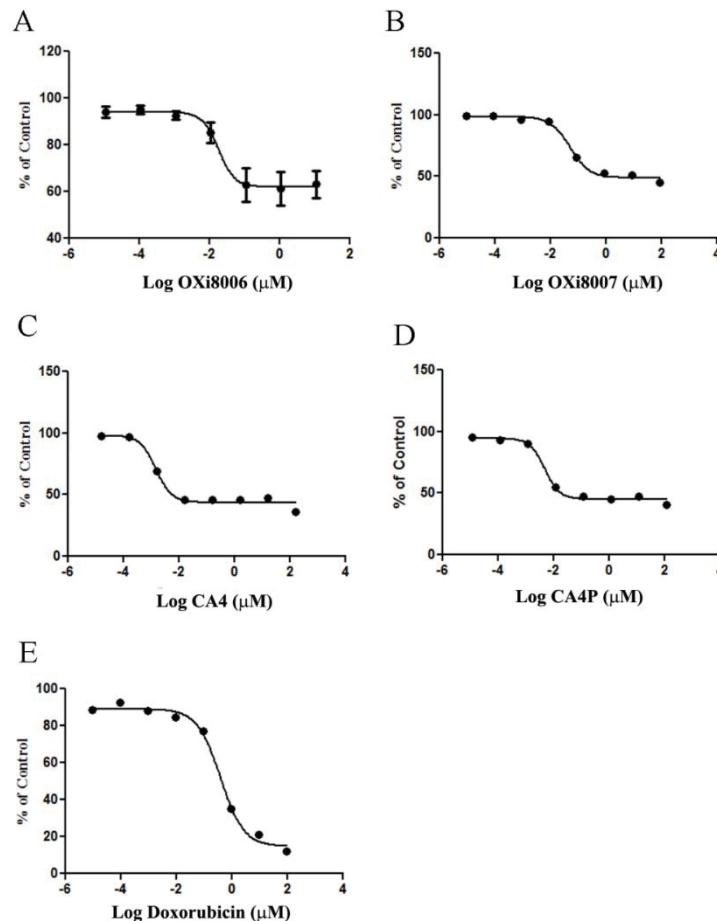


Figure 3.10. The cytotoxicity of tubulin binding VDAs and doxorubicin against nearly confluent HUVECs to model the low proliferating baseline of normal mature endothelium. Cytotoxicity was evaluated using the standard SRB assay for (A) OXi8006 (B) OXi8007 (C) CA4 (D) CA4P and (E) doxorubicin. A decrease in the cytotoxicity was observed for all tested compounds as compared with rapidly proliferating cells (See Table 1). Cytotoxicity reached a plateau and did not increase beyond 50% even at very high OXi8006 concentrations ($> 100 \mu\text{M}$). Similar effects were observed for OXi8007, CA4, and CA4P treatment of confluent HUVECs. In contrast, doxorubicin which has a separate mechanism of action [192] exhibited a typical dose-response curve with an EC_{50} of 400 nM ($38.8 \text{ nM} = \text{GI}_{50}$ for activated HUVECs). It should be noted that the growth controls at 24 h and those at 72 h were not significantly different reflecting the quiescent nature of the confluent HUVEC growth.

Table 3.1. OXi8006 and OXi8007 inhibited the growth of activated human umbilical vein endothelial cells (HUVECs) and human breast cancer cells (MDA-MB-231). Values were derived from SRB assay of a minimum of at least 3 independent experiments and are presented as averaged GI₅₀ values \pm S.D.

	Doxorubicin (nM)	OXi8006 (nM)	OXi8007 (nM)
HUVECs (activated)	48.7 \pm 45.9	33.4 \pm 1.13	40.6 \pm 9.9
MDA-MB-231	116 \pm 101	37.5 \pm 8.5	31.9 \pm 11.6

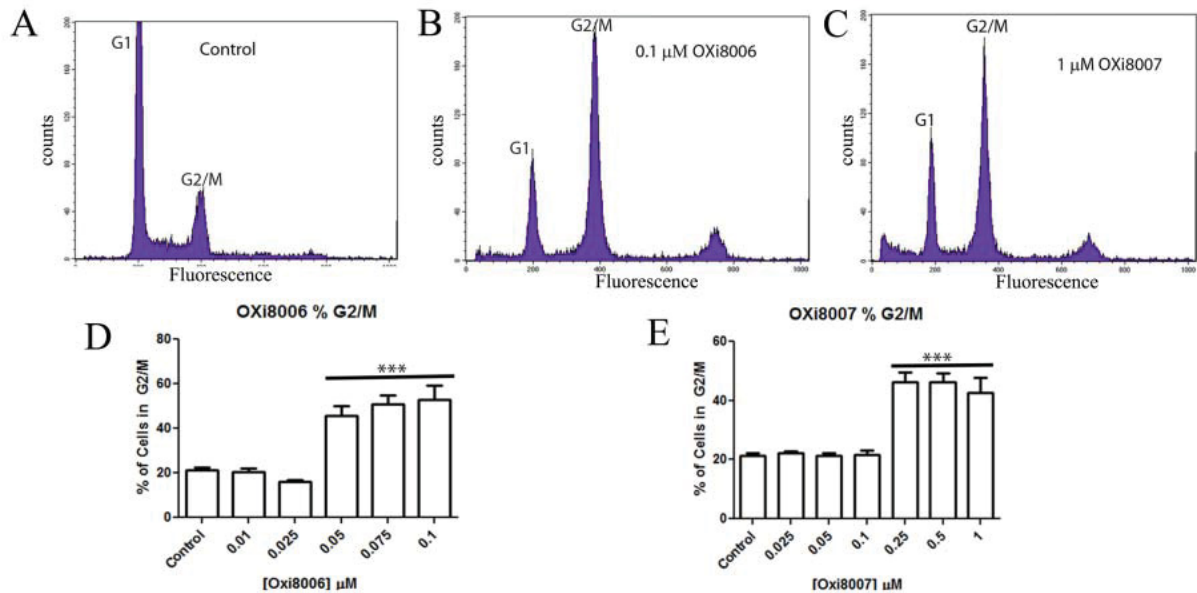


Figure 3.11. OXi8006 and OXi8007 induced G2/M arrest in HUVECs. (A-C) Representative DNA histograms and (D, E) bar graphs show concentration dependent increase in the fraction of cells arrested at the G2/M phase upon OXi8006 and OXi8007 treatment. DNA content was assessed by flow cytometry. Data in bar graphs represent three independent experiments and are presented as mean \pm S.E.M. *** $p < 0.001$

OXi8006 Treatment Resulted in a Disruption of Pre-established Vascular Networks

A property of endothelial cells is their ability to form a network of capillary tubes when plated at sub-confluent concentrations in the presence of an extracellular matrix and appropriate growth factors [177]. Upon plating on a dense coat of Matrigel™, HUVECs attach and generate mechanical forces on the surrounding extracellular support matrix to create tracks or guidance pathways that facilitate cellular migration, eventually resulting in the formation of a network of cells (Figure 3.12) which models neovasculature in two dimensions. This network retains the sensitivity to growth factors and VDAs that exists in the tumor vessels but is mostly absent in remodeled normal vasculature. Exposure of this endothelial tube network to OXi8006 caused a concentration-dependent disruption that resulted in rounded disorganized groups of endothelial cells (Figure 3.12). OXi8006 treatment resulted in significant effects at 0.1 μM with complete destruction of the network observed upon 1 μM treatment (Figure 3.12). OXi8007 demonstrated significant disruption at 1 μM (Figure 3.13).

In vivo Bioluminescence Imaging of the Vascular Disrupting Effects of OXi8007 in a Human Breast Cancer Xenograft in Mice

Tumor vascular disruption blocks the flow of the luciferin substrate to the tumor and results in a quantifiable decrease in bioluminescence signal [148, 184]. For control tumors maximum signal correlated with tumor size. At a volume of approximately 110 mm^3 tumors were evaluated for signal response to OXi8007. Following administration of luciferin substrate to the SCID mice bearing orthotopic luciferase-transfected MDA-MB-231 human breast cancer cells, bioluminescence signal was observed, which increased reaching a maximum intensity after 15-20 minutes followed by a gradual decline over the next 15 minutes (Figure 3.14 A, baseline). Repeat measurements in the control group

showed no significant difference in signal over a period of 24 h. However, dose-escalation with OXi8007 (200-400 mg/kg) demonstrated a dose-dependent decrease in maximum bioluminescence at 6 h after treatment (Figure 3.14 A, B). At each dose the tumors showed significantly lower mean maximum signal at 6 and 24 h compared with the same tumors at baseline ($p<0.05$; Figure 3.14 A, B and C). At 6 h each group showed significantly lower signal than the controls, though at 24 h only the 350 mg/kg group remained significantly different from controls. Thus, a dose of 350 mg/kg was found to be effective and well tolerated by the mice. Dynamic BLI was then used to compare the time dependent effect of OXi8007 versus CA4P (positive VDA control) or saline control on MDA-MB-231-luc xenografts growing in the mammary fat pad in a cohort of mice ($n=5$ each; Figure 3.15). BLI was evaluated before and after (2, 6, and 24 h) administration of VDA or saline. Fresh luciferin was administered on each occasion. Saline gave quite reproducible results with no significant changes in light intensity over 24 h (Figure 3.15 B, C) in terms of light distribution, maximum light intensity, and time to maximum light emission. Administration of OXi8007 (350 mg/kg, Figure 3.15 A, B) induced a decrease in normalized signal within 2 h by approximately 84% ($p<0.001$ vs. baseline), with a further decrease to a value of only 7% of that of the baseline when fresh luciferin was administered at the 6 h time point ($p<0.001$ vs. baseline). The bioluminescence emission remained significantly depressed for 24 h (by 87%) ($p<0.001$ vs. baseline), although some recovery was observed when compared to the 6 h time point. The results were compared to BLI of tumors in mice treated with CA4P (120 mg/kg), a vascular disrupting agent in clinical trials which we have previously verified to cause vascular shutdown in various tumors based on comparison of dynamic BLI, histology and

MRI [184, 193]. OXi8007 treatment resulted in significantly less recovery of BLI signal between 6 and 24 h than CA4P treatment ($p < 0.05$) (Figure. 3.15 D).

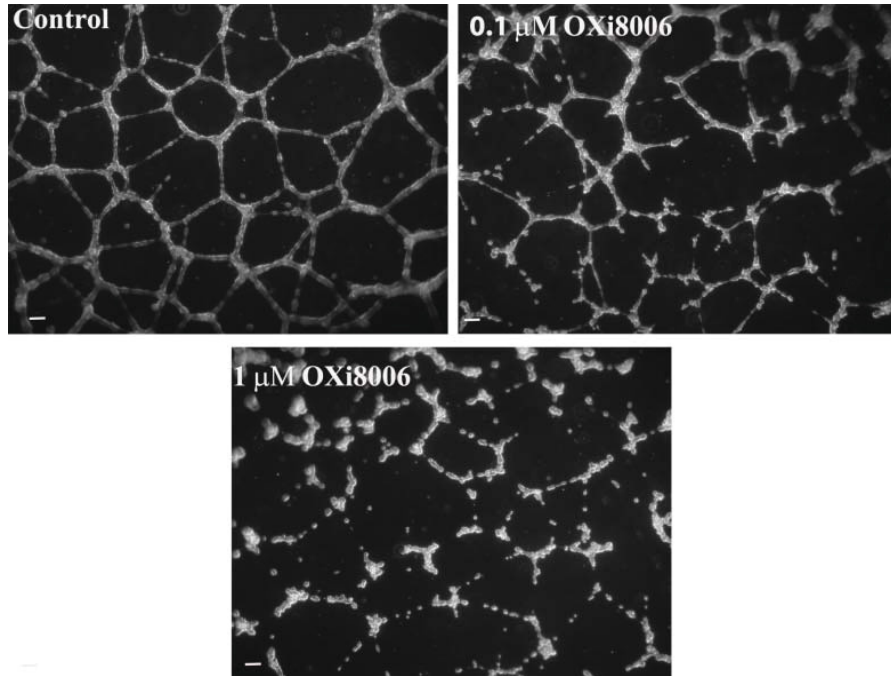


Figure 3.12. OXi8006 treatment disrupts pre-established endothelial capillary-like networks. Treatment (2 h) of pre-established endothelial capillary-like networks with OXi8006 showed a dose dependent increase in tube disruption (0.1 μM , top right, 1 μM , bottom). Cells were imaged with an inverted microscope (5x) and nine fields were photographed per well. A minimum of three independent experiments were carried out for each treatment, and representative images are shown. Bars, 100 μm .

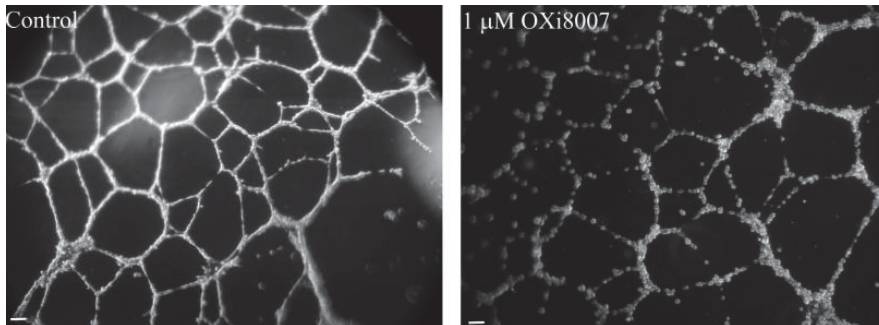


Figure 3.13. OXi8007 treatment disrupts pre-established endothelial capillary-like networks. HUVECs (124,000 cells/well) were seeded on 24 well culture plates densely coated with Matrigel™ and allowed to form capillary tube structures in growth factor enriched medium for 16

h. Treatment with 1 μ M OXi8007 for 2 h demonstrated endothelial tube disruption in approximately 33% of the images compared to vehicle treated (Control) capillary tubes. Cells were imaged with an inverted microscope (5x) and nine fields were photographed per well. A minimum of three independent experiments was carried out for each treatment. Bars, 100 μ m

Histological Confirmation of Decreased Tumor Perfusion after OXi8007 Treatment

To determine perfused vasculature, the fluorescent DNA-binding dye Hoechst 33432, which is rapidly taken up by vascular endothelial cells, was injected into mice at various time points (0, 6, and 24 h) after treatment (Figure. 3.16). Histology showed extensive perfusion of the pre-treated tumor (saline vehicle control) with a well-developed tumor vasculature as seen from CD31 (red) immunofluorescence staining. Tumor sections taken after treatment of mice with OXi8007 (350 mg/kg) showed lower intensity and distribution of the Hoechst perfusion marker (blue) by 6 h and only peripheral perfusion after 24 h. This reduction in perfusion was accompanied by a loss of endothelial cells or a reduction in tumor blood vessel diameter as confirmed by reduced CD31 immunofluorescence at 6 h which was further decreased at 24 h with the exception of the viable outer rim of the tumor. These results are consistent with significant vascular disruption.

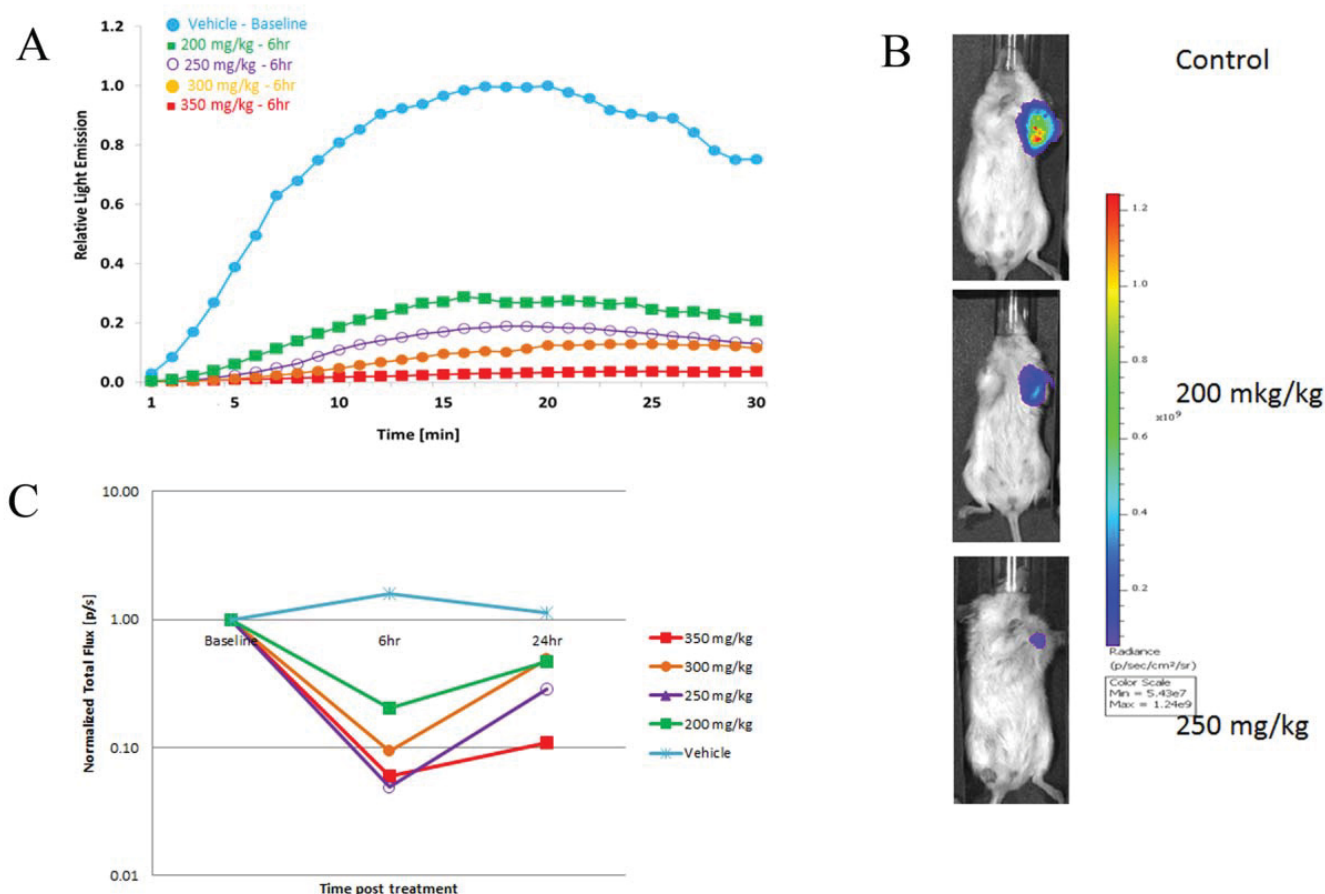


Figure 3.14. Dynamic BLI assessment of dose escalation response to OXi8007. Increasing doses of OXi8007 were administered to SCID mice bearing luciferase expressing MDA-MB-231-luc human breast cancer xenografts. Dynamic BLI was performed at baseline, and repeated 6 h and 24 h after OXi8007 with fresh luciferin administered SC (120 mg/kg) on each occasion. (A) Representative signal intensity curves for individual tumors showing increase of light emission over 15 minutes following administration of luciferin. Highest signal was seen for control tumor (blue) with lower signals for higher doses of OXi8007 (200 mg/kg green, 250 mg/kg purple, 300 mg/kg orange, 350 mg/kg red). (B) Images for control, 200 and 250 mg/kg showing maximum signal about 17 min after luciferin administration. (C) Normalized mean signal intensity for groups of tumors at each dose observed 17 minutes after luciferin was administered showing dose dependent vascular shutdown (n=3 tumors per group except 300 mg/kg where n=2).

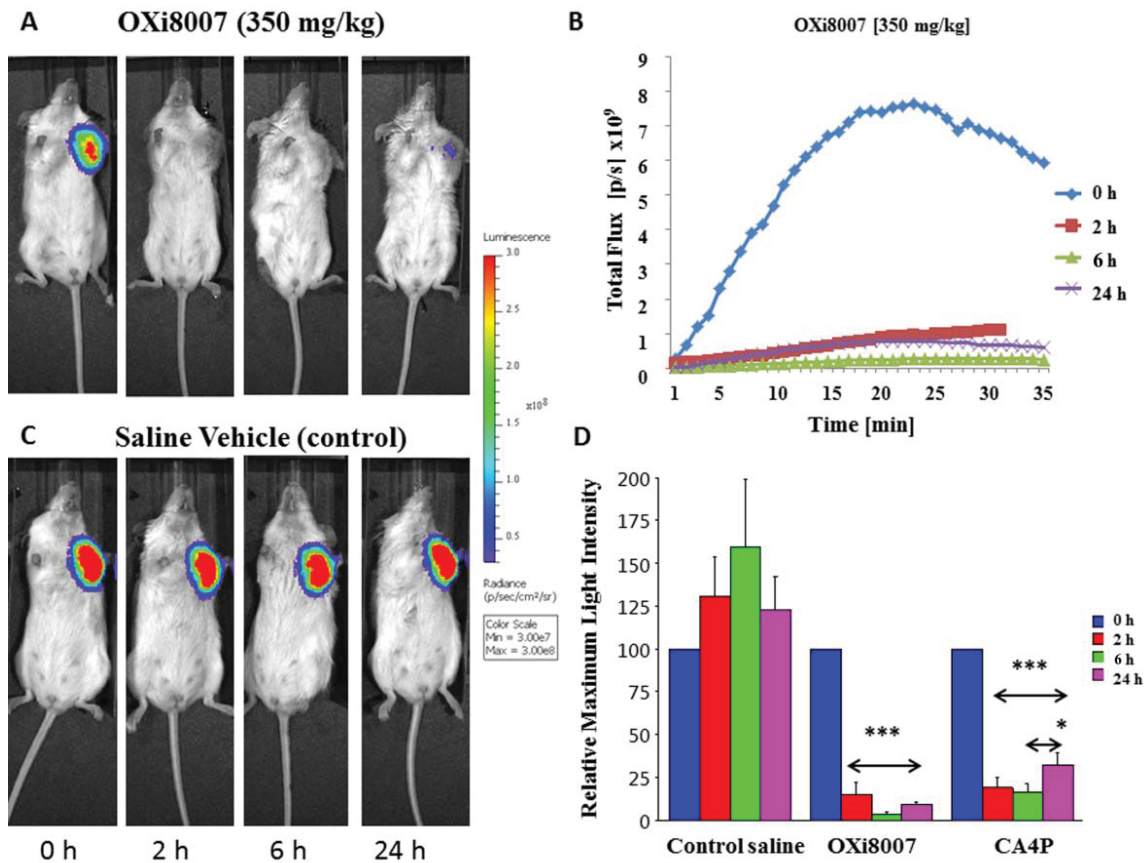


Figure 3.15. MDA-MB-231-luc breast tumor response to OXi8007 treatment assessed by BLI. Sequential images of representative SCID mice bearing orthotopic MDA-MB-231-luc breast tumors growing in the mammary fat pad were obtained following administration of (A) OXi8007 (350 mg/kg) (C) and saline vehicle. Signals were obtained at 2, 6, and 24 h after treatment and 15 minutes after fresh luciferin substrate injection. (B) Representative dynamic BLI showing signal intensity evolution over 35 minutes for an MDA-MB-231-luc tumor from a mouse treated with OXi8007 (350 mg/kg). (D) Bar plot for normalized mean maximum BLI signal \pm S.D. of tumors from cohorts of mice ($n=5$) at different time-points post drug administration. OXi8007 and CA4P induced significant reduction in BLI of tumors (** $p < 0.001$, * $p < 0.05$). OXi8007 BLI signal remained low at 24 h whereas CA4P showed significant recovery between 6 and 24 h post treatment (* $p < 0.05$).

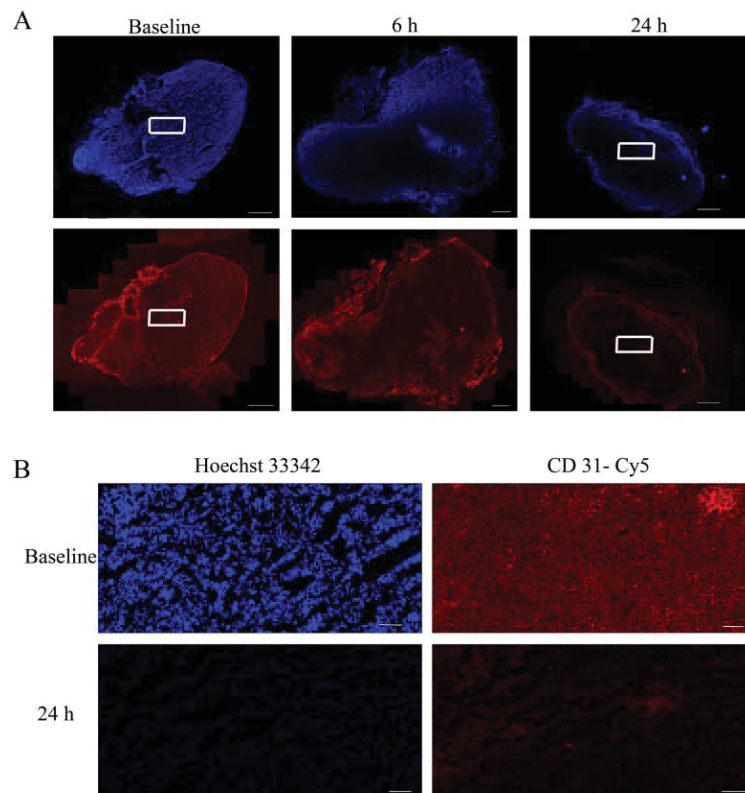


Figure 3.16. Histological evaluation of MDA-MB-231-luc tumor xenografts after OXi8007 administration confirmed vascular shutdown. (A) Hoechst 33342 dye was infused into mice (IV) 1 minute prior to sacrifice to selectively stain perfused regions. Tumor sections revealed tumor perfusion (top panel, blue) based on distribution of Hoechst 33342 and vascular structure based on Cy3-conjugated secondary antibody staining of CD31 (bottom panel, red) to show the presence of endothelial cells. There is general initial perfusion in vehicle treated mice, significant reduction of perfusion 6 h post administration, and only intense peripheral perfusion at 24 h post administration. The pattern of CD31 staining matches the perfusion seen with the Hoechst 33342 staining. Bars, 1000 μ m. (B) 20x images of baseline and 24 h treated tumor sections stained with Hoechst 33342 dye and Cy3-conjugated secondary antibody for CD31. Images are taken from area corresponding to white rectangles in 9A. Bars, 100 μ m.

Discussion

In order to demonstrate the vascular disrupting properties and elucidate the mechanism of action of OXi8006 (the proposed mechanism is shown in Figure 3.17), we performed a series of biochemical and biological experiments in HUVECs. The dynamic assembly and disassembly of microtubules is essential for cell growth, motility, and signaling, thus making it an important anticancer target. OXi8007 is dephosphorylated by non-specific phosphatases, and the effector anti-cancer agent (OXi8006) is proposed to enter cells by simple diffusion (Figure 3.17). In a dose- and time-dependent manner, OXi8006 treatment resulted in microtubule disruption in rapidly proliferating endothelial cells as determined by immunofluorescence confocal microscopy. At a minimal effective concentration of 10 nM, OXi8006 treatment caused significant disruption of microtubules in HUVECs, which started within 5 minutes and progressed over the course of 2 h to a profound loss of the microtubule network (Figure 3.2).

In untreated or vehicle-treated HUVECs, actin is primarily visualized as filaments in the cortical layer at the cell periphery along with a baseline level of thick bundles of actin filaments (stress fibers) that are linked to the cell substratum through focal adhesions. Microtubule disruption, effected by OXi8006 treatment of rapidly proliferating endothelial cells, led to a dose- and time-dependent increase in actin stress fiber formation. With a higher concentration (1 μ M) of OXi8006 treatment, significant blebbing occurred in some cells, and extensive contraction (rounding up) and detachment from the gelatin layer was observed by fluorescence confocal and light microscopy, processes that precede VDA induced apoptosis [194]. Antiparallel actin bundling into stress fibers is aided by a number of actin binding proteins that play a role in the cell

contractile and force generation system. One essential member of this group of proteins is non-muscle myosin II (NM II) which binds and contracts filamentous actin in an ATP-dependent process. Comprised of three pairs of peptides, the two heavy chains of NM II assemble into a long α -helical coiled coil that forms an extended rod-shaped domain and two globular head groups with binding sites for both ATP and actin. The two essential light chains stabilize the heavy chain structure while phosphorylation of its two regulatory light chains at Thr-18 and Ser-19 mediate NM II activation [195]. Activation of NM II is associated with a conformational change leading to its assembly into bipolar filaments through interactions between the rod domains which bind to actin through their head groups, resulting in contractile myosin linked antiparallel actin stress fibers. We observed, by confocal immunofluorescence microscopy, that OXi8006 treatment (100 nM) led to increased phosphorylation of MLC and activation of NM II. This resulted in an increase in stress fiber formation. An examination by western blotting confirmed this increase in phosphorylation of MLC with a maximum occurring at 30 min post-treatment with 1 μ M OXi8006.

Focal adhesions are super assemblies of proteins that form at sites of tight adhesion linking the actin cytoskeleton through integrins to the extracellular matrix. They are made up of integrins and cytoskeletal and signaling proteins such as talin, α -actinin, vinculin, zyxin, paxillin, and focal adhesion kinase (FAK) among other components [188] and increase in response to contraction of the actin-myosin cytoskeleton. An increase in focal adhesions, localized to the ends of actin stress fibers, was observed as determined by anti-vinculin immunofluorescence upon OXi8006 treatment of activated HUVECs. FAK plays significant regulatory and structural roles during focal adhesion

reorganization. Regulation of FAK includes phosphorylation at multiple tyrosine and serine residues. Tyrosine 397 is the initial phosphorylation site of FAK and is involved in its activation [187, 196, 197]. Therefore, we examined the phosphorylation of FAK at this site and found that it increased in a concentration and time dependent manner in response to microtubule disruption as a consequence of OXi8006 treatment.

RhoA is a guanidine triphosphatase that regulates a number of cellular processes, including actin dynamics, cell contractility, and cell adhesion. Previous studies have shown that RhoA plays a significant role in focal adhesion regulation via FAK signaling [190, 198, 199]. Upon dissociation of GDP, RhoA binds GTP and activates Rho-associated kinase (ROCK), which in turn can increase the level of phosphorylation of myosin via direct phosphorylation of the regulatory light chain and/or by phosphorylation and inactivation of MLC phosphatase [200, 201]. In order to ascertain whether OXi8006 functions via this mechanism, activated HUVECs were treated with the RhoA kinase (ROCK) inhibitor Y-27632 prior to OXi8006 treatment. Pretreatment of HUVECs with Y-27632 did not inhibit microtubule disruption upon OXi8006 treatment, but it effectively inhibited the increase in actin stress fiber formation and myosin regulatory light chain phosphorylation. We also determined that pretreatment with Y-27632 prevented the increase in FAK phosphorylation (pY397) previously observed with OXi8006. Consistent with the activity and mechanism of action of a tubulin-binding VDA [98, 164, 185], we have confirmed the role of the intracellular switch RhoA and its downstream effector RhoA kinase in the proposed OXi8006 mechanism (Figure 3.17). We have also demonstrated the importance of FAK phosphorylation (pY397) in the

tubulin-binding VDA mechanism. These studies provided support for the proposed mechanism of OXi8007 action depicted in Figure 3.17.

An evaluation of the cytotoxicity using the standard SRB assay showed that OXi8006 and its corresponding prodrug salt OXi8007 caused significant inhibition of proliferation of activated HUVECs with GI₅₀ values in the low nanomolar range (Table 1). However, when HUVECs were grown to near confluence before treatment as a model for the low proliferating baseline of normal mature endothelium, there was a significant decrease in the cytotoxicity of OXi8006 and its prodrug OXi8007. These results suggest selectivity of OXi8006 and OXi8007 towards rapidly proliferating endothelial cells. These compounds were also very potent against MDA-MB-231 breast cancer cells consistent with their activity on other cancer cell lines [28, 29]. In separate experiments, the tubular capillary network that models tumor neovasculature that is formed by HUVECs plated on MatrigelTM was disrupted by OXi8006 in a concentration dependent manner as endothelial cells retracted and rounded up. The network of HUVEC tube structures began to break down after treatment with 0.1 μ M OXi8006 and was completely disrupted at a concentration of 1 μ M. Related to the microtubule disruption activity and cytotoxicity toward cancer cell lines, OXi8006 is an antimitotic agent and induced a cell cycle blockade at G2/M as determined by flow cytometry of activated HUVECs treated with OXi8006 for 24 h. This transition from cell populations mostly at G1 to a majority of cells at G2/M occurred between 25 and 50 nM OXi8006. OXi8007 treatment of HUVECs showed a similar effect but at a higher concentration (between 100 and 250 nM).

Dynamic bioluminescence imaging is a convenient and effective method to evaluate VDAs in luciferase-expressing cells growing as tumor xenografts in mice [148, 183, 184]. Tumor vascular disruption blocks the delivery of the luciferin substrate to the tumor and results in a quantifiable decrease in bioluminescence signal. From dose escalation studies assessed by BLI in xenograft SCID mice, 350 mg/kg of the water-soluble phosphate prodrug OXi8007 was determined to be the dose that was effective and well tolerated. At this dose, we demonstrated that OXi8007 was a potent VDA in a cohort of mice bearing xenograft tumors of luciferase-transfected human triple negative breast cancer (MDA-MB-231-luc) assessed by BLI. A decrease of 84% in normalized signal was observed within 2 h, with a further decrease (corresponding to 93% total loss) observed at the 6 h time point. Although there was some recovery at the 24 h time point, it was significantly less than what was observed with CA4P treatment, a VDA in human clinical trials [137, 139], used here for comparison. The in vivo BLI results of vascular disrupting activity that were observed after OXi8007 treatment were confirmed by histology. As with other VDAs [36], a persistent "viable rim" of tumor perfusion was observed at the interface of the tumor with normal tissue where the vasculature more closely resembles normal vasculature and which is largely unaffected by VDA action. The viable rim is the site where tumor regrowth is most likely to take place after VDA treatment. The BLI findings with OXi8007 are consistent with the previously observed acute selective tumor vascular shutdown using Color-Doppler ultrasound in a mouse bearing a PC-3 human prostate xenograft [28]. They also match longer term observations in separate cohorts of MDA-MB-231-luc breast tumor bearing mice, which showed severe vascular impairment and hypoxiation by MRI within 4 h and significantly

diminished BLI signal up to 72 h [99]. By contrast, limited effects were seen with OXi8007 in Ewing's sarcoma family (TC-32) of tumors [175], but that study used a lower dose of OXi8007 (200 mg/kg), which we have seen to be considerably less effective (Figure 3.14). Through in vivo dynamic BLI and biochemical and biological experiments on activated endothelial cells, we have demonstrated that OXi8006 and its phosphate prodrug OXi8007 have potent VDA activity. Taken together these results indicate that the prodrug OXi8007 is a very promising VDA that warrants further pre-clinical evaluation.

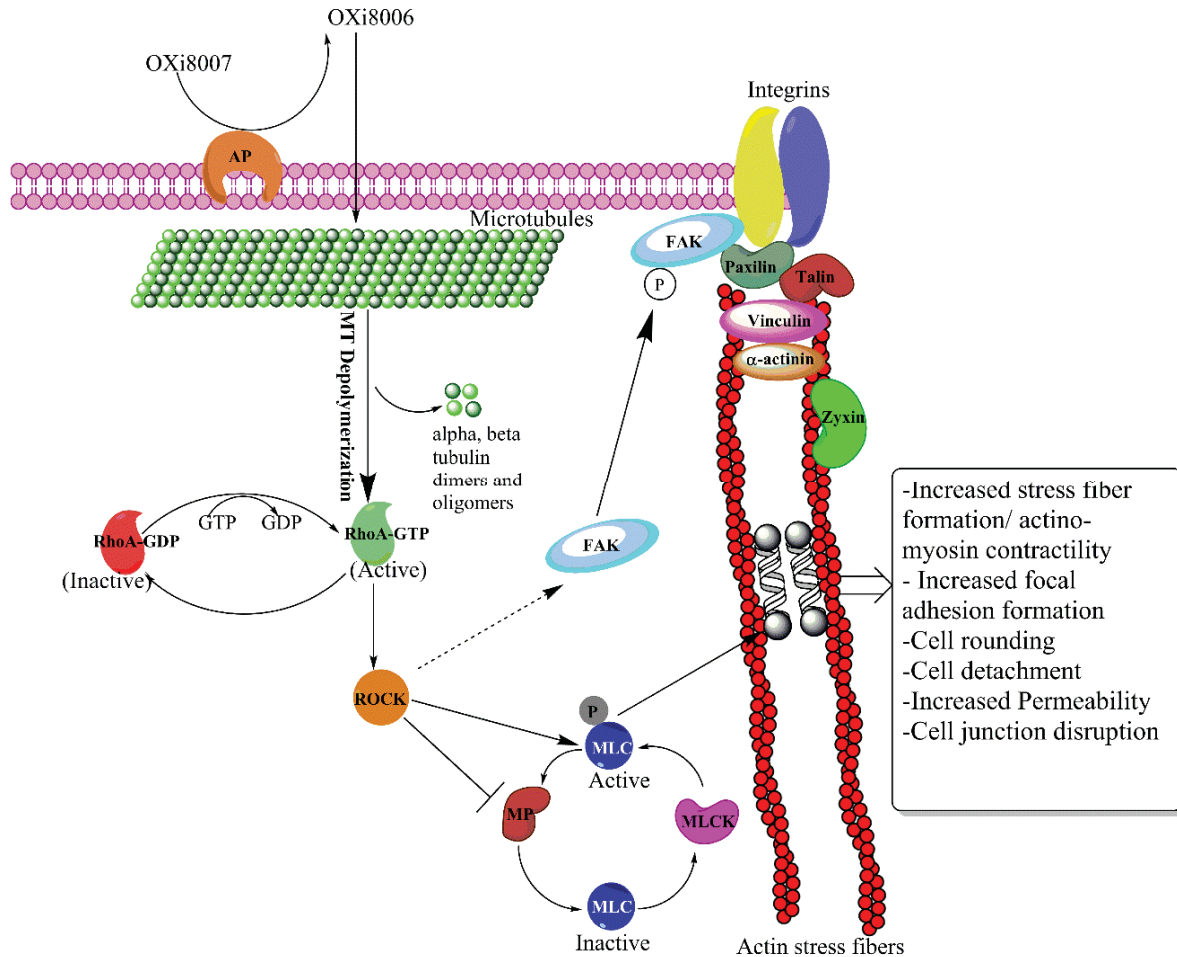


Figure 3.17. Proposed VDA mechanism of action of OXi8007 in activated endothelial cells. Phosphate prodrug OXi8007 is cleaved by a non-specific phosphatase to OXi8006 that enters the endothelial cell and binds to tubulin resulting in microtubule depolymerization and RhoA activation. RhoA kinase (ROCK) is activated by RhoA and phosphorylates MLC and phosphorylates and inactivates MLC phosphatase (MP) leading to increased levels of phosphorylated MLC and activation of non-muscle myosin II which results to actin bundling and stress fiber formation. ROCK also leads to focal adhesion kinase (FAK) phosphorylation and activation contributing to increased focal adhesions.

Acknowledgments

The authors thank Dr. A. Ramirez (Mass Spectrometry Core Facility, Baylor University) and Dr. J. Karban, Dr. C. Moehnke and Dr. M. Nemec (Director) for use of the shared Molecular Biosciences Center at Baylor University. Dr. Kate Luby-Phelps provided invaluable assistance with fluorescent microscopy in the Microscopy Resource of the Cancer Center at UT Southwestern Medical Center. This work was supported by the National Institutes of Health National Cancer Institute [Grant 5R01CA140674] (to K.G.P. and M.L.T. with subcontract to R.P.M.), and OXiGENE, Inc. (Grant to K.G.P. and M.L.T). The content is solely the responsibility of the authors and does not necessarily represent the official views of the National Cancer Institute or the National Institutes of Health. Imaging was facilitated with the assistance of Resources of the Harold C. Simmons Cancer Center supported through an National Institutes of Health National Cancer Institute Cancer Center Support Grant [Grant 1P30 CA142543], specifically, the Southwestern Small Animal Imaging Resource, and Live Cell Imaging Resource. The IVIS Spectrum was purchased with support of 1S10RR024757.

Contributions of Individual Co-Authors

The research presented in Chapter three of this dissertation is a peer-reviewed, published article with fifteen authors who participated to different extents in the various aspects the work published including conception and design of study, acquisition of data, analysis and interpretation of data, writing of the manuscript, and revision of the manuscript before submission and after review for publication. Furthermore, as is the case for most scientific research in the biomedical sciences, the work presented here is part of an extensive and ongoing collaboration - in this case between the the laboratories of Dr. Mary Lynn Trawick and Dr. Kevin Pinney at Baylor University, the research group of Dr. Ralph Mason at UT Southwestern in Dallas, and Mateon Therapeutics (formerly OXiGENE) Incorporated, a biopharmaceutical company located in San Francisco among other collaborators.

Dr. Tracy Strecker and Samuel Odutola were designated as co-first authors due to their equally significant contributions towards the publication of this paper. Both individuals contributed to the conception and design of the study including target selection in the mechanism study, as well as data acquisition and analysis. Specifically, Samuel Odutola, was responsible for designing, performing and evaluating the confocal immunofluorescence microscopy data. Samuel Odutola was also responsible for most of the statistical analysis conducted during evaluation of the data. Both Dr. Tracy Strecker and Samuel Odutola contributed to the acquisition and analysis of the western blot data presented in the study. Both individuals were responsible for the growth and culture of the cells used in the various cell assays presented in this study. Tracy Strecker was responsible for acquiring the cytotoxicity data presented in the study, but Samuel Odutola played the major role in data analysis. Both individuals assisted in some of the other experiments presented including the flow cytometry experiments and the tube disruption assays. Samuel Odutola was also involved in some of the data analysis from the in vivo experiments, particularly the analysis of the immunohistochemical images, and he was responsible for putting the figures together, statistical analysis.

The co-first authors were both heavily involved in the drafting and revisions of the manuscript. Samuel Odutola was responsible for writing the first draft of the manuscript, making and incorporating revisions, and for assembling most of the figures. Tracy Strecker was also significantly involved in various revisions to the manuscript.

Drs. Mallinath Hadimani, Matthew MacDonough and Anjan Ghatak, who were members of the Pinney Research group under Dr. Kevin Pinney were responsible for the synthesis of the compounds analyzed in this study.

Morgan Cooper and Dr. Amanda Charlton were responsible for acquiring the flow cytometry data used in the study, while Justin Tidmore provided the data from the tube disruption assays.

Ramona Lopez, and Li Li and Dr. Li Liu, members and/or associated with the research group of Dr. Ralph Mason at UT Southwestern (Dallas) performed the *in vivo* mouse studies. Dr. Ralph Mason also contributed significantly to the conception and design of the study as well as revisions to the manuscript prior to submission.

Drs. David Chaplin, Kevin Pinney, and Mary Lynn Trawick played major roles in the design of the study. Dr. Mary Lynn Trawick had a major role in writing of the manuscript and Dr. Kevin Pinney and Dr. David Chaplin had significant roles in writing of the manuscript. Members of the Pinney group synthesized the compounds analyzed, the *in vivo* work was carried out by Dr. Ralph Mason and his group, and the cell and molecular biology studies were performed by members of the Trawick group. Funding for the study was supported by the National Institutes of Health National Cancer Institute [Grant 5R01CA140674] (to K.G.P. and M.L.T. with subcontract to R.P.M.), and OXiGENE, Inc. (Grant to K.G.P. and M.L.T), which is now Mateon Therapeutics. Imaging was facilitated with the assistance of Resources of the Harold C. Simmons Cancer Center supported through an National Institutes of Health National Cancer Institute Cancer Center Support Grant [Grant 1P30 CA142543], specifically, the Southwestern Small Animal Imaging Resource, and Live Cell Imaging Resource. The IVIS Spectrum was purchased with support of 1S10RR024757.

CHAPTER FOUR

Evaluation of Mechanism of Action of VDAs in Vitro: The Roles of GEFs and Various Signaling Proteins

In order to produce effective VDAs, it is imperative to have a robust understanding of the mechanisms of action and the various signaling pathways that are activated as a result of exposure of endothelial and tumor cells to VDAs. In the previous chapter, the effects of novel VDAs (OXi8006 and OXi8007) on activated endothelial cytoskeletal components were discussed. The data presented suggested a mechanism of action that involved rapid microtubule disruption which led to the activation of a cell signaling cascade, mediated by RhoA and its effector kinase (ROCK), which led to an increase in cell contractility due to increased actin stress fiber formation as well as initial increase in focal adhesion formation. The eventual outcome of this signaling was resolution of this cell contractility, as seen from endothelial cells shrinking and rounding up, loss of cell-cell and cell-matrix associations, and eventual cell detachment from the extracellular matrix. These events were summarized in Figure 3.17.

In this chapter, a number of the proteins involved in the OXi8006 induced cell signaling cascade in activated endothelial cells will be discussed, with the goal being to further elucidate the mechanism of action. This includes confirmation of the link between microtubule disruption and RhoA activation, examination of some of the downstream targets of ROCK, examination of the roles played by early apoptotic effectors in this signaling cascade, as well as an examination of the effect of VDAs on tumor cell

migration. The suggested cell signaling cascade initiated by OXi8006 treatment is presented in Figure 4.1.

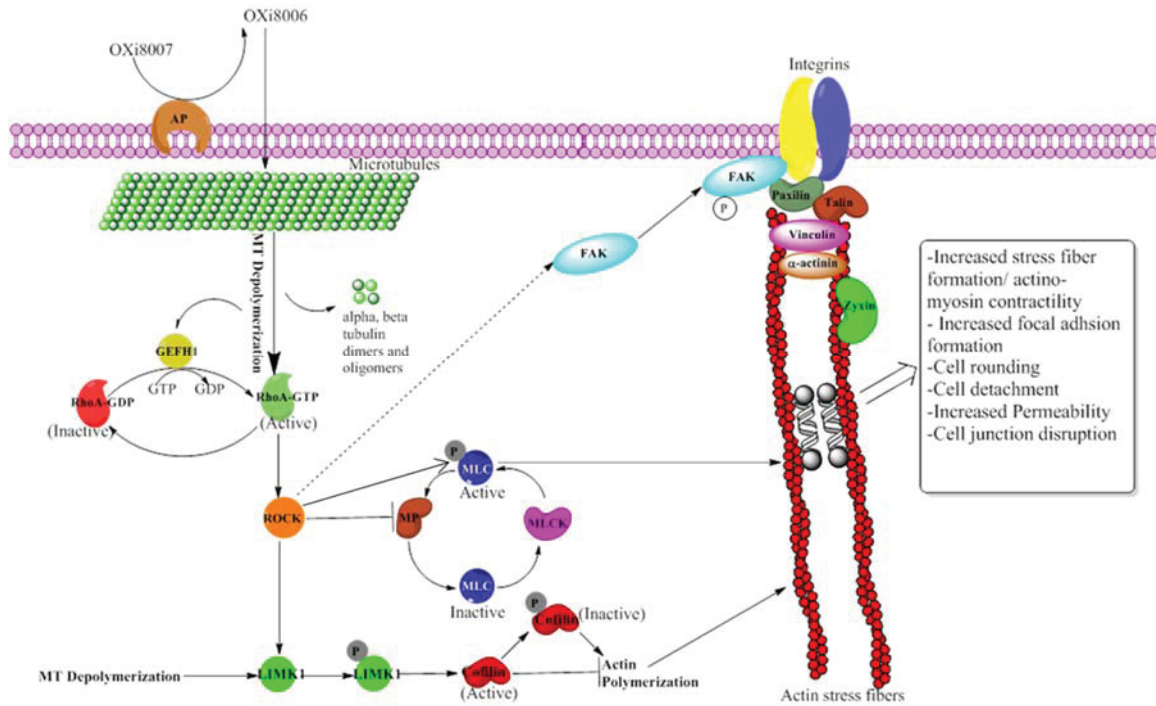


Figure 4.1. Proposed VDA mechanism of action of OXi8007 in activated endothelial cells (modified from Figure 3.17). Phosphate prodrug OXi8007 is cleaved by a non-specific phosphatase to OXi8006 that enters the endothelial cell and binds to tubulin resulting in microtubule depolymerization which leads to release of GEFH1. GEFH1 facilitates GDP to GTP exchange on RhoA resulting in RhoA activation. RhoA kinase (ROCK) is activated by RhoA and phosphorylates MLC and phosphorylates and inactivates MLC phosphatase (MP) leading to increased levels of phosphorylated MLC and activation of non-muscle myosin II which results to actin bundling and stress fiber formation. ROCK also leads to focal adhesion kinase (FAK) phosphorylation and activation contributing to increased focal adhesions. Furthermore, OXi8006 induced microtubule depolymerization also releases LIM Kinase 1 (LIMK1). LIMK1 is phosphorylated and activated by ROCK, thus leading to phosphorylation and inactivation of cofilin. This results in increased actin polymerization and eventual increase in stress fiber formation.

Rho Family GTPases

Rho GTPases are members of the Ras superfamily of monomeric 20-30 kDa GTP-binding proteins. There are twenty-three mammalian genes that encode ten different mammalian Rho GTPases, some with multiple isoforms: Rho (A, B, C isoforms), Rac (1, 2, and 3 isoforms), Cdc42 (Cdc42Hs, G25K isoforms), Rho6, Rho7, RhoE, RhoD, RhoG, TC10 and TTF [202, 203]. The most extensively characterized members of this family of proteins are Rho, Rac and Cdc42. These GTPases act as molecular switches, cycling between an active GTP-bound and an inactive GDP-bound state. When GTP-bound, they are able to interact with effector or target molecules leading to the initiation of downstream signaling cascades. GTPase activity (usually mediated via GTPase activating proteins (GAPs)) returns the proteins to the GDP-bound state, to complete the cycle and terminate signal transduction. Rho family GTPases regulate a wide array of functions, regulate many essential cellular processes, including actin dynamics, gene transcription, cell-cycle progression, cell polarization, migration, and oncogenesis. However, the mechanisms of activation by various stimuli are still being elucidated.

One of the main goals of this research project is to elucidate the mechanism of activation of RhoA as a result of VDA treatment, focusing in particular on regulation by the guanine nucleotide exchange factor GEF-H1, in tumor endothelial cells.

Overview of Functions of Rho GTPases

One of the highly conserved functions of the Rho, Rac, and Cdc42 subfamilies is regulation of the actin cytoskeleton. The Rho GTPase signaling cascades mediate general cellular processes that are dependent on the actin cytoskeleton including cytoskeletal remodeling, microtubule dynamics, vesicle trafficking, cell polarity, cell migration,

regulation of cell permeability, phagocytosis and pinocytosis, and cell differentiation [203]. In addition to their effect on the actin cytoskeleton, this family of proteins also regulates a variety of other biochemical pathways including serum response factor (SRF) and nuclear factor κ B (NF- κ B) transcription factors [204, 205], the c-Jun N-terminal kinase (JNK) and p38 mitogen-activated protein kinase pathways [206, 207], cell-cycle progression [208], secretion in mast cells [209], cell polarity [210] and cell transformation [211, 212]. Therefore, although Rho GTPases are best characterized for their effects on the actin cytoskeleton, there is now much interest in their ability to affect cell proliferation and gene transcription, and the contributions of all of these activities to malignant transformation is an important field of study.

RhoA in particular plays a variety of important roles in cells. RhoA activation plays a vital role in the cell via its effects on the actin cytoskeleton, which results in regulation of various cellular processes. RhoA is prevalent in regulating cell shape, polarity and locomotion via actin polymerization, actinomyosin contractility, cell adhesion, and microtubule dynamics [213]. In addition, RhoA is believed to act primarily at the rear of migrating cells to promote detachment. Signal transduction pathways regulated via RhoA link plasma membrane receptors to focal adhesion formation and the subsequent activation of relevant actin stress fibers, as well as regulating the integrity of the extracellular matrix and the loss of corresponding cell-cell adhesions (adherens and tight junctions) required for cell migration [213, 214].

Rho A Structure

Human RhoA is a ~20 kDa Rho GTPase and has a common G-domain fold, which consists of a six-stranded β -sheet surrounded by 5 α -helices [215]. The β -strands

are arranged in a combination of parallel and antiparallel β -sheets. The GDP- and GTP-bound forms differ in the two loops, known as switch 1 (or the effector loop, residues 28-44) and switch 2 residues (Figure 4.2). Binding of GTP and other analogues typically causes dramatic changes in the conformation of these switches. Given that these switch regions are highly flexible, new interactions with GTP causes structural and dynamic changes in both the loops. This results in reorientation and conformational changes in the effector loop which allows Rho A to associate with downstream effector proteins [216, 217]. RhoA, like other members of the Rho family of proteins, has distinct binding regions for nucleotides and effector proteins. There is also a distinct binding region for Mg^{2+} , which is essential for the high-affinity binding of guanine nucleotides [218]. In the nucleotide-free state, RhoA has the highest affinity towards binding activated Guanine Nucleotide Exchange Factor (GEF). GEFs catalyze the exchange of GDP for GTP. Rho GTPase intermediates that are nucleotide- (and Mg^{2+}) free can be preferentially loaded with GTP since cellular concentrations of GTP are substantially higher than those of GDP [218].

Activation and Regulation of Rho GTPases

Rho GTPases are downstream of various proteins such as G-protein-coupled receptors (GPCRs), tyrosine kinase receptors, integrin clustering or engagement, cell–cell adhesion, and cytokine receptors [219-222]. Rho proteins oscillate between an active GTP-bound state and inactive GDP bound state. This alternation between both states is mediated by GTPase-activating proteins (GAPs) (which promote hydrolysis of GTP bound to the active form and accumulation of GDP on the inactive form) and guanine nucleotide exchange factors (GEFs) (which facilitate exchange of GDP for GTP) (Figure

4.3). Furthermore, inactive GDP-bound Rho proteins are found in the cytosol in complex with another class of regulatory proteins, nucleotide dissociation inhibitors (RhoGDIs). Upon activation, dissociation of RhoGDIs from the complex is required to enable interaction with GEFs and exchange of GDP for GTP [202].

Downstream Effectors of RhoA

Some of the best characterized targets of RhoA are Rho-kinase (ROCK or ROK), the mammalian homolog of the Diaphanous formin (mDia), Protein Kinase N (PKN), rhotekin, raphilin, citron kinase, Phosphatidylinositol-4-phosphate 5-kinase (PIP5-K), and Serum Response Factor (SRF) (Figure 4.4).

ROCK

ROCK, a Ser/Thr kinase, is a major effector activated by RhoA, and leads to activation of several signaling cascades [223] (Figure 4.5). The amino terminus of ROCK contains its kinase domain, while the carboxy-terminal has C-a putative coiled-coil domain in the middle of the protein which interacts with RhoGTP, leading to the activation of the phosphotransferase activity of ROCK [224]. Previous studies have shown that constitutive activation of ROCK results in increased phosphorylation and activation of MLC [225]. ROCK is essential for Rho-induced formation of stress fibers, since its activation of MLC stimulates both, association of actin filaments with myosin II, and the ATPase activity of myosin [225, 226].

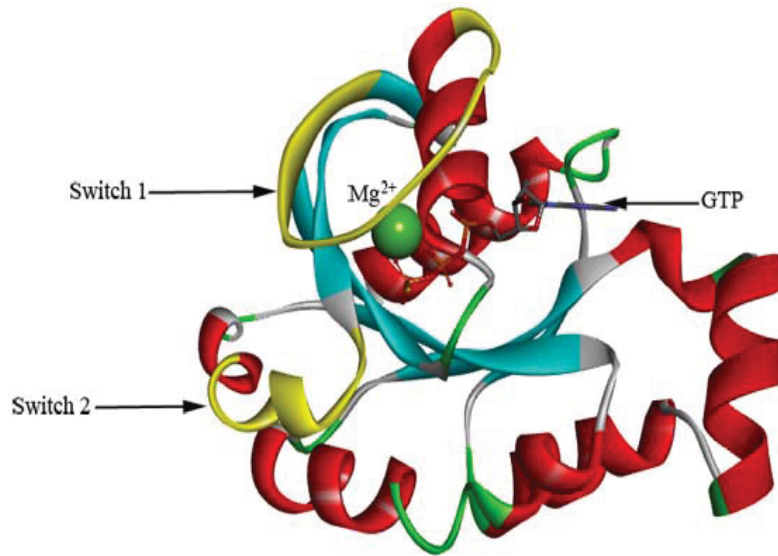


Figure 4.2. Crystal Structure of Human RhoA (PDB ID: 1A2B) [216]. Both switch regions are represented in yellow and the guanosine nucleotide and Mg²⁺ are represented in ball and stick and space filling models respectively

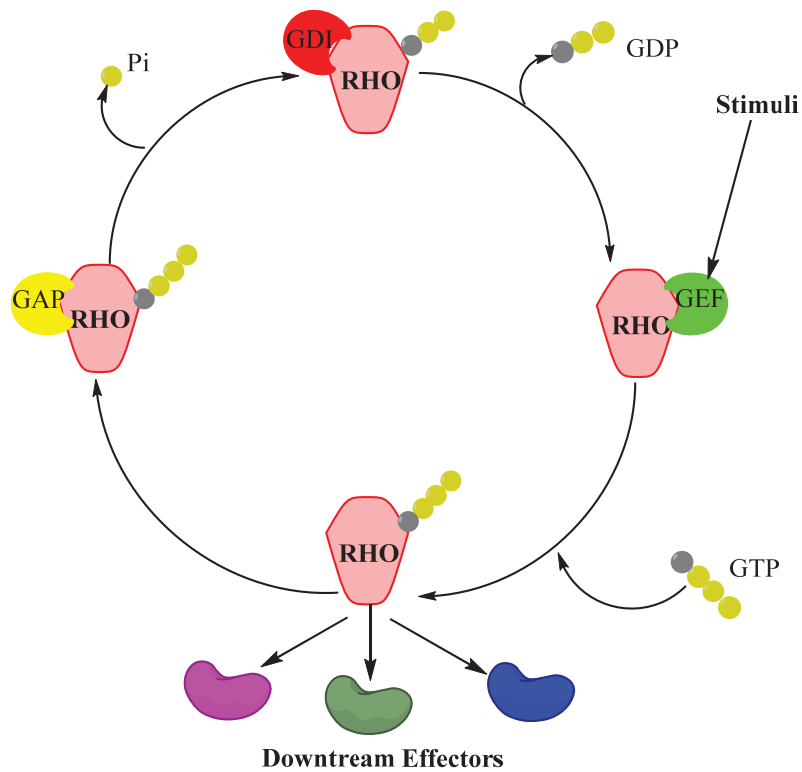


Figure 4.3. Activation/Deactivation cycle of RhoGTPases

ROCK regulates contractility of the actomyosin complex via two mechanisms; by directly phosphorylating Myosin Light Chain (MLC) [225, 226] and by phosphorylating and inhibiting the myosin-binding subunit (MBS) of myosin phosphatase [227]. In addition to MLC, ROCK phosphorylates several other proteins that act further downstream in Rho signaling. LIMK is phosphorylated by ROCK. LIMK then phosphorylates and inactivates the actin depolymerizing protein cofilin, inhibiting its actin-severing ability. This regulates actin cytoskeleton reorganization [228]. Another less well characterized pathway activated by ROCK is the ubiquitous Na^+/H^+ exchanger NHE1. This protein may also contribute to stress fiber and focal adhesion formation [229].

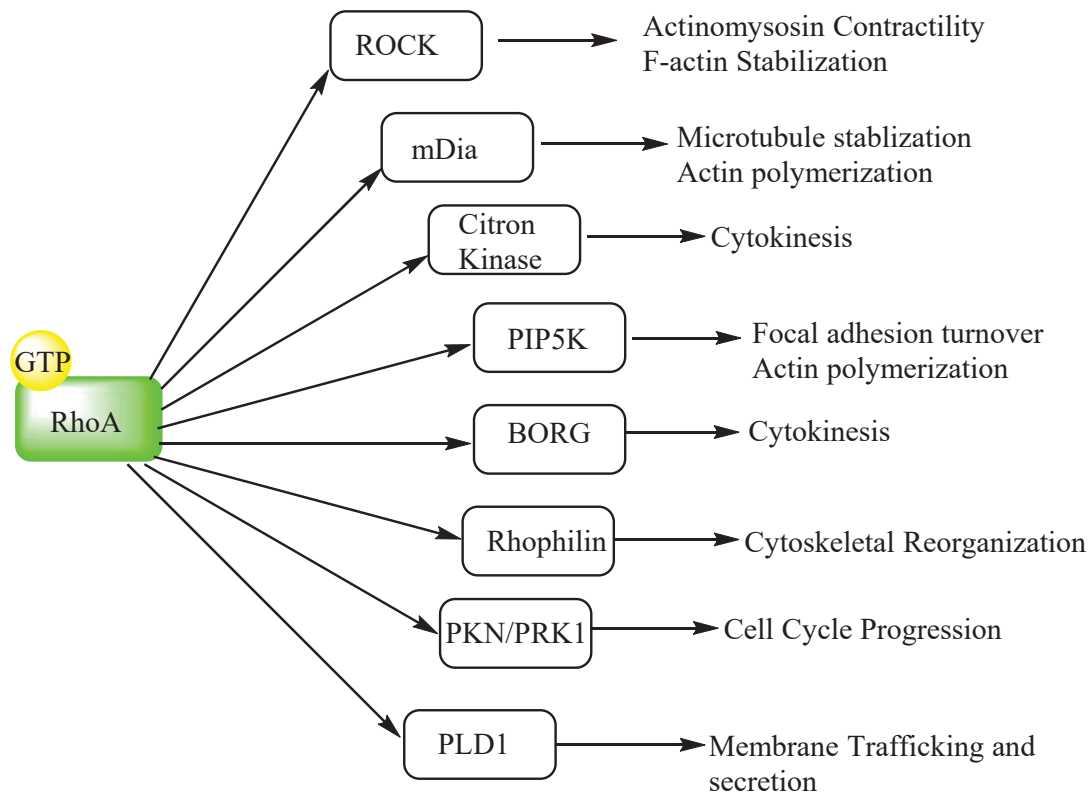


Figure 4.4. Downstream effectors of RhoA

Focal Adhesion Kinase (FAK)

Focal adhesion reorganization is also a significant part of the cytoskeletal reorganization process that results from VDA treatment. Focal adhesions are super assemblies of proteins that form at sites of integrin adhesion to the extracellular matrix [230, 231]. At their cytoplasmic face, focal adhesions provide attachment sites for F-actin stress fibers. They are made up of integrins (which are proteins that constitute a large family of heterodimeric trans-membrane, cell- matrix and/or cell-cell adhesion receptors) and cytoplasmic proteins such as focal adhesion kinase (FAK), talin, vinculin, paxillin SRC-family kinases (SRKs) and so on [188, 232]. Previous studies have shown that Rho family GTPases play a significant role in focal adhesion assembly via FAK signaling [190, 233].

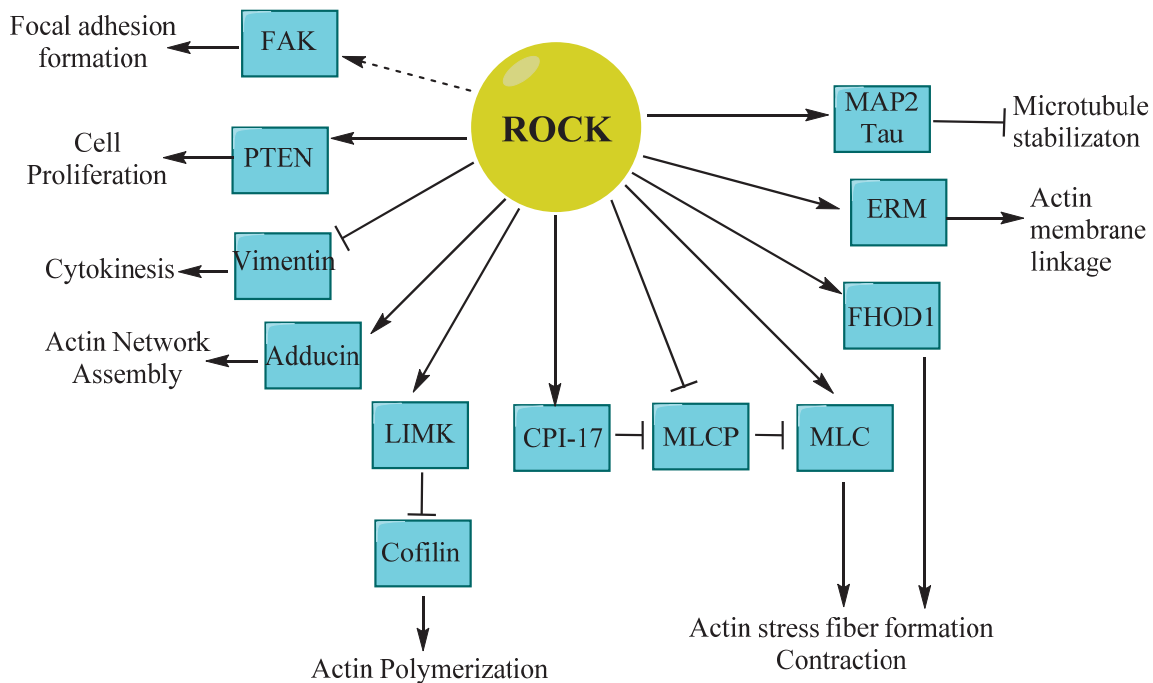


Figure 4.5. Various signaling cascades initiated by activated ROCK

FAK plays an important role in focal adhesion turnover, as this protein is responsible for reinforcement of focal adhesions by promoting talin and src recruitment to the complex, as well as phosphorylation of scaffolding proteins such as paxillin and p130Cas [234]. FAK (after activation) has also been shown to downregulate Rho activity [199]. Regulation of FAK includes phosphorylation at multiple tyrosine and serine residues [196, 197]. Tyrosine 397 is the initial phosphorylation site of FAK, and is involved in its activation [235].

GEF-H1

Ras homology family GTP-binding proteins (Rho-GTPases) function as intracellular switches, causing the activation/deactivation of pathways that facilitate reorganization of the cellular cytoskeleton, cell cycle progression, gene transcription, and cell survival, proliferation and differentiation. GTP exchange factors (GEFs) are proteins that help promote the exchange of GDP for GTP, thus ensuring localized and timely activation of GTPases. The Rho GEF family, also called the Dbl family, consists of approximately 80 members. The GEF proteins usually contain a Dbl homology (DH) domain and a pleckstrin homology (PH) domain that is important for plasma membrane localization, where the activation of Rho GTPases takes place. GEF DH domains interact with Rho GTPase switch regions, modifying their conformation, resulting in release of GDP. This allows free GTP to bind the GTPase, inducing the switch to the active conformation [236].

GEF-H1 is a member of this family that is of particular interest in the context of the mechanism of action VDAs. GEF-H1, along with a few other members of this family (p115RhoGEF, LARG, ECT2, VAV2, Trio, and Rgnef (p190RhoGEF), have been shown

to contribute to RhoA activation, actin stress fiber, focal adhesion formation, cell contractility and migration [236]. However, of these proteins only GEF-H1 and Rgnef have been shown to be microtubule associated and/or regulated.

Structure

Similar to most DH domain-containing GEFs, GEF-H1 has a typical DH-PH domain structure (Figure 4.6). GEF-H1 is one of only two RhoA interacting GEFs that localizes to microtubules. It has a C1 domain which contains a Cys53 residue that is important for microtubule binding and subsequent inactivation [237]. The PH domain and the inhibitory C-terminus (which contains the coiled-coil motif) region in GEF-H1 are also important for microtubule binding. The DH domain of GEF-H1 is the region that interacts with RhoA and Rac, and contains the GEF activity [238]. Mutations in highly conserved residues within the DH domain prevent its catalytic exchange activity towards both RhoA and Rac [237].

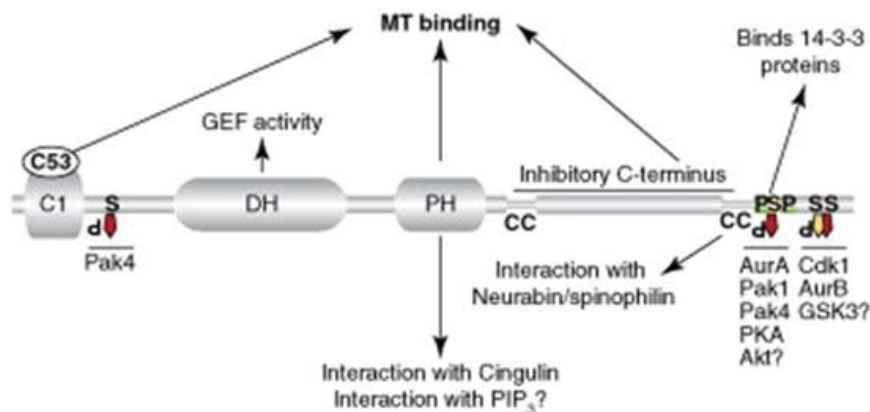


Figure 4.6. Representation of GEF-H1 Structure [237]

Regulation of GEF-H1

GEF-H1 is predominantly localized to the cytosol bound to microtubules and in this form is typically inactive. Stimuli that disrupt this binding activate the exchange factor and allow for downstream activation of the Rho GTPase [237]. GEF-H1 activity can also be regulated by phosphorylation at various sites on the protein. GEF-H1 can be phosphorylated by the Rac/Cdc42 effector PAK1 on its S885 residue, enabling its binding to 14-3-3 proteins and subsequently to microtubules, leading to inactivation [239]. Another study noted that S142 phosphorylation of GEF-H1 (unbound to microtubules) by PAK4 promoted Rho activation and increased stress fiber formation [240].

Materials and Methods

Compounds

CA4 was obtained from OXiGENE Inc. (South San Francisco, CA), and OXi8006 was synthesized as previously described [28, 29].

Cell Culture

HUVECs (Invitrogen) were grown on collagen-I coated flasks (CELLCOAT®) in M200 medium (Invitrogen) supplemented with 1% gentamycin sulfate, 1% amphotericin B, and high growth factor supplement kit (Endothelial Cell Growth Kit-VEGF (ATCC)). HUVECs were not used beyond passage 5. MDA-MB-231 cells (ATCC) were cultured in DMEM supplemented with 10% fetal bovine serum (Gibco One Shot®) and 1% gentamycin sulfate, and passaged according to ATCC recommendations. Cells were maintained at 37 °C in a humidified atmosphere of 5% CO₂, for use in these experiments. Passaging/removal of cells was done using 0.25% Trypsin solution (Corning) for MBA-

MB-231 cells, and Trypsin-EDTA with Trypsin neutralizing solutions (ATCC) for HUVECs.

Gene Silencing via RNAi

GEF-H1 (OnTarget™, Dharmacon) and RGNEF (Silencer® Select, Invitrogen) siRNAs were used at 60 nM and 20 nM final concentrations respectively. For morphology experiments, approximately 200,000 HUVECs grown per well of a 6-well plate were transfected with 2 µl of Lipofectamine RNAiMax (Invitrogen) per ml of cell culture media. For siRNA transfections in different sizes of tissue culture plates (for western blot analysis) or 24-well plates (qRT-PCR analysis), cell numbers, amounts of siRNA duplexes and transfection reagent were adapted to the difference in surface area. Cells were treated with RNAi for 72 h prior to termination of experiment and relevant analyses.

GEF-H1 siRNA SMARTpools were for human ARHGEF2 (accession number NM_004723). The target sequences were:

GUGCGGAGCAGAUGUGUAA

CCACGGAACUGGCAUUACU

GAAUUAAGAUGGAGUUGCA

GAAGGUAGCAGCCGUCUGU

For RGNEF, siRNA used was for human ARHGEF28 (accession numbers NM_001080479.2, NM_001177693.1, and NM_001244364.1).

As a control for potential off-target effects, a pool of four siCONTROL non-targeting siRNAs was used (D-001206-13, non-Specific Control Duplexes – XIII).

Duplex 1: AUGAACGUGAAUUGCUCAA

Duplex 2: UAAGGCUAUGAAGAGAUAC

Duplex 3: AUGUAUUGGCCUGUAUUAG

Duplex 4: UAGCGACUAAACACAUCAA.

RNA Extraction/Purification

RNA extraction was performed using an RNeasy Mini kit (Qiagen). This kit contained various buffers, spin columns, a ribonuclease solution, and various collection tubes. Cells were harvested via trypsinization, and between 350-600 μ l of RLT buffer (from the kit) were added to the cell solution for lysis. Equal volume of 70% ethanol was added to the lysate, after which the solution was transferred to an RNeasy Mini spin column placed in a 2 ml collection tube. Solution was centrifuged for 15 s at 8000 x g and eluate was discarded.

DNA digestion was done by adding 350 μ l of RW1 buffer RW1 to the RNeasy column, centrifuged for 15 s at 8000 x g. Again, eluate was discarded. Following this, a DNase solution (1:7 ratio of DNase stock solution and RDD buffer) was added to the column and incubated for 15 minutes at room temperature. Subsequently, 350 μ l of RW1 buffer was added to the RNeasy column, followed by centrifugation for 15 s at 8000 x g and eluate was discarded.

For RNA purification and elution, 500 μ l of RPE buffer was added to the column, followed by centrifugation for 15 s at 8000 x g and discarding of eluate. This procedure was repeated two more times, after which the column was placed in a new collection tube and the RNA eluted by addition 20-50 μ l of RNase-free water and centrifugation at 8000 x g for 1 minute.

RNA concentrations in ng/μl were determined using a Nanodrop 1000 spectrophotometer (Thermo Fisher), using the RNA-40 setting.

QRT-PCR

Following RNA extraction, cDNA synthesis was performed using a reverse transcription system kit (Promega), using a slightly modified protocol from the one provided by the manufacturer. Briefly, 1~5μg per RNA sample were centrifuged briefly in a microcentrifuge, and then placed on ice. Subsequently, a 20μl reaction (per sample) was prepared by adding the following reagents in the following order:

MgCl ₂ , 25mM	4 μl
Reverse Transcription 10X Buffer	2 μl
dNTP Mixture, 10mM	2 μl
Recombinant RNasin® Ribonuclease Inhibitor	0.5 μl
AMV Reverse Transcriptase (High Conc.) 15u	0.83 μl
Oligo (dT)15 Primer 0.5μg	1 μl
Nuclease-Free Water to a final volume of	20 μl

Using a Techne TC 512 RT-PCR machine, the reaction solutions were then incubated at 42°C for 60 minutes, followed by incubation at 95°C for 5 minutes, and finally incubation at 0–5°C for 5 minutes.

QPCR of the cDNA product was done using a Solaris qPCR master mix and primer probe sets (Thermo Fischer). The reaction was run on a PCR thermal cycler according to the parameters in Table 4.1

Table 4.1. QPCR cycling parameters

	Temp.	Time	Number of cycles
Enzyme activation	95°C	15 min	1 cycle
Denaturation	95°C	15 sec	40 cycles
Annealing/Extension	60°C	60 sec	

Immunofluorescence Imaging of Endothelial Cells

Actively proliferating HUVECs were cultured on glass coverslips coated with 1% gelatin. For the simple compound treated experiments, cells were plated at 10,000 cells/coverslip in 6-well culture plates (Corning) using high growth factor supplemented medium and allowed to incubate at 37 °C for 48 hours (approximately 40% confluence) before being treated with compounds. For RNAi experiments, cells were plated at 100,000 cells per well in 6-well culture plates. Stock solutions of VDA compounds were made by dissolving agents in DMSO, with a final concentration of DMSO less than 0.5% in media. Cells were incubated with specific concentrations of compounds for defined time periods.

After treatment, the cells were fixed and permeabilized via the addition of a solution that comprised 4% paraformaldehyde and 0.5% Triton X (Sigma-Aldrich) in PBS. Microtubules were detected using mouse anti- α -tubulin antibody (Sigma-Aldrich) followed by incubation with FITC-conjugated goat anti-mouse IgG (Jackson ImmunoResearch, West Grove, PA), actin fibers were stained using Texas-red conjugated phalloidin (Invitrogen), and nuclear staining was carried out with DAPI. Phosphorylated focal adhesion kinase (FAK) was stained with anti-pFAK^{Y397} antibody (Abcam, Cambridge, MA). GEF H1 was detected using anti-GEF H1 antibody (Abcam). RGNEF was detected using anti-RGNEF antibody (Abcam). Phosphorylated cofilin was detected using anti-phosphocofilin^{S3} antibody (Abcam). These primary antibodies were

visualized using FITC and Alexa-fluor 647 conjugated goat anti-rabbit secondary antibodies (Jackson ImmunoResearch). Fluorescence and phase contrast images were collected using an Olympus FV 1000 confocal microscope and Olympus fluoview software (Olympus Imaging America Inc., Center Valley, PA) using a 60x oil immersion objective.

Western Blotting

Activated HUVECs were grown on collagen I coated T75 flasks to approximately 70% confluence and treated with 1 μ M OXi8006 for defined periods of time. A higher cell confluence was required to obtain sufficient protein, and with these conditions, a higher OXi8006 concentration was required to obtain similar effects to the morphology experiments on cover slips. For RNAi experiments, cells were exposed to siRNA (60 nM) for 72 h total and OXi8006 for 30 minutes prior to lysis.

After removal of compound, flasks were placed immediately on ice, at which point lysis buffer, made up of ice cold RIPA buffer (Alpha Aesar) containing a phosphatase inhibitor tablet (Roche) and 20uL protease inhibitor cocktail (Sigma) for a total of 10mL lysis solution, was added to proportion of cell count (100uL per 1×10^6 cells) for rapid lysis. For complete collection, flasks were lightly scraped to dislodge any remaining cells into the lysis solution and pool the total lysate for, which was transferred into clean microcentrifuge tubes and incubated for 30 minutes on ice with gentle rocking. The lysate was clarified by centrifugation, at 13,000 rpm for 10 minutes at 4°C using a tabletop microcentrifuge. A small fraction (5 μ L) was collected and analyzed for protein quantitation, using the RC/DC assay protocol and reagents (BioRad), which was analyzed via nanodrop; the remainder was immortalized using the LDS NuPage protocol (Life

Science) in 5% β -mercaptoethanol (Sigma). Briefly, lysates were boiled at 75°C for 10 minutes, given the use of lithium dodecylsulfate, in lieu of sodium dodecylsulfate, as it has a lower boiling temperature and prevents heat damage to the cells, at a 3:1 ratio of clarified lysate to sample buffer, then a 5% volume correction for β -ME.

Lysates were separated via gel electrophoresis in using a NuPage 4-12% bis-tris gel, 1.00 mm X 15 well, in MOPS/SDS buffer, at 125 V for 90 minutes.

Subsequent transfer to PVDF membranes (GE) was done at 25 V for 75 minutes for high molecular proteins (> 60kD) and 65 minutes for lower molecular weight proteins (< 60 kD) using a tank blot module (XCell-II, Invitrogen), in Tris-Glycine transfer buffer with 1 mL of NuPage Antioxidant and 10% methanol.

Lysates (10-30 μ g protein/sample) were combined with NUPAGE™ loading dye and 500 mM DTT solution and heated to denature and immortalize protein. Lysates were separated on NUPAGE™ 4-12% Bis-Tris gels (Invitrogen) using 1x MOPS running buffer (Sigma). Proteins were transferred to an Immobilon-P™ PVDF membranes (EMD Millipore) with. Membranes were incubated with primary antibodies for various proteins being analyzed including pFAK^{Y397} (Abcam), pMLC (Cell Signaling), RGNEF (Abcam), pCofilin^{S3}, GEFH1 and GAPDH (Cell Signaling). Anti-rabbit HRP and anti-mouse HRP secondary antibodies were obtained from Jackson ImmunoResearch. Protein bands were visualized using ECL Prime™ blotting detection reagent (GE) and ImageQuant LAS 4000 imaging system (GE). Analysis of bands was done using Licor Image Studio 4.0 software.

Annexin V Binding Assay

Determination of the effects of OXi8006 treatment on annexin V binding by HUVECs was done via a modified immunofluorescence microscopy protocol. Cells were plated on gelatin coated coverslips at a concentration of about 100,000 cells per coverslip and allowed to plate down for 24 hours. Cells were subsequently treated with 10 nM OXi8006 for a total of 18 h. As positive controls for induction of apoptosis binding, other coverslip plated HUVECs were either treated with 10 nM CA4 for 18 h, or incubated in a hypoxic chamber (at ≤ 10 ppm O₂) for four hours and then incubated in normoxic conditions for 18 h. Subsequently, cells were washed gently with ice cold PBS and then incubated Cy5 conjugated annexin V protein diluted in annexin V binding buffer (from annexin V-Cy5 Apoptosis detection kit, Enzo Life Sciences) for 10 minutes. Cells were then washed 1x with annexin V binding buffer before fixation with 4% paraformaldehyde solution (in annexin V binding buffer) for 10 minutes. It should be noted that staining prior to fixation is necessary because fixation may cause cell membrane disruption which may lead to non-specific binding of annexin V to phosphatidyl serine on the inner surface of the cell membrane. Coverslips were then mounted on slides as previously described and imaged using via fluorescence microscopy.

Wound Assay

MDA-MB-231 cells which have been passaged less than 20 times (cell passaging procedure is described in detail in Chapter eight) were trypsinized to remove from T-75 flasks and counted using an automated cell counter (BD Biosciences). Cells were plated into 6-well plates (Corning) at a concentration of 800,000 cells per well. It should be noted that before cell plating, a sharpie was used to draw a horizontal line as a reference

point about 5 cm from the top of each well so as to serve as a reference point for image acquisition. Cells were incubated until they reached 100% confluence in wells (48-72 h), with a change of 10% FBS containing media every 24 h to promote healthy growth of cells.

VDA concentrations for cell treatment (1 nM, 5 nM, 10 nM and 20 nM) were made using DMEM supplemented with 2% FBS. Prior to treatment, wounds were made in cell monolayers in the wells using a 200 μ l pipette tip to scratch vertically across each well. Subsequently, the 10% FBS DMEM was removed from the cells and replaced with the compound dilutions in 2% FBS DMEM. VDAs used in this assay were OXi8006, OXi8007, and CA4.

After wound creation, each well was imaged immediately and subsequently at 6 h intervals up to 24 h (or up to the point of complete wound closure). Cells were imaged using a Zeiss Axiovert light microscope with a Canon Power shot A460 camera attached. The cells were imaged at 10x magnification on the microscope and at 4x magnification on the camera, which enabled a field of view that encompassed the entire well. Also, when imaging the final time point, the cells were washed once with 1X PBS so as remove cell debris and obtain a clear image.

Measurement of the wound distances for each compound concentration at each time point was done using Adobe Photoshop. The measurement protocol is as follows:

1. Obtain an image of a graticle using the same objective lens and camera magnification used to image the cells (10x objective and 4x magnification respectively).
2. In photoshop, use the measurement tool to draw a straight line across the graticle from the 0 μ m to the 100 μ m markings.
3. Open the analysis tab and record measurements. This opens a table at the bottom of the screen which shows the length of the line in pixels

4. In order for the software to perform subsequent measurements using the right units and scale:
 - a. Convert the pixel value to microns by dividing the pixel value of the line by 100 μm
 - b. Click analysis-set measurement scale- custom
 - c. Input the pixel value, the logical value (i.e. the converted pixel value in microns), and the required unit for the measurements
5. Open the images to be measured, ensuring that the images are the same size and resolution as the graticle image.
6. Using the measurement tool, measure the length from one side of the wound to the other. Obtain measurements at 10 different points on the image so as to get an average wound width. Ensure to click record measurement after each use of the measurement tool.

The data obtained was then analyzed using GraphPad Prism software. The average distance measurements for each compound treatment were normalized using the zero-time point measurements in order to account for slight differences in wound width. It should be noted that results represent data from triplicate assays.

Results and Discussion

GEF-H1 Mediates the Effects of OXi8006 on Contractility in HUVECs

As previously discussed in chapter three, increased actin stress fiber and focal adhesion formation is associated with an increased contractile phenotype in cells. OXi8006 induction of microtubule depolymerization and subsequent increase in cellular contractility was also shown to be mediated via RhoA and ROCK (Figures 3.8, 3.17 and 4.1).

In order to ascertain a connection between OXi8006 induced microtubule disruption and the subsequent contractility as well as activation of other downstream signaling pathways, the activity of GEF-H1 was examined. As discussed earlier, GEF-H1 is a microtubule associated, RhoA-specific guanine nucleotide exchange factor that has

been suggested to link microtubule dynamics and RhoA GTPase regulation of the actin cytoskeleton [241, 242].

GEF-H1 localization to microtubules in HUVECs was confirmed using immunofluorescence co-staining of microtubules and GEF-H1 (Figure 4.7 A). Results showed that in untreated cells, GEF-H1 was significantly localized to the microtubule network. Colocalization analyses of these images using ImageJ software showed that there was significant correlation between microtubules and GEF-H1 (Figure 4.7B), with values of 0.646 and 0.826 Pearson correlation and Mander's overlap coefficients respectively. These correlations are statistical tools typically used to quantify the degree of colocalization between fluorophores [243].

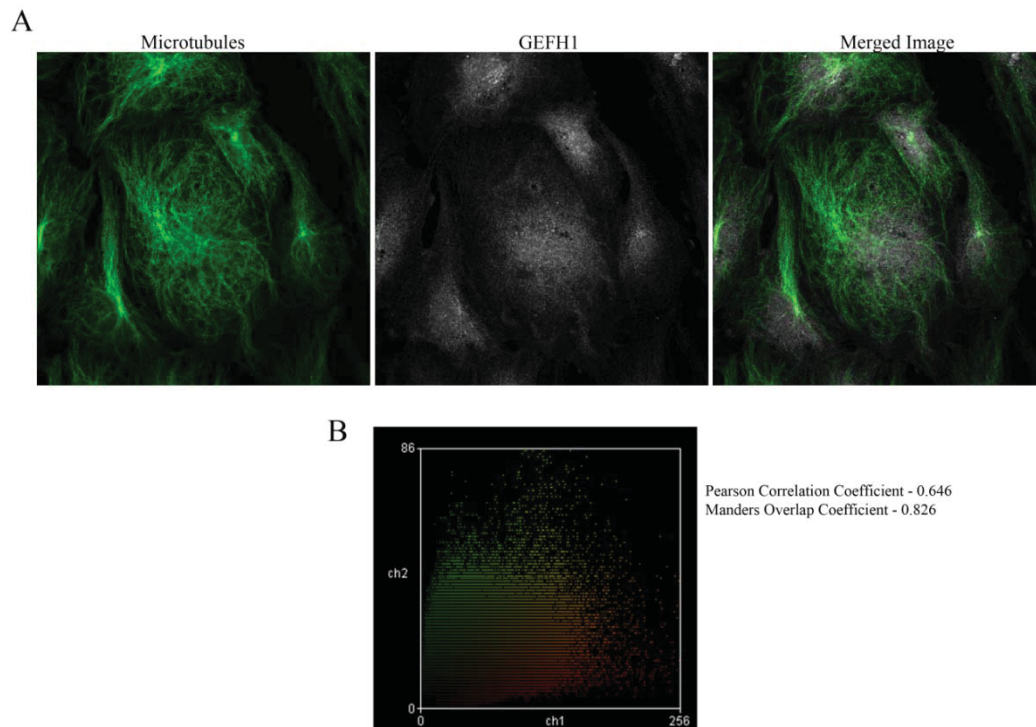


Figure 4.7. Colocalization analysis of microtubules and GEFH1 in HUVECS. A) Confocal immunofluorescence staining showing microtubules, GEF-H1, and merged images. B) Scatter Plot showing colocalization analysis of microtubule and GEF-H1 images. Pearson correlation and Manders overlap coefficient values suggest significant correlation between images.

In order to examine the role played by GEF-H1 in the cell contractility that occurs as a result of OXi8006 treatment in HUVECs, GEF-H1 in HUVECs was depleted via RNAi prior to OXi8006 treatment. Briefly, HUVECs were treated with a GEF-H1 specific siRNA pool as described in the materials and methods section above. Subsequently, cells were treated with OXi8006 and cell morphology and signaling effects analyzed using confocal immunofluorescence microscopy and western blotting. Analysis of the GEF-H1 RNA via qPCR (Figure 4.8) and GEF-H1 protein via immunofluorescence and western blotting (Figure 4.9) after 72 h of siRNA treatment showed that the siRNA treatment resulted in about 90 % reduction in GEF-H1 RNA and 65-75% reduction in GEF-H1 protein levels.

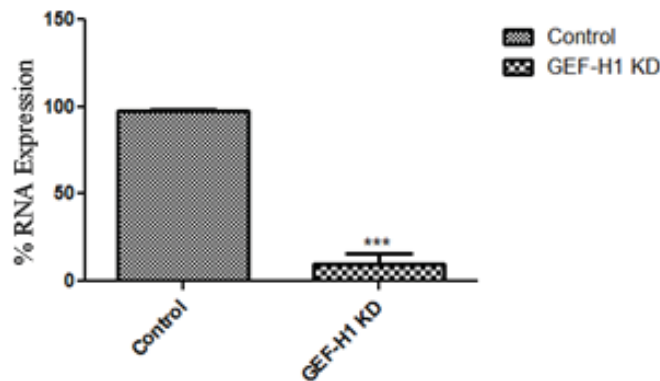


Figure 4.8. GEF-H1 RNAi qPCR.

Similar to previous results, modest actin stress fiber assembly was observed throughout the cell body in control/vehicle treated HUVECs the cell body along with the presence of a modest amount of focal adhesions located at the ends of the stress fibers (Figure 4.10). In GEF-H1 depleted cells (without OXi8006), the baseline stress fiber and focal adhesion levels are significantly reduced compared to control, with increased F-

actin localization to the cell periphery. Furthermore, GEF-H1 depleted cells are seen to adopt a more rounded phenotype compared to control (Figure 4.10). It should be noted that microtubule networks were intact and well organized in both control cells and cells depleted of GEF-H1. OXi8006 treatment of cells with normal GEF-H1 levels resulted in microtubule disruption as well as significantly increased stress fiber and focal adhesion, similar to previous results (Figure 4.10). However, in GEF-H1–depleted cells, OXi8006 induced microtubule disruption was not accompanied by significantly increased stress fiber and/or focal adhesion formation (Figure 4.10). This reduction of OXi8006 induced increase in focal adhesion formation (as seen from increase phosphorylation of FAK at Tyr-397) due to GEFH1 depletion was confirmed by western blotting (Figure 4.11). Therefore, it could be suggested that GEF-H1 knockdown slows down OXi8006 induced stress fiber and focal adhesion formation in HUVECs.

Rgnef Depletion Has No Effect on OXi8006 Induced HUVEC Contractility

GEF-H1 and Rgnef are both microtubule associated proteins and are also known to be involved in RhoA activation. Rgnef, also known as p190 RhoGEF, is a GEF that interacts with Rho, but not with Rac or Cdc42 [236]. Endogenous Rgnef localizes to distinct RhoA-containing regions at the plasma membrane, to the cytosol and along microtubules. In vitro and in vivo binding experiments show that Rgnef directly interacts with microtubules via its C-terminal region adjacent to the catalytic DbpA homology/pleckstrin homology domain [244]. The exact mechanisms of Rgnef activation of RhoA have not been fully elucidated but a mechanism of mediation of RhoA activation via integrins has been suggested [245]. This suggested mechanism involves Rgnef scaffolding function that promotes FAK activation which can then lead to RhoA

activation. Furthermore, the GEF activity of Rgnef toward Rho is also important in the activation of paxillin, another focal adhesion protein [246].

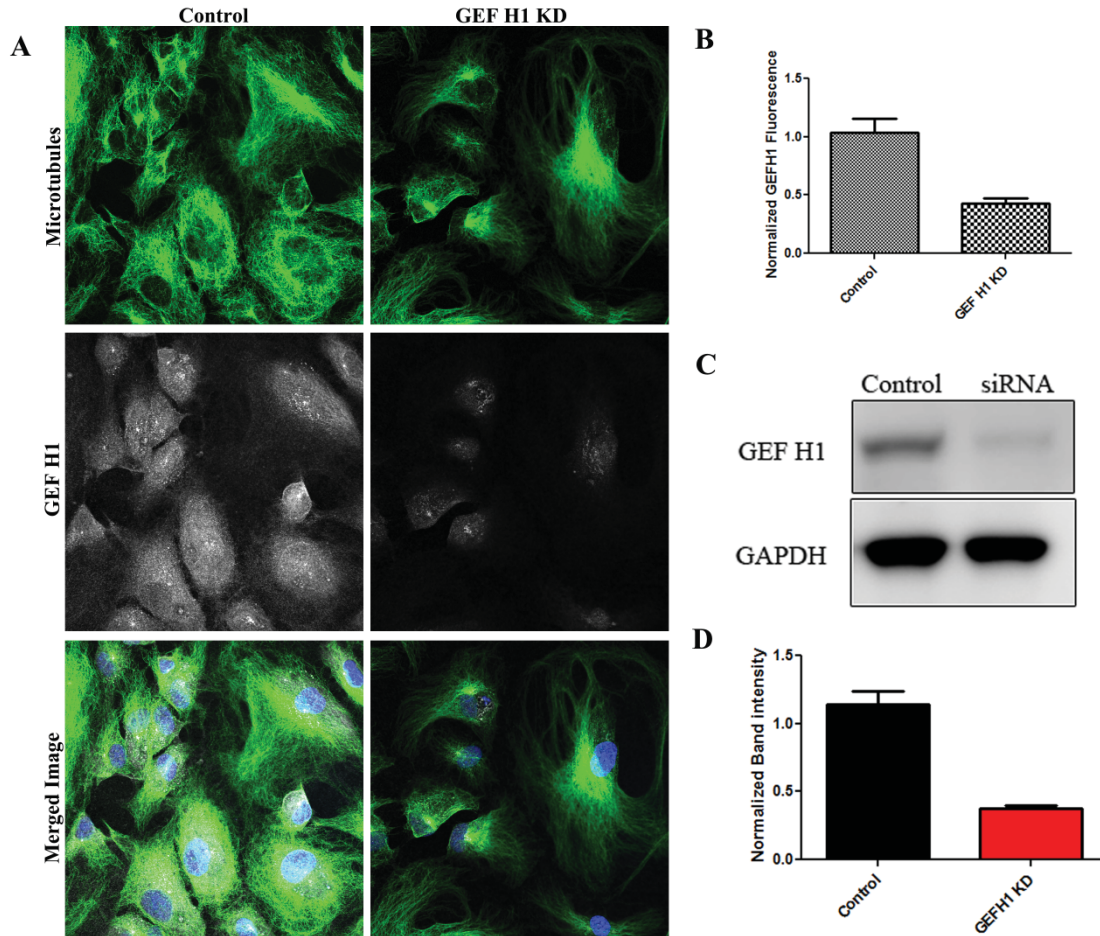


Figure 4.9. GEFH1 RNAi results in reduced protein expression in HUVECs. A) Immunofluorescence confocal images showing effects of siRNA on GEF-H1 levels. B) Quantification of GEF-H1 immunofluorescence. C) Western blot showing GEF-H1 protein depletion. D) Quantification of western blot band intensities.

In order to ascertain that depletion of Rgnef does not have any effect on the cell signaling cascades and morphological changes initiated by OXi8006 treatment, HUVECs were treated with Rgnef specific siRNA prior to OXi8006 treatment. This RNAi procedure resulted in about 60% reduction in Rgnef protein levels (Figure 4.12).

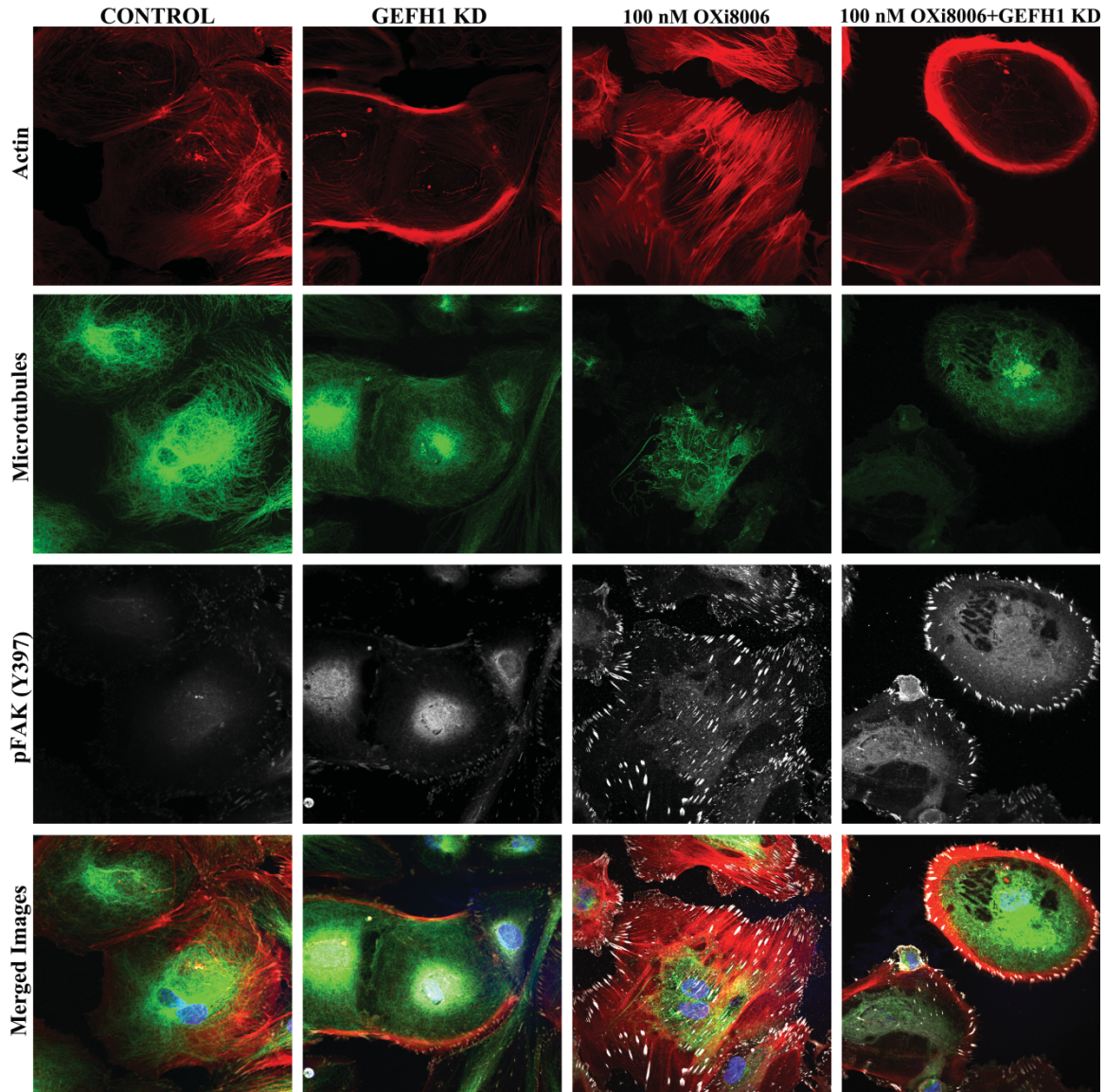


Figure 4.10. Effects of GEFH1 knockdown on OXi8006 treated HUVECs

In contrast to the results seen with GEF-H1, siRNA-mediated depletion of Rgnef (20 nM siRNA for 72 h), had no effect on the contractile and/or ruffling phenotype induced by OXi8006 (Figure 4.13). More specifically, Rgnef depletion did not prevent OXi8006 induced actin stress fiber and focal adhesion formation. This suggests that there is a specific requirement for GEF-H1 in this mechanism. Taken together, this data strongly suggests that OXi8006 induced microtubule depolymerization is linked to the

stimulation of RhoA/ROCK-mediated actomyosin contraction and associated downstream signaling via GEF-H1 activity.

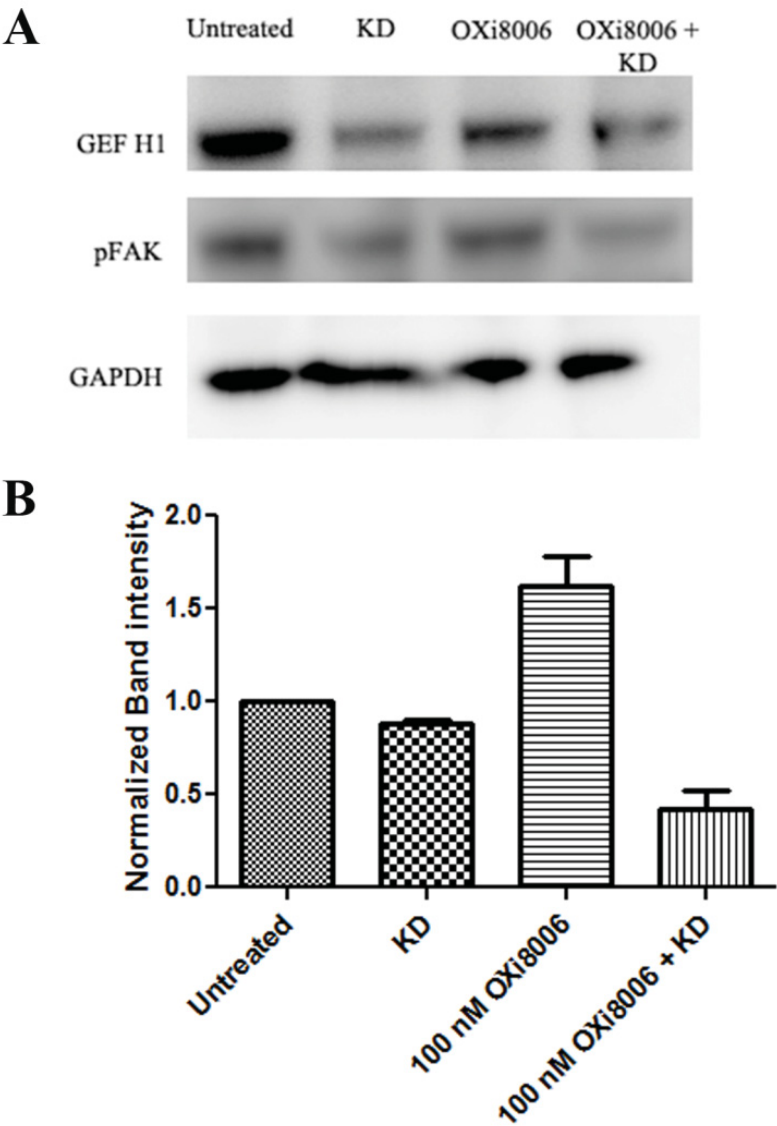


Figure 4.11. Western blot experiment showing effect of GEFH1 knockdown on OXi8006 induced FAK phosphorylation. A) Western blots B) Western blot pFAK band quantification

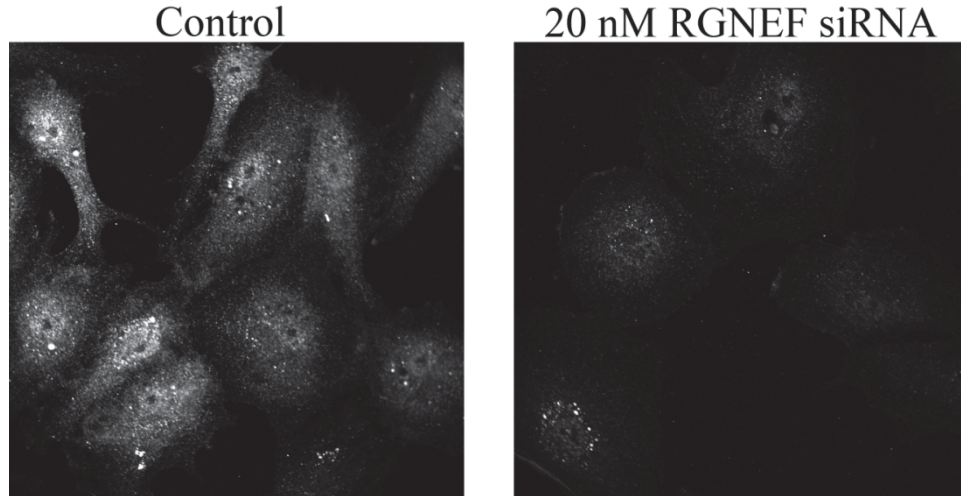


Figure 4.12. HUVECs cells stained with Rggef.

Cofilin Phosphorylation Plays a Significant Role in OXi8006 Induced Cell Contractility

Another method by which the RhoA/ROCK signaling pathway exerts control over cytoskeletal dynamics is via the proteins LIM kinase (LIMK) and cofilin. LIMK is a serine/threonine kinase that plays a role in actin polymerization regulation via phosphorylation and inactivating of the protein cofilin [228]. Cofilin regulates actin dynamics by severing actin filaments and preventing actin monomers from associating with the pointed end of actin filaments, thus preventing actin polymerization and eventual assembly of polymers into stress fibers. Once phosphorylated at serine 3 by LIMK, cofilin can no longer bind to actin, leading to accumulation of actin polymers [247]. LIMK is also a substrate of ROCK and is phosphorylated and activated by ROCK at Thr-508 [228]. In addition, LIMK is also a microtubule associated protein [247]. Therefore, in order to ascertain whether the LIMK/cofilin pathway plays any role in HUVEC contractility that occurs as a result of OXi8006 treatment, the effect of treatment on cofilin phosphorylation was examined.

In order to examine the effect of OXi8006 treatment on cofilin phosphorylation in HUVECs, cells were treated with 100 nM of compound for 2 h before fixation and co-staining with antibodies for actin, α -tubulin, and phospho-cofilin (S3). Confocal imaging of the immunofluorescence stained cells showed that OXi8006 treatment resulted in microtubule disruption and actin stress fiber formation that occurred concurrently with significant increase in cofilin phosphorylation (Figure 4.14). These results were confirmed via western blotting. Here, cells were treated at various time points with 1 μ M OXi8006 before lysate generation. Western blotting showed an initial increase in phosphorylation occurring about 5 minutes after treatment, with maximal phosphorylation seen approximately 60 - 90 minutes after treatment followed by significant decrease in phosphorylation (Figure 4.15 A and B).

The role of LIMK in this mechanism was also examined. Activated HUVECs were pretreated for 12 h with 10 μ M of a LIMK inhibitor (LIM Kinase Inhibitor I, EMD Millipore), after which there were treated for 2 h with OXi8006 and then processed for immunofluorescence imaging. Results show that LIM kinase inhibition not only reduced OXi8006 induced cofilin phosphorylation, but also partially abrogated stress fiber formation in the cells that were co-treated with OXi8006 and the LIMK inhibitor (Figure 4.16). This suggests that the LIMK/cofilin pathway is also activated due to OXi8006 treatment and does play a significant role in the downstream effects of this compound in HUVECs.

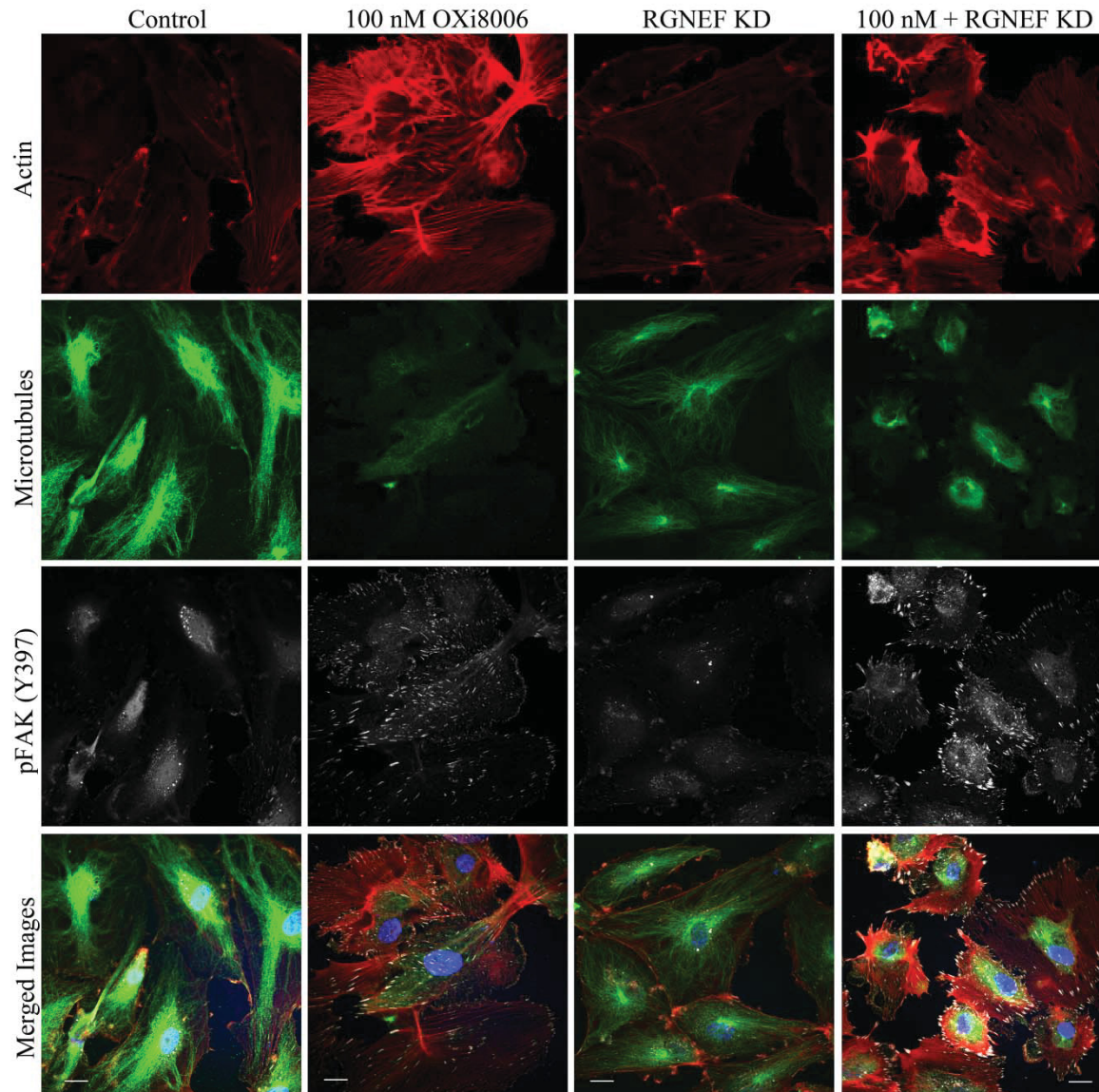


Figure 4.13. Representative confocal images showing p190 RhoGEF (RGNEF) depletion (via RNAi) has minimal effect on OXi8006 induced increase in HUVEC contractility. Treatment with OXi8006 causes similar stress fiber and focal adhesion formation even with RGNEF knockdown.

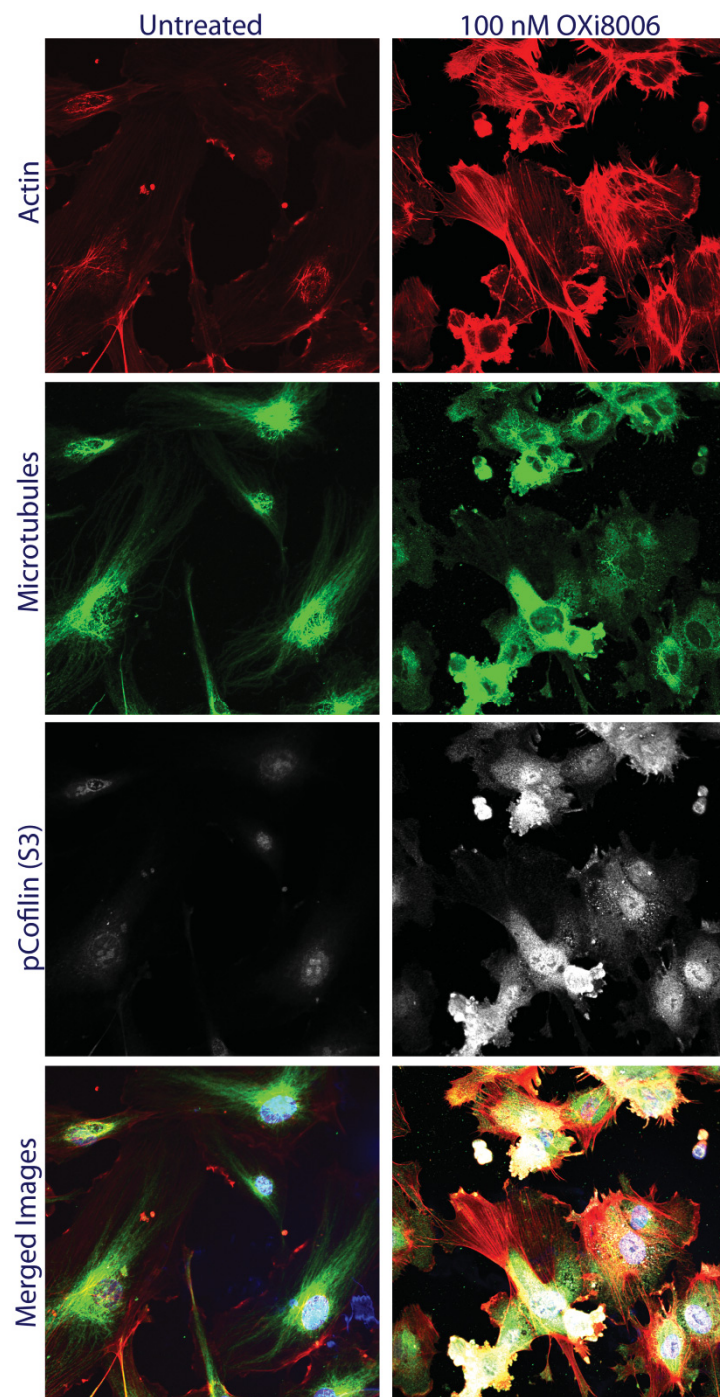


Figure 4.14. Representative confocal images showing effect of OXi8006 treatment on cofilin phosphorylation in HUVECs. OXi8006 treatment causes increased cofilin phosphorylation concurrent with actin stress fiber formation.

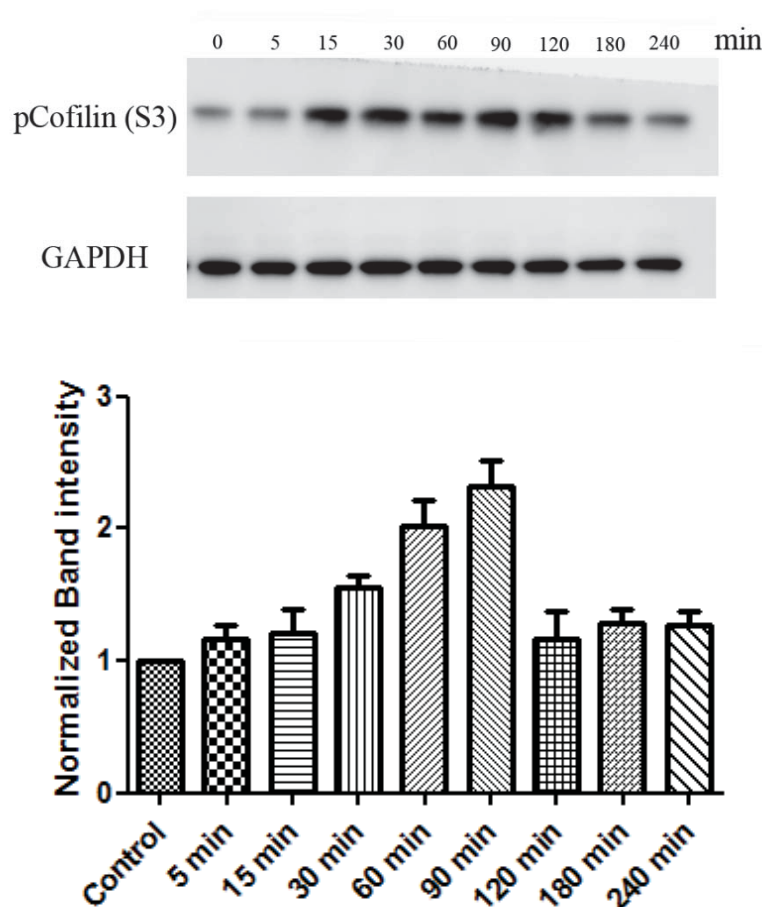


Figure 4.15: Time course experiment showing effect of OXi8006 (1 μ M) on cofilin phosphorylation in HUVECs. A) Western blot. B) Quantification of blots using Image J

OXi8006 Treatment Has a Significant Effect on Tumor Cell Migration

As discussed earlier in Chapter 3, the desired end result of VDA treatment is the rounding up and dissociation of endothelial cells from the basement membrane and from neighboring cells resulting in eventual complete breakdown of the tumor vascular network. However, it is important to ascertain that VDA treatment does lead to increased tumor metastasis due to the fact that it could cause tumor cells to detach from the original tumor site. Therefore, the effects of OXi8006 treatment on MDA-MB-231 cell migration was examined using a scratch assay (as described in the materials and methods section above). Results from this assay showed that treatment with OXi8006 slowed down cell

migration (as evidenced by decreased rate of wound closure compared with vehicle control) in a concentration dependent manner, with effects seen as low as 1 nM OXi8006. As seen from images taken at different time points after OXi8006 treatment (Figure 4.17), wound distances seem to reduce at a significantly slower rate than the controls. Further analyses of these wound distances by measurement and plotting the data into bar graphs (Figure 4.18) confirmed the initial observation. More specifically, the average wound distances of the compound treated monolayers after 12 h were significantly different from the controls ($p < 0.001$ via 2-way ANOVA). Finally, a plot of the average wound distances over time (Figure 4.19) showed rates of 4.2, 3.4, 2.4, and 2.2 % wound distance closure/hr. for control, 1 nM, 5 nM, and 10 nM OXi8006 respectively, showing that treatments as low as 5-10 nM are enough to reduce cell movement/migration by about 50%.

Effect of OXi8006 Treatment on Annexin V Binding in HUVECs

Previous results of our analyses of the effects of OXi8006 on HUVECs showed that OXi8006 treatment eventually leads to cell shrinkage/rounding up and cell membrane blebbing, which are typical morphological criteria associated with apoptosis. Annexin V conjugated dyes are widely employed in cytometry and microscopy as an early marker for apoptosis because of its binding affinity for phosphatidylserine, which is exposed at the cell surface early in the process [248]. In this preliminary experiment, the effects of OXi8006 on induction of annexin V binding by HUVECs were examined via immunofluorescence microscopy.

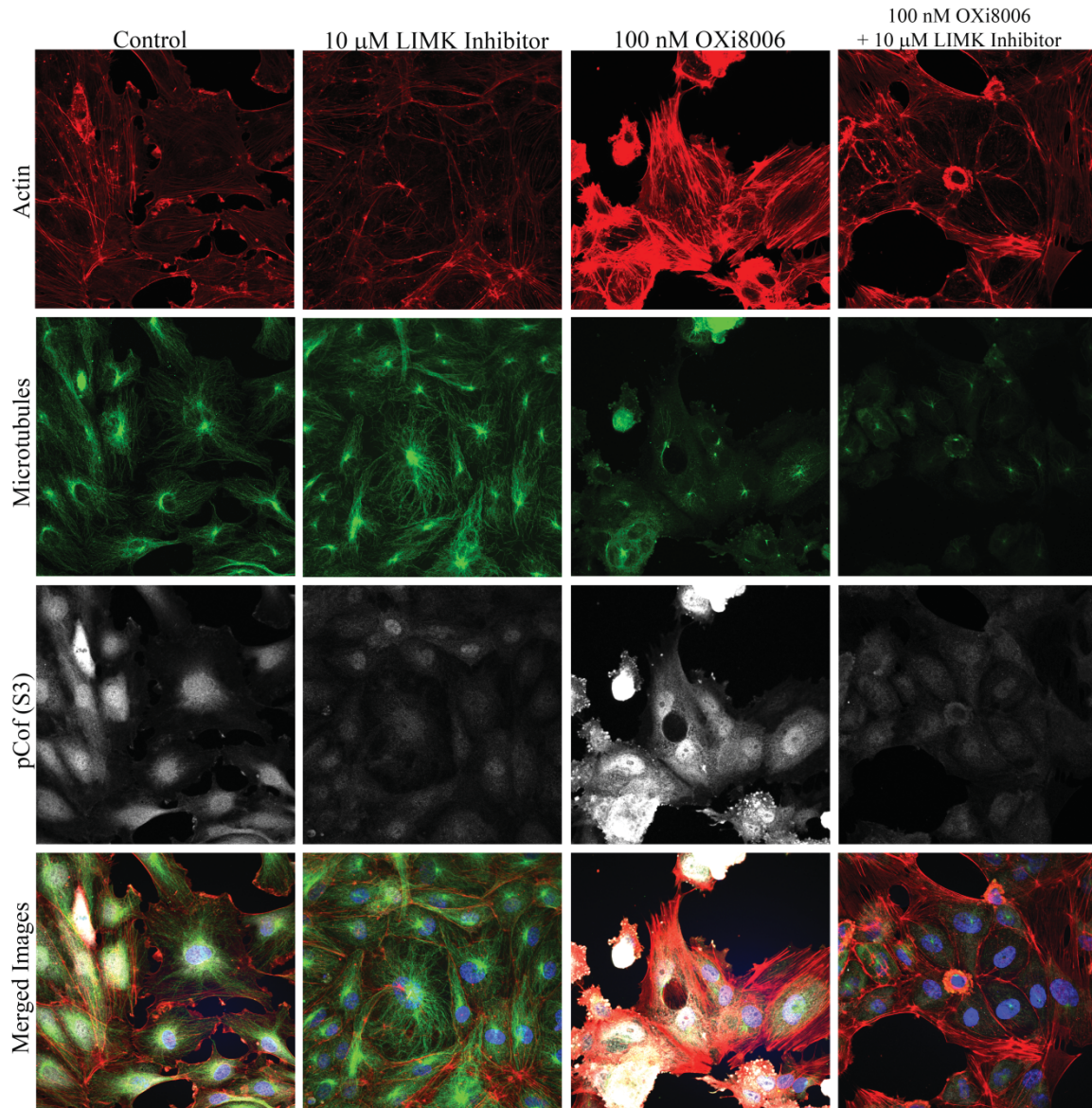


Figure 4.16. Effect of LIM Kinase inhibition on OXi8006 treated HUVECs

As a positive control for increased annexin V binding, cells were treated with CA4, a VDA which has been shown to induce apoptosis in rapidly proliferating HUVECs [128]. As a second positive control, HUVECs were also incubated for 4 h in hypoxic conditions (< 10 ppm O_2) prior to normoxic incubation for another 18 h. This has previously been shown to result in increased apoptotic signaling in human endothelial cells [249]. Results from this experiment showed that treatment of HUVECs with

OXi8006 for 18 h resulted in significantly increased annexin V binding compared to control (Figure 4.20). OXi8006 induced increase in annexin V binding was similar to the increases seen with CA4 treatment and hypoxia. This suggests that OXi8006 induced HUVEC rounding/shrinkage and membrane blebbing could be linked to apoptotic signaling. However, these treatments were done on a longer timescale than the treatments used to determine morphological and cell signaling results (18 h compared to ≤ 2 h), and as such additional experiments using shorter time periods would be required to ascertain that OXi8006 induced increase in HUVEC annexin V binding occurs at similar time points to other morphological and cell signaling changes. Furthermore, in order to confirm that this increase in annexin V binding is indeed due to apoptotic signaling, a concurrent viability assay (using dyes such as PI or trypan blue) must be performed.

Summary

It cannot be overstated how necessary it is to continually add to the landscape of anti-cancer agents currently being researched. There is a lot of potential in targeting the microtubule network as a means of chemotherapeutic development and VDAs represent a promising component to add to the growing arsenal of chemotherapeutic agents. However, a robust understanding of the mechanisms of action of VDAs is still required. The research presented in this chapter suggests some of the mechanisms by which OXi8006 functions in HUVECs. Previously published data from our group [250] which was also discussed in Chapter three suggested that OXi8006/OXi8007 has potent VDA effects in vitro and in vivo. It was also shown that these effects were mediated via microtubule-disruption induced RhoA activation, leading to increased cellular contractility.

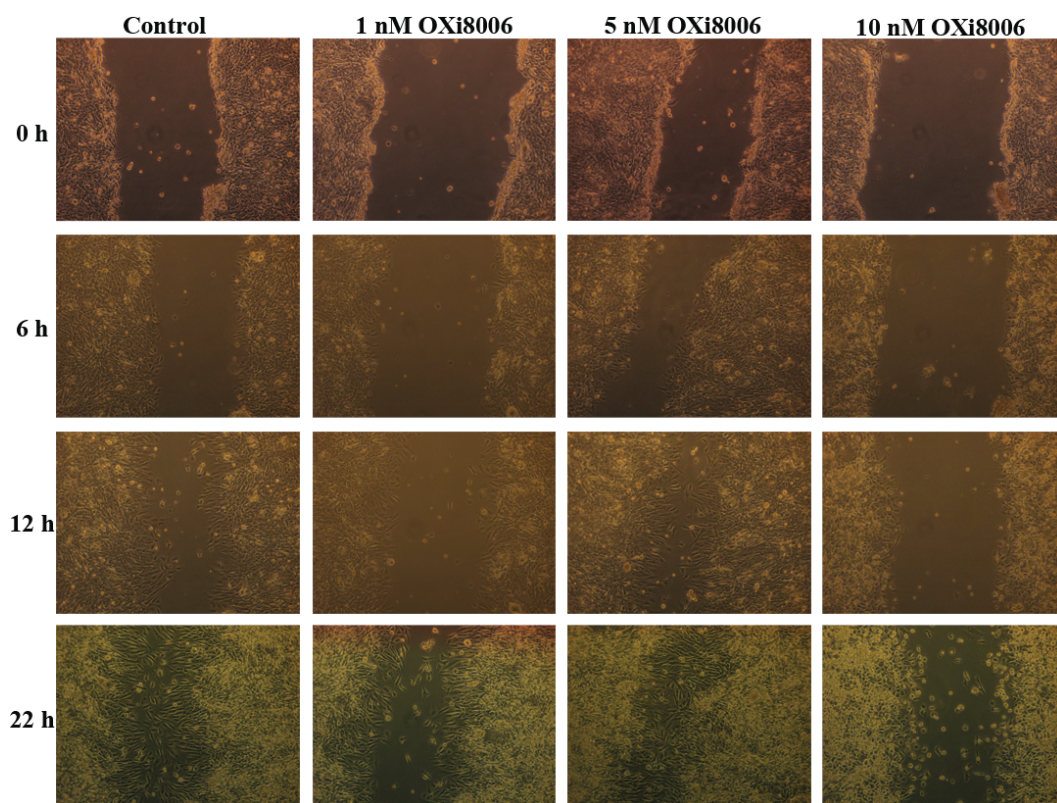


Figure 4.17. Representative images of MDA-MB-231 cell monolayers showing effect of various concentrations of OXi8006 on wound closure over time. OXi8006 treatment results in concentration dependent reduction in wound closure rate.

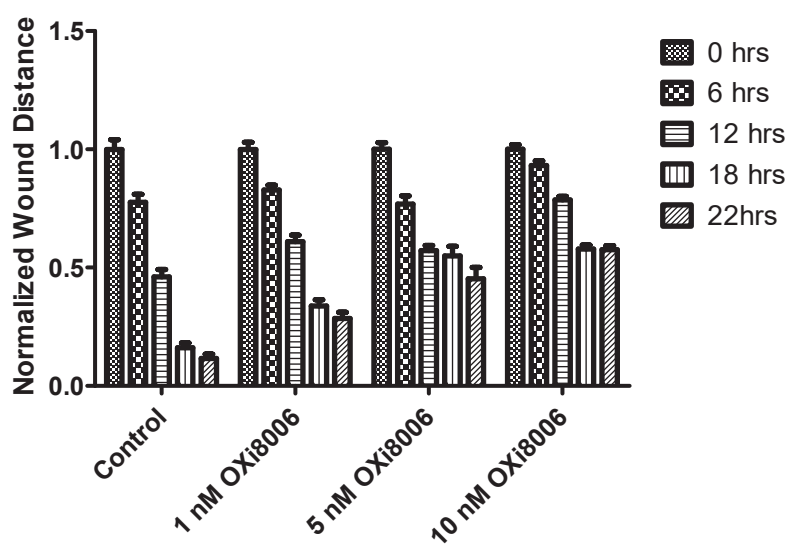


Figure 4.18. Bar graphs showing MDA-MB-231 wound closure over time at different OXi8006 concentrations.

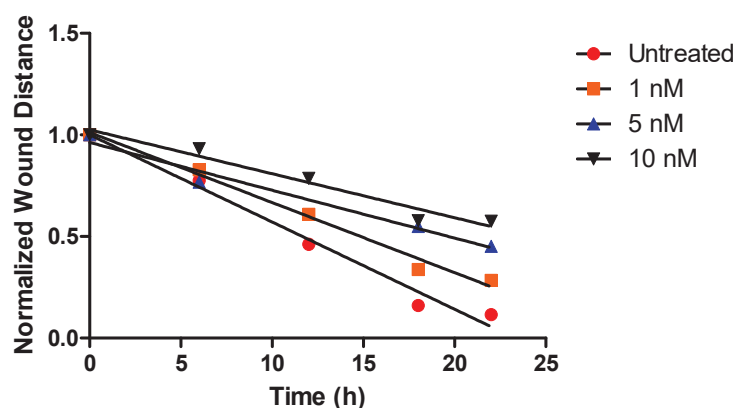


Figure 4.19. Graphical representation of rates of MDA-MB-231 wound closure due to different OXi8006 concentrations.

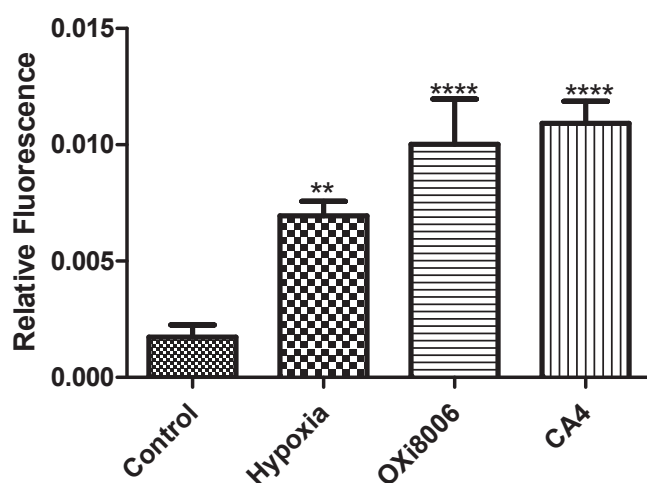


Figure 4.20. Quantification of fluorescence microscopy images showing induction of annexin V binding due to various treatments (**** $p < 0.0001$, ** $p < 0.001$). Treatment with 10 nM OXi8006 for 18 h results in significantly increased annexin V binding compared to control.

However, the microtubule network is not directly involved in the contractile machinery. Previous studies have suggested that the link between RhoA activation and microtubule network dynamics is via GEF-H1 activity [241, 251]. As discussed earlier, GEFs are multifunctional molecules that typically activate Rho GTPases and are important links in various cell signaling cascades. Of these GEFs, GEF-H1 and

p190RhoGEF are the only as microtubule-associated Rho-GEFs which activate RhoA in humans. Furthermore, both of these GEFs have their activity mediated by their microtubule association. The results presented in this chapter suggested that GEF-H1 is necessary for RhoA/ROCK activation following microtubule disruption, as siRNA depletion of GEF-H1 led to abrogation OXi8006 induced contractility. In contrast, release of p190 RhoGEF from microtubules by OXi8006 does not lead to increased HUVEC contractility.

Another facet of the RhoA/ROCK signaling cascade is the activation of LIMK/cofilin. OXi8006 treatment results in significant increase of cofilin phosphorylation which occurs concurrently with actin stress fiber formation. Cofilin phosphorylation increased due to OXi8006 treatment, with maximum phosphorylation observed between 60-90 minutes, after which phosphorylation began to decrease. However, pretreatment of HUVECs with an inhibitor of LIM kinase prior to treatment with OXi8006 abrogated the morphological changes and cell contractility that results from OXi8006 treatment. It should be noted that these results matched the phosphorylation pattern seen with MLC and FAK phosphorylation due to OXi8006 treatment. Furthermore, these phosphorylation patterns also matched the morphological changes seen due to treatment.

A summary of the suggested mechanism is presented in Figure 4.1. Briefly, OXi8006 induced microtubule disruption leads to GEF-H1 release and activation of the RhoA/ROCK pathway. This leads to initial increase in MLC and pFAK phosphorylation resulting in increased stress fiber and focal adhesion formation. There is also an increase in LIMK/cofilin phosphorylation, which leads to a reduction in actin fiber breakdown and

contributes to stress fiber formation. However, the phosphorylation begins to decrease as the cell contractility is resolved and cells begin to round up, shrink, and eventually detach from the extracellular matrix.

In this chapter, the effects of OXi8006 on tumor cell migration were also investigated. While the tumor cells themselves are not the intended primary target of VDA treatment, it is possible that there could be some bystander effects, causing the tumor cells themselves to detach from the basement membrane. This detachment is similar to one of the initial steps seen in the epithelial-mesenchymal transition (EMT) that can contribute to cancer metastasis [252]. Therefore, it is useful to ensure that the drug treatment does not lead to increased cell migration. Results from wound assays on MDA-MB-231 cell monolayers indicate that OXi8006 treatment causes significant concentration dependent inhibition of cell migration, with effects starting at concentrations as low as 1 nM.

Finally, the effect of OXi8006 on the initiation of apoptosis in HUVECs was also examined. A number of the morphological changes that were observed as a result of OXi8006 treatment including cell rounding, shrinkage and blebbing are characteristic of and could result from the initiation of apoptotic signaling [253]. HUVECs were treated with OXi8006 and the resulting effect on annexin V binding was analyzed via an annexin-V binding assay and fluorescence microscopy. Results from this assay indicated that OXi8006 caused a significant increase in annexin V binding by treated cells compared to control. This result suggests that OXi8006 treatment could be causing an increase in apoptotic signaling albeit on a much longer timescale than seen with the initial morphological changes.

CHAPTER FIVE

Introduction to Cysteine Proteases

Proteases constitute the largest class of immensely biodiverse enzymes, with more than 1600 proteases identified in over 1700 organisms; in humans alone, there are approximately 500 proteases observed. Provided such broad abundance, it is not surprising that proteases play significant biochemical roles in regulating many essential signal transducing pathways leading to homeostatic functionality supporting cell, organ, and total system physiology level processes. While these processes are complex, the biochemical action of proteases is the specific cleavage of peptide bonds in proteins, particularly in degradation and processing pathways. Thus the dysfunction of these can give rise to serious physiological and pathological consequences in the expressing organism. Conversely, the completely functional involvement of proteases in the life cycle of disease-causing organisms facilitates their infection and proliferation in human hosts. Given natural ubiquity and essential functionality, focus on targeting protease represents fertile ground for novel therapeutic design and discovery in the management of a broad variety of diseases, including cancer, AIDS, parasitic ailments, and immunological disorders [254].

Proteases can be categorized based on two criteria: substrate specificities or mechanisms of catalysis. Categorization based on substrate specificity results in classifying proteases as either endopeptidases (enzymes cleaving within a polypeptide chain) or exopeptidases (enzymes cleaving at the ends of polypeptide termini).

Categorization based on catalytic mechanisms gives four major protease classes: serine, cysteine, aspartic, and metalloproteases [255].

Aspartic proteases use two catalytic aspartic acid residues in the active site to coordinate the nucleophilic attack of the peptide bond by a water molecule. Serine proteases have a hydroxyl group at the active site that acts as the nucleophile that attacks the peptide bond. In the case of cysteine proteases, a thiolate ion at the active site is used to attack the peptide bond. Metalloproteases use a metal atom to coordinate the substrate and catalyze the nucleophilic attack of a water molecule on the peptide bond [255].

The project presented here is focused mainly on enzymes of the large subfamily of cysteine proteases known as papain-like cysteine proteases (clan CA, family C1), specifically mammalian cathepsins L, B and K, as well as the parasitic cysteine protease cruzipain (or cruzain).

Papain-Like Cysteine Proteases: Sequence, Structure, Mechanism, Expression, Substrate Specificity, and Physiological Functions

Lysosomal cysteine proteases comprise a group of papain-like enzymes, sharing similar amino acid sequences and folds. They are optimally active under the slightly acidic conditions and the molecular weights of the mature forms of these enzymes are usually in the 20-30 kDa range. In their zymogenic (inactive) forms, these enzymes typically have a pro-region, which extends from approximately 60-100 kDa. These zymogenic forms are initially synthesized as pre-proenzymes [256]. Following synthesis, a pre-proenzyme is transformed to the proenzyme during the passage to the endoplasmic reticulum. Pro-cathepsin undergoes proteolytic processing to the active, mature enzyme form in the acidic environment of late endosomes or lysosomes [257]. Limited

proteolysis is thus a crucial step in controlling the proteolytic activity of lysosomal cysteine proteases and numerous other proteases. The mature forms of these enzymes are mostly monomeric. Eleven papain-like cathepsins are expressed in the human genome (B, H, L, S, C, K, O, F, V, X and W) (Figure 5.1) [258, 259].

Name	Synonym	Cleavage specificity	Tissue expression	Function	pH
Cathepsin B	Cathepsin B1, APP secretase	Endopeptidase; peptidyl-dipeptidase	Ubiquitous	Lysosomal, extracellular; proteolytic processing of APP tumor invasion and metastasis	pH 4–6 (optimal), stable to pH 7
Cathepsin C ^a	DPP I, cathepsin J, dipeptidyl-transferase	Peptidyl-dipeptidase, tripeptidyl-peptidase; endopeptidase	Ubiquitous	Lysosomal; activates granulocyte serine proteases, factor XIII neuraminidases	pH 6 (optimal), pH 4–7.5 (stable)
Cathepsin F	SmCF	Endopeptidase	Heart, skeletal muscle, brain, testis, ovary	Lysosomal; role in tumor invasion and metastasis	pH 5.2–6.8 (optimal), pH 4.5–7.2 (stable)
Cathepsin H	Cathepsin B/3, BANA hydrolase	Endopeptidase, aminopeptidase	Brain, kidney, liver; inflamed tonsil	Lysosomal; invariant chain (Ii) degradation	pH 6.8 (optimal), pH 5–8 (stable)
Cathepsin K ^b	Cathepsin O(1), cathepsin O2, cathepsin X	Endopeptidase	Predominantly in bone (osteoclasts); present in most epithelial tissues	Lysosomal, extracellular; osteoclastic bone resorption; fibrinogen and ECM degradation	pH 6 (optimal), pH 4–8 (stable)
Cathepsin L	SPase, cathepsin L1	Endopeptidase	Ubiquitous	Lysosomal, extracellular, nuclear (truncated); antigen presentation (AP), Ii degradation, cell cycle regulation	pH 6 (optimal), pH 4–7 (stable) varying
Cathepsin O	—	Endopeptidase (pending)	Widely expressed	Lysosomal; protein turnover (pending)	
Cathepsin S	—	Endopeptidase	Alveolar macrophages, spleen, testis, epithelial cells; CD4+ T-cells	Lysosomal, extracellular; Ii degradation, arterogenesis, AP, angiogenesis, elastolytic activity	pH 6 (optimal), pH 4.5–8 (stable)
Cathepsin V	Cathepsin L2, cathepsin U	Endopeptidase	Predominantly in thymus, testis; present in brain, corneal epithelium, skin	Lysosomal (potential); AP, Ii degradation	pH 5.7 (optimal), pH ≤4 to ≥7.2 (stable)
Cathepsin W	Lymphopain	Pending	Spleen, natural killer and cytotoxic T-cells	Immune response, regulation of T-cell cytotoxic activity	
Cathepsin X	Cathepsin B2, cathepsin P, cathepsin Z	Carboxymono-peptidase, carboxydipeptidase	Widely expressed; ubiquitously in primary tumors and cancer cell lines	Lysosomal; non-proteolytic in cell adhesion	

Figure 5.1. List of human cysteine cathepsin proteases [258].

Cysteine Protease Amino Acid Sequences and Active Site Residues

Cysteine proteases have numerous similarities, and have a significant number of conserved amino acid sequences (Figure 5.2). All cysteine proteases have a conserved active site, consisting of cysteine, histidine, and asparagine residues. The cysteine residue (Cys-25, papain numbering) is embedded in a highly conserved peptide sequence, CGSCWAFS. Similar to the area around the active site cysteine residues, the vicinities of the histidine and asparagine residues are also conserved. The histidine residue (His-

159) is adjacent to small amino acid residues such as glycine or alanine followed by four aliphatic hydrophobic residues (valine, leucine, isoleucine and glycine) [260]. The catalytic domains of most papain-like cysteine proteases are between 220 and 260 amino acids in length, with the exception of several parasite-derived cysteine proteases which contain a C-terminal extension of unknown function.

The human cathepsin L gene encodes a 333-amino acid cysteine protease that contains a 17-amino acid signal peptide, a 96-amino-acid propeptide, and a 220-amino acid mature region. The 38-kDa procathepsin L is processed to mature, active cathepsin L, and exists either as a single chain form of 30 kDa or as a two-chain form of 25 and 5 kDa [260-262]. There is a high structural similarity between cathepsin L and the parasitic cysteine protease cruzain. The amino acid sequence of the heavy chain is shown in Figure 5.3. The peptide sequence is also about 41% similar to that of papain [263]. The three most abundant residues are glycine, glutamate and serine (25, 19, and 19 residues, respectively), and the least abundant residues are histidine (three residues) and tryptophan (five residues). Hydrophobic residues account for almost one third of the total composition of cathepsin L. Approximately, 41 percent of the composition is comprised of polar, uncharged residues.

Cathepsin K is a homodimeric protein containing 215 residues per monomer with a molecular weight between 25 and 29 kDa [264]. The amino acid sequence of cathepsin K (Fig 5.4) has been reported to be between 50 – 60 % similar to cathepsin L [264]. The three most abundant residues are glycine, asparagine and arginine (24, 19, and 19 residues respectively). The least abundant residues are histidine (2 residues), tryptophan and methionine (four residues each). Cathepsin K is similar to cathepsin L in that

hydrophobic residues account for almost one third of the total composition of the protein. Also, 44 percent of the composition is entirely made of polar, uncharged residues.

Cathepsin B is a 339 amino acid chain in its zymogenic form. Upon maturation (due to cleavage of pro-peptide), it becomes a double chain molecule of approximately 254 amino acids in length. The light chain (residues 80-126) is cross-linked via a disulfide bond to the heavy chain (residues 129-333) and is seen in pink. Residues 1-8 (green) make up a signal peptide, residues 9-79 and residues 334-339 make up the pro-peptide (red), all of which are cleaved during processing leaving residues 80-333 (~254 amino acids) as the mature cathepsin B enzyme (blue). The active site residues on the mature enzyme are Cys29, His199, and Asn281 [265].

Crystal Structures of Cysteine Cathepsins

Cysteine proteases are made up of two major domains, the left (L) and right (R), which are of similar size. The L-domain has three helical regions, the longest being the central helix, about 30-40 residues long, having the catalytic Cys-25 perched at its N terminus. The fold of the R-domain is based on a β -barrel motif of five to six strands and includes a shorter α -helical motif which closes off the β -barrel (Figure 5.6). This domain has the His-159 residue at its C-terminal region. Although the left domain is mainly comprised of the N-terminal half of the enzyme, the polypeptide chain actually starts on the distal right side of the right domain 6. The domains are separated such that a V-shaped active-site cleft is formed, which has residues Cys-25 and His-159 of each domain in the center to form the catalytic site of the enzyme [256, 270].

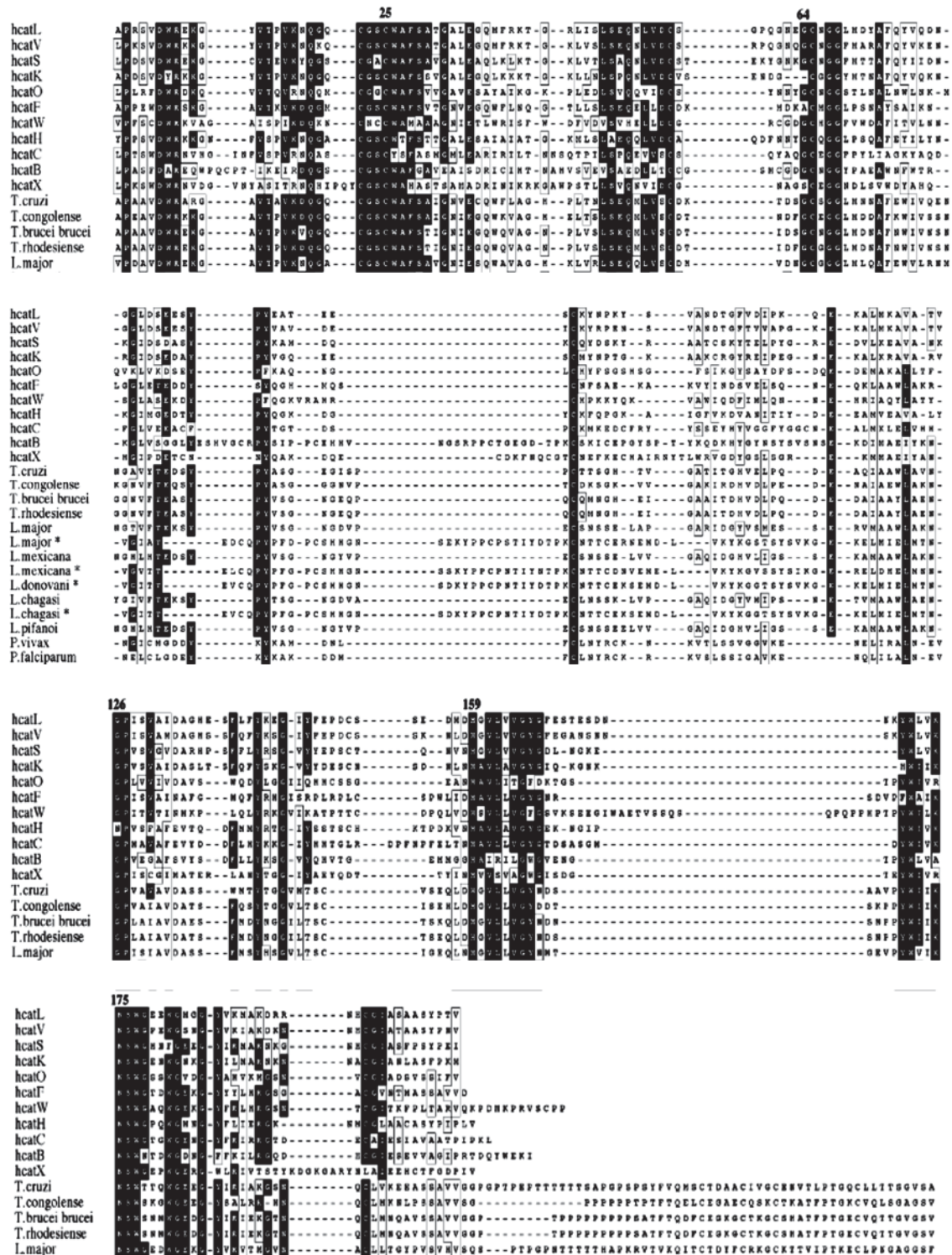


Figure 5.2. Amino acid sequence alignment of human lysosomal cathepsins and related parasite cysteine proteases [266]

1	APRSVDWREK	GYVTPVKNQG	QCGSCWAFSA	TGALEGQMFR	KTGRLISLSE
51	QNLVDCSGPQ	GNEGCNGL	DYAFQYVQDN	GGLDSEESYP	YEATEESCKY
101	NPKYSVANDT	GFVDIPKQEK	ALMKAVATVG	PISVAIDAGH	ESFLFYKEGI
151	YFEPDCSSED	MDHGVLVVGY	GFESTESDNN	KYWLVKNSWG	EEWGMGGYVK
201	MAKDRRNHCG	IASAASYPTV			

Figure 5.3. Amino acid Sequence of Cathepsin L. Legend: Blue, Heavy Chain; Red, Light Chain; Catalytic Residues, Green [267]

```

1  APDSVDYRKKGYVTPVKNQGQCGSCWAFSSVGALEGQLKKKTGKLLNLSP
51 QNLVDCVSENDGCGGGYMTNAFQYVQKNRGIDSEDAYPYVGQEESCMYNP
101 TGKAAKCRGYREIPEGNEKALKRAVARVGPVSVAIDASLTSFQFYSGVY
151 YDESCNSDNLNHAFLAVGYGIQKGNKHWHIKNWGENWGNKGYILMARNK
201 NNACGIANLASFPKM

```

Figure 5.4. Amino Acid Sequence of Cathepsin K (PDB ID: 3KX1) [268].

10	20	30	40	50
MWQLWASLCC	LLVLANARSR	PSFHPLSDEL	VNYVNKRNTT	WQAGHNFYNV
60	70	80	90	100
DMSYLKRLCG	TFLGGPKPPQ	RVMFTEDLKL	PASFDAREQW	PQCPTIKEIR
110	120	130	140	150
DQGSCGSCWA	FGAVEAISDR	ICIHTNAHVS	VEVSAEDLLT	CCGSMCGDGC
160	170	180	190	200
NGGYPAEAWN	FWTRKGLVSG	GLYESHVGC	PYSIPPCEHH	VNGSRPPCTG
210	220	230	240	250
EGDTPKCSKI	CEPGYSPTYK	QDKHYGYSY	SVSNSEKDIM	AEIYKNGPVE
260	270	280	290	300
GAFSVYSDFL	LYKSGVYQHV	TGEMMGGHAI	RILGWGVENG	TPYWLVANSW
310	320	330		
NTDWGDNGFF	KILRGQDHCG	IESEVVAGIP	RTDQYWEKI	

Figure 5.5. Amino acid Sequence of Cathepsin B. Legend: Green, signal peptide; Red, pro-peptide; Pink, light chain of mature enzyme; Blue, Heavy chain of mature enzyme [269].

The active site surface is formed by residues converging from four loops, two from each domain. The L-domain loops are shorter and disulfide-bond connected. The R-domain loops, on the other hand, are larger in length and are placed at the top of the β -barrel motif. Similarly, the mostly C-terminal right domain ends in a strand that extends into the left domain. For many enzymes in this group, two disulfide linkages add stability to the left domain, whereas one is found in the right domain [271]. Cathepsin propeptides

are typically less structured and run in the inverse orientation through the substrate binding cleft (Figure 5.7) [260]. Analysis of the crystal structures of the proenzymes showed that the structure of the mature enzyme is already formed in the zymogen form [272]. The propeptide chain is comprised of an α -helical domain, which continues along the active-site cleft toward the N-terminus of the mature enzyme in a predominantly extended conformation in a direction opposite to substrate binding, thus blocking access to the active site (Figure 5.7) [260]. The activation process is triggered by a pH change that may lead to the weakening of the interactions between the propeptide and the catalytic site. As a consequence, the proenzyme most likely adopts conformation where it is less tightly bound to the active site without the loss of the secondary structure making it more accessible to proteolytic cleavage to form the active enzyme [273].

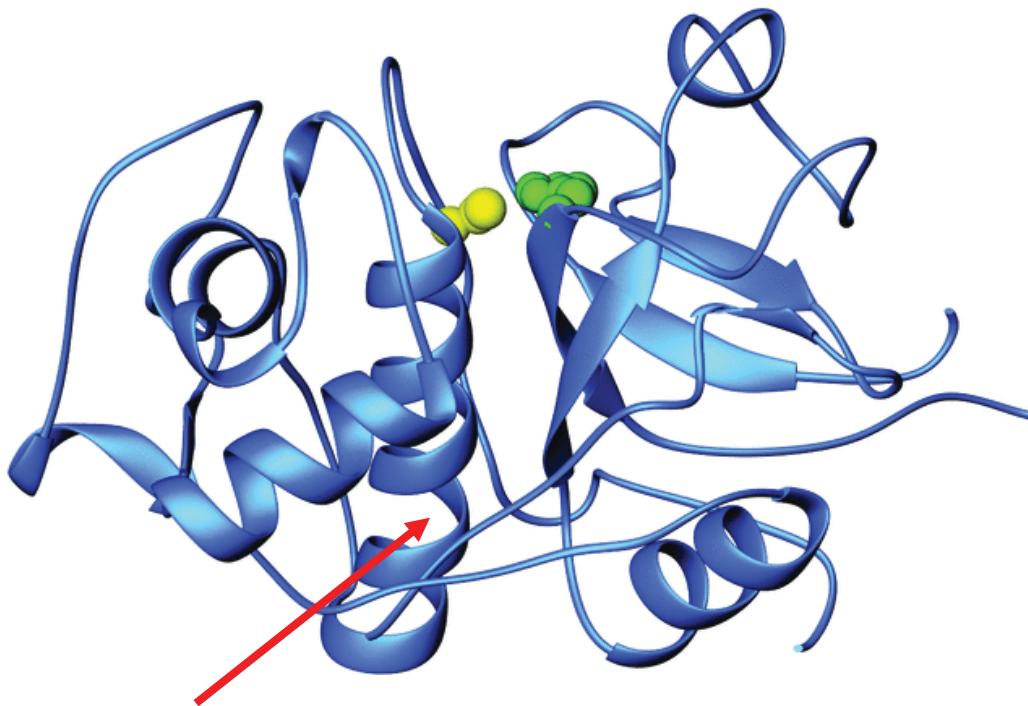


Figure 5.6. Typical cysteine cathepsin (cathepsin L) fold viewed along the two-domain interface and the active site at the top. The side chains of the catalytic residues Cys-25 and His-159 (papain numbering) are shown as yellow and green atom spheres, respectively [260].

Substrate-Binding Sites

There are seven possible substrate-binding sites, which bracket the catalytic dyad of Cys- 25 and His-159 [274].

The carboxyl side of the peptide substrate and corresponding enzyme subsites are conventionally referred to as the prime side and are termed P_1' , P_2' , P_n' and S_1' , S_2' , and S_n' respectively. The amino side of the peptide and corresponding subsites assigned the non-prime side and are designated P_1 , P_2 , P_n and S_1 , S_2 and S_n , respectively (Figure 1.8) [273].

The active site clefts of cysteine proteases consist of three well defined substrate-binding subsites (S_2 , S_1 and S_1'). However, the complete binding area is comparatively broad, with other subsites (S_4 , S_3 , S_2' , S_3') participating in substrate binding [275].

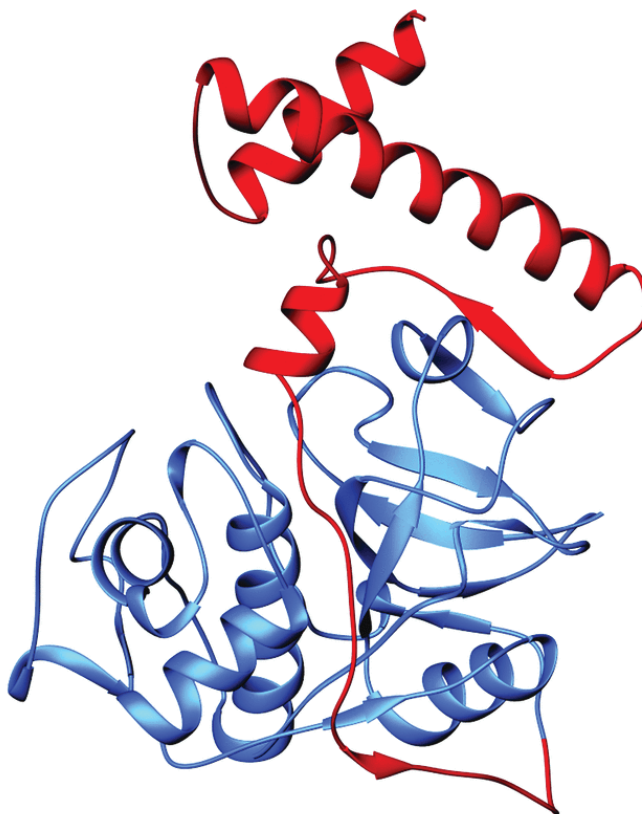


Figure 5.7. Typical procathepsin fold (1cj). The mature enzyme part is shown in blue and the propeptide is shown in red [260]

These binding sites do not exhibit strict specificities, but do have preferences arising from specific exclusions based on substrate type/structure [272]. Cysteine proteases typically react more readily with bulky hydrophobic residues at P2 due to the fact that the S₂ binding site is a deep hydrophobic pocket [263]. In conclusion, subsites S₂, S₁ and S₁' form well-defined binding sites. The S₂ and S₁' substrate binding sites are responsible for the diversity and selectivity of the substrate and inhibitor binding [260, 276].

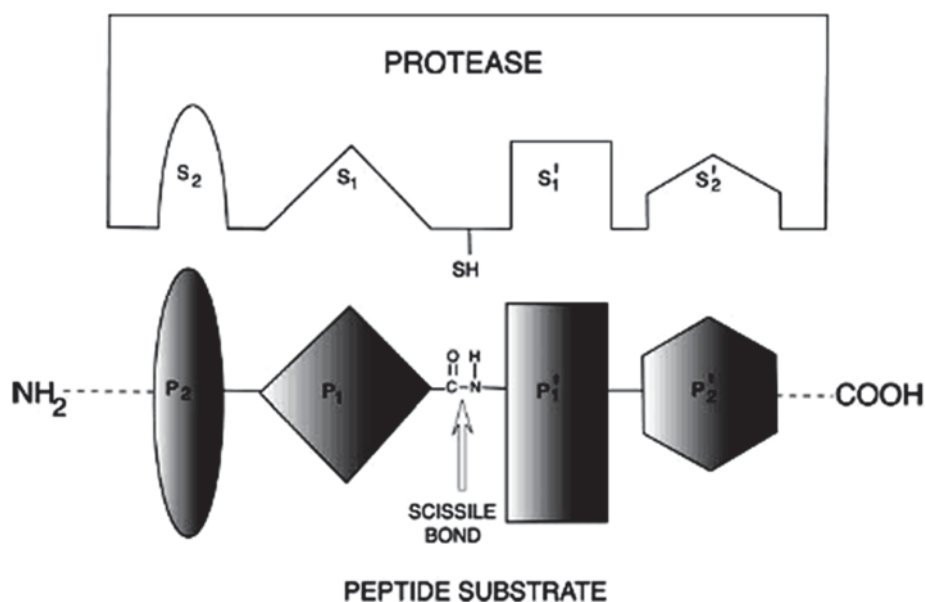


Figure 1.8. Diagrammatic representation of peptide substrate interaction with the active site pockets of a cysteine protease. Amino acid residues from the peptide substrate are denoted by 'P' and the sub-sites that the peptide interacts with are given the letter 'S'. The active site cysteine sulfhydryl nucleophile is represented as SH [273].

Cathepsin L Structure

The structure of cathepsin L has been extensively elucidated, and analysis of cathepsin L by X-ray crystallography revealed important characteristics of the structure [263]. The S' regions of cathepsin L are shallow depressions and have various

similarities with papain. The bottoms of these depressions are made up of interactions various sidechains (Trp189, Gln21, Gly20, Asn18, Glu192, Trp193 and Leu144). The oxyanion hole of cathepsin L is made by three residue side chains (Gln16, Trp189, and His163) and the Cys25 backbone. The S₂ pocket of cathepsin L is highly hydrophobic, which is similar to several cysteine proteases. The bottom S₂ pocket of cathepsin L consists of Met70, Ala135, hydrophobic residues Leu69, Met161 and Gly164. Also, the residues that surround the S₂ site are Asp162, Met161, Asp160, and Ala214. Met70 is the responsible for the S₂ pocket shallow characteristic. The crystal structure of human cathepsin L is shown in figure 5.9. The active site residues that form the catalytic triad (Cys25, His159, and Asn175) are shown in ball and stick form. In figure 5.9, α -Helices are represented in red, β -sheets in cyan, the turns are in green, and coils represented in white [277].

Cathepsin K Structure

Mature cathepsin K is a macromolecule with 215 amino acids. In the structure, Cys25 and His159, two of the members of the catalytic triad, form of an ion pair (thiolate-imidazolium pair), with the third residue Asn175 located close by and protected by Trp77 (papain numbering). The overall structure contains several well defined pockets. Seven of these pockets have the capability to interact with potential cysteine protease inhibitors.

The crystal structure of uninhibited cathepsin K is shown in Figure 5.10 [268]. Three catalytic residues (Cys25, His159, and Asn175) are shown in ball and stick form, α -helices are red, β -sheets are cyan, turns are green, and coils are white. Analysis of the structure revealed a number of important structural components at the active site and

throughout the protein. At the active site, there is a hydrogen bond formed between the carboxyl oxygen of Asn175 and one of the nitrogen atoms of the imidazole ring of His159. The crystal structure also reveals a close proximity between one of the His159 nitrogen atoms and the thiol group of Cys25 (*N-S*: 3.65 Å). The significantly hydrophobic S2 subsite is formed by six residues, (Tyr67, Met, 68, Ala133, Leu157, Ala160, and Leu205). The presence of Leu205 makes the S₂ pocket shallow, which enables preference for bulky substrate residues such as phenylalanine.

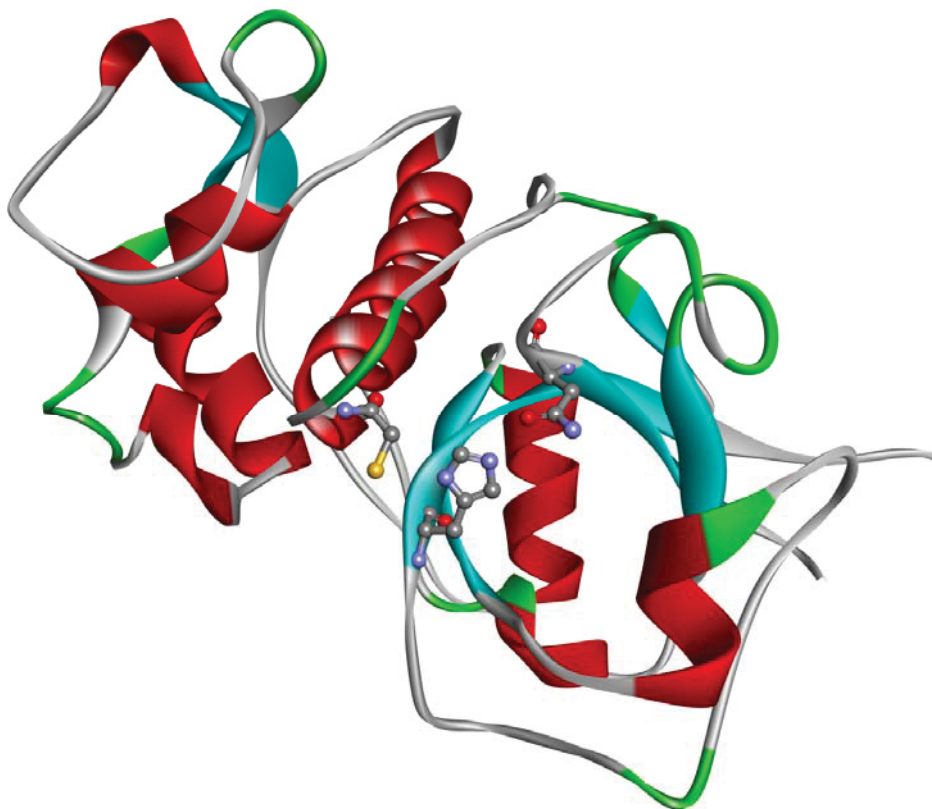


Figure 5.9. Crystal Structure of Human Cathepsin L (PDB ID: 1ICF) [277]

On the other hand, the S₃ pocket is made only with two residues: Tyr67 and Asp61. The P₁' pocket is made up of Asn158, Trp177, and Ala136 side chains. Trp177 (which is the protective group of Asn175) appears to be in close proximity to the

substrate as well. Finally, the key signature of cysteine proteases, a disulfide bond between two cysteine residues was found in cathepsin K (Cys153 and Cys200).

Cathepsin B Structure

Cathepsin B is a bi-lobal protein approximately 30 kDa in size (~38 kDa in its zymogenic form) [265]. The protein is about 30 Å thick with a diameter of approximately 50 Å, and is comprised of two domains and an occluding loop into two domains (Figure 5.11)

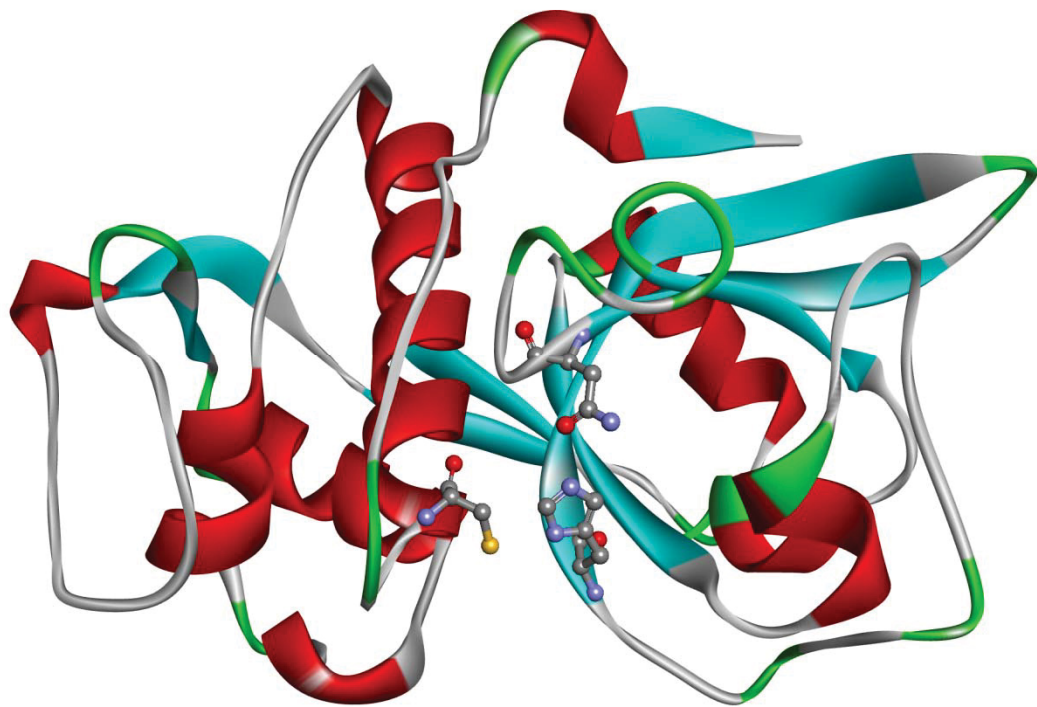


Figure 5.10. Crystal Structure of Human Cathepsin K (PDB: 3KX1) [268]

One domain has a central α -helical structure and is made up of the amino-terminal half of the polypeptide chain from residues 11-148 and the last 4 carboxy-terminal

residues [278]. This domain contains three α -helices arranged perpendicularly and is mostly hydrophobic in nature, containing 18 hydrophobic residues [279]. The other domain is composed of the C-terminal domain, being formed by residues 1-10 and the carboxy terminal end of the protein (residues 149-250) with a secondary structure made up of a β -barrel with 6 sheets arranged in an anti-parallel motif [265]. This domain is surrounded by α -helices, and contains a highly hydrophobic core which comprises of about 19 aromatic residues.

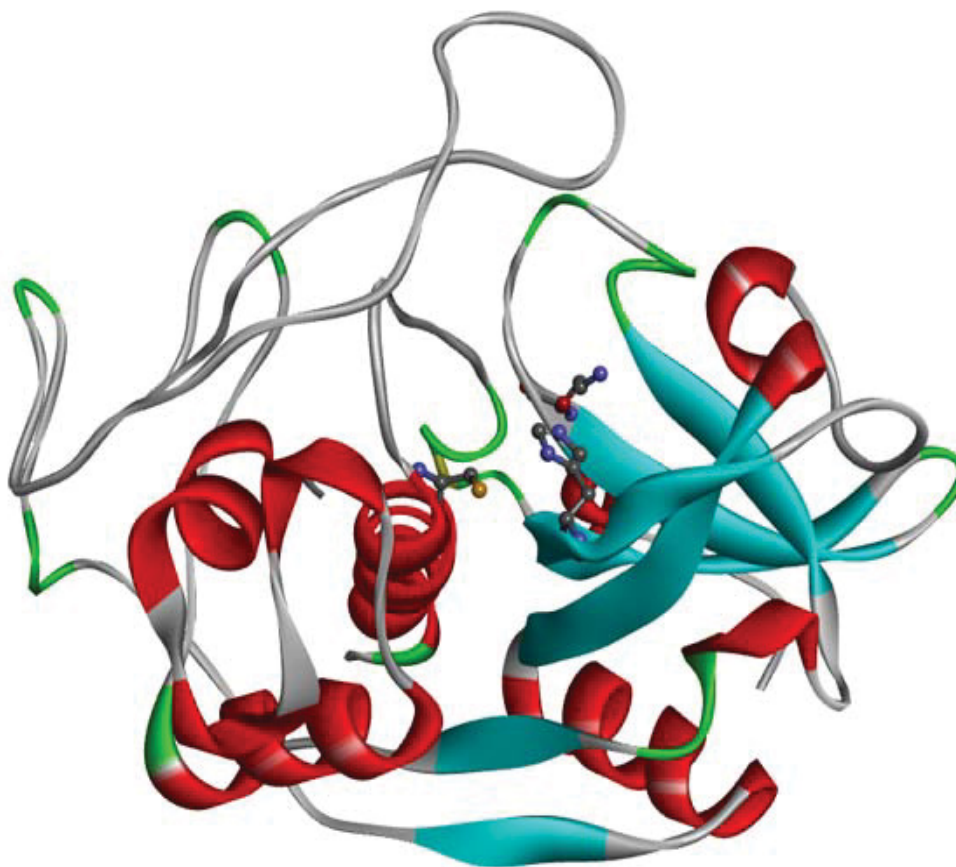


Figure 5.11. Crystal Structure of Human Cathepsin B (PDB: 1HUC) [265]

The two domains interact with each other via an extended polar interface that opens to the V-shaped cleft active site [278]. The active site present at this V-shaped cleft

contains amino acid residues Cys29, Asn281, His199, His110, and His111 (the latter two of which are responsible for the exopeptidase activity of the enzyme), which are important for the catalytic activity of cathepsin B. The active site of cathepsin B contains a cysteine in the catalytic triad of Cys29, Asn281, and His199 as is seen in Figure 5.11. It should also be noted that human cathepsin B contains six total disulfide bridges formed between the following amino acid residues: 93-122, 105-150, 141-207, 142-146, 179-211, and 187-198 [265, 280].

Cathepsin B is unique from many other cathepsins due to its dual role depending on the pH. Cathepsin B can act as a carboxypeptidase at acidic pH and as an endopeptidase (similar to other cysteine cathepsins) at neutral pH [281]. The carboxypeptidase activity occurs due to the presence of the occluding loop composed of 18-20 residues, Ile105-Pro126, that restricts active site access, acting as a flexible “flap” which can open and close. This loop is unique to cathepsin B, and is a covalently closed circular structure which begins and ends with an identical Pro-Pro-Cys sequence which has been suggested to help stabilize the ends of the occluding loop [281]. In order to initiate carboxypeptidase activity, the Cys29 and His199 act as the catalytic nucleophile and general base while Gln23 stabilizes the oxyanion tetrahedral intermediate of the substrate. Furthermore, in this native form and at low pH, Trp221 and Trp225 form a hydrophobic pocket surrounding active site and two salt bridges between Asp22-His110 and Arg116-Asp224 are created. This causes the usually flexible occluding loop to be held in place thus blocking access to the active site [282]. With these structural changes, the histidine residues form the outer boundaries of the S2' subsite. Upon pH increase and in the inhibitory conformation, the His110 becomes deprotonated, allowing for the loop

to freely move and therefore changes the function of cathepsin B from an exopeptidase to an endopeptidase [281]. The two histidine residues account for the cathepsin B preference for carboxypeptidase activity as they can bind the C-terminal carboxylic groups of the substrate. The occluding loop is proposed to contribute to cathepsin B decreased affinity for potent inhibitors of other papain-like enzymes as deletion or shortening of this flexible structure increased binding to this enzyme [283].

Cysteine Protease Catalytic Mechanism

Cysteine proteases catalyze the hydrolysis of amide bonds in proteins via a nucleophilic attack by the active site cysteine thiol on the carbonyl group of the amide bonds [266, 284]. The catalytic site of papain-like cysteine proteases is highly conserved and has a catalytic triad made up of Cys-25, His-159, and Asn-175. Cys-25 and His-159 form an ion pair which is stabilized by Asn-175 via a hydrogen bond [284, 285].

The hydrolysis mechanism of cysteine proteases involves an attack by a negatively charged thiolate group of a cysteine residue on the carbonyl carbon of the peptide bond. This leads to the formation of an acyl enzyme intermediate which is hydrolyzed in the second step (Figure 5.12) [286, 287]. During peptide hydrolysis, the nucleophilic thiolate cysteine attacks the carbonyl carbon of the scissile bond of the bound substrate and forms a tetrahedral intermediate which is stabilized by the so-called oxyanion hole, a crucial element in forming an electrophilic center to stabilize the tetrahedral intermediate during hydrolysis (Figure 5.13) [273, 285, 288].

The thiol group at the active site is a particularly good nucleophile due to the close proximity of an active site histidine residue which acts as a proton donor. The two ionizable groups of the thiolate–imidazolium diad allow a broad pH range of enzymatic

activity. They consist of a pKa for cysteine of approximately 4.0 and a pKa for histidine ionization of approximately 8.5 [271, 273].

Cysteine Protease Intracellular and Tissue Distribution

The majority of cathepsins are ubiquitously expressed in human tissues, indicating that these enzymes are involved in a normal cellular protein degradation and turnover. However some cathepsins show a restricted/specific cell or tissue-specific distribution, indicating their more specific roles [259]. The location of papain-like cysteine proteases is not strictly lysosomal; rather, the enzymes are trafficking between phagosomes, endosomes, and lysosomes. The individual proteases may accumulate in different organelles. Human cathepsins typically have optimum activation under acidic pH, resulting in for full activity within cellular lysosomes.

Cathepsin L is ubiquitously expressed in lysosomes of most human tissues and organs, including skin, liver, thyroid glands, and kidneys. It differs from other cathepsins in that it lacks exopeptidase activity and has the highest proteolytic activity in lysosomes [257, 289]. Cathepsin L is also found as a secreted protease in the secretory vesicles where it participates in the activation of pro-enkephalin confirming that cathepsin L is also selectively secreted under specific conditions. Cathepsin L has also been shown to have nuclear localization in some cells [290].

Cathepsin K is also a lysosomal enzyme, and is mostly expressed in osteoclasts (cells involved in bone resorption), which has led to it being a validated therapeutic target for the treatment of diseases characterized by excessive bone loss, including osteoporosis [291, 292]. Cathepsin K is also found in macrophages, as well as in epithelial cells of the respiratory and gastrointestinal systems [292, 293].

Cathepsin B is present and active intracellularly and extracellularly in almost all tissue types. Intracellularly, it is localized in the lysosomes, whereas extracellularly, it can be found both free and bound to the extracellular matrix proteins [294].

Regulation of Lysosomal Cathepsin Activity

Proteolytic activity is important for normal functioning of an organism and must be rigorously controlled to avoid potentially dangerous excess protein degradation.

Lysosomal cysteine protease activity is regulated in a number of ways, the most important being zymogen activation and inhibition by endogenous protein inhibitors.

The propeptide (part or all of which is removed during activation) aids specific targeting, stability and proper folding of the enzymes [295], as well as being able to specifically inhibit the activity of mature enzymes [256]. The proregions are tightly binding, highly selective and reversible inhibitors that occupy the cleft in a linear, but backwards orientation (Figure 5.7), preventing the premature activation of the catalytic domain of mature cathepsin with K_I values in the nanomolar range [271, 296]. Usually, the inhibition obeys slow-binding kinetics, but the mechanism is also pH dependent [295, 296]. The K_I value for inhibition of human cathepsin L propeptide towards the mature cathepsin L is 0.088 nM at pH 5.5, but increases to 3.0 nM at pH 4.0 [272].

Conversion to the mature form occurs intracellularly in lysosomes at pH 3.0-3.5 via either auto-activation (Figure 5.14) or trans-activation (Figure 5.15) [299]. In extracellular contexts, maturation is supported by negatively charged matrix surfaces at pH 5.5-6.0 [256]. Propeptides of cysteine proteases are thought to dissociate from the protease, unfold, and undergo proteolytic degradation when they are no longer required to inhibit cysteine protease activity [259].

Physiological Roles of Cysteine Proteases

Human cysteine proteases are involved in both general and specialized processes such as protein catabolism, hormone activation, antigen presentation, and tissue remodeling [259, 300]. Cathepsin L plays various roles in the degradation of serum, cytoplasmic and nuclear proteins [290, 301].

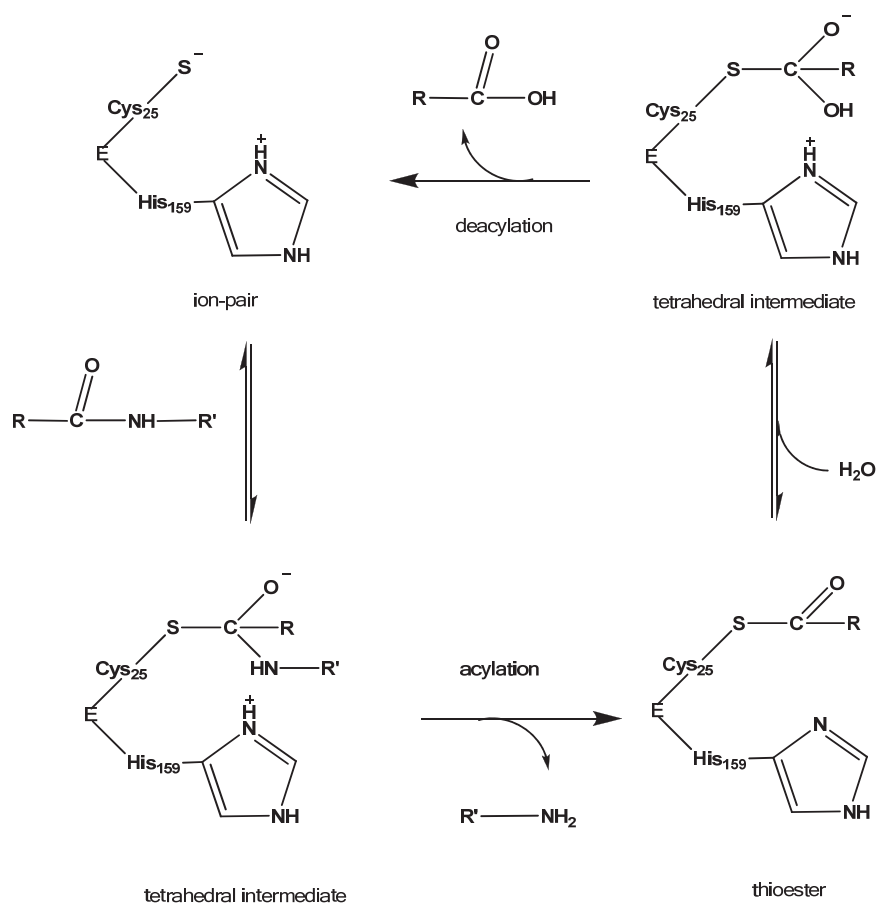


Figure 5.12. Catalytic mechanism of cysteine proteases. Their catalytic site has the Cys-25, His-159 and Asn-175 conserved in all of its members. In this triad, Cys-25 and His-159 form an ion pair which is stabilized by Asn-175 *via* a hydrogen bond allowing peptide hydrolysis [271, 297]

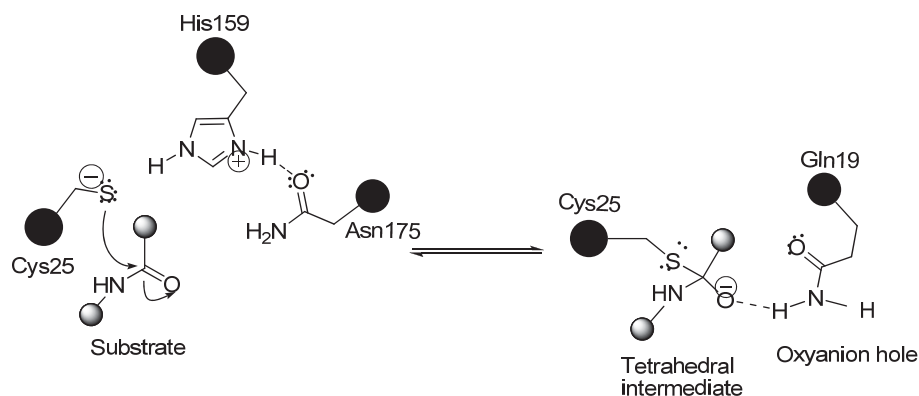


Figure 5.13. Stabilization of the oxyanion generated by the cysteine protease catalytic reaction [298].

In addition, cathepsin L is involved in various processes such as bone resorption, sperm maturation, intestinal neoplasia, processing of thyroglobulin in thyroid glands, and processing of neuropeptides into neurotransmitters and some hormones [302, 303]. Other studies support the role of cathepsin L in the differentiation of keratinocytes and its importance in hair pigmentation and the biology of hair cells [304]. Reproduction cycles (spermatogenesis and oogenesis) also require the activity of this protease [305, 306]. Finally, cathepsin L plays a crucial role in angiogenesis [307].

Cathepsin K distribution is selective in human tissues. Therefore, its physiological function is limited to a specific number of processes. The most well defined process is the participation of cathepsin K in bone resorption. Type I collagen is one of the most abundant fibrillar proteins in the bone matrix and is composed of three helical chains, along with telopeptides at the end of these chains [308]. Other proteases with collagenase activity lack telopeptidase activity. This is not the case for cathepsin K, which has both activities combined (collagenase, telopeptidase) [309].

Cathepsin B has many important physiological functions. This includes remodeling of the extracellular matrix, acting directly or indirectly upon the structure. In

addition, cathepsin B is able to hydrolyze the extracellular matrix components collagen IV, fibronectin and laminin thereby allowing for the tumor cells to permeate surrounding tissues and vasculature [259, 310, 311]. Due to its ubiquitous nature, it is involved in various biological processes such as protein turnover in the lysosomes, bone remodeling, site-specific cleavage of human prorenin processing, and self-protection of cytotoxic T lymphocytes during degranulation [312].

Role of Cysteine Proteases in Pathological Conditions

A large number of pathological conditions are caused by failure of biological control mechanisms for proteolytic activities leading to disturbance of the normal balance of enzymatic activity. Abnormal protease activity typically occurs as a result of the equilibrium between lysosomal enzymes and their endogenous inhibitors in the extracellular space being disturbed. This imbalance could occur due to a variety of reasons including excess release of lysosomal enzymes leading to saturation and reduction in activity of endogenous inhibitors, reduced binding of inhibitors to enzymes due to changes in the binding properties of the inhibitors, as well as increased stability of lysosomal cathepsins which are normally inactive in the extracellular space (creating microenvironments with low pH).

Papain-like cysteine proteases have been shown to play important roles in degenerative, invasive, and immune system related disorders as well as in various parasitic infections [287, 313, 314]. Cysteine proteases have been observed in a number of diseases such as cancer, apoptosis, rheumatoid arthritis, osteoarthritis, bone resorption, Alzheimer's disease, multiple sclerosis, and muscular dystrophy [260, 277, 300, 315, 316]. Impaired cathepsin-L like activity may also play a key role in the establishment of

skin and gingival abnormalities seen in I-cell disease. In addition, reduced activities may play an important role in drug-induced gingival overgrowth [317]. Cathepsin L has also been shown to play a role in the degradation of cartilage and joints in osteoarthritis [263, 289, 295].

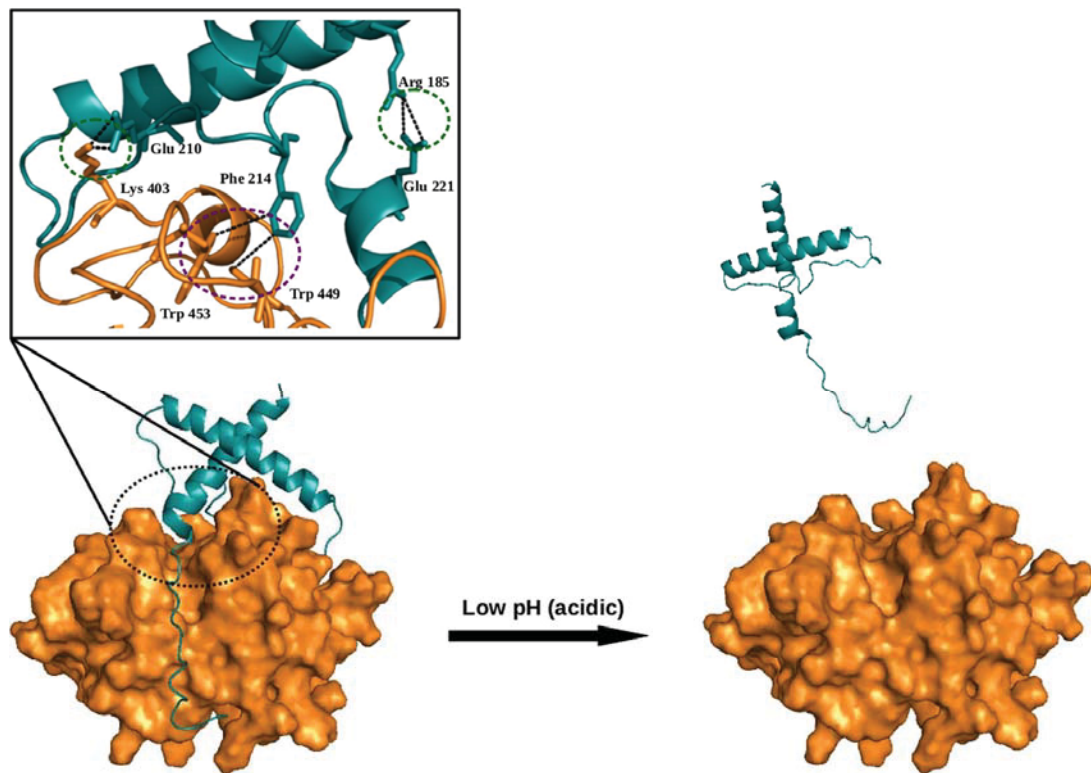


Figure 5.14. Autoactivation of a cysteine protease due to low pH [299]

Role of Cathepsins in Cancer

Proteolytic activities from all major protease classes including papain-like cysteine proteases have been implicated in cancer metastasis. The ability of malignant tumor cells to invade normal surrounding tissue contributes in large part to the significant morbidity and mortality of cancers. Invasiveness requires several distinct cellular functions including adhesion, motility, detachment, and extracellular matrix proteolysis.

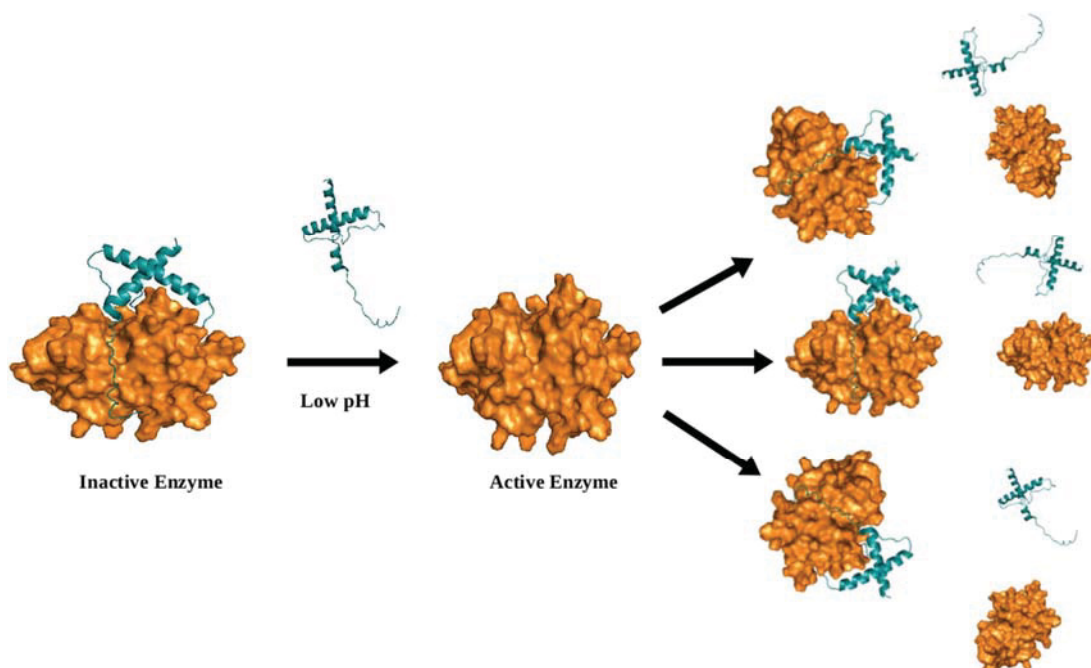


Figure 5.15. Transactivation of a cysteine protease in acidic conditions [299]

Tumor progression and metastasis is a very complicated process, requiring a number of factors including local proteolysis for the spatial expansion of tumors, the generation of tumor supporting blood vessels (angiogenesis), and the migration of transformed cells in and out of the vascular system (metastasis) [318] (Figure 5.16). The largest structural barrier to metastasis and invasive growth of malignant tumors is the connective tissue of the extracellular matrix (ECM), of which the most substantial component the basal membrane, which provides an immunological separation of different tissues surrounding the blood and lymph vessels [319]. This membrane is composed of proteins which can be degraded by cysteine proteases including type IV collagen, proteoglycans, fibronectin, laminin, and entactin [320]. A characteristic of malignant tumors is the destruction of the extracellular matrix (ECM) [318, 321]. It has been shown that the degradation of the ECM, which is necessary for invasion of tumors into neighboring tissue, involves proteolytic enzymes such as plasminogen activators,

cathepsin B, cathepsin L, collagenase, as well as metallo and serine proteases [310, 313, 321, 322]. Furthermore, proteases involved in tumor invasion and metastasis are also expressed by surrounding stromal cells. Tumor cells activate protease expression in stromal fibroblasts which then assist in the degradation of the extracellular matrix [323]. It has been shown that fibroblasts neighboring tumor cells have elevated levels of matrix metallo-protease 9 (MMP9) [324]. Alterations in the balance between endogenous inhibitors and the cathepsins have been postulated to contribute to malignant progression [319]. Cathepsin activity in the plasma membrane fraction has been shown to be significantly higher in tumor cells of various cancer types than in normal cells, indicating that these enzymes are protected from endogenous cysteine protease inhibitors and denaturation through membrane binding. For example, high expression levels of cathepsin B in colorectal cancer patients correlated with shorter survival, and it has been reported that inhibition of cell-surface cathepsin B can prevent the activation of uPA, a well-known prognostic marker in cancer [325, 326]. Elevated expression levels of cathepsin L have been reported in kidney and testicular tumors, meningiomas, non-small cell lung carcinomas, and in most cancers of the breast, ovary, colon, adrenal, bladder, prostate, and thyroid [285, 327]. Increased expression levels of cathepsin B have been observed at the invasive edge of various tumors including bladder, colon, and prostate carcinomas [310, 328, 329], and cathepsin K has been associated with human breast carcinoma [271].

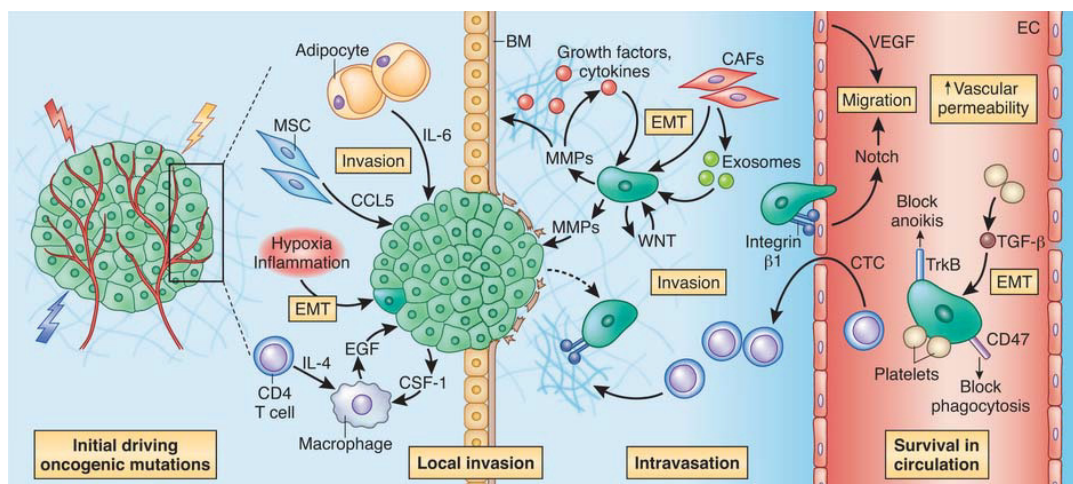


Figure 5.16. Diagrammatic representation of the tumor metastatic process [318]

Introduction to Enzyme Kinetics

Enzymes play an important role in the catalysis of various biochemical reactions. The rate of these reactions is determined by the enzyme that catalyzes the reaction. These reactions are typically complex, however in order to describe them they can be written in a simplified form representing the conversion of substrate (S) to product (P catalyzed) by enzyme (E) (Figure 5.17). Initially, when an enzyme is combined with excess substrate (and no product) there is a short pre-steady state period where the two components build up to their steady state levels. After this initial phase a steady state is achieved where the reaction could proceed as:



Figure 5.17. Simplified enzyme catalyzed reaction

In the reaction above, ES, k_1 , k_{-1} , and k_2 represent the enzyme-substrate complex, ES forward rate constant, ES reverse rate constant, and the forward rate constant for

product formation, respectively. The rate of this reaction can be adequately described by the Michaelis-Menten expression (Eq. 5.1)

$$v_o = k_2[ES] = \frac{V_{\max}[S]}{K_M + [S]} \quad \text{Equation 5.1}$$

The Michaelis-Menten model presents a hyperbolic relationship between enzyme activity and substrate concentration where; K_M : Michaelis-Menten constant, S : substrate concentration, V_{\max} : maximum enzymatic activity, and v : velocity. The Michaelis-Menten constant represents the amount of substrate that is necessary to achieve half maximal activity of the enzyme. The K_M could be viewed as a measure of the enzyme substrate affinity, such that the lower the value, the tighter the interaction is between both species (substrate and enzyme). The graphical representation of this model (Figure 5.18) shows an initial linear portion when the substrate concentration is small, and a plateau reaching V_{\max} when the substrate concentration is much greater than K_M .

Another measure of how well an enzyme can catalyze the conversion of a specific substrate to product is the turnover number of k_{cat} . This is the maximum number of moles of substrate that are converted to product per second. This value can be obtained using equation 5.2;

$$k_{\text{cat}} = V_{\max}/[E] \quad \text{Equation 5.2}$$

This value can further be used to ascertain how active the enzyme is at low substrate concentrations (as seen in physiological conditions), which is given by the ratio k_{cat}/K_M .

This ratio is known as the specificity constant, with high values of this constant denoting high activity of an enzyme against a specific substrate.

Enzyme Inhibition

Enzyme inhibitors are molecules that bind to enzymes resulting in a decrease their activity. Enzyme inhibition can occur in different ways, depending on whether the inhibitors bind the enzyme, the enzyme-substrate complex, or both

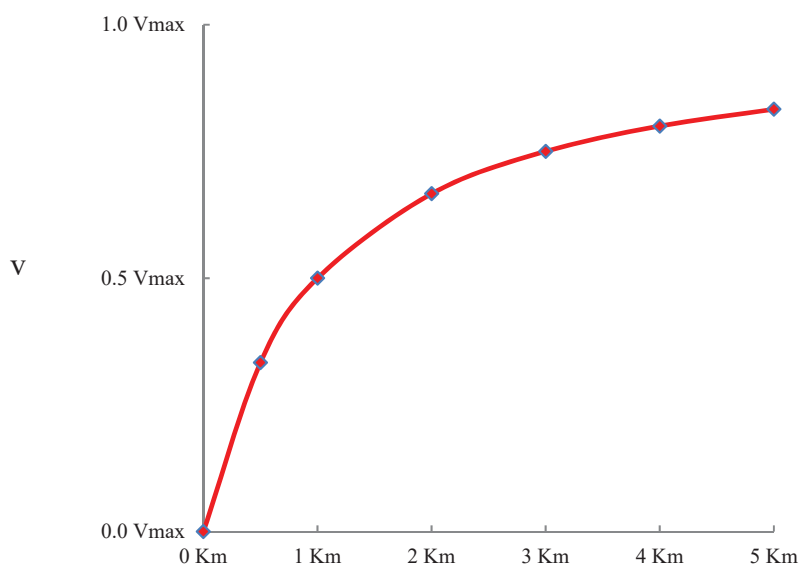


Figure 5.18. Typical Michaelis-Menten Plot.

In order to correctly design suitable candidates for drug discovery as well as to completely elucidate enzyme kinetics in their uninhibited state, it is important to understand the mechanisms of action by which inhibitors affect enzyme activity. The analysis of how the structure of inhibitors relates to their inhibitory activity against enzymes is very important area of study. This research is done so as to optimize advanced pre-clinical and *in vivo* studies, as well as to improve selectivity and potency of inhibitors [330, 331].

Enzyme inhibition can be reversible or irreversible. Reversible inhibition can occur when inhibitors attach to enzymes via non-covalent interactions such as hydrogen bonds, hydrophobic interactions and ionic bonds. Multiple weak bonds between the inhibitor and the active site combine to produce strong and specific binding. Reversible inhibitors generally do not undergo chemical reactions when bound to the enzyme and can be easily removed by dilution or dialysis, resulting in recovery of enzymatic activity. Irreversible inhibitors interact with the target enzyme, typically via a covalent modification at the active site thereby permanently inactivating it.

Reversible inhibitors can be classified based on their mechanism of action. There are three types of reversible inhibitors: competitive, uncompetitive, and noncompetitive or mixed reversible inhibition. A number of these types of inhibitors have been used as effective therapeutics against a variety of pathologies (Table 5.1).

Table 5.1: Examples of Reversible Inhibitors in Clinical Use

Mode of Inhibition	Compound	Medical Condition	Enzyme Target
Competitive	Mevacor (Lovastatin)	High Cholesterol	HMG-CoA reductase
Non-competitive	Tacrine	Alzheimer's	Acetylcholinesterase
Uncompetitive	Ciglitazone	Inflammatory diseases	15-Hydroxyprostaglandin Dehydrogenase

Competitive Inhibition

Competitive inhibitors act by binding at the enzyme active site thus preventing formation of the enzyme substrate complex (Fig 5.19).

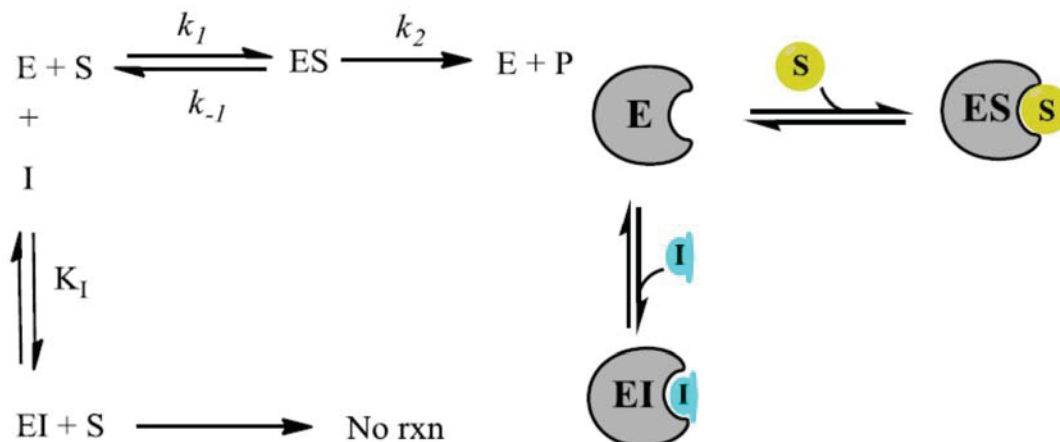


Figure 5.19. Competitive inhibitor reaction scheme [332]

As seen in Fig 5.19, it is assumed that the inhibitor binds to the enzyme to form an EI complex, which is unavailable for substrate binding. This direct competition for the active site does not affect the V_{\max} (Fig. 5.20), but increases the K_M . This alteration of the enzyme kinetics can be accounted for by an addition of another term to the Michaelis-Menten. This term, α , is defined in equation 5.3 where K_I is the dissociation constant for the enzyme substrate complex. The term α is a function of the inhibitor concentration and its affinity for the enzyme and once inserted into the Michaelis-Menten equation, illustrates how competitive inhibitors affect steady state kinetics, as seen in equation 5.4.

$$\alpha = 1 + \frac{[I]}{K_I} \quad \text{Equation 5.3}$$

$$v = \frac{V_{\max}[S]}{S + K_M \left(1 + \frac{[I]}{K_I}\right)} \quad \text{Equation 5.4}$$

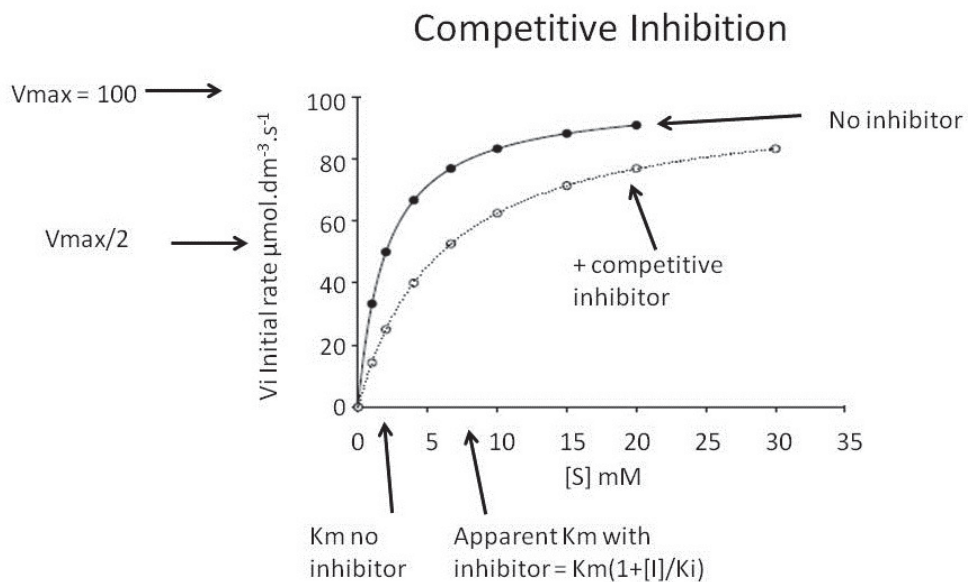
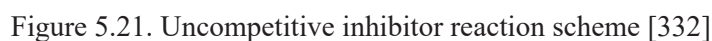
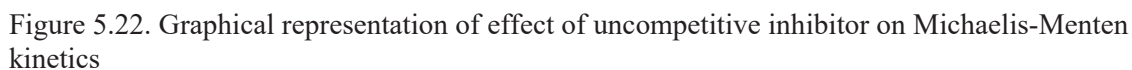


Figure 5.20. Graphical representation of effect of competitive inhibitor on Michaelis-Menten kinetics

Uncompetitive Inhibition

For an uncompetitive inhibitor, the compound binds directly to the enzyme substrate complex but not to free enzyme (Fig 5.21). In uncompetitive inhibition, the substrate binding causes a conformational change in the enzyme. Therefore, the structure of inhibitor compound does not necessarily need to mimic the structure of the substrate. This effect of this type of inhibition on the Michaelis-Menten kinetics can be seen in equations 5.5 and 5.6, as well as figure 5.22. The presence of the α' term in the denominator effects the substrate concentration in this model, thus causing decreases in K_M and V_{\max} with increasing inhibitor concentration.


$$\alpha' = 1 + \frac{[I]}{K_I} \quad \text{Equation 5.5}$$

$$v = \frac{V_{\max}[S]}{\alpha'[S] + K_M} \quad \text{Equation 5.6}$$


Noncompetitive Inhibition

Another modality of reversible inhibition of enzyme activity occurs where the inhibitor binds effectively to the enzyme substrate complex and inhibits product formation from this complex. Noncompetitive inhibition (also known as mixed inhibition), involves binding of the inhibitor to both the enzyme substrate complex and the free enzyme (Fig 5.23). In noncompetitive inhibition (as with uncompetitive inhibition), the binding events occur at an alternative site from the active site.

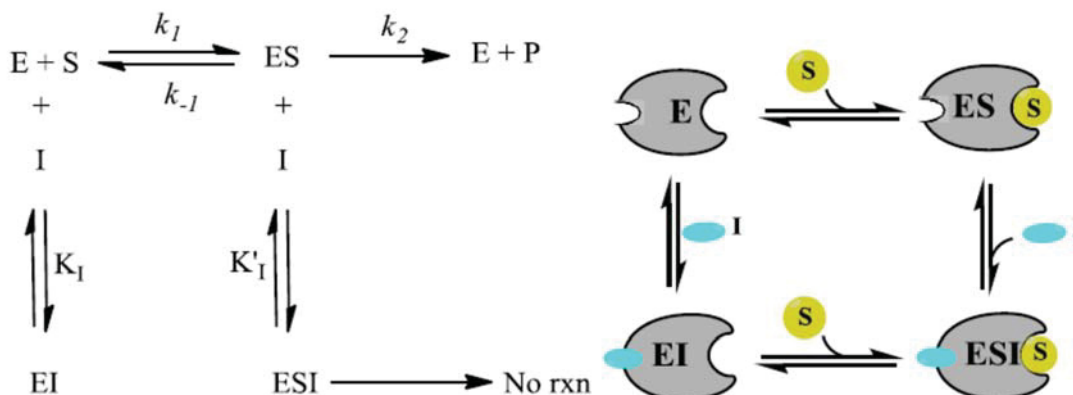


Figure 5.23. Noncompetitive inhibitor reaction scheme [332]

Noncompetitive inhibitors have two distinct dissociation equilibrium constants, one for the binary enzyme inhibitor complex (EI) designated K_I and another for the tertiary enzyme substrate inhibitor complex (ESI) designated K'_I or αK_I . When α is greater than 1, this indicates the preference of the inhibitor for free enzyme; α less than 1 indicates a higher affinity of the inhibitor for the enzyme substrate complex. Noncompetitive inhibitors have differing effects on the Michealis-Menten constants depending on the values of α . The effect of noncompetitive inhibition on the Michaelis-

Menten equation is illustrated in equation 5.7. The terms α and α' in the equation allow for inhibition to be effective at both high and low concentrations of substrate.

$$v = \frac{V_{\max}[S]}{\alpha'[S] + \alpha K_M} \quad \text{Equation 5.7}$$

The effects of all the reversible inhibition modalities on enzyme kinetics are summarized below (Figure 5.24).

Parameter	Inhibition Modality				
	Competitive	Noncompetitive $\alpha > 1$	Noncompetitive $\alpha = 1$	Noncompetitive $\alpha < 1$	Uncompetitive
K_M	Increases linearly with increasing $[I]$	Increases curvilinearly with increasing $[I]$	No effect	Decreases curvilinearly with increasing $[I]$	Decreases curvilinearly with increasing $[I]$
V_{\max}	No effect	Decreases curvilinearly with increasing $[I]$	Decreases curvilinearly with increasing $[I]$	Decreases curvilinearly with increasing $[I]$	Decreases curvilinearly with increasing $[I]$
V_{\max}/K_M	Decreases curvilinearly with increasing $[I]$	Decreases curvilinearly with increasing $[I]$	Decreases curvilinearly with increasing $[I]$	Decreases curvilinearly with increasing $[I]$	No effect
Catalytic step affected	$E + S \rightarrow ES$	$E + S \rightarrow ES^\ddagger$	$E + S \rightarrow ES^\ddagger$	$E + S \rightarrow ES^\ddagger$	$ES \rightarrow ES^\ddagger$

Figure 5.24. Effects of reversible inhibitors on enzyme kinetics

IC₅₀ and K_I: Importance in Inhibition Studies

Two very important and widely used concepts in describing/quantifying enzyme inhibition are IC₅₀ and K_I values.

The IC₅₀ value is the concentration of a specific compound (inhibitor) that is required to inhibit the enzymatic activity of a target by fifty percent. The relationship between enzyme activity and inhibitor concentration is expressed in equation 5.8. Y represents the inhibited activity (compared to control), X is log ([inhibitor]) in M, v_{\min}

and v_{\max} represent the velocities of the enzyme when it is pre-incubated with the highest and lowest inhibitor concentrations, respectively. Finally, the Hill slope value is the slope of the sigmoidal curve. This can be fit to a sigmoidal curve and represented graphically (Figure 5.25).

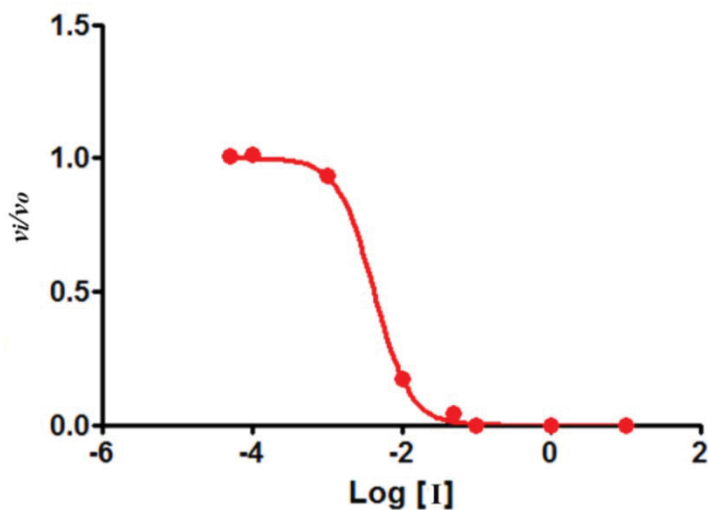


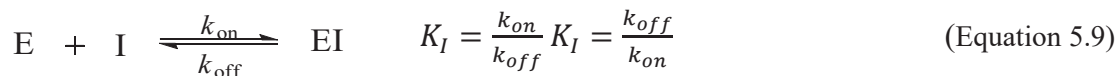
Figure 5.25. IC_{50} sigmoidal dose response curve

The determination of IC_{50} for any enzyme is method dependent. This value is highly dependent on various experimental conditions such as pH, temperature, buffer, solubility, pH, enzyme concentration, pre-incubation time, solvent effect, substrate concentration, substrate inhibition, etc. Thus, the importance of establishing validated, consistent protocols for examining inhibition according to this parameter is important for the sake of comparison and reproducibility.

The inhibition constant (K_i , Eq. 5.9) is another concept that correlates the effect of an inhibitor with a given enzyme (the lower the value, the better the inhibitory activity of

any compound). K_I can be described as the ratio of k_{off} and k_{on} and, the rate constants for the onset of inhibition and inhibitor dissociation respectively.

$$Y = \frac{v_{MIN} + (v_{MAX} - v_{MIN})}{1 + 10^{(\log(IC_{50}-X)*Hillslope)}} \quad (\text{Equation 5.8})$$



There are several approaches that could be used to calculate K_I . Equation 5.9 offers the simplest means to do this, albeit only applying in instances where both k_{on} and k_{off} are already known. Unfortunately, the determination of these rate constants is not always straightforward. As such, several mathematical models to determine this inhibition constant have been suggested [334]. It is important to understand the limitations of each approach in order to guarantee the most exact value for K_I . One such method by which K_I can be calculated is via the transient approach, whereby data sets are fit into a system of multiple differential equations. A significant drawback to this approach is the requirement that the mode of inhibition is previously known, as well the need for a complex mathematical program.

A simpler approach to K_I determination is the Cheng and Prusoff model, which involves a series of equations that correlate IC_{50} values and K_I values [335]. This model comprises three equations which describe the relationships when a reversible inhibitor works as a competitive (Eq. 5.10), noncompetitive (Eq.5.11), and uncompetitive inhibitor (Eq. 5.12).

$$IC_{50} = K_I \left(1 + \frac{[S]}{K_M} \right) \quad (\text{Equation 5.10})$$

$$IC_{50} = \frac{[S] + K_M}{\frac{K_M}{K_I} + \frac{[S]}{\alpha K_I}} \quad (\text{Equation 5.11})$$

$$IC_{50} = \alpha K_I \left(1 + \frac{K_M}{[S]} \right) \quad (\text{Equation 5.12})$$

Time Dependence/Slow Binding Inhibition

Some inhibitors tend to bind to, or dissociate from, their target enzymes slowly, thus leading to time dependence for the onset of inhibition. The true affinity of such compounds can only be assessed after the system has reached equilibrium, where the inhibitor is fully bound to the enzyme. Failure to properly account for the time dependence of inhibition can result in false negatives and potentially cause the researcher to overlook promising inhibitor molecules.

One of the major ways by which evaluation of compounds as slow binding inhibitors is done is by comparing inhibited and uninhibited enzymatic reaction progress curves. Slow binding inhibition typically is manifested as degree of inhibition of a fixed concentration of compound varying over time, as equilibrium is slowly established between the free and enzyme-bound forms of the compound, leading to a curvature of the reaction progress curve over time while the uninhibited reaction progress curve remains linear (Figure 5.26).

For a reaction with fixed concentrations of enzyme, substrate, and slow binding inhibitor, we can fit the progress curve by an equation (Eq. 5.13) that contains terms for the initial and steady state velocities (v_o and v_s), and for the apparent first-order rate

constant for conversion from the initial velocity phase to the steady state velocity phase, k_{obs} . The release of product (P) is dependent of the time (t) of the reaction [336].

$$P = v_s t \frac{(v_o - v_s)}{k_{obs}} (1 - e^{-k_{obs}t}) \quad (\text{Equation 5.13})$$

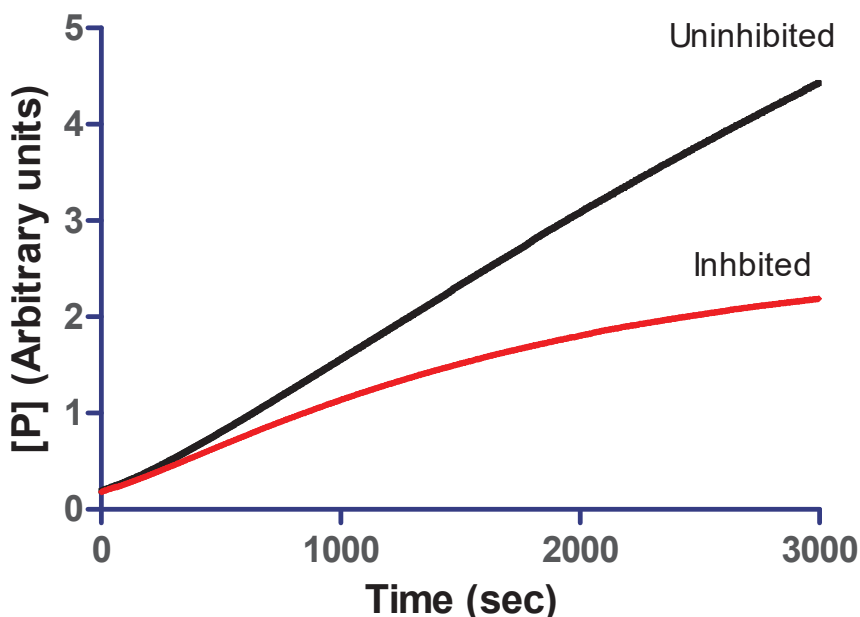


Figure 5.26. Reaction Progress Curves showing Uninhibited (black) and Inhibited Sample with a Slow Binding Inhibitor (red)

It should be noted that the mode of inhibition of slow-binding inhibitors can be determined once k_{obs} values are elucidated. k_{obs} values are substrate dependent (Eq. 5.14, 5.15 and 5.16), and as such the relationship between substrate concentration and k_{obs} values can be used to determine inhibitor modality (Figure 5.27) [337].

For competitive inhibitors, rate constants (k_{obs}) decrease hyperbolically with increasing substrate concentration. In the case of uncompetitive inhibition, rate constants are substrate concentration independent. Finally, the rate constants for non-competitive inhibitors increase hyperbolically with higher substrate concentrations (Figure 5.27).

$$k_{obs} = \frac{k}{1 + \frac{[S]}{K_M}} \quad (\text{Equation 5.14})$$

$$k_{obs} = k \quad (\text{Equation 5.15})$$

$$k_{obs} = \frac{k}{1 + \frac{K_M}{[S]}} \quad (\text{Equation 5.16})$$

Elucidation of the k_{obs} value is also important in determining the mechanism by which slow binding inhibition is occurring [337]. There are a number of mechanisms by which slow binding can occur (Figure 5.28). Equation A of figure 5.28 shows the uninhibited enzyme reaction in which ES complex formation and dissociation are governed by the association rate constant k_1 (i.e., k_{on}) and the dissociation rate constant k_2 (i.e., k_{off}). Equation B shows a simple reversible equilibrium between the enzyme and inhibitor with the onset and offset rate constants (k_3 and k_4). This is very similar to the pattern of inhibition seen with typical reversible inhibitors; however, the values of k_3 and/or k_4 are miniscule, leading to slow inhibition.

Equation C of figure 5.28 illustrates another mechanism of slow binding, where the inhibitor initially binds to the enzyme leading to rapid equilibrium conditions that are very similar to the simple reversible inhibitors. Hence the binding affinity between enzyme and inhibitor in this initial complex (EI) is defined by the ratio of the rate constants k_4/k_3 , which is equal to the K_i of the encounter complex. Subsequent to initial complex formation, the enzyme undergoes an isomerization step (k_5), which is significantly slower than the formation of initial complex.

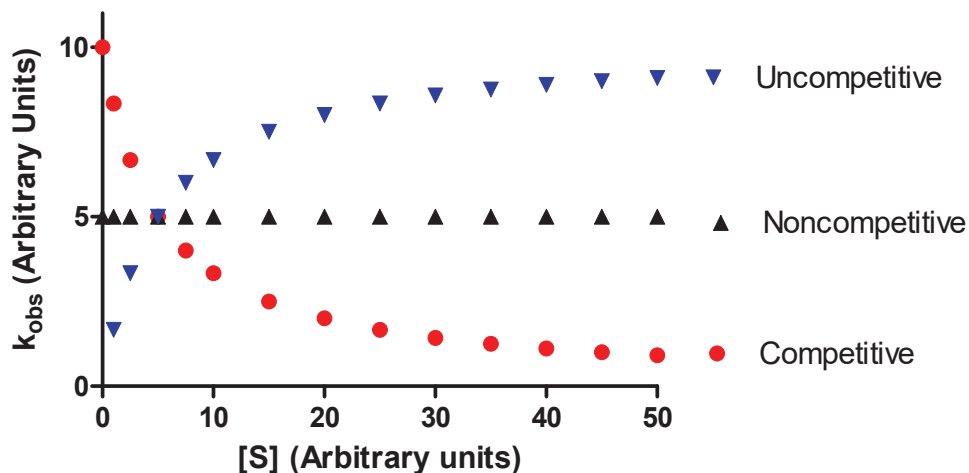


Figure 5.27. Determination of Inhibition Modality for Slow-Binding Inhibitors. Values are in Arbitrary Units.

The isomerization of the enzyme results in a much more significant association between the inhibitor and the new enzyme conformation (E^*). The reverse isomerization step between E^*I and EI is governed by the rate constant k_6 . Since the true affinity of the inhibitor cannot be seen prior to formation of the E^*I complex, any elucidation of slow-binding inhibitor affinity for this mechanism must take into account K_i , k_5 , and k_6 .

The third mechanism that results in slow binding behavior involves covalent inactivation of the enzyme via affinity labeling or mechanism-based inhibition. However, this mechanism is typically only related with irreversible inhibition.

In order to determine which of the two slow binding reversible inhibition mechanisms is taking place the relationship between k_{obs} and inhibitor concentration can be observed using reaction progress curves. With slow binding inhibition that occurs as a result of simple reversible slow binding, k_{obs} depends only on k_3 and k_4 (Eq.5.17).

$$k_{\text{obs}} = k_3[\text{I}] + k_4 \quad \text{Equation 5.17}$$

The above equation can be represented graphically (Fig 5.29), with the relationship between k_{obs} and $[\text{I}]$ resulting in a straight line. This signifies simple reversible slow binding between the enzyme and the inhibitor.

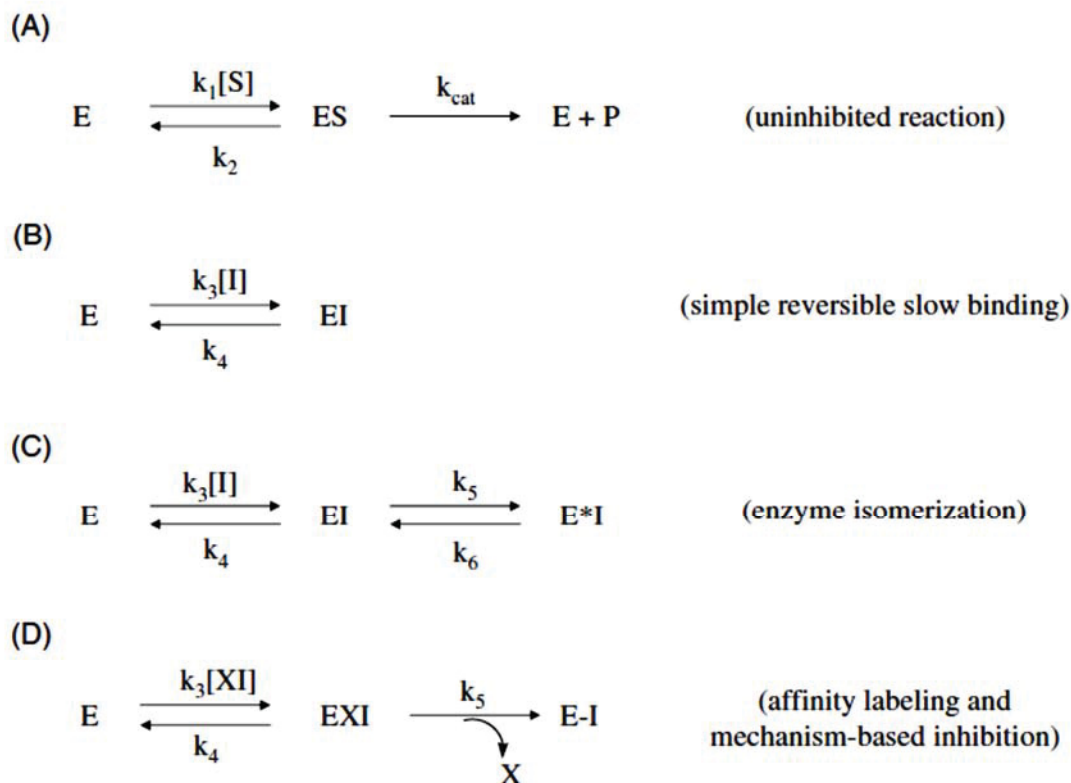


Figure 5.28. Mechanisms for slow binding inhibition of enzymatic reactions [337]. (A) The enzyme reaction in the absence of inhibitor. (B) A single-step binding mechanism for which the association rate (determined by k_3) or dissociation rate (determined by k_4) or both are inherently slow. (C) A two-step binding mechanism for which the first step is simple, rapid equilibrium binding of inhibitor to enzyme to form an encounter complex (EI) and the second step is a slow isomerization of the enzyme to form a higher affinity complex, E^*I . (D) Covalent modification of the enzyme by an affinity label or a mechanism-based inhibitor. The intact inhibitory species (XI) first binds reversibly to the enzyme to form an encounter complex (EI). Subsequently, there is a slower reaction step leading to covalent attachment of the inhibitor to a catalytically essential group on the enzyme and release of the leaving group X.

As far as the enzyme isomerization mechanism for slow binding inhibition, there is a two-step reaction, of which the relationship between k_{obs} and $[I]$, can be represented by the following equation:

$$k_{obs} = k_5 + \left\{ \frac{k_6}{1 + (K_i^{app}/[I])} \right\} \quad \text{Equation 5.18}$$

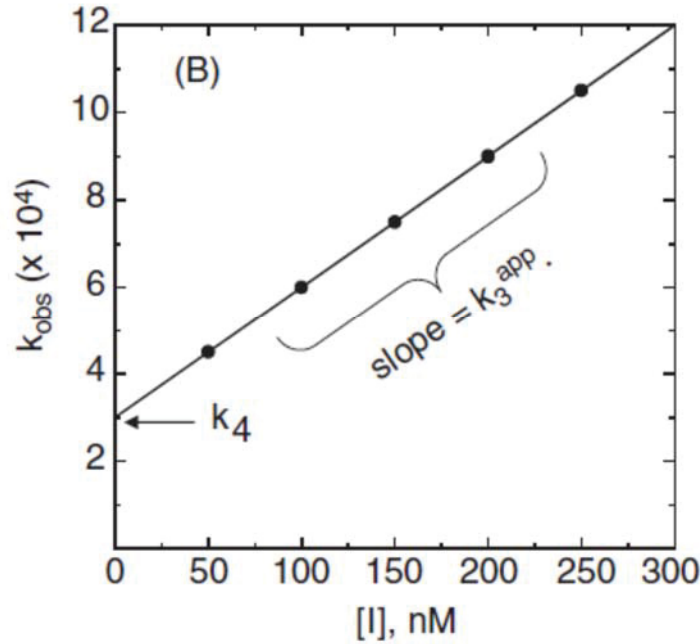


Figure 5.29. Graphical representation of slow binding reversible inhibition. The linear fit of the data estimates the kinetic rate constants k_4 (y-intercept) and of the apparent value of k_3 (slope).

In equation 5.18, K_i^{app} is the apparent value of the K_i for the initial equilibrium (i.e., k_4/k_3 (apparent)). The plot of k_{obs} as a function of inhibitor concentration for this mechanism shows a hyperbolic relationship between these two parameters (Figure 5.30)

Relationship Between Enzyme Concentration and K_I : The Morrison Equation

Slow binding inhibitors in a lot of instances also tend to be tight binding, as high-affinity, or tight binding, interactions with enzymes may occur as a result of a very slow dissociation rate of the enzyme–inhibitor binary complex. One of the best mathematical methods to evaluate the relationship inhibition constants for slow, tight-binding inhibitors is the Morrison’s quadratic equation (equation 5.19). The equation expresses the K_I value in terms of the enzyme species concentrations and can be graphically represented as seen in figure 5.31. Thus, the inhibition constant is dependent of free enzyme and enzyme bound to the inhibitor. Mathematically, the Morrison mathematical model is a quadratic equation; that is, it has two plausible solutions. Obviously, only one solution is physically possible because $K_I > 0$. Nevertheless, the Morrison equation solves the apparent inhibition constant K_I^{app} . Equation 5.20 solves the true inhibition constant K_I by showing a relationship between K_I^{app} , K_I , $[S]$, and K_M .

$$\frac{v_i}{v_o} = 1 - \frac{([E]_T + [I]_T + (K_I(1 + \left(\frac{[S]}{K_M}\right))) - \sqrt{([E]_T + [I]_T + (K_I(1 + \left(\frac{[S]}{K_M}\right)))^2 - 4[E]_T[I]_T})}{2 [E]_T} \quad \text{(Equation 5.19)}$$

$$K_I^{app} = K_I(1 + \left(\frac{[S]}{K_M}\right)) \quad \text{(Equation 5.20)}$$

The Morrison equation shows the relationship between K_I^{app} , K_I , $[S]$, and K_M and inhibitor. K_I^{app} , K_I , inhibited rate (v_i) and uninhibited rate (v_o) can be experimentally determined. Michaelis-Menten constant and substrate concentration are kept constant. Thus, the apparent inhibition constant can be determined by solving the dependence of the fractional activity (i.e. v_i/v_o) versus inhibitor concentration.

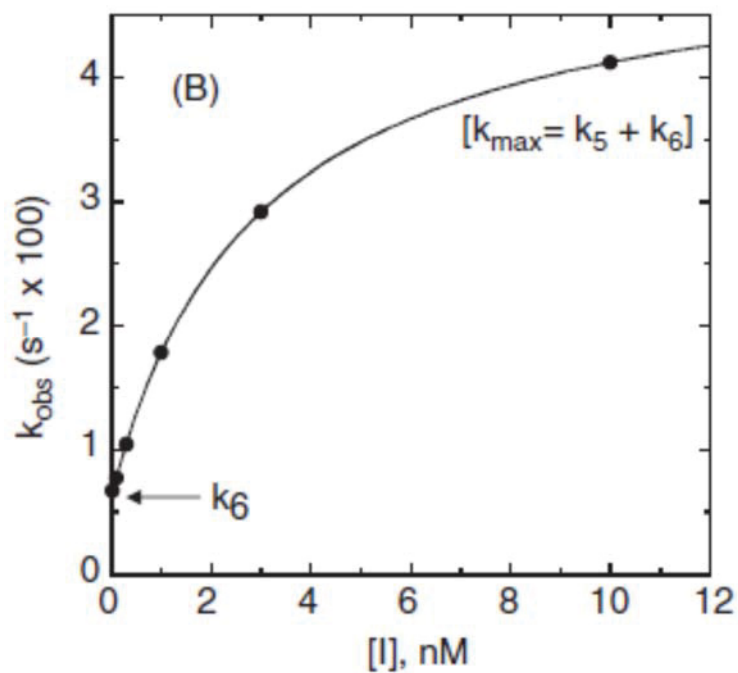


Figure 5.30. Graphical representation of enzyme isomerization slow binding inhibition mechanism. The y-intercept estimates k_5 , while the maximum value of k_{obs} (k_{max}), at infinite inhibitor concentration, reflects the sum of k_5 and k_6 .

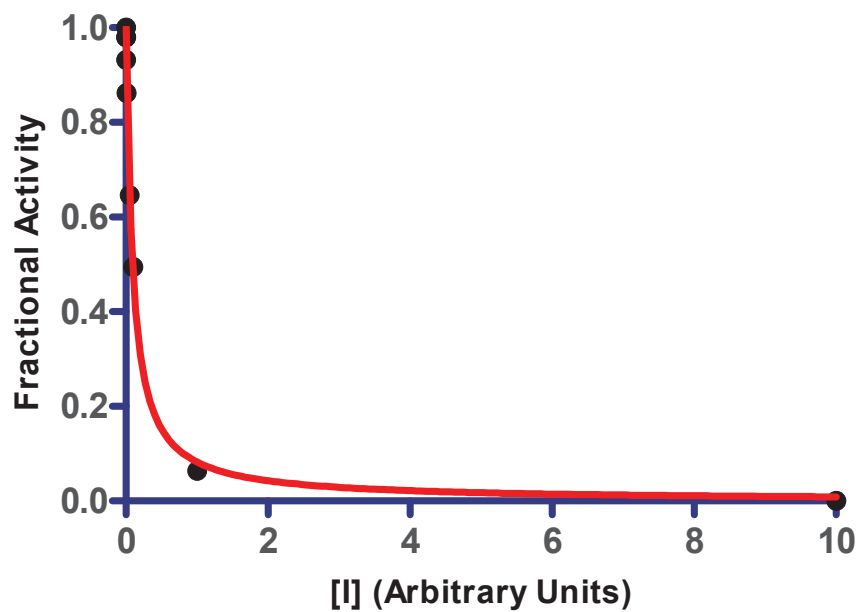


Figure 5.31. Graphical Representation of the Morrison Equation.

Experimental Design for Analysis of Cysteine Proteases

As mentioned in chapter one, one of the goals of this research project is to examine the mechanisms by which a subset of compounds (from a larger library of compounds with a thiosemicarbazone moiety) can inhibit cysteine proteases. This analysis was conducted using an experimental flow chart as seen in figure 5.32. The thiosemicarbazone compounds analyzed could be divided into four main structural scaffolds for ease of analysis: benzophenone thiosemicarbazones, benzophenone (with extended alkyl links) thiosemicarbazones, benzoyl benzophenone thiosemicarbazones, and thiochromanone thiosemicarbazones (Figure 5.33). After validation of enzyme activity, enzymes were treated with compounds at a concentration of 10 μM . Subsequently, compounds that inhibit the enzyme activity by more than 50% were further analyzed to elucidate their IC_{50} and K_i values. Potent inhibitors of the enzymes are further subjected to various advanced kinetic analyses, molecular modeling and mass spectroscopy to further elucidate the mechanisms of inhibition.

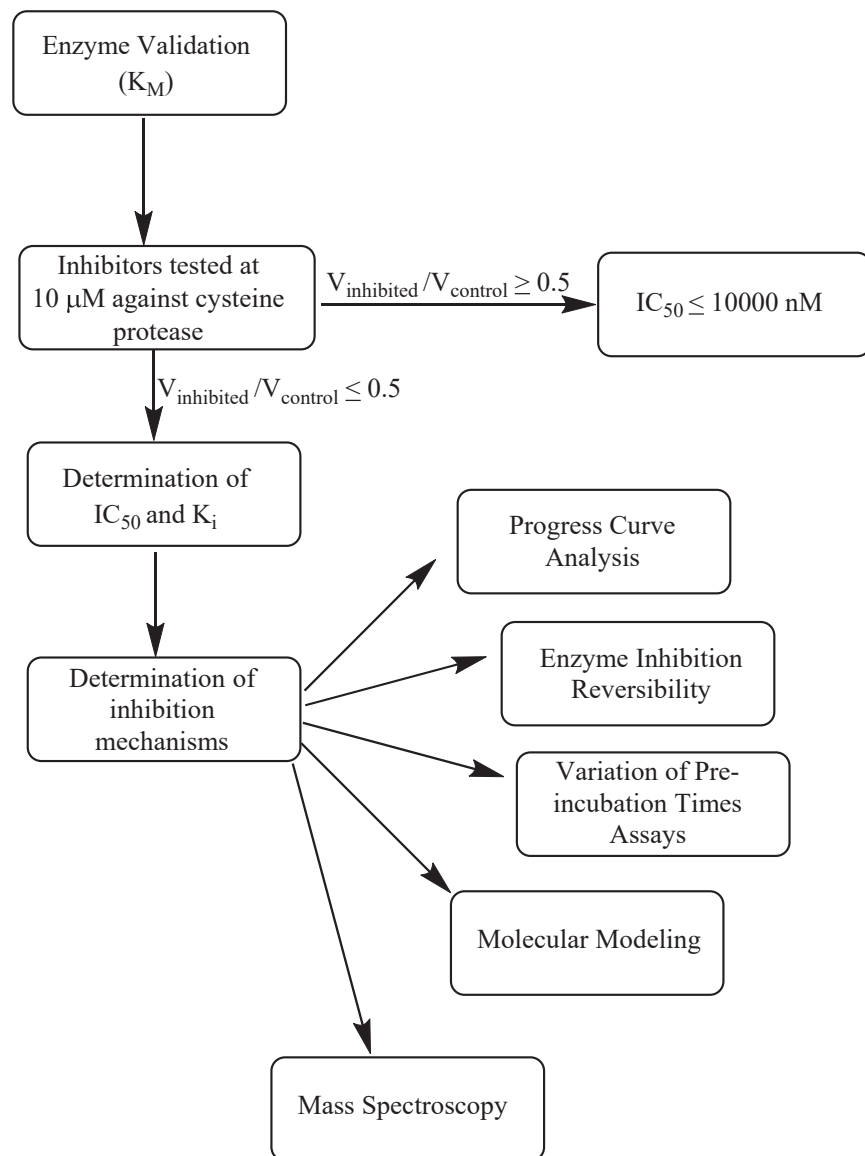
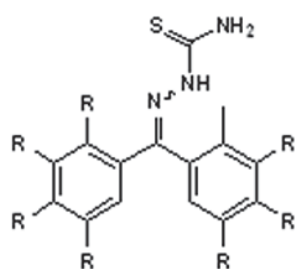
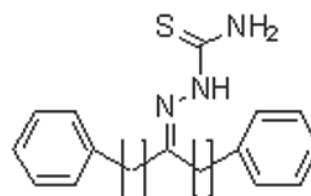


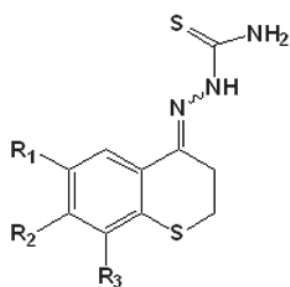
Figure 5.32. Experimental flowchart for analyzing compound inhibition of cysteine proteases



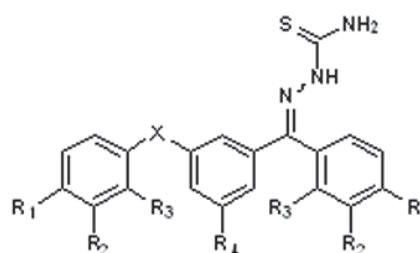
Benzophenone



Benzophenone (with alkyl linkers)



Thiochromanone



Benzoyl Benzophenone

Figure 5.33: Structural scaffolds of thiosemicarbazone compounds tested as cysteine protease inhibitors.

CHAPTER SIX

Chagas' Disease: Epidemiology, Pathology and Treatment

Roles of Parasitic Proteases in Mammals

Parasitic diseases are caused by a large and varied range of eukaryotic organisms and represent a significant global health problem. These diseases are often caused by the parasitic organism life cycle which usually results in deleterious effects on the hosts. These diseases have significant effects on public health, as they have higher morbidity rates than well-known maladies like diabetes [338], with malaria, schistosomiasis, and hookworm or *Ascaris* afflicting more than a billion people worldwide [339]. However, suppression of these diseases has proven to be a challenging task due to a number of factors. First, there is a relative lack of interest in vaccine or drug development against human parasitic diseases, mostly because these diseases primarily affect indigent people. Also, the understanding of parasitic disease pathogenesis is relatively lacking due to the biology of host-parasite relationships being extremely complex as well as the lack of research into this field. Furthermore, parasitic infections may lead to chronic diseases that are more difficult to treat. Some headway has been made towards identifying factors that are important to parasite virulence and pathogenesis. Among the most widely studied of these factors are parasite-derived proteases. Proteases play very important roles in the parasite life cycle and pathogenicity, such as parasite growth and maturation, tissue and cell invasion, breakdown of nutrients, and immune cell evasion [339-342]. Therefore,

parasitic proteases present a promising target for development of therapeutics against the diseases caused by these parasites.

Chagas Disease; History, Epidemiology and Pathology,

Chagas' disease, or American trypanosomiasis is a tropical disease caused by the parasitic protozoan *Trypanosoma cruzi* (*T. cruzi*), poses a significant public health crisis in the western world. It has been identified as one of the five neglected parasitic infections by the United States Center for Disease Control, due to the worldwide volume and severity of infection, exacerbated by poor clinical management and stage dependent detection [343]. This disease was first 'discovered' by Carlos Chagas, a Brazilian physician, in 1909 during an antimalarial campaign, when he observed the presence of a protozoan trypanosome in the gut of a reduviid bug (also known as the kissing bug) and hypothesized that the trypanosome may be the cause of an unknown illness afflicting a significant number of the local population [344-346]. These bugs, members of the family triatominae, are the primary vectors of *T. cruzi*. *T. cruzi* is transmitted during the blood meal consumption of these bugs. Fecal remains left at the bite contain the protozoan, which subsequently enters the bloodstream through the wound. Once blood borne, *T. cruzi* may persist indefinitely in circulation, at which it may be secondarily distributed via blood donation or through the umbilical cord blood during pregnancy [347, 348].

Despite rigorous efforts in Latin America to limit primary outbreak, Chagas' disease remains endemic. Furthermore, the number of infections in other parts of the world is steadily increasing due to global migration (Figure 6.1), with at least 300,000 and 80,000 projected cases in the United States and Europe respectively [343, 348-350]. Historically, not much effort has been directed towards managing Chagas' disease. In

fact, Chagas' disease is considered a neglected tropical disease (NTD) for a number of reasons: (1) the disease is ancient in origin, (2) the primary population infected is poor and lives in rural areas, and (3) the disease has a high burden but low mortality [344]. Furthermore, due to the difficulty of diagnosis there is a large population of people with Chagas' disease who are undiagnosed. Currently, the Centers for Disease Control (CDC) and the World Health Organization (WHO) are focused on creating better vector control parameters to reduce transmission and disease burden [349]. However, there has been relatively little research towards the development of effective therapeutics against this disease, with only two available drugs to treat the acute phase symptoms of the disease. However, it should be noted that these drugs are highly cytotoxic and are ineffective against the chronic phase of the disease. This, along with the mounting threat of advancement of the geographical regions affected by this disease, makes the development of efficient and cost-effective pharmacological agents against this disease increasingly expedient.

Chagas Disease; Symptoms and Diagnosis

There are three non-distinct phases of Chagas disease that can progressively manifest in infected patients. There is an acute phase that is primarily asymptomatic, an indeterminate or latent phase during which the disease is dormant, and a chronic phase. The timing between these phases is irregular and the severity of symptoms is dependent on a variety of variables (Figure 6.2). Furthermore, the mechanism by which infected individual progress through these phases is unknown. In fact, the likelihood that a person develops chronic phase symptoms is less than 33% and this group does not present similar pathology [350].

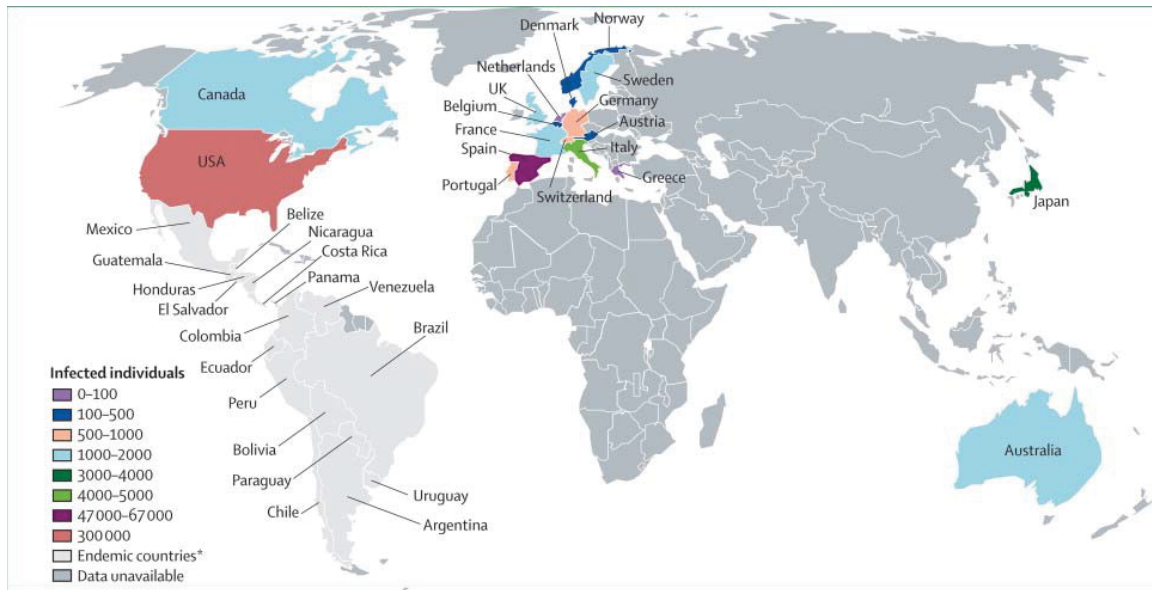


Figure 6.1. Projected worldwide number of *T. cruzi* infections [350]

Acute Phase

The acute phase of the disease is typically asymptomatic (up to 95% of cases are asymptomatic). However, there are some symptoms that may manifest 4-6 days after the initial infection. These symptoms typically present in infants and children, as well as immunocompromised individuals [351]. Two physical manifestations that are fairly reliable signs of Chagas' disease infection are the Romaña's sign and the chagoma. Romaña's sign (Figure. 6.3) occurs as a result of peri-orbital swelling from edema as well as conjunctivitis. A chagoma is a circular inflammatory lesion around the insect bite. Chagoma manifests less frequently than Romaña's sign, but either symptom is distinctly characteristic of Chagas' disease. Other symptoms that may occur during the acute phase include, fever, malaise, muscle and joint pain, somnolence, cramps, diarrhea, vomiting,

lymphadenopathy, edema, cyanosis, comma, meningoencephalitis and myocarditis [344, 351].

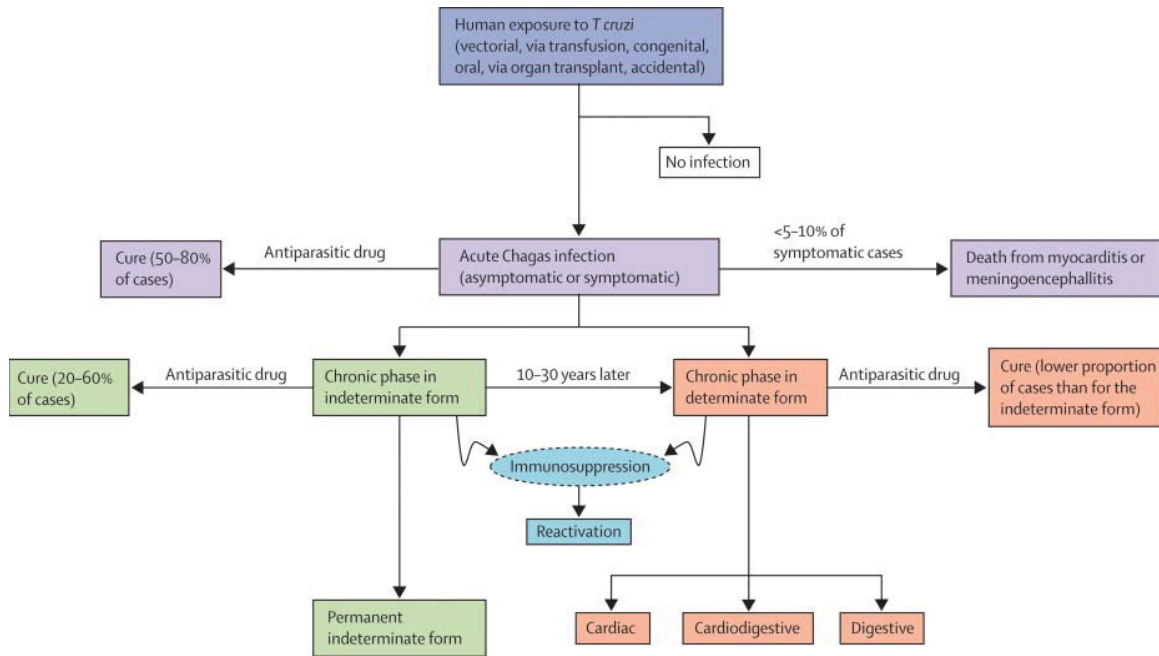


Figure 6.2. Chagas' disease progression [350]

Many of these symptoms are minor and may not be immediately associated with Chagas' disease. As a result, many infected people are not screened for *T. cruzi* infection. Moreover, less than 5% of Chagas disease afflicted patients in the acute phase die because initial manifestations are rarely severe. However, in the few cases with morbidity in the acute phase, the cause of death was a result of myocarditis or meningoencephalitis with concurrent bronchopneumonia [351]. These initial symptoms may digress after 4-8 weeks.



Figure 6.3. Artistic Rendition of Romaña's Sign [352]

Chagas disease diagnosis during the acute phase of the disease is possible due to *T. cruzi* parasites being visible in the blood. Due of this, diagnosis via direct microscopic examination of a blood smear could be done. Giemsa staining could be run concurrently to indicate the presence of parasites, though any kinetoplastid present would also be stained, thus increasing the likelihood of a false positive diagnosis. *T. cruzi* antibodies may also be found in a blood sample, confirming that the parasite has invaded the body. By the latter part of the acute phase, astrocytes (from the brain) and heart tissue have already been invaded by *T. cruzi*. Examination of histological samples from infected patients shows inflammatory mononuclear cell infiltrates and parasite-free host cell lysis. Lysis of parasite-free cells and neurons is a result of a hypersensitive immune response to target cells that in turn affects uninfected cells. As a result, one of the hallmarks of acute phase Chagas' disease is destruction of heart cells and depopulation of neurons [351].

Indeterminate Phase

The acute phase typically lasts for a period of 3-4 months, followed by progression to an indeterminate phase which is relatively asymptomatic compared to the acute and chronic phases. In fact, autopsies of patients that succumbed to other maladies

but were in the indeterminate phase of Chagas' disease revealed no heart lesions or megasyndromes. This implies that the chronic phase of the disease results from a severe outbreak of the parasite, rather than a slow degenerative process as previous studies suggested [351]. During this indeterminate phase the parasites are dormant and serological tests typically do not detect *T. cruzi*. The only noted symptoms from seropositive persons are electrocardiogram abnormalities, including right bundle branch block and left anterior hemi-block. Seropositive patients in this case refers to patients who have *T. cruzi* antibodies, however, not all patients infected by *T. cruzi* make these antibodies for unknown reasons [351, 353]. This indeterminate phase lasts 10 to 30 years after the initial infection.

Diagnosis of Chagas disease is rather difficult during this phase because the parasites have become dormant and are no longer present in large amounts in the blood. Therefore, direct blood smears are not an option and serological tests are not always accurate because infected patients may not make *T. cruzi* antibodies. Detection during this phase can be accomplished through phenotypic and genotypic screening of *T. cruzi* markers with concurrent enzyme-linked immunosorbent assay (ELISA) with parasite lysate [354, 355]. The latter exam typically indicates higher elevation of antibody titers, which may not be present if the person has not made *T. cruzi* antibodies. An emerging exam that may help circumvent this problem is a polymerase chain reaction (PCR) assay to test for *T. cruzi* DNA, although there are currently no PCR based diagnostic tools available for this disease [355].

Chronic Phase

Symptoms of the chronic phase of Chagas' disease are the most severe and diverse. Patients are inflicted with cardiomyopathy, arrhythmias, conduction defects, cardiomegaly, congestive heart failure, thromboembolism, megaesophagus, and megacolon [344, 351]. There are also cases of acquired peripheral neuropathies reported in children afflicted by Chagas' disease [356]. Only 30% of infected persons move onto the chronic phase from the indeterminate phase [357]. Life expectancy on average is reduced by 9 years after the onset of the chronic phase of this disease [350].

Cardiac defects occur in over 90% of cases of chronic Chagas' disease and lead to death in 58% of patients [350, 358]. In South America, Chagas' disease is the leading cause of heart disease, and this disease is the most infectious cause of myocarditis worldwide [350, 357, 359]. Sudden death is the main cause of death in patients with Chagas heart disease, accounting for nearly two thirds of all deaths, followed by refractory heart failure (25–30%), and thromboembolism (10–15%) [360]. Sudden cardiac death can occur even in patients who were previously asymptomatic. It is usually associated with ventricular tachycardia and fibrillation or, more rarely, with complete atrioventricular block or sinus node dysfunction. Leading causes of death vary dependent on the stage of disease, with a clear predominance of sudden death at early stages, and a slight predominance of death from pump failure at advanced stages [359, 360]. The reason for this death is typically due to enlarged hearts, (sometimes twice the original size along with aneurysm formation), inflammatory infiltrates in all layers of the heart, as well as dilated lymphatic vessels leading to the outer layer of the heart. Additionally, destroyed heart tissues become fibrous and exacerbate the hypertrophy and

cardiomyopathy [358]. Further analysis has found that there is decreased acetylcholinesterase activity as a result of progressive autonomic denervation.

Destruction of cardiac tissue is believed to result from involving parasite induced cell lysis and host autoimmune-mediated cell lysis (Figure 6.4) [361, 362].

Another clinical manifestation of chronic Chagas' disease is gastrointestinal dysfunction, manifested typically as megaesophagus or megacolon. These manifestations of the disease are seen mostly south of the Amazon basin (mainly in Argentina, Brazil, Chile, and Bolivia), and is rare in northern parts of South America, Central America, and Mexico. It has been suggested that this geographical distribution is likely as a result of differences in parasite strains [363]. This form of the disease develops in about 10–15% of chronically infected patients, with the severe symptoms manifesting as dysphagia, severe constipation, and then excruciating abdominal and esophageal pain [357]. The pain is caused by the enlargement of these organs from chronic inflammation and destruction of the parasympathetic ganglia from parasitic infiltrates. Furthermore, patients with megaoesophagus have an increased incidence of esophageal cancer [364].

In addition, recent studies have also suggested a link between chronic Chagas disease and neurodegeneration [365, 366]. Necrotizing inflammatory injuries in the grey matter of the central nervous system have been shown to occur as a result of this disease [357]. However, lesions in the sympathetic and parasympathetic peripheral nervous systems are the more common neurodegenerative symptoms [351, 365]. Symptoms of this disorder include weakness, sensory loss, paresthesia, and pain or burning sensation across the body. The most common manifestation of peripheral neuropathy is diminished or absent deep tendon reflexes as well as sensory impairment.

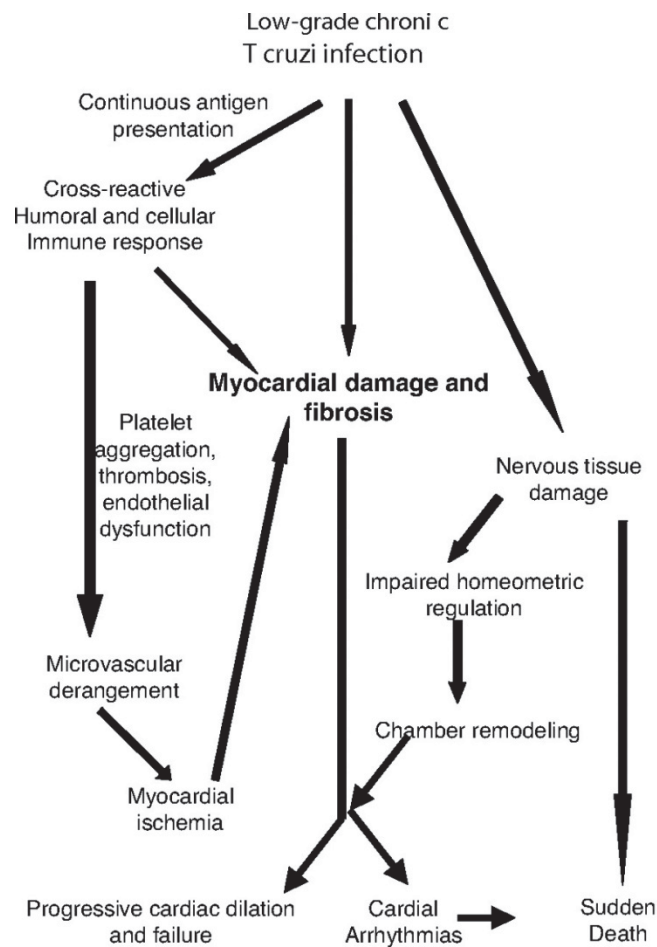


Figure 6.4. Suggested mechanisms of cardiac tissue destruction as a result of chronic Chagas' disease infection. [361]

Diagnosis of chronic Chagas disease typically involves monitoring of the adverse symptoms of the disease. For Chagas' heart disease, this involves the use of electrocardiograms to look for abnormalities such as arrhythmias, tachycardia, heart block and ventricular aneurysms [367]. Diagnosis via symptoms that occur as a result of the gastrointestinal form of the disease can be done using methods such as barium swallow and/or enema with concurrent CT scanning [368]. As with other phases of Chagas' disease, microscopic techniques can be used to detect *T. cruzi* using staining

protocols such as Giemsa or Wright tests. The protozoan can be detected in several human fluids and tissues (blood, and cerebrospinal fluid). Parasite isolation via techniques such as the inoculation of healthy mammals with blood from infected patients, include cell culture, and xenodiagnoses are viable diagnostic tools [351]. However, these tend to be slow and rather expensive. The most common and precise methods of diagnosing chronic Chagas' disease are serologic techniques. Indirect immunofluorescent assay (IFA), Enzyme-linked immunosorbent assay (ELISA), hemagglutination, radio-immunoprecipitation are commonly used with high sensitivity and specificity rates [369]. However, there may be the potential for false positives with other parasites from the Leishmania family. Molecular biology techniques are also quite useful due to the detection of the parasite using polymerase chain reaction (PCR) and immunoblotting protocols [355, 370].

Trypanosoma cruzi

The etiologic agent of Chagas disease is a flagellate, protozoan kinetoplastid. This eukaryote has a single flagellum, one nucleus, one kinetoplast, and an undulating membrane (Figure. 6.5). The trypanosome exists in four distinct stages: trypomastigote, amastigote, sphaeromastigote, and epimastigote [344, 371]. These parasites have unique life-cycles in humans and in their insect-vectors as well as in non-human mammals. There are 11 species of trypanosomes that comprise the *T. cruzi* clade and 6 phylogenetic lineages of the *T. cruzi* species [372].

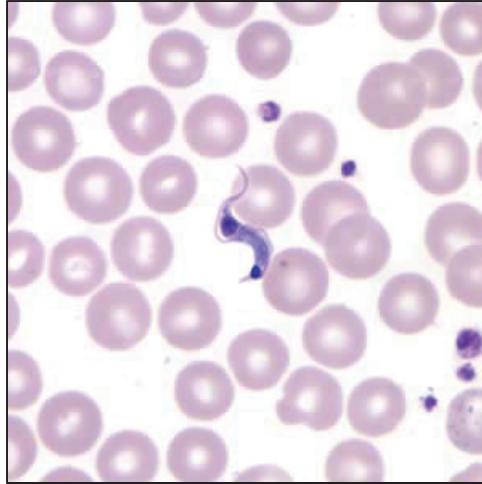


Figure 6.5. Giemsa-stained *T. cruzi* trypomastigote in a thin-blood smear [373]

Evolution

T. cruzi is a protozoan parasite belonging to the class kinetoplastida. These trypanosomes are believed to have branched from the *Trypanosoma brucei* clade (the causative agent of African sleeping sickness) in the mid-Cretaceous period (Figure 6.6). Compared to *T. brucei*, the *T. cruzi* clade is far more widespread and complex in terms of geographical distribution and host range. Furthermore, unlike *T. brucei*, *T. cruzi* has primarily evolved in the absence of humans. In fact, the transmission of *T. cruzi* by triatomine bugs is believed to be a recent evolutionary change, with an estimated the change occurring 1.5 million years ago, 150 million years after the divergence of the *T. cruzi* clade. Human contact with *T. cruzi* is believed to have occurred only 30 to 40,000 years ago [372]. Phylogenetic analysis has led to the organization of *T. cruzi* into two major groups, TcI and TcII. The second group, TcII, was later split into 5 sub-groups (TcII, TcIII, TcIV, TcV, and TcVI). It should be denoted that the different genetic strains have differing pathological manifestation, as well as different geological localization (Figure 6.7) [374]. For example, TcI has a preferential association for marsupials as it is

believed to have evolved in North American opossums. In fact, there are very few cases of TcI infections and it is believed that these parasites are cleared by the human host before manifesting as a chronic disease. On the other hand, TcII groups preferentially infect placental mammals and primarily infect humans. The TcII, TcV, and TcVI lineages, most commonly carried by *Triatoma infestans*, are the most common strains in South American Chagas disease infections. In regards to their pathophysiology, it has been found that TcI, TcV and TcVI are linked with cardiomyopathy and TcII with intestinal megasyndromes (megacolon and megaesophagus) [357].

T. cruzi Life Cycle, Transmission, and Mechanism of Infection

The *Trypanosoma cruzi* life cycle starts in an animal reservoir, usually mammals, wild or domestic, including humans. The vector (a triatomine bug) ingests *T. cruzi* while taking a blood meal. Once in the triatomine bug the parasite goes into the epimastigote stage, making it possible to reproduce. After reproducing through binary fission, the epimastigotes move onto the rectal cell wall, where they become infectious metacyclic trypomastigotes. When the triatomine bug subsequently takes a blood meal from a human, it defecates. The trypomastigotes in the feces can then enter the human host through the bite wound or by crossing mucous membranes.

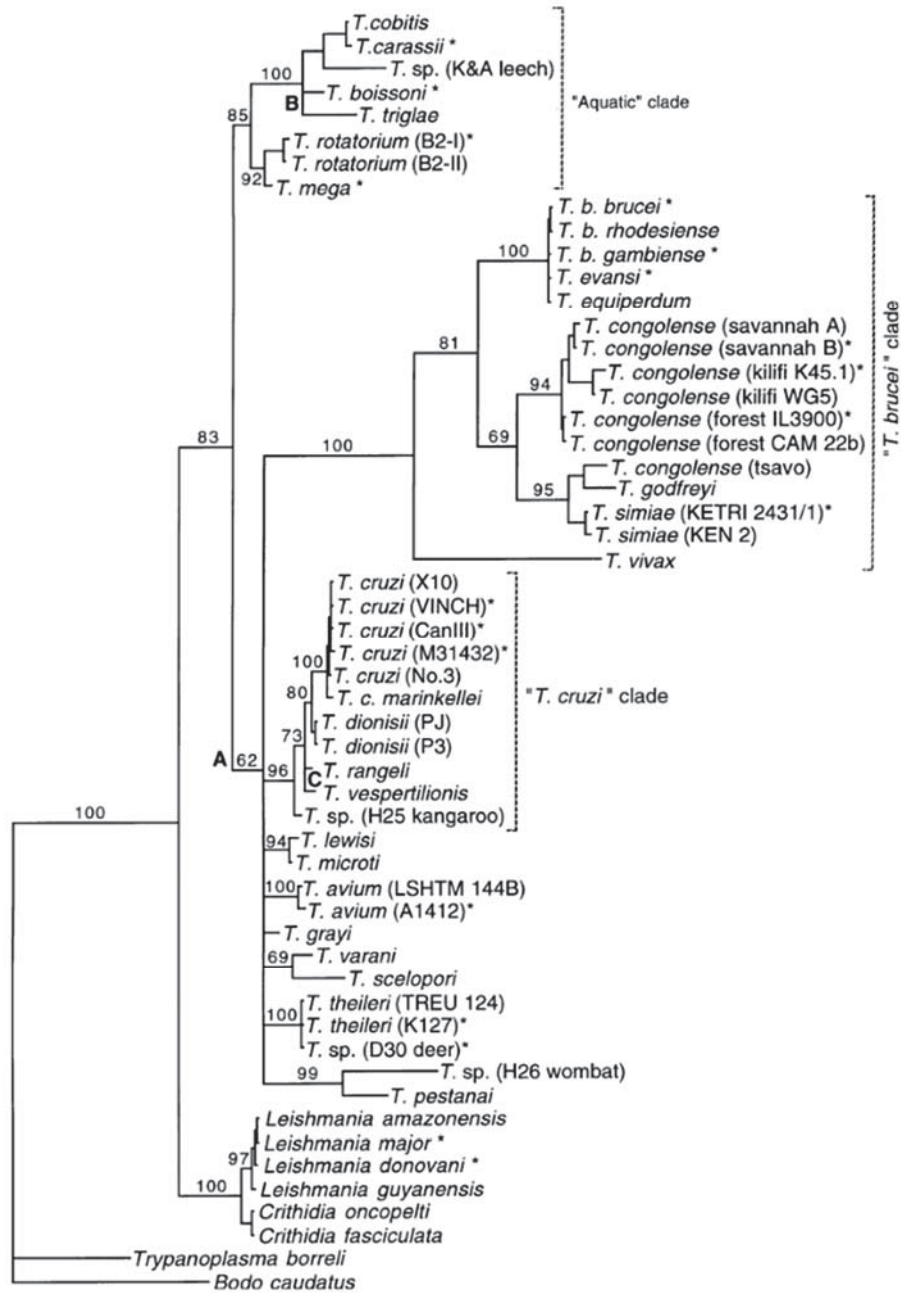


Figure 6.6. Phylogram showing origin of *T. cruzi* clade [372]

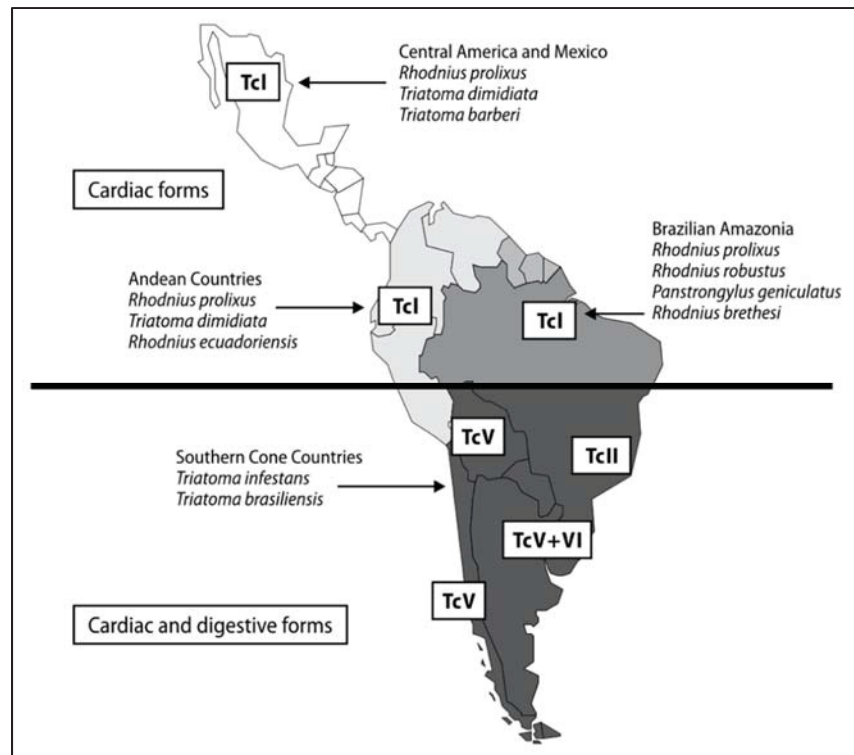


Figure 6.7. Geographic Distribution of *T. cruzi* strains across Central and South America [357]

Upon infection, trypanosomes undergo environmentally stimulated morphological and biochemical stages, oscillating between trypomastigote and amastigote [375] (Figure 6.8). *T. cruzi* host cell invasion and subsequent lysis is a complicated process involving various overlapping pathways. The process of invasion can be broken down into three steps: adhesion between *T. cruzi* and host cell via receptor ligand binding, internalization of *T. cruzi*, and escape from the parasitophorous vacuole. These three steps are multi-variable in the sense that there are multiple proteins, ligands and receptors involved that lead to variation in the pathways.

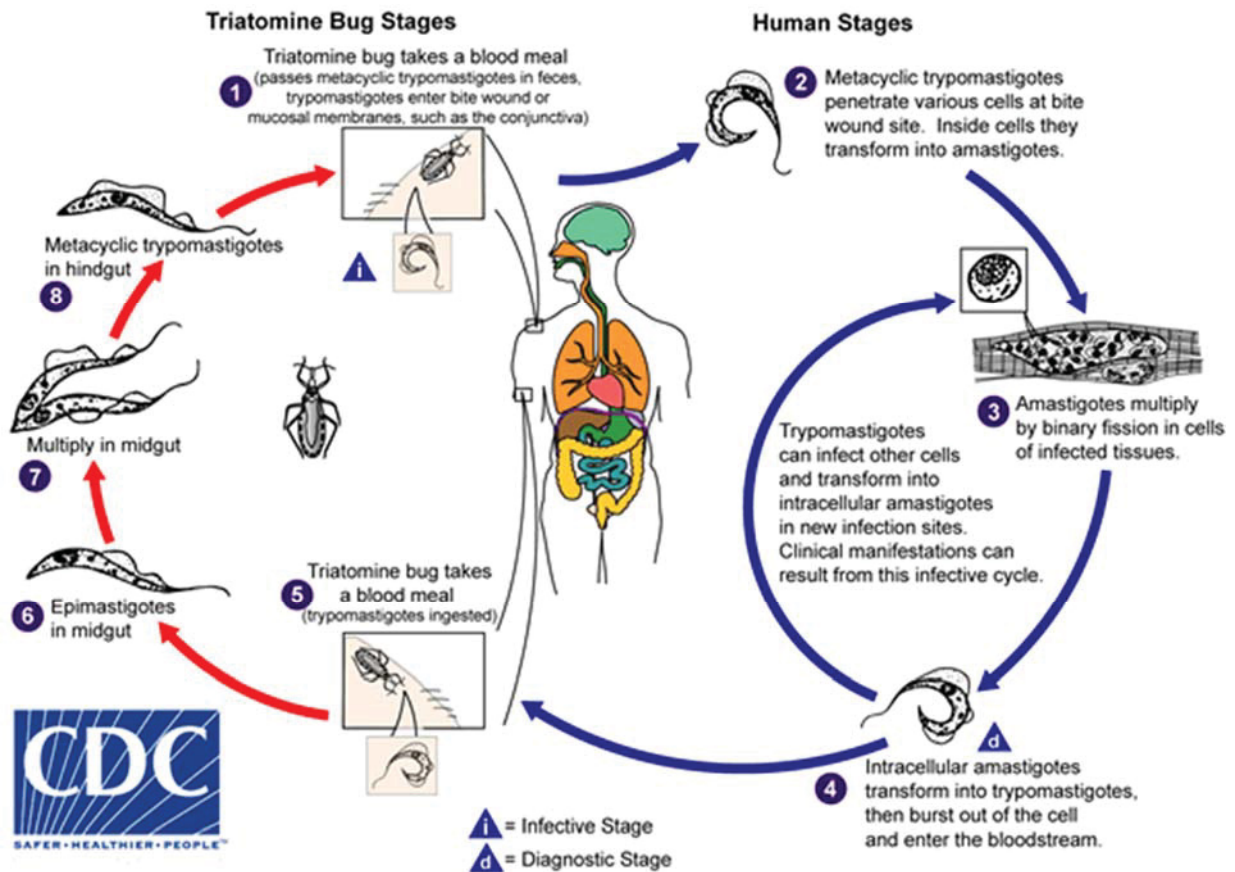


Figure 6.8. Life cycle and transmission of *T. cruzi* [376]

Host Cell Adhesion

The process of adhesion between *T. cruzi* trypomastigotes and host cells involves various surface proteins, compounds and receptors. *T. cruzi* utilizes glycoproteins such as mucins, gp35/50, gp82, gp90 and Tc85, trans-sialidases and proteases such as cruzipain, oligopeptidase B and Tc80 for host cell adhesion (Figure 6.9). Interaction between these and host cell surface markers typically leads to activation of signaling cascades that result in increase in cellular Ca^{2+} concentration, which is important for internalization of the trypomastigote [377]. Also, proteases play an important role in adhesion. POPPTc80

(prolyl-endoprotease), a serine protease that mediates hydrolysis of native collagen (types I and IV) and fibronectin, can degrade the extracellular matrix, thus helping parasite entrance and dissemination. Oligopeptidase B, a serine protease previously implicated in cell invasion by generating a Ca^{2+} agonist necessary for recruitment and fusion of host lysosomes at the site of parasite attachment, is secreted by trypomastigotes [377].

Cruzipain, the most abundant protease expressed as a mixture of isoforms in all forms of *T. cruzi*, plays roles in adhesion through extracellular matrix degradation and immune evasion (via antibody degradation) [378, 379]. For example, cruzipain in *T. cruzi* infection has been associated with its ability to generate bradykinin in the host and acting on B2 type bradykinin receptors (B2R). Cooperative activation of B2R and Toll-like receptor 2 by a mechanism that includes cruzipain has been suggested to be a link between innate and adaptive immunity in *T. cruzi* subcutaneous infection [377].

Host Cell Internalization

The next step after the parasite adhesion to a host cell is internalization. Currently, there are three theoretical pathways for *T. cruzi* internalization: lysosome-dependent exocytosis, actin dependent internalization with plasma membrane expansion, and lysosome-independent plasma membrane invagination. These internalization pathways vary based on the trypomastigote surface proteins used. However, the specific surface interactions leading to each method of internalization have not been completely elucidated. The lysosome-dependent pathway involves Ca^{2+} release leading to host cell exocytosis in order to from lysosomes by which trypomastigotes can be internalized. In the lysosome-independent pathway, PI-3K (phosphoinositide 3-kinase) activation at the site of entry leads to the formation an early endosome with the plasma membrane in order

to enclose the parasite. The early endosome eventually fuses with lysosomes and becomes a lysosome-like vacuole. The actin dependent pathway is basically phagocytosis, with emission of pseudopods by the cell upon trypomastigote adherence. All three pathways eventually lead to the formation of a parasitophorous vacuole that is acidic in nature (Figure 6.10). This vacuole is made up of the host cell plasma membrane and grows in size as it fuses with endosome and lysosome vacuoles [378, 380].

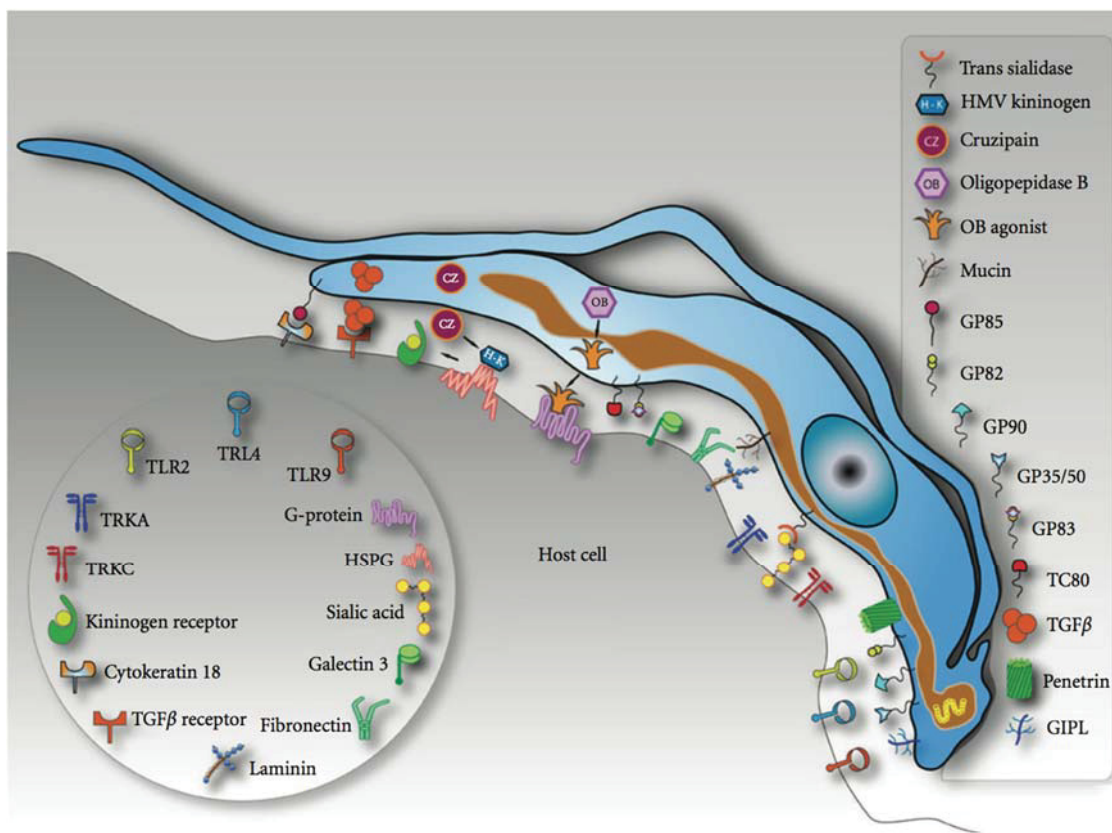


Figure 6.9. Surface interactions between *T. cruzi* trypomastigote and Host cell [378]

Cell Lysis

While enclosed in the parasitophorous vacuole, the trypomastigote parasites release trans-sialidase/neuraminidase enzymes to remove sialic acid from the membrane. This process sensitizes the membrane to the lytic factor LYT1 and the Tc-Tox peptide, released from the parasites, which disintegrates the membrane by creating pores [378, 380]. Concurrently, the trypomastigotes transform into amastigotes as the membrane is degrading. When the parasitophorous vacuole lyses, the amastigotes escape into the cytoplasm of the cell where they replicate exponentially. Once the amastigotes drain the cell of its resources, they cause the cell lysis – though host cell death is not caused by apoptosis but an unknown mechanism. Once the amastigotes lyse the host cell they can proceed to infect other cells. The lysing of cells presents physiologically as the symptoms of Chagas' disease, based on the types of cells being lysed [381]. However, the entire process of host cell invasion does not have a distinct timeline because amastigotes have the ability to lie dormant for long periods of time – hence the asymptomatic nature of the acute/intermediate phases.

Current Therapeutics for Chagas' Disease

Currently there are two types of treatments: antiparasitic and symptomatic treatment. The former results in parasitic death and is effective in the acute phase while the latter is mainly palliative and is used for the chronic phase. Available drugs for the acute phase are nifurtimox and benznidazole (Figure 6.11). These drugs interfere with the organism's genetic synthetic processes and create radicals allowing for antitrypanosomal activity, albeit with significant host toxicity [382, 383]. While antiparasitic therapy addresses acute stages, at the present time, no curative treatment is established for

chronic Chagas' disease. Due to deleterious side effects, benznidazole is banned in some countries like the United States. As a result of the undesirable current treatment, research into alternative therapeutic agents is important.

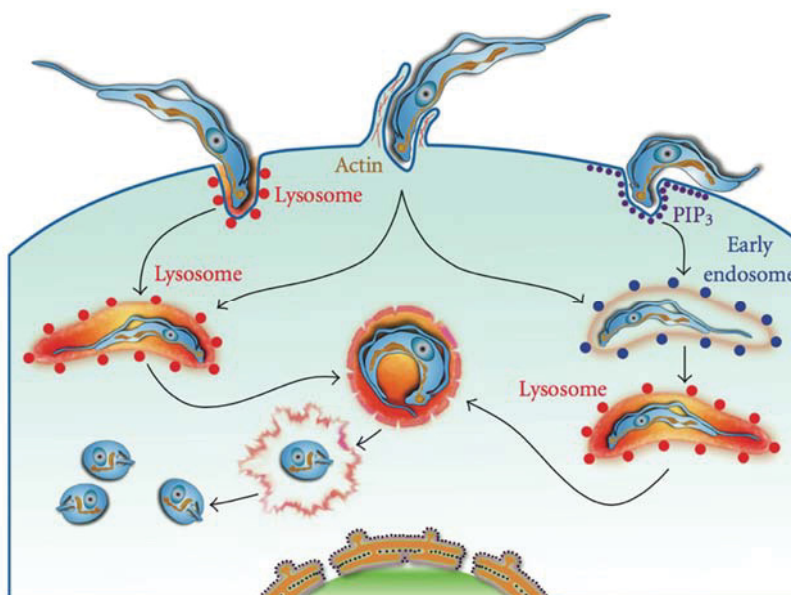


Figure 6.10: Models of *T. cruzi* internalization [378]

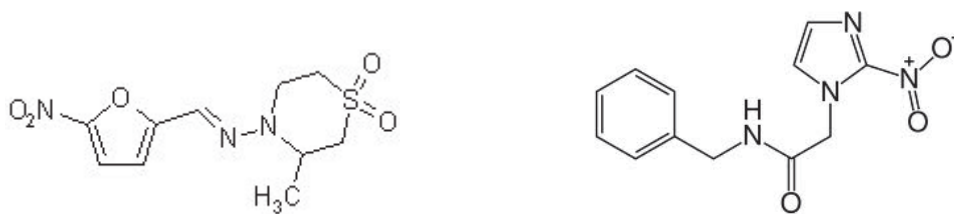


Figure 6.11: Chemical structures of Nifurtimox and Benznidazole.

Potential Targets for Chagas Disease Drug Development

Purine Salvage

The life cycle of *T. cruzi* is well known and the genome has been completely sequenced [384]. Essential parasitic pathways or enzymes that are distinct from the mammalian hosts present potential therapeutic targets. Parasitic nucleotide metabolism are interesting targets for therapeutic drug design, as this interference with this is a means by which replication transcription, RNA, and protein synthesis and all other machinery can be stopped. Mammals and parasitic microbes have distinct mechanisms by which of purines, for use in nucleotide metabolism, are produced. Many parasitic microbes, in contrast to free living organisms, cannot perform *de novo* synthesis of purines; therefore, they must acquire purines from the host through specific purine phosphoribosyltransferases. *T. cruzi* salvages exogenous purines from the host cells via hypoxanthine-guanine phosphoribosyltransferase, which might serve as a potential therapeutic target [385]. However, no inhibitors of this enzyme have thus far been found to adequately reduce parasitemia or show satisfactory. There has also been investigation into subversive substrates as potential drugs. For example, a drug allopurinol acts as a purine analog and is incorporated, through this purine salvage enzyme, into the parasite's DNA thus disrupting the synthesis of RNA and proteins [386]. However, this approach has also failed to produce viable therapeutic candidates

Dihydrofolate Reductase

Nucleotide synthesis can also be disrupted is via the enzyme dihydrofolate reductase [386]. Dihydrofolate reductase catalyzes the reduction of dihydrofolate to tetrahydrofolate, which is converted to methylene tetrahydrofolate in the subsequent step

and functions as a methyl source for the production of thymidine monophosphate (TMP) in trypanosomes (Figure 6.12) [387]. Enzyme substrate analogues are a method that has also been used to target this enzyme. One such compound is methotrexate (Figure 6.13), a dihydrofolate analogue that acts as a competitive inhibitor. The K_I values for *T. cruzi* and human DHFR are 0.038 nM and 0.179 nM, respectively [298]. In cell culture, methotrexate has an IC_{50} value of 9.2 μ M towards *T. cruzi* amastigote form. However, this compound exhibits a relatively low selectivity for *T. cruzi* dihydrofolate reductase, with only a 4.7-fold selectivity quotient against the human form of the enzyme. Research into compounds with better selectivity is ongoing [388-390]

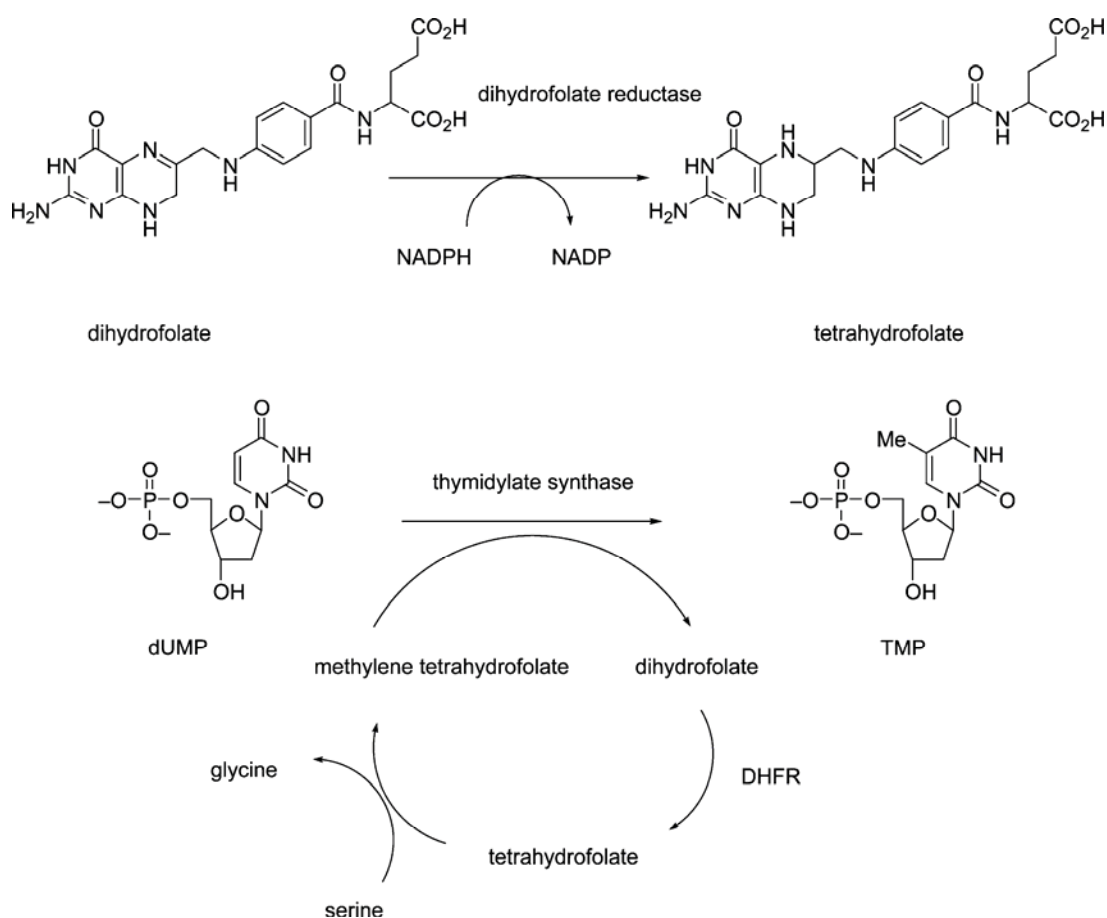


Figure 6.12. Mechanism of dihydrofolate reductase in the biosynthesis thymidine monophosphate

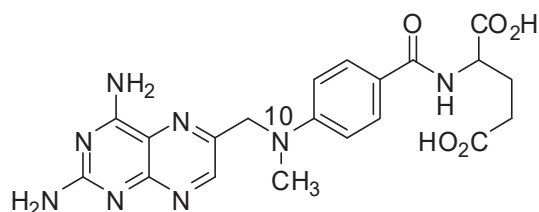


Figure 6.13. Structure of methotrexate

Sterol Biosynthesis

Research in the last two decades has consistently demonstrated that *T. cruzi*, like most fungi and yeasts, requires specific sterols for cell viability and proliferation in all stages of its life cycle and the ergosterol biosynthesis pathway (Figure 6.14), which has various enzymes that are parasite specific, has been chemically validated at many different steps, in vitro [385]. Various inhibitors targeting some of the enzymes in this pathway have been developed. Some of the enzymes that have been targeted for inhibition by therapeutics in this pathway are squalene synthase, squalene epoxidase, oxidosqualene cyclase, and C14 α -demethylase (which exists only in fungi and protozoa). Low EC₅₀ value inhibitors have been developed for these targets.

Squalene synthase catalyzes the first committed step in sterol biosynthesis and was a chemically validated as a chemotherapeutic target in *T. cruzi* and *Leishmania mexicana* [385]. Inhibitors having low nanomolar IC₅₀ values against squalene synthase have been developed. The best compound E5700, a quinuclidine compound, has an EC₅₀ of 30 nM against *T. cruzi* [391]. E5700 was able to provide full protection against death and completely arrested development of parasitemia in a murine model of acute disease when given orally [391]. Selective antiparasitic activity of this compound is most likely

due to the fact that despite them being potent inhibitors of mammalian squalene synthase [392], the host cells can compensate for the blockade of de novo cholesterol synthesis by up-regulating the expression LDL receptors [393]. This is not the case with the parasite as there are no appreciable amounts of ergosterol in the host cells [385, 391]. However, host organs (such as testis) that require elevated endogenous cholesterol supply could pose a significant limitation for the prolonged use of these inhibitors, highlighting the need for parasite specific squalene synthase inhibitors. Recent research has demonstrated progress towards this goal, as the gene coding *T. cruzi* squalene synthase has been cloned and expressed in *E. coli*, allowing the production of a soluble, fully active, recombinant enzyme, which has been used to identify parasite-specific inhibitors [394].

Another promising approach in this area is the validation of oxidosqualene cyclase as a chemotherapeutic target in *T. cruzi* and related parasites [385]. Unfortunately, there have been no reports of in vivo activity of this class of compounds as of yet. However, it should be noted that amiodarone, an antiarrhythmic drug most frequently used in chronic Chagas heart disease patients [359], has intrinsic anti-*T. cruzi* activity in vitro and in vivo. It was found that amiodarone has a dual mechanism of action against this parasite, disruption of Ca^{2+} homeostasis and blockade of de novo ergosterol biosynthesis at the level of oxidosqualene cyclase [395].

Recent research has shown that commercially available azole compounds which are highly effective antifungal agents (such as ketoconazole, itraconazole or terbinafine) have suppressive, but not curative, activity against *T. cruzi* infections in humans or experimental animals [385]. Triazole derivatives of these drugs have been shown to be potent and selective inhibitors of fungal and protozoan cytochrome P-450-dependent

C14 α sterol demethylase (CYP51) [385]. These were the first compounds reported to display curative activity both stages of the disease. Furthermore, such compounds were able to eradicate nitrofuran- and nitroimidazole-resistant *T. cruzi* strains from infected mice, even if the hosts were immunosuppressed [396]. Studies with posaconazole (Figure. 6.15), have shown that this compound can eradicate intracellular amastigote *T. cruzi* forms from cultured cardiomyocytes and at the same time allow the full reassembly of the host cells' cytoskeleton and contractile apparatus [397]. Other triazoles (Figure. 6.15), such as TAK-187, UR-9825 and ravuconazole have also been shown to have trypanocidal activity, both in vitro and in vivo [398-401].

A different family of azole-based CYP51 inhibitors, with potent anti-*T. cruzi* activity in vitro and in vivo, was discovered in the course of a research program to identify parasite-specific protein farnesylation inhibitors. These compounds are structurally simpler than the azole compounds described above and could be interesting alternatives for specific anti-*T. cruzi* drugs [402, 403].

Despite extensive research into the development of ergosterol biosynthesis inhibitors, the results from clinical trials have been variable (cure rates range from 0 – 100%). This may be due to different strains in different locations and acquired ergosterol in patients' diet from plant sources and/or from other vitamin D₂ supplementation, which may compete with chemotherapies in the sterol biosynthesis pathway. As such, it is necessary for more research into this topic to be performed.

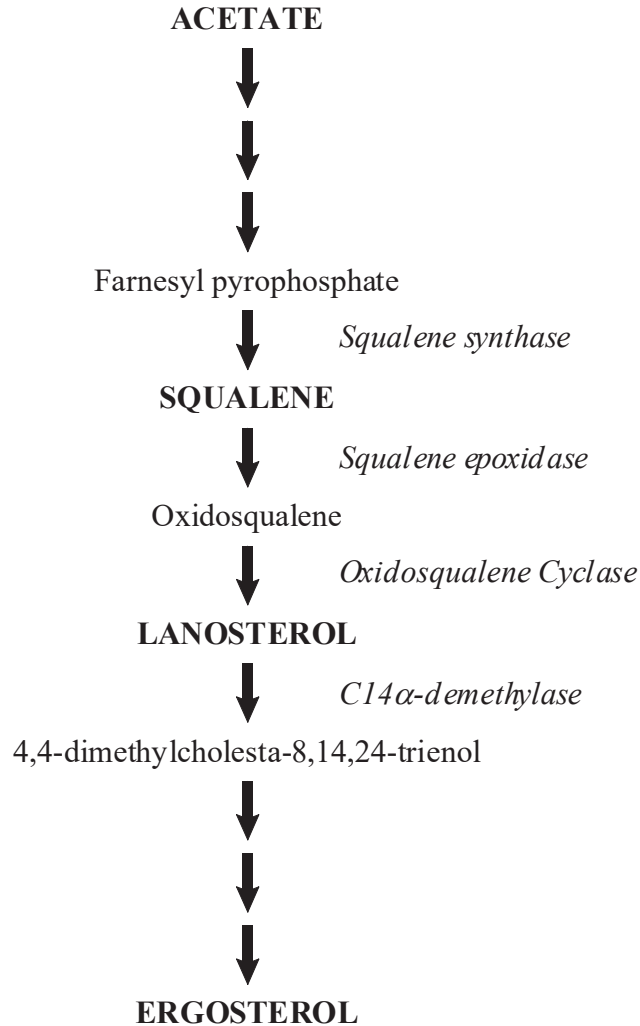


Figure 6.14. Simplified ergosterol biosynthesis in fungi and protozoa. Involved enzymes are in italic. The arrows indicate one or more reaction steps.

Pyrophosphate Metabolism

Pyrophosphate metabolism is another indirect target for sterol biosynthesis.

Trypanosomatid cells specialized organelles called acidocalcisomes, which are involved in polyphosphate and cation storage. The uptake and release of Ca^{2+} from acidocalcisomes is regulated by mechanisms involving Ca^{2+} ATPase, Na^+/H^+ exchanger, and proton pumping ATPase and pyrophosphatases.

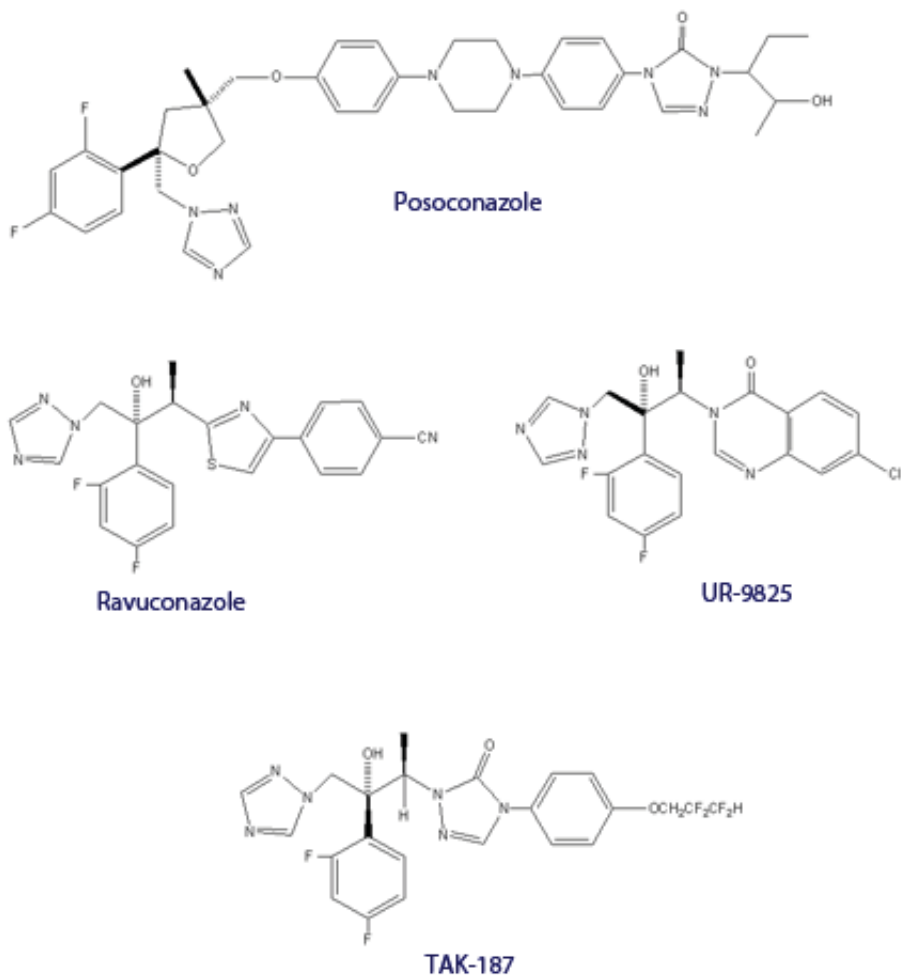


Figure 6.15. Azole ergosterol biosynthesis inhibitors that inhibit CYP51

Bisphosphonate compounds which are used to treat bone resorption disorders were demonstrated to inhibit enzymes that are involved in inorganic and organic pyrophosphate reactions such as farnesyl-pyrophosphate synthase, squalene synthase, or proton-pumping pyrophosphatases. Compounds selective against *T. cruzi* are promising candidates for anti-trypansomal chemotherapy [385, 404-406].

Trypanothione Reductase

Prevention of accumulation of reactive oxygen species is very important for cell survival. In mammalian host cells, removal of reactive oxygen species (superoxide anion, hydroxyl radical, peroxynitrite, and hydroperoxides) is accomplished via a carefully balanced system catalyzed by glutathione related enzymes, superoxide dismutase and catalase. This process is accomplished in *T. cruzi* via a biochemical pathway that is unique to Kinetoplastid protozoa, where it replaces glutathione and glutathione reductase as the main intracellular thiol-redox system, making it a promising target for antiparasitic chemotherapy [385]. Trypanothione (N1, N8-bis (glutathionyl)-spermidine) is unique to trypanosomatids. Recent research has identified the enzymes involved in the synthesis and redox metabolism of trypanothione as potential chemotherapeutic targets. The genes of all the enzymes of this pathway have been cloned and expressed and the 3D structures of these proteins have been determined using X-ray crystallography. Also, several of the enzymes in this pathway, including trypanothione reductase and trypanothione synthase, have been genetically validated [407]. Recent research has led to design/discovery of a number of specific inhibitors of this pathway with in vitro trypanocidal activity [408, 409]. However, there hasn't been much success in development of inhibitors that display high enough selectivity or provide parasitological cure.

Cruzipain: A Validated Target for Drug Development

One of the aims of the cysteine cathepsin inhibitor project being conducted in the Pinney and Trawick laboratories at Baylor University is the development of inhibitors of Cruzipain. Cruzipain is a lysosomal cysteine protease, a papain-like enzyme belonging to Clan 1A family. Cruzipain is a parasitic hydrolase found in *Trypanosoma cruzi* with an

EC number of 3.4.22.51.458 [410]. Cruzipain is also known as cruzain (a recombinant form of the enzyme), antigen GP57/51, or Ag163B6. Cruzain is also considered a cathepsin-L like enzyme due to their structural similarities also has endopeptidase activity. This enzyme is differentially expressed in the four main stages of the parasite life cycle, showing significant higher activity in epimastigotes compared with the other parasite forms [411]. Cruzain inhibition is a promising avenue for therapeutic development because in the event of inhibition, unprocessed cruzipain accumulates in the Golgi apparatus of *T. cruzi* epimastigotes. This accumulation interferes with the secretory pathway which eventually leads to trypanocidal activity [412].

Biological Roles of Cruzain in T. Cruzi Pathology

Cruzain plays numerous roles in the life cycle of *T. cruzi*. Cruzain is mainly found in parasitic lysosomes, similar to cathepsin L (which is expressed in mammalian organisms). Cruzain is transported to the epimastigote lysosome via endoplasmic reticulum and Golgi apparatus [413, 414]. Cruzain is also expressed in every stage of the protozoan life cycle. Specifically, cruzain was found at the surfaces of epimastigotes and amastigotes, as well in transitional forms of the trypomastigote-amastigote pseudo stage [415-417].

As mentioned earlier, cruzain is considered the a very important protease due to its high catalytic activity found in *T. cruzi* as well as its involvement in cell invasion, immune evasion and disease pathogenesis.

Cruzain plays a key role in the parasite's ability to invade host cells via a number of pathways [378, 418]. For example, cruzain kininogenase activity results in the release

of lys-bradykinin (an inflammatory peptide) and prekallikrein (which also generates lys-bradykinin) [419]. These proteins are pro-inflammatory, thus leading to an increase in parasitic uptake in host cells [420].

Cruzain also plays a crucial role in evasion of the host immune system by *T. cruzi*. One such mechanism by which this is achieved is the sequestration and degradation of host NF- κ B on the surface of epimastigotes by cruzain [421]. This protein is crucial for the activation of macrophages. Thus, host macrophages are rendered unresponsive at the outset of infection thus conferring protection on the parasite.

In addition to the functions already mentioned, cruzain plays a variety of other roles in *T. cruzi* life cycle and pathogenesis including: cell remodeling in the epimastigote, activation of bradykinin receptors, metabolism, virulence and mediation of apoptotic processes [314, 421, 422].

Structure of Cruzain

Cruzain is expressed in *Trypanosoma cruzi* as a pre-proenzyme of 467 amino acids residues (Figure 6.16) containing four very well defined portions: a signal peptide (19 residues), the propeptide (104 residues), the mature portion (215 residues) and a carboxy-terminal domain (129 residues) [423]. The signal and prodomain, which account for 123 amino acids, are cleaved under acidic conditions. The function of these domains is to protect unnecessary hydrolytic activity of the enzyme inside of the eukaryotic cells of the parasite, similarly to other cysteine proteases found in mammals. Mature cruzain is a monomer containing 215 residues (Figure 6.17) with a molecular weight of 23 kDa; however, glycosylated cruzain molecular weight is 51 kDa. Finally, the 129-residue carboxyl terminal domain is an unusual feature that is a characteristic of cruzain. To

date, there are no other known enzymes sharing this portion. The C-terminal domain contains significant modifications, including N- and O-glycosylations, and sialylations [424]. Efforts to crystallize cruzain with its C-terminal have been unsuccessful to date. As such, the elucidation of the biological functions of the C-terminal is challenging due to the lack of validated crystal structures. Furthermore, other modifications also exist, but their implications in *in vivo* studies are yet to be fully understood. However, the C-terminal region does not play a role in cruzain catalytic activity.

The three most abundant residues in the cruzain primary structure are alanine, glycine, asparagine and valine (25, 23 and 21 residues respectively). On the other hand, the least abundant residues are histidine (4 residues), arginine and phenylalanine (three residues each). Hydrophobic residues (A, F, I, L, M, P, V and W) account for forty percent of the composition of cruzain. Also, 38 percent of the composition is entirely made of polar, uncharged residues. The secondary structure is made up of seven alpha helices accounting for 25% of the structure (55 residues), with 24% of the sequence made up of beta sheets distributed in seventeen strands (52 residues).

```

1      MSGWARALLLA AVLVMACLVPAATASLHAEETLSQFAEFKQKHGRVYESAAEEAFRLS
61     VFRENLFARLHAAA NPHATFGVTPFSDLTREEFRSRYHNGAAHFAAAQERARVPVKVEV
121    VGAPAAVDWRARGAVTAVKDQGGQCGSCWAFSAIGNVECQWFLAGHPLTNLSEQMLVSCDK
241    PQDEAQIAAWLAVNGPVAVAVDASSWMTYTGGMVMTSCVSEQLDHGVLLVGYNDSAAVPYW
301    IIKNSWTTQWGEEGYIRIAKGSNQCLVKEEASSAVVGGPGPTPEPTTTTTTSAPGPSPSY
361    FVQMSCTDAACIVGCENVTLPTGQCLLTSGVSAIVTCGAETLTEEVFLTSTHCSGPSVR
421    SSVPLNKCNRLLRGSEFFCGSSSSGRLADVDRQRRHQPYHSRHRL

```

Figure 6.16. Amino Acid Sequence of Pre-procruzain. Legend: Green: Signal Peptide; Blue: Propeptide; Red: Mature Cruzain; Purple: C-Terminal [423].

```

1   APAAVDWRARGAVTAVKDQGQCGSCWAFSAIGNVECQWFLAGHPLTNLSE
51  QMLVSCDKTDSGCSGGLMNNAFEWIVQENNGAVYTEDSYPYASGEGISPP
101 CTTSGHTVGATITGHVELPQDEAQIAAWLAVNGPVAVAVDASSWMTYTGG
151 VMTSCVSEQLDHGVLLVGYNDSAAVPYWIKNWTTQWGEEGYIRIAKGS
201 NQCLVKEEASSAVVG

```

Figure 6.17. Amino Acid Sequence of Cruzain (PDB: 1ME3 [425])

The crystal structure of cruzain was first reported by McGrath and colleagues, with a structure solved at 2.35 Å [426]. Since then, numerous crystal structures have been resolved, one of which is presented in Figure 6.18. The cruzain monomer is comprised of two well defined domains: the L-domain which is mainly α -helical and the R-domain with extended antiparallel β -sheet interactions. The domains are linked by a polythreonine rich region. The active site is located at the inner face of the two domains. Similar to cathepsin L and a number of other cysteine proteases, the catalytic triad at the active site is composed of Cys25, His159 and Asn175 (papain numbering). The overall structure of cruzain structure is very similar to papain, the major cysteine protease. Nevertheless, cruzain and papain have differing loops and turns.

A unique feature of cruzain is the presence of a cysteine residue at position 36 (Cys36). To date, there are no other cysteine proteases with this residue located at that position. The thiol group of this residue was found to have weak interactions with two carbonyl oxygen atoms (Ala12, Gly32) and one water molecule.

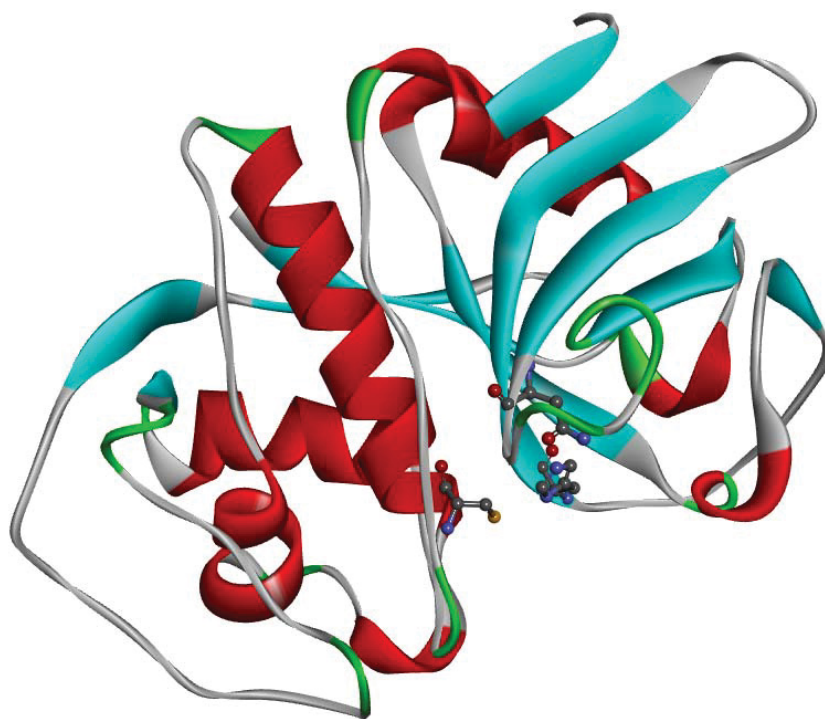


Figure 6.18. Crystal Structure of Cruzain PDB: 1ME3 [425]. Active site residues displayed as ball and stick models.

Cruzain contains eight binding sites for the substrate labeled as S1, S2, S3, S4, S1', S2', S3', and S4' (Figure 6.19). Of particular importance is the deep, hydrophobic S2 pocket, as it aids cruzain substrate specificity. This pocket has a glutamate residue at its base (Glu205). The S2 specificity pocket is able to productively bind arginine and phenylalanine residues. This is because Glu-205 adjusts to restructure the S2 specificity pocket, conferring right binding to both hydrophobic and basic residues. Kinetic analysis of activated peptide substrates shows that substrates placing hydrophobic residues in the specificity pocket are cleaved at a broader pH range than hydrophilic substrates [427].

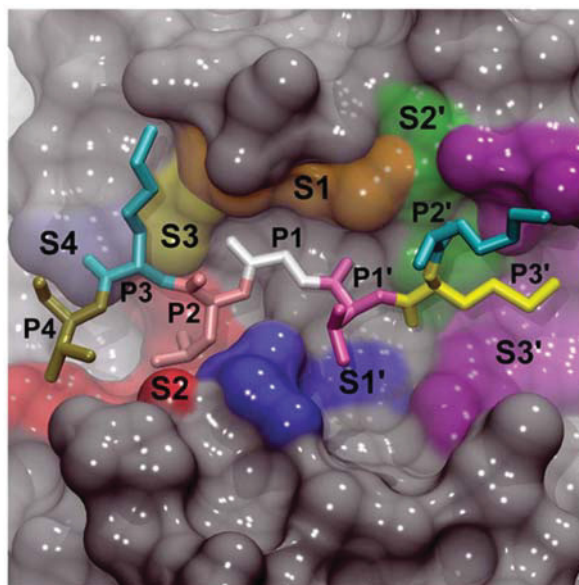


Figure 6.19. Cruzain active site with labelled subsites

Cruzain Substrate Specificity and Mechanism of Action

Cruzain is a cathepsin L-like cysteine protease, and shares not only structural similarities with cysteine cathepsins, but also has a number of similarities in substrate specificity. This has been observed upon comparison of catalytic activities against various substrates [428].

Cruzain enzymatic activity has been well studied due to its major roles in cell invasion and immunogenic procedures. As such, there are a number of natural substrates of cruzain. The enzyme is able to cleave proteins found in the extracellular matrix such as collagen, fibronectin and gelatin, among others [429]. This explains the ability of *T. cruzi* to degrade components of the extracellular matrix, including collagen, laminin, and heparin sulfate [430]. Cruzain also possesses caseinase properties and can also cleave

hemoglobin, bovine serum albumin and immunoglobulin, which speaks to the role played by cruzain in the evasion of the host immune system by *T. cruzi*

In order to clearly elucidate the catalytic/proteolytic capabilities of cruzain, the ability of this parasitic protease to cleave various synthetic fluoregenic substrates has been examined [427]. In this study, different fluoregenic substrates with the motif Z-XR-AMC where X where hydrophilic or hydrophobic residues at the P2 position, were analyzed. The enzymatic activity of cruzain over a broad pH range (3 to 8) was also explored. As mentioned earlier, substrates specificity of cruzain is mainly determined by the presence of hydrophobic residues at the P2 position of the substrate (X= Phe, Ile and Tyr) over hydrophilic ones (Arg, Gln). It should however be noted that there is still catalytic activity against hydrophilic residues at this position albeit to a lesser extent. This study also defined the activity of cruzain over a broad pH range when hydrophobic residues were tested, with highest catalytic activity occurring under acidic conditions (pH 5.5). Studies showed the phenolic ring of phenylalanine can be easily accommodated in a hydrophobic pocket formed by Ala133, Leu157, Gly160 and Glu205 and Met68.

The general mechanism of action of cruzain is mostly similar to the general cysteine protease mechanism (Figure 5.12). To re-iterate, the mechanism involves a nucleophilic attack of the thiolate anion of the catalytic cysteine residue. The cleavage and mechanism of action begins with a deprotonated cysteine thiol group attacking the carbonyl carbon of the substrate. A glutamine residue (Gln 19) facilitates this reaction by hydrogen bonding to the carbonyl oxygen and oxyanion tetrahedral intermediate of the substrate. The electrons temporarily move to the carbonyl oxygen forming a tetrahedral transition state. Following this, the pushed up electrons are brought back down, cleaving

the amide bond. The nitrogen of the amide group receives a proton from the imidazolium cation of the histidine, which acts here as a proton donor. The new amine substrate is temporarily hydrogen bound to the histidine group before deprotonating the imidazolium and leaving; the carboxylic substrate is still bound to the cysteine with a thioester bond. Following this step, a water molecule attacks the remaining substrate causing the oxygen to take on electrons like before forming another tetrahedral transition state. The histidine acts as a proton acceptor in this step and takes one of the water's hydrogen, restoring the imidazolium cation. When the electrons reform the carbonyl double bond, the thioester undergoes deacylation forming a deprotonated thiol group and a carboxyl group, concluding the reaction [431].

Cruzain Inhibitors

For design of effective cruzain inhibitors as possible therapeutics for Chagas' disease, a number of factors must be taken into account. These include; i) effectiveness in both stages, ii) completed under 60 days for clinical use, iii) low molecular weight, iv) highly selective, v) oral bioavailability, vi) marginal toxicity [432].

Identification of potent cruzain inhibitors has typically been done through substrate library screening, molecular docking programs, high-throughput screening (HTS), virtual screening (VS), and quantitative structure-activity relationships (QSAR) established with x-ray crystallography and protein-ligand interactions fingerprint (PLIF) methods. Based on these various screening methods, various compounds have been discovered to be potent inhibitors of cruzain (Figure 6.21). The following section presents a brief overview of compounds/molecules that have been found to inhibit cruzain activity.

Natural Inhibitors

Cruzain is expressed in parasitic organisms as a proenzyme, similar to cysteine cathepsins. One of the major functions of the propeptide is the prevention of enzymatic activity of cruzain within the parasite. Thus, activation occurs within the parasitic lysosome where cruzain activity is mainly found. Cleavage and activation of the enzyme occur under acidic conditions present in the lysosome. Studies have shown that this proregion, (103 residues) with a molecular size of 14 kDa, is a potent inhibitor of mature cruzain, with a dissociation constant as low as 18 pM in *in vitro* studies [433].

Other cruzain inhibitors include natural products such as chagasin and tigutcystatin. Tigutcystatin is a protein produced by a vector of *T. cruzi*, *traiatoma infestans* [434]. This endogenous inhibitor was first shown to tightly and reversibly bind toward cruzipain ($K_i = 3.29$ nM). Structural features of this particular cystatin include a highly conserved N-terminal glycine residue, a principal motif QxVxG (where x refers to any amino acid residue), and two adjacent residues at the carboxyl end-proline and tryptophan. Possible physiological processes involving tigutcystatin include endogenous gastrointestinal cysteine proteases monitoring, inhibition of cruzain upon *T. cruzi* infection, and other innate immune mechanisms [434]. Chagasin is an endogenous *T. cruzi* cruzain inhibitor, most likely used for post-translational regulation of cruzain by the parasite [435].

Synthetic Inhibitors

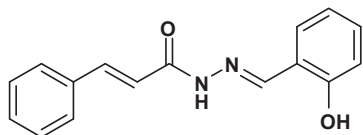
A significant number of compounds exhibiting cysteine protease inhibition activity have been developed and researched as possible candidates for Chagas disease therapy (Fig 6.20). One of the more well-known and researched selective inhibitors of

cruzain is N-methyl-piperazine-urea-F-hF-vinyl-sulfone-phenyl, also known as CRA-3316 or K-777 (Figure. 6.20). This compound has been shown to block the proliferation of both extracellular epimastigotes and intracellular amastigotes and halt the transformation of epimastigotes to metacyclic trypomastigotes in vitro. This led to significant reduction in the parasitemia levels and increased survival in murine models of acute and chronic Chagas disease, with minimal toxicity [436]. Other studies using a canine model [437] and a murine immune-deficient model [438] showed that K-777 caused parasitemia reduction and curative effects. The National Institutes of Health nominated K-777 for development as a potential new treatment for Chagas disease. However, the clinical development of this compound has been slow due to some controversy over issues such as hepatotoxicity and the manufacture of the compound [439]. Studies with structural variants of K777 (with changes at P1, P2, and P3 sites), showed that a hydrophilic heterocycle at P3 site favored hydrogen bonding with Ser61 of S3 pocket [440]. Other compound classes that have been shown to be promising cruzain inhibitors include indoloquinoline alkaloid compounds [441], amino nitrile compounds [442], chalcones and hydrazides [443], acylhydrazones and thiazolylyhydrazones [444], and semicarbazone and thiosemicarbozone compounds [445, 446].

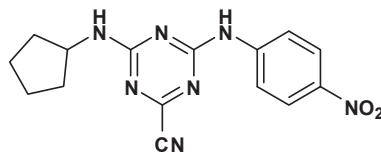
Thiosemicarbazone compounds, which are the focus of this project, represent promising potential antichagasic compounds. The discovery of nonpeptidic thiosemicarbazones as cysteine protease inhibitors was first reported in 2002, when it was observed that 3'-bromopropiophenone thiosemicarbazone had particularly potent inhibitory capability against cruzain [445]. Other research groups, in independent research projects, have reported similar findings [447, 448]. Furthermore, various studies

have shown that this class of compounds have had promising albeit widely variable effects on *T. cruzi* in vitro and in vivo [449-452].

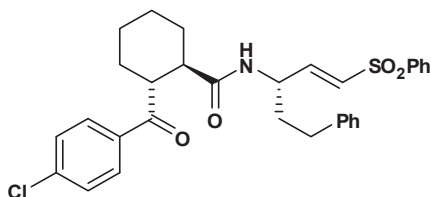
As part of a collaborative project between the laboratories of Dr. Mary Lynn Trawick and Dr. Kevin G. Pinney at Baylor University, the synthesis and evaluation of novel functionalized thiosemicarbazones as cruzain inhibitors have been reported. The list included naphthalenes, benzophenone, propiophenones, among others [298, 447, 453, 454]. The purpose of this segment of the overall collaborative research project is the evaluation of the inhibitory activity of other functionalized thiosemicarbazones that have been subsequently synthesized including benzoyl-benzophenone and thiochromanone moieties [455, 456].



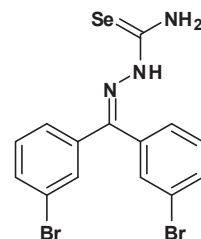
Cinnamic *N*-acylhydrazone (IC_{50} : 52 μ M)



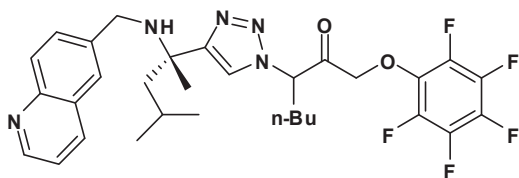
Nitro-substituted triazine (IC_{50} : 1 nM)



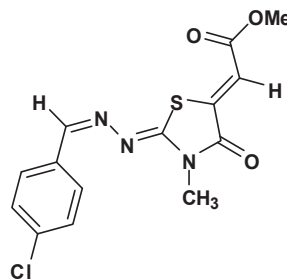
Vinylsulfone Derivative (IC_{50} : 50 nM)



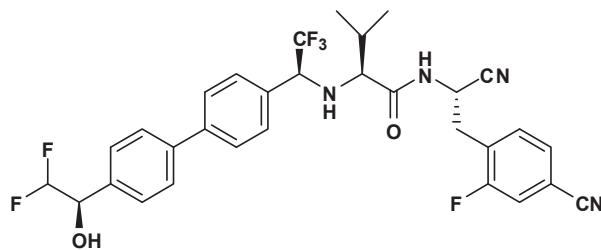
Selenosemicarbazone
(99% inhibition, $[I]$: 10 μ M)



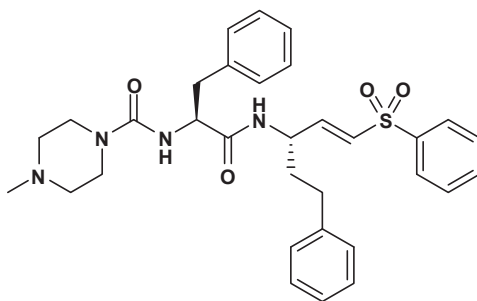
Tetrafluorophenoxymethyl (K_i : 100 nM)



Thiazolidinones (75% inhibition, $[I]$: 100 μ M)



Amino nitrile derivative (IC_{50} : 0.4 nM)



K777 (vinyl sulfone)

Figure 6.20. Selection of potential antichagasic cruzain inhibitors [452]

CHAPTER SEVEN

Evaluation of Thiosemicarbazone Inhibitors of Cruzain as Therapeutics for Chagas' Disease

Material and Methods for the Biological Evaluation of Thiosemicarbazones Derivatives as Inhibitors of Cruzain

Materials and Equipment

Sodium acetate (anhydrous), ethylenediaminetetraacetic acid (EDTA), and dithiothreitol (DTT) were obtained from EMD. 30 % Brij 35, and Z-Phe-Arg-AMC (7-Amino-4-methylcoumarin, N-CBZ-L-phenylalanyl-L-arginine amide, hydrochloride, Z-FR-AMC) was purchased from Sigma Aldrich. Pure (99.9 %) Dimethyl sulfoxide (DMSO) and pure 7-Amino-4-methylcoumarin (AMC) were products from Acros and Anaspec. Recombinant cruzain (1.1 μ M) was expressed and purified by Dr. Wara M. Arispe and Lauren Adamson under the guidance and supervision of Dr. Mary Lynn Trawick. Cruzain DNA plasmid was kindly donated by Elizabeth Hansell and Dr. James McKerrow from the University of California at San Francisco, CA. 18 m Ω ultra-pure water (subsequently referred to as pure water) was generated using an Elga PureLab Flex water purification system. The thiosemicarbazone inhibitor compounds were synthesized by members of the Dr. Kevin G. Pinney laboratory [455, 456] at Baylor University. Black 96 well flat bottom microplates and 0.2 μ m filters were obtained from Corning. Single and twelve-channel pipettes as well pipette tips were obtained from Eppendorf. Range of pipettes used varied between 0.5 and 5000 μ l. Also, a pH meter (Mettler

Toledo) and a Fluoroskan Ascent FL (Thermo) were used to calibrate the pH of the prepared solutions and for fluorometric experiments respectively.

Preparation of Buffers and Stock Solutions

Preparation of 400 mM sodium acetate buffer, pH 5.5. 200 ml of this solution was prepared by dissolving 5.59g of anhydrous sodium acetate in 0.74ml glacial acetic acid and making solution up to 200 ml with pure water. Glacial acetic acid or sodium hydroxide 5 M (MW: 40 g/mol) were used to adjust the pH of the buffer. This solution was stored at 4 °C.

Preparation of 40 mM EDTA. A stock concentration of this solution was prepared by dissolving 14.89 mg (40 µmol) of EDTA (MW: 372.29 g/mol) in one milliliter of water. Fifty milliliters of this solution (744.5 mg; 2 mmol) was prepared for multiple experiments. The solution of 40 mM EDTA was stored at 4 °C.

Preparation of 80 mM DTT. A freshly made stock concentration of this solution was prepared by dissolving 12.3 mg (80 µmol) of DTT (MW: 175 g/mol) in one milliliter of sodium acetate 400 mM, pH 5.5. The 80 mM DTT solutions were made fresh for each experiment.

Preparation of 6 mM AMC. This stock solution was prepared by dissolving 1.38 mg (6 µmol) of AMC (MW: 229.2 g/mol) in one milliliter of pure DMSO. This solution was stable for several months when stored at low temperatures (-20 °C).

Preparation of 6 mM Z-FR-AMC stock solution. This solution was made by dissolving 3.9 mg (6 µmol) of Z-FR-AMC (MW: 649.15 g/mol) in one milliliter of pure DMSO. This solution was stable for several months when stored at low temperatures (-20 °C).

Preparation of 150 μ M Z-FR-AMC solution. This solution was prepared by diluting 25 μ l of the 6 mM Z-FR-AMC stock solution in 975 μ l of pure water, resulting in 1 ml of a 150 μ M (in 2.5% DMSO) Z-FR-AMC solution. This solution was stable for a month when stored at -20 °C.

Thiosemicarbazone derivative stock solutions. A subset of compounds from a library of thiosemicarbazone inhibitors was used to make inhibitor stock solutions (20 mM) in pure DMSO. Typically, one milligram was weighed to give a final volume that varied between 100 and 200 μ l of these stock solutions.

Preparation of inhibitor dilutions. Each inhibitor was serially diluted in pure DMSO to provide six different concentrations (named A-F) with concentrations ranging from 2 nM (solution A) to 20 nM (solution F). Further dilutions of these solutions into a solution that contained 35% DMSO in water (named 1-8) were done. Concentrations of these 35% DMSO in water inhibitor solutions ranged from 200 μ M and 200 pM. Solutions made in pure DMSO were stored for two weeks at -80 °C. 35% DMSO solutions were made prior to the experiment and kept at 4 °C. Tables 7.1A and B show sample calculations for the procedure for preparation of the inhibitor stock solutions in pure and 35% DMSO.

Table 7.1A. Preparation of inhibitor stock solutions in pure DMSO

Inhibitor solutions	Concentration (μM)	Volume from previous solution (μl)	Pure DMSO (μl)	Total Volume (μl)
Stock	20000			
A	2000	10	90	100
B	200	10	90	100
C	20	10	90	100
D	2	10	90	100
E	0.2	10	90	100
F	0.02	10	90	100

Preparation of cruzain assay buffer. Cruzain assay buffer (subsequently assay buffer for future reference) contained 1.3 mM EDTA, 3.25 mM DTT, 0.02% Brij 35 and 130 mM NaOAc pH 5.5. Ten milliliters of assay buffer were made by adding 450 μl of 40 mM EDTA, 675 μl of 80 mM DTT, 6 μl of Brij 35, 3 ml of 400 mM NaOAc pH 5.5, and 5.87 ml of water in a plastic 50 ml conical tube. A summary of a typical calculation sheet used to make different volumes of assay buffer is presented in Table 7.2. The solution was stable up to a maximum of 24 h after preparation.

Preparation of 35% DMSO solution. An aqueous solution of DMSO was prepared by dilution of 35 μl of DMSO with 65 μl of water to bring a total of 0.1 ml. This solution was made up and used for each individual experiment.

Preparation of cruzain secondary stock solution. A secondary stock solution of cruzain was prepared containing 1 mM EDTA, 2.5 mM DTT, 0.01% Brij 35, 0.29 nM cruzain and 100 mM NaOAc pH 5.5. Table 7.3 presents a summary of typical calculations used to prepare different volumes of cruzain stock solution. The solution freshly prepared prior to every kinetic or inhibition experiment.

Table 7.1B. Preparation of inhibitor stock solutions in 35% DMSO

35 % DMSO Solutions (μ M)	100 % DMSO Stock solutions	100 % DMSO Stock Solutions (μ l)	DMSO (μ l)	Water (μ l)
200	A	10	25	65
100	A	5	30	65
20	B	10	25	65
10	B	5	30	65
2	C	10	25	65
1	C	5	30	65
0.2	D	10	25	65
0.02	E	10	25	65
0.01	E	5	30	65
0.002	F	10	25	65
0.001	F	5	30	65
0.0002	F	1	34	65

Preparation of cruzain buffer solution for reversibility studies. 4.8 ml of this solution was made by mixing 1320 μ l of 400 mM NaOAc pH 5.5, 5.28 μ l of 10% Brij 30, 165 μ l of 80 mM DTT, 132 μ l of 40 mM EDTA, and 3177.7 μ l of water. Final conditions were: 100 mM NaOAc pH 5.5, 1 mM EDTA, 2.5 mM DTT, and 0.01% Brij 30.

Preparation of cruzain stock solution for reversibility studies. 100 ml of this solution was made by diluting 1.82 μ l of cruzain enzyme (1.1 μ M) in 98.18 μ l of the cruzain buffer solution for reversibility. Final conditions in this solution were 100 mM NaOAc pH 5.5, 1 mM EDTA, 2.5 mM DTT, and 0.01% Brij 30, and 20 nM cruzain.

Table 7.2. Preparation of Cruzain Assay Buffer

Assay Buffer (μ l)	40 mM EDTA (μ l)	80 mM DTT (μ l)	400 mM NaOAc (μ l)	Water (μ l)	10% Brij (μ l)
1000	32.5	40.625	325	600.575	1.3
2000	65	81.25	650	1201.15	2.6
3000	97.5	121.875	975	1801.725	3.9
4000	130	162.5	1300	2402.3	5.2
5000	162.5	203.13	1625	3002.87	6.5
6000	195	243.75	1950	3603.45	7.8
7000	227.5	284.38	2275	4204.02	9.1
8000	260	325	2600	4804.6	10.4
9000	292.5	365.63	2925	5405.17	11.7
10000	325	406.25	3250	6005.75	13
11000	357.5	446.88	3575	6606.32	14.3
12000	390	487.5	3900	7206.9	15.6

Table 7.3. Preparation of Cruzain Stock Solution

Cruzain Stock Solution (μ l)	40 mM EDTA (μ l)	80 mM DTT (μ l)	400 mM NaOAc (μ l)	Water (μ l)	10% Brij (μ l)	1.1 μ M Cruzain (μ l)
600	15	18.75	150	415.49	0.6	0.16
1200	30	37.5	300	830.99	1.2	0.31
1800	45	56.25	450	1246.48	1.8	0.47
2400	60	75	600	1661.98	2.4	0.62
3000	75	93.75	750	2077.47	3	0.78
3600	90	112.5	900	2492.96	3.6	0.94
4200	105	131.25	1050	2908.46	4.2	1.09
4800	120	150	1200	3323.95	4.8	1.25
5400	135	168.75	1350	3739.45	5.4	1.4
6000	150	187.5	1500	4154.94	6	1.56
6600	165	206.25	1650	4570.43	6.6	1.72
7200	180	225	1800	4985.93	7.2	1.87

Experimental Section

Kinetic Cruzain Assay

Kinetic studies to determine the catalytic activity of cruzain against Z-FR-AMC substrate were carried in 96-well black microplates using a Thermo Fluoroskan microplate reader. The total reaction volume was 200 μ l per well, with each well containing 100 μ l of assay buffer, 10 μ l of 35% DMSO solution, 70 μ l cruzain solution, and 20 μ l of varying concentrations (in 2.5% DMSO) of Z-FR-AMC solution. Serial dilutions were used to prepare Z-FR-AMC solutions that were 10x the final concentrations in the well (Table 7.4). The reaction mixture containing assay buffer, enzyme solution, and 35% DMSO was preincubated at 25 °C for 5 minutes after which the reaction was initiated by the addition of Z-FR-AMC to each well. The production of AMC was monitored for 5 minutes at 25 °C using excitation and emission references of 355 and 460 nm respectively. Readings were taken every 15 seconds for five minutes. Reactions were carried out in triplicate. The final concentrations of the kinetic assay are: 100 mM NaOAc pH 5.5, 1 mM EDTA, 2.5 mM DTT, 0.01% Brij 35, 0.1 nM cruzain and 2% DMSO. Final concentrations of Z-FR-AMC varied between 0.2 and 15 μ M.

Preliminary Inhibition Studies

A subset of compounds from a library of thiosemicarbazone analogs (synthesized by members of the laboratory of Dr. Kevin G. Pinney) was assayed to determine inhibitory activity against cruzain. The total volume of the reaction was 200 μ l, with each well containing 100 μ l of assay buffer, 10 μ l of 35% DMSO (control) or 10 μ l of a 200 μ M dilution of compound (to give a final concentration of 10 μ M in the well), 70 μ l

cruzain solution, and 20 µl of 150 µM Z-FR-AMC solution. The enzyme-inhibitor mixtures (180 µl of assay buffer, 35% DMSO (control) or inhibitor, and cruzain solution) was preincubated at 25 °C for a duration of 5 minutes in 96-well black microplates, after which reactions were initiated by addition of 20 µl of Z-FR-AMC. The release of AMC product from the substrate in the inhibited and uninhibited reactions was monitored for five minutes. The final concentrations of the preliminary inhibitory reactions were: 100 mM NaOAc pH 5.5, 1 mM EDTA, 2.5 mM DTT, 0.01% Brij 35, 0.1 nM cruzain, 10 µM of the screened inhibitor and 15 µM of Z-FR-AMC. Readings were taken every 15 seconds for five minutes and reactions were carried out in triplicate. Compounds that did not have cruzain inhibitory activity more than 50% (i.e. $v_i/v_o \leq 0.5$) compared to the uninhibited control reactions were considered 'inactive' compounds and a general IC₅₀ value greater than 10000 nM was assumed. Compounds that inhibited cruzain inhibitory activity more than 50% were further assayed and an exact IC₅₀ value was determined.

Table 7.4. Dilution table for varying substrate concentrations (in 2.5% DMSO and water)

Final Concentration (µM)	Concentration prepared (µM)	Volume of previous Substrate (µl)	Water (µl)	DMSO (µl)
	6000 (stock)			
15	150	25	975	
10	100	666.7	325	8.3
7.5	75	750	243.75	6.25
5	50	666.7	325	8.3
2.5	25	500	487.5	12.5
1	10	400	585	15
0.5	5	500	487.5	12.5
0.25	2.5	500	487.5	12.5

Cruzain Inhibition Assay (IC₅₀ Determination)

Thiosemicarbazone analogues were analyzed for their inhibitory activity against cruzain using a modified protocol of the preliminary inhibition assays described above. In this case however, eight different inhibitor dilutions (with final concentrations in the wells of ranging from 10 μ M and 10 pM) were used. Total volume of the reaction was 200 μ l, with each well containing 100 μ l of assay buffer, 10 μ l of 35% DMSO or 10 μ l of inhibitor dilutions, 70 μ l cruzain stock solutions, and 20 μ l of Z-FR-AMC stock solution. A 180 μ l reaction mixture containing assay buffer, 35% DMSO or inhibitor, and cruzain was pre-incubated at 25 °C for 5 minutes in 96-well black microplates, after which reactions were initiated by addition of 20 μ l of Z-FR-AMC. The release of AMC product from the substrate in the inhibited and uninhibited reactions was monitored for five minutes. The final concentrations of the preliminary inhibitory reactions were: 100 mM NaOAc pH 5.5, 1 mM EDTA, 2.5 mM DTT, 0.01% Brij 35, 0.1 nM cruzain, 10 μ M of the screened inhibitor and 15 μ M of Z-FR-AMC. Readings were taken every 15 seconds for five minutes and reactions were carried out in triplicate.

Construction of AMC Calibration Curve

In order to validate the fluorimeter at the excitation and emission wavelengths used (355 and 460 nm respectively) as well for enzyme activity standardization purposes, an aminomethylcoumarin (AMC) standard curve was created monitoring the fluorescence of varying concentrations of AMC. Dilutions were made to include at eight different concentrations of AMC ranging from 15-0.2 μ M in 2% DMSO in a manner similar to that described in table 7.4.

Effect of Inhibitor Concentration on Cruzain Progress Curves

Final concentrations, conditions, and volumes were similar to the cruzain inhibition assay. Assay buffer, inhibitors (final concentrations varied between 1 nM and 10 μ M) and Z-FR-AMC (final concentration: 15 μ M) were added to the 96-well black plates (volume of the substrate-inhibitor mixture: 130 μ l). Then 70 μ l of cruzain solution was added immediately without any pre-incubation of enzyme and inhibitor. Readings were taken every 30 seconds for sixty minutes.

Effect of Substrate Concentration in Cruzain Progress Curves

This assay was also similar to the cruzain inhibition assay. Assay buffer, inhibitor (final 1 μ M) and Z-FR-AMC (with varying concentrations ranging from 1-15 μ M) were added to the 96-well black plates (volume of the substrate-inhibitor mixture: 130 μ l). Then 70 μ l of cruzain solution were added immediately without any pre-incubation time. Readings were taken every 30 seconds for sixty minutes.

Effect on Pre-incubation on Cruzain Inhibition

Pre-incubation studies with some of the compounds were carried via an assay similar to the cruzain inhibition assay described earlier. In this assay, solutions containing assay buffer, inhibitor and cruzain were pre-incubated for varying time periods ranging from 0 and 120 min. Fluorescence readings were taken every 15 s for 5 min total and reactions were carried out in triplicate.

Determination of K_{iapp} Using Morrison's Quadratic Equation

Data obtained from preincubation assays were further analyzed as possibly being tight binding inhibitors of cruzain. This was done by fitting the data via a nonlinear regression using Morrison's quadratic equation so as to determine the apparent K_i of the inhibition.

Cruzain Reversibility Studies

A 4.8 ml of volume assay buffer for reversibility studies was prepared. 20 μ l of cruzain solution for reversibility was pre-incubated assay buffer for reversibility studies with an equal amount of a concentrated solution of the inhibitor (at a concentration of 20x the pre-determined IC_{50} value) at 25 °C between one and four hours. This results in a solution containing 10 nM cruzain (10x the normal assay amount), compound with 10x IC_{50} concentration, and 50% DMSO. 20 μ l of cruzain solution for reversibility was also incubated with an equal amount of a 50% DMSO solution to serve as the untreated control. Subsequently, 2 μ l of the enzyme-inhibitor mixture (or control solution) were rapidly mixed with 178 μ l of cruzain assay buffer for reversibility and 20 μ l of Z-FR-AMC to start the reaction. Total reaction volume was 200 μ l. Readings were taken every thirty seconds for four hours. Final concentrations are equivalent to those described previously. Final conditions were: 100 mM NaOAc, pH 5.5, 1 mM EDTA, 2.5 mM EDTA, 0.01% Brij 35, 0.1 nM cruzain and 15 μ M of Z-FR-AMC.

Molecular Modeling Studies

Computational studies were performed using Discovery Studio 2016 Client. First, a crystal structure was obtained from the PDB database. The molecule used for this

analysis was 1ME3 [425]. Previous experiments conducted with this molecule by previous members of Trawick group were used to verify the accuracy of the results [298, 452].

Preparation of the Protein

The selected crystal structure is related to the analysis of recombinant cruzain bound to a synthetic ketone inhibitor. Therefore, the protein needed to be prepared and validated using a high affinity substrate as reported [425]. Water molecules and other ligands (synthetic ketones) were removed. The structure was re-examined to correct possible structural disorders, protein residue connectivity, bond-orders, and missing side-chain or backbone atoms. The pH of the system was also changed in order to modify the protonation state of the enzyme termini and side chain residues. The pH value used for this analysis was 6.8. Finally, the binding site was defined according to default specifications from PDB records.

Preparation of the Ligand (Thiosemicarbazones)

Compound **28** was selected to be modeled with cruzain in order to verify mode of inhibition and observe major interactions. Compound **1** was used as a comparison because it was previously modeled with cruzain [298]. Each molecule was drawn in ChemDraw 6.0 and copied into Discovery Studio 2016. Each molecule was prepared as ‘ligands’. For each ligand, changes in ionization states, and canonical tautomers were allowed to be carried out. At the end of the run, a list of tautomers was generated for each compound.

Docking Simulations

CDOCKER, a dock ligand protocol was used to docking the selected ligands into the macromolecule. The algorithm allows the simulation of several ligands with a single receptor protein simultaneously. The input receptor was the cruzain molecule (1ME3) and the ligands were the entire list of tautomers for each compound. The total number of top hits was set up to 200. The site sphere coordinates were set as: 5.1024, 9.25127, 6.43005, 8.4. These coordinates were set according to the PDB files default conditions and they established the permitted area where both ligand and receptor (thiosemicarbazones and cruzain respectively) could interact. The number of ‘orientations to refine’ was set to 20. Similarly, the ‘maximum bad orientation’ and ‘orientation vdW Energy Threshold numbers were 800 and 800 respectively. The selected force field was CHARMM and the ligand partial charge method was changed to MMFF. CHARMM was used due to its extensive use when modeling organic molecules with proven accuracy and works quite well with a variety of solvents used in in vitro studies in several receptor-ligand studies where ligands are synthetic molecules. Similarly, MMFF is type of force field derived from experimental calculations. MMFF is extensively used in pharmaceutical industries for studies involving changes in conformation energies and nonbonded interactions. MMFF also gives accurate results for a wide range of organic molecules but fails when parallel processing is required. Docking simulations took several minutes to be performed. For each compound, the number of conformations varied from a couple of dozen to hundreds to possible conformations. These conformations were arranged based on the interaction energies to localize the conformations with highest interaction energies for the compounds analyzed.

A visible conformation was selected in order to observe interactions between cruzain and its inhibitors. Finally, a selection filtering residues having interactions with every ligand was set. Distances for selected atoms were selected and calculated. Also, hydrogen bonds in that region were chosen and selected. Discovery Studio 2016 Client set hydrogen bonds less than 2.5 Å, but this distance was also modified depending on each case.

Results and Discussion

Previous studies into the potency of compounds with a thiosemicarbazone moiety as inhibitors of cruzain have elicited promising results [445, 447]. Therefore, a subset of compounds from a library of thiosemicarbazone inhibitors was biochemically evaluated for potency of inhibition against cruzain. This study was performed as part of a larger collaborative project between the Kevin G. Pinney and Mary Lynn Trawick laboratories at Baylor University. Synthetic non-peptidic thiosemicarbazones were provided by members of the laboratory of Dr. Kevin G. Pinney at Baylor University. Investigation of the inhibitory activity of these compounds against cruzain included evaluation of inhibitory potency (IC₅₀) values, elucidation of modes of inhibition using advanced kinetic studies, and elucidation of binding interactions between compounds and the protein via molecular modelling.

In order to study the various factors concerning the inhibitory activity of these compounds against cruzain, enzyme-inhibitor-substrate mixtures were assayed fluorometrically. Cruzain studies were carried out using a 96-well microplate fluorometric based assay (Figure 7.1). Z-FR-AMC is a validated fluorogenic substrate that for serine and cysteine proteases. Substrate concentration was set to 15 µM so as to

avoid substrate inhibition that may occur at excessive substrate concentrations. Final conditions for the cruzain fluorometric assay are: 100 mM NaOAc pH 5.5, 1 mM EDTA, 2.5 mM DTT, 0.01% Brij 35, 2% DMSO, 0.1 nM cruzain, and 0.5 – 15 μ M Z-FRM-AMC.

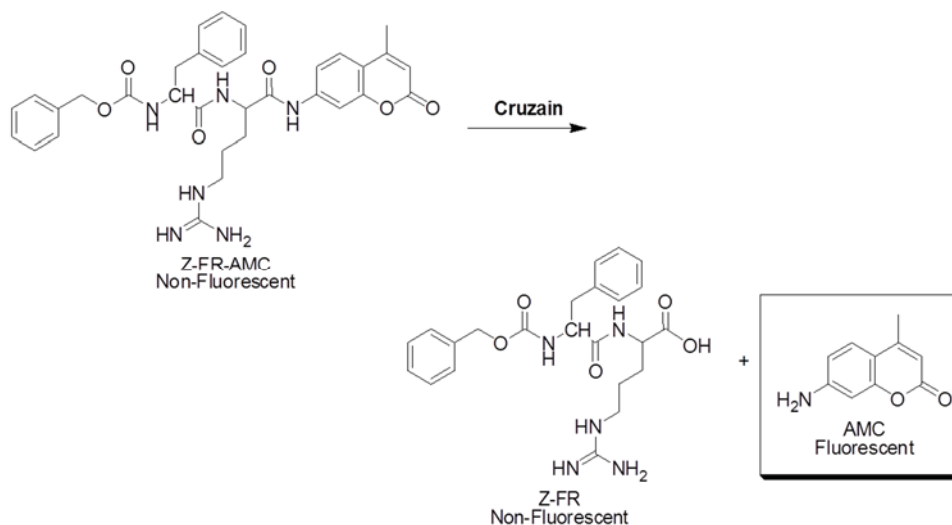


Figure 7.1. Fluorometric enzyme assay reaction. Z-FR-AMC is hydrolyzed by cruzain resulting in a fluorescent product (AMC)

Construction of AMC Calibrations Curves

Fluorometric based assays were used to study the potency, mechanism, and mode of inhibition of thiosemicarbazones as cruzain inhibitors. This assay relies on the ability of cruzain to cleave AMC, a fluorophore, from Z-FR-AMC, a less fluorescent synthetic substrate that is extensively used in research involving cysteine proteases (Figure 7.1).

The construction of AMC standard curves was necessary in order to convert the relative fluorescence units (RFU) into the concentration of the fluorophore. The curve allowed the validation of enzymatic activities, kinetic and inhibition assays. Also, kinetic parameters, velocities and rates could be compared to standard concentration units that

can be found in the literature. The standard curves were constructed, using GraphPad Prism™ software, by plotting varying concentrations of AMC over time (Figure 7.2). Linear regressions of these values were performed and the y-intercept values corresponding to each AMC solution were obtained. These y-intercept relative fluorescence values were plotted over the AMC concentrations and a second linear regression performed (Figure 7.3). Results of the second linear regression give an equation that can correlate RFU and AMC concentration. The equation is $\text{RFU} = 146 \text{ AMC (in } \mu\text{M}) + 38$ and the linear coefficient (r^2) calculated to give a value of 0.9985.

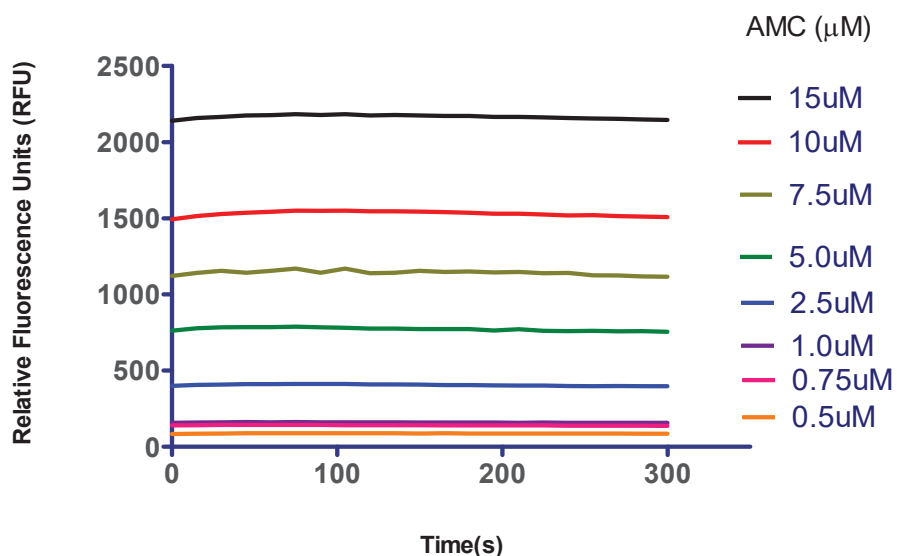


Figure 7.2. Fluorescence values of AMC plotted over time

Determination of Kinetic parameters (K_M , V_{max} , and k_{cat})

Kinetic parameters of the recombinant cruzain with the fluorogenic synthetic peptide substrate (Z-FR-AMC), were based on the steady state assumption, and indicate that cruzain velocity as a function of substrate concentration is consistent with the Michaelis-Menten equation (Eq. 5.1).

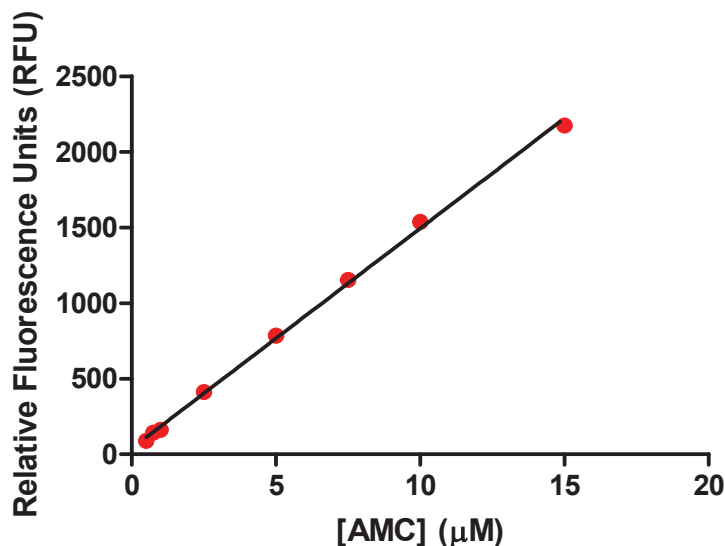


Figure 7.3. AMC Calibration Curve

K_M , V_{max} and k_{cat} for this enzymatic reaction were determined using experiments that observed the catalytic activity of a fixed concentration of cruzain (0.1 nM) with varying concentrations of Z-FR-AMC (0.2 -15 μ M). Experiments were carried out in triplicate. Catalytic rates were calculated by applying linear regression to a plot of relative fluorescence obtained from the varying substrate concentrations over time. The slopes obtained from these linear regressions are the reaction rates/velocities. Subsequently, these rates were plotted against Z-FR-AMC concentration and a nonlinear regression analysis using the Michaelis-Menten equation (Eq. 5.1) was performed to calculate K_M and V_{max} values. These plots, regressions and calculations were done using GraphPad Prism 5.0 software. The k_{cat} constant value was determined using equation 5.2. The parameter v_0 is the initial rate velocity at a specific substrate concentration. The V_{max} is the maximum velocity, K_M is the Michaelis-Menten constant, $[S]$ is the substrate

concentration, and k_{cat} is the catalytic rate constant. The K_M value was found to be $2.37 \pm 0.04 \mu\text{M}$, similar to previously reported literature values [457]. The V_{max} was determined to be $2.13 \pm 0.15 \text{ nM/s AMC}$. The k_{cat} value was calculated to be 21.3 s^{-1} . The R^2 of the fit was 0.96.

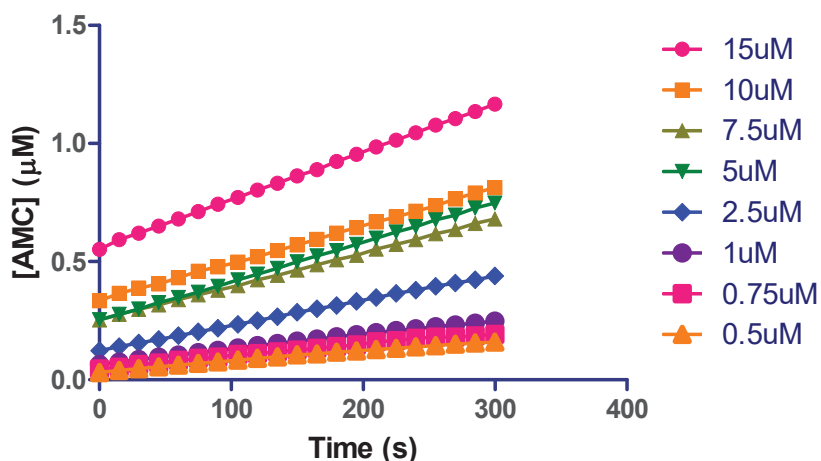


Figure 7.4. Catalytic activity of cruzain over time with varying substrate concentrations

$$v_o = \frac{V_{MAX}[S]}{K_M + [S]} \quad (\text{Eq. 5.1}) \quad k_{CAT} = \frac{V_{MAX}}{[E]} \quad \text{Eq. (5.2)}$$

Preliminary Inhibition Assays of Thiosemicarbazones with Cruzain

The first set of inhibitory experiments was performed to screen for compounds in the library of thiosemicarbazones that could be potential cruzain inhibitors. Compounds that caused inhibition of the catalytic activity of cruzain 50% (compared to untreated control) were selected for further analysis of inhibitory activity.

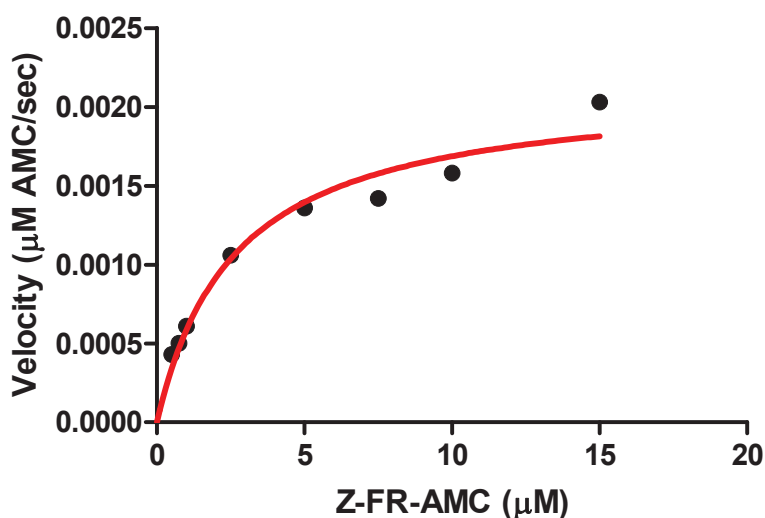


Figure 7.5. Dependence of cruzain activity on substrate concentration. The curve was fit to the Michaelis-Menten equation via non-linear regression using the GraphPad Prism 5.0 software.

Three independent sets of experiments of untreated ([I]: 0 μM) and treated samples ([I]: 10 μM) were preincubated with 0.1 nM cruzain for 5 minutes at 25 $^{\circ}\text{C}$. Inhibitory activities were monitored when reactions were started by adding 15 μM Z-FR-AMC as a fluorogenic substrate. Reactions demonstrated a linear behavior for at least the first five minutes. Active compounds were further analyzed to determine an exact IC_{50} value. If the rate of the reaction of the inhibited reaction was greater than 50% (i.e. inhibition less than 50%), then the compounds were not considered potential inhibitors and an approximated IC_{50} value > 10000 nM was assigned to them.

Cruzain Inhibition Assay (IC_{50} Determination)

A subset of compounds from the library of thiosemicarbazone inhibitors was assayed to ascertain their potency as inhibitors of the catalytic activity of cruzain. A 96-well microplate fluorometric assay was utilized to determine the inhibitory activity of each of these inhibitors. Uninhibited cruzain catalytic activity showed linear behavior

when 15 μM Z-FR-AMC was used for reactions times that were 5 minutes long. The determination of the IC_{50} values was carried out with experiments that observe the inhibitory capacity of the synthetic compounds when a fixed concentration of cruzain (0.1 nM) was preincubated for 5 minutes at 25 $^{\circ}\text{C}$. The final concentration of each compound varied between 10 pM and 10 μM . Experiments for each tested inhibitor were done in triplicate. Catalytic rates of uninhibited and inhibited samples were calculated by linear regression of the data ([AMC]: dependent variable and time (seconds): the independent variable). The slopes from this linear regression (representing the reaction rates for each compound concentration-enzyme mixture) were then plotted over the compound concentrations. The data was consistent with a sigmoidal dose response relationship, thus a nonlinear regression using equation 5.8 was performed to calculate IC_{50} values. The value Y represents the inhibited activity (normalized relative to control), and the X is $\log([\text{inhibitor}])$ in μM . The velocities v_{min} and v_{max} represent when cruzain was preincubated with the highest and lowest inhibitor concentrations respectively (10 μM and 0 pM or control). The Hill slope value is the slope of the sigmoidal curve. $\text{IC}_{50} \pm \text{S.E.}$ values represent the average and standard errors of at least three independent experiments. The data from these experiments is presented in Tables 7.6-7.10.

Table 7.6. IC₅₀ values of benzophenone thiosemicarbazone compounds against cruzain

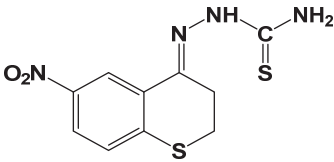
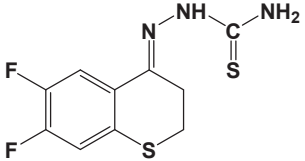
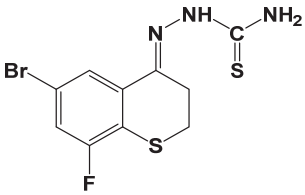
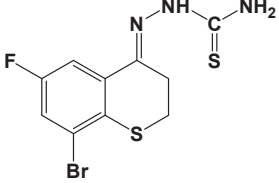
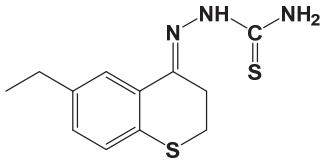
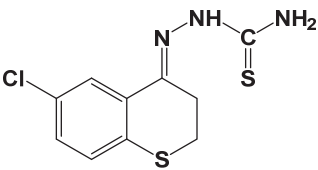
Compound	Structure	IC ₅₀ ± S.E. (nM)
1 ₁		11.17±2.9
2 ₂		30.3±3.3
3 ₃		> 10000
4		70.37±6.4
5		> 10000
6		> 10000
13		> 10000

¹ Synthesis Reference- R. Siles et al. Bioorg. Med. Chem. Lett., 16 (2006) 4405-4409

² Synthesis Reference- G.D.K. Kumar et al. Bioorg. Med. Chem. Lett., 20 (2010) 6610-6615.

³ Synthesis Reference- G.D.K. Kumar et al. Bioorg. Med. Chem. Lett., 20 (2010) 1415-1419.

Table 7.7. IC₅₀ values of thiochromanone thiosemicarbazone compounds against cruzain

Compound	Structure	IC ₅₀ ± S.E. (nM)
14 ⁴		47.93±5.9
15 ⁴		158.1±23
16 ⁴		40.74±2.3
17 ⁴		91.77±26
18 ⁴		87.03±19.38
19 ⁴		14.08±3.3

⁴ Synthesis Reference- J. Song et al. ACS Med Chem Lett, 3 (2012) 450-453.

Table 7.7 (continued). IC₅₀ values of thiochromanone thiosemicarbazone compounds against cruzain

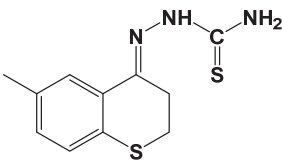
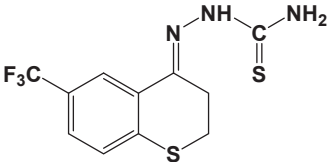
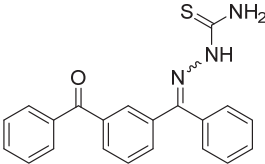
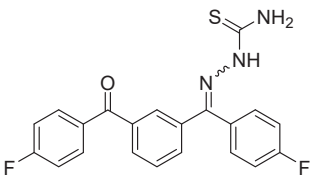
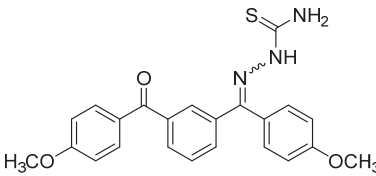
Compound	Structure	IC ₅₀ ± S.E. (nM)
20 ⁴		627.6±116
21 ⁴		39.58±3.58

Table 7.8. IC₅₀ values of benzoyl benzophenone thiosemicarbazone compounds against cruzain

Compound	Structure	IC ₅₀ ± S.E. (nM)
22 ⁵		70.24±12.9
23 ⁵		45.9±4.1
24 ⁵		≈10000

⁵ E.N. Parker, et al., Bioorg Med Chem, 23 (2015) 6974-6992.

Table 7.8 (continued). IC₅₀ values of benzoyl benzophenone thiosemicarbazone compounds against cruzain

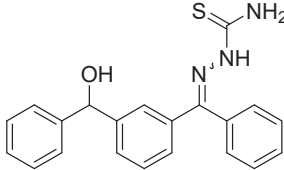
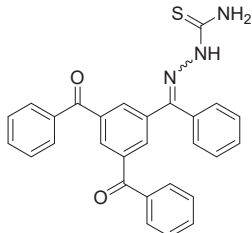
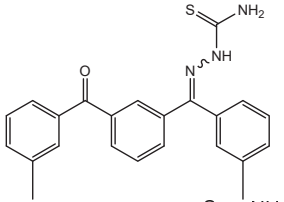
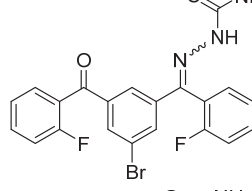
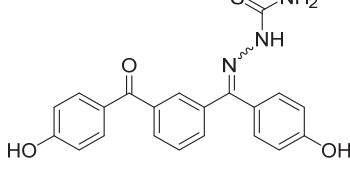
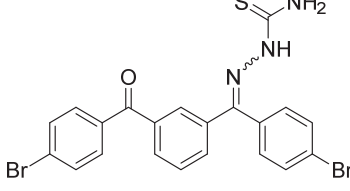
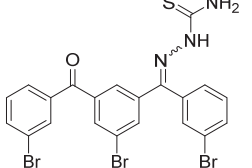
Compound	Structure	IC ₅₀ ± S.E. (nM)
25 ⁵		1248±157
26 ⁵		36.22±9.1
27 ⁵		217±45
28 ⁵		12.86±3.75
29 ⁵		117±8.5
30 ⁵		334±29
33 ⁵		≈ 10000

Table 7.9. IC₅₀ values of benzophenone (with alkyl linkers) thiosemicarbazone compounds against cruzain

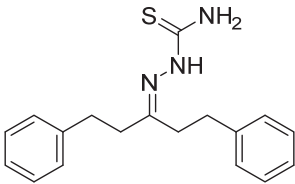
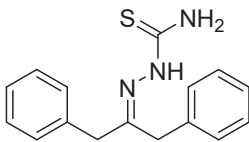
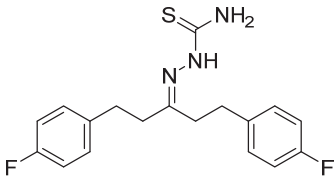
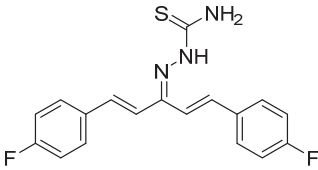
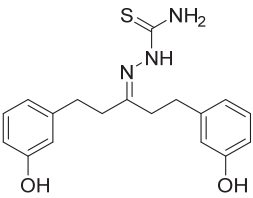
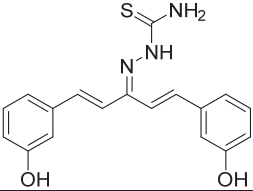
Compound	Structure	IC ₅₀ ± S.E. (nM)
34		> 10000
35		> 10000
36		> 10000
37		> 10000
38		≈ 10000
39		≈ 10000

Table 7.9 (continued). IC₅₀ values of benzophenone (with alkyl linkers) thiosemicarbazone compounds against cruzain

Compound	Structure	IC ₅₀ ± S.E. (nM)
40		> 10000
42		> 10000
44		> 10000
45		> 10000

A significant number of the compounds assayed proved to be potent inhibitors of cruzain (IC₅₀ < 100 nM) (Figure 7.6), with some others showing moderate activity (100 nM < IC₅₀ < 10 μM). In addition, the compounds that showed inhibitory activity against cruzain represented all four of the structural scaffolds (Figure 5.33) around the thiosemicarbazone moiety.

Advanced Kinetic Studies

A number of the compounds demonstrating inhibitory activity against cruzain (and representing the four different scaffolds) were further assayed using various kinetic

methods in order to determine time dependence of inhibition, elucidate the mechanism by which this class of compounds inhibit cruzain, as well as determine the reversibility of inhibition of this class of compounds.

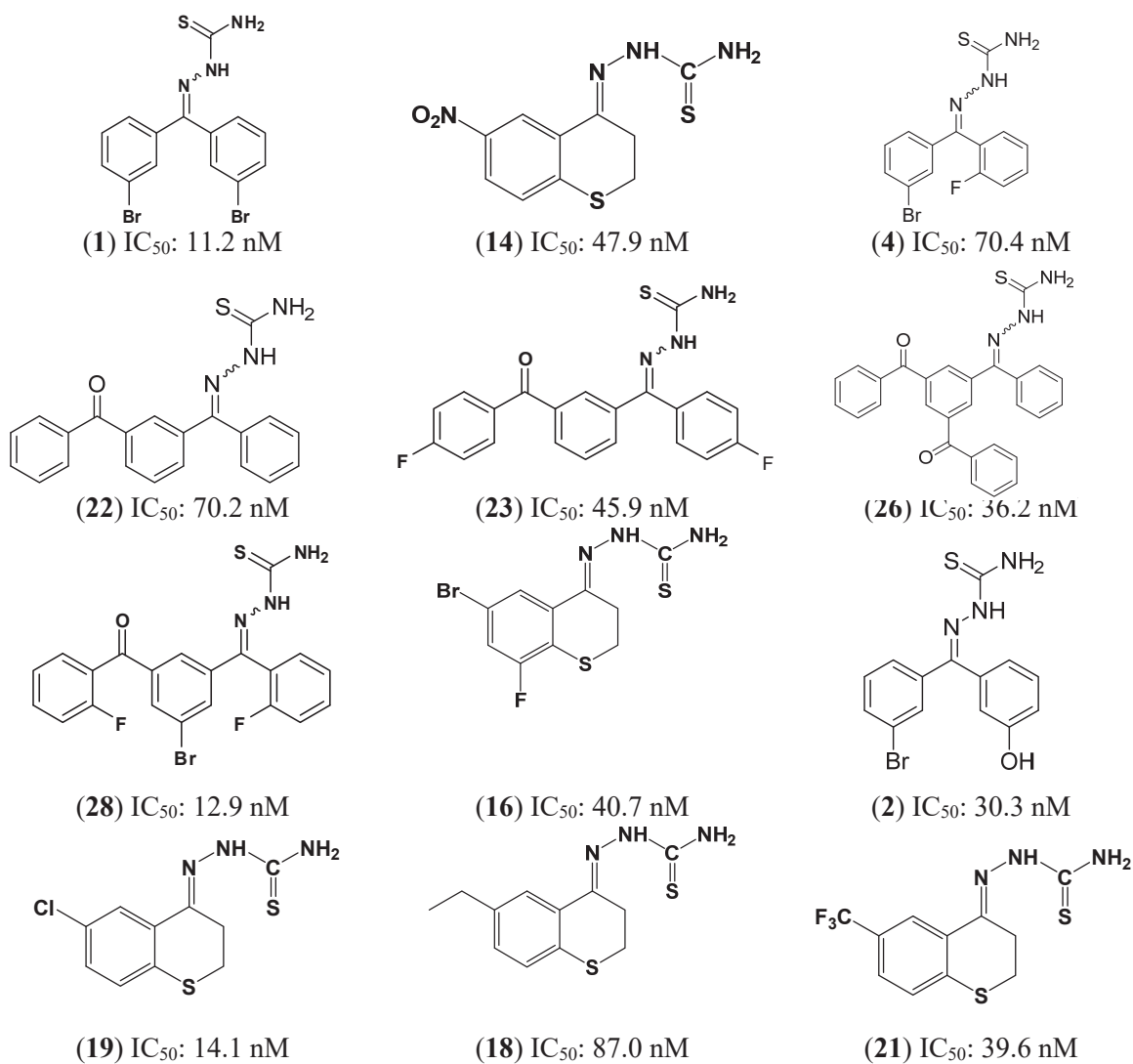


Figure 7.6. Potent thiosemicarbazone inhibitors of cruzain

Effects of Thiosemicarbazone Inhibitors on Cruzain Progress Curves

To assess the time dependence of the inhibition, the reaction rates were monitored as a function of time. For this experiment, the enzyme was treated with various concentrations of inhibitor in the presence 15 μM substrate Z-FR-AMC. Reactions were initiated by the addition of the enzyme to the inhibitor substrate mixture without preincubation and fluorescence measurements were taken every 15 seconds up to 3000 seconds. The components were added in the sequence noted in order to observe the initial interactions of the enzyme with the inhibitor. For time dependent curves, a change in slope over time should be observed where the inhibition increases as the reaction progresses. This is due to the initial velocity of enzyme catalyzed substrate cleavage followed by a change to a steady state velocity. Analysis of progress curves of the activity of cruzain inhibited with compound **23** shows that this compound inhibits cruzain in a time dependent manner (Figure 7.7), suggesting slow binding inhibition of cruzain.

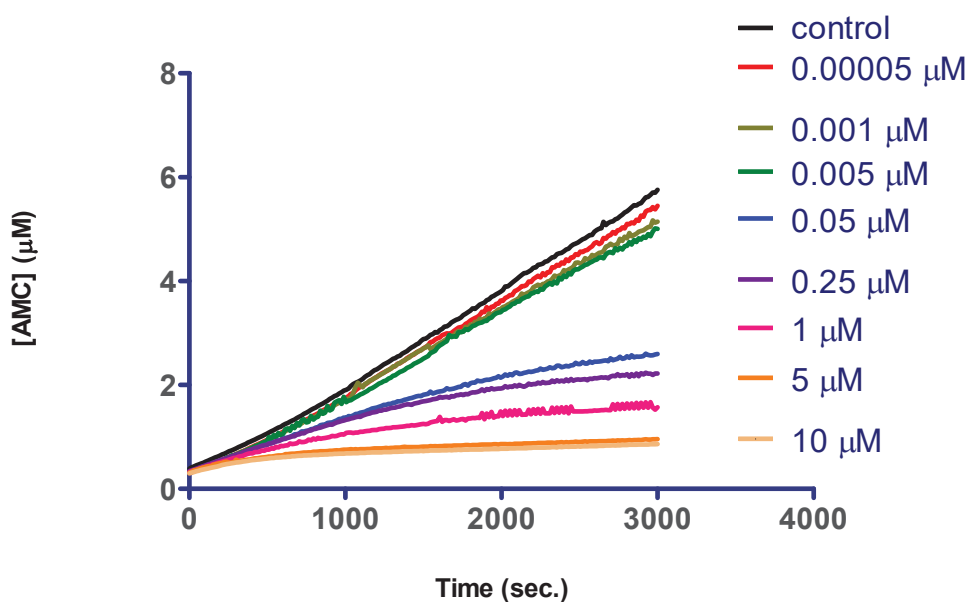


Figure 7.7. Cruzain progress curves with varying concentrations of compound **23**

As mentioned in Chapter five, further examination of the exact mechanism of slow binding inhibition was performed by fitting the data to equation 5.13, by nonlinear regression analysis using GraphPad Prism 5.0 software. P is the concentration of product (μM), v_o and v_s are the initial and steady-state velocities ($\mu\text{M/s}$), t is the time in seconds and k_{obs} the rate constant for conversion of the initial velocity v_o to the steady state velocity v_s . The rate constant (k_{obs}) units are given in s^{-1} . In equation 5.13, P and t are the dependent and independent variables, while the velocities and the rate constant are unknowns. For each case, the constraints for their calculation were to give positive values (i.e. $k_{obs} \geq 0$). It is also worth noting the equation is only valid when substrate depletion is insignificant [336, 337]. Various kinetic parameters obtained from this analysis are presented in Table 7.10.

$$P = v_s t \frac{(v_o - v_s)}{k_{obs}} (1 - e^{-k_{obs}t}) \quad (\text{Equation 5.12})$$

Table 7.10. Calculated Kinetic Parameters for Cruzain Progress Curves with compound **23**

[I] (μM)	10	5	2.5	1	0.05
v_s ($\mu\text{M/s}$)	0.0001085	0.0001307	0.0002868	0.0003478	0.0004961
v_o ($\mu\text{M/s}$)	0.005748	0.006306	0.003130	0.002461	0.002286
k_{obs} (s^{-1})	0.01019	0.01044	0.003514	0.001691	0.001512

When k_{obs} is plotted over inhibitor concentration (Figure 7.8), a hyperbolic curve is observed. This suggests that the mechanism of slow binding inhibition is one that involves an initial simple slowly reversible binding step followed by the cruzain-inhibitor complex undergoing isomerization or covalent modification, to form a more stable enzyme-inhibitor complex.

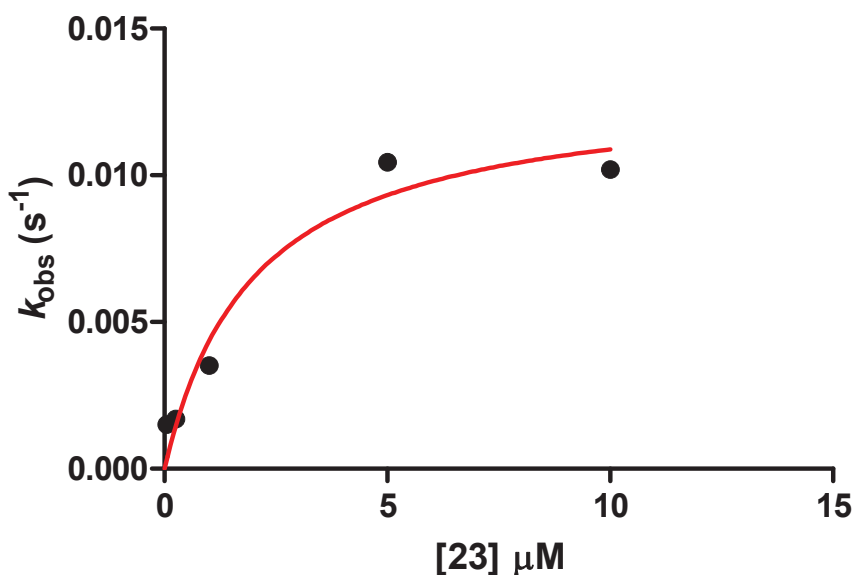


Figure 7.8. Graphical representation of relationship between k_{obs} and **23**.

Effect of Substrate Concentration on Thiosemicarbazone Inhibition of Cruzain Activity

A useful assay to determine mode of slow binding inhibition of an enzyme is to generate progress curves with different concentrations of substrate while keeping the inhibitor concentration constant. For this experiment, progress curves were generated by addition of 1 μM of compound **19** to cruzain and initiating the reaction with Z-FR-AMC concentrations ranging from 1-15 μM . Analysis of these progress curves (Figure 7.9) indicated time dependence of inhibition (as seen from reduction in slopes over time).

As discussed in Chapter five, the mode of inhibition for a slow binding inhibitor can be determined by observing the effects of substrate concentration on the value of k_{obs} at a fixed inhibitor concentration [337, 458, 459]. For a competitive inhibitor the value of k_{obs} will diminish hyperbolically with increasing substrate concentration as seen from Figure 5.27 and equation 5.14. In order to confirm this, the data from this experiment was

fit into Equation 5.12 in order to calculate the k_{obs} values for each substrate concentration (Table 7.11). Plotting the calculated k_{obs} values against substrate concentrations results in an inverse hyperbolic curve (Figure 7.10). This indicates the occurrence of competitive inhibition

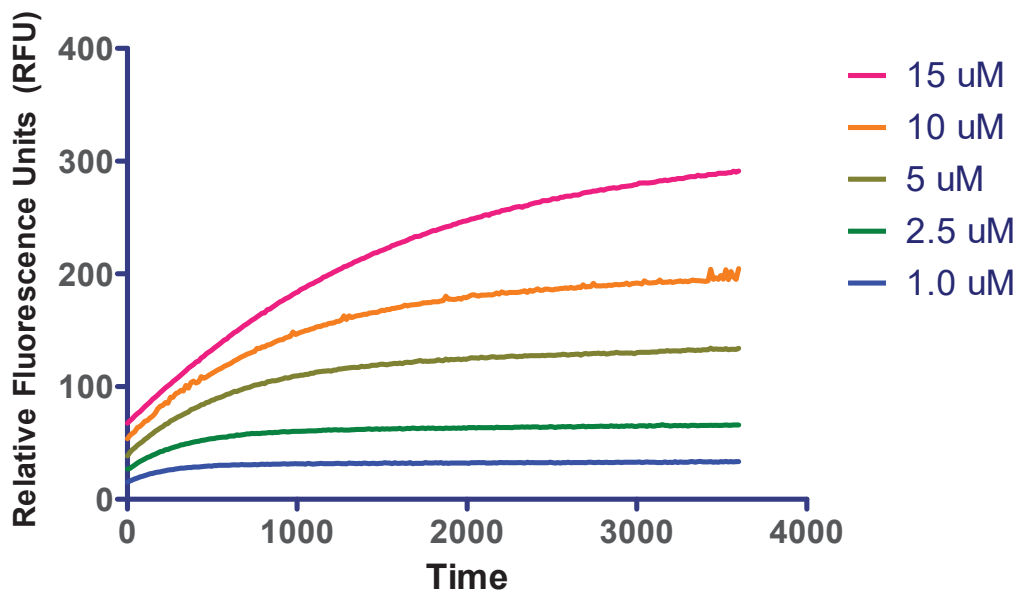


Figure 7.9. Cruzain progress curves with varying substrate concentration and 1 μ M of compound **19**

Table 7.11. Kinetic parameters for Cruzain substrate progress curves with compound **19**

[S] (μ M)	15	10	5	2.5	1
v_s (μ M/s)	0.0002251	0.00011	5.599e-005	1.851e-005	6.991e-006
v_o (μ M/s)	0.002841	0.002852	0.002534	0.002659	0.002226
k_{obs} (s^{-1})	0.002778	0.003489	0.004188	0.008157	0.01299

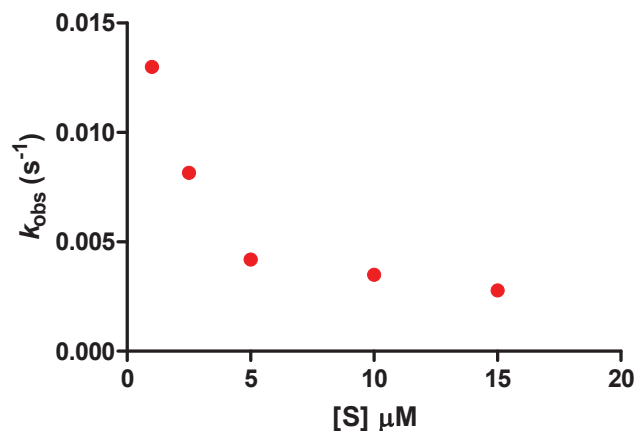


Figure 7.10. Graphical representation of relationship between k_{obs} and substrate concentration when cruzain is inhibited with compound **19**

Effects of Pre-incubation Time on IC₅₀ Values

Progress curves provided strong evidence for the occurrence of time dependent/slow-binding inhibition. Therefore, the effect of pre-incubation time on the inhibitory potency of thiosemicarbazones on their IC₅₀ values was examined. The IC₅₀ values of a number of thiosemicarbazone compounds were determined at different pre-incubation times ranging between 0 and 120 minutes. Final inhibitor concentration ranged 0 and 10 μM. The data from these experiments is presented in Table 7.12

Table 7.12. Effect of Pre-incubation Time on IC₅₀ Values with various compounds (ND - not determined)

Compounds	IC ₅₀ Values (nM)				
	0 min	5 min	30 min	60 min	120 min
2	> 10000	30.3±3.3	6.8±1.1	4.4±0.4	ND
23	9072±2004	45.9±4.1	10.6±0.7	4.3±1.1	ND
22	> 10000	70.2±12.9	9.2±4.2	0.1±0.03	ND
28	≈ 5000	12.9±3.7	2.5±1.3	1.8±0.8	ND
25	> 10000	1248±156.9	110±14.5	49.9±4.2	5.3±0.8
18	> 10000	87.0±19.4	10.8±1.0	7.6±0.9	ND
26	> 10000	36.2±9.1	4.9±1.0	0.62±0.01	ND

As presented in Table 7.12, the effect of pre-incubation on the effectiveness of cruzain inhibition of these compounds is significant. For instance, the unsubstituted benzoyl benzophenone compound (compound **25**) showed minimal inhibitory activity with no pre-incubation with the cruzain. However, there was a significant increase in inhibition when the pre-incubation time was increased to 5 minutes, showing a greater than 100-fold increase in inhibitory potency with an IC_{50} value of 70.2 nM. There was further significant increase in potency with longer pre-incubation times, culminating in an IC_{50} less than 10 nM when cruzain was pre-incubated with the compound for 2 hours (Figure 7.11). Analysis of other thiosemicarbazone compounds showed similar trends. These results confirmed the strong dependence of IC_{50} value determination with respect to the pre-incubation time parameter. Uninhibited controls were monitored for every time period so as to ensure that no significant loss of catalytic activity at longer pre-incubation times occurred.

It should be noted that inhibitory assays typically differ in this specific parameter when inhibitory assays are reported in the literature, making comparison of IC_{50} values a somewhat difficult proposition. It is thus expedient to standardize this parameter to get an accurate measure of how various inhibitors, especially time-dependent ones, compare to others in inhibitory potency.

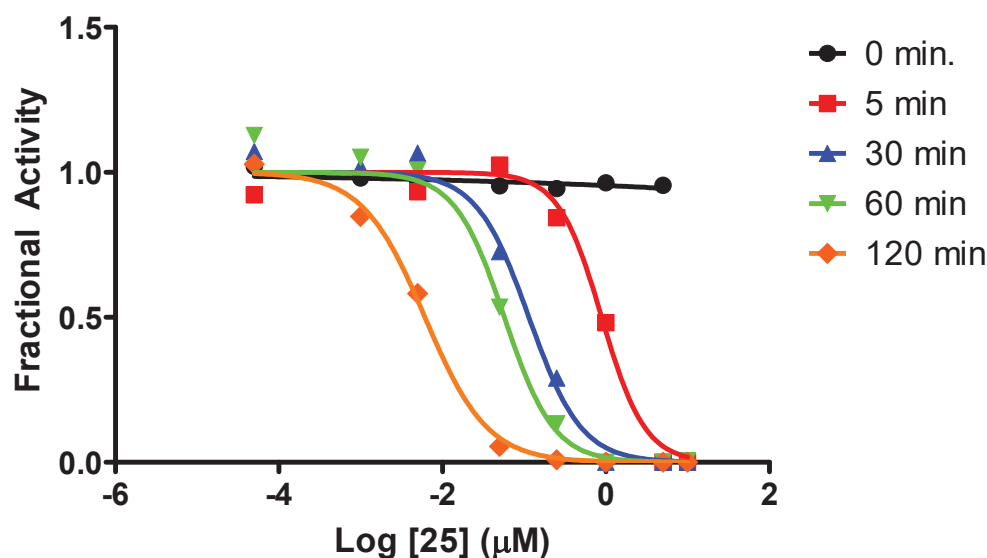


Figure 7.11. Effect of increasing pre-incubation times on IC_{50} of compound **25** against cruzain

Analysis of Tight Binding Inhibition: Determination of K_I using the Morrison Equation

In order to ascertain whether these compounds were tight binding inhibitors of cruzain, the Williams Morrison equation (equation 5.17) was used to determine the apparent binding constant for the inhibitor to the enzyme, the K_I^{app} , after specified pre-incubation times. A number of compounds with high inhibitory potency against cruzain were further analyzed using this equation in order to elucidate the extent of their binding affinity to cruzain. The data obtained from the IC_{50} determination studies (5-minute pre-incubation time) were input into this equation in order to determine the K_I^{app} values.

$$\frac{v_i}{v_o} = 1 - \frac{([E]_T + [I]_T + (K_I(1 + \left(\frac{[S]}{K_M}\right))) - \sqrt{([E]_T + [I]_T + (K_I(1 + \left(\frac{[S]}{K_M}\right)))^2 - 4[E]_T[I]_T}}{2[E]_T} \quad \text{(Equation 5.17)}$$

The rates v_i and v_o are the inhibited and uninhibited cruzain velocities (RFU/s); $[E]_T$ (nM) is, the total concentration of enzyme found in solution (free enzyme and inhibitor-enzyme complex); $[I]_T$ (nM) is the total concentration of inhibitor present in solution (free inhibitor and inhibitor-enzyme complex); and K_I (nM) is the inhibition constant, often referred as the dissociation constant. GraphPad 5.0 was used to fit the data to the non-linear regression curve generated from the equation. The residual activity (or v_i/v_o) was normalized to 1 (i.e. v_o : 1 and $0 \leq v_i \leq 1$). Normalized residual activity and $[I]$ were defined as the dependent and independent variables respectively. Nonlinear regression was applied using the following conditions: $[S]$: 15 μ M, K_M : 2.37 μ M, $[E]_T$: 0.0001 μ M and v_o : 1.

As seen from the results presented in Table 7.13, the thiosemicarbazone compounds with high inhibitor potency also turned out to be tight-binding inhibitors of cruzain, with K_I values in the low nanomolar range. Furthermore, the graphical representation of the Morrison equation with these compounds results in a very robust fit, with R^2 values close to 1 (Figure 7.12 and 7.13).

Table 7.13. IC_{50} and K_I^{app} values of potent thiosemicarbazone inhibitors of cruzain (5 minute preincubation)

<i>Compound</i>	<i>IC₅₀ (nM)</i>	<i>K_I^{app} (nM)</i>
1	11.17	1.53
2	30.30	4.68
14	47.93	6.12
19	14.08	1.51
23	45.92	7.98
22	70.24	18.66
25	1248	100
26	36.20	7.30
27	217.0	47.60
28	12.86	1.06
29	117.0	21.6

This data suggests that these thiosemicarbazone compounds from the three different scaffolds being examined act as tight binding inhibitors of cruzain.

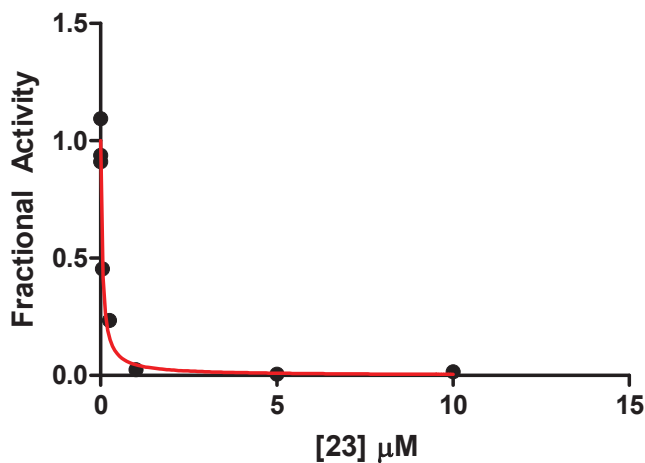


Figure 7.12. Graphical representation of Morrison Analysis of tight binding of **23** to cruzain

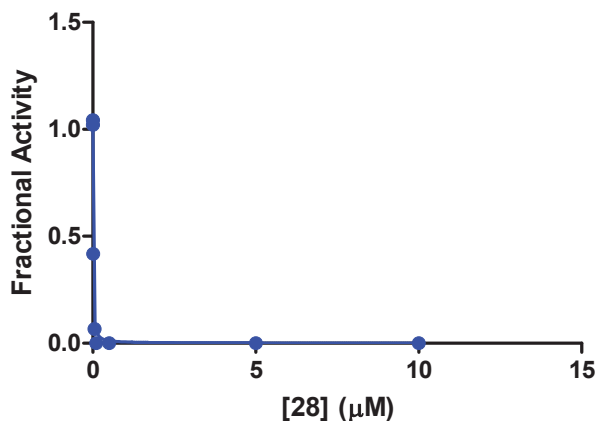


Figure 7.13. Graphical representation of Morrison Analysis of tight binding of **28** to cruzain

Cruzain Reversibility Studies

Thiosemicarbazone compounds were found to be competitive and time-dependent inhibitors of cruzain based on the progress curve assays and pre-incubation studies.

Therefore, the next step taken was the exploration of the reversibility of inhibition of these compounds. A mixture containing 10 nM cruzain and 1 μM compound **14** were

incubated at 25 °C for 4 h. The reaction was initiated by rapid dilution of the mixture (100-fold) with assay buffer containing Z-FR-AMC. Experiments were set up in order to monitor these reactions almost immediately initiation. The final reaction conditions were 0.1 nM cruzain, 10 nM of the thiosemicarbazone compound and 15 μ M of Z-FR-AMC substrate. A control experiment with cruzain incubated with DMSO vehicle control was carried out simultaneously. The release of AMC over the first 5000 seconds is observed, as presented in Figure 7.14. Recovery of catalytic activity of cruzain occurred after the rapid dilution with assay buffer containing Z-FR-AMC. The results showed cathepsin L was recovered up to 80% after 5000 seconds of reaction. Furthermore, a closer inspection of the early time-points in the reaction showed that cruzain recovered its activity within the first 300 seconds of the reaction up to about 60% (Figure 7.15).

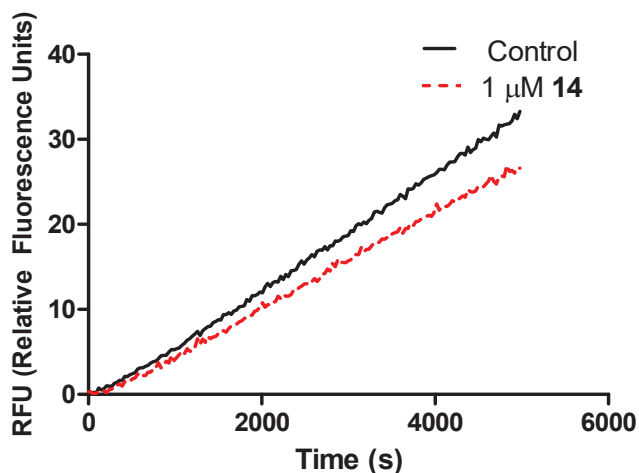


Figure 7.14. Reversibility curves for cruzain incubated with compound **14**

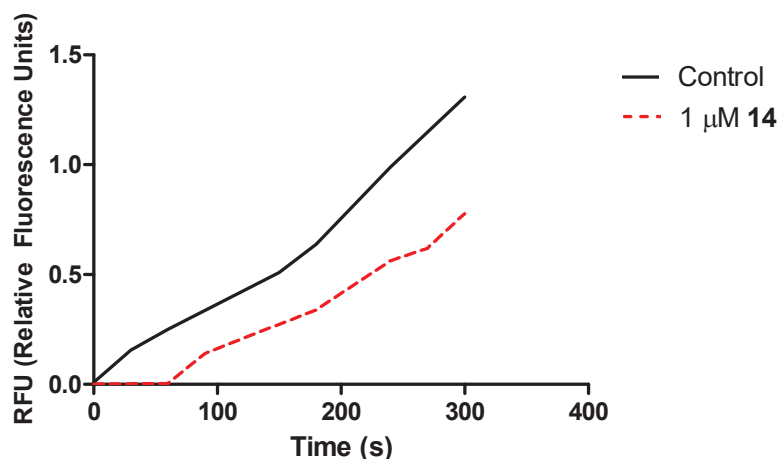


Figure 7.15. First 500 s of reversibility reaction showing rapid recovery of cruzain activity

Molecular Modeling

In order to further understand the interactions between the thiosemicarbazone compounds and cruzain towards optimization of drug candidates as therapeutic agents against *T. cruzi*, detailed information on how the inhibitor structures interact with cruzain is required. Molecular modeling is a very important tool in drug design and development. This technique has been used with the aid of computer technology to screen and develop potential drug-like molecules and to visualize the abstractive receptor-ligand complex in two- or three-dimensions.

The active site of cruzain is described using the X-ray structure 1ME3. As discussed in Chapter six, the cruzain active site consists of 8 subsites (S1, S2, S3, S4, S1', S2', S3', and S4'). Based on previous molecular modeling studies done by past members of the Trawick research group, it has been ascertained that thiosemicarbazone compounds that are potent inhibitors of cruzain typically interact with the enzyme at subsites S1, S2, and/or S3. The S3 subsite is composed of Thr-59, Asp-60, Ser-61, Ser-64, Gly-65, Gly-66, Leu-67, and Asn-70. Ala-133, Leu-157, Glu-205, and part of Leu-67 and Met-68

along with Gly-66, Asp-158, His-159, and Gly-160 form the deep hydrophobic S2 pocket. The S1 subsite is made up of Cys-25, Ala-30, part of Trp-26 and Ser-61, Asp-60, Thr-59, Asn-70, part of Leu-67 and Met-68, Gly-160, and Asp-158 compose the S1 pocket.

An evaluation of the library of thiosemicarbazones showed several compounds are outstanding inhibitors of cruzain with IC₅₀ values less than 100 nM. One of the potent benzoyl benzophenone thiosemicarbazone compounds (**28**) was docked with cruzain using 1ME3 as a reference structure. Also a compound with no inhibitory activity (**24**) was modeled for comparison purposes. The results from the kinetic assays along with molecular models suggested the formation of covalent bonds between the thiocarbonyl carbon of the TSC and Cys25 (papain numbering) thiolate group of cruzain (C–S[−]), the active residue in the catalytic triad. The proximity between these groups of less than 5 Å promotes the formation of a transient covalent bond.

Molecular Docking of 28 with Cruzain

Benzoyl benzophenone analog **28** was one of the more potent inhibitors analyzed, with an IC₅₀ value of 12.1 nM. Molecular modeling using the parameters stated in the experimental section resulted in a large number of possible conformations of the compound at the active site. The most likely binding conformation was selected based on the relative interaction energy with the enzyme. The conformation with the highest relative interaction energy was then examined to elucidate important interactions and possible hydrogen bond formation (Figures 7.16). Closer examination of the compound docked at the active site revealed a number of key interactions (Figure 7.17). This model places the thiosemicarbazone moiety in the S1 pocket such that the thiocarbonyl is in

close proximity with the Cys-25 residue. The benzophenone arm of the inhibitor is located in the deep, hydrophobic S2 pocket, the bromophenyl arm is positioned at the interphase between the S1 and S2 pockets, and the fluorophenyl arm attached to the thiosemicarbazone moiety is located on the right-hand side of the S3 pocket close to the S1 pocket. Some other important interactions between **28** and the active site of cruzain are:

- Hydrogen bond between one of the hydrogens on the backbone carbonyl of Asp158 and the fluorine on the benzophenone ring, which possibly helps secure this ring in the deep S2 pocket.
- The (C–S⁻) distance is 4.216 Å
- A hydrogen bond between the thiocarbonyl sulfur of the inhibitor and a hydrogen on Cys25 at the active site, which may contribute to placing the thiocarbonyl carbon atom of the inhibitor in close proximity to the Cys25 thiolate

Molecular Docking of 24 with Cruzain

For comparison purposes, molecular docking studies were also carried out with analogue **24**, which was inactive against cruzain. Molecular modeling indicated that analogue **24** did not bind in a manner that would facilitate formation of a covalent bond (Figure 7.18). Unlike the orientation seen with analogue **28**, analogue **24** binds in a manner such that the TSC group is oriented away from the enzyme towards the solvent. The benzophenone ring resides in the S1 subsite while the phenyl ring closest to the TSC moiety resides in the S2 pocket. In each of the top binding orientations, the thiocarbonyl carbon atom of analogue **24** was positioned no closer than 8 Å from the Cys25 thiolate

ion of cruzain. This comparison further suggests that formation of a transient covalent bond is necessary for activity against cruzain in this series of compounds.

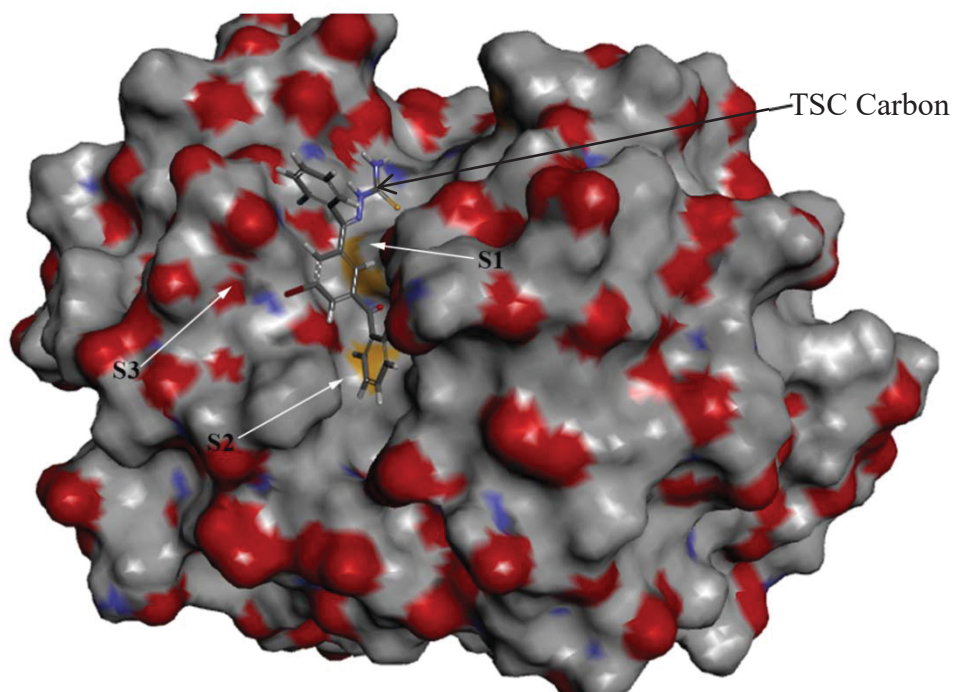


Figure 7.16. Molecular docking of compound **28** with cruzain (1ME3). Compound **28** is docked with a Connolly surface model of cruzain with the active site subsites labelled.

Summary

A series of benzophenone and other functionalized thiosemicarbazones were analyzed as potential inhibitors of cruzain. A few of these compounds were shown to be potent inhibitors of cruzain, with IC_{50} values less than 100 nM (Figure 7.6). Advanced kinetics analyses were performed in order to investigate the mechanism by which some of the more potent compounds inhibit cruzain. These compounds were determined to be competitive, time dependent, tight-binding, and reversible inhibitors of cruzain. For one of the most potent inhibitors, molecular docking with cruzain showed that

thiosemicarbazones are placed at the S1 subsite in close proximity to cruzain Cys25 and in the correct orientation such that bond formation between these groups is possible.

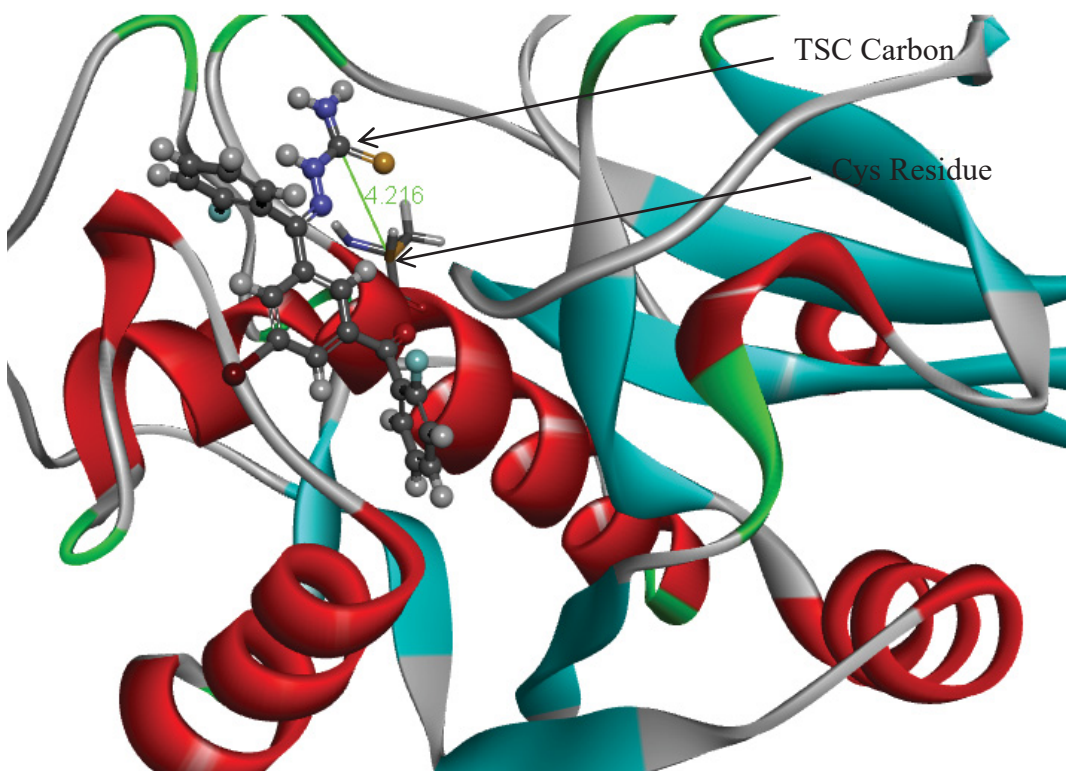


Figure 7.17. Compound **28** docked at the active site of cruzain with thiosemicarbazone carbon to Cys-25 sulfur distance labelled. Cruzain is represented with ribbons, active site Cys-25 is represented as a stick model, and compound is represented as a ball and stick model.

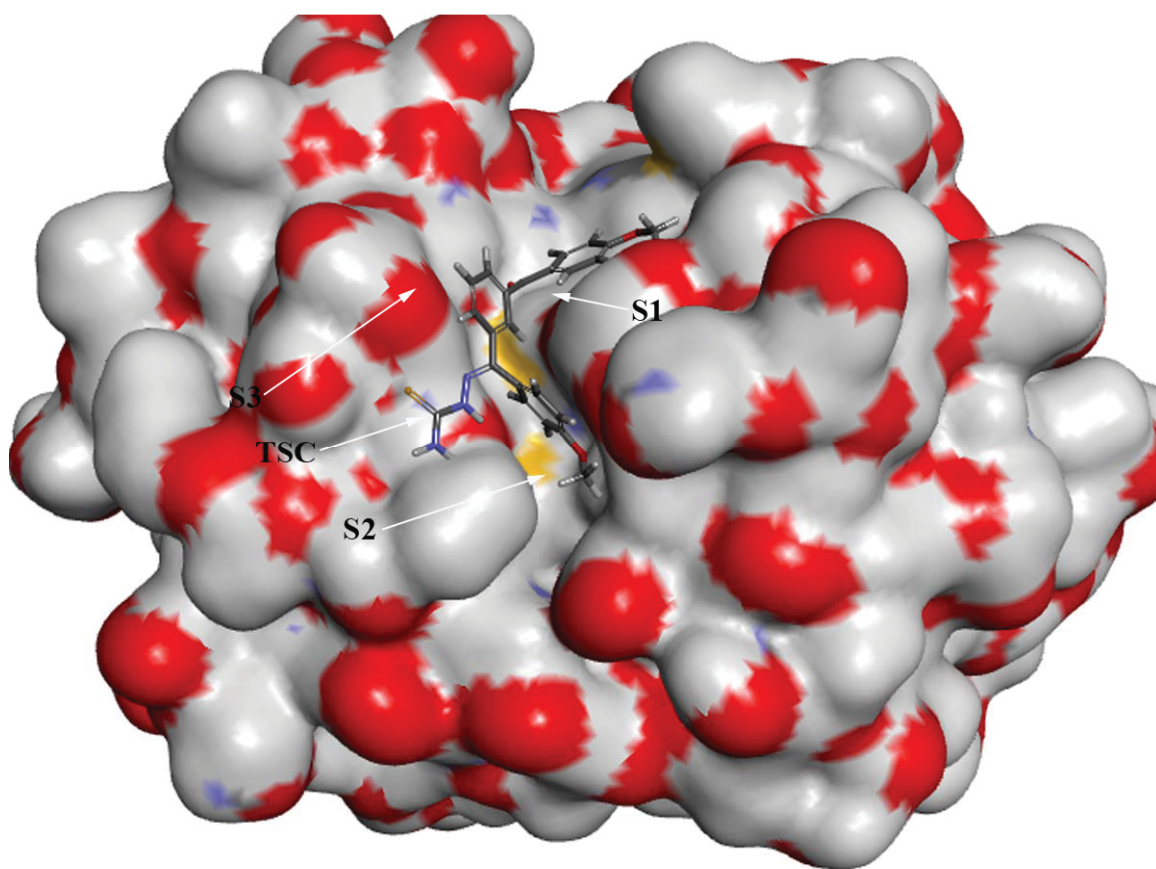


Figure 7.18. Molecular docking of compound **24** with cruzain (1ME3). Compound **24** is docked with a Connolly surface model of cruzain with the active site subsites labelled.

CHAPTER EIGHT

Inhibition of Cysteine Cathepsins by Thiosemicarbazone Compounds

Materials and Methods for the Evaluation of Thiosemicarbazone Compounds as Cysteine Protease Inhibitors

Materials and Equipment

Sodium acetate (anhydrous), ethylenediaminetetraacetic acid (EDTA), and dithiothreitol (DTT) were obtained from EMD. Z-Phe-Arg-AMC (7-Amino-4-methylcoumarin, N-CBZ-L-Phenylalanyl-L-arginine amide, hydrochloride, Z-FR-AMC) the substrate used for analysis of cathepsin L and K was purchased from Sigma Aldrich. Z-Arg-Arg-AMC Pure (99.9 %) Dimethyl sulfoxide (DMSO) and pure 7-Amino-4-methylcoumarin (AMC) were purchased from Acros and Anaspec respectively. Cathepsin L was purchased from Sigma Aldrich, cathepsin K from Enzo life sciences, and cathepsin B from Calbiochem. Human recombinant caspase 3 enzyme, fluorogenic peptide substrate of caspase 3 Acetyl-Asp-Met-Gln-Asp-amino-4-methylcoumarin (Ac-DMQD-AMC) and a validated aldehyde inhibitor of caspase 3 acetyl-Asp-Glu-Val-Asp-aldehyde (Ac-DEVD-CHO) were all purchased from Sigma Aldrich. The thiosemicarbazone inhibitor compounds were synthesized by members of the Dr. Kevin G. Pinney laboratory at Baylor University. Black 96 well flat bottom microplates (3991) and 0.2 μm filters were obtained from Corning. Single and twelve-channel pipettes as well pipette tips were obtained from Eppendorf. Range of pipettes used varied between 0.5 and 5000 μl . 18 m Ω ultra-pure water was generated using a Elga PureLab Flex water

purification system. Also, a pH meter (Mettler Toledo) and a Fluoroskan Ascent FL (Thermo) were used to calibrate the pH of the prepared solutions and for fluorometric experiments respectively. MDA-MB-231 cells used for invasion and migration assays were obtained from ATCC. Matrigel™ invasion and migration assay kits were purchased from BD Biosciences. DMEM media (VWR), FBS (Gibco), and DIFF QUIK (Imeb) were all used for the cell invasion and migration assays.

Preparation of Buffers and Stock Solutions for Cathepsin L Assays

Preparation of 400 mM sodium acetate buffer, pH 5.5. 200 ml of this solution was prepared by dissolving 5.59g of anhydrous sodium acetate in 0.74ml glacial acetic acid and making solution up to 200 ml with pure water. Glacial acetic acid or sodium hydroxide 5 M (MW: 40 g/mol) were used to adjust the pH of the buffer. This solution was stored at 4 °C.

Preparation of 40 mM EDTA. A stock concentration of this solution was prepared by dissolving 14.89 mg (40 µmol) of EDTA (MW: 372.29 g/mol) in one milliliter of water. Fifty milliliters of this solution (744.5 mg; 2 mmol) was prepared for multiple experiments. The solution of 40 mM EDTA was stored at 4 °C.

Preparation of 80 mM DTT. A freshly made stock concentration of this solution was prepared by dissolving 12.3 mg (80 µmol) of DTT (MW: 175 g/mol) in one milliliter of sodium acetate 400 mM, pH 5.5. The 80 mM DTT solutions were made fresh for each experiment.

Preparation of 20 mM AMC. This stock solution was prepared by dissolving 1.38 mg (6 µmol) of AMC (MW: 229.2 g/mol) in one milliliter of pure DMSO. This solution was stable for several months when stored at low temperatures (-20 °C).

Preparation of 20 mM Z-FR-AMC stock solution. This solution was made by dissolving 12.99 mg (20 μ mol) of Z-FR-AMC (MW: 649.15 g/mol) in one milliliter of pure DMSO. This solution was stable for several months when stored at low temperatures (-20 °C).

Preparation of 500 μ M Z-FR-AMC solution. This solution was prepared by diluting 25 μ l of the 20 mM Z-FR-AMC stock solution in 975 μ l of pure water, resulting in 1 ml of a 500 μ M (in 2.5% DMSO) Z-FR-AMC solution. This solution was stable for a month when stored at -20 °C.

Thiosemicarbazone derivative stock solutions. A subset of compounds from a library of thiosemicarbazone inhibitors was used to make inhibitor stock solutions (20 mM) in pure DMSO. Typically, one milligram was weighed to give a final volume that varied between 100 and 200 μ l of these stock solutions.

Preparation of inhibitor dilutions. Inhibitor solutions were prepared as previously discussed for the cruzain assays in Chapter seven. Tables 7.1A and B show sample calculations for the procedure for preparation of the inhibitor stock solutions in pure and 35% DMSO.

Preparation of cathepsin L assay buffer. Cathepsin L assay buffer contained 1.8 mM EDTA, 5.4 mM DTT, 0.02% Brij 35 and 180 mM NaOAc pH 5.5. Ten milliliters of assay buffer were made by adding 450 μ l of 40 mM EDTA, 675 μ l of 80 mM DTT, 20 μ l of 10% Brij 30, 4.5 ml of 400 mM NaOAc pH 5.5, and 4.36 ml of water in a plastic 50 ml conical tube. A summary of a typical calculation sheet used to make different volumes of assay buffer is presented in Table 8.1. The solution was stable up to a maximum of 24 h after preparation.

Preparation of 35% DMSO solution. An aqueous solution of DMSO was prepared by dilution of 35 μ l of DMSO with 65 μ l of water to bring a total of 0.1 ml. This solution was made up and used for each individual experiment.

Preparation of cathepsin L secondary stock solution. This solution contained 1 mM EDTA, 3 mM DTT, 0.01% Brij 35, 10 nM cathepsin L (enzyme stock concentration \approx 9 μ M) and 100 mM NaOAc pH 5.5. Table 8.2 presents a summary of typical calculations used to prepare different volumes of cathepsin L stock solution. The solution was made prior to every kinetic or inhibition experiment.

Preparation of buffer solution for reversibility studies. 4.8 ml of this solution was made by mixing 1320 μ l of 400 mM NaOAc pH 5.5, 5.28 μ l of 10% Brij 30, 180 μ l of 80 mM DTT, 132 μ l of 40 mM EDTA, and 3162.7 μ l of water. Final conditions were: 100 mM NaOAc pH 5.5, 1 mM EDTA, 3 mM DTT, and 0.01% Brij 30.

Preparation of cathepsin L stock solution for reversibility studies. 100 ml of this solution was made by diluting 1.9 μ l of cathepsin L enzyme (9 μ M stock solution) in 98.12 μ l of the buffer solution for reversibility. Final conditions in this solution were 100 mM NaOAc pH 5.5, 1 mM EDTA, 2.5 mM DTT, and 0.01% Brij 30, and 200 nM cathepsin L.

Preparation of Buffers and Stock Solutions for Cathepsin K Assays

Preparation of 400 mM sodium acetate buffer, pH 5.5. 200 ml of this solution was prepared by dissolving 5.59g of anhydrous sodium acetate in 0.74ml glacial acetic acid and making solution up to 200 ml with pure water. Glacial acetic acid or sodium hydroxide 5 M (MW: 40 g/mol) were used to adjust the pH of the buffer. This solution was stored at 4 °C.

Table 8.1. Preparation of Cathepsin L Assay Buffer

Columns	Volume(μ l)	EDTA (μ l)	DTT(μ l)	NaOAc(μ l)	Water(μ l)	Brij(μ l)
1	1000	45	67.5	450	435.5	2
2	2000	90	135	900	871	4
3	3000	135	202.5	1350	1306.5	6
4	4000	180	270	1800	1742	8
5	5000	225	337.5	2250	2177.5	10
6	6000	270	405	2700	2613	12
7	7000	315	472.5	3150	3048.5	14
8	8000	360	540	3600	3484	16
9	9000	405	607.5	4050	3919.5	18
10	10000	450	675	4500	4355	20
11	11000	495	742.5	4950	4790.5	22
12	12000	540	810	5400	5226	24

Table 8.2. Preparation of Cathepsin L Secondary Stock Solution

Columns	Volume(μ l)	EDTA(μ l)	DTT(μ l)	NaOAc(μ l)	Water(μ l)	Brij(μ l)	Cathepsin L(μ l)
1	200	5	7.5	50	137.07	0.2	0.23
2	400	10	15	100	274.14	0.4	0.46
3	600	15	22.5	150	411.21	0.6	0.69
4	800	20	30	200	548.28	0.8	0.92
5	1000	25	37.5	250	685.35	1	1.15
6	1200	30	45	300	822.42	1.2	1.38
7	1400	35	52.5	350	959.49	1.4	1.61
8	1600	40	60	400	1096.56	1.6	1.84
9	1800	45	67.5	450	1233.63	1.8	2.07
10	2000	50	75	500	1370.7	2	2.3
11	2200	55	82.5	550	1507.77	2.2	2.53
12	2400	60	90	600	1644.84	2.4	2.76

Preparation of 40 mM EDTA. A stock concentration of this solution was prepared by dissolving 14.89 mg (40 μ mol) of EDTA (MW: 372.29 g/mol) in one milliliter of water. Fifty milliliters of this solution (744.5 mg; 2 mmol) was prepared for multiple experiments. The solution of 40 mM EDTA was stored at 4 °C.

Preparation of 80 mM DTT. A freshly made stock concentration of this solution was prepared by dissolving 12.3 mg (80 μ mol) of DTT (MW: 175 g/mol) in one milliliter of sodium acetate 400 mM, pH 5.5. The 80 mM DTT solutions were made fresh for each experiment.

Preparation of 20 mM Z-FR-AMC stock solution. This solution was made by dissolving 12.99 mg (20 μ mol) of Z-FR-AMC (MW: 649.15 g/mol) in one milliliter of pure DMSO. This solution was stable for several months when stored at low temperatures (-20 °C).

Preparation of 500 μ M Z-FR-AMC solution. This solution was prepared by diluting 25 μ l of the 20 mM Z-FR-AMC stock solution in 975 μ l of pure water, resulting in 1 ml of a 500 μ M (in 2.5% DMSO) Z-FR-AMC solution. This solution was stable for a month when stored at -20 °C.

Thiosemicarbazone derivative stock solutions. A subset of compounds from a library of thiosemicarbazone inhibitors was used to make inhibitor stock solutions (20 mM) in pure DMSO. Typically, one milligram was weighed to give a final volume that varied between 100 and 200 μ l of these stock solutions.

Preparation of inhibitor dilutions. Inhibitor serial dilutions were made similarly to those for the cruzain and cathepsin L assays described earlier. However, the difference here is that solutions contained 75% DMSO in water.

Preparation of cathepsin K assay buffer. Cathepsin K assay buffer contained 1.8 mM EDTA, 4.5 mM DTT, 0.02% Brij 35 and 270 mM NaOAc pH 5.5. Ten milliliters of assay buffer were made by adding 450 μ l of 40 mM EDTA, 562.5 μ l of 80 mM DTT, 20 μ l of 10% Brij 30, 6.75 ml of 400 mM NaOAc pH 5.5, and 2.22 ml of water in a plastic

50 ml conical tube. A summary of a typical calculation sheet used to make different volumes of assay buffer is presented in Table 8.3. The solution was stable up to a maximum of 24 h after preparation.

Preparation of 75% DMSO solution. An aqueous solution of DMSO was prepared by dilution of 75 μ l of DMSO with 25 μ l of water to bring a total of 0.1 ml. This solution was made up and used for each individual experiment.

Preparation of cathepsin K secondary stock solution. This solution contained 1 mM EDTA, 2.5 mM DTT, 0.01% Brij 35, 3 nM cathepsin K (stock concentration \approx 0.9 μ M) and 150 mM NaOAc pH 5.5. Table 8.2 presents a summary of typical calculations used to prepare different volumes of cruzain stock solution. The solution was made prior to every kinetic or inhibition experiment.

Preparation of Buffers and Stock Solutions for Cathepsin B Assays

Preparation of 400 mM phosphate buffer, pH 6.0. 200 ml of this solution was prepared by dissolving 1.36 g of dibasic sodium phosphate (48 mM) and 9.58 g of monobasic potassium phosphate with pure water. Hydrochloric acid or sodium hydroxide 5 M (MW: 40 g/mol) were used to adjust the pH of the buffer. This solution was stored at 4 °C.

Preparation of 40 mM EDTA. A stock concentration of this solution was prepared by dissolving 14.89 mg (40 μ mol) of EDTA (MW: 372.29 g/mol) in one milliliter of water. Fifty milliliters of this solution (744.5 mg; 2 mmol) was prepared for multiple experiments. The solution of 40 mM EDTA was stored at 4 °C.

Preparation of 80 mM DTT. A freshly made stock concentration of this solution was prepared by dissolving 12.3 mg (80 μ mol) of DTT (MW: 175 g/mol) in one milliliter

of sodium acetate 400 mM, pH 5.5. The 80 mM DTT solutions were made fresh for each experiment.

Table 8.3. Preparation of Cathepsin K Assay Buffer

Columns	Volume(μl)	EDTA (μl)	DTT(μl)	NaOAc(μl)	Water(μl)	Brij(μl)
1	1000	45	56.25	675	221.75	2
2	2000	90	112.5	1350	443.5	4
3	3000	135	168.75	2025	665.25	6
4	4000	180	225	2700	887	8
5	5000	225	281.25	3375	1108.75	10
6	6000	270	337.5	4050	1330.5	12
7	7000	315	393.75	4725	1552.25	14
8	8000	360	450	5400	1774	16
9	9000	405	506.25	6075	1995.75	18
10	10000	450	562.5	6750	2217.5	20
11	11000	495	618.75	7425	2439.25	22
12	12000	540	675	8100	2661	24

Table 8.4. Preparation of Cathepsin K Secondary Stock Solution

Columns	Volume (μl)	EDTA (μl)	DTT(μl)	NaOAc (μl)	Water (μl)	Brij (μl)	Cathepsin K (μl)
1	200	5	6.25	75	112.87	0.2	0.68
2	400	10	12.5	150	225.74	0.4	1.36
3	600	15	18.75	225	338.61	0.6	2.04
4	800	20	25	300	451.48	0.8	2.72
5	1000	25	31.25	375	564.35	1	3.4
6	1200	30	37.5	450	677.22	1.2	4.08
7	1400	35	43.75	525	790.09	1.4	4.76
8	1600	40	50	600	902.96	1.6	5.44
9	1800	45	56.25	675	1015.83	1.8	6.12
10	2000	50	62.5	750	1128.7	2	6.8
11	2200	55	68.75	825	1241.57	2.2	7.48
12	2400	60	75	900	1354.44	2.4	8.16

Preparation of 20 mM AMC. This stock solution was prepared by dissolving 1.38 mg (6 μ mol) of AMC (MW: 229.2 g/mol) in one milliliter of pure DMSO. This solution was stable for several months when stored at low temperatures (-20 °C).

Preparation of 24 mM Z-RR-AMC stock solution. This solution was made by dissolving 16.67 mg (24 μ mol) of Z-RR-AMC (MW: 621.29 g/mol) in one milliliter of pure DMSO. This solution was stable for several months when stored at low temperatures (-20 °C).

Preparation of 600 μ M Z-RR-AMC solution. This solution was prepared by diluting 25 μ l of the 24 mM Z-RR-AMC stock solution in 975 μ l of pure water, resulting in 1 ml of a 600 μ M (in 2.5% DMSO) Z-RR-AMC solution. This solution was stable for a month when stored at -20 °C.

Thiosemicarbazone derivative stock solutions. A subset of compounds from a library of thiosemicarbazone inhibitors was used to make inhibitor stock solutions (20 mM) in pure DMSO. Typically, one milligram was weighed to give a final volume that varied between 100 and 200 μ l of these stock solutions.

Preparation of inhibitor dilutions. Inhibitor solutions were prepared as previously discussed for the cruzain assays in Chapter seven. Tables 7.1A and B show sample calculations for the procedure for preparation of the inhibitor stock solutions in pure and 35% DMSO.

Preparation of cathepsin B assay buffer. Cathepsin B assay buffer contained 1.8 mM EDTA, 5.4 mM DTT, 0.02% Brij 35 and 216 mM K-Na phosphate buffer pH 6.0. Ten milliliters of assay buffer were made by adding 450 μ l of 40 mM EDTA, 675 μ l of 80 mM DTT, 20 μ l of 10% Brij 30, 5.4 ml of 400 mM Phosphate buffer pH 6.0, and 3.46

ml of water in a plastic 50 ml conical tube. A summary of a typical calculation sheet used to make different volumes of assay buffer is presented in Table 8.5. The solution was stable up to a maximum of 24 h after preparation.

Preparation of 35% DMSO solution. An aqueous solution of DMSO was prepared by dilution of 35 μ l of DMSO with 65 μ l of water to bring a total of 0.1 ml. This solution was made up and used for each individual experiment.

Preparation of Cathepsin B secondary stock solution. This solution contained 1 mM EDTA, 3 mM DTT, 0.01% Brij 35, 10 nM cathepsin B (enzyme stock concentration \approx 12.8 μ M) and 120 mM K-Na phosphate pH 6.0. Table 8.6 presents a summary of typical calculations used to prepare different volumes of cruzain stock solution. The solution was made prior to every kinetic or inhibition experiment.

Table 8.5. Preparation of cathepsin B assay buffer

Volume (μ l)	EDTA (μ l)	DTT (μ l)	K-Na Phosphate (μ l)	Water (μ l)	Brij (μ l)
1000	45	67.5	540	345.5	2
2000	90	135	1080	691	4
3000	135	202.5	1620	1036.5	6
4000	180	270	2160	1382	8
5000	225	337.5	2700	1727.5	10
6000	270	405	3240	2073	12
7000	315	472.5	3780	2418.5	14
8000	360	540	4320	2764	16
9000	405	607.5	4860	3109.5	18
10000	450	675	5400	3455	20
11000	495	742.5	5940	3800.5	22
12000	540	810	6480	4146	24

Table 8.6. Preparation of cathepsin B secondary stock solutions

Volume(μ l)	EDTA (μ l)	DTT (μ l)	K-Na Phosphate (μ l)	Water (μ l)	Brij (μ l)	Cathepsin B (μ l)
200	5	7.5	60	127.14	0.2	0.16
400	10	15	120	254.29	0.4	0.31
600	15	22.5	180	381.43	0.6	0.47
800	20	30	240	508.57	0.8	0.63
1000	25	37.5	300	635.72	1	0.78
1200	30	45	360	762.86	1.2	0.94
1400	35	52.5	420	890	1.4	1.1
1600	40	60	480	1017.15	1.6	1.25
1800	45	67.5	540	1144.29	1.8	1.41
2000	50	75	600	1271.43	2	1.57
2200	55	82.5	660	1398.58	2.2	1.72
2400	60	90	720	1525.72	2.4	1.88

Experimental Section

Kinetic Cysteine Protease Assays

Kinetic studies to determine the catalytic activity of their respective substrates against substrates were carried out in 96-well black microplates using a Thermo Fluoroskan microplate reader. The total reaction volume was 200 μ l per well, with each well containing 100 μ l of assay buffer, 10 μ l of vehicle (DMSO) solution, 20 μ l enzyme solution, and 20 μ l of varying concentrations (in 2.5% DMSO) of substrate solution. Serial dilutions were used to prepare substrate solutions that were 10x the final concentrations in the well (Table 7.4). After combining all the assay components, the production of AMC was monitored for 5 minutes at 25 °C, using excitation and emission references of 355 and 460 nm respectively. Readings were taken every 15 seconds for 5 minutes total. Reactions were carried out in triplicate. The final parameters of each of the respective enzyme kinetic assays are:

- Cathepsin L - 100 mM NaOAc pH 5.5, 1 mM EDTA, 3 mM DTT, 0.01% Brij 35, 1 nM cathepsin L and 2% DMSO. Final concentrations of Z-FR-AMC varied between 0.2 and 15 μ M.
- Cathepsin K – 150 mM NaOAc pH 5.5, 1 mM EDTA, 2.5 mM DTT, 0.01% Brij 35, 0.3 nM cathepsin K and 4% DMSO. Final concentrations of Z-FR-AMC varied between 1 and 15 μ M.
- Cathepsin B – 120 mM K-Na Phosphate pH 6.0, 1 mM EDTA, 3 mM DTT, 0.01% Brij 35, 1 nM cathepsin B and 2% DMSO. Final concentrations of Z-RR-AMC varied between 1 and 60 μ M

Preliminary Inhibition Studies

A subset of compounds from a library of thiosemicarbazone analogs (synthesized by members of the laboratory of Dr. Kevin G. Pinney) was assayed to determine inhibitory activity against all three cathepsin enzymes. Components of this assay are similar to those described in the kinetic assay protocol above, in addition to 10 μ M of the compounds being screened. Compounds failing to inhibit cysteine protease activity by more than 50% (i.e. $v_i/v_o \leq 0.5$) compared to the uninhibited control reactions were considered ‘inactive’ compounds; a general IC_{50} value greater than 10000 nM was assumed. Compounds that inhibited cysteine protease activity by more than 50% were assayed to determine exact IC_{50} values against the enzymes.

Cathepsin Inhibition Assay (IC_{50} Determination)

Thiosemicarbazone analogues were analyzed for their inhibitory activity against the cathepsins L, B and K using a protocol similar to the one described for cruzain analysis in Chapter seven. Total volume of the reaction was 200 μ l, with each well containing 100 μ l of assay buffer, 50 μ l of water, 10 μ l of vehicle or 10 μ l of inhibitor dilutions, 20 μ l enzyme secondary stock solutions, and 20 μ l of substrate solution

(500 μ M Z-FR-AMC solution for cathepsin L and K, and 600 μ M Z-RR-AMC for cathepsin B). A 180 μ l reaction mixture containing assay buffer, vehicle or inhibitor, and enzyme was pre-incubated at 25 °C for 5 minutes in 96-well black microplates, after which reactions were initiated by addition of 20 μ l of substrate solution. The release of AMC product from the substrate in the inhibited and uninhibited reactions was monitored for 5 minutes. The final concentrations of the preliminary inhibitory reactions were:

- Cathepsin L - 100 mM NaOAc pH 5.5, 1 mM EDTA, 3 mM DTT, 0.01% Brij 35, 1 nM cathepsin L, 50 μ M of Z-FR-AMC, and varying concentrations of inhibitor compounds.
- Cathepsin K – 150 mM NaOAc pH 5.5, 1 mM EDTA, 2.5 mM DTT, 0.01% Brij 35, 0.3 nM cathepsin K, 50 μ M of Z-FR-AMC, and varying inhibitor concentrations.
- Cathepsin B – 120 mM K-Na phosphate buffer pH 6.0, 1 mM EDTA, 3 mM DTT, 0.01% Brij 35, 1 nM cathepsin B, 60 μ M of Z-RR-AMC, and varying inhibitor concentrations

Readings were taken every 15 seconds for five minutes and reactions were carried out in triplicate.

Construction of AMC Calibration Curve

AMC calibration curves were constructed as previously described in Chapter seven.

Effect of Inhibitor Concentration on Cathepsin L Progress Curves

Final concentrations, conditions, and volumes are similar to the cathepsin L inhibition assay. Assay buffer, inhibitors (final concentrations varied between 100 nM and 10 μ M) and Z-FR-AMC (final concentration: 50 μ M and 10 μ M) were added to the 96-well black plates (volume of the substrate-inhibitor mixture: 180 μ l). Then 20 μ l of

cathepsin L solution were added immediately without any pre-incubation time. Readings were taken every 30 seconds for sixty minutes.

Determination of K_{iapp} Using Morrison's Quadratic Equation

Data obtained from preincubation assays were further analyzed as potential tight binding inhibitors of cruzain. To determine the apparent K_i of the inhibition, the data was fit via nonlinear regression by applying Morrison's quadratic equation.

Reversibility Studies

Cathepsin L reversibility solution for was pre-incubated with an equal amount of a concentrated solution of inhibitor (at a concentration of 20 μ M) at 25 °C for 3 hours. The cathepsin L reversibility assay solution contained 100 nM cathepsin L (10x the normal assay amount), 10 μ M compound, and 50% DMSO. Enzyme solution for reversibility was also incubated with an equal amount of a 50% DMSO solution to serve as the untreated control. After the 3 h incubation, 2 μ l of the enzyme-inhibitor mixture (or control solution) were rapidly mixed with 178 μ l of cruzain assay buffer for reversibility and 20 μ l of Z-FR-AMC to start the reaction. Total reaction volume was 200 μ l. Readings were taken every thirty seconds for four hours. Final concentrations are equivalent to those described previously. Final conditions were: 100 mM NaOAc, pH 5.5, 1 mM EDTA, 3 mM EDTA, 0.01% Brij 35, 1 nM cathepsin L and 10 μ M of Z-FR-AMC.

Alkaline Phosphatase (AP) Activity Assay

An assay buffer comprising 10 mM glycine-NaOH buffer (pH 8.6) with 2 mM $MgCl_2$ was prepared. Stock enzyme solution was made by dissolving 0.26 mg human

placental alkaline phosphatase enzyme (Sigma Aldrich) in 260 μ l DI H₂O (about 1.2 units/100 μ l solution). At optimum conditions, 1 unit of AP converts 1 μ mol of 4-nitrophenyl phosphate (substrate) to 4-nitrophenol (product) per minute. A 60 mM substrate stock solution was prepared; 0.02-unit alkaline phosphatase aliquots were made and used for the assay. Final assay conditions in the cuvette were: 1.4 ml of assay buffer (10 mM Gly-NaOH, 2mM MgCl₂, pH 8.6), 50 μ l of 0.02-unit enzyme aliquots, and 50 μ l of 60 mM substrate solution (to give a final substrate concentration of 2mM). Assay was performed at 37°C for 50 minutes in a UV/Vis spectrophotometer with absorbance readings taken at 405 nm every 6 seconds.

Preliminary Inhibition Assay for Thiosemicarbazone Phosphate Analogue

A modified preliminary inhibition assay protocol was used to determine the percentage inhibition of cathepsin L by 10 μ M of a phosphate analogue of compound **2**, compound **46** (Figure 8.1). In this assay, the reaction solution contained 0.1% Tween (as opposed to 0.01% Brij used in other reactions).

Alkaline Phosphatase Activation of Thiosemicarbazone Analogue Assay

AP (1.2 units per sample) was incubated with 200 μ M of compound **46** for 18 hr. at 37°C. HPLC was used to confirm amount of conversion of KGP420 to KGP94 due to cleavage of the phosphate group. 2% DMSO was added to a separate sample and also incubated under the same conditions. This was done because KGP94 is not very soluble in water and could possibly precipitate due to the AP activity on KGP420.

In order to ascertain the inhibitory capacity of alkaline phosphatase-treated **47** on cathepsin L, a modified version of the preliminary inhibition assay was used. The assay was run using the following conditions:

- Assay buffer; 100 mM Sodium acetate-acetic acid buffer (pH 5.5), 1 mM EDTA, 3 mM DTT, 0.1% Tween.
- 1 nM Cathepsin L
- 50 μ M substrate (Z-FR-AMC)
- 10 μ l AP-KGP420 solution to give a final solution of 10 μ M of compound in 200 μ l reaction solution.

Cathepsin L was allowed to incubate with the AP-**46** mixture for 5 minutes before reaction was initiated with addition of Z-FR-AMC. 10 μ l volumes of AP-**46** in 2%DMSO, glycine NaOH buffer and AP alone (1 unit) were also incubated with cathepsin L in other reaction solutions. Fluorescence readings over 5 minutes were obtained and the % inhibition compared to control was calculated for AP-**46**, AP, glycine NaOH buffer, and AP-**46** in 2% DMSO.

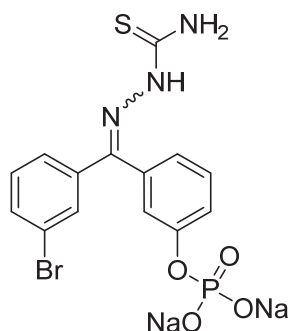


Figure 8.1. Structure of Compound **46**, a phosphate analogue of compound **2**

Caspase 3 Inhibition Assay

Assays to determine the effects of on thiosemicarbazone inhibitors (using compound **2**) on the activity of recombinant human caspase 3 (Sigma Aldrich) were carried out using the fluoregenic peptide substrate Acetyl-Asp-Met-Gln-Asp-amino-4-

methylcoumarin (Ac-DMQD-AMC) [460, 461]. A validated aldehyde inhibitor of caspase 3, acetyl-Asp-Glu-Val-Asp-aldehyde (Ac-DEVD-CHO) [461], was used as a positive control for enzyme inhibition. Inhibitors (1 μ M compound **2** or 100 nM Ac-DEVD-CHO) were not pre-incubated with enzyme before initiation of the assay. The final assay conditions were 1 mM EDTA, 10 mM DTT, 0.1% v/v CHAPS, 50 mM HEPES, 2% v/v DMSO, 10% v/v glycerol, 100 mM NaCl, pH 7.4, 5 nM caspase 3, and 50 μ M of Ac-DMQD-AMC and inhibitor in a total reaction volume of 200 μ l. The release of AMC from the substrate was monitored at 15 second intervals over 30 minutes at 25°C in black 96 well Corning 3686 assay microplates using a Thermo Fluoroskan Ascent FL microplate reader at excitation and emission filter wavelengths of 355 nm and 460 nm respectively. Analysis of data was performed with GraphPad Prism 5.0 software.

MDA-MB-231 Cell Culture

MDA-MB-231 cells that were stored under cryogenic conditions were thawed and plated (using fetal bovine serum (FBS) supplemented DMEM medium) in T-75 flasks and incubated at 37 °C and 5% CO₂/air. Supplemented DMEM medium was replaced every two days. Cells were passaged (removed and placed at lower cell densities in new flasks) once they reached about 80-90% confluence.

Passaging was carried out by removing DMEM medium from confluent cells and immediately adding 4 ml of trypsin-EDTA solution to induce cell detachment and lift off into culture media. After 5-minute incubation at 37°C, cells were observed under the microscope to confirm if they were completely rounded and detached from the flask surface. Equal volumes of FBS supplemented DMEM media were added to the flasks in order to neutralize the proteolytic activity of trypsin. Trypsinized cells were used to seed

a new generation of cells by transfer to new T-75 flasks containing fresh DMEM media. New passages were cultured and maintained as previously described.

Cell Freezing Protocol

Trypsinized cells were periodically frozen to keep and maintain an inventory for future experiments. Stock solutions were centrifuged at 10000 rpm for 5 minutes to form a cell pellet. Suspended media was removed and replaced with DMEM medium that is supplemented with 5% DMSO. A cell counter was used to determine cell concentration in the new stock solutions. Cell concentration varied between one and 5 million cells/ml. These cell stock solutions were transferred to cryogenic vials. Cells were kept under cryogenic conditions (liquid nitrogen).

Cell Invasion Assays

Invasion assays were carried out using the BD Bioscience MatrigelTM invasion kit assay. MDA-MB-231 cells were cultured and passaged as described. Cells were trypsinized when they were 80% confluent. However, trypsin neutralization was done with DMEM with no FBS. Cell density was determined with a Beckman Coulter Z-Coulter cell counter. Cell solutions were diluted with DMEM with no FBS in order to reach a 200,000 cell/ml concentration in each case. Thiosemicarbazone inhibitors (compounds **22**, **23**, and **28**) with high cathepsin L activity were selected to test its efficacy by delaying cell invasion. Also, E-64, a validated pan-cysteine protease inhibitor was used as a positive control.

Compound dilutions were made by diluting 20 mM compound stock into DMEM media (with no FBS) to give 50 and 20 μ M solutions. Simultaneously, several BD

BioCoat Matrigel® invasion chambers, which contain an 8-micron pore size PET membrane with a layer of Matrigel basement, were prepared for the experiment. Both sides of each matrix were rehydrated using 500 µl DMEM media with no FBS for two hours in a 5% CO₂ environment at 37 °C. Media was removed and inserts were ready to be used to start the invasion assay. The experiment was initiated by adding 750 µl of DMEM supplemented with 10% FBS (which functions as a chemoattractant) and gentamicin to a 24-well microplate (i.e. lower chamber). Then, the inserts were carefully placed on top of the wells containing the chemoattractant, avoiding air bubbles between the bottom part of the insert and medium. Two hundred fifty microliters of the cell stock solutions (400,000 cells/ml) and 250 µl of 50 and 20 µM of each compound to be tested were added to every insert. Final conditions for treated cells were: 2% DMSO, 100,000 cells and 25 or 10 µM of the compounds. Final conditions for untreated (controls) cells are: 2% DMSO and 100,000 cells. The 24-well plates containing the invasion studies chambers were placed in an incubator with a 5% CO₂ environment for 24 hours at 37 °C.

Reactions were terminated by removing medium from the inserts. Each insert was cleaned twice with cotton swabs to remove cells located at the top side of the membrane. Membranes were stained with a Diff-Quik staining kit (IMEB, Inc.) and fixed with 100% methanol for two minutes. Then, membranes were rinsed with deionized water and consecutive staining solutions of azure and xanthenes dyes. Samples were placed in each solution for a minimum of two minutes and rinsed with water in between. Finally, samples were air-dried for a minimum for two hours in a biological safety cabinet.

Membranes were removed using sterile scalpels and placed on glass slides. Each sample was observed under a Zeiss Axiovert 40 CFL inverted microscope with and attached Canon Powershot camera. Ten fields were chosen and observed under a 40X objective. Eight fields were located at the periphery of the circular sample and numbered clockwise. Two more fields were counted at the middle of each sample, as depicted in Figure 8.2. Experiments were performed in triplicate. Counting of the invaded cells was done using Adobe Photoshop counting tool. The inhibition of the invasiveness of MDA-MB-231 cells was measured by using the formula: treated cells that invaded the Matrigel™ layer/untreated cells that invaded the Matrigel™ layer.

Cell Migration Assays

The experimental procedure for the determination of the ability of MDA-MB-231 to migrate is similar to that described for the cell invasion assays. However, the inserts with an 8 μm did not contain the Matrigel™ layer. Both, invasion and migration assays were performed simultaneously and used the same MDA-MB-231 cell stock solutions. The inhibition of the motility of MDA-MB-231 cells was measured by using the formula: treated cells that migrated to the 8 μm membrane/untreated cells that migrated to the 8 μm layer.

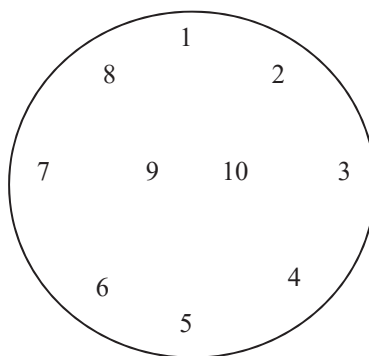


Figure 8.2. Invasion and Migration Assay Sample Fields

Results and Discussion

As part of a collaborative project between the Pinney and Trawick research groups at Baylor University, a small library of thiosemicarbazone compounds were synthesized, which led to the discovery of a number of thiosemicarbazone derivatives as inhibitors of cruzain and cathepsin L, with some also showing inhibitory activity towards other cysteine proteases.

The characterization of compounds that could be used as potential therapeutic agents involved numerous evaluations. Understanding the kinetic effect of these inhibitors helped to identify their mechanism of action. Fluorometric based assays were used to study inhibitor potency, determine K_i , as well as determine whether or not these thiosemicarbazone compounds are reversible inhibitors of cathepsin L. Two dimensional cell based assays (colorimetric cell invasion and cell migration assays) were used to determine the ability of these compounds to inhibit invasion and migration in a metastatic breast cancer cell line. Furthermore, in order to ascertain selectivity of the different compounds to cysteine cathepsins, these compounds were also assayed against cathepsins B, L and caspase 3. Furthermore, as part of the ongoing effort to develop these compounds as therapeutics, a phosphate analogue (which is more water soluble than the parent thiosemicarbazone compound) was developed and assayed as a phosphatase substrate and for its inhibitory activity against cathepsin L.

Cathepsin studies were carried out using a 96-well microplate fluorometric based assay, similar to the studies used for cruzain analysis. The major advantage of this type of assay is that a relatively large number of experiments can be performed in a short period of time without compromising the reproducibility of the results. Microplate-based

assays are commonly used in drug discovery; furthermore, high throughput screening is also available where hundreds or thousands of samples can be evaluated simultaneously. As mentioned earlier, Z-FR-AMC is a validated fluorogenic substrate for serine and cysteine proteases. This substrate was used for the Fluorometric assays involving cathepsins L and K (Figure 8.3). Cathepsin B, due to the presence of the active site occluding loop, has slightly different substrate specificity to the other cysteine cathepsins (see Chapter five), and as such the fluoregenic substrate Z-RR-AMC is used for this assay (Figure 8.4).

Construction of AMC Calibrations Curves

AMC calibration curves were constructed in a similar manner to those used for the cruzain assays, so as to be able to convert the relative fluorescence units into the concentration of the fluorophore. The standard curves were constructed, using GraphPad Prism™ software, by plotting varying concentrations of AMC over time (Figure 7.2). Linear regressions of these values were performed and the y-intercept values corresponding to each AMC solution were obtained. These y-intercept relative fluorescence values were plotted over the AMC concentrations and a second linear regression performed (Fig 7.3). Results of the second linear regression give an equation that can correlate RFU and AMC concentration. The equation is $\text{RFU} = 146 \text{ AMC (in } \mu\text{M}) + 38$ and the linear coefficient (r^2) calculated to give a value of 0.9985.

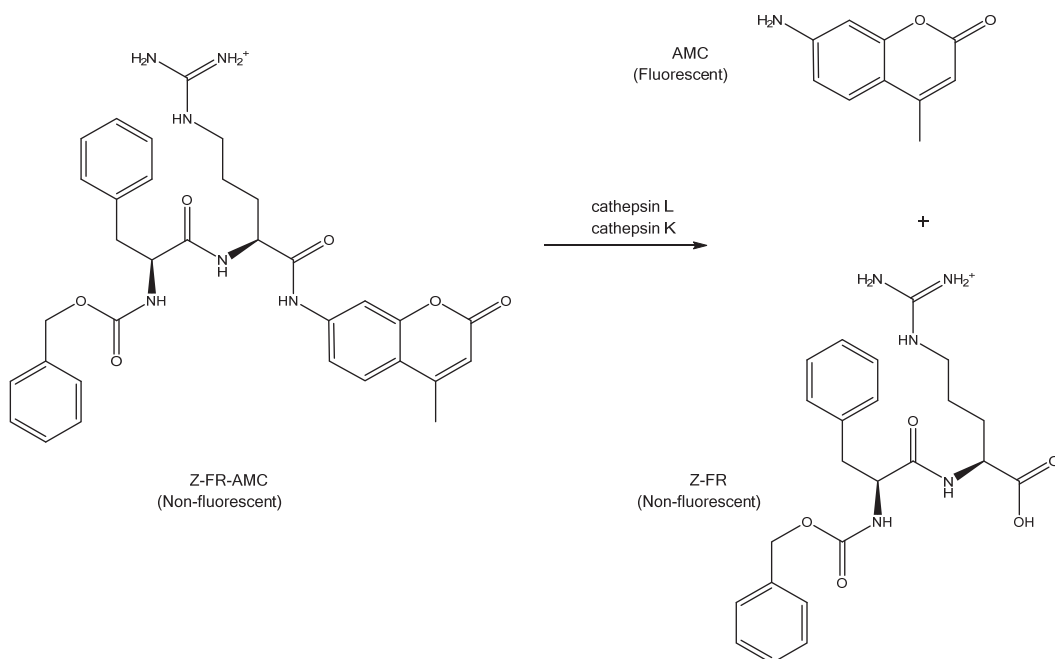


Figure 8.3. Cathepsin L/K catalyzed hydrolysis of Z-FR-AMC

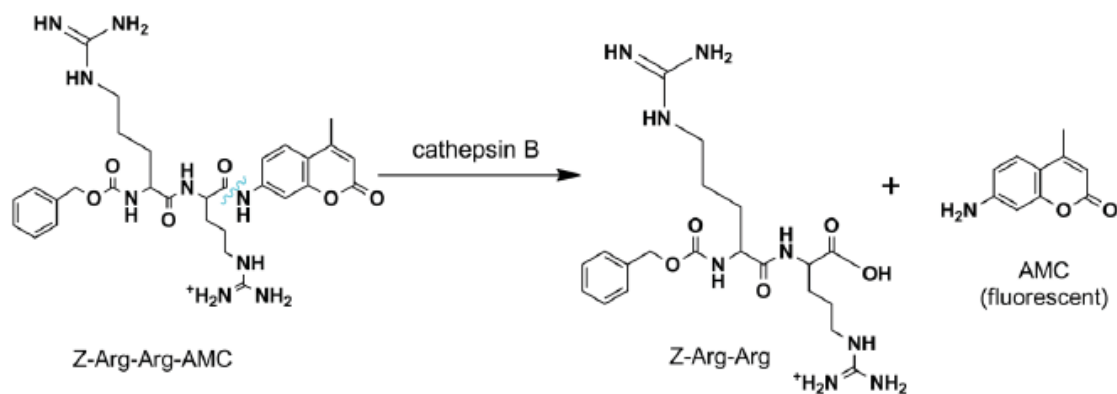


Figure 8.4. Cathepsin B catalyzed hydrolysis of Z-RR-AMC

Determination of Kinetic Parameters (K_M , V_{max} , and k_{cat}) for Cathepsins L, K, and B

Kinetic parameters for the cysteine proteases with fluorogenic synthetic peptide substrates Z-FR-AMC (for cathepsins L and K) and Z-RR-AMC (cathepsin B), were based on the steady state assumption, and indicate that reaction rates of these enzymes as

a function of substrate concentration were consistent with the Michaelis-Menten equation (Eq. 5.1).

K_M , V_{max} and k_{cat} values for these reactions were obtained using a similar method to the one described for cruzain in Chapter seven. Briefly, kinetic parameters were determined by observing the catalytic activity of a fixed concentration of enzyme with varying concentrations of substrate, applying linear regression to ascertain the rates of these reactions, plotting these rates against substrate concentration, and then applying nonlinear regression analysis using the Michaelis-Menten equation (Eq. 5.1), in order to calculate K_M and V_{max} values. These analyses were done using GraphPad Prism 5.0 software. The k_{cat} constant value was determined using equation 5.2. The parameter v_o is the initial rate velocity at a specific substrate concentration. The V_{max} is the maximum velocity, K_M is the Michaelis-Menten constant, $[S]$ is the substrate concentration, and k_{cat} is the catalytic rate constant. The final reaction values for all the enzyme assays are presented in the experimental section.

For cathepsin L, the K_M value was found to be $1.65 \pm 0.2 \mu\text{M}$, similar to the previously reported literature values [462]. The V_{max} was determined to be $1.34 \pm 0.11 \text{ nM/s AMC}$. The K_{cat} value was calculated to be 1.34 s^{-1} . The R^2 of the fit was 0.96. The plot of the change in $[\text{AMC}]$ over time as a result of cathepsin L activity is graphically represented in Figure 8.5 A, and the graphical representation of the Michaelis-Menten equation showing cathepsin L activity is presented in Figure 8.5 B.

For cathepsin K, the K_M value was found in our assays to be $61.95 \pm 4.98 \mu\text{M}$. The V_{max} was determined to be 3.18 nM/s of AMC . The k_{cat} value was calculated to be 206.5 s^{-1} . It should be noted from the kinetic results that cathepsins K and L values

reveals a considerable difference in proteolytic activity against Z-FR-AMC between both enzymes.

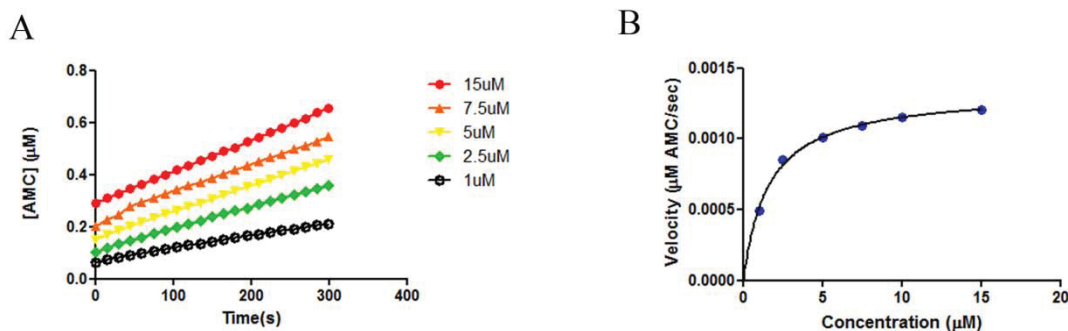


Figure 8.5. Graphical representation of the kinetic parameters for cathepsin L against Z-FR-AMC synthetic fluorogenic substrate.

Z-FR-AMC is an excellent cathepsin L substrate (K_M : 1 μM). However, that is not the case for cathepsin K. Literature values show the K_M to be roughly 10 times higher than that of cathepsin L [463] (60 times higher in the assay presented here) and this difference could be occurring as a result of differences in substrate affinity. Cathepsin K has been shown to have a specific preference for proline, and other substrates (Z-GPR-AMC) have been developed to test cathepsin K activity in other studies [464]. The plot of the change in [AMC] over time as a result of cathepsin K activity is graphically represented in Figure 8.6 A, and the graphical representation of the Michaelis-Menten equation showing cathepsin L activity is presented in Figure 8.6 B.

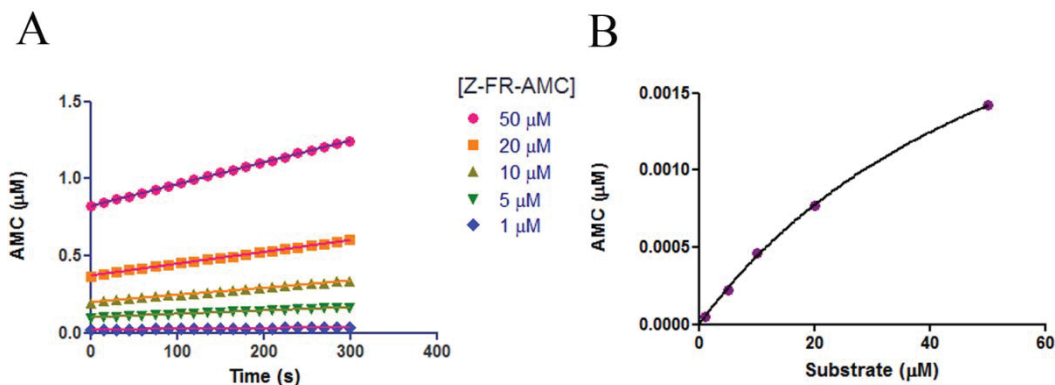


Figure 8.6. Graphical representation of the kinetic parameters for cathepsin K against Z-FR-AMC synthetic fluorogenic substrate.

Kinetic parameters for cathepsin B were determined by a previous member of the Trawick laboratory, Dr. Amanda Charlton-Sevcik using very similar conditions to the ones used for the inhibition analyses of the thiosemicarbazone compounds against cathepsin B. The K_M value was found to be 200.8 μM [465].

Preliminary Inhibition Assays of Thiosemicarbazones with Cysteine Proteases

The first set of experiments that were performed to screen for compounds in the library of thiosemicarbazones that could be potential inhibitors cathepsins L, B, and K. Compounds that caused inhibition of the catalytic activity by more than 50% (compared to untreated control) were selected for further analysis of inhibitory activity. Three independent sets of experiments of untreated ($[I]: 0 \mu\text{M}$) and treated samples ($[I]: 10 \mu\text{M}$) were preincubated with enzyme for 5 minutes at 25 $^{\circ}\text{C}$. Inhibitory activities were monitored when reactions were started by adding substrate. Reactions demonstrated a linear behavior for at least the first five minutes. Active compounds were further analyzed to determine an exact IC_{50} value. If the rate of the reaction of the inhibited

reaction was greater than 50% (i.e. inhibition less than 50%), then the compounds were not considered potential inhibitors and an approximated IC₅₀ value > 10000 nM was assigned to them.

Cathepsin Inhibition Assay (IC₅₀ Determination)

Forty six compounds from the total library of thiosemicarbazone inhibitors were assayed to ascertain their potency as inhibitors of the catalytic activities of cathepsins L, B and K. The synthetic compounds were synthesized by members of the Pinney research laboratory as part of a larger collaborative project between the Pinney and Trawick research groups. A 96-well microplate fluorometric assay was utilized to determine the inhibitory activity of these inhibitors. The determination of the IC₅₀ values was carried out with experiments that observe the inhibitory capacity of the synthetic compounds when a fixed concentration of each of the enzymes was preincubated for 5 minutes at 25 °C with thiosemicarbazone compounds being analyzed. The final concentration of each compound varied between 10 pM and 10 µM. Experiments for each tested inhibitor were done in triplicate. Catalytic rates of uninhibited and inhibited samples were calculated by linear regression of the data ([AMC]: dependent variable and time (seconds): the independent variable). The slopes from this linear regression (representing the reaction rates for each compound concentration-enzyme mixture) were then plotted over the compound concentrations. The data was consistent with a sigmoidal dose response relationship, thus a nonlinear regression using equation 5.8 was performed to calculate IC₅₀ values. The value Y represents the inhibited activity (normalized relative to control), and the X is log ([inhibitor]) in µM. The velocities v_{min} and v_{max} represent the highest and lowest velocities for the reactions. The Hill slope value is the slope of the sigmoidal

curve. $IC_{50} \pm S.E.$ values represent the average and standard errors of at least three independent experiments. The various IC_{50} values and thiosemicarbazone compound structures are shown in Tables 8.7-8.10 below (some of the IC_{50} values presented were also previously reported by past members of the Trawick research group [452, 465]).

Of the thiosemicarbazone compounds analyzed against cathepsin L, 8 of them proved to be particularly potent inhibitors with IC_{50} values less than 100 nM (Figure 8.7). Compounds from three of the four different structural scaffolds (Figure 5.33) were represented in this group of potent cathepsin L inhibitors, with only the compounds having the benzophenone with extended alkyl link structure not showing any inhibitory activity against cathepsin L. There were also a few other compounds assayed that showed moderate inhibitory activity against cathepsin L (i.e. $100 \text{ nM} < IC_{50} < 10 \text{ }\mu\text{M}$).

There were also a significant number of compounds assayed that showed moderate to potent activity against cathepsin K, with about 9 compounds having inhibitory activity less than 100 nM (Figure 8.8) and another 10 compounds having inhibitory activity between 100 nM and 10 μM . It should also be noted that while a number of compounds displayed significant inhibitory activity against both cathepsin L and cathepsin K, a number of compounds showed inhibitory specificity against one or the other cathepsin (Figure 8.9). Finally, this group of thiosemicarbazones had insignificant inhibitory effect on cathepsin B activity, as only compound **1** had an IC_{50} value below 10 μM . This is likely due to the difference in the active site cavity of cathepsin B compared to cathepsins L and K.

Advanced Kinetic Studies with Cathepsin L

A number of the compounds shown to have inhibitory activity against cathepsin L (and representing the various compound scaffolds) were further assayed using various kinetic methods in order to elucidate the mode of inhibition. These assays were done to determine time dependence of inhibition, elucidate the mechanism by which this class of compounds inhibit cathepsin L, as well as determine the reversibility of inhibition of this class of compounds.

Effects of Thiosemicarbazone Inhibitors on Cathepsin L Progress Curves

To assess the time dependence of the inhibition, the reaction rates were monitored as a function of time. For this experiment, cathepsin L was treated with various concentrations of inhibitor in the presence 10 μM substrate Z-FR-AMC. Reactions were initiated by the addition of the enzyme to the inhibitor substrate mixture without preincubation and fluorescence measurements were taken every 30 seconds up to 50 minutes. For time dependent curves, a change in slope over time should be observed where the inhibition increases as the reaction progresses. This is due to the initial velocity of enzyme catalyzed substrate cleavage followed by a change to a steady state velocity. Further examination of the exact mechanism of slow binding inhibition of cathepsin L by compound **22** was performed by fitting the data to equation 5.13, by nonlinear regression analysis using GraphPad Prism 5.0 software. P is the concentration of product (μM), v_o and v_s are the initial and steady-state velocities ($\mu\text{M/s}$), t is the time in seconds and k_{obs} the rate constant for conversion of the initial velocity v_o to the steady state velocity v_s .

Table 8.7. IC₅₀ values of benzophenone thiosemicarbazone compounds against cysteine cathepsins

Compound	Structure	R ₁	IC ₅₀ ± S.E (nM)		
			Cathepsin L	Cathepsin K	Cathepsin B
1 ¹			16.2±3.1	26.5±1.9	2185±189
2 ²			189±11	53.3±3.4	>10000
3 ³			> 10000	524.8±31.2	>10000
4 ³			175.1±19.5	61.7±5.5	>10000
5			> 10000	> 10000	>10000
6			7200±751	> 10000	>10000
7 ⁶			202±3.2	ND	>10000
8 ⁶			> 10000	104.7±3.6	>10000

⁶ Synthesis Reference- E.N. Parker, et al. Bioorg. Med. Chem. Lett. (2016).

Table 8.7 (continued). IC₅₀ values of benzophenone thiosemicarbazone compounds against cysteine cathepsins

Compound	Structure	R ₁	IC ₅₀ ± S.E		
			Cathepsin L	Cathepsin K	Cathepsin B
9 ⁶			> 10000	203.3±10.7	>10000
10 ⁶			> 10000	> 10000	>10000
11 ⁶			> 10000	> 10000	>10000
12 ⁶			> 10000	368.9±46.1	>10000
13			1876±124	>10000	>10000

Table 8.8. IC₅₀ values of thiochromanone thiosemicarbazone compounds against cysteine cathepsins

Compound	Structure	R ₁	IC ₅₀ ± S.E (nM)		
			Cathepsin L	Cathepsin K	Cathepsin B
14 ⁴			67.8±6.8	164.7±14.9	>10000
15 ⁴			54±7.6	176.6±14.3	>10000

Table 8.8 (continued). IC₅₀ values of thiochromanone thiosemicarbazone compounds against cysteine cathepsins

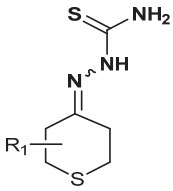
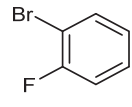
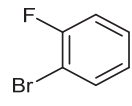
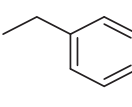
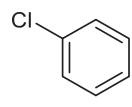
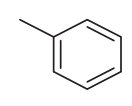
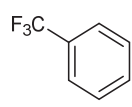
Compound	Structure	R ₁	IC ₅₀ ± S.E (nM)		
			Cathepsin L	Cathepsin K	Cathepsin B
16 ⁴			434.2±14.8	44.2±2.9	>10000
17 ⁴			> 10000	419.4±21.6	>10000
18 ⁴			2720±240	29.1±1.8	>10000
19 ⁴			228.4±11.6	62.9±2.3	>10000
20 ⁴			213.8±16.4	80.8±2.6	>10000
21 ⁴			284.1±10.7	21.49±2.1	>10000

Table 8.9. IC₅₀ values of benzoyl benzophenone thiosemicarbazone compounds against cysteine cathepsins

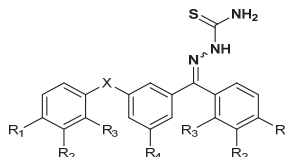
Cmp	Structure	R ₁	R ₂	R ₃	R ₄	X	Cathepsin IC ₅₀ ± S.E (nM)		
							L	K	B
22 ⁵		H	H	H	H	C=O	19.63±3.3	17.38±1.4	> 10000

Table 8.9 (continued). IC₅₀ values of benzoyl benzophenone thiosemicarbazone compounds against cysteine cathepsins

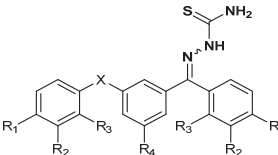
<i>Cmp d</i>	<i>Structure</i>	<i>R</i> ₁	<i>R</i> ₂	<i>R</i> ₃	<i>R</i> ₄	<i>X</i>	Cathepsin IC ₅₀ ±S.E (nM)		
							L	B	K
23 ⁵		F	H	H	H	C=O	14.4±4.5	8500±664	>10000
24 ⁵		OCH 3	H	H	H	C=O	5117±600	2105±129	>10000
25 ⁵		H	H	H	H	C-OH	528±62.5	296.5±5.1	>10000
26 ⁵		H	H	H	HC=O Bz	C=O	56±19	2796±20	>10000
27 ⁵		H	H	H	CH ₃	C=O	729±110	1034±68	>10000
28 ⁵		H	H	Br	F	C=O	8.12±0.5	>10000	>10000
29 ⁵		OH	H	H	H	C=O	340.5±30	≈10000	>10000
30 ⁵		Br	H	H	H	C=O	1522± 325	≈10000	>10000
31 ⁵		H	OH	H	Br	C=O	71.6±6.8	>10000	≈10000

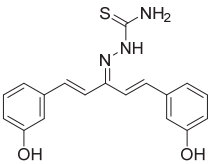
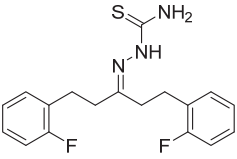
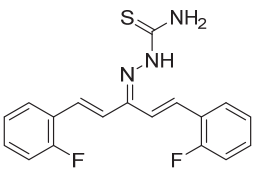
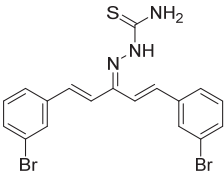
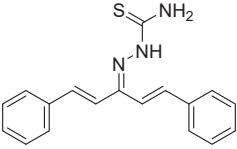
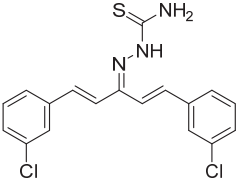
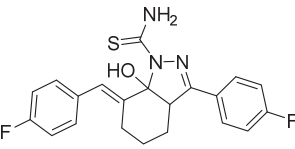
Table 8.9 (continued). IC₅₀ values of benzoyl benzophenone thiosemicarbazone compounds against cysteine cathepsins

<i>Cmpd</i>	<i>Structure</i>	<i>R</i> ₁	<i>R</i> ₂	<i>R</i> ₃	<i>R</i> ₄	<i>X</i>	Cathepsin IC ₅₀ ± S.E (nM)		
							<i>L</i>	<i>K</i>	<i>B</i>
32⁵		H	Br	H	OH	C=O	>10000	≈10000	>10000
33⁵		H	Br	H	Br	C=O	≈10000	>10000	>10000

Table 8.10. IC₅₀ values of benzophenone thiosemicarbazone compounds (with alkyl chain linkers) against cysteine cathepsins

<i>Compound</i>	<i>Structure</i>	<i>Cathepsin L</i>	IC ₅₀ ± S.E (nM)	
			<i>Cathepsin K</i>	<i>Cathepsin B</i>
34		>10000	>10000	>10000
35		>10000	>10000	>10000
36		>10000	>10000	>10000
37		>10000	>10000	>10000
38		>10000	>10000	>10000

Table 8.10 (continued). IC₅₀ values of benzophenone thiosemicarbazone compounds (with alkyl chain linkers) against cysteine cathepsins

<i>Cmpd</i>	<i>Structure</i>	<i>IC</i> ₅₀ ± <i>S.E</i> (nM)		
		<i>Cathepsin L</i>	<i>Cathepsin K</i>	<i>Cathepsin B</i>
39		>10000	>10000	>10000
40		>10000	>10000	>10000
41		>10000	>10000	>10000
42		>10000	>10000	>10000
43		>10000	>10000	>10000
44		>10000	>10000	>10000
45		≈10000	>10000	>10000

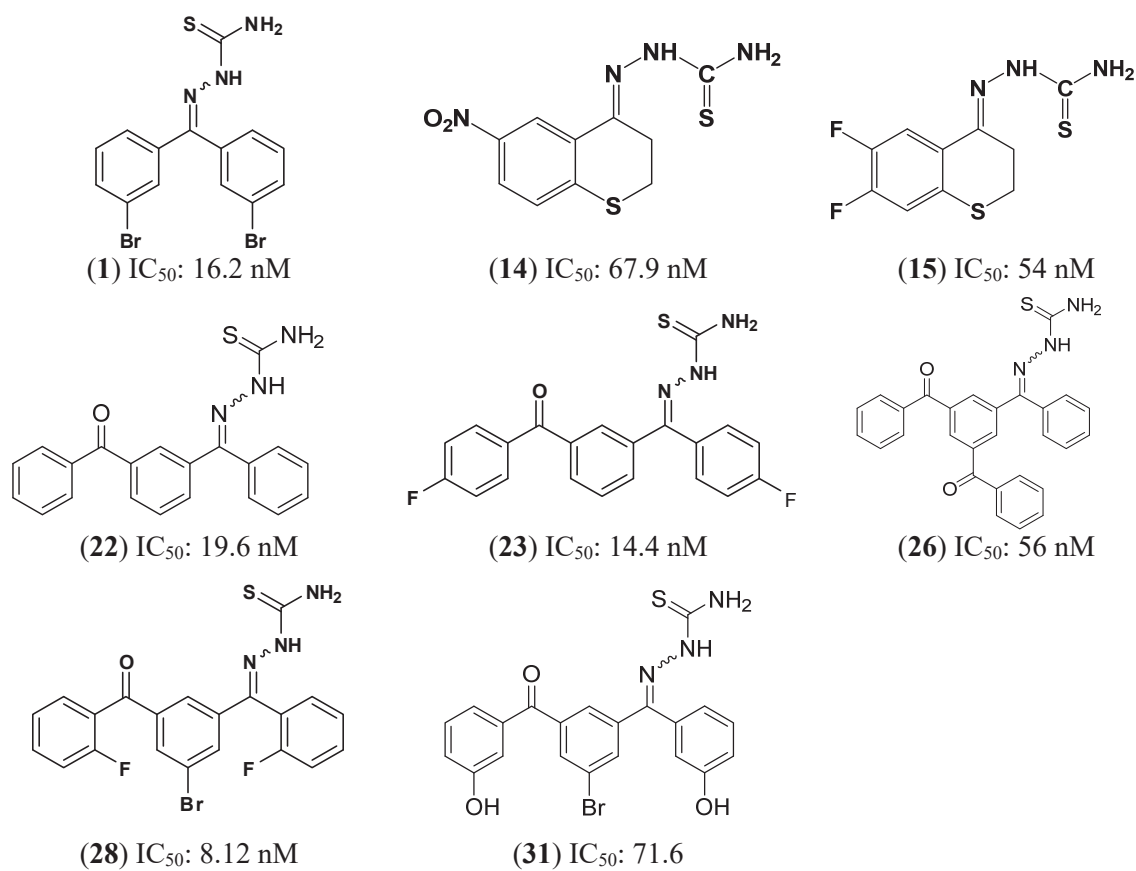


Figure 8.7: Potent thiosemicarbazone inhibitors ($IC_{50} < 100$ nM) of cathepsin L

The rate constant (k_{obs}) units are given in s^{-1} . In equation 5.13, P and t are the dependent and independent variables, while the velocities and the rate constant are unknowns. For each case, the constraints for their calculation were to give positive values (i.e. $k_{obs} \geq 0$). The kinetic parameters obtained from this analysis are presented in Table 8.11.

Observation of a plot of k_{obs} over inhibitor concentration (Figure 8.12) suggests that the relationship between these two parameters is a linear one. This suggests that the mechanism of slow binding inhibition of cathepsin L by compound **22** is one that involves simple slowly reversible inhibition. However, analysis of the mechanism of

slow binding inhibition of compound **28** against cathepsin L suggests a different outcome. The relationship between k_{obs} and inhibitor concentration observed here is a hyperbolic one (Figure 8.13), suggesting that the mechanism of inhibition may involve an initial simple slowly reversible binding step followed by the cruzain-inhibitor complex undergoing isomerization or covalent modification, to form a more stable enzyme-inhibitor complex.

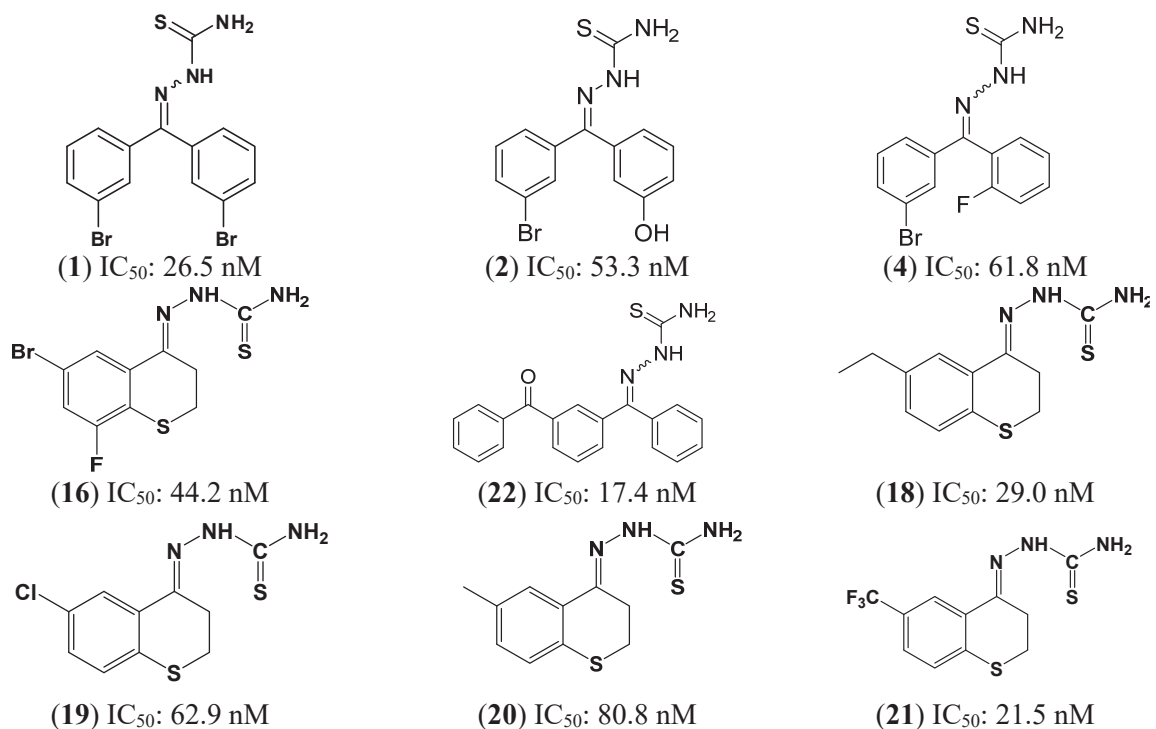


Figure 8.8. Potent thiosemicarbazone inhibitors ($\text{IC}_{50} < 100$ nM) of cathepsin K

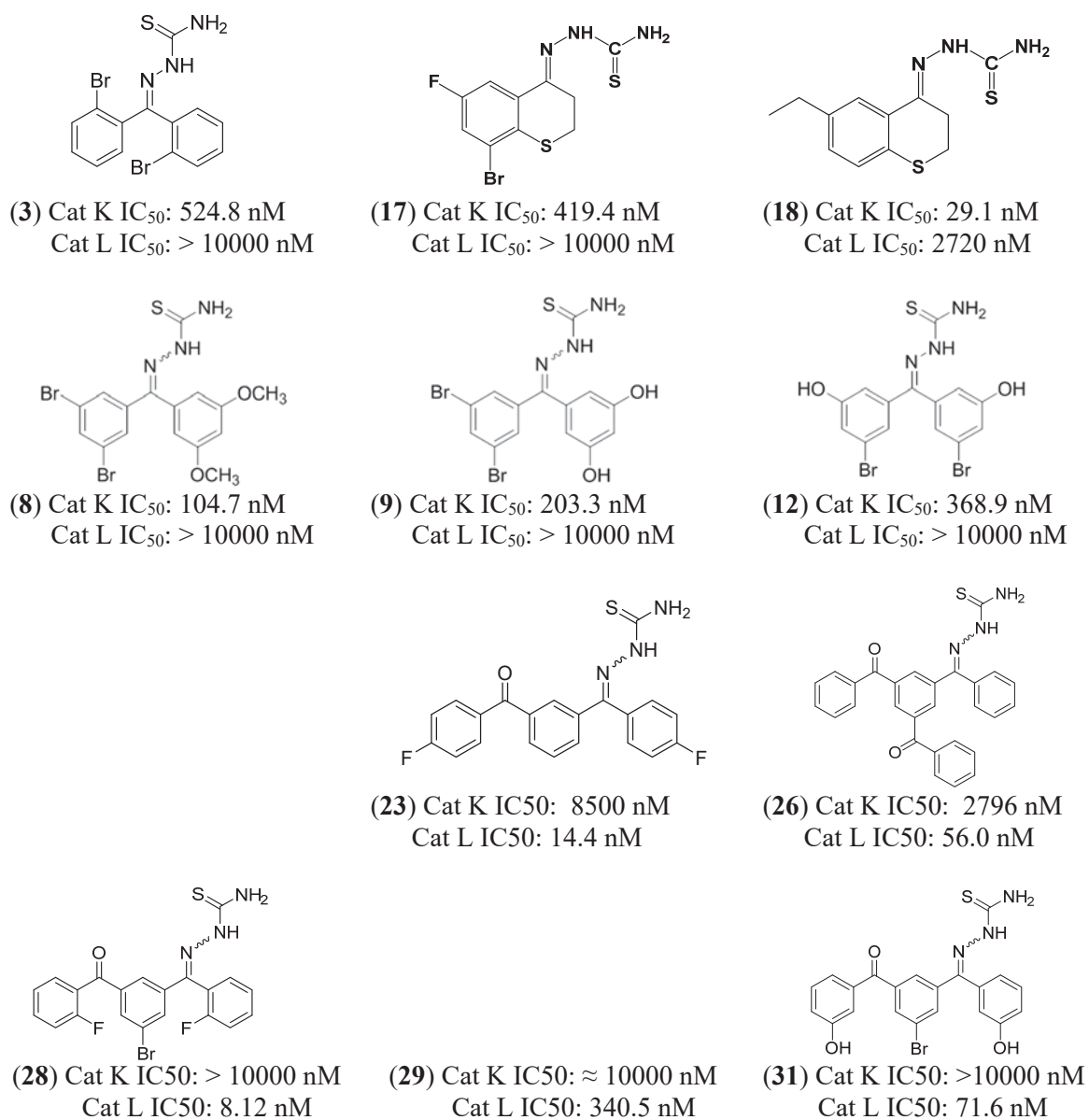


Figure 8.9: Thiosemicarbazone compounds selective for cathepsin L and/or K

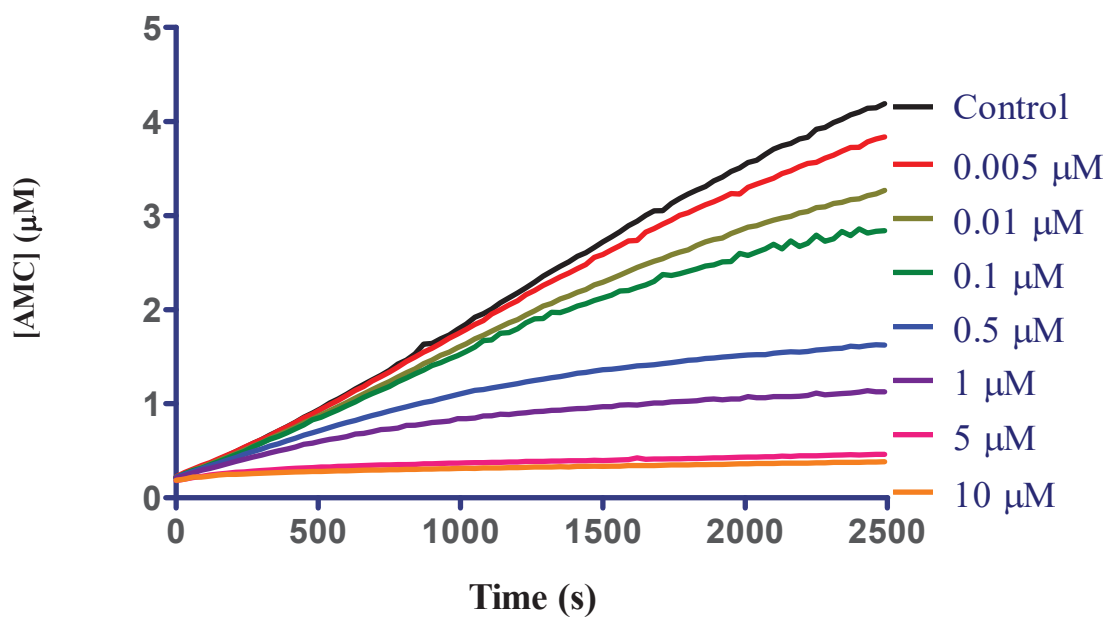


Figure 8.10. Progress curves of cathepsin L activity inhibited with varying concentrations of compound 22

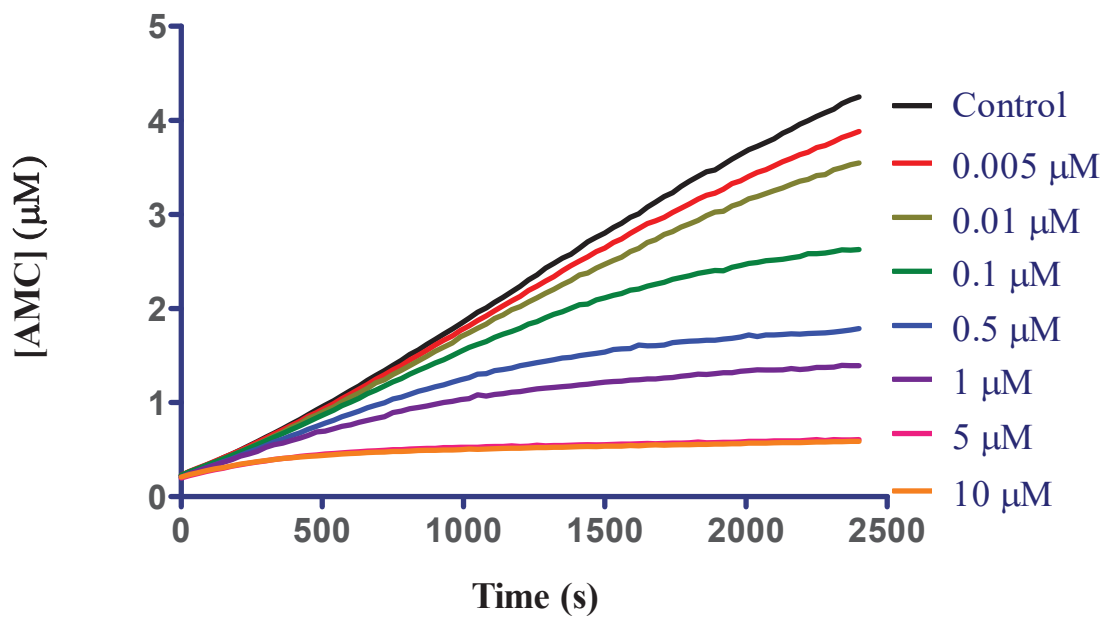


Figure 8.11. Progress curves of cathepsin L activity inhibited with varying concentrations of compound 28

Table 8.11. Kinetic parameters obtained from non-linear regression analysis of progress curves of cathepsin L inhibited by compound **22**

[22] (μM)	10	5	1	0.5	0.1	0.01	0.005
v_s ($\mu\text{M/s}$)	5.645e-005	7.572e-005	0.0001982	0.0002630	1.551e-014	2.019e-014	4.701e-014
v_o ($\mu\text{M/s}$)	0.01095	0.006306	0.002321	0.002127	0.001936	0.001910	0.001982
$k_{obs}(s^{-1})$	0.04373	0.02199	0.003213	0.001854	0.0004476	0.0003145	0.0002009

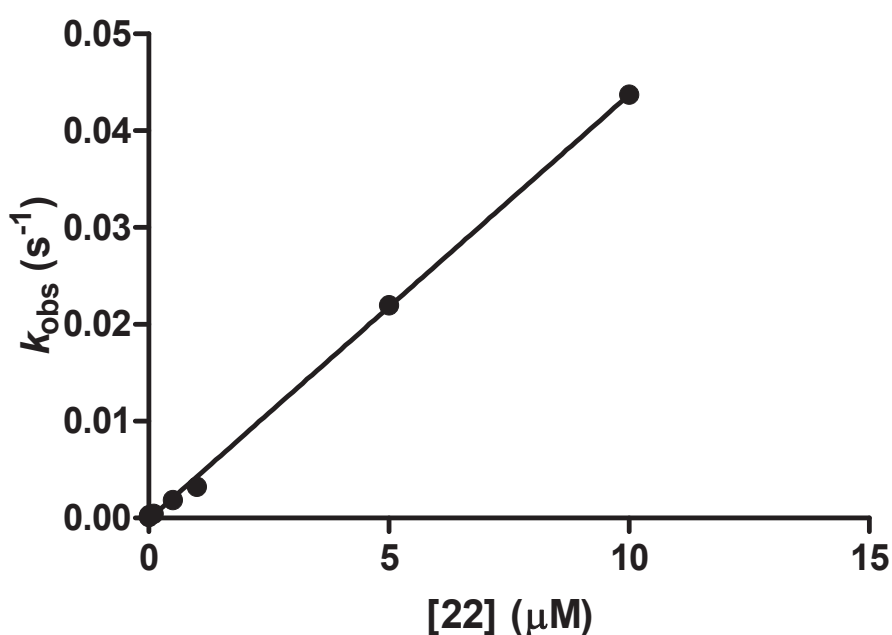


Figure 8.12. Graphical representation of the relationship between k_{obs} and [**22**]

Analysis of Tight Binding Inhibition: Determination of K_I using the Morrison Equation

Analysis of tight binding inhibition of cathepsin L by thiosemicarbazone compounds using the Williams Morrison equation (equation 5.17) was used to determine the binding constant for the inhibitor to the enzyme, the K_I , at specified pre-incubation times.

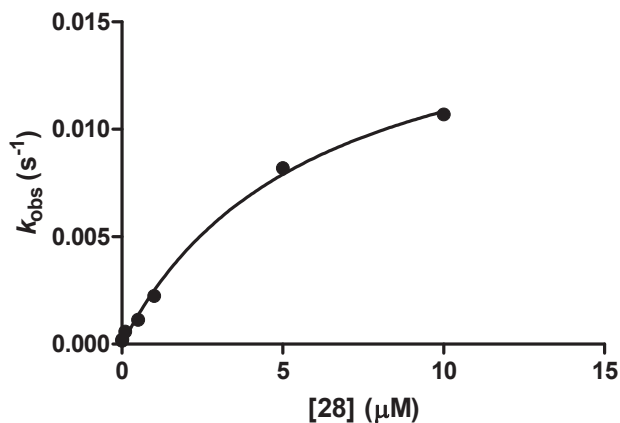


Figure 8.13. Graphical representation of the relationship between k_{obs} and [28]

A number of compounds with high inhibitory potency against cathepsin L were further analyzed using this equation in order to elucidate the extent of their binding affinity to cruzain. The data obtained from the IC₅₀ determination studies (5-minute pre-incubation time) were input into this equation in order to determine the K_I values.

$$\frac{v_i}{v_o} = 1 - \frac{([E]_T + [I]_T + (K_I(1 + \left(\frac{[S]}{K_M}\right))) - \sqrt{([E]_T + [I]_T + (K_I(1 + \left(\frac{[S]}{K_M}\right)))^2 - 4[E]_T[I]_T}}{2[E]_T} \quad (\text{Equation 5.17})$$

The rates v_i and v_o are the inhibited and uninhibited cruzain velocities (RFU/s); $[E]_T$ (nM) is, the total concentration of enzyme found in solution (free enzyme and inhibitor-enzyme complex); $[I]_T$ (nM) is the total concentration of inhibitor present in solution (free inhibitor and inhibitor-enzyme complex); and K_I (nM) is the inhibition constant, often referred as the dissociation constant. The equation may be solved to give two possible answers. However, the equation is written so that there is only one possible answer that fits physiological conditions (i.e. $K_I^{\text{app}} > 0$). GraphPad 5.0 was used to fit the

data to the non-linear regression curve generated from the equation. The residual activity (or v_i/v_o) was normalized to 1 (i.e. v_o : 1 and $0 \leq v_i \leq 1$). Normalized residual activity and [I] were defined as the dependent and independent variables respectively. Nonlinear regression was applied using the following conditions: [S]: 15 μ M, K_M : 2.37 μ M, [E]_T: 0.0001 μ M and v_o : 1.

As seen from the results presented in Table 8.12, the thiosemicarbazone compounds with high inhibitor potency also turned out to be tight-binding inhibitors of cathepsin L, with K_I^{app} values in the low nanomolar range. Furthermore, the graphical representation of the Morrison equation with a representative compound results in a very robust fit, with R^2 values close to 1 (Figure 8.14). This data suggests that these thiosemicarbazone compounds from the three different scaffolds being examined act as tight binding inhibitors of cathepsin L.

Table 8.12. K_I values of a selection of thiosemicarbazone inhibitors of cathepsin L

<i>Compound</i>	<i>IC₅₀ (nM)</i>	<i>K_I^{app} (nM)</i>
1	16.2	0.39
2	223	38.9
7	202	7.60
23	14.4	1.83
26	56.0	0.81
28	8.12	1.04
31	71.6	2.71

Cleavage and Inhibition Studies of a Thiosemicarbazone Phosphate Analogue against Cathepsin L

In this research project as well as in previous studies, Compound **2** has been shown to be a potent, slowly reversible, time-dependent inhibitor of cathepsin L [466]. Furthermore, the low cytotoxicity against human umbilical vein endothelial cells

(HUVECs), the ability to inhibit the invasive and migratory potential of both PC-3ML (prostate cancer cell line) and MDA-MB-231 (breast cancer cell line) in vitro, and the ability to reduce metastatic tumor burden and increase survival rate in PC-3ML tumor bearing mice has led to the identification of this compound as a pre-clinical candidate for potential development as an anti-metastatic agent, functioning through a potent inhibition of cathepsin L [455, 466].

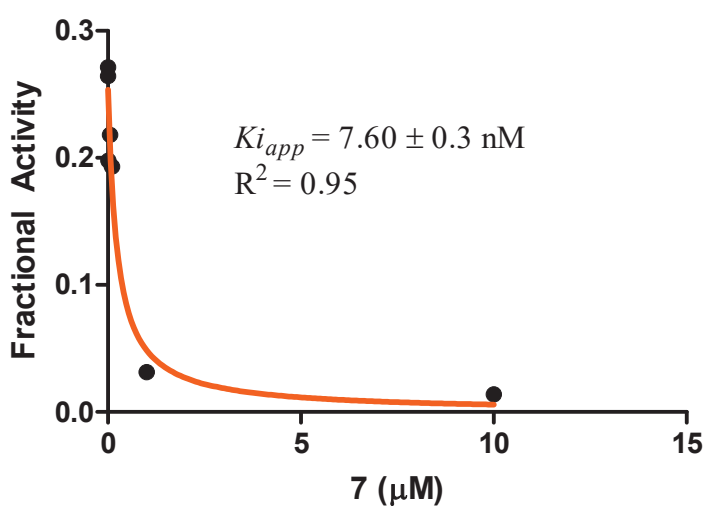


Figure 8.14. Graphical representation of Morrison analysis of tight binding of compound 7 to cathepsin L

However, compound 2, like most of the other thiosemicarbazone compounds being analyzed, has limited solubility in water. Therefore, a water-soluble prodrug salt, compound 46 (Figure 8.1), was synthesized so as to further the pre-clinical development of this promising agent. This phosphate prodrug had low inhibitory activity against cathepsin L ($IC_{50} > 10000 \text{ nM}$). However, the phosphate prodrug can be converted to the parent compound by endogenous phosphatases in vivo (Figure 8.15).

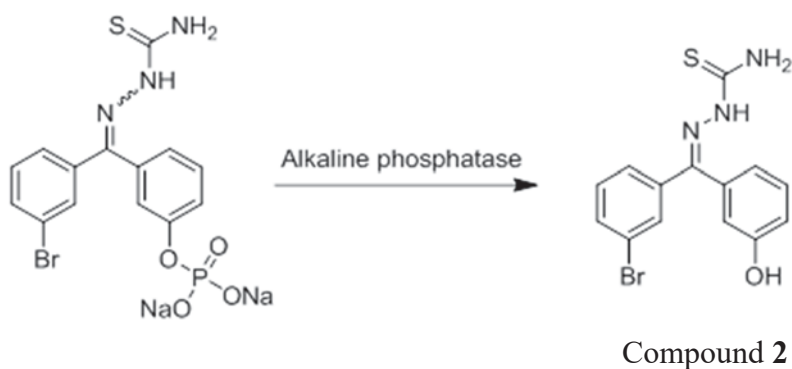


Figure 8.15. Conversion of compound **46** to compound **2**

Initial in vitro analysis of this compound involved a preliminary inhibition assay of cathepsin L with compound **46**, an alkaline phosphatase activity assay, alkaline phosphatase treatment of compound **46**, and finally a cathepsin L preliminary inhibition assay using the product of the reaction between alkaline phosphatase and compound **46**. The enzymatic activity of alkaline phosphatase (from human placenta) was determined by monitoring the conversion of 4-nitrophenyl phosphate (Sigma-Aldrich) substrate (Sigma-Aldrich) to 4-nitrophenol. This enzymatic assay was carried out as described in the experimental section, and showed that the alkaline phosphatase enzyme converted substrate to product at a rate of roughly 0.002 $\mu\text{mol}/\text{min}$ (1 μmol 4-nitrophenol = 1 absorbance unit) (Figure 8.16). This alkaline phosphatase activity was about 10 fold less active than expected (at optimum conditions, 1 unit of AP converts 1 μmol of 4-nitrophenyl phosphate (substrate) to 4-nitrophenol (product) per minute; 0.02 units of alkaline phosphatase were used), mostly likely due to sub-optimal assay pH. However, this activity was still deemed to be comparable to conditions in cells and sufficient to adequately convert the phosphate prodrug into the parent drug.

The cleavage of prodrug **46** with ALP was carried out by incubation at 37 °C in 10 mM glycine buffer solution (pH 8.6, with 2 mM MgCl₂) over 48 h. HPLC analysis of both compounds (Agilent Technologies 1200 series, with a ZORBAX Eclipse XDB-18 column) isocratically in 50% acetonitrile and 50% water (containing 0.05% TFA) at 1 mL/min showed retention times of 1.565 minutes for **46** and 5.582 for **2** (Figure 8.17). Once these retention times for the compounds were determined, compound **46** (200 µM) was incubated with alkaline phosphatase (1.2 units) in glycine buffer solution for 18 h as previously stated in the experimental section. Subsequently, conversion of compound **46** to compound **2** was monitored via HPLC. It should be noted that 2% DMSO was added to a separate sample and also incubated under the same conditions.

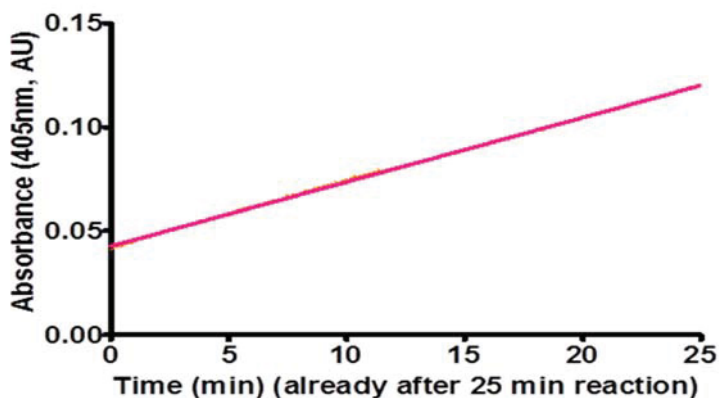


Figure 8.16. Alkaline phosphatase enzymatic assay

This was done because compound **2** is not very soluble in water and could possibly precipitate due to the alkaline phosphatase activity on compound **46**. Incubation of compound **46** with alkaline phosphatase resulted in almost complete conversion to compound **2** due to cleavage of the phosphate group (Figure 8.18).

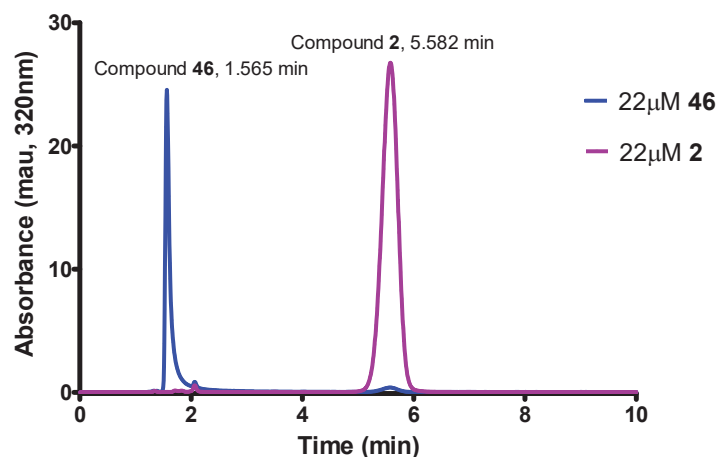


Figure 8.17. HPLC Chromatogram of Compounds **2** and **46**

Addition of 2% DMSO to the reaction solution also produced similar results (Figure 8.19). It should be noted that compound **47** was incubated for 48 h in glycine buffer solution without ALP at 37 °C, minor hydrolysis (5.6%) to form **2** was observed (Data not shown). When **47** was stored at 4 °C at a 20 µM concentration in water, no hydrolysis to form **2** was observed. This suggested that minimal spontaneous hydrolysis occurs with these compounds under these conditions.

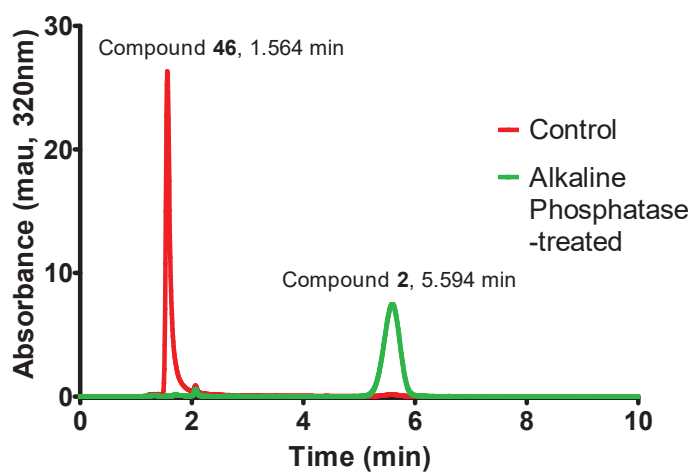


Figure 8.18. HPLC chromatogram of alkaline phosphatase treated compound **46**

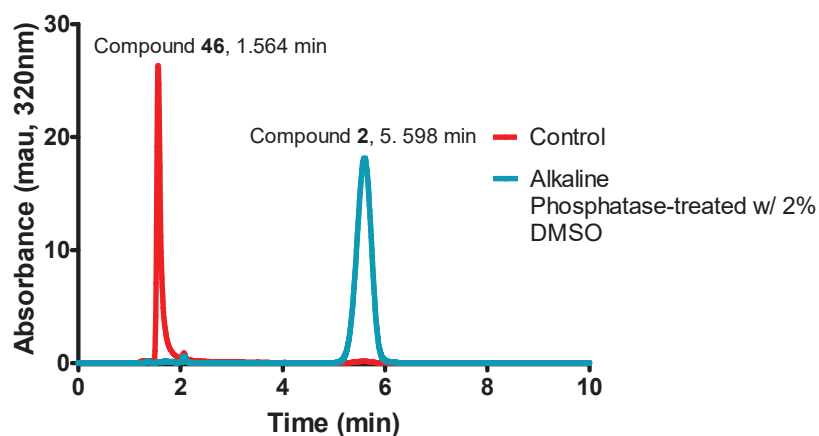


Figure 8.19. HPLC chromatogram of alkaline phosphatase treated compound **46** in 2% DMSO

Subsequently, the cleavage product was assayed against cathepsin L to determine the inhibitory activity. This was compared to the inhibitory activity at 10 μ M (5 minute pre-incubation) of compounds **2** and **47**. Analysis of the cleavage product against cathepsin L showed that incubation of **47** with alkaline phosphatase restored the inhibitory activity against cathepsin L that was seen with treatment of cathepsin L with **2** (Figure 8.20).

Caspase 3 Inhibition Assay

In order to ascertain that thiosemicarbazone inhibitors specifically target cysteine cathepsin proteases, the inhibitory activity of a potent cathepsin L inhibitor from this group of compounds (compound **2**) was determined against caspase 3. Caspases are cysteine aspartyl proteases that play important roles in apoptosis and inflammation. Caspase 3 is one of the downstream effector caspases that are activated by initiator caspases during apoptosis, leading to selective hydrolysis of cellular proteins in the pathways leading to cell death [467].

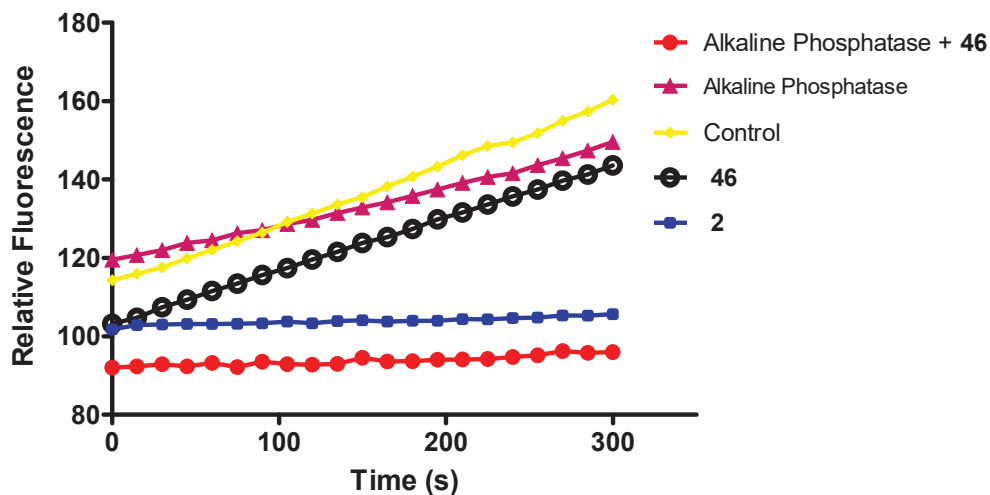


Figure 8.20. Effect of alkaline phosphatase activity on cathepsin L inhibition by **46**

Caspase activity is highly regulated in the cell. Improper caspase activity has been shown to play roles in many severe human diseases, including neuronal crush injury, stroke, heart failure, and neurodegenerative diseases such as Alzheimer's, Parkinson's, and Huntington's diseases are associated with increased activities of caspases [467]. On the other hand, caspase activity is suppressed in cancer, autoimmune diseases and viral infections [467].

Using the fluoregenic assay described earlier, compound **2** was shown to inhibit caspase 3 activity by only 4.5% at 1 μ M, compared with over 90% inhibition of caspase 3 activity by 100 nM of the positive control inhibitor (Ac-DEVD-CHO) (Figure 8.21). This indicates that this compound is inactive against caspase 3 and as such would not cause any significant change in caspase activity in cells.

Inhibition of Cell Invasion and Migration

Cysteine cathepsins have been shown to play a significant role in tumor metastasis and have been shown to be upregulated in various highly metastatic tumors

[327, 468]. Tumor metastasis involves increased cell motility and degradation of extracellular matrices. Therefore, we decided to explore the potency of some of the thiosemicarbazone compounds to reduce invasion and motility of MDA-MB-231 cells, a human breast cancer cell line that has been previously investigated and showed high levels of cathepsin L, invasiveness and motility properties.

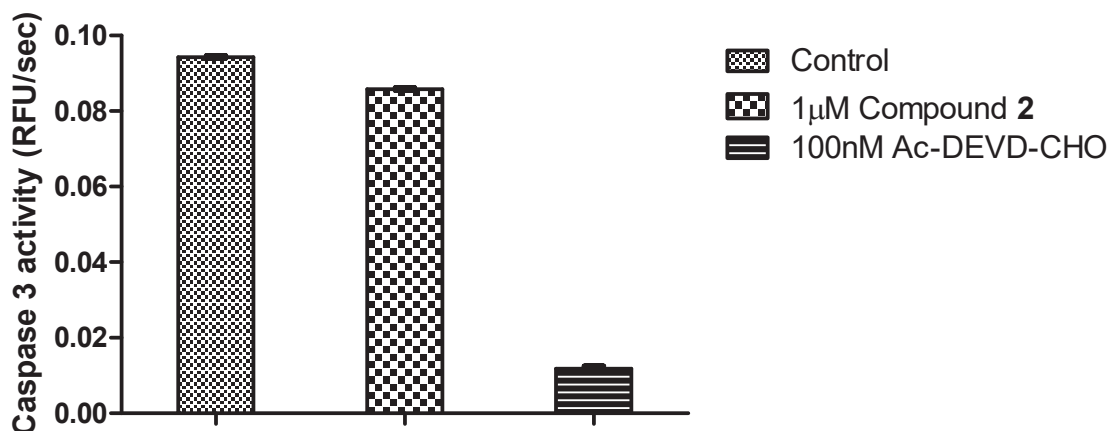


Figure 8.21. Caspase 3 Inhibition Assay

Three benzoyl benzophenone thiosemicarbazone compounds (Compounds **22**, **23** and **28**) were analyzed, and E-64, a nonspecific cysteine protease irreversible inhibitor was used as a positive control to verify the activity of the compounds. E-64 was selected because it is highly selective towards cysteine proteases and not reacting with other enzymes, as well as its ability to inhibit tumor migration and invasion [469, 470].

Invasion and migration assays were carried out using MDA-MB-231 cells that have been harvested with DMEM media supplemented with 10% FBS, as previously described in the experimental section. Final conditions were 50,000 cells per well/insert, 2% DMSO, and 10 or 25 µM of compounds **22**, **23**, **28** and E-64. Samples were incubated for 24 h at 37 °C in 5% CO₂/air environment. After incubation time, media was removed, and the

inner sides of the membranes were cleaned to remove cells that did not invade or migrate. Then, membranes were stained with DiffQuik staining kit with azure and xanthenes dyes. Membranes were air-dried and placed on slides. Manual cell counting was performed using a Zeiss inverted microscope. Slides were placed onto the instrument, and were observed under a 40X objective. Cell that migrated the 8 μ m membrane or cells that invaded the Matrigel® layer have a dark purple shade with a round shape. The purple coloration is due that cytoplasmic matter and nuclei are sensitive to both dyes. The dark color is also easier to follow and distinguish from other particles.

Analysis of the experimental data produced shows that treatment of MDA-MB-231 cells with thiosemicarbazone compounds **22**, **23**, and **28** has significant effects on cell invasion of Matrigel and on cell motility (Figure 8.22). Treatment of cells with 10 μ M of compound **28** caused significant inhibition of cell invasion (67% compared to control) which is similar to the inhibition seen with E-64 treatment. However, at this concentration compounds **22** and **23** have barely any inhibitory effect on cell invasion (Figure 8.21 A). At 25 μ M, all compounds **22**, **23**, and **28** inhibit cell invasion by 30, 65 and 67% respectively (Figure 8.22 B). It should be noted that the inhibitory activity of compound **28** does not seem to increase between 10 and 25 μ M concentrations which is unexpected, as the other compounds and E-64 show a concentration dependent increase in inhibition of MDA-MB-231 cell invasion.

All three compounds also significantly inhibit cell migration at both 10 and 25 μ M concentrations. At 10 μ M, compounds **22**, **23**, and **28** inhibit cell migration by 40, 42 and 25% respectively (Figure 8.21 C). At 25 μ M, the inhibition of migration increases to 75%, 50% and 60 % respectively (Figure 8.22 D).

Overall, all three compounds seem to cause significant inhibition of cell invasion and migration that is comparable to E-64, with moderate increase in inhibitory potency due to increased compound concentration.

Cathepsin L Reversibility Studies

Similar to the results seen with cruzain, thiosemicarbazone compounds were found to be time-dependent inhibitors of cathepsin L based on the progress curve assays and pre-incubation studies. In order to get a more robust understanding of the mode of inhibition, it was necessary to ascertain whether the inhibition of cathepsin L by these compounds is a reversible process. A mixture containing 10 nM cruzain and 5 μ M compound **22** were incubated at 25 °C for four hours. The reaction was initiated by rapid dilution of the mixture (100-fold) with assay buffer containing Z-FR-AMC. Experiment was set up in order to monitor these reactions almost immediately initiation of reaction. Final conditions are 1 nM cruzain, 50 nM of the thiosemicarbazone compound and 10 μ M of Z-FR-AMC substrate. A control experiment with cathepsin L incubated with DMSO vehicle control was carried out simultaneously. The release of AMC over the course of 7500 s was observed, and results presented in Figure 8.23. Observation of the reaction over the course 7500 s showed complete initial inhibition of enzyme activity by both compounds for about the first 1000s. However, there was slow recovery of enzyme activity in the inhibited reactions as observed from the increase in the rate of product release over time (Figure 8.22 inset). Cathepsin L activity for the uninhibited reaction was found to be 1.47 nM/s, compared with 0.26 nM/s for compound **22**. This indicates reversibility of inhibition.

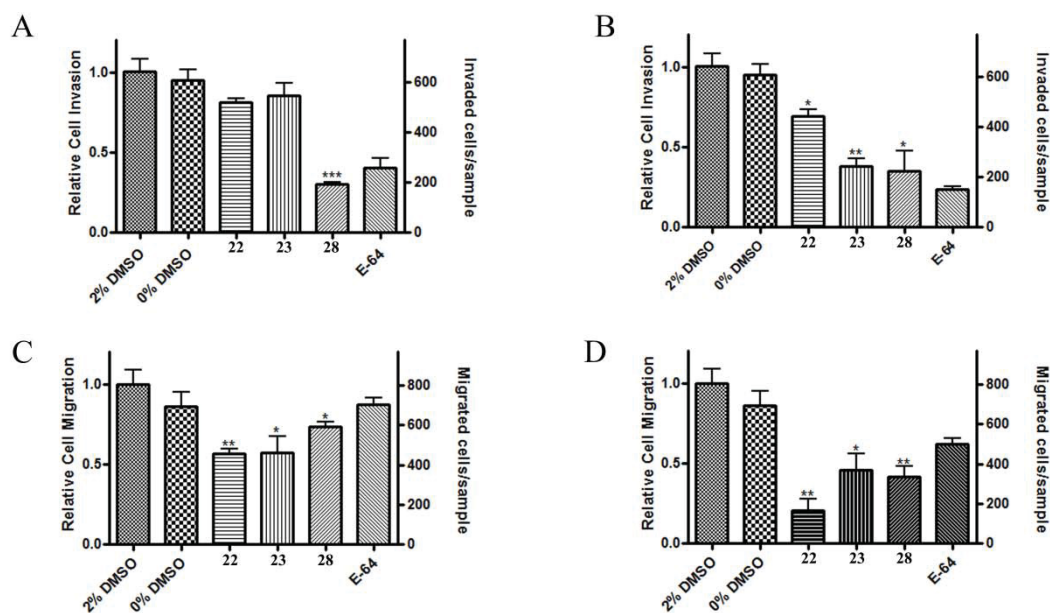


Figure 8.22. MDA-MB-231 invasion and migration data for 10 and 25 μ M of thiosemicarbazone compounds and E-64.

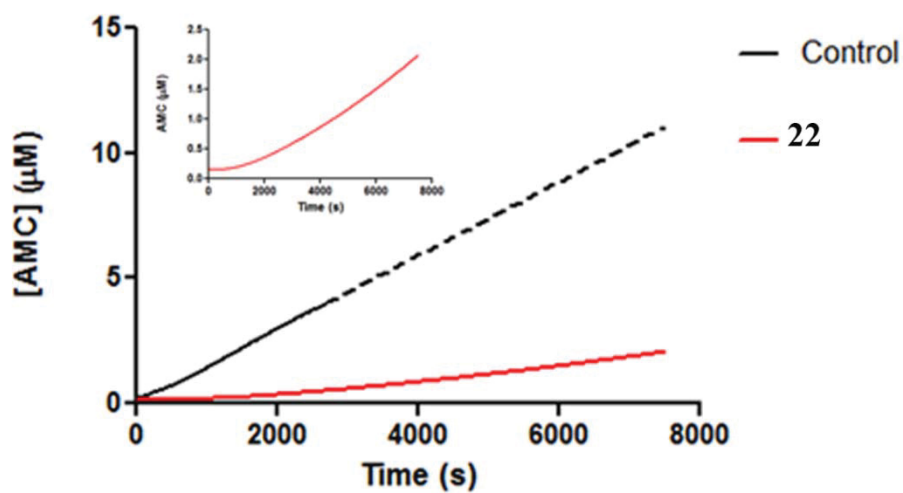


Figure 8.23. Reversibility curves for cathepsin L incubated with compound 22. Inset shows clearer view of slow recovery of enzyme activity over time.

Summary

The research presented in this chapter described assays aimed at analyzing a subset of thiosemicarbazone compounds with various functionalizations as inhibitors of cathepsins L, K, and B. A number of these compounds proved have significant inhibitory activity against cathepsin L and K, with a few showing selectivity towards either cathepsin L or K. However, only compound **1** showed any inhibitory activity towards cathepsin B.

In order to elucidate the mechanism of action of this class of compounds against cathepsin L, advanced kinetic assays were performed using a number of the more potent cathepsin L inhibitors. Based on these assays, these compounds were determined to be tight binding, time dependent and reversible inhibitors of cathepsin L. To further confirm selectivity towards cathepsins, one of the relatively potent inhibitors of cathepsin L (compound **2**) was assayed against caspase 3. It was found that this compound exhibited minimal inhibitory activity against caspase 3.

A number of the more potent thiosemicarbazone compounds analyzed also showed the ability to significantly inhibit invasion and migration of MDA-MB-231 breast cancer cells. Inhibition of invasion and migration suggests that these compounds may have some anti-metastatic properties.

Finally, analysis of a phosphate prodrug (compound **46**) of one of the promising cathepsin L inhibitors (compound **2**) was conducted. This compound was derivatized so as to improve its aqueous solubility in order to position it as a viable therapeutic candidate. Results from cathepsin L inhibition assays showed that the phosphate prodrug did not have significant inhibitory activity against cathepsin L. However, this compound

was also shown to be readily cleaved by alkaline phosphatase to release the parent drug, which led to restoration of the inhibitory activity towards cathepsin L.

CHAPTER NINE

Conclusions

The research presented in this dissertation involved pre-clinical analyses and evaluation of a number of small molecule compounds as possible therapeutic candidates targeting tumor vasculature and cysteine proteases using various biochemical and molecular biology techniques.

Vascular Disrupting Agents

VDAs, in contrast to AIAs, selectively target the established tumor vasculature of larger solid tumors. VDAs cause rapid breakdown of the tumor vascular network leading to reduction in blood flow and subsequent tumor necrosis. Amongst the most promising of VDAs are the small molecule microtubule-targeting agents which increase microtubule depolymerization in ECs as a means of inducing tumor vascular dysfunction. However, the number of drug candidates is still relatively limited, some compounds suffer from severe side effects, and VDAs are yet to be FDA approved for cancer therapy. Therefore, it is important to continue to make progress in this field by discovering, characterizing and evaluating new compounds.

In this study, the indole compounds OXi8006 and its phosphate prodrug OXi8007 were evaluated as prospective VDAs. These analyses were done in vitro (using activated HUVECs as a model for tumor vasculature) and in vivo (using MDA-MB-231 luc tumor xenograft models). Results presented show that OXi8006 treatment of activated

endothelial cells resulted in rapid disruption of the microtubule network, increase in myosin light chain phosphorylation along with increased actin stress fiber formation, and increased phosphorylation of FAK leading to increased focal adhesion formation. In addition, OXi8006 treatment also leads to increased phosphorylation and inactivation of cofilin by LIMK, also contributing to stress fiber formation and increase in EC contractility. This initial increase in contractility was eventually followed by resolution of cellular contractility as the cells begin to shrink, round up, undergo membrane blebbing, and eventually detach from the extracellular matrix. Furthermore, OXi8006-induced tubulin depolymerization and resulting EC contractility is mediated via activation of the RhoA/ROCK pathway. It was also ascertained that the link between OXi8006-induced microtubule disruption and activation of the RhoA/ROCK signaling pathway is the activation of a specific microtubule associated and RhoA binding guanine-nucleotide exchange factor, GEF-H1. Analysis of another microtubule associated exchange OXi8006 and OXi8007 treatment also led to significant cell cycle arrest at G2/M in HUVECs, suggesting antimitotic effects of these compounds. The results obtained from an annexin V/microscopy experiment showed that OXi8006 treatment led to increased annexin V binding by HUVECs, suggesting that this compound may induce significant apoptosis in these cells, albeit at an extended time period compared to the early signaling and morphological changes.

In vivo results indicated that a single dose of OXi8007 (350 mg/kg) significantly decreased blood flow in a cohort of mice bearing xenograft tumors of luciferase-transfected human triple negative breast cancer (MDA-MB-231-luc) assessed by BLI. This dose was well tolerated and led to rapid and significant decrease in tumor

vasculature within 6 h, albeit with some recovery of signal at the 24 h time point.

However, this recovery was significantly less than what was observed with CA4P treatment, a VDA in human clinical trials.

All these results taken together suggest that OXi8006/7 exerts strong vascular disrupting activities in vitro and selectively impairs tumor blood perfusion in vivo, thus positioning this compound as a promising pre-clinical candidate for antivasular tumor treatment.

Cysteine Protease Inhibitors

Cysteine proteases are ubiquitous enzymes that play numerous biological roles. These proteases have been shown to be upregulated in various cancers and have been implicated to play crucial roles in tumor growth and metastasis (Figure 9.1). Cysteine proteases also play important roles in the pathogenesis and disease progression of numerous parasitic ailments. This presents these enzymes as a viable target for therapeutic development.

The research presented in this study involved the evaluation of small molecule compounds with a thiosemicarbazone functional group as inhibitors of four different cysteine proteases; cathepsin L, cathepsin K, cathepsin B, and cruzain.

A subset containing 46 compounds (part of a larger library of thiosemicarbazone compounds synthesized by the Pinney laboratory) were assayed to determine their inhibitory capability against cathepsins L, K, and B. A number of these compounds were potent inhibitors of cathepsin L (Figure 8.7) and cathepsin K (Figure 8.8), with IC₅₀ values less than 100 nM. Furthermore, a few of these compounds showed some measure of selectivity against either cathepsin L or K (Figure 8.9). Of the 46 compounds analyzed,

only one showed any measure of inhibitory activity against cathepsin B. The likely reason for this is the presence of an occluding loop at the active site cavity of cathepsin B which might prevent association of these compounds with the active site. In addition, one of the lead thiosemicarbazone compounds showed minimal activity against caspase 3.

Subsequently, some of the more potent inhibitors of cathepsin L were subjected to *in vitro* analyses to determine the mechanisms of inhibition and evaluate their performance and efficacy. Kinetic analysis was used to investigate the mechanism and mode of inhibition of these compounds. The results show that these compounds were time-dependent/slow-binding, reversible, and competitive inhibitors of the fluorogenic substrate of cathepsin L. Also, analysis of the results via the Morrison quadratic equation suggested either a tight binding interaction between the compounds and the enzyme or the formation of a transient covalent intermediate. However, the observed interaction energies obtained from the molecular modeling studies were somewhat lower than what would be expected for a tight binding interaction, which suggests a covalent interaction as the more likely mechanism of inhibition. Furthermore, the results suggested that the inhibition occurred via one of two mechanisms; a simple reversible inhibition or a more complex two-step mechanism of inhibition. Also, some of the potent cathepsin L inhibitors were shown to significantly inhibit invasion and migration of the breast cancer MDA-MB-231 cell line, suggesting the promise of these compounds as anti-metastatic agents. In addition, a derivative of compound **2** (the phosphate prodrug compound **47**) was assayed to determine its water solubility, its inhibitory activity against cathepsin L, how efficiently it could be cleaved by alkaline phosphatase, and the inhibitory activity of the cleavage product against cathepsin L. It was determined that this compound was very

soluble in aqueous conditions and showed minimal inhibitory activity against cathepsin L. Furthermore, the compound proved to be a good substrate for alkaline phosphatase, and the product of the alkaline phosphatase reaction had significantly increased activity against cathepsin L compared to the activity of **47**, and similar to the activity of **2**.

A number of the compounds assayed against the cysteine cathepsins were also assayed for their inhibitory activity against cruzain. As with cathepsins L and K, a number of compounds were found to be potent inhibitors of cruzain (Figure 7.6). Further kinetic analyses also showed these compounds to be competitive, reversible, time-dependent inhibitors of recombinant cruzain. As with the cysteine cathepsins, the suggested mechanisms of inhibition of cruzain by this series of compounds is via either a simple reversible slow binding or via a more complex two step enzyme isomerization mechanism. Furthermore, these suggested mechanisms are most likely to involve the formation of a transient covalent bond between the thiocarbonyl carbon and the sulfur of the Cys-25 at the active site.

This suggested mechanism is supported by advanced kinetic studies with cruzain and cathepsin L using a number of the more potent inhibitors of these enzymes, as well as molecular docking using the aforementioned inhibitors and cruzain. Therefore, it is reasonable to assume that the presence of the thiosemicarbazone moiety in these molecules is vital for their inhibitory potency.

These preliminary studies have contributed to understanding the characteristics of thiosemicarbazones as potential anticancer and/or anti-Chagas' disease agents. The proposed mode of inhibition based on these studies involves a transient covalent modification due to the interactions between the thiocarbonyl carbon of the

thiosemicarbazone moiety and the thiolate group of cysteine 25, one of the catalytic triad residues and a key residue in the activity of these cysteine proteases (Figure 9.2).

Following the formation of a transient covalent bond, the mechanism may proceed as a simple slow binding reversible inhibition to recover the active enzyme. However, there is a distinct possibility that thiocarbamoylated cruzain, cathepsin L or cathepsin K is formed followed by slow hydrolysis. Thus, a future direction for this study would be to confirm this using a technique such as mass spectrometry.

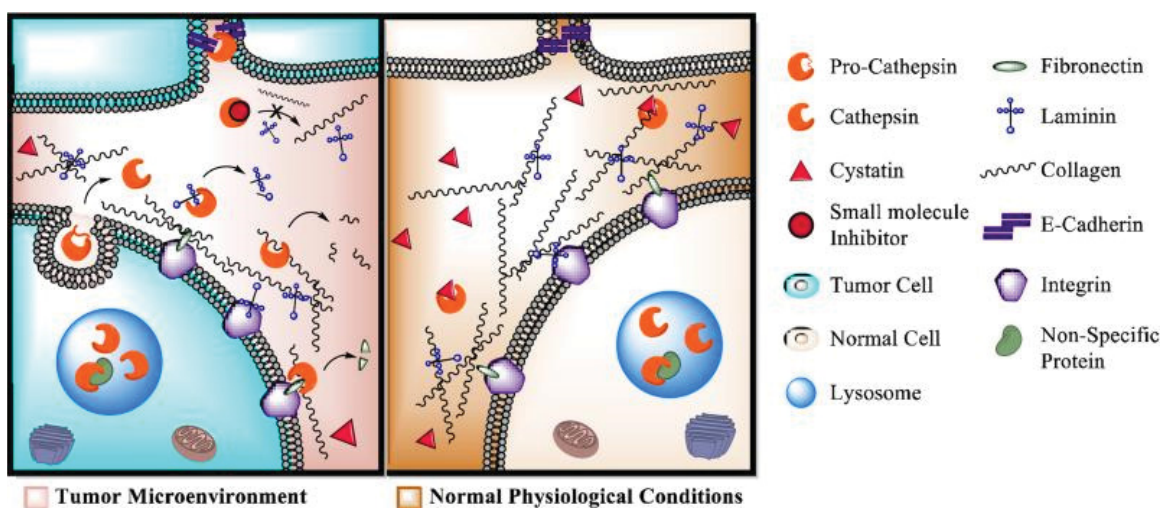


Figure 9.1. Overview of roles of cysteine cathepsins in invasion and metastasis. Upregulation of certain cathepsins in the tumor microenvironment along with downregulation of endogenous inhibitors, increase of proteolytic capability of cathepsins due to extracellular acidification, and extracellular secretion of cathepsins contributes to increased invasion and metastasis of malignant tumors. Small-molecule cathepsin inhibitors have the potential to inhibit the invasive nature of malignant cells [455].

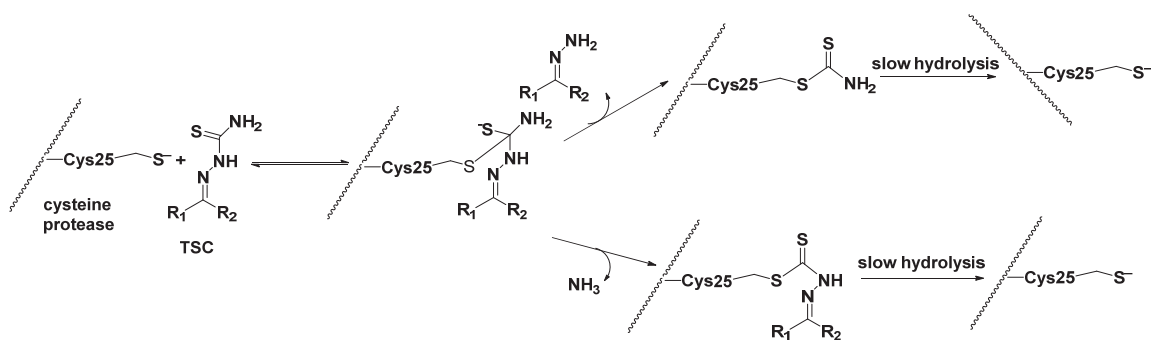


Figure 9.2. Proposed mechanism for thiosemicarbazone inhibition of cysteine proteases

APPENDICES

APPENDIX A

Immunofluorescence Microscopy Experiments

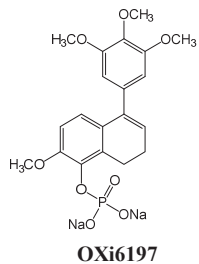
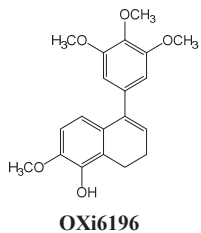
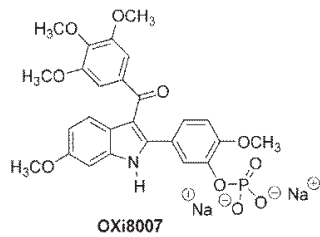
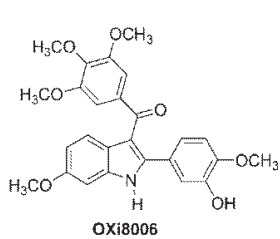
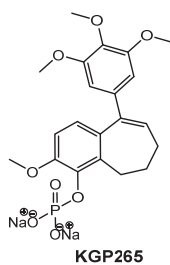
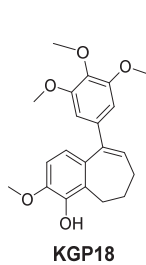
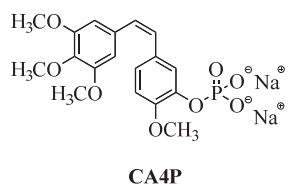
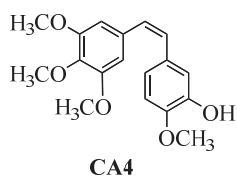


Figure A1. VDA Compound Structures. KGP18 and KGP265 syntheses in [471]. OXi6196 and OXi6197 syntheses in [176]

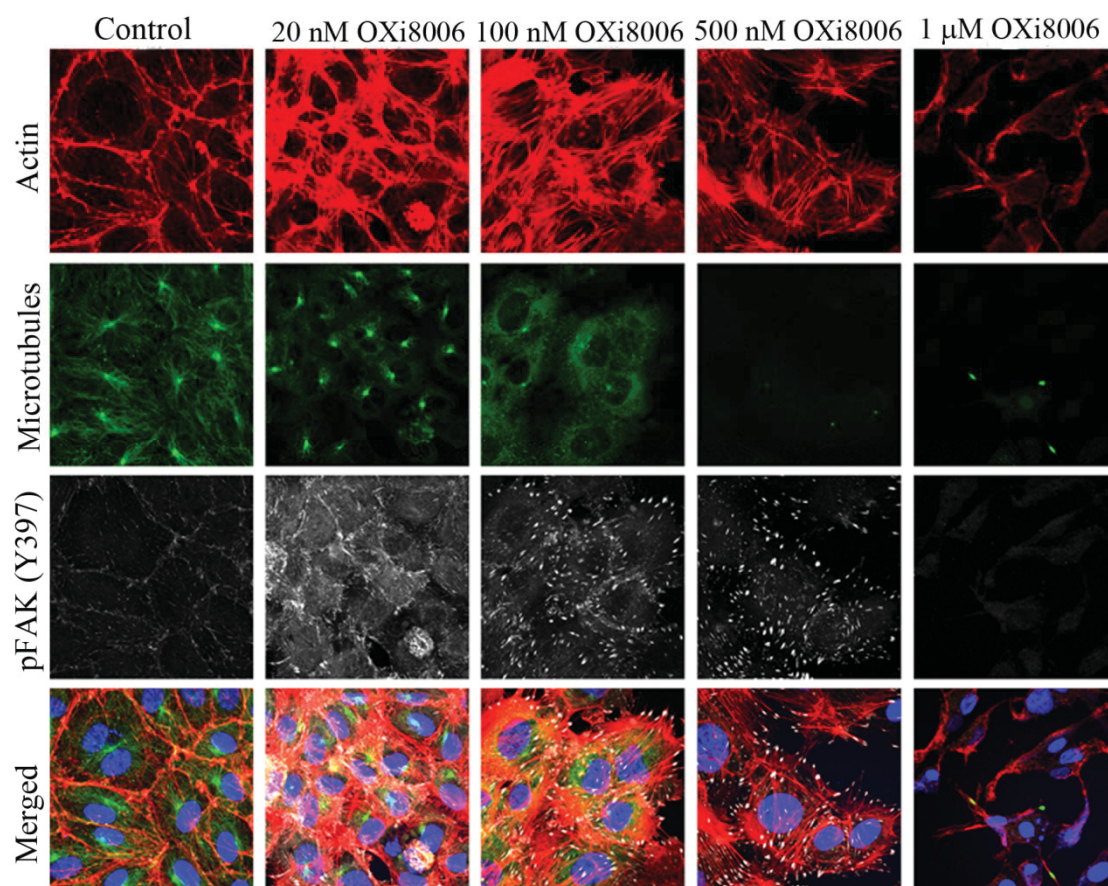


Figure A2. Effects of OXi8006 treatment on confluent monolayers of HUVECs.

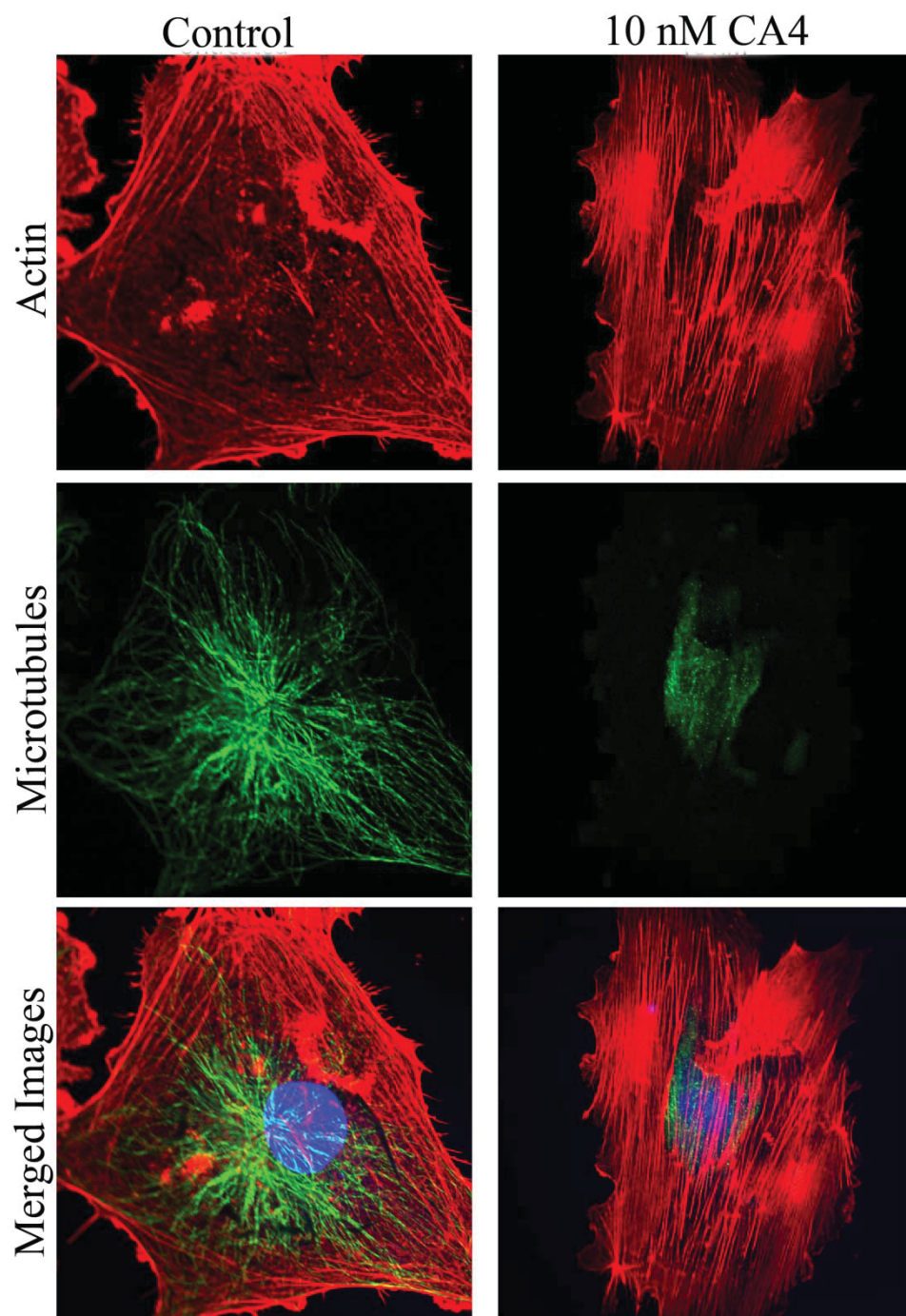


Figure A3. Effects of CA4 treatment on HUVECs

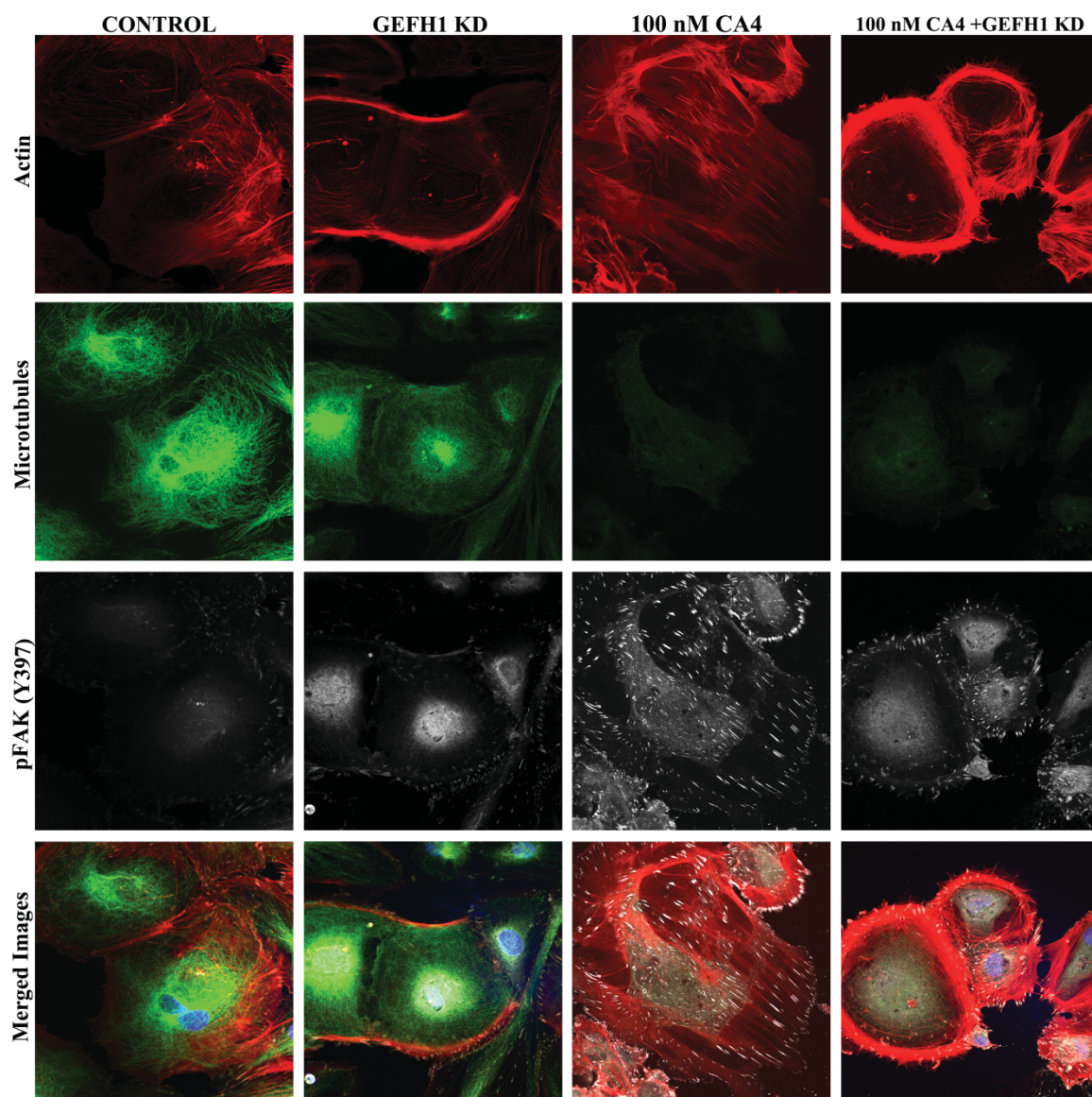


Figure A4. Effects of GEFH1 knockdown on CA4 treated HUVECs

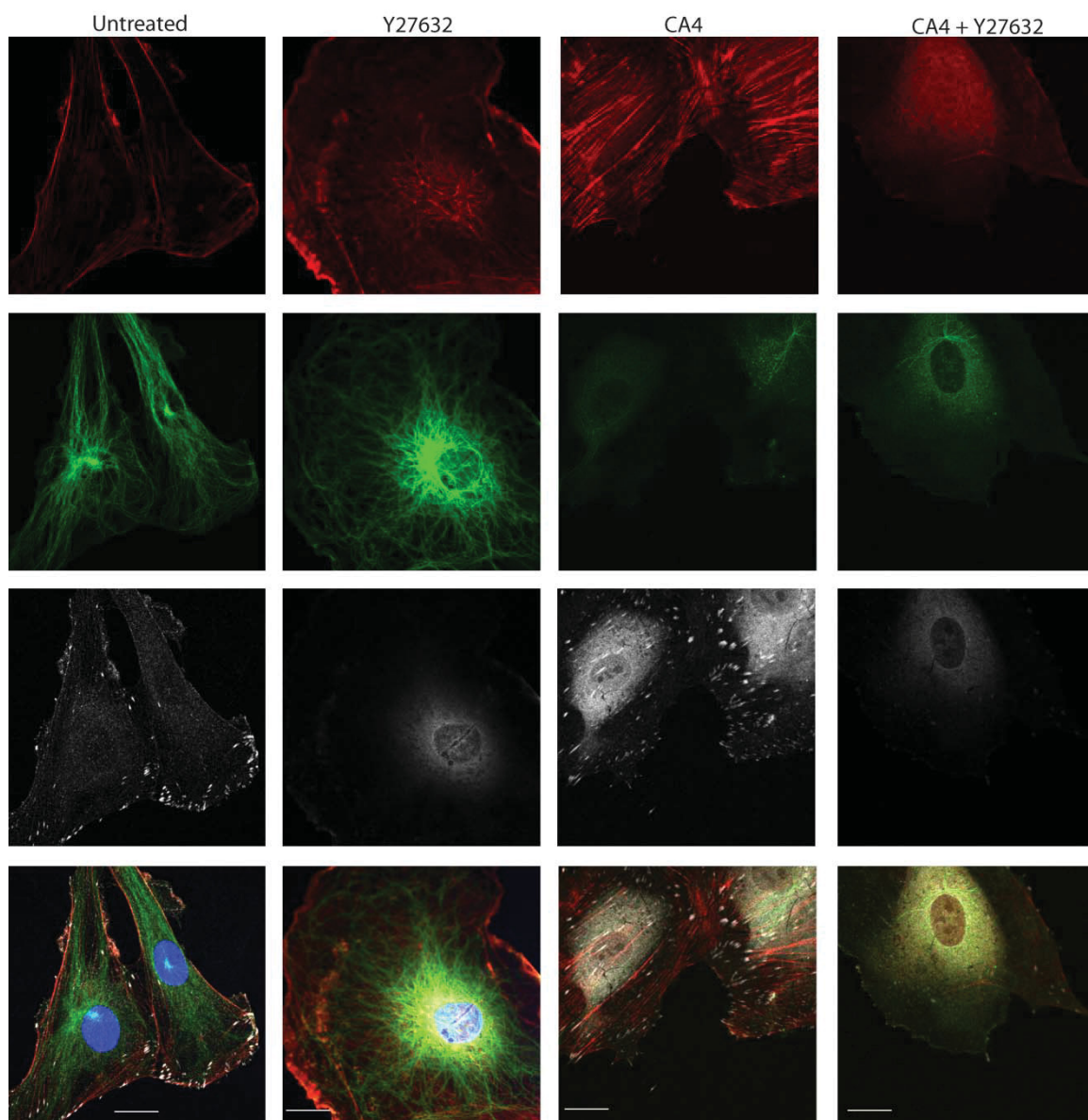


Figure A5. Inhibition of ROCK activity via pretreatment with a ROCK inhibitor (Y27632, 10 μ M, 30 min), abrogates CA4 induced effects in HUVECs

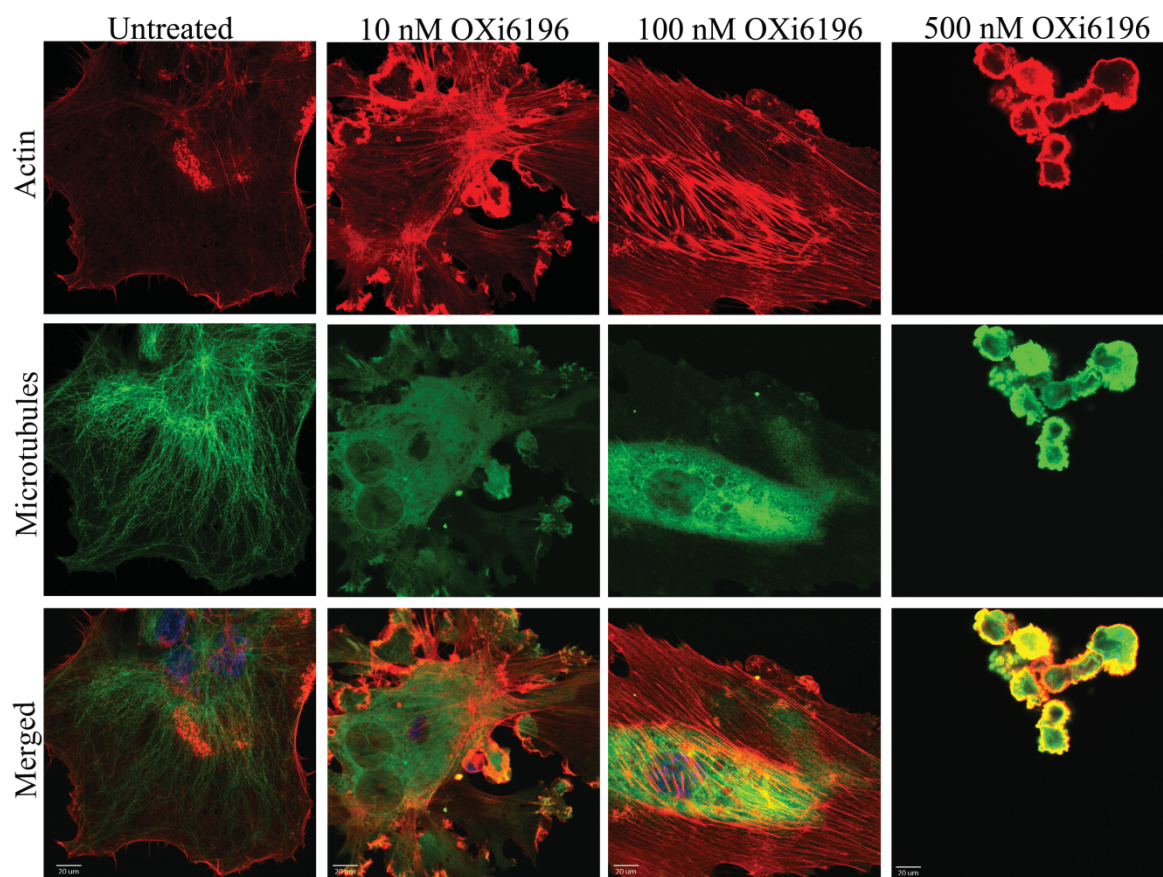


Figure A6. Effects of OXi6196 treatment on HUVECs

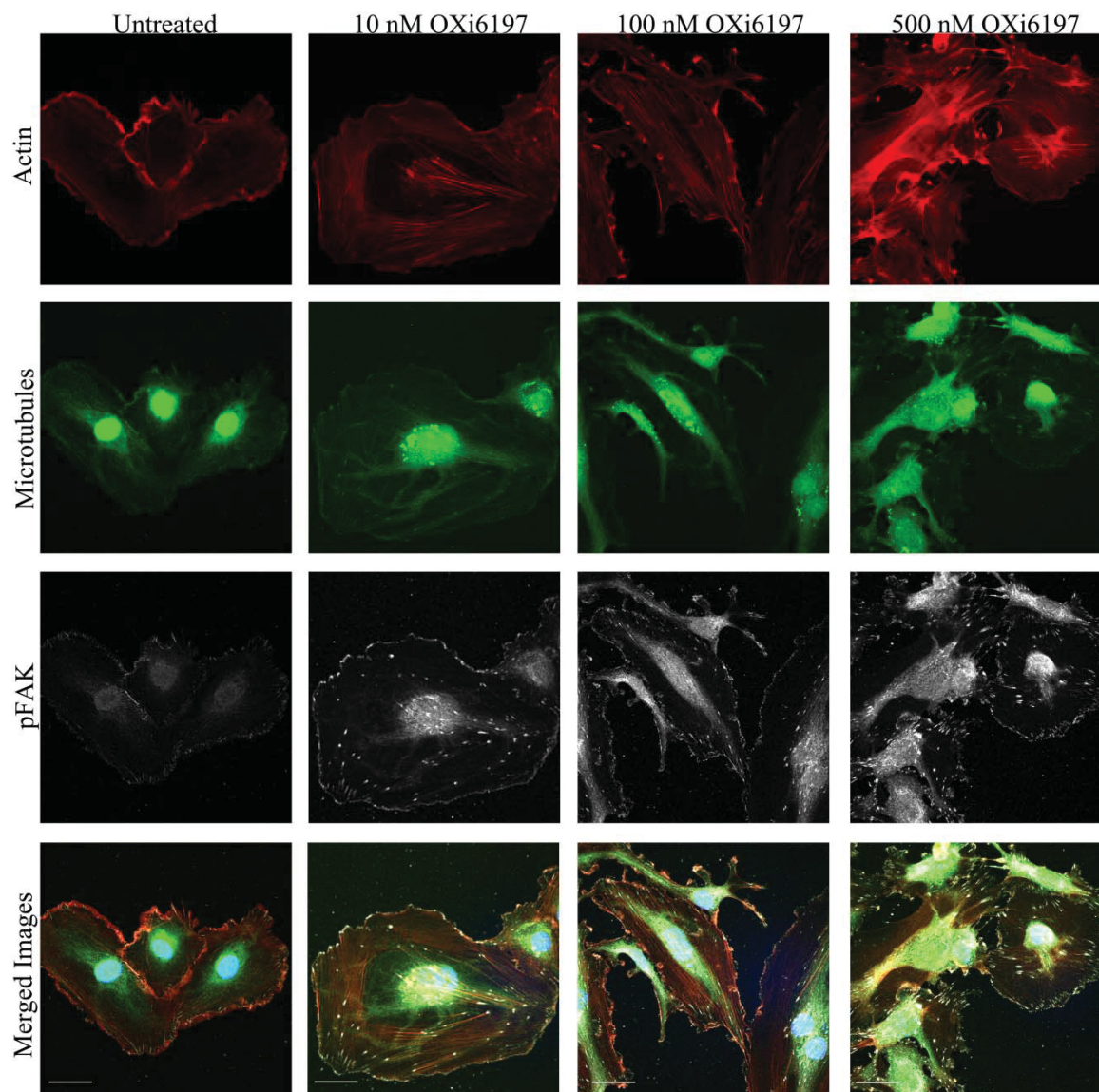


Figure A7. Effects of OXi6197 treatment on HUVECs

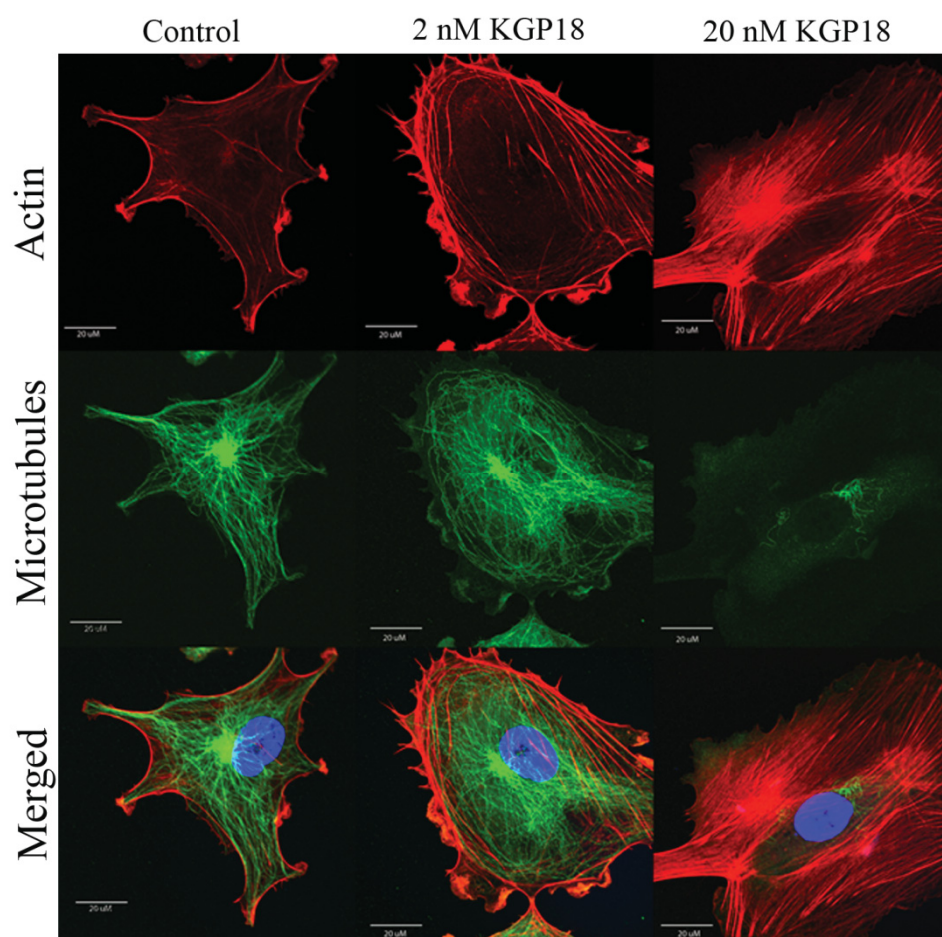


Figure A8. Effects of KGP18 treatment on HUVECs

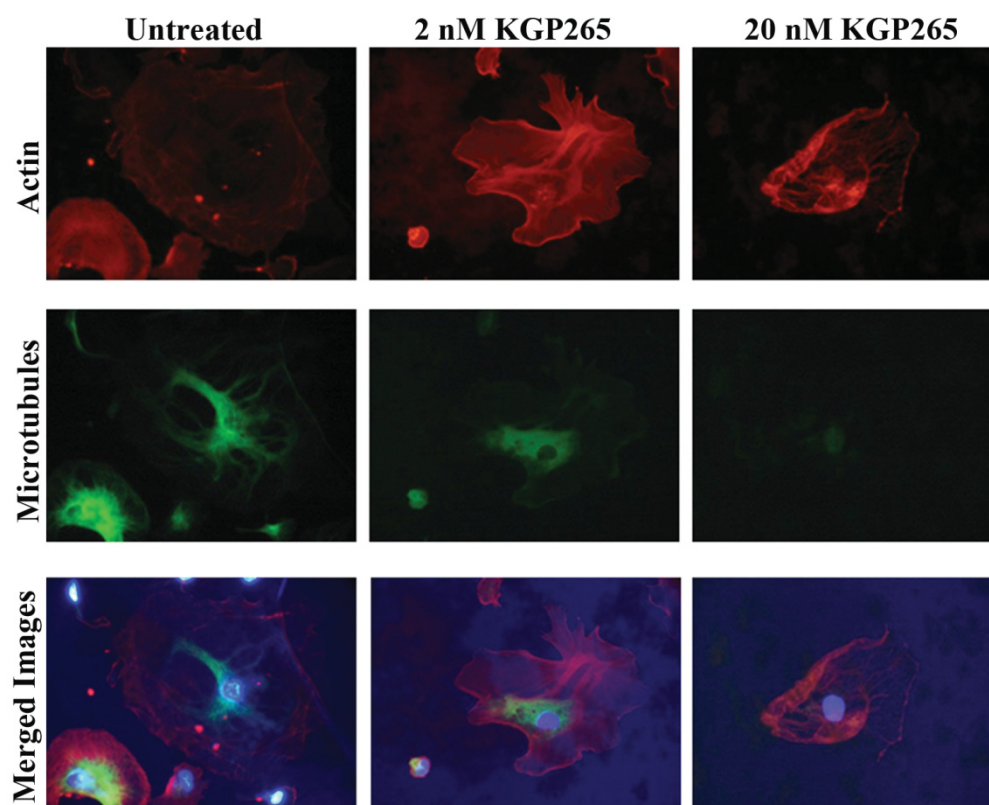


Figure A9. Effects of KGP265 treatment on HUVECs

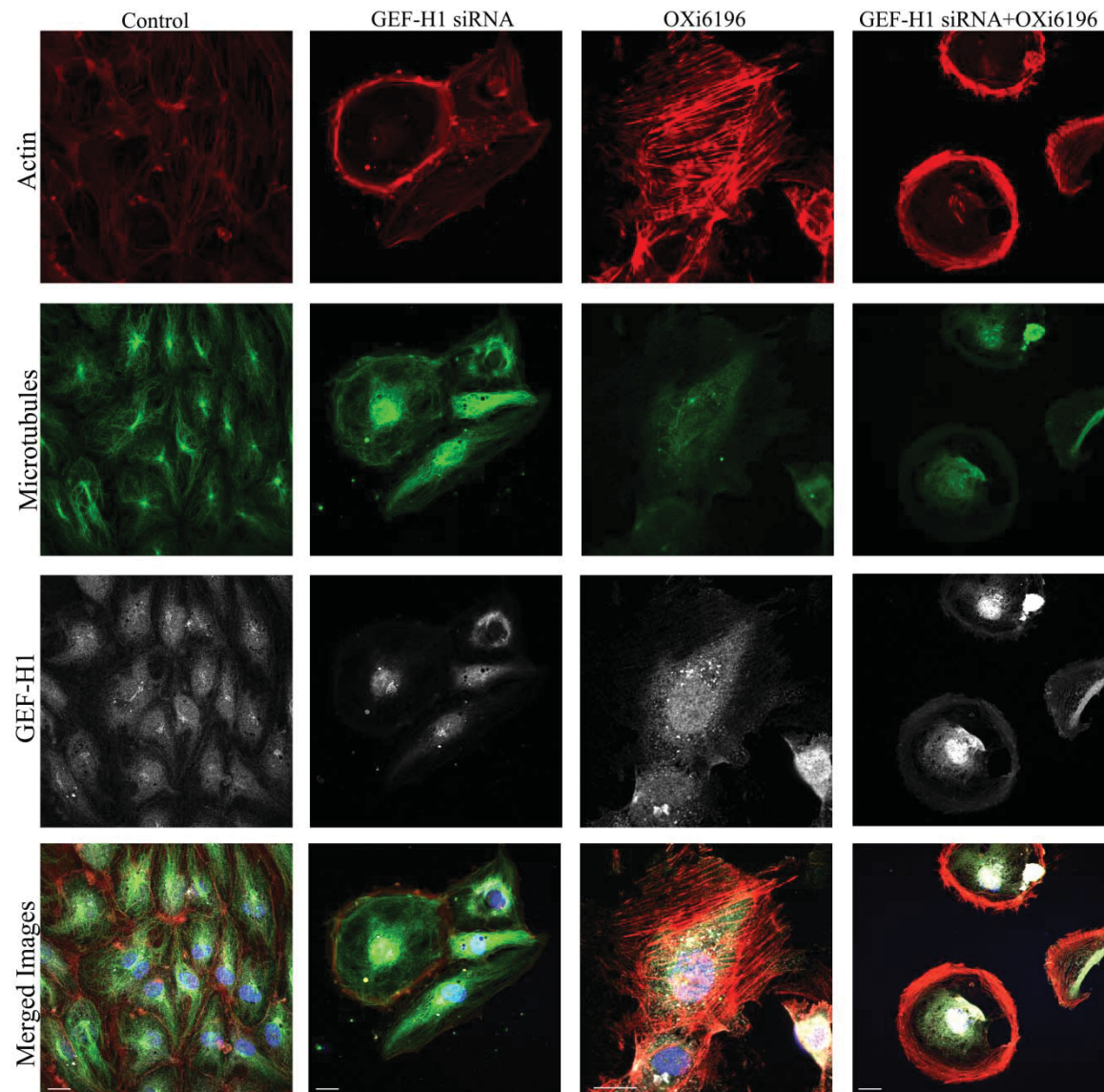


Figure A10. Effects of GEFH1 knockdown on OXi6196 treated HUVECs

APPENDIX B

Wound Assays

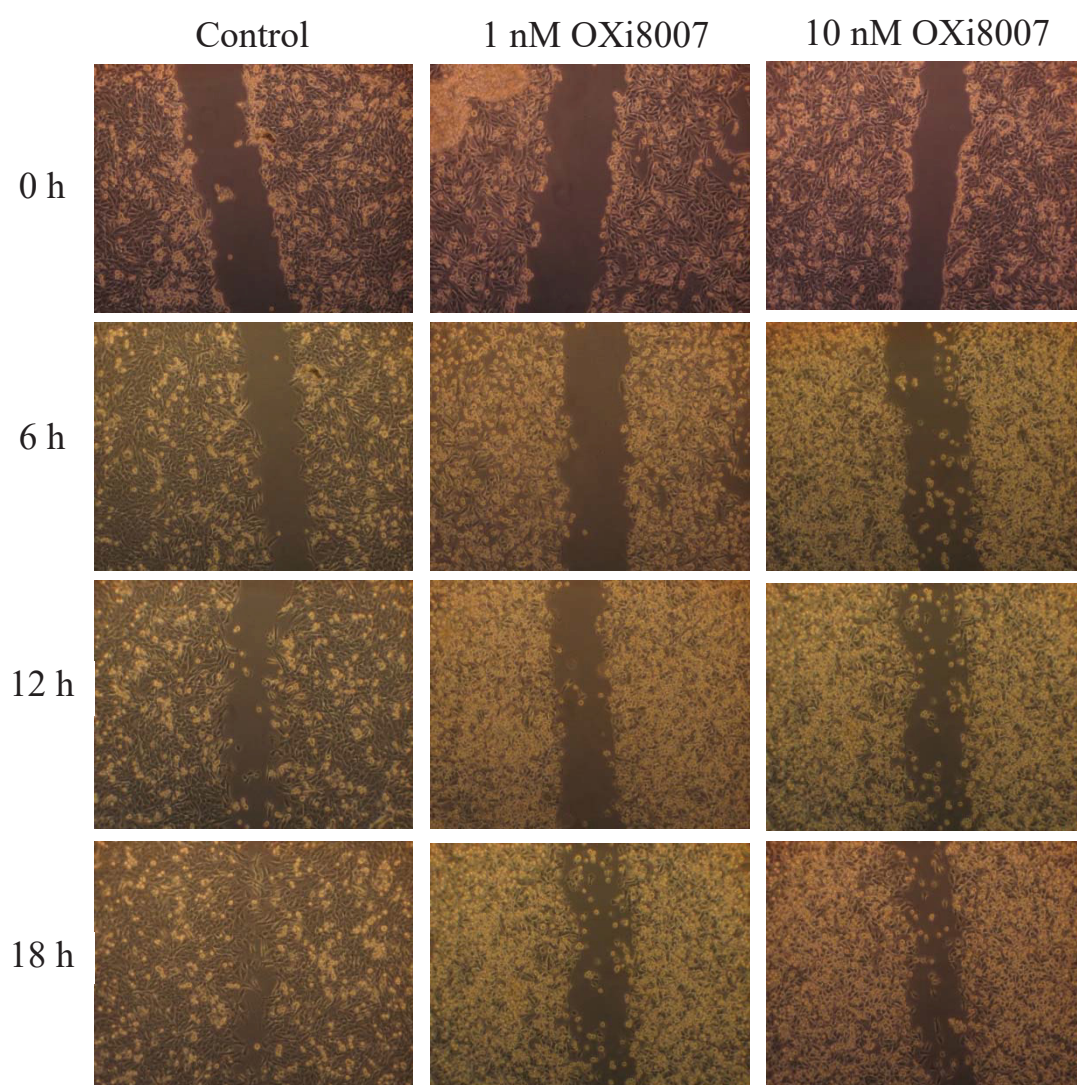


Figure B1. Representative phase contrast images showing effects of OXi8007 treatment on wound closure in MDA-MB-231 monolayers

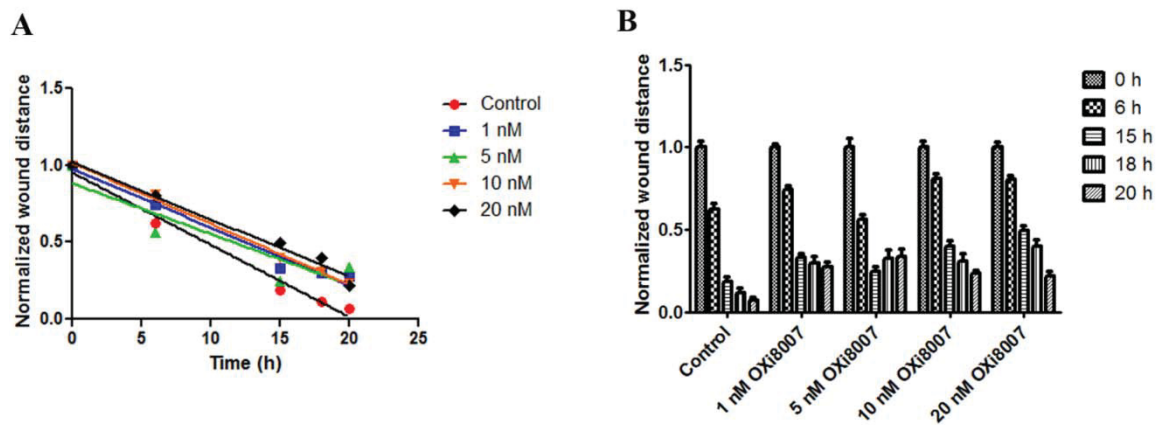


Figure B2. Quantification of effects of OXi8007 on MDA-MB-231 wound closure. A) Graphical representation of rates of MDA-MB-231 wound closure due to different OXi8007 concentrations. B) Bar graphs showing MDA-MB-231 wound closure over time at different OXi8007 concentrations.

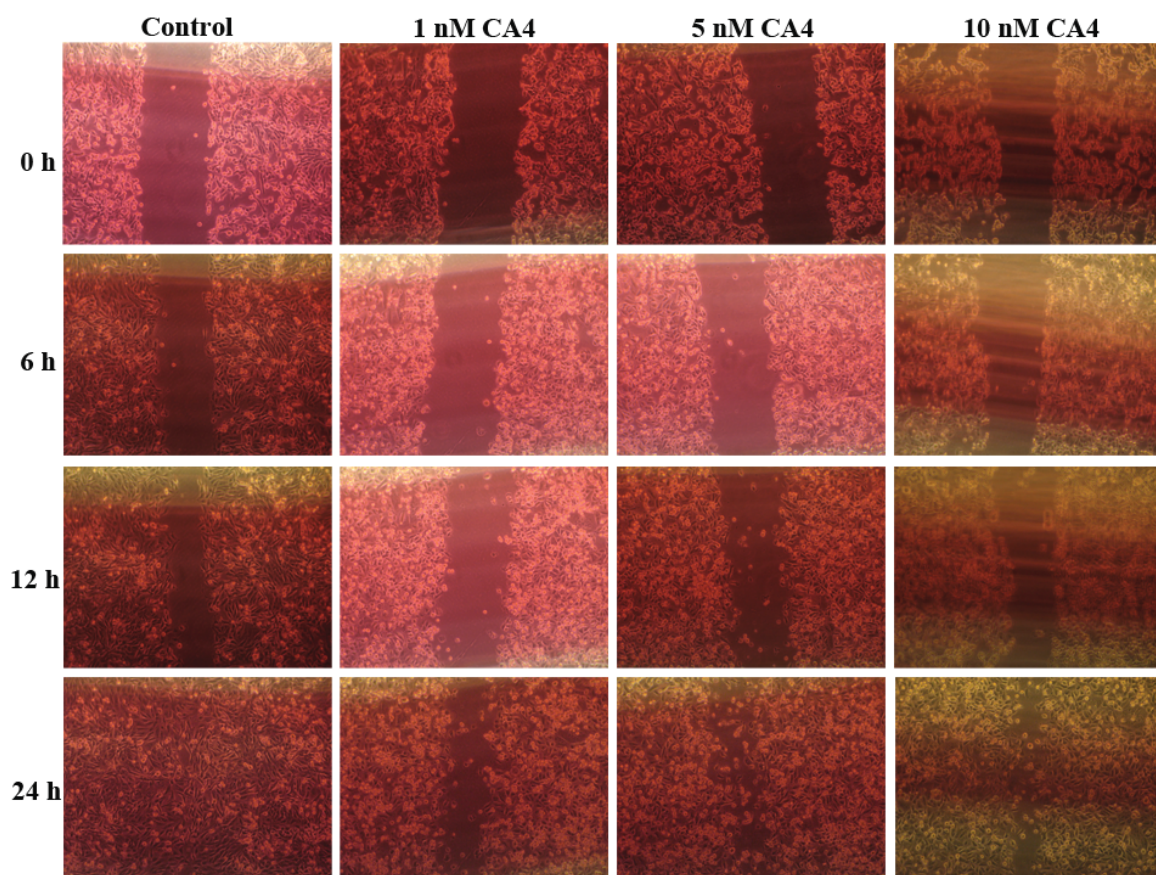


Figure B3. Representative phase contrast images showing effects of CA4 treatment on wound closure in MDA-MB-231 monolayers

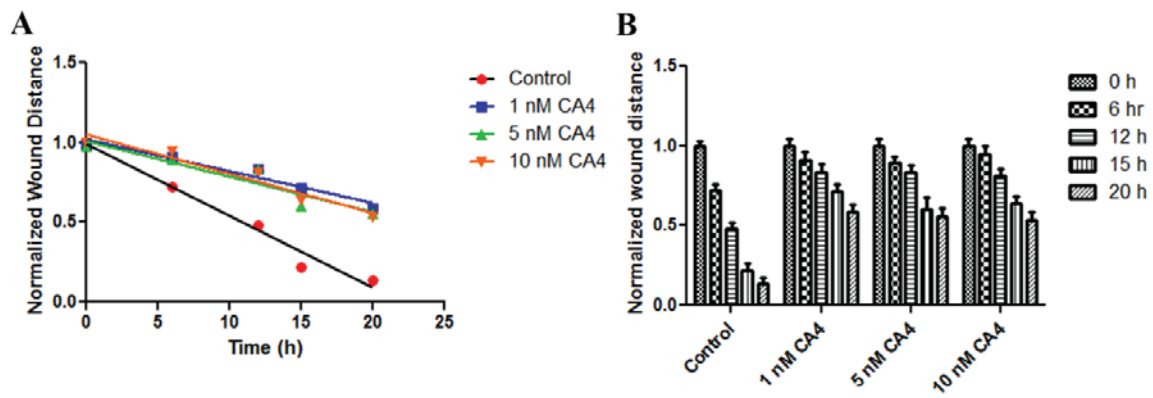


Figure B4. Quantification of effects of CA4 on MDA-MB-231 wound closure. A) Graphical representation of rates of MDA-MB-231 wound closure due to different CA4 concentrations. B) Bar graphs showing MDA-MB-231 wound closure over time at different CA4 concentrations.

REFERENCES

- [1] M.J. Maceilag, Chemical properties of antibacterials and their uniqueness in: T.J. Dougherty, M.J. Pucci (Eds.) *Antibiotic Discovery and Development* 2012, pp. 801-802.
- [2] D.F. Veber, S.R. Johnson, H.Y. Cheng, B.R. Smith, K.W. Ward, K.D. Kopple, Molecular properties that influence the oral bioavailability of drug candidates, *J Med Chem*, 45 (2002) 2615-2623.
- [3] C.A. Lipinski, Lead- and drug-like compounds: the rule-of-five revolution, *Drug Discov Today Technol*, 1 (2004) 337-341.
- [4] M.E. Bunnage, Getting pharmaceutical R&D back on target, *Nat Chem Biol*, 7 (2011) 335-339.
- [5] J.D. Benson, Y.N. Chen, S.A. Cornell-Kennon, M. Dorsch, S. Kim, M. Leszczyniecka, W.R. Sellers, C. Lengauer, Validating cancer drug targets, *Nature*, 441 (2006) 451-456.
- [6] K. Quon, P.D. Kassner, RNA interference screening for the discovery of oncology targets, *Expert Opin Ther Targets*, 13 (2009) 1027-1035.
- [7] R. Brough, J.R. Frankum, S. Costa-Cabral, C.J. Lord, A. Ashworth, Searching for synthetic lethality in cancer, *Curr Opin Genet Dev*, 21 (2011) 34-41.
- [8] A.P. Russ, S. Lampel, The druggable genome: an update, *Drug Discov Today*, 10 (2005) 1607-1610.
- [9] S.H. Kaufmann, Paul Ehrlich: founder of chemotherapy, *Nat Rev Drug Discov*, 7 (2008) 373.
- [10] B.K. Shoichet, Screening in a spirit haunted world, *Drug Discov Today*, 11 (2006) 607-615.
- [11] N. Thorne, D.S. Auld, J. Inglese, Apparent activity in high-throughput screening: origins of compound-dependent assay interference, *Curr Opin Chem Biol*, 14 (2010) 315-324.
- [12] P.J. Hajduk, J. Greer, A decade of fragment-based drug design: strategic advances and lessons learned, *Nat Rev Drug Discov*, 6 (2007) 211-219.
- [13] J.A. Beutler, Natural Products as a Foundation for Drug Discovery, *Current protocols in pharmacology / editorial board*, S.J. Enna (editor-in-chief) ... [et al.], 46 (2009) 9.11.11-19.11.21.

- [14] A.L. Harvey, R. Edrada-Ebel, R.J. Quinn, The re-emergence of natural products for drug discovery in the genomics era, *Nat Rev Drug Discov*, 14 (2015) 111-129.
- [15] E. Rajesh, L.S. Sankari, L. Malathi, J.R. Krupaa, Naturally occurring products in cancer therapy, *Journal of Pharmacy & Bioallied Sciences*, 7 (2015) S181-S183.
- [16] J. Mann, Natural products in cancer chemotherapy: past, present and future, *Nature reviews. Cancer*, 2 (2002) 143-148.
- [17] P. Ripphausen, B. Nisius, L. Peltason, J. Bajorath, Quo vadis, virtual screening? A comprehensive survey of prospective applications, *J Med Chem*, 53 (2010) 8461-8467.
- [18] S. Ekins, J.D. Honeycutt, J.T. Metz, Evolving molecules using multi-objective optimization: applying to ADME/Tox, *Drug Discov Today*, 15 (2010) 451-460.
- [19] J.S. de Bono, A. Ashworth, Translating cancer research into targeted therapeutics, *Nature*, 467 (2010) 543-549.
- [20] T.A. Yap, P. Workman, Exploiting the cancer genome: strategies for the discovery and clinical development of targeted molecular therapeutics, *Annu Rev Pharmacol Toxicol*, 52 (2012) 549-573.
- [21] S.I. Hay, C.A. Guerra, A.J. Tatem, P.M. Atkinson, R.W. Snow, Tropical infectious diseases: Urbanization, malaria transmission and disease burden in Africa, *Nature Reviews Microbiology*, 3 (2005) 81-90.
- [22] A.R. Renslo, J.H. McKerrow, Drug discovery and development for neglected parasitic diseases, *Nat Chem Biol*, 2 (2006) 701-710.
- [23] C.C. Wang, Validating targets for antiparasite chemotherapy, *Parasitology*, 114 Suppl (1997) S31-44.
- [24] R. Pink, A. Hudson, M.-A. Mouries, M. Bendig, Opportunities and Challenges in Antiparasitic Drug Discovery, *Nat Rev Drug Discov*, 4 (2005) 727-740.
- [25] T. Mackey, A policy analysis of funding for ambitious interventional gerontology: the possibility of rejuvenation research at the National Institute on Aging, *Rejuvenation Res*, 7 (2004) 211-222.
- [26] M. Bogyo, S. Verhelst, V. Bellingard-Dubouchaud, S. Toba, D. Greenbaum, Selective targeting of lysosomal cysteine proteases with radiolabeled electrophilic substrate analogs, *Chem Biol*, 7 (2000) 27-38.
- [27] Z.A. Knight, K.M. Shokat, Features of selective kinase inhibitors, *Chem Biol*, 12 (2005) 621-637.

- [28] M.B. Hadimani, M.T. MacDonough, A. Ghatak, T.E. Strecker, R. Lopez, M. Sriram, B.L. Nguyen, J.J. Hall, R.J. Kessler, A.R. Shirali, L. Liu, C.M. Garner, G.R. Pettit, H. Ernest, D.J. Chaplin, R.P. Mason, M.L. Trawick, K.G. Pinney, Synthesis of a 2-Aryl-3-aryl Indole Salt (OXi8007) Resembling Combretastatin A-4 with Application as a Vascular Disrupting Agent, *J. Nat. Prod.*, 76 (2013) 1668-1678.
- [29] M.T. MacDonough, T.E. Strecker, E. Hamel, J.J. Hall, D.J. Chaplin, M.L. Trawick, K.G. Pinney, Synthesis and biological evaluation of indole-based, anti-cancer agents inspired by the vascular disrupting agent 2-(3'-hydroxy-4'-methoxyphenyl)-3-(3",4",5"-trimethoxybenzoyl)-6-methoxyindole (OXi8006), *Bioorgan Med Chem*, 21 (2013) 6831-6843.
- [30] J. Denekamp, Endothelial cell proliferation as a novel approach to targeting tumour therapy, *Br J Cancer*, 45 (1982) 136-139.
- [31] J. Denekamp, Inadequate vasculature in solid tumours: consequences for cancer research strategies, *BJR Suppl*, 24 (1992) 111-117.
- [32] D. Hanahan, J. Folkman, Patterns and emerging mechanisms of the angiogenic switch during tumorigenesis, *Cell*, 86 (1996) 353-364.
- [33] P. Carmeliet, Mechanisms of angiogenesis and arteriogenesis, *Nat Med*, 6 (2000) 389-395.
- [34] P. Carmeliet, Angiogenesis in health and disease, *Nat Med*, 9 (2003) 653-660.
- [35] P. Carmeliet, R.K. Jain, Angiogenesis in cancer and other diseases, *Nature*, 407 (2000) 249-257.
- [36] D.W. Siemann, The unique characteristics of tumor vasculature and preclinical evidence for its selective disruption by Tumor-Vascular Disrupting Agents, *Cancer treatment reviews*, 37 (2011) 63-74.
- [37] H.F. Dvorak, J.A. Nagy, J.T. Dvorak, A.M. Dvorak, Identification and characterization of the blood vessels of solid tumors that are leaky to circulating macromolecules, *Am J Pathol*, 133 (1988) 95-109.
- [38] P. Baluk, S. Morikawa, A. Haskell, M. Mancuso, D.M. McDonald, Abnormalities of basement membrane on blood vessels and endothelial sprouts in tumors, *Am J Pathol*, 163 (2003) 1801-1815.
- [39] H. Hashizume, P. Baluk, S. Morikawa, J.W. McLean, G. Thurston, S. Roberge, R.K. Jain, D.M. McDonald, Openings between Defective Endothelial Cells Explain Tumor Vessel Leakiness, *The American Journal of Pathology*, 156 (2000) 1363-1380.

- [40] Y. Boucher, L.T. Baxter, R.K. Jain, Interstitial pressure gradients in tissue-isolated and subcutaneous tumors: implications for therapy, *Cancer research*, 50 (1990) 4478-4484.
- [41] H.F. Dvorak, J.A. Nagy, A.M. Dvorak, Structure of solid tumors and their vasculature: implications for therapy with monoclonal antibodies, *Cancer Cells*, 3 (1991) 77-85.
- [42] M.A. Konerding, E. Fait, A. Gaumann, 3D microvascular architecture of pre-cancerous lesions and invasive carcinomas of the colon, *Br J Cancer*, 84 (2001) 1354-1362.
- [43] A.J. Leu, D.A. Berk, A. Lymboussaki, K. Alitalo, R.K. Jain, Absence of functional lymphatics within a murine sarcoma: a molecular and functional evaluation, *Cancer research*, 60 (2000) 4324-4327.
- [44] T.P. Padera, A. Kadambi, E. di Tomaso, C.M. Carreira, E.B. Brown, Y. Boucher, N.C. Choi, D. Mathisen, J. Wain, E.J. Mark, L.L. Munn, R.K. Jain, Lymphatic metastasis in the absence of functional intratumor lymphatics, *Science*, 296 (2002) 1883-1886.
- [45] R.K. Jain, Normalization of tumor vasculature: an emerging concept in antiangiogenic therapy, *Science*, 307 (2005) 58-62.
- [46] W. Mueller-Klieser, P. Vaupel, R. Manz, R. Schmidseder, Intracapillary oxyhemoglobin saturation of malignant tumors in humans, *Int J Radiat Oncol Biol Phys*, 7 (1981) 1397-1404.
- [47] P. Vaupel, M. Hockel, Blood supply, oxygenation status and metabolic micromilieu of breast cancers: characterization and therapeutic relevance, *Int J Oncol*, 17 (2000) 869-879.
- [48] R.T. Tong, Y. Boucher, S.V. Kozin, F. Winkler, D.J. Hicklin, R.K. Jain, Vascular normalization by vascular endothelial growth factor receptor 2 blockade induces a pressure gradient across the vasculature and improves drug penetration in tumors, *Cancer research*, 64 (2004) 3731-3736.
- [49] P. Vaupel, K. Schlenger, C. Knoop, M. Hockel, Oxygenation of human tumors: evaluation of tissue oxygen distribution in breast cancers by computerized O₂ tension measurements, *Cancer research*, 51 (1991) 3316-3322.
- [50] A.R. Pries, A.J. Cornelissen, A.A. Sloot, M. Hinkeldey, M.R. Dreher, M. Hopfner, M.W. Dewhirst, T.W. Secomb, Structural adaptation and heterogeneity of normal and tumor microvascular networks, *PLoS Comput Biol*, 5 (2009) e1000394.
- [51] P. Vaupel, A. Mayer, Hypoxia in cancer: significance and impact on clinical outcome, *Cancer Metastasis Rev*, 26 (2007) 225-239.

- [52] J.A. Forsythe, B.H. Jiang, N.V. Iyer, F. Agani, S.W. Leung, R.D. Koos, G.L. Semenza, Activation of vascular endothelial growth factor gene transcription by hypoxia-inducible factor 1, *Mol Cell Biol*, 16 (1996) 4604-4613.
- [53] J. Gu, H. Yamamoto, M. Ogawa, C.Y. Ngan, K. Danno, H. Hemmi, N. Kyo, I. Takemasa, M. Ikeda, M. Sekimoto, M. Monden, Hypoxia-induced up-regulation of angiopoietin-2 in colorectal cancer, *Oncol Rep*, 15 (2006) 779-783.
- [54] G. Melillo, T. Musso, A. Sica, L.S. Taylor, G.W. Cox, L. Varesio, A hypoxia-responsive element mediates a novel pathway of activation of the inducible nitric oxide synthase promoter, *J Exp Med*, 182 (1995) 1683-1693.
- [55] K. Kuwabara, S. Ogawa, M. Matsumoto, S. Koga, M. Clauss, D.J. Pinsky, P. Lyn, J. Leavy, L. Witte, J. Joseph-Silverstein, et al., Hypoxia-mediated induction of acidic/basic fibroblast growth factor and platelet-derived growth factor in mononuclear phagocytes stimulates growth of hypoxic endothelial cells, *Proc Natl Acad Sci U S A*, 92 (1995) 4606-4610.
- [56] T.G. Graeber, C. Osmanian, T. Jacks, D.E. Housman, C.J. Koch, S.W. Lowe, A.J. Giaccia, Hypoxia-mediated selection of cells with diminished apoptotic potential in solid tumours, *Nature*, 379 (1996) 88-91.
- [57] J.K. Mohindra, A.M. Rauth, Increased cell killing by metronidazole and nitrofurazone of hypoxic compared to aerobic mammalian cells, *Cancer research*, 36 (1976) 930-936.
- [58] S. Koch, F. Mayer, F. Honecker, M. Schittenhelm, C. Bokemeyer, Efficacy of cytotoxic agents used in the treatment of testicular germ cell tumours under normoxic and hypoxic conditions in vitro, *Br J Cancer*, 89 (2003) 2133-2139.
- [59] S. Rockwell, I.T. Dobrucki, E.Y. Kim, S.T. Marrison, V.T. Vu, Hypoxia and radiation therapy: past history, ongoing research, and future promise, *Curr Mol Med*, 9 (2009) 442-458.
- [60] D.M. McDonald, P.L. Choyke, Imaging of angiogenesis: from microscope to clinic, *Nat Med*, 9 (2003) 713-725.
- [61] J. Folkman, Endothelial cells and angiogenic growth factors in cancer growth and metastasis. Introduction, *Cancer Metastasis Rev*, 9 (1990) 171-174.
- [62] J. Folkman, Angiogenesis and apoptosis, *Semin Cancer Biol*, 13 (2003) 159-167.
- [63] G. Bergers, L.E. Benjamin, Tumorigenesis and the angiogenic switch, *Nature reviews. Cancer*, 3 (2003) 401-410.
- [64] J. Holash, S.J. Wiegand, G.D. Yancopoulos, New model of tumor angiogenesis: dynamic balance between vessel regression and growth mediated by angiopoietins and VEGF, *Oncogene*, 18 (1999) 5356-5362.

- [65] V. Baeriswyl, G. Christofori, The angiogenic switch in carcinogenesis, *Semin Cancer Biol*, 19 (2009) 329-337.
- [66] A.E. El-Kenawi, A.B. El-Remessy, Angiogenesis inhibitors in cancer therapy: mechanistic perspective on classification and treatment rationales, *British journal of pharmacology*, 170 (2013) 712-729.
- [67] K. Jain, A.R. Berger, Y.H. Yucil, H.D. McGowan, Vasoproliferative tumours of the retina, *Eye (Lond)*, 17 (2003) 364-368.
- [68] E. Fagiani, G. Christofori, Angiopoietins in angiogenesis, *Cancer letters*, 328 (2013) 18-26.
- [69] V.W. van Hinsbergh, P. Koolwijk, Endothelial sprouting and angiogenesis: matrix metalloproteinases in the lead, *Cardiovasc Res*, 78 (2008) 203-212.
- [70] J.M. Whitelock, A.D. Murdoch, R.V. Iozzo, P.A. Underwood, The degradation of human endothelial cell-derived perlecan and release of bound basic fibroblast growth factor by stromelysin, collagenase, plasmin, and heparanases, *J Biol Chem*, 271 (1996) 10079-10086.
- [71] I. Vlodavsky, Y. Friedmann, Molecular properties and involvement of heparanase in cancer metastasis and angiogenesis, *J Clin Invest*, 108 (2001) 341-347.
- [72] C. Murdoch, M. Muthana, S.B. Coffelt, C.E. Lewis, The role of myeloid cells in the promotion of tumour angiogenesis, *Nature reviews. Cancer*, 8 (2008) 618-631.
- [73] P. Cirri, P. Chiarugi, Cancer associated fibroblasts: the dark side of the coin, *Am J Cancer Res*, 1 (2011) 482-497.
- [74] K.M. Cook, W.D. Figg, Angiogenesis inhibitors: current strategies and future prospects, *CA Cancer J Clin*, 60 (2010) 222-243.
- [75] R.S. Samant, L.A. Shevde, Recent advances in anti-angiogenic therapy of cancer, *Oncotarget*, 2 (2011) 122-134.
- [76] R. Kerbel, J. Folkman, Clinical translation of angiogenesis inhibitors, *Nature reviews. Cancer*, 2 (2002) 727-739.
- [77] D. Ribatti, Endogenous inhibitors of angiogenesis: a historical review, *Leuk Res*, 33 (2009) 638-644.
- [78] T.M. Mundel, R. Kalluri, Type IV collagen-derived angiogenesis inhibitors, *Microvasc Res*, 74 (2007) 85-89.
- [79] J. Folkman, Angiogenesis: an organizing principle for drug discovery?, *Nat Rev Drug Discov*, 6 (2007) 273-286.

- [80] J.Y. Hsu, H.A. Wakelee, Monoclonal antibodies targeting vascular endothelial growth factor: current status and future challenges in cancer therapy, *BioDrugs*, 23 (2009) 289-304.
- [81] S. Baka, A.R. Clamp, G.C. Jayson, A review of the latest clinical compounds to inhibit VEGF in pathological angiogenesis, *Expert Opin Ther Targets*, 10 (2006) 867-876.
- [82] A. Zivi, L. Cerbone, F. Recine, C.N. Sternberg, Safety and tolerability of pazopanib in the treatment of renal cell carcinoma, *Expert Opin Drug Saf*, 11 (2012) 851-859.
- [83] N. Ferrara, R.S. Kerbel, Angiogenesis as a therapeutic target, *Nature*, 438 (2005) 967-974.
- [84] NCI, www.cancer.gov, National Cancer Institute, www.cancer.gov.
- [85] H.J. Lenz, Antiangiogenic agents in cancer therapy, *Oncology (Williston Park)*, 19 (2005) 17-25.
- [86] J. Holash, S. Davis, N. Papadopoulos, S.D. Croll, L. Ho, M. Russell, P. Boland, R. Leidich, D. Hylton, E. Burova, E. Ioffe, T. Huang, C. Radziejewski, K. Bailey, J.P. Fandl, T. Daly, S.J. Wiegand, G.D. Yancopoulos, J.S. Rudge, VEGF-Trap: a VEGF blocker with potent antitumor effects, *Proc Natl Acad Sci U S A*, 99 (2002) 11393-11398.
- [87] J.S. Rudge, J. Holash, D. Hylton, M. Russell, S. Jiang, R. Leidich, N. Papadopoulos, E.A. Pyles, A. Torri, S.J. Wiegand, G. Thurston, N. Stahl, G.D. Yancopoulos, VEGF Trap complex formation measures production rates of VEGF, providing a biomarker for predicting efficacious angiogenic blockade, *Proc Natl Acad Sci U S A*, 104 (2007) 18363-18370.
- [88] D. Huang, Y. Ding, Y. Li, W.M. Luo, Z.F. Zhang, J. Snider, K. Vandenbeltd, C.N. Qian, B.T. Teh, Sunitinib acts primarily on tumor endothelium rather than tumor cells to inhibit the growth of renal cell carcinoma, *Cancer research*, 70 (2010) 1053-1062.
- [89] S.P. Ivy, J.Y. Wick, B.M. Kaufman, An overview of small-molecule inhibitors of VEGFR signaling, *Nat Rev Clin Oncol*, 6 (2009) 569-579.
- [90] J.M. Llovet, S. Ricci, V. Mazzaferro, P. Hilgard, E. Gane, J.F. Blanc, A.C. de Oliveira, A. Santoro, J.L. Raoul, A. Forner, M. Schwartz, C. Porta, S. Zeuzem, L. Bolondi, T.F. Greten, P.R. Galle, J.F. Seitz, I. Borbath, D. Haussinger, T. Giannaris, M. Shan, M. Moscovici, D. Voliotis, J. Bruix, S.I.S. Group, Sorafenib in advanced hepatocellular carcinoma, *N Engl J Med*, 359 (2008) 378-390.
- [91] G. Gasparini, R. Longo, M. Toi, N. Ferrara, Angiogenic inhibitors: a new therapeutic strategy in oncology, *Nat Clin Pract Oncol*, 2 (2005) 562-577.

- [92] L.S. Chan, J. Daruwalla, C. Christophi, Selective targeting of the tumour vasculature, *ANZ J Surg*, 78 (2008) 955-967.
- [93] D. Keppler, M. Sameni, K. Moin, B.F. Sloane, T. Mikkelsen, C.A. Diglio, Tumor progression and angiogenesis: cathepsin B & Co, *Biochemistry and cell biology*, 74 (1996) 799-810.
- [94] B. Vincenzi, D. Santini, L. Rocci, G. Tonini, Bisphosphonates: new antiangiogenic molecules in cancer treatment?, *Ann Oncol*, 14 (2003) 806-807.
- [95] F. Shojaei, M. Singh, J.D. Thompson, N. Ferrara, Role of Bv8 in neutrophil-dependent angiogenesis in a transgenic model of cancer progression, *Proc Natl Acad Sci U S A*, 105 (2008) 2640-2645.
- [96] S.M. Weis, D.A. Cheresh, Tumor angiogenesis: molecular pathways and therapeutic targets, *Nat Med*, 17 (2011) 1359-1370.
- [97] S. Huveneers, H. Truong, H.J. Danen, Integrins: signaling, disease, and therapy, *Int J Radiat Biol*, 83 (2007) 743-751.
- [98] G.M. Tozer, C. Kanthou, B.C. Baguley, Disrupting tumour blood vessels, *Nat. Rev. Cancer*, 5 (2005) 423-435.
- [99] H. Zhou, R.R. Hallac, R. Lopez, R. Denney, M.T. MacDonough, L. Li, L. Liu, E.E. Graves, M.L. Trawick, K.G. Pinney, R.P. Mason, Evaluation of tumor ischemia in response to an indole-based vascular disrupting agent using BLI and 19F MRI, *Am. J. Nucl. Med. Mol. Imaging*, 5 (2015) 143-153.
- [100] D.W. Siemann, D.J. Chaplin, P.A. Walicke, A review and update of the current status of the vasculature-disabling agent combretastatin-A4 phosphate (CA4P), *Expert Opin Investig Drugs*, 18 (2009) 189-197.
- [101] P.E. Thorpe, Vascular targeting agents as cancer therapeutics, *Clin Cancer Res*, 10 (2004) 415-427.
- [102] F.J. Burrows, P.E. Thorpe, Eradication of large solid tumors in mice with an immunotoxin directed against tumor vasculature, *Proc Natl Acad Sci U S A*, 90 (1993) 8996-9000.
- [103] G. Thurston, J.W. McLean, M. Rizen, P. Baluk, A. Haskell, T.J. Murphy, D. Hanahan, D.M. McDonald, Cationic liposomes target angiogenic endothelial cells in tumors and chronic inflammation in mice, *J Clin Invest*, 101 (1998) 1401-1413.
- [104] S. Krasnici, A. Werner, M.E. Eichhorn, M. Schmitt-Sody, S.A. Pahernik, B. Sauer, B. Schulze, M. Teifel, U. Michaelis, K. Naujoks, M. Dellian, Effect of the surface charge of liposomes on their uptake by angiogenic tumor vessels, *Int J Cancer*, 105 (2003) 561-567.

- [105] S. Ran, P.E. Thorpe, Phosphatidylserine is a marker of tumor vasculature and a potential target for cancer imaging and therapy, *Int J Radiat Oncol Biol Phys*, 54 (2002) 1479-1484.
- [106] H.G. Augustin, D.H. Kozian, R.C. Johnson, Differentiation of endothelial cells: analysis of the constitutive and activated endothelial cell phenotypes, *Bioessays*, 16 (1994) 901-906.
- [107] R. Kunstfeld, G. Wickenhauser, U. Michaelis, M. Teifel, W. Umek, K. Naujoks, K. Wolff, P. Petzelbauer, Paclitaxel encapsulated in cationic liposomes diminishes tumor angiogenesis and melanoma growth in a "humanized" SCID mouse model, *J Invest Dermatol*, 120 (2003) 476-482.
- [108] M. Schmitt-Sody, S. Strieth, S. Krasnici, B. Sauer, B. Schulze, M. Teifel, U. Michaelis, K. Naujoks, M. Dellian, Neovascular targeting therapy: paclitaxel encapsulated in cationic liposomes improves antitumoral efficacy, *Clin Cancer Res*, 9 (2003) 2335-2341.
- [109] J. Wu, A. Lee, Y. Lu, R.J. Lee, Vascular targeting of doxorubicin using cationic liposomes, *Int J Pharm*, 337 (2007) 329-335.
- [110] G.P. Smith, S.B. Calveley, M.J. Smith, B.C. Baguley, Flavone acetic acid (NSC 347512) induces haemorrhagic necrosis of mouse colon 26 and 38 tumours, *Eur J Cancer Clin Oncol*, 23 (1987) 1209-1211.
- [111] T.H. Corbett, M.C. Bissery, A. Wozniak, J. Plowman, L. Polin, E. Tapazoglou, J. Dieckman, F. Valeriote, Activity of flavone acetic acid (NSC-347512) against solid tumors of mice, *Invest New Drugs*, 4 (1986) 207-220.
- [112] D.J. Kerr, T. Maughan, E. Newlands, G. Rustin, N.M. Bleehen, C. Lewis, S.B. Kaye, Phase II trials of flavone acetic acid in advanced malignant melanoma and colorectal carcinoma, *Br J Cancer*, 60 (1989) 104-106.
- [113] G.W. Rewcastle, G.J. Atwell, Z.A. Li, B.C. Baguley, W.A. Denny, Potential antitumor agents. 61. Structure-activity relationships for in vivo colon 38 activity among disubstituted 9-oxo-9H-xanthene-4-acetic acids, *J Med Chem*, 34 (1991) 217-222.
- [114] C.J. Lash, A.E. Li, M. Rutland, B.C. Baguley, L.J. Zwi, W.R. Wilson, Enhancement of the anti-tumour effects of the antivascular agent 5,6-dimethylxanthenone-4-acetic acid (DMXAA) by combination with 5-hydroxytryptamine and bioreductive drugs, *Br J Cancer*, 78 (1998) 439-445.
- [115] L.M. Ching, Z. Cao, C. Kieda, S. Zwain, M.B. Jameson, B.C. Baguley, Induction of endothelial cell apoptosis by the antivascular agent 5,6-Dimethylxanthenone-4-acetic acid, *Br J Cancer*, 86 (2002) 1937-1942.

- [116] B.C. Baguley, Antivascular therapy of cancer: DMXAA, *Lancet Oncol*, 4 (2003) 141-148.
- [117] L.L. Thomsen, L.M. Ching, L. Zhuang, J.B. Gavin, B.C. Baguley, Tumor-dependent increased plasma nitrate concentrations as an indication of the antitumor effect of flavone-8-acetic acid and analogues in mice, *Cancer research*, 51 (1991) 77-81.
- [118] L.M. Ching, D. Goldsmith, W.R. Joseph, H. Korner, J.D. Sedgwick, B.C. Baguley, Induction of intratumoral tumor necrosis factor (TNF) synthesis and hemorrhagic necrosis by 5,6-dimethylxanthenone-4-acetic acid (DMXAA) in TNF knockout mice, *Cancer research*, 59 (1999) 3304-3307.
- [119] S. Zhou, P. Kestell, B.C. Baguley, J.W. Paxton, 5,6-dimethylxanthenone-4-acetic acid (DMXAA): a new biological response modifier for cancer therapy, *Invest New Drugs*, 20 (2002) 281-295.
- [120] L.J. Zwi, B.C. Baguley, J.B. Gavin, W.R. Wilson, Correlation between immune and vascular activities of xanthenone acetic acid antitumor agents, *Oncol Res*, 6 (1994) 79-85.
- [121] T. Hida, M. Tamiya, M. Nishio, N. Yamamoto, T. Hirashima, T. Horai, H. Tanii, M.M. Shi, K. Kobayashi, Y. Horio, Phase I study of intravenous ASA404 (vadimezan) administered in combination with paclitaxel and carboplatin in Japanese patients with non-small cell lung cancer, *Cancer Sci*, 102 (2011) 845-851.
- [122] M.J. McKeage, M. Reck, M.B. Jameson, M.A. Rosenthal, D. Gibbs, P.N. Mainwaring, L. Freitag, R. Sullivan, J. Von Pawel, Phase II study of ASA404 (vadimezan, 5,6-dimethylxanthenone-4-acetic acid/DMXAA) 1800mg/m² combined with carboplatin and paclitaxel in previously untreated advanced non-small cell lung cancer, *Lung Cancer*, 65 (2009) 192-197.
- [123] P.N. Lara, Jr., J.Y. Douillard, K. Nakagawa, J. von Pawel, M.J. McKeage, I. Albert, G. Losonczy, M. Reck, D.S. Heo, X. Fan, A. Fandi, G. Scagliotti, Randomized phase III placebo-controlled trial of carboplatin and paclitaxel with or without the vascular disrupting agent vadimezan (ASA404) in advanced non-small-cell lung cancer, *J Clin Oncol*, 29 (2011) 2965-2971.
- [124] Novartis discontinues ASA404 clinical trial program and shifts focus to other cancer compounds in early and late stage development [press release]. Novartis, Basel, Switzerland, 2010.
- [125] Y. Lu, J. Chen, M. Xiao, W. Li, D.D. Miller, An Overview of Tubulin Inhibitors That Interact with the Colchicine Binding Site, *Pharmaceutical research*, 29 (2012) 2943-2971.

- [126] A.T. McGown, B.W. Fox, Structural and biochemical comparison of the anti-mitotic agents colchicine, combretastatin A4 and amphethinile, *Anti-Cancer Drug Design*, 3 (1989) 249-254.
- [127] E. Boyland, M.E. Boyland, Studies in tissue metabolism: The action of colchicine and *B. typhosus* extract, *Biochem J*, 31 (1937) 454-460.
- [128] G.M. Tozer, C. Kanthou, C.S. Parkins, S.A. Hill, The biology of the combretastatins as tumour vascular targeting agents, *Int J Exp Pathol*, 83 (2002) 21-38.
- [129] G.M. Tozer, V.E. Prise, J. Wilson, R.J. Locke, B. Vojnovic, M.R. Stratford, M.F. Dennis, D.J. Chaplin, Combretastatin A-4 phosphate as a tumor vascular-targeting agent: early effects in tumors and normal tissues, *Cancer research*, 59 (1999) 1626-1634.
- [130] A.C. Brooks, C. Kanthou, I.H. Cook, G.M. Tozer, P.R. Barber, B. Vojnovic, G.B. Nash, C.S. Parkins, The vascular targeting agent combretastatin A-4-phosphate induces neutrophil recruitment to endothelial cells in vitro, *Anticancer Res*, 23 (2003) 3199-3206.
- [131] J.A. Woods, J.A. Hadfield, G.R. Pettit, B.W. Fox, A.T. McGown, The interaction with tubulin of a series of stilbenes based on combretastatin A-4, *Br J Cancer*, 71 (1995) 705-711.
- [132] D.J. Chaplin, S.A. Hill, The development of combretastatin A4 phosphate as a vascular targeting agent, *Int J Radiat Oncol Biol Phys*, 54 (2002) 1491-1496.
- [133] D.J. Chaplin, G.J. Dougherty, Tumour vasculature as a target for cancer therapy, *Br. J. Cancer*, 80 Suppl 1 (1999) 57-64.
- [134] C.D. Thomas, C. Walczak, J. Kaffy, R. Pontikis, J. Jouanneau, A. Volk, Early effects of combretastatin A4 phosphate assessed by anatomic and carbogen-based functional magnetic resonance imaging on rat bladder tumors implanted in nude mice, *Neoplasia*, 8 (2006) 587-595.
- [135] L. Li, A.M. Rojiani, D.W. Siemann, Preclinical evaluations of therapies combining the vascular targeting agent combretastatin A-4 disodium phosphate and conventional anticancer therapies in the treatment of Kaposi's sarcoma, *Acta Oncol*, 41 (2002) 91-97.
- [136] K. Grosios, P.M. Loadman, D.J. Swaine, G.R. Pettit, M.C. Bibby, Combination chemotherapy with combretastatin A-4 phosphate and 5-fluorouracil in an experimental murine colon adenocarcinoma, *Anticancer Res*, 20 (2000) 229-233.

- [137] G.J. Rustin, G. Shreeves, P.D. Nathan, A. Gaya, T.S. Ganesan, D. Wang, J. Boxall, L. Poupard, D.J. Chaplin, M.R. Stratford, J. Balkissoon, M. Zweifel, A Phase Ib trial of CA4P (combretastatin A-4 phosphate), carboplatin, and paclitaxel in patients with advanced cancer, *Br. J. Cancer*, 102 (2010) 1355-1360.
- [138] M. Zweifel, G. Jayson, N. Reed, R. Osborne, B. Hassan, G. Shreeves, L. Poupard, P.A. Walicke, J. Balkissoon, D.J. Chaplin, G. Rustin, Combretastatin A-4 phosphate (CA4P) carboplatin and paclitaxel in patients with platinum-resistant ovarian cancer: Final phase II trial results., *J. Clin. Oncol.*, 27 (2009).
- [139] P. Nathan, M. Zweifel, A.R. Padhani, D.M. Koh, M. Ng, D.J. Collins, A. Harris, C. Carden, J. Smythe, N. Fisher, N.J. Taylor, J.J. Stirling, S.P. Lu, M.O. Leach, G.J. Rustin, I. Judson, Phase I trial of combretastatin A4 phosphate (CA4P) in combination with bevacizumab in patients with advanced cancer, *Clinical cancer research : an official journal of the American Association for Cancer Research*, 18 (2012) 3428-3439.
- [140] C.B. Pattillo, B. Venegas, F.J. Donelson, L. Del Valle, L.C. Knight, P.L. Chong, M.F. Kiani, Radiation-guided targeting of combretastatin encapsulated immunoliposomes to mammary tumors, *Pharm Res*, 26 (2009) 1093-1100.
- [141] S.A. Hill, G.M. Toze, G.R. Pettit, D.J. Chaplin, Preclinical evaluation of the antitumour activity of the novel vascular targeting agent Oxi 4503, *Anticancer Res*, 22 (2002) 1453-1458.
- [142] G.R. Pettit, M.P. Grealish, D.L. Herald, M.R. Boyd, E. Hamel, R.K. Pettit, Antineoplastic agents. 443. Synthesis of the cancer cell growth inhibitor hydroxyphenstatin and its sodium diphosphate prodrug, *J Med Chem*, 43 (2000) 2731-2737.
- [143] K. Hori, S. Saito, K. Kubota, A novel combretastatin A-4 derivative, AC7700, strongly stanches tumour blood flow and inhibits growth of tumours developing in various tissues and organs, *Br J Cancer*, 86 (2002) 1604-1614.
- [144] D.C. Blakey, F.R. Westwood, M. Walker, G.D. Hughes, P.D. Davis, S.E. Ashton, A.J. Ryan, Antitumor activity of the novel vascular targeting agent ZD6126 in a panel of tumor models, *Clin Cancer Res*, 8 (2002) 1974-1983.
- [145] P.D. Davis, G.J. Dougherty, D.C. Blakey, S.M. Galbraith, G.M. Tozer, A.L. Holder, M.A. Naylor, J. Nolan, M.R. Stratford, D.J. Chaplin, S.A. Hill, ZD6126: a novel vascular-targeting agent that causes selective destruction of tumor vasculature, *Cancer research*, 62 (2002) 7247-7253.
- [146] M. Otani, T. Natsume, J.I. Watanabe, M. Kobayashi, M. Murakoshi, T. Mikami, T. Nakayama, TZT-1027, an antimicrotubule agent, attacks tumor vasculature and induces tumor cell death, *Jpn J Cancer Res*, 91 (2000) 837-844.

- [147] J.C. Lee, H.Y. Lee, C.H. Moon, S.J. Lee, W.H. Lee, H.J. Cha, S. Park, Y.H. Lee, H.J. Park, H.-T. Song, Y.J. Min, Arsenic Trioxide as a Vascular Disrupting Agent: Synergistic Effect with Irinotecan on Tumor Growth Delay in a CT26 Allograft Model, *Translational Oncology*, 6 (2013) 83-91.
- [148] R.P. Mason, D. Zhao, L. Liu, M.L. Trawick, K.G. Pinney, A perspective on vascular disrupting agents that interact with tubulin: preclinical tumor imaging and biological assessment, *Integr. Biol.*, 3 (2011) 375-387.
- [149] H. Li, D.J. DeRosier, W.V. Nicholson, E. Nogales, K.H. Downing, Microtubule structure at 8 Å resolution, *Structure*, 10 (2002) 1317-1328.
- [150] A. Desai, T.J. Mitchison, Microtubule polymerization dynamics, *Annu Rev Cell Dev Biol*, 13 (1997) 83-117.
- [151] E. Nogales, Structural insights into microtubule function, *Annual Review of Biochemistry*, 69 (2000) 277-302.
- [152] T. Mitchison, M. Kirschner, Microtubule assembly nucleated by isolated centrosomes, *Nature*, 312 (1984) 232-237.
- [153] C. Conde, A. Caceres, Microtubule assembly, organization and dynamics in axons and dendrites, *Nat Rev Neurosci*, 10 (2009) 319-332.
- [154] C.M. O'Connor, J.U. Adams, *Essentials of Cell Biology*, NPG Education, Cambridge, MA, 2010.
- [155] B. Bhattacharyya, D. Panda, S. Gupta, M. Banerjee, Anti-mitotic activity of colchicine and the structural basis for its interaction with tubulin, *Medicinal research reviews*, 28 (2008) 155-183.
- [156] E. Nogales, Structural insight into microtubule function, *Annu Rev Biophys Biomol Struct*, 30 (2001) 397-420.
- [157] R.B. Ravelli, B. Gigant, P.A. Curmi, I. Jourdain, S. Lachkar, A. Sobel, M. Knossow, Insight into tubulin regulation from a complex with colchicine and a stathmin-like domain, *Nature*, 428 (2004) 198-202.
- [158] D. Panda, J.E. Daijo, M.A. Jordan, L. Wilson, Kinetic stabilization of microtubule dynamics at steady state in vitro by substoichiometric concentrations of tubulin-colchicine complex, *Biochemistry*, 34 (1995) 9921-9929.
- [159] E. Nogales, M. Whittaker, R.A. Milligan, K.H. Downing, High-resolution model of the microtubule, *Cell*, 96 (1999) 79-88.

- [160] H.J. Park, Y. Zhang, S.P. Georgescu, K.L. Johnson, D. Kong, J.B. Galper, Human umbilical vein endothelial cells and human dermal microvascular endothelial cells offer new insights into the relationship between lipid metabolism and angiogenesis, *Stem Cell Rev*, 2 (2006) 93-102.
- [161] G.G. Dark, S.A. Hill, V.E. Prise, G.M. Tozer, G.R. Pettit, D.J. Chaplin, Combretastatin A-4, an agent that displays potent and selective toxicity toward tumor vasculature, *Cancer research*, 57 (1997) 1829-1834.
- [162] K.J. Chavez, S.V. Garimella, S. Lipkowitz, Triple negative breast cancer cell lines: one tool in the search for better treatment of triple negative breast cancer, *Breast Dis*, 32 (2010) 35-48.
- [163] L. Hui, Y. Zheng, Y. Yan, J. Bargonetti, D.A. Foster, Mutant p53 in MDA-MB-231 breast cancer cells is stabilized by elevated phospholipase D activity and contributes to survival signals generated by phospholipase D, *Oncogene*, 25 (2006) 7305-7310.
- [164] C. Kanthou, G.M. Tozer, The tumor vascular targeting agent combretastatin A-4-phosphate induces reorganization of the actin cytoskeleton and early membrane blebbing in human endothelial cells, *Blood*, 99 (2002) 2060-2069.
- [165] D.W. Siemann, M.R. Horsman, Vascular targeted therapies in oncology, *Cell Tissue Res.*, 335 (2009) 241-248.
- [166] D.W. Siemann, M.C. Bibby, G.G. Dark, A.P. Dicker, F.A.L.M. Eskens, M.R. Horsman, D. Marmé, P.M. LoRusso, Differentiation and definition of vascular-targeted therapies, *Clinical cancer research : an official journal of the American Association for Cancer Research*, 11 (2005) 416-420.
- [167] G. Bergers, S. Song, N. Meyer-Morse, E. Bergsland, D. Hanahan, Benefits of targeting both pericytes and endothelial cells in the tumor vasculature with kinase inhibitors, *J. Clin. Investig.*, 111 (2003) 1287-1295.
- [168] X. Ren, M. Dai, L.P. Lin, P.K. Li, J. Ding, Anti-angiogenic and vascular disrupting effects of C9, a new microtubule-depolymerizing agent, *Br. J. Pharm.*, 156 (2009) 1228-1238.
- [169] M.A. Jordan, L. Wilson, Microtubules as a target for anticancer drugs, *Nature reviews. Cancer*, 4 (2004) 253-265.
- [170] X.P. Xu, X.D. Wu, G.L. Liang, W.S. Huang, L. Wang, H.Y. Jing, S.L. Zhong, Pharmacokinetics, excretion, and distribution of combretastatin A4 phosphate in rats, *Die Pharmazie*, 67 (2012) 529-533.

- [171] C.H. Shen, J.J. Shee, J.Y. Wu, Y.W. Lin, J.D. Wu, Y.W. Liu, Combretastatin A-4 inhibits cell growth and metastasis in bladder cancer cells and retards tumour growth in a murine orthotopic bladder tumour model, *British journal of pharmacology*, 160 (2010) 2008-2027.
- [172] M.M. Mita, L. Sargsyan, A.C. Mita, M. Spear, Vascular-disrupting agents in oncology, *Expert opinion on investigational drugs*, 22 (2013) 317-328.
- [173] J.A. Sosa, R. Elisei, B. Jarzab, C.S. Bal, H. Koussis, A.W. Gramza, R. Ben-Yosef, B.J. Gitlitz, B. Haugen, S.M. Karandikar, F.R. Khuri, L.F. Licitra, S.C. Remick, S. Marur, C. Lu, F.G. Ondrey, S. Lu, J. Balkissoon, A randomized phase II/III trial of a tumor vascular disrupting agent fosbretabulin tromethamine (CA4P) with carboplatin (C) and paclitaxel (P) in anaplastic thyroid cancer (ATC): Final survival analysis for the FACT trial., *J. Clin. Oncol.*, 29 (2011).
- [174] K.G. Pinney, G.R. Pettit, M.L. Trawick, C. Jelinek, D.J. Chaplin, The Development and Discovery of the Combretastatins, in: G.M. Cragg, Kingston, D. G. I., Newman, D. J. (Ed.) *Antitumor Agents from Natural Products*, CRC Press, Taylor and Francis Group, Boca Raton, FL, 2011, pp. 227-263.
- [175] S. Dalal, S.A. Burchill, Preclinical evaluation of vascular-disrupting agents in Ewing's sarcoma family of tumours, *European journal of cancer*, 45 (2009) 713-722.
- [176] K.G. Pinney, F. Wang, M.B. Hadimani, Indole-containing and combretastatin-related anti-mitotic and anti-tubulin polymerization agents, US Patent US 6,849,656 B1 Feb 1, 2005, 2005.
- [177] K.L. DeCicco-Skinner, G.H. Henry, C. Cataisson, T. Tabib, J.C. Gwilliam, N.J. Watson, E.M. Bullwinkle, L. Falkenburg, R.C. O'Neill, A. Morin, J.S. Wiest, Endothelial cell tube formation assay for the in vitro study of angiogenesis, *Journal of visualized experiments : JoVE*, (2014) e51312.
- [178] Q. Zhou, W.B. Kiosses, J. Liu, P. Schimmel, Tumor endothelial cell tube formation model for determining anti-angiogenic activity of a tRNA synthetase cytokine, *Methods*, 44 (2008) 190-195.
- [179] N.S. Patel, J.L. Li, D. Generali, R. Poulsom, D.W. Cranston, A.L. Harris, Up-regulation of delta-like 4 ligand in human tumor vasculature and the role of basal expression in endothelial cell function, *Cancer research*, 65 (2005) 8690-8697.
- [180] V. Vichai, K. Kirtikara, Sulforhodamine B colorimetric assay for cytotoxicity screening, *Nat. Protoc.*, 1 (2006) 1112-1116.

- [181] A. Monks, D. Scudiero, P. Skehan, R. Shoemaker, K. Paull, D. Vistica, C. Hose, J. Langley, P. Cronise, A. Vaigro-Wolff, et al., Feasibility of a high-flux anticancer drug screen using a diverse panel of cultured human tumor cell lines, *Journal of the National Cancer Institute*, 83 (1991) 757-766.
- [182] P. Skehan, R. Storeng, D. Scudiero, A. Monks, J. McMahon, D. Vistica, J.T. Warren, H. Bokesch, S. Kenney, M.R. Boyd, New colorimetric cytotoxicity assay for anticancer-drug screening, *Journal of the National Cancer Institute*, 82 (1990) 1107-1112.
- [183] L. Liu, H. Beck, X. Wang, H.-P. Hsieh, R.P. Mason, X. Liu, Tubulin-destabilizing agent BPR0L075 induces vascular-disruption in human breast cancer mammary fat pad xenografts, *PloS one*, 7 (2012) e43314.
- [184] D. Zhao, E. Richer, P.P. Antich, R.P. Mason, Antivascular effects of combretastatin A4 phosphate in breast cancer xenograft assessed using dynamic bioluminescence imaging and confirmed by MRI, *FASEB J.*, 22 (2008) 2445-2451.
- [185] C. Kanthou, G.M. Tozer, Tumour targeting by microtubule-depolymerizing vascular disrupting agents, *Expert opinion on therapeutic targets*, 11 (2007) 1443-1457.
- [186] G. Kremmidiotis, A.F. Leske, T.C. Lavranos, D. Beaumont, J. Gasic, A. Hall, M. O'Callaghan, C.A. Matthews, B. Flynn, BNC105: a novel tubulin polymerization inhibitor that selectively disrupts tumor vasculature and displays single-agent antitumor efficacy, *Mol. Cancer Ther.*, 9 (2010) 1562-1573.
- [187] D.D. Schlaepfer, C.R. Hauck, D.J. Sieg, Signaling through focal adhesion kinase, *Prog. Biophys. Mol. Biol.*, 71 (1999) 435-478.
- [188] S.K. Sastry, K. Burridge, Focal Adhesions: A Nexus for Intracellular Signaling and Cytoskeletal Dynamics, *Exp. Cell Res.*, 261 (2000) 25-36.
- [189] C.E. Tolbert, P.M. Thompson, R. Superfine, K. Burridge, S.L. Campbell, Phosphorylation at Y1065 in Vinculin Mediates Actin Bundling, Cell Spreading, and Mechanical Responses to Force, *Biochemistry*, 53 (2014) 5526-5536.
- [190] S.K. Mitra, D.A. Hanson, D.D. Schlaepfer, Focal adhesion kinase: in command and control of cell motility, *Nat. Rev. Mol. Cell Biol.*, 6 (2005) 56-68.
- [191] S. Narumiya, T. Ishizaki, M. Ufhata, Use and properties of ROCK-specific inhibitor Y-27632, in: C.J.D. W.E. Balch, H. Alan (Eds.) *Methods in enzymology*, Academic Press 2000, pp. 273-284.
- [192] C.F. Thorn, C. Oshiro, S. Marsh, T. Hernandez-Boussard, H. McLeod, T.E. Klein, R.B. Altman, Doxorubicin pathways: pharmacodynamics and adverse effects, *Pharmacogenetics and genomics*, 21 (2011) 440-446.

- [193] L. Liu, R.P. Mason, B. Gimi, Dynamic bioluminescence and fluorescence imaging of the effects of the antivascular agent Combretastatin-A4P (CA4P) on brain tumor xenografts, *Cancer Lett.*, 356 (2015) 462-469.
- [194] S. Iyer, D.J. Chaplin, D.S. Rosenthal, A.H. Boulares, L.Y. Li, M.E. Smulson, Induction of apoptosis in proliferating human endothelial cells by the tumor-specific antiangiogenesis agent combretastatin A-4, *Cancer research*, 58 (1998) 4510-4514.
- [195] M.A. Conti, R.S. Adelstein, Nonmuscle myosin II moves in new directions, *J. Cell Sci.*, 121 (2008) 11-18.
- [196] S. Dahmani, C. Reynaud, A. Tesnière, D. Rouelle, J.-M. Desmonts, J. Mantz, Lidocaine increases phosphorylation of focal adhesion kinase in rat hippocampal slices, *Eur. J. Pharm.*, 489 (2004) 55-58.
- [197] Y. Lim, I. Han, J. Jeon, H. Park, Y.-Y. Bahk, E.-S. Oh, Phosphorylation of focal adhesion kinase at tyrosine 861 is crucial for Ras transformation of fibroblasts, *Journal of Biological Chemistry*, 279 (2004) 29060-29065.
- [198] A.J. Ridley, A. Hall, The small GTP-binding protein rho regulates the assembly of focal adhesions and actin stress fibers in response to growth factors, *Cell*, 70 (1992) 389-399.
- [199] X.-D. Ren, W.B. Kiosses, D.J. Sieg, C.A. Otey, D.D. Schlaepfer, M.A. Schwartz, Focal adhesion kinase suppresses Rho activity to promote focal adhesion turnover, *J. Cell Sci.*, 113 (2000) 3673-3678.
- [200] M. Amano, M. Ito, K. Kimura, Y. Fukata, K. Chihara, T. Nakano, Y. Matsuura, K. Kaibuchi, Phosphorylation and activation of myosin by Rho-associated kinase (Rho-kinase), *Journal of Biological Chemistry*, 271 (1996) 20246-20249.
- [201] J.C. Sandquist, K.I. Swenson, K.A. DeMali, K. Burridge, A.R. Means, Rho kinase differentially regulates phosphorylation of nonmuscle myosin II isoforms A and B during cell rounding and migration, *Journal of Biological Chemistry*, 281 (2006) 35873-35883.
- [202] A.L. Bishop, A. Hall, Rho GTPases and their effector proteins, *Biochem J*, 348 Pt 2 (2000) 241-255.
- [203] S. Etienne-Manneville, A. Hall, Rho GTPases in cell biology, *Nature*, 420 (2002) 629-635.

- [204] H.W. Liu, A.J. Halayko, D.J. Fernandes, G.S. Harmon, J.A. McCauley, P. Kocieniewski, J. McConville, Y. Fu, S.M. Forsythe, P. Kogut, S. Bellam, M. Dowell, J. Churchill, H. Lesso, K. Kassiri, R.W. Mitchell, M.B. Hershenson, B. Camoretti-Mercado, J. Solway, The RhoA/Rho kinase pathway regulates nuclear localization of serum response factor, *American journal of respiratory cell and molecular biology*, 29 (2003) 39-47.
- [205] L. Tong, V. Tergaonkar, Rho protein GTPases and their interactions with NFκB: crossroads of inflammation and matrix biology, *Bioscience Reports*, 34 (2014) e00115.
- [206] H. Teramoto, P. Crespo, O.A. Coso, T. Igishi, N. Xu, J.S. Gutkind, The Small GTP-binding Protein Rho Activates c-Jun N-terminal Kinases/Stress-activated Protein Kinases in Human Kidney 293T Cells: EVIDENCE FOR A Pak-INDEPENDENT SIGNALING PATHWAY, *Journal of Biological Chemistry*, 271 (1996) 25731-25734.
- [207] S. Zhang, J. Han, M.A. Sells, J. Chernoff, U.G. Knaus, R.J. Ulevitch, G.M. Bokoch, Rho Family GTPases Regulate p38 Mitogen-activated Protein Kinase through the Downstream Mediator Pak1, *Journal of Biological Chemistry*, 270 (1995) 23934-23936.
- [208] P. Villalonga, A.J. Ridley, Rho GTPases and cell cycle control, *Growth factors* (Chur, Switzerland), 24 (2006) 159-164.
- [209] L.S. Price, J.C. Norman, A.J. Ridley, A. Koffer, The small GTPases Rac and Rho as regulators of secretion in mast cells, *Current Biology*, 5 (1995) 68-73.
- [210] N.A. Mack, M. Georgiou, The interdependence of the Rho GTPases and apicobasal cell polarity, *Small GTPases*, 5 (2014) 1-16.
- [211] F.M. Vega, A.J. Ridley, Rho GTPases in cancer cell biology, *FEBS Letters*, 582 (2008) 2093-2101.
- [212] X. Chi, S. Wang, Y. Huang, M. Stamnes, J.-L. Chen, Roles of Rho GTPases in Intracellular Transport and Cellular Transformation, *International Journal of Molecular Sciences*, 14 (2013) 7089-7108.
- [213] X. Zhou, Y. Zheng, Cell Type-specific Signaling Function of RhoA GTPase: Lessons from Mouse Gene Targeting, *Journal of Biological Chemistry*, 288 (2013) 36179-36188.
- [214] A.P. Wheeler, A.J. Ridley, Why three Rho proteins? RhoA, RhoB, RhoC, and cell motility, *Experimental Cell Research*, 301 (2004) 43-49.
- [215] I.R. Vetter, A. Wittinghofer, The guanine nucleotide-binding switch in three dimensions, *Science*, 294 (2001) 1299-1304.

- [216] K. Ihara, S. Muraguchi, M. Kato, T. Shimizu, M. Shirakawa, S. Kuroda, K. Kaibuchi, T. Hakoshima, Crystal structure of human RhoA in a dominantly active form complexed with a GTP analogue, *The Journal of biological chemistry*, 273 (1998) 9656-9666.
- [217] T. Hakoshima, T. Shimizu, R. Maesaki, Structural basis of the Rho GTPase signaling, *J Biochem*, 134 (2003) 327-331.
- [218] K.L. Rossman, C.J. Der, J. Sondek, GEF means go: turning on RHO GTPases with guanine nucleotide-exchange factors, *Nat Rev Mol Cell Biol*, 6 (2005) 167-180.
- [219] V.P. Sah, T.M. Seasholtz, S.A. Sagi, J.H. Brown, The role of Rho in G protein-coupled receptor signal transduction, *Annu Rev Pharmacol Toxicol*, 40 (2000) 459-489.
- [220] G.P. van Nieuw Amerongen, V.W. van Hinsbergh, Cytoskeletal effects of rho-like small guanine nucleotide-binding proteins in the vascular system, *Arterioscler Thromb Vasc Biol*, 21 (2001) 300-311.
- [221] E. Kardash, M. Reichman-Fried, J.-L. Maitre, B. Boldajipour, E. Papusheva, E.-M. Messerschmidt, C.-P. Heisenberg, E. Raz, A role for Rho GTPases and cell-cell adhesion in single-cell motility in vivo, *Nat Cell Biol*, 12 (2010) 47-53.
- [222] R. Singh, B. Wang, A. Shirvaikar, S. Khan, S. Kamat, J.R. Schelling, M. Konieczkowski, J.R. Sedor, The IL-1 receptor and Rho directly associate to drive cell activation in inflammation, *Journal of Clinical Investigation*, 103 (1999) 1561-1570.
- [223] M. Schwartz, Rho signalling at a glance, *J Cell Sci*, 117 (2004) 5457-5458.
- [224] K. Kaibuchi, Regulation of cytoskeleton and cell adhesion by Rho targets, *Prog Mol Subcell Biol*, 22 (1999) 23-38.
- [225] M. Chrzanowska-Wodnicka, K. Burridge, Rho-stimulated contractility drives the formation of stress fibers and focal adhesions, *J Cell Biol*, 133 (1996) 1403-1415.
- [226] A. Ridley, Rho GTPases. Integrating integrin signaling, *J Cell Biol*, 150 (2000) F107-109.
- [227] F. Matsumura, G. Totsukawa, Y. Yamakita, S. Yamashiro, Role of myosin light chain phosphorylation in the regulation of cytokinesis, *Cell structure and function*, 26 (2001) 639-644.
- [228] K. Ohashi, K. Nagata, M. Maekawa, T. Ishizaki, S. Narumiya, K. Mizuno, Rho-associated Kinase ROCK Activates LIM-kinase 1 by Phosphorylation at Threonine 508 within the Activation Loop, *Journal of Biological Chemistry*, 275 (2000) 3577-3582.

- [229] N. Berthelsen, H. Pantera, J. Sauer, J. Lawrence, M. Wallert, J. Provost, RhoA Kinase Phosphorylation of NHE1 impact on Growth Factor and G Protein Coupled Receptor Signaling, *The FASEB Journal*, 27 (2013) 1045.1044.
- [230] K. Burridge, K. Fath, T. Kelly, G. Nuckolls, C. Turner, Focal adhesions: transmembrane junctions between the extracellular matrix and the cytoskeleton, *Annu Rev Cell Biol*, 4 (1988) 487-525.
- [231] V. Petit, J.P. Thiery, Focal adhesions: structure and dynamics, *Biol Cell*, 92 (2000) 477-494.
- [232] D.J. Webb, J.T. Parsons, A.F. Horwitz, Adhesion assembly, disassembly and turnover in migrating cells -- over and over and over again, *Nat Cell Biol*, 4 (2002) E97-100.
- [233] E.J. Ezratty, M.A. Partridge, G.G. Gundersen, Microtubule-induced focal adhesion disassembly is mediated by dynamin and focal adhesion kinase, *Nature cell biology*, 7 (2005) 581-590.
- [234] K. Burridge, M. Chrzanowska-Wodnicka, Focal adhesions, contractility, and signaling, *Annu Rev Cell Dev Biol*, 12 (1996) 463-518.
- [235] K.E. Michael, D.W. Dumbauld, K.L. Burns, S.K. Hanks, A.J. García, Focal Adhesion Kinase Modulates Cell Adhesion Strengthening via Integrin Activation, *Molecular Biology of the Cell*, 20 (2009) 2508-2519.
- [236] J.D. van Buul, D. Geerts, S. Huveneers, Rho GAPs and GEFs: controlling switches in endothelial cell adhesion, *Cell Adh Migr*, 8 (2014) 108-124.
- [237] J. Birkenfeld, P. Nalbant, S.H. Yoon, G.M. Bokoch, Cellular functions of GEF-H1, a microtubule-regulated Rho-GEF: is altered GEF-H1 activity a crucial determinant of disease pathogenesis?, *Trends Cell Biol*, 18 (2008) 210-219.
- [238] Y. Ren, R. Li, Y. Zheng, H. Busch, Cloning and characterization of GEF-H1, a microtubule-associated guanine nucleotide exchange factor for Rac and Rho GTPases, *The Journal of biological chemistry*, 273 (1998) 34954-34960.
- [239] F.T. Zenke, M. Krendel, C. DerMardirossian, C.C. King, B.P. Bohl, G.M. Bokoch, p21-activated kinase 1 phosphorylates and regulates 14-3-3 binding to GEF-H1, a microtubule-localized Rho exchange factor, *The Journal of biological chemistry*, 279 (2004) 18392-18400.
- [240] M.G. Callow, S. Zozulya, M.L. Gishizky, B. Jallal, T. Smeal, PAK4 mediates morphological changes through the regulation of GEF-H1, *J Cell Sci*, 118 (2005) 1861-1872.

- [241] A.A. Birukova, D. Adyshev, B. Gorshkov, G.M. Bokoch, K.G. Birukov, A.D. Verin, GEF-H1 is involved in agonist-induced human pulmonary endothelial barrier dysfunction, *Am J Physiol Lung Cell Mol Physiol*, 290 (2006) L540-548.
- [242] M. Krendel, F.T. Zenke, G.M. Bokoch, Nucleotide exchange factor GEF-H1 mediates cross-talk between microtubules and the actin cytoskeleton, *Nat Cell Biol*, 4 (2002) 294-301.
- [243] J. Adler, I. Parmryd, Quantifying colocalization by correlation: the Pearson correlation coefficient is superior to the Mander's overlap coefficient, *Cytometry Part A*, 77 (2010) 733-742.
- [244] F.P.G. van Horck, M.R. Ahmadian, L.C. Haeusler, W.H. Moolenaar, O. Kranenburg, Characterization of p190RhoGEF, A RhoA-specific Guanine Nucleotide Exchange Factor That Interacts with Microtubules, *Journal of Biological Chemistry*, 276 (2001) 4948-4956.
- [245] N.L.G. Miller, C. Lawson, X.L. Chen, S.-T. Lim, D.D. Schlaepfer, Rgnef (p190RhoGEF) Knockout Inhibits RhoA Activity, Focal Adhesion Establishment, and Cell Motility Downstream of Integrins, *PLoS ONE*, 7 (2012) e37830.
- [246] N.L.G. Miller, C. Lawson, E.G. Kleinschmidt, I. Tancioni, S. Uryu, D.D. Schlaepfer, A non-canonical role for Rgnef in promoting integrin-stimulated focal adhesion kinase activation, *Journal of Cell Science*, 126 (2013) 5074-5085.
- [247] M. Gorovoy, J. Niu, O. Bernard, J. Profirovic, R. Minshall, R. Neamu, T. Voynoyasenetskaya, LIM kinase 1 coordinates microtubule stability and actin polymerization in human endothelial cells, *The Journal of biological chemistry*, 280 (2005) 26533-26542.
- [248] R. Gatti, S. Belletti, G. Orlandini, O. Bussolati, V. Dall'Asta, G.C. Gazzola, Comparison of Annexin V and Calcein-AM as Early Vital Markers of Apoptosis in Adherent Cells by Confocal Laser Microscopy, *Journal of Histochemistry & Cytochemistry*, 46 (1998) 895-900.
- [249] M. Dhar-Mascareño, J.M. Cárcamo, D.W. Golde, Hypoxia–reoxygenation-induced mitochondrial damage and apoptosis in human endothelial cells are inhibited by vitamin C, *Free Radical Biology and Medicine*, 38 (2005) 1311-1322.
- [250] T.E. Strecker, S.O. Odutola, R. Lopez, M.S. Cooper, J.K. Tidmore, A.K. Charlton-Sevcik, L. Li, M.T. MacDonough, M.B. Hadimani, A. Ghatak, L. Liu, D.J. Chaplin, R.P. Mason, K.G. Pinney, M.L. Trawick, The vascular disrupting activity of OXi8006 in endothelial cells and its phosphate prodrug OXi8007 in breast tumor xenografts, *Cancer letters*, 369 (2015) 229-241.

- [251] Y.C. Chang, P. Nalbant, J. Birkenfeld, Z.F. Chang, G.M. Bokoch, GEF-H1 couples nocodazole-induced microtubule disassembly to cell contractility via RhoA, *Mol Biol Cell*, 19 (2008) 2147-2153.
- [252] R. Kalluri, R.A. Weinberg, The basics of epithelial-mesenchymal transition, *The Journal of Clinical Investigation*, 119 (2009) 1420-1428.
- [253] S. Elmore, Apoptosis: A Review of Programmed Cell Death, *Toxicologic pathology*, 35 (2007) 495-516.
- [254] J. Reiser, B. Adair, T. Reinheckel, Specialized roles for cysteine cathepsins in health and disease, *J Clin Invest*, 120 (2010) 3421-3431.
- [255] J.K. McDonald, An overview of protease specificity and catalytic mechanisms: aspects related to nomenclature and classification, *The Histochemical Journal*, 17 (1985) 773-785.
- [256] A. Brinker, E. Weber, D. Stoll, J. Voigt, A. Muller, N. Sewald, G. Jung, K.H. Wiesmuller, P. Bohley, Highly potent inhibitors of human cathepsin L identified by screening combinatorial pentapeptide amide collections, *Eur J Biochem*, 267 (2000) 5085-5092.
- [257] K. Ishidoh, E. Kominami, Multi-step processing of procathepsin L in vitro, *FEBS Lett*, 352 (1994) 281-284.
- [258] K. Brix, A. Dunkhorst, K. Mayer, S. Jordans, Cysteine cathepsins: cellular roadmap to different functions, *Biochimie*, 90 (2008) 194-207.
- [259] V. Turk, V. Stoka, O. Vasiljeva, M. Renko, T. Sun, B. Turk, D. Turk, Cysteine cathepsins: from structure, function and regulation to new frontiers, *Biochim Biophys Acta*, 1824 (2012) 68-88.
- [260] D. Turk, G. Guncar, Lysosomal cysteine proteases (cathepsins): promising drug targets, *Acta Crystallogr D Biol Crystallogr*, 59 (2003) 203-213.
- [261] A. Klose, P. Zigrino, R. Denhofer, C. Mauch, N. Hunzelmann, Identification and discrimination of extracellularly active cathepsins B and L in high-invasive melanoma cells, *Anal Biochem*, 353 (2006) 57-62.
- [262] S.M. Smith, M.M. Gottesman, Activity and deletion analysis of recombinant human cathepsin L expressed in *Escherichia coli*, *J Biol Chem*, 264 (1989) 20487-20495.
- [263] A. Fujishima, Y. Imai, T. Nomura, Y. Fujisawa, Y. Yamamoto, T. Sugawara, The crystal structure of human cathepsin L complexed with E-64, *FEBS Lett*, 407 (1997) 47-50.

- [264] J. Guay, J.-P. Falgout, A. Ducret, M.D. Percival, J.A. Mancini, Potency and selectivity of inhibition of cathepsin K, L and S by their respective propeptides, *European Journal of Biochemistry*, 267 (2000) 6311-6318.
- [265] D. Musil, D. Zucic, D. Turk, R.A. Engh, I. Mayr, R. Huber, T. Popovic, V. Turk, T. Towatari, N. Katunuma, et al., The refined 2.15 Å X-ray crystal structure of human liver cathepsin B: the structural basis for its specificity, *EMBO J*, 10 (1991) 2321-2330.
- [266] F. Lecaille, J. Kaleta, D. Bromme, Human and parasitic papain-like cysteine proteases: their role in physiology and pathology and recent developments in inhibitor design, *Chem Rev*, 102 (2002) 4459-4488.
- [267] R.T. Shenoy, J. Sivaraman, Structural basis for reversible and irreversible inhibition of human cathepsin L by their respective dipeptidyl glyoxal and diazomethylketone inhibitors, *J Struct Biol*, 173 (2011) 14-19.
- [268] Z. Rankovic, J. Cai, J. Kerr, X. Fradera, J. Robinson, A. Mistry, E. Hamilton, G. McGarry, F. Andrews, W. Caulfield, I. Cumming, M. Dempster, J. Waller, P. Scullion, I. Martin, A. Mitchell, C. Long, M. Baugh, P. Westwood, E. Kinghorn, J. Bruin, W. Hamilton, J. Uitdehaag, M.v. Zeeland, D. Potin, L. Sanieri, A. Fouquet, F. Chevallier, H. Deronzier, C. Dorleans, E. Nicolai, Design and optimization of a series of novel 2-cyano-pyrimidines as cathepsin K inhibitors, *Bioorganic & medicinal chemistry letters*, 20 (2010) 1524-1527.
- [269] A. Ritonja, W. Machleidt, A.J. Barrett, Amino acid sequence of the intracellular cysteine proteinase inhibitor cystatin B from human liver, *Biochem Biophys Res Commun*, 131 (1985) 1187-1192.
- [270] R. Loser, K. Schilling, E. Dimmig, M. Gutschow, Interaction of papain-like cysteine proteases with dipeptide-derived nitriles, *J Med Chem*, 48 (2005) 7688-7707.
- [271] M.E. McGrath, The lysosomal cysteine proteases, *Annu Rev Biophys Biomol Struct*, 28 (1999) 181-204.
- [272] Y. Yamamoto, M. Kurata, S. Watabe, R. Murakami, S.Y. Takahashi, Novel cysteine proteinase inhibitors homologous to the proregions of cysteine proteinases, *Curr Protein Pept Sci*, 3 (2002) 231-238.
- [273] M. Sajid, J.H. McKerrow, Cysteine proteases of parasitic organisms, *Mol Biochem Parasitol*, 120 (2002) 1-21.
- [274] I. Schechter, A. Berger, On the size of the active site in proteases. I. Papain, *Biochemical and Biophysical Research Communications*, 27 (1967) 157-162.
- [275] V.K. Dubey, M. Pande, B.K. Singh, M.V. Jagannadham, Papain-like proteases: Applications of their inhibitors, *African Journal of Biotechnology*, 6 (2007).

- [276] F. Lecaille, E. Authie, T. Moreau, C. Serveau, F. Gauthier, G. Lalmanach, Subsite specificity of trypanosomal cathepsin L-like cysteine proteases. Probing the S2 pocket with phenylalanine-derived amino acids, *Eur J Biochem*, 268 (2001) 2733-2741.
- [277] G. Guncar, G. Pungercic, I. Klemencic, V. Turk, D. Turk, Crystal structure of MHC class II-associated p41 Ii fragment bound to cathepsin L reveals the structural basis for differentiation between cathepsins L and S, *EMBO J*, 18 (1999) 793-803.
- [278] A. Premzl, V. Zavasnik-Bergant, V. Turk, J. Kos, Intracellular and extracellular cathepsin B facilitate invasion of MCF-10A neoT cells through reconstituted extracellular matrix in vitro, *Exp Cell Res*, 283 (2003) 206-214.
- [279] B.F. Sloane, K. Moin, E. Krepele, J. Rozhin, Cathepsin B and its endogenous inhibitors: the role in tumor malignancy, *Cancer Metastasis Rev*, 9 (1990) 333-352.
- [280] A. Yamamoto, K. Tomoo, K. Matsugi, T. Hara, Y. In, M. Murata, K. Kitamura, T. Ishida, Structural basis for development of cathepsin B-specific noncovalent-type inhibitor: crystal structure of cathepsin B-E64c complex, *Biochim Biophys Acta*, 1597 (2002) 244-251.
- [281] I. Redzynia, A. Ljunggren, M. Abrahamson, J.S. Mort, J.C. Krupa, M. Jaskolski, G. Bujacz, Displacement of the occluding loop by the parasite protein, chagasin, results in efficient inhibition of human cathepsin B, *The Journal of biological chemistry*, 283 (2008) 22815-22825.
- [282] J.C. Krupa, S. Hasnain, D.K. Nagler, R. Menard, J.S. Mort, S2' substrate specificity and the role of His110 and His111 in the exopeptidase activity of human cathepsin B, *Biochem J*, 361 (2002) 613-619.
- [283] C. Naudin, F. Lecaille, S. Chowdhury, J.C. Krupa, E. Purisima, J.S. Mort, G. Lalmanach, The occluding loop of cathepsin B prevents its effective inhibition by human kininogens, *J Mol Biol*, 400 (2010) 1022-1035.
- [284] F. Willenbrock, K. Brocklehurst, A general framework of cysteine-proteinase mechanism deduced from studies on enzymes with structurally different analogous catalytic-site residues Asp-158 and -161 (papain and actinidin), Gly-196 (cathepsin B) and Asn-165 (cathepsin H). Kinetic studies up to pH 8 of the hydrolysis of N-alpha-benzoyloxycarbonyl-L-arginyl-L-arginine 2-naphthylamide catalysed by cathepsin B and of L-arginine 2-naphthylamide catalysed by cathepsin H, *Biochem J*, 227 (1985) 521-528.

- [285] R. Mosi, I.R. Baird, J. Cox, V. Anastassov, B. Cameron, R.T. Skerlj, S.P. Fricker, Rhenium inhibitors of cathepsin B (ReO(SYS)X (where Y = S, py; X = Cl, Br, SPhOMe-p)): Synthesis and mechanism of inhibition, *J Med Chem*, 49 (2006) 5262-5272.
- [286] T. Schirmeister, A. Klockow, Cysteine protease inhibitors containing small rings, *Mini Rev Med Chem*, 3 (2003) 585-596.
- [287] T. Schirmeister, U. Kaeppler, Non-peptidic inhibitors of cysteine proteases, *Mini Rev Med Chem*, 3 (2003) 361-373.
- [288] M. Rzychon, D. Chmiel, J. Stec-Niemczyk, Modes of inhibition of cysteine proteases, *Acta Biochim Pol*, 51 (2004) 861-873.
- [289] H. Tsuge, T. Nishimura, Y. Tada, T. Asao, D. Turk, V. Turk, N. Katunuma, Inhibition mechanism of cathepsin L-specific inhibitors based on the crystal structure of papain-CLIK148 complex, *Biochem Biophys Res Commun*, 266 (1999) 411-416.
- [290] S. Sullivan, M. Tosetto, D. Kevans, A. Coss, L. Wang, D. O'Donoghue, J. Hyland, K. Sheahan, H. Mulcahy, J. O'Sullivan, Localization of nuclear cathepsin L and its association with disease progression and poor outcome in colorectal cancer, *Int J Cancer*, 125 (2009) 54-61.
- [291] J.Y. Gauthier, N. Chauret, W. Cromlish, S. Desmarais, L.T. Duong, J.P. Falgout, D.B. Kimmel, S. Lamontagne, S. Leger, T. LeRiche, C.S. Li, F. Masse, D.J. McKay, D.A. Nicoll-Griffith, R.M. Oballa, J.T. Palmer, M.D. Percival, D. Riendeau, J. Robichaud, G.A. Rodan, S.B. Rodan, C. Seto, M. Therien, V.L. Truong, M.C. Venuti, G. Wesolowski, R.N. Young, R. Zamboni, W.C. Black, The discovery of odanacatib (MK-0822), a selective inhibitor of cathepsin K, *Bioorganic & medicinal chemistry letters*, 18 (2008) 923-928.
- [292] M.J. Bossard, T.A. Tomaszek, S.K. Thompson, B.Y. Amegadzie, C.R. Hanning, C. Jones, J.T. Kurdyla, D.E. McNulty, F.H. Drake, M. Gowen, M.A. Levy, Proteolytic activity of human osteoclast cathepsin K. Expression, purification, activation, and substrate identification, *The Journal of biological chemistry*, 271 (1996) 12517-12524.
- [293] F. Buhling, A. Reisenauer, A. Gerber, S. Kruger, E. Weber, D. Bromme, A. Roessner, S. Ansorge, T. Welte, C. Rocken, Cathepsin K--a marker of macrophage differentiation?, *J Pathol*, 195 (2001) 375-382.
- [294] S. Roshy, B.F. Sloane, K. Moin, Pericellular cathepsin B and malignant progression, *Cancer Metastasis Rev*, 22 (2003) 271-286.

- [295] R. Menard, E. Carmona, S. Takebe, E. Dufour, C. Plouffe, P. Mason, J.S. Mort, Autocatalytic processing of recombinant human procathepsin L. Contribution of both intermolecular and unimolecular events in the processing of procathepsin L in vitro, *The Journal of biological chemistry*, 273 (1998) 4478-4484.
- [296] R. Jerala, E. Zerovnik, J. Kidric, V. Turk, pH-induced conformational transitions of the propeptide of human cathepsin L. A role for a molten globule state in zymogen activation, *The Journal of biological chemistry*, 273 (1998) 11498-11504.
- [297] D. Bromme, J. Kaleta, Thiol-dependent cathepsins: pathophysiological implications and recent advances in inhibitor design, *Curr Pharm Des*, 8 (2002) 1639-1658.
- [298] S.E. Chen, Modeling, design, and development of potential inhibitors of γ -glutamylamine cyclotransferase and inhibitors of cruzain as therapeutic agents for Chagas' disease., Baylor University, Waco, Texas, 2008.
- [299] S. Verma, R. Dixit, K.C. Pandey, Cysteine Proteases: Modes of Activation and Future Prospects as Pharmacological Targets, *Frontiers in Pharmacology*, 7 (2016) 107.
- [300] B. Werle, A. Staib, B. Julke, W. Ebert, P. Zladoidsky, A. Sekirnik, J. Kos, E. Spiess, Fluorometric microassays for the determination of cathepsin L and cathepsin S activities in tissue extracts, *Biol Chem*, 380 (1999) 1109-1116.
- [301] C. Rocken, R. Menard, F. Buhling, S. Vockler, J. Raynes, B. Stix, S. Kruger, A. Roessner, T. Kahne, Proteolysis of serum amyloid A and AA amyloid proteins by cysteine proteases: cathepsin B generates AA amyloid proteins and cathepsin L may prevent their formation, *Ann Rheum Dis*, 64 (2005) 808-815.
- [302] T. Nagaya, Y. Murata, S. Yamaguchi, Y. Nomura, S. Ohmori, M. Fujieda, N. Katunuma, P.M. Yen, W.W. Chin, H. Seo, Intracellular proteolytic cleavage of 9-cis-retinoic acid receptor alpha by cathepsin L-type protease is a potential mechanism for modulating thyroid hormone action, *J Biol Chem*, 273 (1998) 33166-33173.
- [303] F. Boudreau, C.R. Lussier, S. Mongrain, M. Darsigny, J.L. Drouin, G. Doyon, E.R. Suh, J.F. Beaulieu, N. Rivard, N. Perreault, Loss of cathepsin L activity promotes claudin-1 overexpression and intestinal neoplasia, *FASEB J*, 21 (2007) 3853-3865.
- [304] D.J. Tobin, K. Foitzik, T. Reinheckel, L. Mecklenburg, V.A. Botchkarev, C. Peters, R. Paus, The Lysosomal Protease Cathepsin L Is an Important Regulator of Keratinocyte and Melanocyte Differentiation During Hair Follicle Morphogenesis and Cycling, *The American Journal of Pathology*, 160 1807-1821.

- [305] W.W. Wright, L. Smith, C. Kerr, M. Charron, Mice that express enzymatically inactive cathepsin L exhibit abnormal spermatogenesis, *Biology of reproduction*, 68 (2003) 680-687.
- [306] S. Oksjoki, M. Soderstrom, E. Vuorio, L. Anttila, Differential expression patterns of cathepsins B, H, K, L and S in the mouse ovary, *Mol Hum Reprod*, 7 (2001) 27-34.
- [307] A. Rebbaa, F. Chu, T. Sudha, C. Gallati, U. Dier, E. Dyskin, M. Yalcin, C. Bianchini, O. Shaker, S.A. Mousa, The anti-angiogenic activity of NSITC, a specific cathepsin L inhibitor, *Anticancer Res*, 29 (2009) 4473-4481.
- [308] B.R. Troen, The role of cathepsin K in normal bone resorption, *Drug News Perspect*, 17 (2004) 19-28.
- [309] P. Garnero, O. Borel, I. Byrjalsen, M. Ferreras, F.H. Drake, M.S. McQueney, N.T. Foged, P.D. Delmas, J.M. Delaisse, The collagenolytic activity of cathepsin K is unique among mammalian proteinases, *The Journal of biological chemistry*, 273 (1998) 32347-32352.
- [310] R. Frlan, S. Gobec, Inhibitors of cathepsin B, *Curr Med Chem*, 13 (2006) 2309-2327.
- [311] S. Inayat, A. Larsson, G.K. Ronquist, G. Ronquist, N. Egberg, R. Eliasson, L. Carlsson, High levels of cathepsins B, L and S in human seminal plasma and their association with prostasomes, *Andrologia*, 44 (2012) 423-427.
- [312] I. Susic, B. Mirkovic, K. Arenz, B. Stefane, J. Kos, S. Gobec, Development of new cathepsin B inhibitors: combining bioisosteric replacements and structure-based design to explore the structure-activity relationships of nitroxoline derivatives, *J Med Chem*, 56 (2013) 521-533.
- [313] T. Nomura, N. Katunuma, Involvement of cathepsins in the invasion, metastasis and proliferation of cancer cells, *J Med Invest*, 52 (2005) 1-9.
- [314] M. Klemba, D.E. Goldberg, Biological roles of proteases in parasitic protozoa, *Annu Rev Biochem*, 71 (2002) 275-305.
- [315] I.E. James, R.W. Marquis, S.M. Blake, S.M. Hwang, C.J. Gress, Y. Ru, D. Zembryki, D.S. Yamashita, M.S. McQueney, T.A. Tomaszek, H.J. Oh, M. Gowen, D.F. Veber, M.W. Lark, Potent and selective cathepsin L inhibitors do not inhibit human osteoclast resorption in vitro, *The Journal of biological chemistry*, 276 (2001) 11507-11511.
- [316] A.M. Sadaghiani, S.H. Verhelst, V. Gocheva, K. Hill, E. Majerova, S. Stinson, J.A. Joyce, M. Bogyo, Design, synthesis, and evaluation of in vivo potency and selectivity of epoxysuccinyl-based inhibitors of papain-family cysteine proteases, *Chem Biol*, 14 (2007) 499-511.

- [317] F. Nishimura, H. Naruishi, K. Naruishi, T. Yamada, J. Sasaki, C. Peters, Y. Uchiyama, Y. Murayama, Cathepsin-L, a key molecule in the pathogenesis of drug-induced and I-cell disease-mediated gingival overgrowth: a study with cathepsin-L-deficient mice, *Am J Pathol*, 161 (2002) 2047-2052.
- [318] L. Wan, K. Pantel, Y. Kang, Tumor metastasis: moving new biological insights into the clinic, *Nat Med*, 19 (2013) 1450-1464.
- [319] P. Gopal, R.U. Rehman, K.S. Chadha, M. Qiu, R. Colella, Matrigel influences morphology and cathepsin B distribution of prostate cancer PC3 cells, *Oncol Rep*, 16 (2006) 313-320.
- [320] M. Zhang, S. Altuwaijri, S. Yeh, RRR-alpha-tocopheryl succinate inhibits human prostate cancer cell invasiveness, *Oncogene*, 23 (2004) 3080-3088.
- [321] Y. Hashimoto, C. Kondo, T. Kojima, H. Nagata, A. Moriyama, T. Hayakawa, N. Katunuma, Significance of 32-kDa cathepsin L secreted from cancer cells, *Cancer Biother Radiopharm*, 21 (2006) 217-224.
- [322] R. Colella, T. Jackson, E. Goodwyn, Matrigel invasion by the prostate cancer cell lines, PC3 and DU145, and cathepsin L+B activity, *Biotech Histochem*, 79 (2004) 121-127.
- [323] B.P. Himelstein, R. Canete-Soler, E.J. Bernhard, R.J. Muschel, Induction of fibroblast 92 kDa gelatinase/type IV collagenase expression by direct contact with metastatic tumor cells, *J Cell Sci*, 107 (Pt 2) (1994) 477-486.
- [324] B.P. Himelstein, R. Canete-Soler, E.J. Bernhard, D.W. Dilks, R.J. Muschel, Metalloproteinases in tumor progression: the contribution of MMP-9, *Invasion Metastasis*, 14 (1994) 246-258.
- [325] B. Bian, S. Mongrain, S. Cagnol, M.J. Langlois, J. Boulanger, G. Bernatchez, J.C. Carrier, F. Boudreau, N. Rivard, Cathepsin B promotes colorectal tumorigenesis, cell invasion, and metastasis, *Molecular Carcinogenesis*, 55 (2016) 671-687.
- [326] C.S. Gondi, J.S. Rao, Cathepsin B as a Cancer Target, *Expert opinion on therapeutic targets*, 17 (2013) 281-291.
- [327] M.M. Mohamed, B.F. Sloane, Cysteine cathepsins: multifunctional enzymes in cancer, *Nature reviews. Cancer*, 6 (2006) 764-775.
- [328] D.W. Visscher, B.F. Sloane, M. Sameni, J.W. Babiarz, J. Jacobson, J.D. Crissman, Clinicopathologic significance of cathepsin B immunostaining in transitional neoplasia, *Mod Pathol*, 7 (1994) 76-81.

- [329] A.A. Sinha, D.F. Gleason, O.F. Deleon, M.J. Wilson, B.F. Sloane, Localization of a biotinylated cathepsin B oligonucleotide probe in human prostate including invasive cells and invasive edges by in situ hybridization, *Anat Rec*, 235 (1993) 233-240.
- [330] F. Xue, J. Huang, H. Ji, J. Fang, H. Li, P. Martasek, L.J. Roman, T.L. Poulos, R.B. Silverman, Structure-based design, synthesis, and biological evaluation of lipophilic-tailed monocationic inhibitors of neuronal nitric oxide synthase, *Bioorg Med Chem*, 18 (2010) 6526-6537.
- [331] J. Lanter, X. Zhang, Z. Sui, Chapter sixteen - Medicinal Chemistry Inspired Fragment-Based Drug Discovery, *Fragment-Based Drug Design Tools, Practical Approaches, and Examples*, Academic Press 2011, pp. 421-445.
- [332] A. Fersht, *Structure and mechanism in protein science: A guide to enzyme catalysis and protein folding.*, Macmillan 1999.
- [333] D.W. Strelow J., Iversen P.W. et al Mechanism of action assay for enzymes. , <http://www.ncbi.nlm.nih.gov/books/NBK92001>., In: Sittampalam GS, Coussens NP, Nelson H, et al., editors. *Assay Guidance Manual* [Internet]. Bethesda (MD): Eli Lilly & Company and the National Center for Advancing Translational Sciences; 2004-. 2012.
- [334] T. Kakkar, H. Boxenbaum, M. Mayersohn, Estimation of K_i in a competitive enzyme-inhibition model: comparisons among three methods of data analysis, *Drug metabolism and disposition: the biological fate of chemicals*, 27 (1999) 756-762.
- [335] C. Yung-Chi, W.H. Prusoff, Relationship between the inhibition constant (K_i) and the concentration of inhibitor which causes 50 per cent inhibition (I_{50}) of an enzymatic reaction, *Biochemical pharmacology*, 22 (1973) 3099-3108.
- [336] M. Golićnik, J. Stojan, Slow-binding inhibition: A theoretical and practical course for students. , *Biochemistry and Molecular Biology Education* 2006, pp. 228-235.
- [337] R.A. Copeland, *Slow Binding Inhibitors, Evaluation of Enzyme Inhibitors in Drug Discovery*, John Wiley & Sons, Inc. 2013, pp. 203-244.
- [338] Special Programme for Research and Training in Tropical Diseases, <http://www.who.int/tdr/tropics>, 2004.
- [339] J.H. McKerrow, C. Caffrey, B. Kelly, P. Loke, M. Sajid, Proteases in parasitic diseases, *Annu Rev Pathol*, 1 (2006) 497-536.
- [340] H. Li, M.A. Child, M. Bogoy, Proteases as regulators of pathogenesis: examples from the Apicomplexa, *Biochim Biophys Acta*, 1824 (2012) 177-185.

- [341] G. Bart, M.J. Frame, R. Carter, G.H. Coombs, J.C. Mottram, Cathepsin B-like cysteine proteinase-deficient mutants of *Leishmania mexicana*, *Mol Biochem Parasitol*, 88 (1997) 53-61.
- [342] P.B. Joshi, B.L. Kelly, S. Kamhawi, D.L. Sacks, W.R. McMaster, Targeted gene deletion in *Leishmania major* identifies leishmanolysin (GP63) as a virulence factor, *Mol Biochem Parasitol*, 120 (2002) 33-40.
- [343] S.P. Montgomery, M.C. Starr, P.T. Cantey, M.S. Edwards, S.K. Meymandi, Neglected parasitic infections in the United States: Chagas disease, *Am J Trop Med Hyg*, 90 (2014) 814-818.
- [344] P.J. Hotez, *Forgotten People, Forgotten Diseases: The Neglected Tropical Diseases and Their Impact on Global Health and Development*, 1 ed., American Society of Microbiology 2008.
- [345] J.C. Dias, J.R. Coura, Emmanuel Dias and *Trypanosoma cruzi* discovery: two centenaries to celebrate--editorial, *Mem Inst Oswaldo Cruz*, 103 (2008) 415-416.
- [346] J.C. Dias, A. Prata, D. Correia, Problems and perspectives for Chagas disease control: in search of a realistic analysis, *Rev Soc Bras Med Trop*, 41 (2008) 193-196.
- [347] F.R. Martins-Melo, A.N. Ramos, Jr., C.H. Alencar, J. Heukelbach, Prevalence of Chagas disease in Brazil: a systematic review and meta-analysis, *Acta Trop*, 130 (2014) 167-174.
- [348] P.T. Cantey, S.L. Stramer, R.L. Townsend, H. Kamel, K. Ofafa, C.W. Todd, M. Currier, S. Hand, W. Varnado, E. Dotson, C. Hall, P.L. Jett, S.P. Montgomery, The United States *Trypanosoma cruzi* Infection Study: evidence for vector-borne transmission of the parasite that causes Chagas disease among United States blood donors, *Transfusion*, 52 (2012) 1922-1930.
- [349] M.C. Nunes, W. Dones, C.A. Morillo, J.J. Encina, A.L. Ribeiro, C. Council on Chagas Disease of the Interamerican Society of, Chagas disease: an overview of clinical and epidemiological aspects, *J Am Coll Cardiol*, 62 (2013) 767-776.
- [350] A. Rassi, Jr., A. Rassi, J.A. Marin-Neto, Chagas disease, *Lancet*, 375 (2010) 1388-1402.
- [351] A.R. Teixeira, N. Nitz, M.C. Guimaro, C. Gomes, C.A. Santos-Buch, Chagas disease, *Postgrad Med J*, 82 (2006) 788-798.
- [352] J.A. Rozendaal, *Vector Control: Methods for Use by Individuals and Communities*, World Health Organization, Switzerland, 1997.
- [353] C.A. Buscaglia, J.M. Di Noia, *Trypanosoma cruzi* clonal diversity and the epidemiology of Chagas' disease, *Microbes Infect*, 5 (2003) 419-427.

- [354] G.d.A. Pereira, F. Louzada-Neto, V.d.F. Barbosa, M.M. Ferreira-Silva, H. de Moraes-Souza, Performance of six diagnostic tests to screen for Chagas disease in blood banks and prevalence of *Trypanosoma cruzi* infection among donors with inconclusive serologyscreening based on the analysis of epidemiological variables, *Revista Brasileira de Hematologia e Hemoterapia*, 34 (2012) 292-297.
- [355] P.E.A.A. Brasil, L. De Castro, A.M. Hasslocher-Moreno, L.H.C. Sangenis, J.U. Braga, ELISA versus PCR for diagnosis of chronic Chagas disease: systematic review and meta-analysis, *BMC Infectious Diseases*, 10 (2010) 337-337.
- [356] O. Genovese, C. Ballario, R. Storino, E. Segura, R.E. Sica, Clinical manifestations of peripheral nervous system involvement in human chronic Chagas disease, *Arq Neuropsiquiatr*, 54 (1996) 190-196.
- [357] M. Barrett, Research priorities for Chagas disease, human African trypanosomiasis and leishmaniasis, World Health Organization technical report series, (2012) v-xii, 1-100.
- [358] R.J.A. Marin-Neto J.A. , Maciel B.C., Simões M.V., Schmidt A., Chagas Heart Disease, in: C.J.A. Yusuf S. , Camm A.J., Fallen E.L., Gersh B.J. (Ed.) *Evidence Based Cardiology*, BMJ Books, London, 2010, pp. 823-841.
- [359] A. Rassi, Jr., A. Rassi, W.C. Little, Chagas' heart disease, *Clin Cardiol*, 23 (2000) 883-889.
- [360] A. Rassi, Jr., S.G. Rassi, A. Rassi, Sudden death in Chagas' disease, *Arq Bras Cardiol*, 76 (2001) 75-96.
- [361] K.M. Bonney, D.M. Engman, Chagas heart disease pathogenesis: one mechanism or many?, *Curr Mol Med*, 8 (2008) 510-518.
- [362] M.S. Braga, L. Lauria-Pires, E.R. Arganaraz, R.J. Nascimento, A.R. Teixeira, Persistent infections in chronic Chagas' disease patients treated with anti-*Trypanosoma cruzi* nitroderivatives, *Rev Inst Med Trop Sao Paulo*, 42 (2000) 157-161.
- [363] D.A. Campbell, S.J. Westenberger, N.R. Sturm, The determinants of Chagas disease: connecting parasite and host genetics, *Curr Mol Med*, 4 (2004) 549-562.
- [364] M.A. Henry, M.M. Lerco, W.K. Oliveira, [Esophageal cancer in patient with chagasic megaesophagus], *Arquivos de gastroenterologia*, 44 (2007) 151-155.
- [365] M.O. Py, Neurologic manifestations of Chagas disease, *Current neurology and neuroscience reports*, 11 (2011) 536-542.
- [366] E. Cordova, E. Maiolo, M. Corti, T. Orduna, Neurological manifestations of Chagas' disease, *Neurological research*, 32 (2010) 238-244.

- [367] A. Rassi, Jr., A. Rassi, C. Franco-Paredes, A Latin American man with palpitations, dizziness, episodes of nonsustained ventricular tachycardia, and an apical aneurysm, *PLoS neglected tropical diseases*, 5 (2011) e852.
- [368] J.A. Perez-Molina, A.M. Perez, F.F. Norman, B. Monge-Maillo, R. Lopez-Velez, Old and new challenges in Chagas disease, *Lancet Infect Dis*, 15 (2015) 1347-1356.
- [369] A.K. Malan, E. Avelar, S.E. Litwin, H.R. Hill, C.M. Litwin, Serological diagnosis of *Trypanosoma cruzi*: evaluation of three enzyme immunoassays and an indirect immunofluorescent assay, *J Med Microbiol*, 55 (2006) 171-178.
- [370] P. Wincker, M.F. Bosseno, C. Britto, N. Yaksic, M.A. Cardoso, C.M. Morel, S.F. Breniere, High correlation between Chagas' disease serology and PCR-based detection of *Trypanosoma cruzi* kinetoplast DNA in Bolivian children living in an endemic area, *FEMS Microbiol Lett*, 124 (1994) 419-423.
- [371] K.M. Tyler, D.M. Engman, The life cycle of *Trypanosoma cruzi* revisited, *Int J Parasitol*, 31 (2001) 472-481.
- [372] J.R. Stevens, H.A. Noyes, G.A. Dover, W.C. Gibson, The ancient and divergent origins of the human pathogenic trypanosomes, *Trypanosoma brucei* and *T. cruzi*, *Parasitology*, 118 (Pt 1) (1999) 107-116.
- [373] CDC, American Trypanosomiasis
<http://www.cdc.gov/dpdx/trypanosomiasisAmerican/gallery.html>.
- [374] A.M. Macedo, R.P. Oliveira, S.D. Pena, Chagas disease: role of parasite genetic variation in pathogenesis, *Expert Rev Mol Med*, 4 (2002) 1-16.
- [375] J. Clayton, Chagas disease 101, *Nature*, 465 (2010) S4-5.
- [376] Y. Jackson, L. Getaz, H. Wolff, M. Holst, A. Mauris, A. Tardin, J. Sztajzel, V. Besse, L. Loutan, J.M. Gaspoz, J. Jannin, P. Albajar Vinas, A. Luquetti, F. Chappuis, Prevalence, clinical staging and risk for blood-borne transmission of Chagas disease among Latin American migrants in Geneva, Switzerland, *PLoS neglected tropical diseases*, 4 (2010) e592.
- [377] M.J. Alves, W. Colli, *Trypanosoma cruzi*: adhesion to the host cell and intracellular survival, *IUBMB Life*, 59 (2007) 274-279.
- [378] W. de Souza, T.M.U. de Carvalho, E.S. Barrias, Review on *Trypanosoma cruzi*: Host Cell Interaction, *International Journal of Cell Biology*, 2010 (2010).
- [379] P. Berasain, C. Carmona, B. Frangione, J.J. Cazzulo, F. Goni, Specific cleavage sites on human IgG subclasses by cruzipain, the major cysteine proteinase from *Trypanosoma cruzi*, *Mol Biochem Parasitol*, 130 (2003) 23-29.

- [380] B.F. Hall, Trypanosoma cruzi: mechanisms for entry into host cells, Semin Cell Biol, 4 (1993) 323-333.
- [381] C.L. Epting, B.M. Coates, D.M. Engman, Molecular mechanisms of host cell invasion by Trypanosoma cruzi, Exp Parasitol, 126 (2010) 283-291.
- [382] B.S. Hall, S.R. Wilkinson, Activation of benznidazole by trypanosomal type I nitroreductases results in glyoxal formation, Antimicrob Agents Chemother, 56 (2012) 115-123.
- [383] J.A. Castro, M.M. de Mecca, L.C. Bartel, Toxic side effects of drugs used to treat Chagas' disease (American trypanosomiasis), Hum Exp Toxicol, 25 (2006) 471-479.
- [384] N.M. El-Sayed, P.J. Myler, D.C. Bartholomeu, D. Nilsson, G. Aggarwal, A.N. Tran, E. Ghedin, E.A. Worthey, A.L. Delcher, G. Blandin, S.J. Westenberger, E. Caler, G.C. Cerqueira, C. Branche, B. Haas, A. Anupama, E. Arner, L. Aslund, P. Attipoe, E. Bontempi, F. Bringaud, P. Burton, E. Cadag, D.A. Campbell, M. Carrington, J. Crabtree, H. Darban, J.F. da Silveira, P. de Jong, K. Edwards, P.T. Englund, G. Fazelina, T. Feldblyum, M. Ferella, A.C. Frasch, K. Gull, D. Horn, L. Hou, Y. Huang, E. Kindlund, M. Klingbeil, S. Kluge, H. Koo, D. Lacerda, M.J. Levin, H. Lorenzi, T. Louie, C.R. Machado, R. McCulloch, A. McKenna, Y. Mizuno, J.C. Mottram, S. Nelson, S. Ochaya, K. Osoegawa, G. Pai, M. Parsons, M. Pentony, U. Pettersson, M. Pop, J.L. Ramirez, J. Rinta, L. Robertson, S.L. Salzberg, D.O. Sanchez, A. Seyler, R. Sharma, J. Shetty, A.J. Simpson, E. Sisk, M.T. Tammi, R. Tarleton, S. Teixeira, S. Van Aken, C. Vogt, P.N. Ward, B. Wickstead, J. Wortman, O. White, C.M. Fraser, K.D. Stuart, B. Andersson, The genome sequence of Trypanosoma cruzi, etiologic agent of Chagas disease, Science, 309 (2005) 409-415.
- [385] J.A. Urbina, R. Docampo, Specific chemotherapy of Chagas disease: controversies and advances, Trends Parasitol, 19 (2003) 495-501.
- [386] M. Paulino, F. Iribarne, M. Dubin, S. Aguilera-Morales, O. Tapia, A.O. Stoppani, The chemotherapy of chagas' disease: an overview, Mini Rev Med Chem, 5 (2005) 499-519.
- [387] I.H. Gilbert, Inhibitors of dihydrofolate reductase in Leishmania and trypanosomes, Biochim Biophys Acta, 1587 (2002) 249-257.
- [388] F. Zuccotto, R. Brun, D. Gonzalez Pacanowska, L.M. Ruiz Perez, I.H. Gilbert, The structure-based design and synthesis of selective inhibitors of Trypanosoma cruzi dihydrofolate reductase, Bioorganic & medicinal chemistry letters, 9 (1999) 1463-1468.

- [389] N. Schormann, S.E. Velu, S. Murugesan, O. Senkovich, K. Walker, B.C. Chenna, B. Shinkre, A. Desai, D. Chattopadhyay, Synthesis and characterization of potent inhibitors of *Trypanosoma cruzi* dihydrofolate reductase, *Bioorganic & Medicinal Chemistry*, 18 (2010) 4056-4066.
- [390] F. Zuccotto, M. Zvelebil, R. Brun, S.F. Chowdhury, R. Di Lucrezia, I. Leal, L. Maes, L.M. Ruiz-Perez, D. Gonzalez Pacanowska, I.H. Gilbert, Novel inhibitors of *Trypanosoma cruzi* dihydrofolate reductase, *European journal of medicinal chemistry*, 36 (2001) 395-405.
- [391] J.A. Urbina, J.L. Concepcion, A. Caldera, G. Payares, C. Sanoja, T. Otomo, H. Hiyoshi, In vitro and in vivo activities of E5700 and ER-119884, two novel orally active squalene synthase inhibitors, against *Trypanosoma cruzi*, *Antimicrob Agents Chemother*, 48 (2004) 2379-2387.
- [392] T. Ishihara, H. Kakuta, H. Moritani, T. Ugawa, I. Yanagisawa, Synthesis and biological evaluation of novel propylamine derivatives as orally active squalene synthase inhibitors, *Bioorg Med Chem*, 12 (2004) 5899-5908.
- [393] J.L. Goldstein, M.S. Brown, Molecular medicine. The cholesterol quartet, *Science*, 292 (2001) 1310-1312.
- [394] S. Orenes Lorente, R. Gomez, C. Jimenez, S. Cammerer, V. Yardley, K. de Luca-Fradley, S.L. Croft, L.M. Ruiz Perez, J. Urbina, D. Gonzalez Pacanowska, I.H. Gilbert, Biphenylquinuclidines as inhibitors of squalene synthase and growth of parasitic protozoa, *Bioorg Med Chem*, 13 (2005) 3519-3529.
- [395] G. Benaim, J.M. Sanders, Y. Garcia-Marchan, C. Colina, R. Lira, A.R. Caldera, G. Payares, C. Sanoja, J.M. Burgos, A. Leon-Rossell, J.L. Concepcion, A.G. Schijman, M. Levin, E. Oldfield, J.A. Urbina, Amiodarone has intrinsic anti-*Trypanosoma cruzi* activity and acts synergistically with posaconazole, *J Med Chem*, 49 (2006) 892-899.
- [396] J.A. Urbina, Chemotherapy of Chagas disease, *Curr Pharm Des*, 8 (2002) 287-295.
- [397] D.T. Silva, S.L.d.M.M. de Nazareth, D. Almeida, J.A. Urbina, M.C. Pereira, Cytoskeleton reassembly in cardiomyocytes infected by *Trypanosoma cruzi* is triggered by treatment with ergosterol biosynthesis inhibitors, *Int J Antimicrob Agents*, 27 (2006) 530-537.
- [398] M. Corrales, R. Cardozo, M.A. Segura, J.A. Urbina, M.A. Basombrio, Comparative efficacies of TAK-187, a long-lasting ergosterol biosynthesis inhibitor, and benznidazole in preventing cardiac damage in a murine model of Chagas' disease, *Antimicrob Agents Chemother*, 49 (2005) 1556-1560.
- [399] P.M.M. Guedes, J.L.R. Fietto, M. Lana, M.T. Bahia, Advances in Chagas Disease Chemotherapy, *Anti-Infective Agents in Medicinal Chemistry*, 5 (2006) 175-186.

- [400] P.M. Guedes, J.A. Urbina, M. de Lana, L.C. Afonso, V.M. Veloso, W.L. Tafuri, G.L. Machado-Coelho, E. Chiari, M.T. Bahia, Activity of the new triazole derivative albaconazole against *Trypanosoma* (*Schizotrypanum*) *cruzi* in dog hosts, *Antimicrob Agents Chemother*, 48 (2004) 4286-4292.
- [401] J.A. Urbina, G. Payares, C. Sanoja, R. Lira, A.J. Romanha, In vitro and in vivo activities of ravuconazole on *Trypanosoma cruzi*, the causative agent of Chagas disease, *Int J Antimicrob Agents*, 21 (2003) 27-38.
- [402] P.K. Suryadevara, S. Olepu, J.W. Lockman, J. Ohkanda, M. Karimi, C.L. Verlinde, J.M. Kraus, J. Schoepe, W.C. Van Voorhis, A.D. Hamilton, F.S. Buckner, M.H. Gelb, Structurally simple inhibitors of lanosterol 14 α -demethylase are efficacious in a rodent model of acute Chagas disease, *J Med Chem*, 52 (2009) 3703-3715.
- [403] F. Buckner, K. Yokoyama, J. Lockman, K. Aikenhead, J. Ohkanda, M. Sadilek, S. Sebti, W. Van Voorhis, A. Hamilton, M.H. Gelb, A class of sterol 14-demethylase inhibitors as anti-*Trypanosoma cruzi* agents, *Proc Natl Acad Sci U S A*, 100 (2003) 15149-15153.
- [404] S.H. Szajnman, G.E. Garcia Linares, Z.H. Li, C. Jiang, M. Galizzi, E.J. Bontempi, M. Ferella, S.N. Moreno, R. Docampo, J.B. Rodriguez, Synthesis and biological evaluation of 2-alkylaminoethyl-1,1-bisphosphonic acids against *Trypanosoma cruzi* and *Toxoplasma gondii* targeting farnesyl diphosphate synthase, *Bioorg Med Chem*, 16 (2008) 3283-3290.
- [405] R. Docampo, S.N. Moreno, The acidocalcisome, *Mol Biochem Parasitol*, 114 (2001) 151-159.
- [406] R. Docampo, S.N. Moreno, Bisphosphonates as chemotherapeutic agents against trypanosomatid and apicomplexan parasites, *Curr Drug Targets Infect Disord*, 1 (2001) 51-61.
- [407] A. Schmidt, R.L. Krauth-Siegel, Enzymes of the trypanothione metabolism as targets for antitrypanosomal drug development, *Curr Top Med Chem*, 2 (2002) 1239-1259.
- [408] H.W. Rivarola, J.M. Bustamante, S. Lo Presti, A.R. Fernandez, J.E. Enders, S. Gea, R. Fretes, P. Paglini-Oliva, *Trypanosoma cruzi*: chemotherapeutic effects of clomipramine in mice infected with an isolate obtained from an endemic area, *Exp Parasitol*, 111 (2005) 80-86.
- [409] H.W. Rivarola, A.R. Fernandez, J.E. Enders, R. Fretes, S. Gea, M. Suligoy, J.A. Palma, P. Paglini-Oliva, Thioridazine treatment modifies the evolution of *Trypanosoma cruzi* infection in mice, *Ann Trop Med Parasitol*, 93 (1999) 695-702.

- [410] Enzyme Database, http://www.brenda-enzymes.info/php/result_flat.php4?ecno=3.4.22.51.
- [411] J.J. Cazzulo, Intermediate metabolism in *Trypanosoma cruzi*, *J Bioenerg Biomembr*, 26 (1994) 157-165.
- [412] M. Sajid, S.A. Robertson, L.S. Brinen, J.H. McKerrow, Cruzain : the path from target validation to the clinic, *Adv Exp Med Biol*, 712 (2011) 100-115.
- [413] J.C. Engel, P.S. Doyle, J. Palmer, I. Hsieh, D.F. Bainton, J.H. McKerrow, Cysteine protease inhibitors alter Golgi complex ultrastructure and function in *Trypanosoma cruzi*, *J Cell Sci*, 111 (Pt 5) (1998) 597-606.
- [414] J.C. Engel, C. Torres, I. Hsieh, P.S. Doyle, J.H. McKerrow, Upregulation of the secretory pathway in cysteine protease inhibitor-resistant *Trypanosoma cruzi*, *J Cell Sci*, 113 (Pt 8) (2000) 1345-1354.
- [415] A. Teixeira, M. Vinaud, A.M. Castro, *Emerging Chagas Disease*, Bentham Books 2011.
- [416] A.E. Nascimento, W. de Souza, High resolution localization of cruzipain and Ssp4 in *Trypanosoma cruzi* by replica staining label fracture, *Biol Cell*, 86 (1996) 53-58.
- [417] C.M. Batista, R.L. Kessler, I. Eger, M.J. Soares, *Trypanosoma cruzi* Intracellular Amastigotes Isolated by Nitrogen Decompression Are Capable of Endocytosis and Cargo Storage in Reserosomes, *PLoS ONE*, 10 (2015) e0130165.
- [418] I.M. Aparicio, J. Scharfstein, A.P. Lima, A new cruzipain-mediated pathway of human cell invasion by *Trypanosoma cruzi* requires trypomastigote membranes, *Infect Immun*, 72 (2004) 5892-5902.
- [419] E. Del Nery, M.A. Juliano, A.P.C.A. Lima, J. Scharfstein, L. Juliano, Kininogenase Activity by the Major Cysteiny Proteinase (Cruzipain) from *Trypanosoma cruzi*, *Journal of Biological Chemistry*, 272 (1997) 25713-25718.
- [420] G. Bras, O. Bochenska, M. Rapala-Kozik, I. Guevara-Lora, A. Faussner, W. Kamysz, A. Kozik, Release of biologically active kinin peptides, Met-Lys-bradykinin and Leu-Met-Lys-bradykinin from human kininogens by two major secreted aspartic proteases of *Candida parapsilosis*, *Peptides*, 48 (2013) 114-123.
- [421] P.S. Doyle, Y.M. Zhou, I. Hsieh, D.C. Greenbaum, J.H. McKerrow, J.C. Engel, The *Trypanosoma cruzi* Protease Cruzain Mediates Immune Evasion, *PLoS Pathogens*, 7 (2011) e1002139.

- [422] P. Aoki Mdel, R.C. Cano, A.V. Pellegrini, T. Tanos, N.L. Guinazu, O.A. Coso, S. Gea, Different signaling pathways are involved in cardiomyocyte survival induced by a *Trypanosoma cruzi* glycoprotein, *Microbes Infect*, 8 (2006) 1723-1731.
- [423] A.E. Eakin, A.A. Mills, G. Harth, J.H. McKerrow, C.S. Craik, The sequence, organization, and expression of the major cysteine protease (cruzain) from *Trypanosoma cruzi*, *J Biol Chem*, 267 (1992) 7411-7420.
- [424] J.J. Cazzulo, J. Martínez, A.J.A. Parodi, C. Wernstedt, U. Hellman, On the post-translational modification at the C-terminal domain of the major cysteine proteinase (cruzipain) from *Trypanosoma cruzi*, *FEMS Microbiology Letters*, 100 (1992) 411-416.
- [425] L. Huang, L.S. Brinen, J.A. Ellman, Crystal structures of reversible ketone-Based inhibitors of the cysteine protease cruzain, *Bioorganic & Medicinal Chemistry*, 11 (2003) 21-29.
- [426] M.E. McGrath, A.E. Eakin, J.C. Engel, J.H. McKerrow, C.S. Craik, R.J. Fletterick, The crystal structure of cruzain: a therapeutic target for Chagas' disease, *J Mol Biol*, 247 (1995) 251-259.
- [427] S.A. Gillmor, C.S. Craik, R.J. Fletterick, Structural determinants of specificity in the cysteine protease cruzain, *Protein Science : A Publication of the Protein Society*, 6 (1997) 1603-1611.
- [428] J.A. Huete-Perez, J.C. Engel, L.S. Brinen, J.C. Mottram, J.H. McKerrow, Protease trafficking in two primitive eukaryotes is mediated by a prodomain protein motif, *J Biol Chem*, 274 (1999) 16249-16256.
- [429] C. Pina-Vazquez, M. Reyes-Lopez, G. Ortiz-Estrada, M. de la Garza, J. Serrano-Luna, Host-parasite interaction: parasite-derived and -induced proteases that degrade human extracellular matrix, *J Parasitol Res*, 2012 (2012) 748206.
- [430] J. Duaso, E. Yanez, C. Castillo, N. Galanti, G. Cabrera, G. Corral, J.D. Maya, I. Zulantay, W. Apt, U. Kemmerling, Reorganization of extracellular matrix in placentas from women with asymptomatic chagas disease: mechanism of parasite invasion or local placental defense?, *J Trop Med*, 2012 (2012) 758357.
- [431] V.G. Duschak, A.S. Couto, Cruzipain, the major cysteine protease of *Trypanosoma cruzi*: a sulfated glycoprotein antigen as relevant candidate for vaccine development and drug target. A review, *Curr Med Chem*, 16 (2009) 3174-3202.
- [432] S.A. Robertson, A.R. Renslo, Drug discovery for neglected tropical diseases at the Sandler Center, *Future medicinal chemistry*, 3 (2011) 1279-1288.

- [433] F.C. Reis, T.F. Costa, T. Sulea, A. Mezzetti, J. Scharfstein, D. Bromme, R. Menard, A.P. Lima, The propeptide of cruzipain--a potent selective inhibitor of the trypanosomal enzymes cruzipain and brucipain, and of the human enzyme cathepsin F, *FEBS J*, 274 (2007) 1224-1234.
- [434] D.S. Buarque, L.M. Spindola, R.M. Martins, G.R. Braz, A.S. Tanaka, Tigutcystatin, a cysteine protease inhibitor from *Triatoma infestans* midgut expressed in response to *Trypanosoma cruzi*, *Biochem Biophys Res Commun*, 413 (2011) 241-247.
- [435] C.C. Santos, C. Sant'Anna, A. Terres, N.L. Cunha-e-Silva, J. Scharfstein, A.P.C. de A. Lima, Chagasin, the endogenous cysteine-protease inhibitor of *Trypanosoma cruzi*, modulates parasite differentiation and invasion of mammalian cells, *Journal of Cell Science*, 118 (2005) 901-915.
- [436] J.C. Engel, P.S. Doyle, I. Hsieh, J.H. McKerrow, Cysteine protease inhibitors cure an experimental *Trypanosoma cruzi* infection, *J Exp Med*, 188 (1998) 725-734.
- [437] S.C. Barr, K.L. Warner, B.G. Kornreic, J. Piscitelli, A. Wolfe, L. Benet, J.H. McKerrow, A cysteine protease inhibitor protects dogs from cardiac damage during infection by *Trypanosoma cruzi*, *Antimicrob Agents Chemother*, 49 (2005) 5160-5161.
- [438] P.S. Doyle, Y.M. Zhou, J.C. Engel, J.H. McKerrow, A cysteine protease inhibitor cures Chagas' disease in an immunodeficient-mouse model of infection, *Antimicrob Agents Chemother*, 51 (2007) 3932-3939.
- [439] J.H. McKerrow, P.S. Doyle, J.C. Engel, L.M. Podust, S.A. Robertson, R. Ferreira, T. Saxton, M. Arkin, I.D. Kerr, L.S. Brinen, C.S. Craik, Two approaches to discovering and developing new drugs for Chagas disease, *Memorias do Instituto Oswaldo Cruz*, 104 (2009) 263-269.
- [440] P. Jaishankar, E. Hansell, D.-M. Zhao, P.S. Doyle, J.H. McKerrow, A.R. Renslo, Potency and selectivity of P2/P3-modified inhibitors of cysteine proteases from trypanosomes, *Bioorganic & medicinal chemistry letters*, 18 (2008) 624-628.
- [441] H. Cerecetto, M. González, Chemotherapy of Chagas' disease: status and new developments, *Current topics in medicinal chemistry*, 2 (2002) 1187-1213.
- [442] C. Beaulieu, E. Isabel, A. Fortier, F. Masse, C. Mellon, N. Methot, M. Ndao, D. Nicoll-Griffith, D. Lee, H. Park, W.C. Black, Identification of potent and reversible cruzipain inhibitors for the treatment of Chagas disease, *Bioorganic & medicinal chemistry letters*, 20 (2010) 7444-7449.

- [443] D.M. Borchhardt, A. Mascarello, L.D. Chiaradia, R.J. Nunes, G. Oliva, R.A. Yunes, A.D. Andricopulo, Biochemical evaluation of a series of synthetic chalcone and hydrazide derivatives as novel inhibitors of cruzain from *Trypanosoma cruzi*, *Journal of the Brazilian Chemical Society*, 21 (2010) 142-150.
- [444] S.A. Carvalho, L.O. Feitosa, M. Soares, T.E. Costa, M.G. Henriques, K. Salomao, S.L. de Castro, M. Kaiser, R. Brun, J.L. Wardell, S.M. Wardell, G.H. Trossini, A.D. Andricopulo, E.F. da Silva, C.A. Fraga, Design and synthesis of new (E)-cinnamic N-acylhydrazones as potent antitrypanosomal agents, *European journal of medicinal chemistry*, 54 (2012) 512-521.
- [445] X. Du, C. Guo, E. Hansell, P.S. Doyle, C.R. Caffrey, T.P. Holler, J.H. McKerrow, F.E. Cohen, Synthesis and structure-activity relationship study of potent trypanocidal thio semicarbazone inhibitors of the trypanosomal cysteine protease cruzain, *J Med Chem*, 45 (2002) 2695-2707.
- [446] R.V. Guido, G.H. Trossini, M.S. Castilho, G. Oliva, E.I. Ferreira, A.D. Andricopulo, Structure-activity relationships for a class of selective inhibitors of the major cysteine protease from *Trypanosoma cruzi*, *J Enzyme Inhib Med Chem*, 23 (2008) 964-973.
- [447] R. Siles, S.E. Chen, M. Zhou, K.G. Pinney, M.L. Trawick, Design, synthesis, and biochemical evaluation of novel cruzain inhibitors with potential application in the treatment of Chagas' disease, *Bioorganic & medicinal chemistry letters*, 16 (2006) 4405-4409.
- [448] I. Chiyanzu, E. Hansell, J. Gut, P.J. Rosenthal, J.H. McKerrow, K. Chibale, Synthesis and evaluation of isatins and thiosemicarbazone derivatives against cruzain, falcipain-2 and rhodesain, *Bioorganic & medicinal chemistry letters*, 13 (2003) 3527-3530.
- [449] D.C. Greenbaum, Z. Mackey, E. Hansell, P. Doyle, J. Gut, C.R. Caffrey, J. Lehrman, P.J. Rosenthal, J.H. McKerrow, K. Chibale, Synthesis and structure-activity relationships of parasitocidal thiosemicarbazone cysteine protease inhibitors against *Plasmodium falciparum*, *Trypanosoma brucei*, and *Trypanosoma cruzi*, *J Med Chem*, 47 (2004) 3212-3219.
- [450] A.C.L. Leite, R.S. de Lima, D.R.d.M. Moreira, M.V.d.O. Cardoso, A.C.G. de Brito, L.M.F. dos Santos, M.Z. Hernandez, A.C. Kiperstok, R.S. de Lima, M.B. Soares, Synthesis, docking, and in vitro activity of thiosemicarbazones, aminoacyl-thiosemicarbazides and acyl-thiazolidones against *Trypanosoma cruzi*, *Bioorganic & medicinal chemistry*, 14 (2006) 3749-3757.

- [451] A. Pérez-Rebolledo, L.R. Teixeira, A.A. Batista, A.S. Mangrich, G. Aguirre, H. Cerecetto, M. González, P. Hernández, A.M. Ferreira, N.L. Speziali, 4-Nitroacetophenone-derived thiosemicarbazones and their copper (II) complexes with significant in vitro anti-trypanosomal activity, *European journal of medicinal chemistry*, 43 (2008) 939-948.
- [452] G.E. Chavarria, Kinetic characterization of thiosemicarbazones as cysteine protease inhibitors and their potential use as therapeutic agents against metastatic cancer and Chagas' disease., Baylor University, Waco, Texas, 2013.
- [453] R. Siles, Design, synthesis and biological evaluation of new anti-Cancer nitrogen-containing combretastatins and novel cysteine protease inhibitors for the treatment of Chagas., Baylor University, Waco, Texas, 2005.
- [454] A. Angulo, Inhibitors of human cathepsin L and cruzain as therapeutic agents., Baylor University, Waco, Texas., 2008.
- [455] E.N. Parker, J. Song, G.D. Kishore Kumar, S.O. Odutola, G.E. Chavarria, A.K. Charlton-Sevcik, T.E. Strecker, A.L. Barnes, D.R. Sudhan, T.R. Wittenborn, D.W. Siemann, M.R. Horsman, D.J. Chaplin, M.L. Trawick, K.G. Pinney, Synthesis and biochemical evaluation of benzoylbenzophenone thiosemicarbazone analogues as potent and selective inhibitors of cathepsin L, *Bioorg Med Chem*, 23 (2015) 6974-6992.
- [456] J. Song, L.M. Jones, G.D. Kumar, E.S. Conner, L. Bayeh, G.E. Chavarria, A.K. Charlton-Sevcik, S.E. Chen, D.J. Chaplin, M.L. Trawick, K.G. Pinney, Synthesis and biochemical evaluation of thiochromanone thiosemicarbazone analogues as inhibitors of cathepsin L, *ACS Med Chem Lett*, 3 (2012) 450-453.
- [457] A.E. Eakin, M.E. McGrath, J.H. McKerrow, R.J. Fletterick, C.S. Craik, Production of crystallizable cruzain, the major cysteine protease from *Trypanosoma cruzi*, *J Biol Chem*, 268 (1993) 6115-6118.
- [458] R.A. Copeland, J. Retey, *Enzymes: a practical introduction to structure, mechanism, and data analysis*, VCH Publishers New York:1996.
- [459] W.X. Tian, C.L. Tsou, Determination of the rate constant of enzyme modification by measuring the substrate reaction in the presence of the modifier, *Biochemistry*, 21 (1982) 1028-1032.
- [460] N.A. Maiani, D. Roos, T.W. Kuijpers, Bid truncation, bid/bax targeting to the mitochondria, and caspase activation associated with neutrophil apoptosis are inhibited by granulocyte colony-stimulating factor, *J Immunol*, 172 (2004) 7024-7030.

- [461] N. Margolin, S.A. Raybuck, K.P. Wilson, W. Chen, T. Fox, Y. Gu, D.J. Livingston, Substrate and inhibitor specificity of interleukin-1 beta-converting enzyme and related caspases, *J Biol Chem*, 272 (1997) 7223-7228.
- [462] P.P. Shah, M.C. Myers, M.P. Beavers, J.E. Purvis, H. Jing, H.J. Grieser, E.R. Sharlow, A.D. Napper, D.M. Huryn, B.S. Cooperman, A.B. Smith, 3rd, S.L. Diamond, Kinetic characterization and molecular docking of a novel, potent, and selective slow-binding inhibitor of human cathepsin L, *Mol Pharmacol*, 74 (2008) 34-41.
- [463] D. Bromme, K. Okamoto, B.B. Wang, S. Biroc, Human cathepsin O2, a matrix protein-degrading cysteine protease expressed in osteoclasts. Functional expression of human cathepsin O2 in *Spodoptera frugiperda* and characterization of the enzyme, *The Journal of biological chemistry*, 271 (1996) 2126-2132.
- [464] F. Lecaille, E. Weidauer, M.A. Juliano, D. Bromme, G. Lalmanach, Probing cathepsin K activity with a selective substrate spanning its active site, *Biochem J*, 375 (2003) 307-312.
- [465] A.K. Charlton-Sevcik, Targeting Cancer through Inhibition of Cathepsin B by Non-peptidic Small Molecule Thiosemicarbazones and Disruption of Pre-existing Vasculature by Colchicine-like Benzosuberene Analogues, *Chemistry and Biochemistry*, Baylor University, Waco, 2014.
- [466] G.E. Chavarria, M.R. Horsman, W.M. Arispe, G.D. Kumar, S.E. Chen, T.E. Strecker, E.N. Parker, D.J. Chaplin, K.G. Pinney, M.L. Trawick, Initial evaluation of the antitumour activity of KGP94, a functionalized benzophenone thiosemicarbazone inhibitor of cathepsin L, *European journal of medicinal chemistry*, 58 (2012) 568-572.
- [467] B. Fang, G. Fu, J. Agniswamy, R.W. Harrison, I.T. Weber, Caspase-3 binds diverse P4 residues in peptides as revealed by crystallography and structural modeling, *Apoptosis*, 14 (2009) 741-752.
- [468] G.-J. Tan, Z.-K. Peng, J.-P. Lu, F.-Q. Tang, Cathepsins mediate tumor metastasis, *World Journal of Biological Chemistry*, 4 (2013) 91-101.
- [469] Y. Shoji-Kasai, M. Senshu, S. Iwashita, K. Imahori, Thiol protease-specific inhibitor E-64 arrests human epidermoid carcinoma A431 cells at mitotic metaphase, *Proc Natl Acad Sci U S A*, 85 (1988) 146-150.
- [470] R. Navab, J.S. Mort, P. Brodt, Inhibition of carcinoma cell invasion and liver metastases formation by the cysteine proteinase inhibitor E-64, *Clin Exp Metastasis*, 15 (1997) 121-129.

- [471] M. Sriram, J.J. Hall, N.C. Grohmann, T.E. Strecker, T. Wootton, A. Franken, M.L. Trawick, K.G. Pinney, Design, synthesis and biological evaluation of dihydronaphthalene and benzosuberene analogs of the combretastatins as inhibitors of tubulin polymerization in cancer chemotherapy, *Bioorg Med Chem*, 16 (2008) 8161-8171.